Olena Fesenko
Leonid Yatsenko   *Editors*

Nanooptics and Photonics, Nanochemistry and Nanobiotechnology, and Their Applications

Selected Proceedings of the IX International Conference Nanotechnology and Nanomaterials (NANO2021), 25–28 August 2021, Lviv, Ukraine

Springer

Springer Proceedings in Physics

Volume 280

Indexed by Scopus

The series Springer Proceedings in Physics, founded in 1984, is devoted to timely reports of state-of-the-art developments in physics and related sciences. Typically based on material presented at conferences, workshops and similar scientific meetings, volumes published in this series will constitute a comprehensive up-to-date source of reference on a field or subfield of relevance in contemporary physics. Proposals must include the following:

– Name, place and date of the scientific meeting
– A link to the committees (local organization, international advisors etc.)
– Scientific description of the meeting
– List of invited/plenary speakers
– An estimate of the planned proceedings book parameters (number of pages/ articles, requested number of bulk copies, submission deadline).

Please contact:

For Americas and Europe: Dr. Zachary Evenson; zachary.evenson@springer.com
For Asia, Australia and New Zealand: Dr. Loyola DSilva; loyola.dsilva@springer. com

Olena Fesenko · Leonid Yatsenko

Editors

Nanooptics and Photonics, Nanochemistry and Nanobiotechnology, and Their Applications

Selected Proceedings of the IX International Conference Nanotechnology and Nanomaterials (NANO2021), 25–28 August 2021, Lviv, Ukraine

Springer

Editors
Olena Fesenko
Institute of Physics
National Academy of Sciences of Ukraine
Kyiv, Ukraine

Leonid Yatsenko
Institute of Physics
National Academy of Sciences of Ukraine
Kyiv, Ukraine

Preface

This book highlights the most recent advances in nanoscience from leading researchers in Ukraine, Europe, and beyond. It features contributions from participants of the 10th International Research and Practice Conference "Nanotechnology and Nanomaterials" (NANO-2021), held in Lviv, Ukraine, on August 25–27, 2021. This event was organized jointly by the Institute of Physics of the National Academy of Sciences of Ukraine, Taras Shevchenko National University of Kyiv (Ukraine), University of Tartu (Estonia), University of Turin (Italy), and Pierre and Marie Curie University (France). Internationally recognized experts from a wide range of universities and research institutes shared their knowledge and key results in the areas of nanocomposites and nanomaterials, nanostructured surfaces, microscopy of nanoobjects, nano-optics and nanophotonics, nanoplasmonics, nanochemistry, nanobiotechnology, and surface-enhanced spectroscopy.

Today, nanotechnology is becoming one of the most actively developing and promising fields of science. Numerous nanotechnology investigations are already producing practical results that can be applied in various areas of human life from science and technology to medicine and pharmacology. The aim of these books is to highlight the latest investigations from different areas of nanoscience and to stimulate new interest in this field. Volume I of this two-volume work covers such important topics as nanoplasmonics, enhanced vibrational spectroscopy, nanochemistry and nanobiotechnology.

This book is divided into two parts: Part I—*Nanochemistry and Biotechnology*, Part II—*Nanooptics and Photonics*. Parts covering nanocomposites and nanostructured surfaces can be found in Volume II: *Nanomaterials and Nanocomposites, Nanostructured Surfaces and Their Applications.*

The papers published in these four parts fall under the broad categories of nanomaterial preparation and characterization, nanobiotechnology, nanodevices and

quantum structures, and spectroscopy and nano-optics. We hope that both volumes will be equally useful and interesting for young scientists or Ph.D. students and mature scientists alike.

Kyiv, Ukraine   Olena Fesenko
                                                                                     Leonid Yatsenko

Contents

Contributors

B. Abu Sal Applied Physics Department Faculty of Science, Tafila Technical University, Tafila, Jordan

O. M. Alekseev Taras Shevchenko National University of Kyiv, Kyiv, Ukraine

M. A. Alieksandrov Taras Shevchenko National University of Kyiv, Kyiv, Ukraine

D. A. Andrusenko Taras Shevchenko National University of Kyiv, Kyiv, Ukraine

L. I. Ardanova Minnesota State University, Mankato, MN, USA

Natalia M. Babenko Department of Cryopathophysiology and Immunology, Institute for Problems of Cryobiology and Cryomedicine of the National Academy of Sciences of Ukraine, Kharkiv, Ukraine

V. A. Barbash National Technical University of Ukraine "Igor Sikorsky Kyiv Polytechnic Institute", Kyiv, Ukraine

Liliya Batyuk Kharkov National Medicine University, Kharkiv, Ukraine

N. I. Berezovska Faculty of Physics, Taras Shevchenko National University of Kyiv, Kyiv, Ukraine

Tetiana Bezugla Taras Shevchenko National University of Kyiv, Kyiv, Ukraine

I. V. Blonskyi Photon Processes Department, Institute of Physics of NAS of Ukraine, Kyiv, Ukraine

M. E. Bondarenko I.N. Frantsevich Institute for Problems of Materials Science of NASU (IPMS), Kyiv, Ukraine

Mykola O. Bondarovych Department of Cryopathophysiology and Immunology, Institute for Problems of Cryobiology and Cryomedicine of the National Academy of Sciences of Ukraine, Kharkiv, Ukraine

T. Bulavinets Department of Photonics, Lviv Polytechnic National University, Lviv, Ukraine

T. O. Busko   Taras Shevchenko National University of Kyiv, Kyiv, Ukraine

Ludmila Chernyshenko   Institute for Problems of Cryobiology and Cryomedicine, National Academy of Sciences of Ukraine, Kharkiv, Ukraine

V. Chumachenko   Taras Shevchenko National University of Kyiv, Kyiv, Ukraine

E. M. Demianenko   Chuiko Institute of Surface Chemistry of National Academy of Sciences of Ukraine, Kyiv, Ukraine

R. V. Dinzhos   V.O. Sukhomlynskyi Mykolaiv National University, Nikolaev, Ukraine;
Institute of Engineering, Thermophysics of NAS of Ukraine, Kyiv, Ukraine

I. M. Dmitruk   Faculty of Physics, Taras Shevchenko National University of Kyiv, Kyiv, Ukraine

O. P. Dmytrenko   Taras Shevchenko National University of Kyiv, Kyiv, Ukraine

A. M. Dmytruk   Photon Processes Department, Institute of Physics of NAS of Ukraine, Kyiv, Ukraine

Roman Dmytryshyn   Faculty of Mathematics and Computer Science, Vasyl Stefanyk Precarpathian National University, Ivano-Frankivsk, Ukraine

Tetiana Dontsova   Kyiv, Ukraine

Volodymyr Doroschuk   Taras Shevchenko National University of Kyiv, Kyiv, Ukraine

Katerina Dorozhko   Kyiv, Ukraine

I. K. Doycho   Odesa I.I. Mechnikov National University, Odesa, Ukraine

Tetiana G. Dubrava   Department of Cryopathophysiology and Immunology, Institute for Problems of Cryobiology and Cryomedicine of the National Academy of Sciences of Ukraine, Kharkiv, Ukraine

Z. A. Duriagina   Department of Materials Science and Engineering, Lviv Polytechnic National University, Lviv, Ukraine;
Department of Materials Engineering, The John Paul II Catholic University of Lublin, Lublin, Poland

N. M. Fialko   Institute of Engineering, Thermophysics of NAS of Ukraine, Kyiv, Ukraine

L. M. Filevska   Odesa I.I. Mechnikov National University, Odesa, Ukraine

O. V. Filonenko   Chuiko Institute of Surface Chemistry of National Academy of Sciences of Ukraine, Kyiv, Ukraine

Yuliia O. Gaevska   Department of Cryopathophysiology and Immunology, Institute for Problems of Cryobiology and Cryomedicine of the National Academy of Sciences of Ukraine, Kharkiv, Ukraine

E. I. Get'man Vasyl' Stus Donetsk National University, Vinnytsia, Ukraine

S. A. Gevelyuk Odesa I.I. Mechnikov National University, Odesa, Ukraine

E. Ya. Glushko Institute of Semiconductor Physics, Kyiv, Ukraine

A. Goltsev Department of Cryopathophysiology and Immunology, Institute for Problems of Cryobiology and Cryomedicine of the National Academy of Sciences of Ukraine, Kharkiv, Ukraine

A. Grebenyuk Chuiko Institute of Surface Chemistry of National Academy of Sciences of Ukraine, Kyiv, Ukraine

V. S. Grinevych Odesa I.I. Mechnikov National University, Odesa, Ukraine

S. V. Gryn Taras Shevchenko National University of Kyiv, Kyiv, Ukraine

Ersin Güler "Faculty of Science, Department of Chemistry", University of Selcuk, Konya, Turkey

D. O. Holochalov Physics, Electronics and Computer Systems Department, Oles Honchar Dnipro National University, Dnipro, Ukraine

L. A. Honcharova Institute of Macromolecular Chemistry of National Academy of Sciences of Ukraine, Kyiv, Ukraine

Ye. S. Hrabovskyi Faculty of Physics, Taras Shevchenko National University of Kyiv, Kyiv, Ukraine

V. V. Hutiv Department of Theoretical Physics and Computer Simulation, Yuriy Fedkovych Chernivtsi National University, Chernivtsi, Ukraine

L. V. Karabanova Institute of Macromolecular Chemistry of National Academy of Sciences of Ukraine, Kyiv, Ukraine

Hanna V. Karakurkchi National Defence University of Ukraine Named After Ivan Cherniakhovskyi, Kyiv, Ukraine

Oksana Kharchenko Kyiv Taras Shevchenko National University, Kyiv, Ukraine

O. Y. Khyzhun I.N. Frantsevich Institute for Problems of Materials Science of NASU (IPMS), Kyiv, Ukraine

Natalya Kizilova Warsaw University of Technology, Warsaw, Poland;
V.N. Karazin Kharkov National University, Kharkov, Ukraine

Vladimir K. Klochkov Nanostructured Materials Department Named By Yu.V. Malyukin, Institute for Scintillation Materials of the National Academy of Sciences of Ukraine, Kharkiv, Ukraine

Ya. Kobzar Institute of Macromolecular Chemistry, National Academy of Sciences of Ukraine, Kyiv, Ukraine

Oleksiy Kolendo Kyiv Taras Shevchenko National University, Kyiv, Ukraine

R. S. Kolodka Faculty of Physics, Taras Shevchenko National University of Kyiv, Kyiv, Ukraine

O. F. Kolomys V.E. Lashkaryov Institute of Semiconductor Physics NAS of Ukraine, Kyiv, Ukraine

Alla N. Korohodska National Technical University «Kharkiv Polytechnic Institute», Kharkiv, Ukraine

A. Kovalchuk Institute of Macromolecular Chemistry, National Academy of Sciences of Ukraine, Kyiv, Ukraine

V. I. Kovalchuk Taras Shevchenko National University of Kyiv, Kyiv, Ukraine

T. M. Kovbasiuk Department of Materials Science and Engineering, Lviv Polytechnic National University, Lviv, Ukraine

S. I. Kovtun Institute of Animals Breeding and Genetics nd.a. M.V. Zubets, National Academy of Agrarian Sciences of Ukraine, Pogrebnjaka Boryspil District, Kyiv Region, Ukraine

I. G. Kovzun F.D. Ovcharenko Institute of Biocolloidal Chemistry of NAS of Ukraine, Kyiv, Ukraine

Oksana Krasuliak Kyiv, Ukraine

R. Kravchuk Institute of Physics, National Academy of Sciences of Ukraine, Kyiv, Ukraine

Grygory Krymets Kyiv, Ukraine

V. Krysa Ivano-Frankivsk National Medical University, Ivano-Frankivsk, Ukraine

M. P. Kulish Taras Shevchenko National University of Kyiv, Kyiv, Ukraine

V. V. Kulyk Department of Materials Science and Engineering, Lviv Polytechnic National University, Lviv, Ukraine

Yu. Kurioz Institute of Physics, National Academy of Sciences of Ukraine, Kyiv, Ukraine

Ahmed Nuri Kursunlu "Faculty of Science, Department of Chemistry", University of Selcuk, Konya, Turkey

N. Kutsevol Taras Shevchenko National University of Kyiv, Kyiv, Ukraine

Svitlana Kyrii Kyiv, Ukraine

Ivanna Lapchuk Department of Chemistry, Vasyl Stefanyk Precarpathian National University, Ivano-Frankivsk, Ukraine

O. M. Lavrynenko I.N. Frantsevich Institute for Problems of Materials Science of NASU (IPMS), Kyiv, Ukraine

M. M. Lazarenko Taras Shevchenko National University of Kyiv, Kyiv, Ukraine

Sergey Lelyushok Taras Shevchenko National University of Kyiv, Kyiv, Ukraine

I. A. Lemishka Department of Materials Science and Engineering, Lviv Polytechnic National University, Lviv, Ukraine

V. V. Lobanov Chuiko Institute of Surface Chemistry of National Academy of Sciences of Ukraine, Kyiv, Ukraine

T. F. Lobunets I.N. Frantsevich Institute for Problems of Materials Science of NASU (IPMS), Kyiv, Ukraine

E. A. Lysenkov Petro Mohyla Black Sea National University, Mykolayiv, Ukraine

O. Yu Lyzogub Institute of Animals Breeding and Genetics nd.a. M.V. Zubets, National Academy of Agrarian Sciences of Ukraine, Pogrebnjaka Boryspil District, Kyiv Region, Ukraine

A. Maizelis National Technical University «Kharkiv Polytechnic Institute», Kharkiv, Ukraine

A. K. Melnyk Institute for Sorption and Problems of Endoecology, Kyiv, Ukraine

A. I. Misiura Taras Shevchenko National University of Kyiv, Kyiv, Ukraine

V. N. Moiseyenko Physics, Electronics and Computer Systems Department, Oles Honchar Dnipro National University, Dnipro, Ukraine

A. I. Momot Taras Shevchenko National University of Kyiv, Kyiv, Ukraine

Iu. Mukha Chuiko Institute of Surface Chemistry, NAS of Ukraine, Kyiv, Ukraine

O. Nadtoka Taras Shevchenko National University of Kyiv, Kyiv, Ukraine

V. Nazarenko Institute of Physics, National Academy of Sciences of Ukraine, Kyiv, Ukraine

S. G. Nedilko Taras Shevchenko National University of Kyiv, Kyiv, Ukraine

O. M. Nikipelova Engineering and Technology Institute "Biotechnika" of NAAS of Ukraine, Odes'ka Oblast, Ukraine;
Odessa State Environmental University, Odessa, Ukraine

O. V. Ohiienko Physics, Electronics and Computer Systems Department, Oles Honchar Dnipro National University, Dnipro, Ukraine

Yu. A. Oleksii Vasyl' Stus Donetsk National University, Vinnytsia, Ukraine

V. O. Oliinyk F.D. Ovcharenko Institute of Biocolloidal Chemistry of NAS of Ukraine, Kyiv, Ukraine

Ostap Olkhovyy Faculty of Pharmacy, Jagiellonian University Medical College, Kraków, Poland

A. P. Onanko Taras Shevchenko National University of Kyiv, Kyiv, Ukraine

Maksym V. Ostankov Department of Cryopathophysiology and Immunology, Institute for Problems of Cryobiology and Cryomedicine of the National Academy of Sciences of Ukraine, Kharkiv, Ukraine

A. V. Panko F.D. Ovcharenko Institute of Biocolloidal Chemistry of NAS of Ukraine, Kyiv, Ukraine

O. Yu. Pavlenko I.N. Frantsevich Institute for Problems of Materials Science of NASU (IPMS), Kyiv, Ukraine

T. M. Pinchuk-Rugal Taras Shevchenko National University of Kyiv, Kyiv, Ukraine

V. M. Popruzhko Taras Shevchenko National University of Kyiv, Kyiv, Ukraine

V. A. Prokopenko F.D. Ovcharenko Institute of Biocolloidal Chemistry of NAS of Ukraine, Kyiv, Ukraine;
National Technical University of Ukraine «KPI», Kyiv, Ukraine

S. V. Radio Vasyl' Stus Donetsk National University, Vinnytsia, Ukraine

R. Sadkovskyi Department of Photonics, Lviv Polytechnic National University, Lviv, Ukraine

Nikolay D. Sakhnenko National Technical University «Kharkiv Polytechnic Institute», Kharkiv, Ukraine

V. P. Scherbatskyi Taras Shevchenko National University of Kyiv, Kyiv, Ukraine

Ju. O. Seti Department of Theoretical Physics and Computer Simulation, Yuriy Fedkovych Chernivtsi National University, Chernivtsi, Ukraine

O. V. Shcherbak Institute of Animals Breeding and Genetics nd.a. M.V. Zubets, National Academy of Agrarian Sciences of Ukraine, Pogrebnjaka Boryspil District, Kyiv Region, Ukraine

O. Shekera Institute of Macromolecular Chemistry, National Academy of Sciences of Ukraine, Kyiv, Ukraine

V. Shevchenko Institute of Macromolecular Chemistry, National Academy of Sciences of Ukraine, Kyiv, Ukraine

D. O. Shevtsov Taras Shevchenko National University of Kyiv, Kyiv, Ukraine

T. V. Shvets Physics, Electronics and Computer Systems Department, Oles Honchar Dnipro National University, Dnipro, Ukraine

P. M. Silenko I.N. Frantsevich Institute for Problems of Materials Science of NASU (IPMS), Kyiv, Ukraine

O. Smirnova Chuiko Institute of Surface Chemistry, NAS of Ukraine, Kyiv, Ukraine

Vitaliy Smokal Kyiv Taras Shevchenko National University, Kyiv, Ukraine

Larisa Sokil Institute for Problems of Cryobiology and Cryomedicine, National Academy of Sciences of Ukraine, Kharkiv, Ukraine

Yu. M. Solonin I.N. Frantsevich Institute for Problems of Materials Science of NASU (IPMS), Kyiv, Ukraine

O. P. Stanovyi Faculty of Physics, Taras Shevchenko National University of Kyiv, Kyiv, Ukraine

Iryna I. Stepanova National Technical University «Kharkiv Polytechnic Institute», Kharkiv, Ukraine

Ludmila Stepanyuk Institute for Problems of Cryobiology and Cryomedicine, National Academy of Sciences of Ukraine, Kharkiv, Ukraine

Tetiana Tatarchuk Department of Chemistry, Vasyl Stefanyk Precarpathian National University, Ivano-Frankivsk, Ukraine;
Faculty of Chemistry, Jagiellonian University, Kraków, Poland

M. I. Terebinska Chuiko Institute of Surface Chemistry of National Academy of Sciences of Ukraine, Kyiv, Ukraine

M. V. Tkach Department of Theoretical Physics and Computer Simulation, Yuriy Fedkovych Chernivtsi National University, Chernivtsi, Ukraine

I. Tkachenko Institute of Macromolecular Chemistry, National Academy of Sciences of Ukraine, Kyiv, Ukraine

O. A. Tsyganovich F.D. Ovcharenko Institute of Biocolloidal Chemistry of NAS of Ukraine, Kyiv, Ukraine;
National Technical University of Ukraine «KPI», Kyiv, Ukraine

B. D. Vasyliv Department of Hydrogen Technologies and Alternative Energy Materials, Karpenko Physico-Mechanical Institute of the NAS of Ukraine, Lviv, Ukraine

V. V. Vira Department of Strength of Materials and Structural Mechanics, Lviv Polytechnic National University, Lviv, Ukraine

P. Virych Taras Shevchenko National University of Kyiv, Kyiv, Ukraine

N. Vityuk Chuiko Institute of Surface Chemistry, NAS of Ukraine, Kyiv, Ukraine

O. M. Voitsekhivska Department of Theoretical Physics and Computer Simulation, Yuriy Fedkovych Chernivtsi National University, Chernivtsi, Ukraine

Nataliia Volkova Institute for Problems of Cryobiology and Cryomedicine, National Academy of Sciences of Ukraine, Kharkiv, Ukraine

K. S. Yablochkova Taras Shevchenko National University of Kyiv, Kyiv, Ukraine

O. S. Yakymenko National Technical University of Ukraine "Igor Sikorsky Kyiv Polytechnic Institute", Kyiv, Ukraine

Olena Yanushevska Kyiv, Ukraine

Gulmira Sh. Yar-Mukhamedova Institute of Experimental and Theoretical Physics, Al-Farabi Kazakh National University, Almaty, Kazakhstan

I. Yaremchuk Department of Photonics, Lviv Polytechnic National University, Lviv, Ukraine

O. V. Yashchenko National Technical University of Ukraine "Igor Sikorsky Kyiv Polytechnic Institute", Kyiv, Ukraine

Oleg Yeshchenko Taras Shevchenko National University of Kyiv, Kyiv, Ukraine

Mariia Yukhta Institute for Problems of Cryobiology and Cryomedicine, National Academy of Sciences of Ukraine, Kharkiv, Ukraine

M. M. Zahornyi I.N. Frantsevich Institute for Problems of Materials Science of NASU (IPMS), Kyiv, Ukraine

R. M. Zakharko National Technical University of Ukraine "Igor Sikorsky Kyiv Polytechnic Institute", Kyiv, Ukraine

Svitlana I. Zyubanova National Technical University «Kharkiv Polytechnic Institute», Kharkiv, Ukraine

Part I
Nanochemistry and Biotechnology

Chapter 1
The Effect of Medium Acidity and Basicity on the Stability of Tryptophan and Formylkynurenine Species with Silver

O. Smirnova, A. Grebenyuk, Iu. Mukha, and N. Vityuk

1.1 Introduction

The variety of functions performed by substances of a protein nature in a living organism is determined by the nature of their constituent amino acids. At the same time, the most common reaction of these substances is complexation with ions of various metals, including silver, the use of its preparations in medicine being expanding every year, because of the lack of resistance to them in microorganisms. According to available data, silver has a detrimental effect on 650,700 species of microorganisms. Its mechanism of action on a microbial cell is that silver ions, after penetrating into it, inhibit the enzymes of the respiratory chain, and also uncouple the processes of oxidation and oxidative phosphorylation, as a result of which the cell dies. These enzymes include catalases, dehydrase, and peroxidases.

Noble metal nanoparticles (NPs) prepared in the presence of biocompatible surface-capping ligands, peptides, and proteins can be highly effective as imaging and delivery agents, catalysts, etc. The combination of bioactive substance moiety and metal nanoparticles can introduce novel chemical and biochemical functionalities [1–3].

Since silver preparations are very sensitive to the effects of various external factors, the search for ways to increase their stability is quite urgent. Complexation of silver with organic compounds improves the stability of the resulting substances. The coordination compounds of silver with polyacrylic, glutamic acids, phenylalanine, proline, and arginine obtained in recent years have antimicrobial and hemostatic

O. Smirnova (✉) · A. Grebenyuk · Iu. Mukha · N. Vityuk

Chuiko Institute of Surface Chemistry, NAS of Ukraine, 17 General Naumov Str, Kyiv 03680, Ukraine

e-mail: olsmirnova2001@ukr.net

effects. In addition to the named, one of the very promising components for the preparation of pharmacologically active compounds is tryptophan (Trp, $C_{11}N_2H_{12}O_2$), which has immuno- and neurotropic properties.

There is a great perspective for the use of tryptophan-containing systems for the preparation of pharmacologically active compounds [4–6].

Tryptophan (Trp) as a biocompatible agent can reduce the toxicity of nanosized system and promote the anticancer effect of metal NPs [7–9].

Trp as bifunctional agent can act as reducer of metal ions, as well as the stabilizer of nanoparticles. As a result of redox reaction, Trp is oxidized, and earlier with quantum mechanical calculations we revealed that during Ag NPs formation (the reaction between Trp and Ag^+ ions) the transformation of Trp goes to N-formylkynurenine (NFK) [10]. Trp as a stabilizer can remain untransformed. So, for the purposeful development of such nano-objects there is still question about the state of the molecule that binds to NPs in Trp-containing system.

Trp as a ligand contains three electron-donor functional groups, which are potential centers of coordination with the metal ion: the oxygen of the carboxyl group, the nitrogen atom of the amino group, and aromatic electrons of the indole ring.

Based on the foregoing, coordination compounds based on silver and tryptophan can become a basis for drugs with a wide spectrum of action. For their purposeful development, it is necessary to first study the process of complexation of silver and tryptophan.

Tryptophan as a ligand contains three electron-donor groups, which are potential centers of coordination with the metal ion: the oxygen of the carboxyl group, the nitrogen atom of the amino group, and the nitrogen atom of the indole ring. The reference data [11] do not provide the acid dissociation constants of the NH group of the indole ring.

The constants of acid dissociation of tryptophan are well known: Literature values of pK_1 and pK_2, respectively, are 2.44 and 9.38. From these data, it follows that at pH 3–8 tryptophan is in three ionic forms.

Coordination compounds of silver and tryptophan are usually obtained through the formation of an intermediate silver hydroxide.

The formation of protonated coordination compounds occurs at pH 7–9; an increase in pH value due to hydroxide ions added to the system leads to their deprotonization [12].

Earlier [10] we revealed the mechanism of metal reduction and particles stabilization in the system including Trp and Ag ions occurring due to transformation of Trp to NFK. The quantum mechanical calculations appeared to be useful tool to investigate the properties of metal/Trp systems starting from the single molecules.

According to DFT calculations performed in [13], the binding of Trp to NPs is possible with the participation of all functional groups, and the most energetically advantageous is the binding simultaneously through the carboxyl group and the indole moiety, which gives a mixed structure.

In this work, we applied spectroscopic methods (absorption and fluorescence) to study Ag NPs colloid and performed quantum chemical calculations of the energy characteristics of structural changes in the $Ag_n(Ag^+)$/Trp (NFK) system to identify

the molecule attached to the nanoparticle surface during stabilization process under the influence of changes in the acidity of the medium: neutral, acidic, and alkaline media.

1.2   Experimental and Theoretical Methods

1.2.1   Silver Colloids

Two types of silver colloids were investigated: (I) colloid 8*obtained at boiling temperature (T100 °C) and (II) colloid obtained under LED irradiation at t° = 25 °C (UV25 °C) according to [10, 14], respectively. For the synthesis of Ag NPs, silver nitrate (AgNO$_3$) and amino acid tryptophan (Trp) were used in aqueous medium with concentration of metal $C = 1 \times 10^{-4}$ M and molar ratio of components Ag:Trp = 1:2. The pH = 10 of the system was reached with the 1 N solution of NaOH.

Colloids were divided by centrifugation into supernatant (marked as "I/II-1") and fraction that was washed twice by deionized water and then exposed to thiol-containing ligands, namely mercaptoundecanoic acid (MUA) (marked as "I/II-2") and centrifuged. Mercaptoundecanoic acid (MUA) was used for displacing the ligand from the surface of Ag NPs. Centrifugation was performed with 16,000 rpm during 60 min in 16,000 rpm.

1.2.2   Investigation Methods

The absorption spectra of the Au NPs colloids were recorded in a 1 cm quartz cell using a spectrophotometer PerkinElmer Lambda 35 and Specord 210. The photo-luminescence spectra were recorded by a luminescence spectrometer PerkinElmer LS 55.

1.2.3   Details of Calculations

The optimal structures of single molecules NFormylKyn and their complexes with hydrated ions Ag$^+$ and proton were systematically studied using the density functional theory (B3LYP/3-21G*) method using the PC GAMESS software package [15]. The electronic absorption spectra of the studied structures were calculated by the TDDFT method [16].

1.3   Results and Discussion

Silver nanoparticles (Ag NPs) in colloids were synthesized in the presence of trypto-phan (Trp) via chemical (marked as "I") and photochemical (marked as "II") methods. The chemical reaction between Ag^+ and Trp proceeded in alkaline medium in boiling solution, while photochemical reaction occurred under UV irradiation at $\lambda = 280$ nm at $t° = 25$ °C. Both methods allow one to obtain stable colloids of Ag NPs with value of zeta potential around 25 mV and pronounced localized surface plasmon resonance (LSPR) band in a visible range with a maximum at 419 and 428 nm, respectively (Fig. 1.1a).

The absorption spectrum of the aqueous Trp solution contains two bands—an intense band at 220 nm and long-wavelength band with a weak oscillatory structure, which has a shoulder of about 270 nm and two maxima at 279 and 288 nm. Both bands of tryptophan are due to π-π*-transitions in the indole ring [17].

During oxidation by noble metals, Trp forms oxidation products according to kynurenine pathway through indole ring cleavage, as was shown in [18].

The interpretation of products should be based on the spectral data of commer-cially available model compounds, as was done, for example, in [19] for tryptophan, N-formylkynurenine (NFK), and kynurenine (Kyn). NFK, that was synthesized by formulation of commercially available kynurenine, has an absorption peak at 320 nm, whereas kynurenine has a longer wavelength maximum at 365 nm. The maximum absorption of NFK depends on the solvent, showing a position at 318 for aqueous solution.

For further identification of stabilizer attached to the nanoparticle, the target molecule was removed from Ag NPs surface to solution by ligand exchange with mercaptoundecanoic acid (MUA).
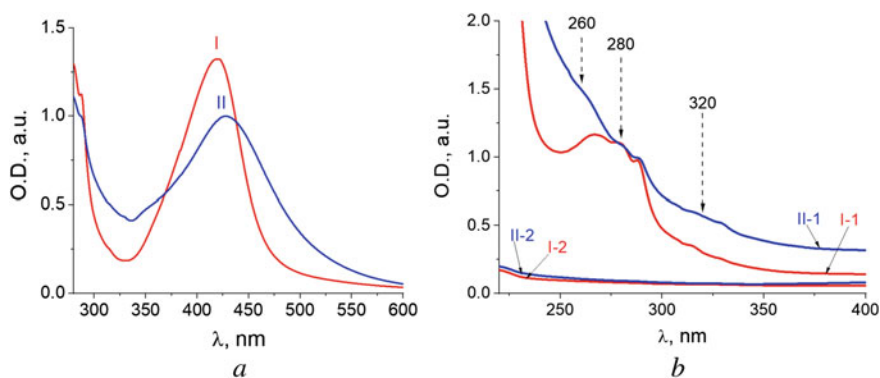
Fig. 1.1 Absorption spectra of colloids of Ag NPs obtained in the presence of tryptophan via chemical (I) and photochemical (II) methods in the range of LSPR band of silver **a** and fractions of colloids **b**, where "I/II-1" refers to supernatant of Ag NPs colloid after 1st step of centrifugation, "I/II-2"—supernatant of centrifuged Ag NPs after interaction with MUA

In prepared colloids for both fraction of supernatants (after 1st step of centrifugation, and after interaction with MUA), there were no pronounced band maximum around mentioned location in absorption spectra, except some shoulders at 280 nm that reflect oscillatory structure characteristic for Trp (Fig. 1.1b). But there is increased intensity around 260 and 320 nm in the range of NFK absorption.

According to the data in [20], when NFK is excited with a wavelength $\lambda_{ex} = 325$ nm, which corresponds to the absorption maximum at 322 nm, there is a wide emission band in the region of 370–500 nm with a maximum at 434 nm that does not occur when excited with $\lambda_{ex} = 280$ nm. So, the fluorescence spectroscopy was applied to study the oxidation products and stabilizer.

For the supernatant after 1st step of centrifugation for both colloids (I-1 and II-1) the emission bands with a maximum at 350 nm were observed when exited with $\lambda_{ex} = 280$ nm (Fig. 1.2a), indicating the presence of Trp in solution. Therewith the same bands were fixed for washed Ag NPs that interacted with MUA (Fig. 1.2c) (The excitation at $\lambda_{ex} = 260$ nm gives the same result due to overlap of absorption bands.).

In its turn, when exited with $\lambda_{ex} = 320$ nm (in NFK absorption maximum) for both systems in solution there were bands in fluorescence spectra with a maximum located at 395 nm (Fig. 1.2b), but no emission bands were observed in this region for washed Ag NPs (Fig. 1.2d).

The excitation spectra were recorded for studied samples using $\lambda = 350$ and 400 nm. For both solution and washed Ag NPs, the bands with a maximum at 275 nm were present in extinction spectra when exited with $\lambda = 350$ nm (Fig. 1.2a, c) that corresponds to Trp. When $\lambda = 400$ nm was applied, the spectra were recorded only for supernatant after 1st step of centrifugation of colloid. The shoulder for chemically obtained colloid (I) and individual peak for photochemically obtained colloid (II) at 315 nm were fixed (Fig. 1.2b). It is in accordance with absorption spectra and indicates the deeper oxidation of Trp in case of photochemical reaction.

Analyzing different spectroscopic data, we can conclude that stabilizer molecule attached to the surface of formed silver nanoparticles is untransformed tryptophan, as the emission and excitation spectra reflect spectroscopic properties of Trp, while its oxidation products, most likely NFK, remains in solution (Fig. 1.3).

In the previous work [10], the processes of oxidation of tryptophan to NFK by silver ions in the presence of water and oxygen molecules were considered. From the optical spectra of a stable colloid of silver nanoparticles obtained in the presence of tryptophan, it follows that with increasing ultraviolet irradiation, the intensity of the absorption band (about 270–290 nm) corresponding to tryptophan decreases whereas and the intensity of the absorption band (400–450 nm) corresponding to silver nanoparticles increases. This conclusion is supported by the results of quantum chemical calculations of the absorption spectra of the Ag_{14} cluster (absorption maximum at 456 nm, Fig. 1.4) and tryptophan-carboxylanion (formed in alkaline medium) in a complex with four water molecules (absorption maximum at 265 nm, Fig. 1.5).

NFK is formed as a result of the oxidation reaction of Trp with oxygen in water in the presence of silver ions.
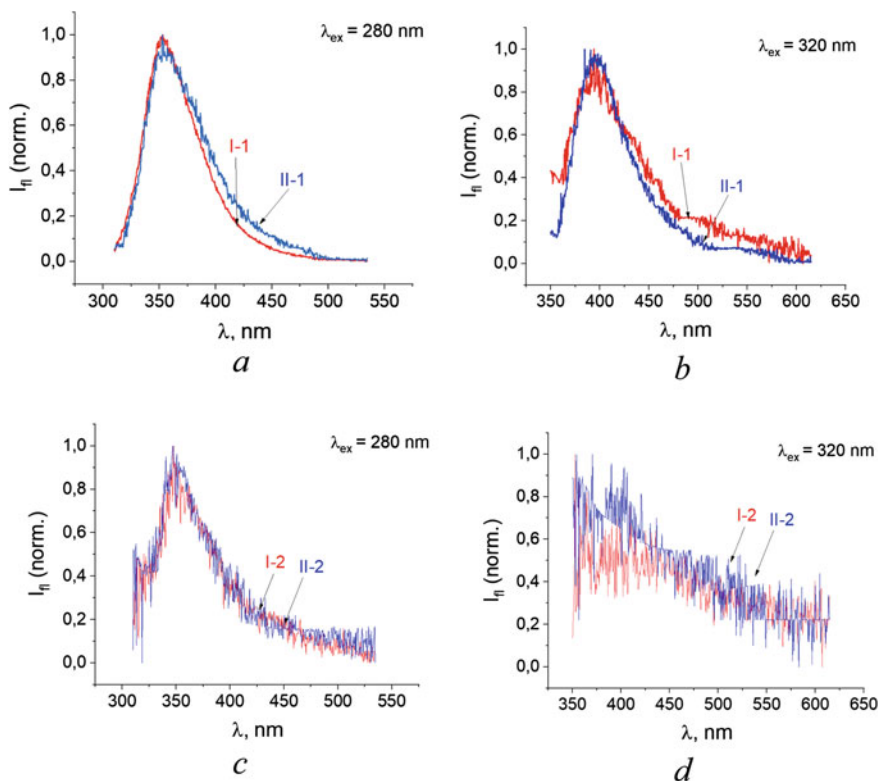
Fig. 1.2 Normalized emission spectra of the fractions of Ag NPs colloids, namely supernatant of Ag NPs colloid after the 1st step of centrifugation **a**, **b** and supernatant of centrifuged Ag NPs after interaction with MUA **c**, **d** excited at the wavelength $\lambda_{ex} = 280$ **a**, **c** and 320 nm **b**, **d**

The spatial structures of the participants in the process of washing out silver ions from the complex with NFK and corresponding UV spectra of the reaction products (NFK and its complex with silver ions and the protonated form) are shown in Fig. 1.6.

Spatial structure and corresponding values of the total energy and the change in the Gibbs free energy during the transition from 0 to 298 K silver complexes in acidic and alkaline media, hydrated forms of hydroxide ions, hydronium, water dimer, and monomer are shown in Figs. 1.7 and 1.8.

In an acidic medium, the transformation of the complex of silver ion with NFK proceeds according to the equation:

$$NFK \cdot Ag^+ \cdot H_2O + H_5O_2^+ = NFK \cdot H^+ \cdot H_2O + Ag^+ \cdot (H_2O)_2 \qquad (1.1)$$

The calculated value of the energy effect of the reaction is $E = -17.46$ kJ/mol, and the Gibbs free energy at 298 K is $E = -15.09$ kJ/mol. So, silver ions are washed out from the NFK $\cdot$ Ag$^+$ $\cdot$ H$_2$O complex.
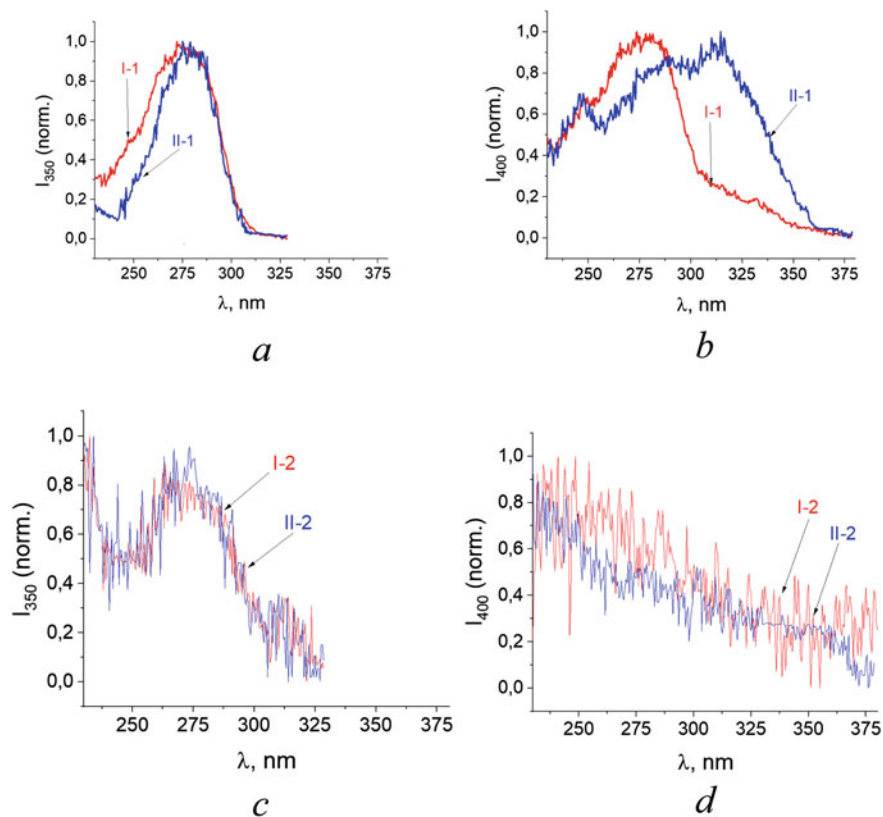
Fig. 1.3 Normalized excitation spectra of fractions of Ag NPs colloids, namely supernatant of Ag NPs colloid after 1st step of centrifugation **a**, **b** and supernatant of centrifuged Ag NPs after interaction with MUA **c**, **d** excited at the wavelength $\lambda_{ex} = 350$ **a**, **c** and 400 nm **b**, **d**
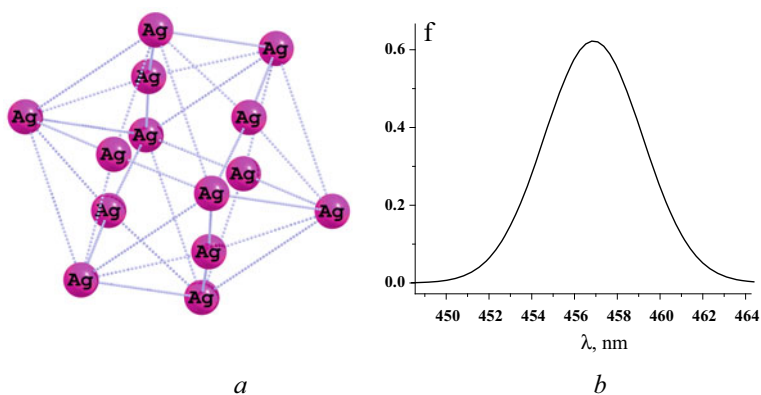
Fig. 1.4 Cluster **a** and related UV spectrum **b** Ag$_{14}$
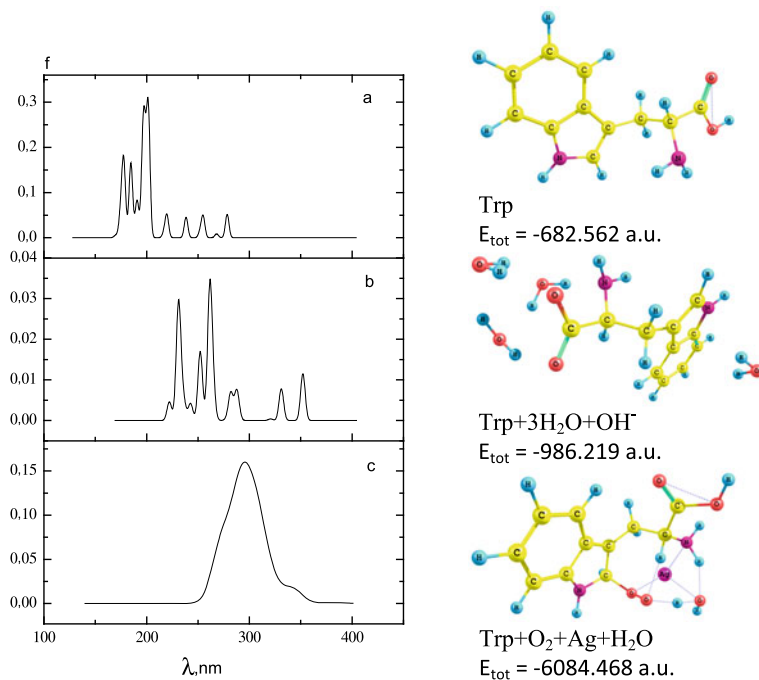
Fig. 1.5 UV spectrum of Trp **a**, Trp in alkaline medium **b**, and its complex with silver ions **c** and corresponding spatial structures

In an alkaline medium, the transformation of the complex of silver ion with NFK proceeds according to the equation:

$$NFK \cdot Ag^+ \cdot H_2O + H_3O_2^- = NFK + H_2O \cdot AgOH + H_2O \qquad (1.2)$$
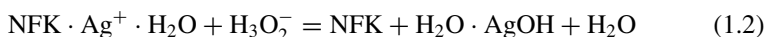
The calculated value of the energy effect of the reaction is $E = -1524.23$ kJ/mol, and the Gibbs free energy at 298 K is $E = -1484.34$ kJ/mol. As a result of the reaction, a solid phase of hydrated silver hydroxide is formed.

In the case of reduced silver, in an acidic medium, the transformation of the complex of silver atom with NFK proceeds according to the equation:

$$NFK \cdot Ag \cdot H_2O + H_5O_2^+ = NFK \cdot H^+ \cdot H_2O + Ag \cdot (H_2O)_2 \qquad (1.3)$$
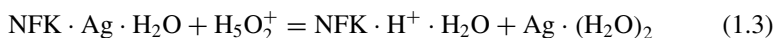
The calculated value of the energy effect of the reaction is -12.32 kJ/mol, and the Gibbs free energy at 298 K is 39.90 kJ/mol. Consequently, silver ions are washed with excess of acid out from the NFK $\cdot$ Ag $\cdot$ H$_2$O complex.

In an alkaline medium, the transformation of the complex of silver ion with NFK proceeds according to the equation:
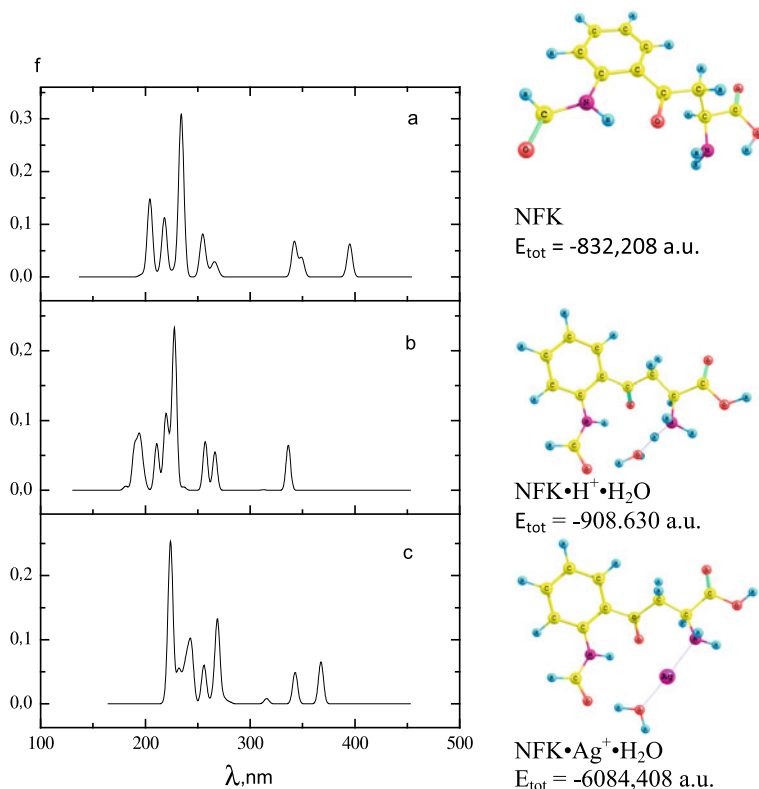
Fig. 1.6 UV spectra NFK **a**, protonated form **b**, and its complex with silver ions **c** and corresponding spatial structure and corresponding values of the total energy

$$NFK \cdot Ag^+ \cdot H_2O + H_3O_2^- = NFK + H_2O \cdot AgOH + H_2O \qquad (1.4)$$
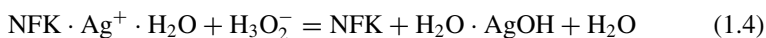
The calculated value of the energy effect of the reaction is –56.87 kJ/mol, and the Gibbs free energy at 298 K is –3.31 kJ/mol. As a result of the reaction, a hydrated solid phase of silver hydroxide is formed.

From the results of quantum chemical calculations, it follows that in an alkaline medium, the process of destruction of the complexes including both oxidized and reduced silver proceeds much more efficiently than in an acidic medium. Provided taken into account the influence of the medium, the concentration of acid or alkali, and the fact that the particles of the solid phase of silver hydroxide consist of many formula units, the numerical values of the energy characteristics can be substantially approximated to experiment. This consideration is especially important when considering processes in an alkaline environment.

In the NFK · H$^+$ · H$_2$O system, the long-wavelength absorption band (340 nm) corresponds by 98% to the transition between the frontier orbitals (Nos. 67–68).

Ag$^+$•(H$_2$O)$_2$
E$_{tot}$ = -5328,135a.u.

a

H$_2$O•Ag$^+$OH
E$_{tot}$ = -5328,14 a.u.

b

Ag^0•(H$_2$O)$_2$
E$_{tot}$ = -5328,279 a.u.

c

H$_2$O•Ag^{0}OH$^-$
E$_{tot}$ = -5327,703

d
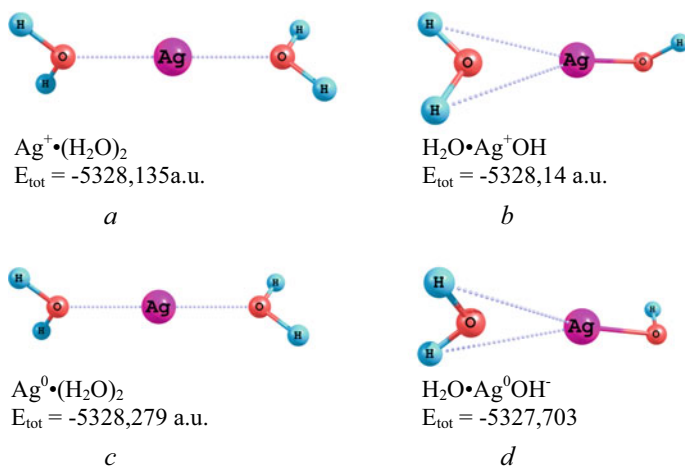
Fig. 1.7 Spatial structure and corresponding values of the total energy of silver complexes in acidic **a**, **c** and alkaline **c**, **d** media

Fig. 1.8 Spatial structure and corresponding values of the total energy of hydrated forms of hydroxide ions **a**, hydronium **b**, water dimer **c**, and monomer **d**

H$_2$O_OH_A
E$_{tot}$ = -151,329 a.u.

a

H$_2$O_H$_3$O_K
E$_{tot}$ = -152,351 a.u.

b

H$_2$O_D
E$_{tot}$ = -151,971 a.u.

c

H$_2$O
E$_{tot}$ = -75,974 a.u.

d
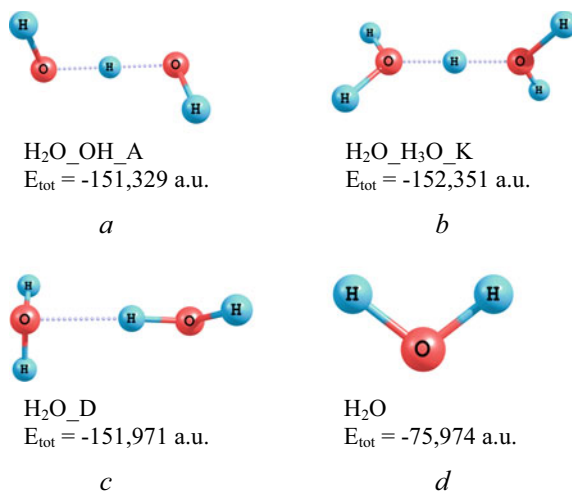
A similar transition occurs in systems NFK · Ag$^+$ · H$_2$O (367 nm, 91%, Nos. 90–91) и NFK (395 nm, 97% Nos. 62–63).

The spatial structure and formation energies of the complexes between silver metal Ag$_{14}$ clusters (Fig. 1.9) and Trp or NFK molecules were calculated. It has been found that the equilibrium structure of the associates formed can be interpreted as a π-complex with additional amino group—silver coordination bond.

The formation energies of these complexes are equal to −79 kJ/mol (Trp) and −83 kJ/mol (NFK).

a　　　　　　　　　　　　*b*
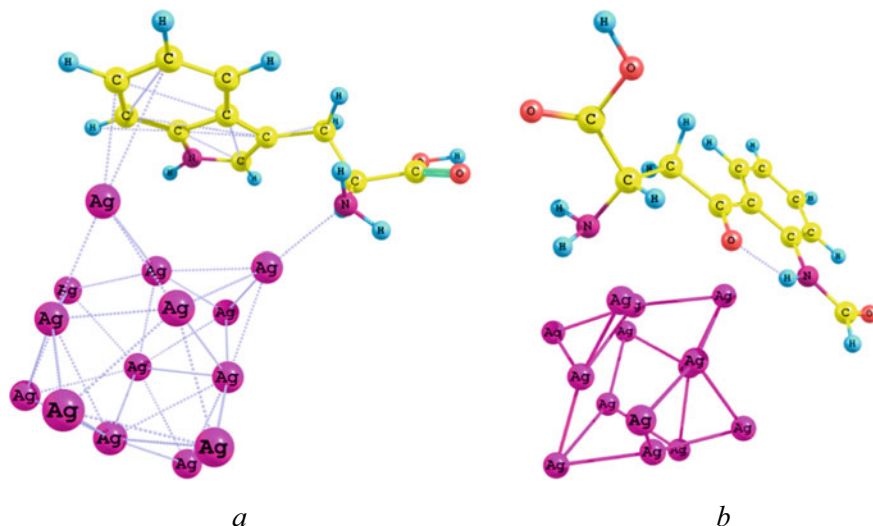
Fig. 1.9 Spatial structures of the complexes between silver metal Ag$_{14}$ clusters and Trp **a** or NFK **b**

The calculated value of the interaction energy of tryptophan and NFK with silver is approximately the same. This can be explained by the presence in the molecules of both compounds of aromatic rings and amino groups, which act as the main sites of interaction with silver.

Since NFK and kynurenine are involved in further transformations, their experimentally determined concentration is very low. In addition, these compounds have a significantly lower extinction coefficient than the initial tryptophan, so it is very difficult to observe them experimentally.

1.4 Conclusion

When passing from a neutral to an acidic medium, the absorption bands of NFK hypsochromic shift from 367 toward 340 nm, which is obeyed by protonation of the amino group. In an alkaline medium, there is a bathochromic shift of absorption bands from 367 to 395 nm corresponding to the elimination of the neutral form NFK.

From the results of quantum chemical calculations, it follows that on going from a neutral to an acidic medium, the NFK complex with silver decomposes with the formation of hydrated silver ions and the protonated form of NFK. In an alkaline environment, the free form of NFK and the solid phase of silver hydroxide are formed. In an alkaline environment, the process proceeds more efficiently, since it is thermodynamically more advantageous than in an acidic environment.

References

1. Si S, Mandal TK (2007) Tryptophan-based peptides to synthesize gold and silver nanoparticles: a mechanistic and kinetic study. Chem Eur J 13(11):3160–3168. https://doi.org/10.1002/chem.200601492
2. Nasrolahi ShA, Tiwari RK, Oh D, Sullivan B, McCaffrey K, Mandal D, Parang K (2013) Surface decorated gold nanoparticles by linear and cyclic peptides as molecular transporters. Mol Pharm 10(8):3137–3151. https://doi.org/10.1021/mp400199e
3. Sun YN, Ding XY, Du LN, Jiang Z, Xu H, Yu YB, Li Ya, Zhang QQ (2011) Synthesis of gold nano- and microplates by tryptophan and 5-hydroxy-tryptophan. Adv Mater Res 194–196; 397–401. https://doi.org/10.4028/www.scientific.net/amr.194-196.397
4. Nasrolahi ShA, Mandal D, Tiwari RK, Guo L, Lu W, Parang K (2012) Cyclic peptide-capped gold nanoparticles as drug delivery systems. Mol. Pharm 10(2):500–511. https://doi.org/10.1021/mp300448k
5. Daima Hemant K, Selvakannan PR, Bhargava Suresh K, Shastry SK, Bansal V (2014) Amino acids-conjugated gold, silver and their alloy nanoparticles: role of surface chemistry and metal composition on peroxidase-like activity. In: From nanotechnology 2014: graphene, CNTs, particles, films and composites, technical proceedings of the NSTI nanotechnology conference and expo, Washington, DC, United States, 15–18 June 2014, pp 275–278
6. Dubey K, Anand BG, Badhwar R, Bagler G, Navya PN, Daima HK, Kar K (2015) Tyrosine- and tryptophan-coated gold nanoparticles inhibit amyloid aggregation of insulin. Amino Acids 47(12):2551–2560. https://doi.org/10.1007/s00726-015-2046-6
7. Mukha Iu, Vityuk N, Grodzyuk G, Shcherbakov S, Lyberopoulou A, Efstathopoulos EP, Gazouli M (2017) Anticancer effect of Ag, Au, and Ag/Au bimetallic nanoparticles prepared in the presence of tryptophan. J Nanosci Nanotechnol 17(12):8987–8994
8. Shmarakov I, Mukha Iu, Vityuk N, Borschovetska V, Zhyshchynska N, Grodzyuk G, Eremenko A (2017) Antitumor activity of alloy and core-shell-type bimetallic AgAu nanoparticles. Nanoscale Res Lett 12:333–10
9. Katifelis H, Lyberopoulou A, Mukha Iu, Vityuk N, Grodzyuk G, Theodoropoulos GE, Efstathopoulos EP, Gazouli M (2018) Ag/Au bimetallic nanoparticles induce apoptosis in human cancer cell lines via P53, CASPASE-3 and BAX/BCL-2 pathways. Artif Cells Nanomed Biotechnol 46(3):S389–S398
10. Smirnova O, Grebenyuk A, Mukha Iu, Vityuk N (2020) Mechanisms of tryptophan transformations involving the photochemical formation of silver nanoparticles. In: Nanooptics and photonics, nanochemistry and nanobiotechnology, and their applications, pp 237–244
11. Jakubke KhD, Eshkait Kh (1985) CRC handbook of chemistry and physics
12. Sufiev Tui Davlatovich Biological properties of silver and triptofan coordination compounds 14.00.25—Pharmacology, Clinical Pharmacology Abstract dissertation for the degree of candidate of biological sciences Dushanbe-2009 003474286b, pp 1–24
13. Joshi P, Shewale V, Pandey R, Shanker V, Hussain S, Karna SP (2011) Tryptophan-gold nanoparticle interaction: a first-principles quantum mechanical study. J Phys Chem C 115(46):22818–22826. https://doi.org/10.1021/jp2070437
14. Mukha Iu, Vityuk N, Khodko A, Kachalova N, Fedyshyn O, Malysheva M, Eremenko A (2019) Photo- and temperature-dependent formation of tryptophan/silver nanoparticles. Res Chem Intermed 45(8):4053–4066
15. Schmidt M, Baldridge K, Boatz J, Elbert S, Gordon M, Jensen J, Koseki S, Matsunaga N, Nguyen K, Su S, Windus T, Dupuis M, Montgomery J (1993) General atomic and molecular electronic structure system. J Comput Chem 14:1347
16. Runge E, Gross EKU (1984) Density-functional theory for time-dependent systems. Phys Rev Lett 52(12):997
17. Demchenko AP (1986) Ultraviolet spectroscopy of proteins. Springer, Berlin, p 312
18. Mukha Iu, Vityuk N, Severynovska O, Eremenko A, Smirnova N (2016) The pH-dependent structure and properties of Au and Ag nanoparticles produced by tryptophan reduction. Nanoscale Res Lett 11:101–107

19. Dreaden TM, Chen J, Rexroth S, Barry BA (2011) N-formylkynurenine as a marker of high light stress in photosynthesis. J Biol Chem 286(25):22632–22641. https://doi.org/10.1074/jbc.m110.212928
20. Fukunaga Y, Katsuragi Y, Izumi T, Sakiyama F (1982) Fluorescence characteristics of kynurenine and N-formylkynurenine, their use as reporters of the environment of tryptophan 62 in hen egg-white lysozyme1. J Biochem 92(1):129–141. https://doi.org/10.1093/oxfordjournals.jbchem.a133909

Chapter 2
Dielectric Properties of Blood Cells as Biomarkers for Stroke Diagnostics

Liliya Batyuk and Natalya Kizilova

2.1 Introduction

Red blood cells (RBCs) and other isometric cells with diameters $d \sim 5\text{--}10\ \mu\text{m}$ can be modeled as microparticles in agglomerates and aquatic suspensions, and their movement can be considered within the mathematical models of microfluids with complex electromechanical properties [1]. Besides mechanical parameters (density, rigidity, fluidity), biological tissues are characterized by electric properties which are high frequency, temperature, and age dependent and important for clinical diagnostics of pathologies [2]. The surface density of the electric charge $\sigma_e = q/S$, where q is the electric charge and S is surface area, is an important characteristic of cells, tissues, and organs. The surface charge of the red blood cells (RBCs) is produced by the charged proteins embedded into the membrane, dissociation of the surface molecules, and adsorption of ions from blood plasma. The charged particles form electrical double layer (EDL) around the cells in water-based solvents. The monomolecular layer of adsorbed ions (Stern layer) is surrounded by a diffuse layer of solvated ions (Gouy–Chapman layer). This structure of EDL is proper to washed RBCs, while in the native RBCs the membrane is covered by glycoproteins forming the complex 3D structure (glycocalyx). The positive and negative charged groups are nonuniformly distributed in the glycocalyx that changes the structure of EDL. The Debye length for biological cells is $\kappa^{-1} = 8\ \text{Å}$ at normal values of ionic strength $I_i = 0.5 \sum_i C_i z_i^2$ of the solvent, where C_i and z_i are concentrations and valency of ions.

L. Batyuk
Kharkov National Medicine University, Pr. Nauki 2, Kharkiv 61022, Ukraine

N. Kizilova (✉)
Warsaw University of Technology, ul. Nowowiejska 24, 00-665 Warsaw, Poland
e-mail: n.kizilova@gmail.com

V.N. Karazin Kharkov National University, Svobody sq., 4, Kharkov 61022, Ukraine

Dielectric permittivity is also an important characteristic of biological cells and tissues. It is a complex value $\varepsilon = \varepsilon' + i\varepsilon''$ because the tissues are not ideal dielectrics and some part of the electromagnetic energy is transformed into heat due to the electric conductivity of the tissues. The dielectric loss $\varphi_\varepsilon = a\tan(\varepsilon''/\varepsilon')$ characterizes the amount of the energy spent to the heat transfer due to conductivity and dielectric losses. Dielectric permittivity of blood increases with concentration of RBC and blood plasma proteins.

Biological cells and tissues are characterized by dispersion of their electric conductivity k and dielectric permittivity ε in the range of low frequencies (LF) $f = 10–10^3$ Hz (α-dispersion), radio frequencies $f = 10^4–10^8$ Hz (β-dispersion), and high frequencies (HF, microwaves) $f > 10^{10}$ Hz (γ-dispersion). In human blood and RBC suspensions, α-dispersion is almost absent [3]. Low blood conductivity at LF is explained by high conductance ($\sim 10^{-2}$ F/m^2) of the RBC membranes [3], and the dispersion is determined by ionic diffusion processes at the cellular membranes.

Ischemic stroke (IS) is a clinical syndrome manifesting itself as a sharp disruption of the brain's local functions, lasting more than a day, or resulting in death as a result of a reduction in cerebral blood flow, thrombosis, or embolism associated with heart, vascular, or blood diseases. More than 140,000 people die each year from stroke in the USA, 152,000 in the UK, and almost 100,000 in Ukraine [4, 5]. According to the World Health Organization, 15 million people suffer a stroke worldwide each year. The mortality rises up to 35%, and 75–85% are related to the IS which is caused by the carotid stenoses in 30–50% of patients.

The methods for predicting the risk of ischemic disorders of cerebral blood flow include blood lipid profile determinations, magnetic resonance imaging, computed tomography, transcranial dopplerography, and others. These methods do not allow revealing the functional state of the microcirculatory system [6] or red blood cell (RBC) malfunctioning [7]. Indicators of hemostasis, kinetics parameters of aggregation and disaggregation of erythrocytes, and their deformability are associated with blood flow through microvessels under different pathological conditions including cerebral ischemia. In addition, the deterioration of rheological properties of blood and parameters of hemostasis is in some connection with the clinical features: the stage, severity, and extent of IS, as well as with the prognosis of the course of the disease [7]. Nevertheless, at the moment there are practically no experimental and clinical studies devoted to the complex analysis of hemostatic and hemorheological factors with an assessment of their effect on microcirculation in patients with thrombolytic therapy of IS and also on the functional outcome of the disease. Thus, it seems relevant to study these blood indices in the acute period of IS, including intravenous thrombolytic therapy.

In this paper, the dielectric parameters of RBC have been measured by two-channel microwave dielectrometer at a frequency $f = 9.2$ GHz. Complex dielectric permittivity of RBC in the RBS suspensions of healthy donors has been compared with those of patients with IS.

2.2   Microwave Dielectrometry Technique in Complex Study of Microparticles

Microwave dielectrometry (MD) in the region of relaxation of free water molecules (γ-dispersion) allows studying the state of water in biological systems [8, 9]. Water determines the mobility of macromolecules (MM), allows them to associate and dissociate, makes possible the proton transfer, and facilitates a large number of biochemical processes [10]. The water interacting with MM can be described as belonging to one of the following three types: free water, associated water, and strongly bound structured water. The physical properties of the three types of water are different. The molecules of bound water have less mobility than molecules of bulk water. Immobilization of certain part of water in the hydration shells of the MM or cells in aquatic suspensions leads to a decrease in the permittivity of the solution/suspension compared to that of the pure solvent. Amount of the bound water depends on the conformations of the MM [11–15].

MD at GHz frequencies can distinguish the bulk water from the bound. The dipole relaxation of free water molecules contributes most to the dielectric constant of biological tissues at microwaves, so the content of free water or redistribution of water molecules between free and bound state could be traced, and thus, the content of free water in a sample could be used as a marker of conformational transitions of MM [11].

The degree of water incorporation into macromolecules in turn is related to the state of the patient's cells, which depends on natural factors and medications administered. This connection is very complex and has not yet been fully understood. It is known that in cardiovascular diseases, hypertensive disease, and IS, there is a gradual desensitization and a decrease in the number of β-adrenergic receptors due to prolonged activating effect of increased concentrations of neurohormones and a decrease in the number of viable myocardial cells, formation of cardiofibrosis, and apoptosis or necrosis processes. Clinically, this is manifested by aggravation of symptoms and progression of the disease, a decrease in the effectiveness of the drugs [16, 17].

The use of the microwave dielectrometry method is an addition to studies of the state of cells in vitro [11, 18, 19]. Unlike many traditional research methods used in biology and medicine, this integrated approach makes it possible to study biological objects in real time and without interfering their native state. Analysis of the cell state based on their dielectric parameters is performed by evaluating the rearrangement of the membrane-receptor complex of the cell under the action of specific bioregulators relative to control (intact) samples [20].

Human RBC was selected as a model for studying molecular mechanisms of control systems of cells due to the presence of adrenergic receptors in their membrane functionally and structurally similar to adrenoreceptors of vascular cells under conditions of acute disturbance of cerebral circulation, neurohumoral pathology of myocardium, and other organs [21, 22]. The state of hypoxia of organs and tissues is an important mechanism in the pathogenesis of cerebral ischemia, which affects

the structural and functional properties of erythrocytes that determine their oxygen transport function [23, 24]. In addition, it is known that erythrocytes are involved in the pathogenesis of microcirculatory disorders in patients with cerebrovascular diseases [25, 26].

The simplicity of organization of erythrocytes makes it possible to study the functional properties of cell membranes without interference imparted by intracellular membrane formations and organelles. Structural disturbances of erythrocyte membranes in various pathological processes can be extrapolated to other membrane systems. There are extensive literature data on methods for measuring the permittivity of biological substances [27–31], blood [32–34], and RBC [35–38].

The state of cells and their reaction is expressed in a change in the ratio of free water and water bound by the macromolecules of the cell membranes. This ratio affects the complex value of the permittivity, since in bound water the mechanical moment is determined by the mass of the macromolecule. Dielectric parameters of blood parameters in clinical samples of patients make it possible to obtain information not only about the state of its vascular system, but also to determine the development of pathologies in the early stages, and the optimal path of treatment taking into account the pathology [20, 37–39]. The most informative measurements will be in γ-relaxation frequency range, including the frequency of free water relaxation ($f \sim$ 10 GHz [40, 41]), which determines the relationship between bound and free water and involves measurements in the frequency range of relaxation of water molecules, i.e., near the frequency of. Another feature of these measurements is the need to minimize the volume of biological samples.

Experimental study of the temperature dependences of the complex dielectric permittivity $\varepsilon = \varepsilon' + i\varepsilon''$ of polar liquids in the microwave range makes it possible to obtain important information on the polarization processes, which can be used both for estimating theoretical ideas about the fundamental characteristics of substances and for practical purposes [42]. A systematic study of the dielectric properties of RBC in the microwave region at different temperatures was practically not performed [8, 43, 44].

2.3   Materials and Method

The dielectric characteristics of RBC in patients with IS were studied before and after the baseline therapy prescribed [44]. The study involved 20 patients aged between 38 and 45 years who underwent IS. The preliminary diagnosis was confirmed on the basis of the generally accepted European recommendations for the prevention and treatment of IS [45, 46]. The diagnosis was based on the history, clinical symptoms of IS, neurological and somatic status, general and biochemical blood tests, CT scan of the brain, duplex scanning of brachiocephalic arteries, ECG, and Echo-KG [47]. The classification of diagnosis of vascular lesions of the brain and spinal cord has been used [48, 49]. The control group consisted of 20 healthy donors of the same age. The normal distribution test was carried out using the Shapiro–Wilk test [50].

To compare the changes in the dielectric parameters of the blood erythrocytes of patients before and after treatment, the Wilcoxon test was used [51, 52].

Venous blood samples (2 ml) were stabilized with 0.1 ml of heparin solution with 5000 IU activity. RBCs were separated from blood plasma and leukocytes by centrifugation (600 g, 10 min) at 4 °C and washed 3 times with phosphate-buffered saline (PBS: 150 mM NaCl, 8.1 mM Na_2HPO_4, and 1.9 mM NaH_2PO_4, pH 7.4). A standard erythrocyte suspension was prepared by diluting the resuspended washed erythrocytes with medium and obtaining a suspension with cell concentration ~4.8×10^6 cells/ml that was verified using Gorjaev's chamber.

The character of frequency dependence of the dielectric parameters of soft tissues is the same for all tissues of the human body, namely $\varepsilon'(f)$ is a decreasing function. The relaxation characteristics of free water molecules in blood do not differ from those of pure water and in the region of γ-dispersion can be described by the Debye equation [2]

$$\varepsilon' = \text{Re}(\varepsilon^*) = \varepsilon_\infty + \frac{\varepsilon_0 - \varepsilon_\infty}{1 + (f/f_d)^2}, \quad \varepsilon'' = \text{Im}(\varepsilon^*) = \frac{\omega\tau(\varepsilon_0 - \varepsilon_\infty)}{1 + (f/f_d)^2}, \quad (2.1)$$

where ε_0 and ε_∞ are the high-frequency and low-frequency (static) permittivity (the asymptotic values of the dielectric constant at frequencies above and below the dispersion region, respectively), and f_d and f are the frequencies of the dielectric relaxation and the frequency of the external microwave field. In our calculations, we assume $\varepsilon_\infty = 5.6$ (as the permittivity in the infrared range) [53].

In the case of any polarization mechanism and single relaxation time τ, the Debye theory gives the following expressions

$$\varepsilon_0 = \varepsilon' + \frac{\varepsilon''^2}{\varepsilon' - \varepsilon_\infty}, \quad f_d = \frac{f(\varepsilon' - \varepsilon_\infty)}{\varepsilon''}, \quad (2.2)$$

The value ε_0 does not depend on the frequency and is smaller for concentrated solutions where the amount of bound water is bigger. The parameter f_d characterizes the mobility of molecules in the microwave field and consequently the degree of its interaction with the environment.

As long as we were not able to perform measurements at different frequencies, we did scan our samples over the temperature. Based on [54] and using the dependence $f_d(T)$ [55], one can obtain

$$f_d = \frac{k_B T}{2\pi h} \exp\left(\frac{\Delta S(T)}{k_B} \exp\left[-\frac{\Delta H}{k_B T}\right]\right), \quad (2.3)$$

where k_B and h are Boltzmann and Planck constants, respectively, T is the absolute temperature, $\Delta S(T)$ is the entropy, and ΔH is the enthalpy. The activation energy of the process of dielectric relaxation of water molecules was determined from the linear fit of the data in the coordinates $\ln(f)$ and $1/T$.

The dielectric permittivity of the RBC suspensions was measured according to the test sample-study design. The individual features of donors affect measured values of ε' and ε''. These features include the hematocrit, the concentration of ions, and the distribution of RBC in size and shape. To compensate for these changes, we worked with suspensions of washed RBC. To increase the accuracy, each measurement was repeated at least 5 times, after which the average value was found.

A cylindrical resonator with operating frequency $f = 9.2$ GHz has been used for the measurements. The water–acetone mixtures with different molar fractions of water and known values of ε' and ε'' have been used for calibration of the capillary. The RBC suspension was collected in a capillary with $d = 2$ mm and placed in the resonator, and a shift between the resonant frequencies of the empty and loaded resonator was recorded. The attenuation due to sample loading in the resonator was also recorded for further calculations of the ε'' values. The values ε' and ε'' have been calculated from the measured frequency shifts and attenuation factors by using regression equation for calibrated water–acetone mixtures with known values of ε' and ε''. The value ε'' was corrected for electrical conductivity due to the presence of inorganic ions in the medium. The electrical conductivity of the RBC suspensions was measured by a bridge method at a frequency of 1 kHz at room temperature. The absolute error in a value of ε' did not exceed $\pm$ 0.2, and for the ε'', the error did not exceed $\pm$ 0.5. The temperature of the samples in the capillary varied in the range from 2 to 45 °C and was measured with a copper-constantan thermocouple with an accuracy of $\pm$ 0.1 °C.

The quantities ε_0 and f_d were calculated using Eq. (2.2). The hydration level of the RBC has been computed as [43]

$$\Delta\varepsilon_0 = \varepsilon_0^{\text{PBS}} - \varepsilon_0^{\text{RBS}},$$

where $\Delta\varepsilon_0$ is the decrement of the static permittivity of the RBC suspension relatively the PBC.

2.4 Mathematical Modeling of RBC Dielectric Properties

Numerous experimental and theoretical study of the cellular electromagnetic activity uncovered the microtubules as major source of electromagnetic interactions [56, 57]. Probably, the most interesting phenomenon connected with the microtubule research is water ordering at the cellular interfaces [58–60]. The layers of water without solutes bounded by microtubules are called clear zones [61]. The bound water molecules resemble a gel, i.e., the viscoelastic solid body. Formation of clear zones depends on the negative electrostatic charge at the microtubule surface [62]. A theory of the ordering of water molecules at the charged interfaces has been developed in [63]. Interfacial water ordering may be formed up to a distance of about 0.1 mm from the charged surface. Ordered water layers are formed around mitochondria and influence their functions [64, 65].

In that way, the water in the cell suspensions is a mixture of two phases of water: bound ordered water forming coherent domains and gas-like water (bulk water). The clear zones display macroscopic separation of these two phases of water by the interfaces caused by a strong electric field. The molecules of the bound water and dissolved substances in the centimeter wavelength diapason are less movable than the molecules of the free water. In this case, the bound water molecules are in composition of hydrated layers of salts, biomacromolecules, microfilaments and tubules, internal membranes of mitochondria, nuclei, and other organelles, as well as bound by the cell membranes. In this state, the membrane plays a role of a shock absorber at abrupt external changes ensuring the survival of cells [66].

Therefore, the healthy and cancerous cells possess different ordering of macromolecules and bound water molecules at their internal and external membranes, organelles, and cytoskeleton, that result in different membrane surface shape and conductivity, entropy and noise of signaling networks, mechanical and dielectric properties of single cells, and cell suspensions.

Development of mathematical models of biological tissues is important for studying their mechanical and dielectric properties. Bernstein with co-authors elaborated the cell membrane theory, in which the cell membrane modeled as a capacitor is mostly responsible for decreasing of tissue electrical impedance with increasing frequency [66]. Philippson proposed the resistance–capacitance model for biological tissues composed by dielectric cells with a conducting internal matter [67]. Numerous experimental data confirmed existence of three distinct dispersions (or relaxations) frequency ranges (α-, β-, γ-dispersions) [68, 69] with additional small δ-dispersion.

The α-dispersion is located within the frequency range $f \sim$ Hz kHz and is usually centered at about 100 Hz [70–73]. The low-frequency α-dispersion is determined by ionic diffusion processes at the cellular membranes. It is not easy to measure because of interference from electrode polarization effects [74].

The β-dispersion is located within the 10 kHz–10 MHz range and centered around 100 kHz [75]. At these higher frequencies, the cell membrane is charged only partially and the current can flow through the lipid cell membranes, charging the intracellular structures and producing a capacitive properties. The β-dispersion is connected with electric polarization of organic macromolecules, cell membranes, and other interfaces (interfacial polarization or Maxwell–Wagner effect) [76–79]. When the membrane is disrupted, the β-dispersion is absent [80]. Therefore, the peculiarities of this dispersion reflect variations in the membrane shape [81], the properties of cytoplasm, and the extracellular medium [76].

The high-frequency γ-dispersion ($f \sim$ GHz, centered at 10 GHz) is produced by polarization of tissue water molecules [71, 82–84]. In this range, the external field can reorient proteins and organelles, and the dispersion is mostly determined by reorientation of free (bulk) water molecules. In some studies, the δ-dispersion region becomes visible between β- and γ-dispersion regions. This type of dispersion is attributed to reorientation of molecules of biopolymers and bound water molecules. Those protein-water interactions demonstrate long-ranged behavior and correlated collective dynamics [85].

The theories used to model the dielectric behavior of cell suspensions are essentially based on the dielectric mixture theory of Maxwell [86] and Wagner [87], on the single(multi)-shell particle models [88, 89] and on the non-equilibrium thermodynamics of the dielectric relaxation processes.

The dielectric behavior of cell suspensions as homogenous particles in the electric field is determined by the charges distributed and oriented at the interfaces (interfacial polarization). The charges need time to be accumulated, and, therefore, their magnitudes depend on the field frequency. The temporal respond of each dipole structure to an imposed electric field can be described by the Debye theory of relaxation of the polarization in an isotropic and homogeneous material with single relaxation time [90].

$$\frac{\partial \overline{P}}{\partial t} = -\frac{\overline{P} - \chi \overline{E}}{\tau}, \tag{2.4}$$

where $\overline{P}$ is the polarization vector, χ is the static dielectric susceptibility, and τ is the relaxation time.

Then, the scalar dielectric permittivity of the system $\varepsilon^* = \overline{D}/\overline{E}$ can be expressed as

$$\varepsilon^*(\omega) = \varepsilon_\infty + \frac{\varepsilon_0 - \varepsilon_\infty}{1 + i\omega\tau}, \tag{2.5}$$

where ω is the angular frequency of the electromagnetic wave, and ε_∞ and ε_0 are permittivity at the limiting high ($\omega\tau \gg 1$) and low ($\omega\tau \ll 1$) frequencies.

Then from (2.5), one can obtain

$$\varepsilon' = \text{Re}(\varepsilon^*) = \varepsilon_\infty + \frac{\varepsilon_0 - \varepsilon_\infty}{1 + (\omega\tau)^2}, \quad \varepsilon'' = \text{Im}(\varepsilon^*) = \frac{\omega\tau(\varepsilon_0 - \varepsilon_\infty)}{1 + (\omega\tau)^2}, \tag{2.6}$$

where $\varepsilon''/\varepsilon' = \tan(\delta)$ is the tangent of dielectric losses.

The Debye model introduces the dielectric permittivity in the limits of high and zero frequencies which needs knowledge on approximation of the $\varepsilon'(\omega)$ and $\varepsilon''(\omega)$ curves based on detailed measurements, which is not convenient from the practical point of view [91].

Deviation from the Debye dispersion in the β-dispersion frequency range can be described by the Cole–Cole dispersion function that differs from (2.5) by the Cole–Cole factor $a \in [0, 1[$

$$\varepsilon^*(\omega) = \varepsilon_\infty + \frac{\varepsilon_0 - \varepsilon_\infty}{1 + (i\omega\tau)^{1-a}}. \tag{2.7}$$

A suspension of polarizable particles can be treated as an assembly of induced electric dipoles, and its electrical polarization $\overline{P}(\omega)$ (or dielectric constant $\varepsilon^*(\omega)$) inversely depends on the frequency of applied electric field $\overline{E}(\omega)$. According to

the mixture theory, the dielectric constant of the suspension is described by the Maxwell–Wagner [92, 93] mixture equation:

$$\varepsilon^* = \varepsilon_f^* \frac{(1 + 2C)\varepsilon_p^* + 2(1 - C)\varepsilon_f^*}{(1 - C)\varepsilon_p^* + (2 + C)\varepsilon_f^*}, \tag{2.8}$$

where C is the mass concentration of the particles, ε^*, ε_f^*, ε_p^* are complex dielectric permittivity of the suspension, fluid, and particles correspondingly.

Equation (2.5) describes very well the dielectric polarization of dilute suspensions when the electric field around each particle is not perturbed by the neighbor particles; anyway, applicability of (2.8) has been shown till $C = 0.4$ [94].

The dielectric properties of non-uniform particles like erythrocytes considered as shells (membranes) filled with a concentrated hemoglobin solution can be approximated by the single-shell model [95]

$$\varepsilon^* = \varepsilon_m^* \frac{\left(\frac{r}{r-h}\right)^3 + 2\left(\frac{\varepsilon_{\text{in}}^* - \varepsilon_m^*}{\varepsilon_{\text{in}}^* + 2\varepsilon_m^*}\right)}{\left(\frac{r}{r-h}\right)^3 - \left(\frac{\varepsilon_{\text{in}}^* - \varepsilon_m^*}{\varepsilon_{\text{in}}^* + 2\varepsilon_m^*}\right)} \tag{2.9}$$

where $\varepsilon_m^* = \varepsilon_m - i\sigma_m/\omega$ and $\varepsilon_{\text{in}}^* = \varepsilon_{\text{in}} - i\sigma_{\text{in}}/\omega$ are the effective complex permittivity of the cell membrane and the interior of the cell, accordingly, r is the cell radius, h is the membrane thickness, and σ_m and σ_{in} are electric conductivities.

Due to the relationship $\sigma_m \ll \sigma_{\text{in}}$, at the frequencies well below the Maxwell–Wagner effect (~MHz)

$$\frac{\varepsilon_{\text{in}}^* - \varepsilon_m^*}{\varepsilon_{\text{in}}^* + 2\varepsilon_m^*} \approx 1.$$

The membrane thickness h is very small relative to cell radius ($h \ll r$), then

$$\varepsilon_p^* = \frac{r}{h}\varepsilon_m^* = r\left(C_{\text{spec}} - i\frac{G_{\text{spec}}}{\omega}\right),$$

where C_{spec} and G_{spec} are the specific membrane capacitance and conductance, accordingly.

By using the single-shell model, reliable values of erythrocyte internal conductivity and permittivity have been obtained [96]. Also, the reported values of the membrane capacitance per unit surface [17, 94] were found to be in a good agreement with those of the solvent-free cellular membranes [97, 98].

The single-shell model (2.9) has been generalized for a two-layer particle if the $\varepsilon_{\text{in}}^*$ is also presented in the same form (2.9) with its own additional membrane ε_{m2}^* and internal contents $\varepsilon_{\text{in}2}^*$. By using iteration, the two-layer model can be generalized to the n-layer model which needs material parameters of all the layers included. The 2-shell model has been shown fit well the experimental data measured on the yeast

cells [99]. The second shell has been attributed to the intracellular structure. The n-layer model has been applied to the dielectric properties of lymphoma cells [89].

The non-equilibrium thermodynamic approach for dielectric behavior has been developed in [100–102] and recently used for deeper understanding of the non-equilibrium processes in healthy and malignant cells and tissues in the external electromagnetic fields of low and high frequencies [102, 103]. In this consideration, the specific entropy $s = S/\rho$, where S is the entropy and ρ is the density, was postulated as a function of specific internal energy $u = U/\rho$, strain tensor ε_{ik}, specific polarization vector $p_i = P_i/\rho$, and additional vector field $p_i^{(1)}$ in the form $s = s(u, \varepsilon_{ik}, p_i, p_i^{(1)})$. Therefore, the polarization vector $p_i = p_i^{(0)} + p_i^{(1)}$ was composed of two vectors $p_i^{(0)}$ and $p_i^{(1)}$ corresponded to molecule deformation and rotation polarizations [103].

Then, the partial derivatives $\frac{\partial s}{\partial p_i} = -\frac{1}{T} E_i^{\text{eq}}$ and $\frac{\partial s}{\partial \varepsilon_{ik}} = -\frac{1}{T} \sigma_{ik}^{\text{eq}}$ determine the equilibrium electric field E_i^{eq} and stress tensor σ_{ik}^{eq}, while $\frac{\partial s}{\partial p_i^{(1)}} = -\frac{1}{T} E_i^{(1)}$ determines the electric field $E_i^{(1)}$ corresponded to $p_i^{(1)}$.

The irreversible electric field E_i^{irr} and stress tensor σ_{ik}^{irr} related to irreversible electromechanical processes can be defined then as $E_i^{\text{irr}} = E_i - E_i^{\text{eq}}, \sigma_{ik}^{\text{irr}} = \sigma_{ik} - \sigma_{ik}^{\text{eq}}$.

For an isotropic medium neglecting the cross-coupled effects, the following phenomenological relations have been obtained [102]:

$$E_i^{\text{irr}} = L^{(0,0)} \frac{dP_i}{dt}, \quad \frac{dP_i^{(1)}}{dt} = L^{(1,1)} E_i^{(1)} \tag{2.10}$$

and the relaxation equation for polarization vector

$$\chi_{\text{EP}}^{(0)} E_i + \frac{dE_i}{dt} = \chi_{\text{PE}}^{(0)} P_i + \chi_{\text{PE}}^{(1)} \frac{dP_i}{dt} + \chi_{\text{PE}}^{(2)} \frac{d^2 P_i}{dt^2}, \tag{2.11}$$

where $\chi_{\text{EP}}^{(0)} = a^{(1,1)} L^{(1,1)}$, $\chi_{\text{PE}}^{(0)} = a^{(0,0)}(a^{(1,1)} - a^{(0,0)}) L^{(1,1)}$, $\chi_{\text{PE}}^{(1)} = a^{(0,0)} + a^{(1,1)} L^{(0,0)} L^{(1,1)}$, $\chi_{\text{PE}}^{(2)} = L^{(0,0)}$, and $a^{(0,0)}$ and $a^{(1,1)}$ are state coefficients.

Accounting for the cross-effects, the phenomenological relations (2.7) have the form [103]

$$E_i^{\text{irr}} = L^{(0,0)} \frac{dP_i}{dt} + L^{(0,1)} E_i^{(1)},$$
$$\frac{dP_i^{(1)}}{dt} = L^{(1,0)} \frac{dP_i}{dt} + L^{(1,1)} E_i^{(1)}, \tag{2.12}$$

where $L^{(0,1)} = L^{(1,0)}$ according to the Onsager–Casimir reciprocal relations.

When the material is subjected to a harmonic perturbation of the polarization vector $P = P_0 e^{i\omega t}$, where P_0 is the amplitude, the electric field will oscillate with the same frequency and the phase lag φ ($E = E_0 e^{i(\omega t + \varphi)}$) supposing the linear

response theory is valid for the system. Then, the dielectric storage Γ_1 and loss Γ_2, phenomenological, and state coefficients can be computed as [103, 104]

$$\Gamma_1 = \frac{E_0(\omega)}{P_0} \cos(\varphi(\omega)), \quad \Gamma_2 = \frac{E_0(\omega)}{P_0} \sin(\varphi(\omega)),$$

$$a^{(0,0)}(\omega) = \Gamma_1 + \frac{\Gamma_2^{(1)}}{\omega\tau}, \quad a^{(1,1)}(\omega) = \frac{(\Gamma_2^{(1)} + \Gamma_1\omega\tau)^2}{\omega\tau\Gamma_2^{(1)}(1 + \omega^2\tau^2)},$$

$$L^{(1,1)}(\omega) = \frac{\omega\Gamma_2^{(1)}(1 + \omega^2\tau^2)}{(\Gamma_2^{(1)} + \Gamma_1\omega\tau)^2} = (\tau a^{(1,1)})^{-1}, \quad L^{(0,0)}(\omega) = \frac{\Gamma_{20}}{\omega}, \qquad (2.13)$$

where $\Gamma_1 = \frac{\varepsilon' - \varepsilon^0}{(\varepsilon' - \varepsilon^0)^2 + \varepsilon''^2}$ and $\Gamma_2 = \frac{\varepsilon''}{(\varepsilon' - \varepsilon^0)^2 + \varepsilon''^2}$ are the real and imaginary parts of the complex dielectric susceptibility, $\Gamma_2^{(1)} = \Gamma_2 - \omega L^{(0,0)}$ is the dissipation associated to internal degree of freedom, Γ_{20} is the Γ_2 in the low-frequency limit, and ε^0 is the dielectric constant in vacuum.

Therefore, based on the measurements of ε' and ε'', one can compute the differences in the dielectric properties, input of the equilibrium and non-equilibrium processes, and other important state parameters like entropy production

$$\sigma^{(s)} = \frac{P_0^2}{T}\left(\omega L^{(0,0)} + \frac{\Gamma_2^{(1)}}{(1 + \omega^2\tau^2)}\right)\omega\cos^2(\omega t) \qquad (2.14)$$

for different cells and tissues in healthy and impaired states.

The Cole–Cole model can be derived as a particular case of the extended Kluitenberg's model [103]. The dependencies $\overline{E}^{eq}(\omega), \overline{E}^{irr}(\omega)\overline{E}^{(1)}(\omega), P^{(0)}(\omega), P^{(1)}(\omega), \sigma_s(\omega)$ have been computed for liquid m-toluidine [91], normal and diabetic human blood in the range of $f \sim 10^6 - 10^7$ Hz [94], and normal and malignant liver tissues in the range of $f \sim 10^{10} - 10^{11}$ Hz [2, 3].

The model with two relaxation times [96] is based on the relaxation equation which is a generalization of (2.8)

$$m_2\frac{d^2 E_i}{dt^2} + m_1\frac{dE_i}{dt} + E_i = \chi_0 P_i + k_1\frac{dP_i}{dt} + k_2\frac{d^2 P_i}{dt^2}. \qquad (2.15)$$

Then, for a harmonic varying polarization $P_i = P_i^0 e^{i\omega t}$ the electric field oscillations will be determined from (2.15) as

$$E_i = P_i^0 e^{i(\omega t + \phi)} + C_1 e^{-t/\tau_1} + C_2 e^{-t/\tau_2}, \qquad (2.16)$$

where $\phi = a\tan\left(\frac{\omega k_1}{\chi_0 - \omega^2 k_2}\right)$, $C_{1,2}$ are integration constants, and $\tau_{1,2}$ are roots of the quadratic equation $m_2 + m_1\tau^1 + \tau^2 = 0$.

The Debye model has been generalized for a medium with a set of relaxation phenomena at different scales with different relaxation times $\{\tau_j\}_{j=1}^{N}$ as [105]

$$\varepsilon^*(\omega) = \varepsilon_\infty + (\varepsilon_0 - \varepsilon_\infty) \int_0^\infty \frac{\zeta(\tau)}{1 + i\omega\tau} d\tau, \qquad (2.17)$$

where $\zeta(t)$ is the memory function that describes the non-Markovian relaxation process.

Therefore, the measurement data of the ε' and ε'' values can be used for computations of the following parameters:

(1) from Debye model (2.4)–(2.6): the dielectric loss coefficient $\delta = a \tan(\varepsilon''/\varepsilon')$; the dielectric relaxation frequency of water $f_d = f(\varepsilon' - \varepsilon_\infty)/\varepsilon''$ in the solution/suspension where f is the frequency of the external field; and the activation energy of dipole relaxation ΔF of the water molecules in studied systems $\Delta F = RT \ln\left(\frac{RT}{hN}\tau\right)$, where τ is the time of dielectric relaxation, h is the Plank constant, R is the gas constant, and N is the Avogadro number;

(2) from the single-shell model (2.9): dielectric permittivity ε_m and ε_{in} of the membrane and the internal matter (cytoplasm, free and bound water) separately, provided the values σ_m and σ_{in} and the membrane thickness h are known from other measurements/experiments;

(3) from the non-equilibrium thermodynamic model (2.10)–(2.11) with single relaxation time: phenomenological and state coefficients of the model (2.13) and entropy production (2.14).

2.5 Results and Discussion

2.5.1 Temperature Effects

The temperature dependence of ε' and ε'' for the RBC suspension in PBS of healthy donors and patients with IS before and after therapy is presented in Table 2.1. As it is known for PBS, ε' value increases while ε'' decreases monotonously with temperature [14]. For all studied temperatures, the magnitudes of the permittivity ε' and dielectric losses ε'' in RBC suspensions of ISB patients were significantly higher compared to healthy donors. The applied treatment reduces this tendency for ε' and ε''; a less significant increase in these parameters is observed for ISA samples in comparison with the RBC suspensions of healthy donors.

The temperature dependences of the static permittivity of the erythrocyte suspension of healthy donors and patients with IS before and after the therapy prescribed are shown in Fig. 2.1. The results show that stroke leads to the increase in the static dielectric permittivity of erythrocyte suspensions compared to that of healthy donors practically over the entire temperature range (Fig. 2.1). For a given frequency

Table 2.1 Temperature dependence of the measured ε' and ε'' values for RBC suspensions of healthy donors and patients with IS before and after treatment

T, °C	Erythrocytes (control)		Erythrocytes (ischemic stroke)		Erythrocytes (after therapy)	
	ε'	ε''	ε'	ε''	ε'	ε''
2	34.1 ± 1.0	34.9 ± 0.7	41.7 ± 1.1[a]	33.2 ± 0.8	35.0 ± 1.0[a]	35.4 ± 1.0[a]
5	42.0 ± 1.2	33.3 ± 0.8	44.2 ± 0.7	31.8 ± 0.9	42.6 ± 1.4	34.0 ± 0.9[a]
10	43.2 ± 1.1	32.1 ± 0.8	46.9 ± 1.1[a]	30.4 ± 1.0[a]	42.8 ± 1.2	32.8 ± 1.3
15	47.8 ± 1.2	29.3 ± 1.1	50.5 ± 1.1	28.6 ± 1.0	46.1 ± 1.0	30.3 ± 1.1
20	50.1 ± 1.0	27.0 ± 0.7	53.5 ± 0.8	26.0 ± 1.2	51.1 ± 1.0	27.9 ± 1.1[a]
25	52.8 ± 1.3	25.3 ± 1.1	56.9 ± 1.1[a]	24.2 ± 1.1	53.4 ± 1.0[a]	25.5 ± 1.1[a]
30	54.3 ± 1.3	23.2 ± 0.9	58.6 ± 1.0[a]	22.1 ± 1.0	53.6 ± 1.3	23.4 ± 1.1
35	55.4 ± 1.1	21.2 ± 1.0	59.4 ± 0.9[a]	19.0 ± 1.1	55.6 ± 1.4	22.0 ± 1.4
40	56.5 ± 1.2	19.6 ± 0.8	61.6 ± 0.8[a]	18.4 ± 0.7	58.9 ± 1.1	19.2 ± 1.2
44	57.0 ± 1.0	18.3 ± 0.4	62.9 ± 1.2[a]	16.0 ± 1.0[a]	60.8 ± 1.0[a]	17.3 ± 1.2

[a] reliability of differences in comparison with control (healthy donors), $p \leq 0.05$

$f = 9.2$ GHz, the static dielectric permittivity decreases when increasing temperature. With rise in temperature, both the strength and extent of the hydrogen bond decrease. This promotes the reorientation of dipoles and allows the water molecule to oscillate at higher frequencies; temperature as well reduces the drag to the rotation of the water molecules [14]. Compared to the PBS solutions, in the case of RBC suspensions the dependencies of $\varepsilon_0(T)$ are of non-monotonous character with some deviations from monotonous (increase of ε_0 values at these temperatures in contrast to monotonous decrease of ε_0 values with rise in temperature) in temperature intervals 4–8, 12–15, and ~ 22–26 °C for HD; 12–18 °C for ISB; and 7–9 °C and 25–27 °C for ISA samples. Peculiarities in the same temperature regions were observed for RBC suspensions of different donors within each studied group. In the temperature ranges of 12–20 and 26–36 °C, the maximal statistically significant difference ($p < 0.05$) between values of ε_0 for ISB and HD/ISA groups is observed.

Non-monotonous changes in the static dielectric permittivity ε_0 of RBC suspensions with temperature are determined by the changes in the degree of water binding to erythrocytes and the redistribution of free and bound water in the vicinity of the cell surface due to the rearrangement or oxidation of membrane lipids or conformational changes of membrane proteins. Such changes of ε_0 can also arise from cell aggregation. Erythrocytes under conditions of impaired cerebral circulation adsorb fibrinogen and fibrin lysis products, impair their ability to deform, and lose part of the surface electric charge. All these factors increase the risk of cell disruption and spontaneous mutual aggregation. However, in the temperature interval and cell concentration studied in the present work no formation of cell aggregates or associates was reported in the available literature. Moreover, concentration dependencies of ε' and ε'' were linear in the cell concentration range studied (not illustrated) that

Fig. 2.1 Temperature
dependence of static
permittivity ε_0 for the RBC
suspension in 0.15 M sodium
phosphate buffer
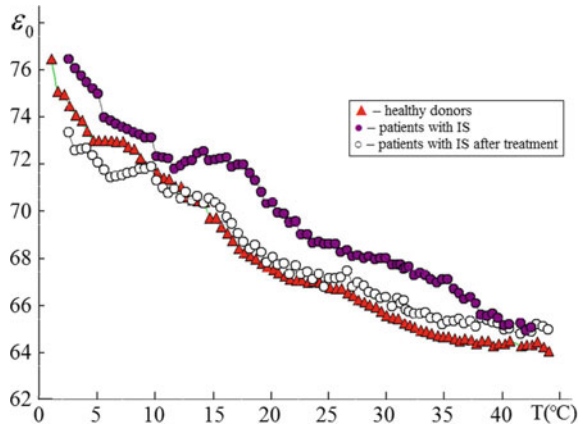
evidences no cell aggregation in our experiments. Thus, we attribute peculiarities observed on the ε', ε'', and ε_0 temperature dependencies (Fig. 2.1 and Table 2.1) to the cell membrane protein conformational change and membrane lipid rearrangements under the action of temperature. Profound increase of ε_0 in the range of $T = 12–18$ °C for ISB samples indicates dehydration of RBC membranes of ischemic patients at these temperatures.

It is known that the increment of static permittivity ε_0 of the cell suspension relative to the solvent is proportional to the hydration of erythrocyte cell membrane [54]. The degree of hydration of the erythrocyte membrane of ISB patients decreases in the temperature range from 5 to 10 °C, in the ranges of $T \sim 12–18$ and 26–36 °C. In IS patients, an increase in the static dielectric permittivity ε_0 may indicate a decrease in the thickness of the hydrated perimembrane unstirred layer of erythrocyte, decrease of the amount of bound water in it. Deviations from the monotonous decrease in the static dielectric permittivity ε_0 of erythrocytes of patients with stroke in the temperature ranges of 5–10 and 37–44 °C indicate a decrease in the amount of free water and thus increase in the hydration of the cell membrane.

IS is associated with the activation of free radical oxidation of lipids in the erythrocyte membrane. The increase in the amount of free water molecules in the erythrocyte suspensions in the ranges of $T = 12–20$ and 26–36 °C is a consequence of the damage of cell membranes by reactive oxygen species. IS contributes to the fluidization of the lipid bilayer of the RBC membrane and the formation of channels of passive permeability due to the formation of hydroperoxides of fatty acids. Changes in the static dielectric permittivity ε_0 of RBC of patients after therapy approach the values of the static permittivity of healthy donors, which indicates a decrease in the amount of free water in the system, which is the "marker" of the disease.

2.5.2   Time of Dielectric Relaxation Study

The dielectric properties of cell suspensions in the microwave range of frequencies are mainly determined by the presence of free water. Water interacts with molecules through hydrogen bond clusters. Cell suspensions exhibit a basic dispersion of the Debye type or close to the Debye type at microwaves. The mechanism of this dispersion is rotational diffusion of polar water molecules or their clusters [36, 37].

   The mean values of the frequency of the dielectric relaxation f_d of the water molecules in erythrocyte suspensions of the groups under study are shown in Fig. 2.2. It can be seen that after the therapy, the temperature dependences for HD and ISA groups practically coincide in the temperature range from 2 to 26 °C. The results [10–14] confirm the assumption that the dielectric properties of intracellular water are the same as in free water. According to our data, the mean value of the frequency of the dielectric relaxation f_d of water molecules in the erythrocyte suspension at a temperature of 20 °C in the group of healthy donors is $f = 15.1$ GHz, which is somewhat less than that of pure water (16.4 GHz). The obtained value is close to the value of f_d of bulk water molecules at 20 °C (13.6 GHz) obtained in [53–55] and close to the data obtained by other authors ($f = 16.7$, 15.8, and 12.6 GHz) given in the same papers. The value of the frequency of the dielectric relaxation f_d of erythrocyte water molecules in the group of patients in the acute period of IS is 17 GHz, which is somewhat higher than in pure water (16.4 GHz), and this can indicate the presence of some amount of free water and the disorganization of the erythrocyte membrane.

   Frequency of dielectric relaxation of free water molecules f_d for water and thin electrolyte solution increases with temperature practically linearly [10]. Value of frequency of dielectric relaxation f_d characterizes the mobility of free water molecules in external electromagnetic fields. The bound water is excluded from

Fig. 2.2 Temperature dependence of dielectric relaxation frequency f_d of the water molecules in RBC suspensions
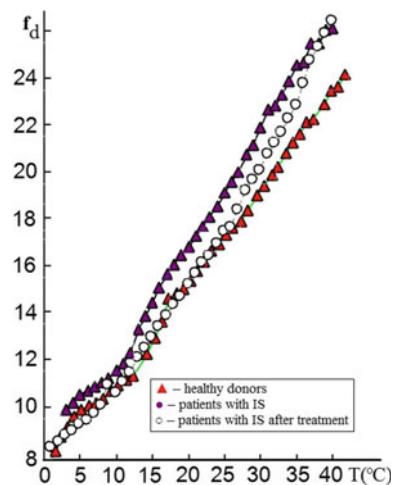
the total water relaxation in solution because its mobility is less than mobility of free water. Thus, in the case of RBC suspensions we have less amount of free water molecules and, consequently, lower value of f_d. Temperature dependencies of f_d for RBC suspensions have a number of kinks. In Fig. 2.2, four linear segments can be distinguished on the temperature dependences of f_d: below and above 12, 26 and 36 °C.

Arrhenius plots of the f_D allowed us to calculate activation energy of the dielectric relaxation for free water molecules in studied RBC suspensions. For the suspension of HD erythrocytes in the temperature ranges of 2–12, 12–20, 26–36, and 36–45 °C, observed kinks on $f_D(T)$ plots are accompanied by an increase in the activation energy by 11 kJ/mol at 12 °C, decrease by 14 kJ/mol at 36 °C, and an increase in the activation energy in the temperature range of 36–45 °C by 5.08 kJ/mol. For the suspension of ISB erythrocytes, activation energy in the range of 12 °C increased by 10.47 kJ/mol and by 3.44 kJ/mol in the range of 36–45 °C. The significant changes in the values of activation energy of the dielectric relaxation of water molecules, which approach the values of activation energy of the dielectric relaxation of water molecules of healthy donors, have been observed after therapy.

If the energy of the hydrogen bond is estimated at 12.5 kJ/mol [39], then in the RBC suspensions of healthy donors each water molecule forms 1.5 to 2.5 H-bonds with neighboring molecules (Table 2.2). In the RBC suspensions of IS patients, each water molecule forms 1–2 H-bonds with neighboring molecules. Along with our data on the change in the activation energy of the process of dielectric relaxation of free water molecules in the erythrocyte suspension, the results presented here suggest that the reason for the change in the dielectric relaxation frequency of water molecules in the suspensions in patients with IS in comparison with healthy donors is an increase in the thickness of hydration layer of their RBC membrane.

Structural transition in the IS RBC membrane observed at $T = 12$–20 °C is accompanied by a change in the ratio of free and bound water (Figs. 2.1 and 2.2). In addition, the mobility of free water varies. These data show that in the region of 12–20 °C the structural transition in the erythrocyte membrane of IS patients occurs, which can be attributed to the zone of protein-rich phospholipids. Increasing the hydration of erythrocyte membranes leads to an increase in the thickness of the hydrate layer, which can lead to a slowing of the diffusion of water through the

Table 2.2 Activation energy of the dielectric relaxation of water molecules in RBC suspensions

	Control	IS	IS after treatment
T, °C	ΔE, kJ/mol	ΔE, kJ/mol	ΔE, kJ/mol
2–12	19.03 ± 0.6	13.54 ± 0.6*	19.05 ± 0.3*
12–20	30.31 ± 0.4	24.01 ± 0.5*	29.82 ± 0.6*
26–36	16.21 ± 0.6	11.12 ± 0.6*	16.39 ± 0.4*
36–45	21.29 ± 0.6	14.56 ± 0.3*	23.16 ± 0.6

*Statistical significance (or significance level) is the probability of the study rejecting the null hypothesis, given that the null hypothesis is true

membrane. It has been repeatedly reported in the literature that changes in the lipid composition and fatty acid spectrum of membranes in IS patients can lead to the formation of a less dense hydrocarbon zone at the center of the bilayer and to a lesser structural strength of membrane.

The development of IS is largely due to the progressing athero- and arteriosclerotic processes in the vessels of the brain. These include a change in blood flow velocity, a decrease in the electric charge of the cell wall, and a change in the pH level of the environment due to chronic hypoxia. At the same time, the anticoagulant properties of the endothelium decrease, and the vascular wall reactivity is impaired by increasing its rigidity. An increase in the cholesterol content in erythrocyte membranes plays an important role in the pathogenesis of many diseases, including cerebrovascular pathology. The incorporation of cholesterol molecules into the erythrocyte membrane leads to an increase in their size and a change in the shape of the cells, affects the receptor apparatus, and reduces the mobility of the cell in the electric field, which sharply disrupts the filtration capacity, increasing the amount of free water. The phase state of lipids is an important factor in regulating membrane plasticity and its permeability. A huge number of erythrocytes in the bloodstream, a large adsorption surface, and an intensive exchange of cholesterol between erythrocytes and blood plasma create a powerful and rapidly exchanging erythrocyte-plasma pool. Violations of the regulation of the exchange of this pool due to changes in the composition and physical organization of erythrocyte membranes lead to the occurrence of hypercholesterolemia, which is an important risk factor for acute cerebral circulation impairment.

Since the realization of the stress reaction of the organism is directly related to the functional state of the membrane-receptor complex of cells, investigation of the relationship of cerebrovascular disorders with the features of the membrane complex will allow personifying approaches to the prevention of development and progression of cerebral circulation disorders. The detected temperature-dependent changes in the dielectric parameters, namely ε_0 and f_d, of the PBS suspension of RBC of IS patients could be used as complementary diagnostic facility for clinical application. Further considerations and more sophisticated models of water relaxation with measurements at several frequencies in GHz range could bring new insights on the molecular mechanisms of ischemic stroke cellular effects.

2.6 Conclusions

Temperature-dependent changes in the dielectric parameters of the erythrocyte suspensions in patients with IS were studied. It was shown that the activation energy of dipole relaxation of water in RBC suspension of healthy donors and IS patients after therapy is close to each other, which indicates a similar molecular mechanism of disease development and recovery after the treatment. Both processes involve breakup of a certain number of hydrogen bonds between water molecules.

Temperature-induced structural rearrangements of erythrocyte membranes cause changes in the structure of the solvent. Structural transition of membranes of erythrocytes in patients in the temperature ranges of $T = 2–12$ °C and $T = 12–20$ °C is accompanied by a change in the ratio of bound and free water and an increase in the frequency of dielectric relaxation of water in the suspensions of patients compared with healthy donors, which leads to an increase in the amount of free water. In the temperature ranges of 2–12, 12–20, 26–36, and 36–45 °C, increase of the activation energy of dipole relaxation occurs.

The structural transition in RBC membranes is preceded by the dehydration of the membrane components, which results in a decrease in the mobility of the water molecules in the erythrocytes as compared with the mobility of water in the surrounding physiological solution. The unidirectional character of the violations of the temperature dependence of the frequency of the dielectric relaxation of the water molecules of the erythrocyte suspension in patients with IS found during the study shows that these disorders can be considered as non-specific signs of involvement of the RBC into the complex set of changes in the body that accompany the development of cerebral circulation disorders.

The method of microwave dielectrometry at $f = 9.2$ GHz is a promising method for the integral assessment of pathology, associated with ischemic stroke.

References

1. Cherevko V, Kizilova N (2017) Complex flows of micro/nanofluids with velocity slip boundary conditions. In: Fesenko O, Yatsenko L (eds) Nanophysics, nanomaterials, interface studies, and applications. Springer Proceedings in Physics, vol 183, pp 207–230
2. Kizilova N (2019) Electromagnetic properties of blood and its interaction with electromagnetic fields. In: Berhardt LV (ed) Advances in medicine and biology, vol 137. NOVA Sci. Publ, pp 1–74
3. Batyuk L, Kizilova N (2018) Modeling of dielectric permittivity of the erythrocytes membrane as a three-layer model. In: Development trends in medical science and practice: the experience of countries of Eastern Europe and prospects of Ukraine. Baltija Publishing, Riga, pp 18–37
4. GBD 2019 Stroke Collaborators (2021) Global, regional, and national burden of stroke and its risk factors, 1990–2019: a systematic analysis for the Global Burden of Disease Study 2019. Lancet 20:795–820
5. Americal Heart Association. 2021 Heart disease and stroke statistical update fact sheet. Electronic resource. https://www.heart.org/-/media/PHD-Files-2/Science-News/2/2021-Heart-and-Stroke-Stat-Update/2021_Stat_Update_factsheet_Global_Burden_of_Disease.pdf
6. del Zoppo GJ, Mabuchi T (2003) Cerebral microvessel responses to focal ischemia. J Cereb Blood Flow Metab 23:879–894
7. Mozos I (2015) Links between vitamin D deficiency and cardiovascular diseases. Biomed Res Int 2015:109275
8. Batyuk LV, Gatash SV, Gorobchenko OA, Nikolov TO (2003) The study of hydration of erythrocyte membranes before and after radiation therapy. Biophys Bull 13:72–78
9. Frauenfelder H, Fenimore PW, McMahon BH (2002) Hydration, slaving and protein function. Biophys Chem 98:35–48
10. Jenin PC, Schwan HP (1980) Some observations on the dielectric properties of hemoglobin's suspending medium inside human erythrocytes. Biophys J 3:285–294

11. Robinson GW, Zhu SB, Singh S, Evans MW (1996) Water in biology, chemistry, and physics: experimental overviews and computational methodologies. World Scientific, Singapore

12. Hackl EV, Gatash SV, Nikolov OT (2005) UHF-dielectrometry to study protein structural transitions. J Biochem Biophys Meth 63:137–148

13. Levin RL, Cravalho EG, Huggins CE (1976) Effect of hydration on the water content of human erythrocytes. Biophys J 16:1411–1426

14. Steinhoff H-J, Kramm B, Hess G, Owerdieck C, Redhardt A (1993) Rotational and translational water diffusion in the hemoglobin hydration shell: dielectric and proton nuclear relaxation measurement. Biophys J 65:1486–1495

15. Lo EH, Dalkara T, Moskowitz MA (2003) Mechanisms, challenges and opportunities in stroke. Nat Rev Neurosci 4:399–415

16. Sundquist J, Blas S, Hogan JE, Davis FB, Davis PJ (1992) The alpha 1-adrenergic receptor in human erythrocyte membranes mediates interaction in vitro of epinephrine and thyroid hormone at the membrane Ca(2+)-ATPase. Cell Signal 4:795–799

17. Asami K, Takahashi Y, Takashima S (1989) Dielectric properties of mouse lymphocytes and erythrocytes. Biochim Biophys Acta 1010:49–55

18. Batyuk L (2015) Influence of cancer disease on dielectric characteristics of structural-functional state of erythrocyte membranes. ScienceRise Med Sci 7:11–17

19. Batyuk L, Shckorbatov Y, Kizilova N, Astapovich D, Berest V (2017) Study of the influence of the electromagnetic field on the state of erythrocytes of patients with acute ischemic stroke by the method of UHF dielectrometry. In: International Turkish congress on molecular spectroscopy (TURCMOS2017), Bodrum, Turkey, pp 182–183

20. Sager G, Jacobsen S (1985) Effect of plasma on human erythrocyte beta-adrenergic receptors. Biochem Pharmacol 34:3767–3771

21. Massaccesi L, Galliera E, Romanelli MMC (2020) Erythrocytes as markers of oxidative stress related pathologies. Mech Ageing Devel 191:111333

22. Kiefer CR, Snyder LM (2010) Oxidation and erythrocyte senescence. Curr Opin Hematol 7:113–116

23. Momtselidze N, Mantskava M, Mchedlishvili G (2006) Hemorheological disorders during ischemic brain infarcts in patients with and without diabetes mellitus. Clin Hemorheol Microcirc 35:261–264

24. Hatamian H, Saberi A, Pourghasem M (2014) The relationship between stroke mortality and red blood cell parameters. Iran J Neurol 13:237–240

25. Pethig R (1984) Dielectric properties of biological materials: biophysical and medical applications. IEEE Trans Electr Insul E1–19:453–547

26. Foster KR, Schwan HP (1989) Dielectric properties of tissues and biological materials: a critical review. Crit Rev Biomed Eng 17:25–104

27. Gabriel C, Gabriel S, Corthout E (1996) The dielectric properties of biological tissues: I. Literature survey. Phys Med Biol 41:2231–2249

28. Gabriel S, Lau R, Gabriel C (1996) The dielectric properties of biological tissues: II. Measurements in the frequency range 10 to 20 GHz. Phys Med Biol 4:2251–2269

29. Peyman A, Gabriel C (2012) Dielectric properties of porcine glands, gonads and body fluids. Phys Med Biol 57:339–344

30. Alison J, Sheppard R (1993) Dielectric properties of human blood at microwave frequencies. Phys Med Biol 3:971–978

31. Jaspard F, Nadi M, Rouane A (2003) Dielectric properties of blood: an investigation of haematocrit dependence. Physiol Meas 24:137–147

32. Lonappan A, Thomas V, Bindu G, Rajasekaran C, Mathew KT (2007) Nondestructive measurement of human blood at microwave frequencies. J Electromagn Waves Appl 21:1131–1139

33. Lisin R, Ginzburg BZ, Schlesinger M, Feldman Y (1996) Erythrocytes and ghosts. Biochimica et Biophysics Acta 1280:34–40

34. Bonincontro A, CamettiC, Rosi A, Sportelli L (1989) Electrical parameters of erythrocyte membranes deduced from radiowave conductivity measurements. J Membrane Sci 41:345–352

35. Dix JA, Solomon AK (1984) Role of membrane proteins and lipids in water diffusion across red cell membranes. Biochim Biophys Acta 773:219–230
36. Kashyap SC (1981) Dielectric properties of blood plasma. Electron Lett 17:713–714
37. Gallagher PG (2017) Disorders of erythrocyte hydration. Blood 130:2699–2708
38. Kontogeorgis GM, Maribo-Mogensen B, Thomsen K (2018) The Debye-Hückel theory and its importance in modeling electrolyte solutions. Fluid Phase Equilib 462:130–152
39. Grimnes S, Martinsen OG (2008) Bioimpedance and bioelectricity basics. Academic Press, San Diego, USA
40. Sodhi CS, de Sena LC, Ozelim M, Rathie PN (2021) Dielectric relaxation model of human blood as a superposition of Debye functions with relaxation times following a modified-Weibull distribution. Heliyon 7:e06606
41. Tuvia S, Moses A, Gulayev N, Levin S, Korenstein R (1999) β-Adrenergic agonists regulate cell membrane fluctuations of human erythrocytes. J Physiol 516:781–792
42. Satoru M, Shinichi K, Shin Y (1989) The dielectric relaxation of mixtures of water and primary alcohol. J Chem Phys 90:3292–3294
43. Gatash SV (1999) Very high frequency dielectrometer for the study of dynamical properties in disperse water systems. Radiophys Electron 4:129–132
44. Chelidze T (2002) Dielectric spectroscopy of blood. J Non-cryst Solids 305:285–294
45. (2003) European stroke initiative recommendations for stroke management-update. Cerebrovasc Dis 16:311–337
46. Kjellstrom T, Norrving B, Shatchkute A (2007) Helsingborg declaration 2006 on European stroke strategies. Cerebrovasc Dis 23:231–241
47. Current principles of diagnosis and treatment of patients with acute ischemic stroke and TIA. Evidence based adapted clinical guideline: order of MoH of Ukraine 03.08.2012 No. 602
48. Spetzler RF, Detwiler PW, Riina HA, Porter RW (2002) Modified classification of spinal cord vascular lesions. J Neurosurg 96:145–156
49. Adibhatla RM (2002) Citicoline: neuroprotective mechanisms in cerebral ischemia. J Neurochem 80:12–13
50. Razali NM, Wah YB (2011) Power comparisons of Shapiro-wilk, kolmogorov-smirnov, lilliefors and anderson-darling tests. J Statist Mode Analytics 2:21–33
51. Altman DG (1991) Practical statistics for medical research. Chapman and Hall, London
52. Sachs L (2004) AngewandteStatistik: Anwendungstatistischer Methoden. Springer, Berlin Heidelberg
53. Suzuki M, Shigematsu J, Kodama T (1996) Hydration study of proteins in solution by microwave dielectric analysis. J Phys Chem 100:7279–7282
54. Kuwabara Sh (1987) Dielectric relaxation time and structure of bound water in biological materials. J Phys Chem 91:6337–6338
55. Frohlich H (1987) Theory of dielectrics: dielectric constant and dielectric loss, 2nd ed. Oxford Univ. Press
56. Tuszynski JA, Hameroff S, Satari MV, Trpisova CB, Nip MLA (1995) Ferroelectric behavior in microtubule dipole lattices: implications for information processing, signaling and assembly/disassembly. J Theor Biol 174:371–380
57. Pokorny J, Hasek J, Jelinek F, Saroch J, Palan B (2001) Electromagnetic activity of yeast cells in the M-phase. Electro-Magnetobiol 20:371–396
58. Zheng J, Pollack GH (2003) Long-range forces extending from polymer-gel surfaces. Phys Rev E 68:031408
59. Zheng J, Chin W, Khijniak E, Khijniak Jr, Pollack GH (2006) Surfaces and interfacial water: evidence that hydrophilic surfaces have long-range impact. Adv Colloid Interface Sci 127:19–27
60. Pollack G, Cameron I, Wheatley D (2006) Water and the cell. Springer, Dordrecht, the Netherlands
61. Amos LA (1979) Structure of microtubules. In: Roberts K, Hyam JS (eds) Microtubules Academic Press, London, UK, pp 1–64

62. Stebbings H, Hunt C (1982) The nature of the clear zone around microtubules. Cell Tissue Res 227:609–617
63. Ling GN (2003) A new theoretical foundation for the polarized oriented multilayer theory of cell water and for inanimate systems demonstrating long-range dynamic structuring of water molecules. Physiol Chem Phys Med NMR 35:91–130
64. Tyner KM, Kopelman R, Philbert MA (2007) Nanosized voltmeter' enables cellular-wide electric field mapping. Biophys J 93:1163–1174
65. Pokorny J (2012) Physical aspects of biological activity and cancer. AIP Adv 2:011207
66. Tiffert T, Lew VL, Ginsburg H et al (2005) The hydration state of human red blood cells and their susceptibility to invasion by Plasmodium falciparum. Blood 105:4853–4860
67. Seyfarth EA (2006) Julius Bernstein (1839–1917): pioneer neurobiologist and biophysicist. Biol Cybern 94:2–8
68. Schwan HP (1957) Electrical properties of tissue and cell suspensions. In: Lawrence JH, Tobias CA (eds) Advances in biological and medical physics, vol 5. New York, Academic, pp 147–209
69. Polk Ch, Postow E (1995) Handbook of biological effects of electromagnetic fields, 3rd ed, 2-volume Set. CRC Press
70. Duck FA (1990) Physical properties of tissue: a comprehensive reference book. Academic Press, London
71. Gabriel C, Gabriel S, Corthout E (1996) The dielectric properties of biological tissues: I. Literature survey. Phys Med Biol 41:2231–2249
72. Gabriel S, Lau RW, Gabriel C (1996) The dielectric properties of biological tissues: II. Measurements in the frequency range 10 to 20 GHz. Phys Med Biol 41:2251–2269
73. Grimnes S, Martinsen OG (2000) Bioimpedance and bioelectricity basics. Academic Press, London
74. Asami K (2011) Design of a measurement cell for low-frequency dielectric spectroscopy of biological cell suspensions. Meas Sci Technol 22:085801
75. Asami K (2002) Characterization of biological cells by dielectric spectroscopy. J Non-Cryst Solids 305:268–277
76. Bao J-Z, Davis ChC, Swicord ML (1994) Microwave dielectric measurements of erythrocyte suspensions. Biophys J 66:2173–2180
77. Foster KR, Schwan HP (1996) Dielectric properties of tissues. In: Polk C, Postow E (eds) Handbook of biological effects of electromagnetic fields, 2nd ed. CRC Press
78. Pethig R, Kell DB (1987) The passive electrical properties of biological systems: their significance in physiology, biophysics and biotechnology. Phys Med Biol 32:933–970
79. Gimsa J, Wachner D (1998) A unified resistor–capacitor model for impedance, dielectrophoresis, electrorotation, and induced transmembrane potential. Biophys J 75:1107–1116
80. Asami K, Hanai T, Koizumi N (1977) Dielectric properties of yeast cells: effect of some ionic detergents on the plasma membranes. J Membr Biol 34:145–156
81. Hayashi Y, Oshige I, Katsumoto Y, Omori Sh, Yasuda A, Asami K (2008) Dielectric inspection of erythrocyte morphology. Phys Med Biol 53:2553–2564
82. Schwan HP, Foster KR (1980) RF-field interactions with biological systems: electrical properties and biophysical mechanisms. Proc IEEE 68:104–113
83. Pething R (1984) Dielectric properties of biological materials: biophysical and medical applications. IEEE Trans Electr Insul 19:453–473
84. Gabriel C, Peyman A (2018) Dielectric properties of biological tissues; variation with age, Chapter 69. In: Conn's handbook of models for human aging, 2nd ed., pp 939–952
85. Braun D, Schmollngruber M, Steinhauser O (2017) Towards a complete characterization of the delta-dispersion in dielectric spectroscopy of protein-water systems. Phys Chem Chem Phys 19:26980–26985
86. Maxwell JC (1891) A treatise on electricity and magnetism, vol 1. Clarendon Pres, Oxford
87. Wagner KW (1914) Erklarung der dielectricshen-narchwirkugen auf grund maxwellscher vorstellungen. Arch Electrotech 2:371–387

88. Pauly H, Schwan HP (1959) The impedance of a suspension of spherical particles surrounded by a shell. Z Naturforsch 14:125–131
89. Irimajiri A, Hanai T, Inouye A (1979) A dielectric theory of "multi-stratified shell" model with its application to a lymphoma cell. J Theor Biol 78:251–269
90. Debye P (1945) Polar mollecules. Dover Publications, New York
91. Farsaci F, Rogolino P (2012) An alternative dielectric model for low and high frequencies: a non-equilibrium thermodynamic approach. J Non-Equilib Thermodyn 37:27–41
92. Rao CR, Jaleeli KA, Bellubbi BS, Ahmad A (2009) Dielectric nature of cancerous erythrocytes. J. Pure Appl Phys 21:201–203
93. Damadian R (1971) Tumor detection by nuclear magnetic resonance. Science 171:1151–1153
94. Davey CL, Davey HM, Kell DB (1992) On the dielectric properties of cell suspensions at high volume fractions. Bioelectrochem Bioenerg 28:319–340
95. Jones TB (1995) Electromechanics of particles. Cambridge University Press, New York
96. Kaneko H, Asami K, Hanai T (2011) Dielectric analysis of sheep erythrocyte ghost. Examination of applicability of dielectric mixture equations. Colloid Polym Sci 269:1039–1044
97. Benz R, Janko K (1976) Voltage-induce capacitance relaxation of lipid bilayer membranes. Effects of membrane composition. Biochim Biophys Acta 455:721–738
98. Fettiplace R (1999) The influence of the lipid on the water permeability of artificial membranes. Biochim Biophys Acta 513:1–10
99. Raicu V, Raicu G, Turcu G (1996) Dielectric properties of yeast cells as simulated by the two-shell model. Bioch Biophys Acta 1274:143–148
100. Kluitenberg GA (1973) On dielectric and magnetic relaxation phenomena and non-equilibrium thermodynamics. Physica 68:75–82
101. Kluitenberg GA (1977) On dielectric and magnetic relaxation phenomena and vectorial internal degrees. Physica A 87:302–330
102. Kluitenberg GA (1981) On vectorial internal variables and dielectric and magnetic relaxation phenomena. Physica A 109:91–122
103. Farsaci F, Ficarra S, Russo A et al (2015) Dielectric properties of human diabetic blood: thermodynamic characterization and new prospective for alternative diagnostic techniques. J Adv Diel 5:1550021
104. McCrum NG, Read BE, Williams G (1967) Anelastic and dielectric effects in polymeric solids. Wiley, London
105. Pérez-Madrid A, Lapas LC, Rubí JM (2017) Multiscale model for the dielectric permittivity. Z Naturforsch 72:109–114
106. Wang J-R, Sun B-Y, Wang H-X, Pang S, Xu X, Sun Q (2014) Experimental study of dielectric properties of human lung in vitro. J Med Biol Eng 34:598–604
107. Ciancio V, Farsaci F, Rogolino P (2009) Phenomenological approach on wave propagation in dielectric media with two relaxation times. Physica B 404:320–324

Chapter 3
Catalysis of Wastewater Pollutants by Ruthenium Nanooxide in Porous Glass

I. K. Doycho, S. A. Gevelyuk, L. M. Filevska, and V. S. Grinevych

3.1 Introduction

Phenol is one of the main wastewater pollutants in industry and in everyday life. Usually, this strong antiseptic is used in medicine as a disinfectant. However, due to its disinfecting properties, it gets into the environment and has a detrimental effect on flora and fauna. Therefore, for environmental reasons, wastewater should be purified from phenol. Since the oxides of phenol derivatives are insoluble in water, the oxidation of the pollutant is the simplest way to purify wastewater. Due to the peculiarities of the molecular structure of phenol and its derivatives, wastewater purification is usually done by catalytic oxidation, which makes it possible the transition to closed waste-free technologies.

3.2 The Formulation of the Problem

Phenol is highly soluble in water and therefore is a persistent environmental pollutant. It is difficultly oxidized, as this would lead to the formation of energetically extremely disadvantageous dangling bonds. A phenol derivative, hydroquinone, upon oxidation forms water-insoluble oxides without dangling bonds. Consequently, the conversion of phenol to hydroquinone followed by oxidation on air [1–3] and precipitation of the oxide is one of the simplest ways to remove phenol from wastewater. Hydroquinone has two tautomeric forms: hydroquinone-2, the oxide of which is schematically shown in Figs. 3.1 and 3.3), and hydroquinone-4, (Figs. 3.1 and 3.4). The unequal

I. K. Doycho · S. A. Gevelyuk · L. M. Filevska (✉) · V. S. Grinevych
Odesa I.I. Mechnikov National University, Dvoryanska Str., 2, Odesa 65082, Ukraine
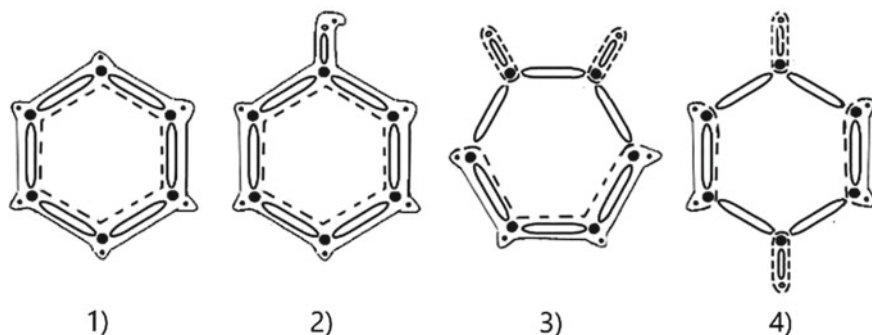e-mail: lfilevska@gmail.com

Fig. 3.1 Schematic distribution of the electron charge density in benzene (1), phenol (2), hydroquinone-2 oxide (3), and hydroquinone-4 oxide (4). Large black circles represent carbon, small ones—hydrogen, medium white—oxygen. Solid thick lines indicate the region of propagation of $ss\sigma$ and $pp\sigma$ bonds, thin solid ones—$sp\sigma$ bonds and dashed ones—$pp\pi$ bonds

distribution of the electron charge density in both oxides differs significantly from the uniform charge distribution in benzene or phenol.

Thus, in order to carry out the transition of phenol to hydroquinone with subsequent oxidation, it is necessary to change significantly the electronic configuration inside the benzene ring, which requires catalytic oxidation. The phenol molecule is a benzene ring, five carbon atoms in which have the same configuration as benzene, and the sixth is physically isolated. It, as in benzene, is bonded to the rest of the ring atoms by two $ss\sigma$ and one $pp\pi$ bonds and is bonded to the oxygen of the hydroxyl group by a $pp\sigma$ bond. Therefore, the uniformity of the electron charge density on the benzene ring in the case of phenol is somewhat distorted (compare positions 1 and 2) in Fig. 3.1. Phenol is difficult to oxidize, since this would lead to the formation of energetically extremely unfavorable dangling bonds, whereas its derivative, hydroquinone, being oxidized, does not form the dangling bonds, and its oxides are insoluble in water. Thus, the simplest way to remove phenol from wastewater is to convert it into hydroquinone, followed by oxidation and precipitation of the oxide. The distribution of the charge density of the oxides of both tautomeric forms of hydroquinone is shown schematically in positions (3) and (4) of Fig. 3.1. It can be seen that in both cases, it differs significantly from the uniform charge distribution in benzene or phenol. Thus, in order to carry out the transition of phenol to hydroquinone, followed by oxidation, catalytic oxidation should be used to change the electronic configuration in the desired direction. The role of a catalyst can be played by a substance which can as easily capture and also easily return electrons back. According to the Frank-Kondom principle, such processes occur simultaneously and instantly, and thus, inside the benzene ring, the electronic charge can be significantly redistributed, despite its inertness. At the same time, the atoms of the catalyst will play the role of a kind of "pantry" where a hindering electron can be placed, and then, taken back and moved to the required node. A metal with two uncompleted electron shells, the upper one of which is s-shell, can play the role of

such a catalyst [4, 5]. The capture of an electron to complete the upper shell in this case will be energetically unfavorable, since in this case, the lower shell will remain incomplete and the metal will tend to return the captured electron.

Thus, the catalytic properties are associated with the contradiction between the Pauli principle and the principle of minimum total energy of the system. Platinum group metals have such properties, and the cheapest of them is ruthenium with an external electronic configuration of $4d^7 5s^1$. Since the surface atoms will participate most actively in the catalytic process, in order to increase the efficiency of the reaction, the maximum development of the surface should be achieved [6, 7]. Aiming this, it is advisable to transform ruthenium into an ensemble of nanoparticles within a suitable matrix.

3.3 The Choice of Matrix

The creation of an appropriate ensemble of nanoparticles needs a suitable matrix, within which it will be formed. Ruthenium as a metal practically cannot be inserted into any kind of porous matrix. But the matrix can be impregnated by a solution of some ruthenium compound, soluble in water. This compound is an aqueous ruthenium trichloride $RuCl_3 \times H_2O$. By co-precipitation at high temperatures in the presence of caprylic acid and NaOH, this salt interacts with atmospheric oxygen, forming, depending on the process temperature, ruthenium dioxide or tetroxide. Both are insoluble in water, but ruthenium dioxide is preferred for the catalytic oxidation of phenol. It retains two free orbitals $5s^1$ and $4d^{10}$, which carry out catalysis by the "capture-return of an electron" mechanism rearranging the electronic configuration in the benzene ring. In ruthenium tetroxide, all orbitals are occupied and catalysis by the indicated mechanism is impossible [8, 9].

The matrix that will be used to form an ensemble of nanoparticles must correspond to a number of requirements. First of all, it must be mechanically strong. In addition, since the process of formation of nanoparticles occurs directly in the pores, it must be chemically inert. Therefore, porous silicon should be immediately considered unsuitable due to several reasons. It is mechanically enough fragile, and, since it is created from silicon wafers by anodizing for p-type and with simultaneous illumination for n-type wafers, it may be considered unstable to electric current and photoexcitation. Co-precipitation occurs at a sufficiently high temperature: if the process temperature is more than 700 °C, then ruthenium tetroxide will be predominantly synthesized, and at temperatures below 700 °C, ruthenium dioxide will be synthesized. Regarding this, the authors of [10] have developed heat-resistant organosilicate rods based on carbon in the form of graphene [11]. They are well resistant to temperatures of 700 °C, at which co-precipitation occurs as quickly as possible. At the same time, this advantage is rather arbitrary, since the formation of both RuO_2 and RuO_4 nanoparticles is possible at such a co-precipitation temperature. Since ruthenium dioxide, like hydroquinone oxide, is insoluble in water, its high adhesion to the matrix walls is very important. This will prevent the catalyst

from leaching out and precipitating along with the hydroquinone oxide, which would lead to an increase in catalyst consumption. Organosilicate rods [12–14] are rather large-pored and therefore attempt to use them as a matrix give a rather high catalyst leakage (over 5% in one cleaning session, which lasts about 8 h). Thus, as a matrix for the formation of an ensemble of RuO_2 nanoparticles, porous silicate glass can be used, which is sufficiently strong mechanically and chemically inert. In reality, heating above 650 °C destroys its structure, but there is no such need [8, 9]. Mainly, RuO_2 can also be formed at 400 °C, but its co-precipitation process will be much slower. At the same time, during slow thermosynthesis, smaller nanoparticles will be formed [15], which means that their active surface will be larger and the catalytic oxidation of phenol will be more efficient.

Depending on the technological features of the formation, four types of porous silicate glass A, B, C, and D are usually considered. The technology for producing each of these types of glasses is described in detail in [16]. An electron microscopic image of their structure is shown in Fig. 3.2. The types of glass differ in pores sizes and in the presence or absence of secondary silica in them. Glasses of type A and B are fine-pored, while glasses C and D are large-pore. Glasses of type A and C contain secondary silica in their pores. Glasses of type B are depleted of them, and in glasses of type D, it is practically absent. The silica particles in Fig. 3.2 are visible as white spots.
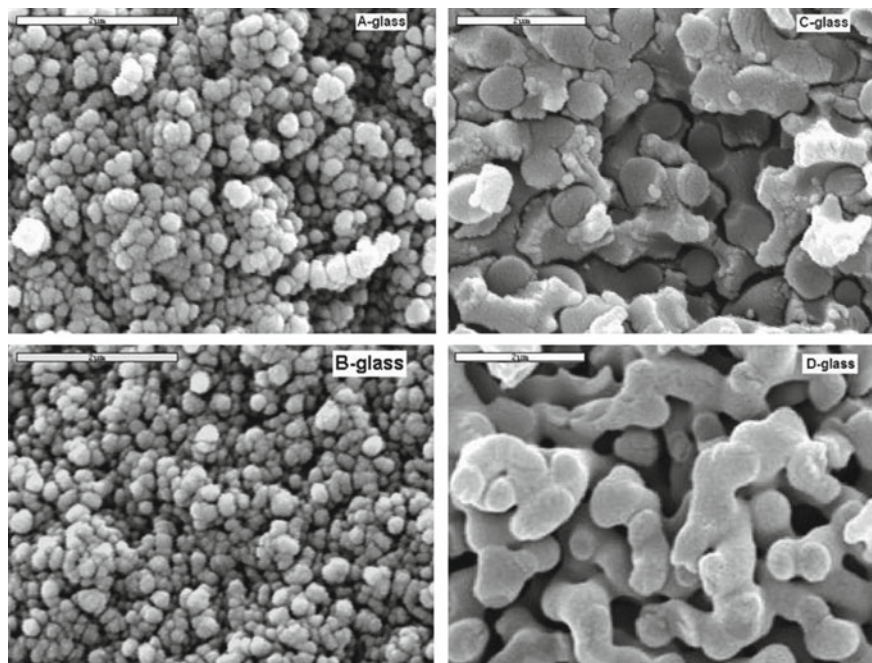
Fig. 3.2 Electron microscopic images of four types of silicate porous glass A, B, C and D [16]
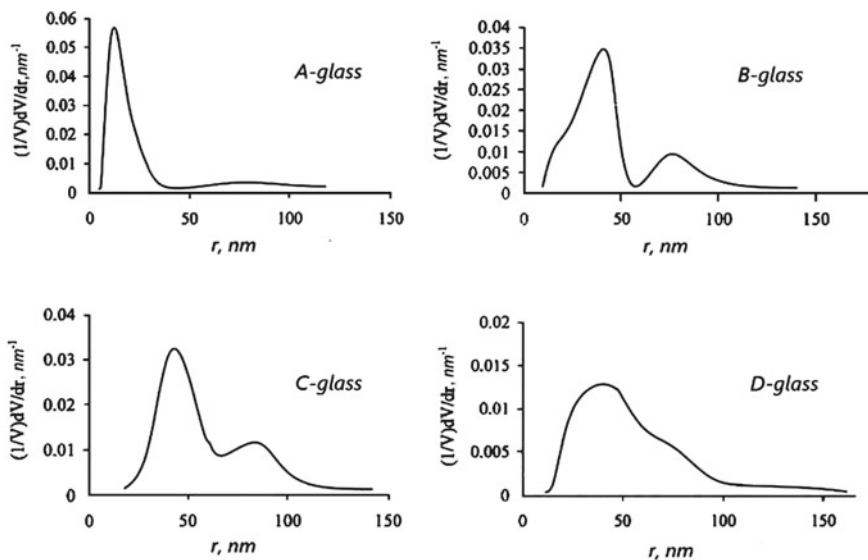
Fig. 3.3 Pore size distribution for different types of porous silicate glass

Fig. 3.4 Photoluminescence spectra of phenol, hydroquinone, and its oxides
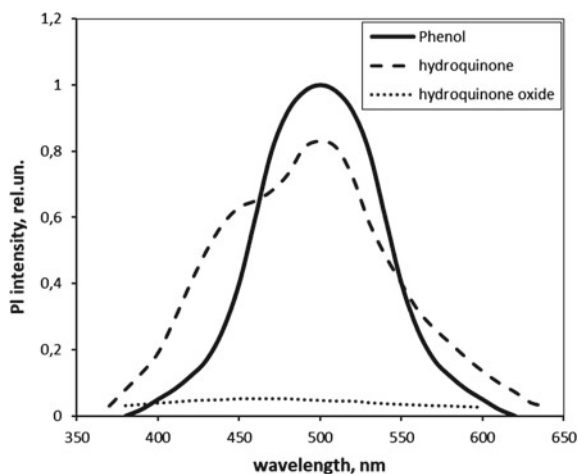
The predominant pore size distribution for all four types of glasses, obtained by the adsorption–desorption of water during capillary evaporation from mesopores [17], is shown in Fig. 3.3. It can be seen that the pore sizes in glass D approximately correspond to the pore sizes in organosilicate rods, so that the use of this type of glass will not provide any advantages being impractical. Comparison of the distributions for glasses of type B and C shows that they are very similar. However, if the pore size distribution in glass B arises due to the removal of silica gel from the pores of

type A glass during their some etching, then the opposite picture takes place for glass C. In this case, the large pores are clogged with silica gel and therefore behave like small pores. Matrices based on glasses of type B and C give a slightly better result in washing out the catalyst from the pores (about 3.5–4% per session) than when using organosilicate rods.

The use of finely porous silicate glass with residual silica gel inside the pores (type A) differs significantly for the better both from the use of organosilicate rods and other types of glass. Such a good result is explained, on one hand, by the rather small size of the nanoparticles of the ensemble (less than 20 nm due to the limitation by the predominant pore size) and, on the other hand, by the separation properties of silica gel, preventing the aggregation of the forming nanoparticles, which additionally. In addition, the filling of voids in the pores with silica gel prevents leaching of the catalyst and improves the adhesion of the matrix, which makes it possible to reduce the leaching of the catalyst to hundredths of a percent per session. Thus, the use of porous silicate glass of type A as a matrix in the catalytic oxidation of phenol is preferable.

3.4 Luminescent Studies

The wastewater treatment process end recording needs no necessity to use high-precision expensive equipment for counting oxidized and non-oxidized particles in solution [10]. Taking into account the structural features of the phenol and hydroquinone oxides molecule, the equipment may be limited to a standard luminescent setup consisting of an SF-4 quartz monochromator, an FEU-69 photomultiplier tube with a sensitivity of 280–850 nm, as a photodetector and a selective amplifier for synchronization with the exciting laser frequency. To excite the spectra, an LCS-DTL-374QT ultraviolet laser with a wavelength of 335 nm and a power of 1.5 mW is used, and the result is transmitted through an analog-to-digital converter using the USB oscillography program to a computer monitor [18].

The phenol molecule can be represented as a hydrazone fragment with a hydroxyl substituent of a tetravalent tin-based dye molecule. In this case, the hydrogen atom will simply play the role of the coordination node. Our previous luminescence studies of dyes of this type [16] showed that, upon hydroxyl substitution, the intensity of their luminescence arising from transitions between the electronic-vibrational sublevels of the system weakly depends on the nature of the coordination site, but may depends on the tautomeric form. Phenol-tautomeric forms are absent, and therefore, the spectrum of its photoluminescence has a Gaussian-like shape with one peak, Fig. 3.4.

In the oxidation process, phenol is first converted into hydroquinone, the presence of which in wastewater is also harmful to the environment. Like phenol, its molecule can also be represented as a hydrazone fragment with a hydroxyl substituent of a tetravalent tin-based dye molecule. But the second hydroxyl group will play the role of a coordination site for it. In this case, two tautomeric forms are possible: 2 and 4. During oxidation, they will arise randomly and it is impossible to separate them. By

analogy with dyes, tautomeric form 4 glows approximately one and a half times less intensive than tautomeric form 2, and its luminescence peak is slightly shifted toward short waves side. The both tautomeric forms will contribute to the total luminescence spectrum, and therefore, it looks somewhat more diffuse in comparison with phenol, with a slightly lower intensity, greater width, and with two peaks clearly distinguished in it, corresponding to two tautomeric forms, Fig. 3.4.

It should be noted that the areas under the curve for the spectra of phenol and hydroquinone coincide, which indicates the same number of molecules in both systems.

After the end of the catalytic oxidation process, both tautomeric forms of hydroquinone lose hydrogen from hydroxyl groups and their place are occupied by oxygen substituents linked to the benzene ring by a strong double bond, Figs. 3.1, 3.3 and 3.4. In such systems, electronic-vibrational levels are practically absent, and therefore, they practically do not luminesce, Fig. 3.4. Thus, the completion of the catalytic oxidation of phenol can be noticed by the termination of the luminescence of the system.

3.5   Conclusion

The use of ruthenium dioxide as a catalyst for the purification of waste water from phen6ol is one of the most preferred methods of purification. Moreover, the formation of this catalyst in the form of ensembles of nanoparticles in the matrix of porous silicate glass of type A prevents its washout during the cleaning process. The indicator of the end of the oxidation process of phenol and its derivative, hydroquinone, is indicated by the termination of the luminescence of the catalytic system.

References

1. Luck F (1999) Wet air oxidation: past, present and future. Catal Today 53(1):81–91. https://doi.org/10.1016/S0920-5861(99)00112-1
2. Bhargava SK, Tardio J, Prasad J et al (2006) Wet oxidation and catalytic wet oxidation. Ind Eng Chem Res 45(4):1221–1258. https://doi.org/10.1021/ie051059n
3. Stüber F, Font J, Fortuny A et al (2005) Carbon materials and catalytic wet air oxidation of organic pollutants in wastewater. Top Catal 33:3–50. https://doi.org/10.1007/s11244-005-2497-1
4. Santiago M, Stüber F, Fortuny A et al (2005) Modified activated carbons for catalytic wet air oxidation of phenol. Carbon 43(10):2134–2145. https://doi.org/10.1016/j.carbon.2005.03.026
5. Huang H-H, Lu M-C, Chen J-N, Lee C-T (2003) Influence of surface modification on catalytic activity of activated carbon toward decomposition of hydrogen peroxide and 2-chlorophenol. J Environ Sci Health A 38(7):1233–1246. https://hero.epa.gov/hero/index.cfm/reference/details/reference_id/645938
6. Levec J, Pintar A (2007) Catalytic wet-air oxidation processes: a review. Catal Today 124:172–184. https://doi.org/10.1016/j.cattod.2007.03.035

7. Besson M, Gallezot P (2005) Stability of ruthenium catalysts supported on TiO_2 or ZrO_2 in catalytic wet air oxidation. Top Catal 33(1–4):101–108. https://doi.org/10.1007/s11244-005-2517-1

8. Gallezot P, Chaumet S, Perrard A, Isnard P (1997) Catalytic wet air oxidation of acetic acid on carbon-supported ruthenium catalysts. J Catal 168(1):104–109. https://doi.org/10.1006/jcat.1997.1633

9. Cao S, Chen G, Hu X, Yue PL (2003) Catalytic wet air oxidation of wastewater containing ammonia and phenol over activated carbon supported Pt catalysts. Catal Today 88(1–2):37–47. https://doi.org/10.1016/j.cattod.2003.08.005

10. Taran OP, Polyanskaya EM, Descorme C et al (2010) Ruthenium carbon-based catalysts for catalytic wet air oxidation of phenol. J Siberian Federal Univ Chem 3(3):245–252. http://elib.sfu-kras.ru/handle/2311/2182

11. Ma H, Kong D, Xu Y et al (2017) Disassembly-reassembly approach to RuO_2/graphene composites for ultrahigh volumetric capacitance supercapacitor. Small 13(30):1701026. https://doi.org/10.1002/smll.201701026

12. Suzuki H, Nitta S, Tomita O et al (2017) Highly dispersed RuO_2 hydrates prepared via simple adsorption as efficient cocatalysts for visible-light-driven Z-scheme water splitting with an IO_3^-/I^- redox mediator. ACS Catal 7(7):4336–4343. https://doi.org/10.1021/acscatal.7b00953

13. Zhou R, Zheng Y, Jaroniec M, Qiao S-Z (2016) Determination of the electron transfer number for the oxygen reduction reaction: from theory to experiment. ACS Catal 6(7):4720–4728. https://doi.org/10.1021/acscatal.6b01581

14. Nagaoka K, Eboshi T, Takeishi Y et al (2017) Carbon-free H_2 production from ammonia triggered at room temperature with an acidic RuO_2/γ-Al_2O_3 catalyst. Sci Adv 3(4):e1602747. https://doi.org/10.1126/sciadv.1602747

15. Gevelyuk SA, Grinevych VS, Doycho IK et al (2019) Photoluminescence of SnO_2 nanoparticle ensemble in porous glass with column structure. In: 2019 IEEE 8th international conference on advanced optoelectronics and lasers (CAOL), pp 416–419. https://doi.org/10.1109/CAOL46282.2019.9019433

16. Doycho IK (2015) Investigation of photoluminescence properties of nanoparticle ensembles of dyes. In: Smyntyna VA (ed) No-equilibrium processes in the sensoric structures. ONU, Odessa, pp 120–170 (in Russian)

17. Doycho IK, Grinevych VS, Filevska LM (2020) Porous silica glasses as a model medium for the formation of nanoparticles ensembles: review. In: Bonča J, Kruchinin S (eds) Advanced nanomaterials for detection of CBRN. NATO science for peace and security series a: chemistry and biology. Springer, Dordrecht. https://doi.org/10.1007/978-94-024-2030-2_21

18. Gevelyuk SA, Doycho IK, Lishchuk DV et al (2000) Linear extension of porous glasses with modified internal surface in humid environment. Optica Applicata 30(4):605–611. https://opticaapplicata.pwr.edu.pl/article.php?id=2000400605

Chapter 4
Physical, Nanostructural, and Biocolloid-Chemical Transformations of Marine Iron-Aluminosilicate Sediments and Their Chemical, and Mineral Ore Conversions

A. V. Panko, I. G. Kovzun, V. A. Prokopenko, O. M. Nikipelova, O. A. Tsyganovich, and V. O. Oliinyk

4.1 Introduction

Natural disperse rocks in form of polymineral nano- and microdisperse iron-aluminosilicate systems and materials (IASs) are common in the earth's crust. Colloid-chemical research of transformations of such systems and materials based on iron and iron-manganese ores, marine and lake sediments (oozes), and sands of different origins attracts great attention in recent decades [1–7]. They have been actively studied not only from the viewpoint of the influence on their properties of physical processes but also of colloid-chemical, nanochemical, and physicochemical geomechanics laws [3–7] to find out the mechanisms of complex biocolloidal interactions [3, 8, 9]. However, the interpretation of such influences on polymineral IASs in many specific cases is not yet completed because of the uncertainty of complex physical, physicochemical, geomechanochemical, colloid-chemical, biocolloidal, and

A. V. Panko (✉) · I. G. Kovzun · V. A. Prokopenko · O. A. Tsyganovich · V. O. Oliinyk
F.D. Ovcharenko Institute of Biocolloidal Chemistry of NAS of Ukraine, 42, Ak.Vernadskogo Blvd, Kyiv 03142, Ukraine
e-mail: phd.wiz@gmail.com

V. A. Prokopenko · O. A. Tsyganovich
National Technical University of Ukraine «KPI», 37, Peremohy Ave., Building 4, Kyiv 03056, Ukraine

O. M. Nikipelova
Engineering and Technology Institute "Biotechnika" of NAAS of Ukraine, Maiakska St, 26, Khlibodarske, Odes'ka Oblast 67667, Ukraine

Odessa State Environmental University, Lvivska Str., 15, Odessa 65016, Ukraine

biomedical methods of their research and the ambiguity of relevant conclusions. In general, it is known that physical, physicochemical, colloid-chemical, nanochemical transformations, and contact interphase interactions in marine IASs based on clay-containing sediments aided with bacterial processes lead to the chemical–mineralogical transformations and formation of new disperse polymineral materials with new properties, which may deteriorate under the action of anthropogenic polluting surfactants. Such IASs consist of iron, aluminum, and silicon oxides, and also, but in smaller quantities, of many other inorganic and polluting organic components. The role of the last ones in similar processes is not clear yet [8–25].

The practical importance of both IASs and nanostructural materials extracted from them is growing permanently. That is why the attention to them of technologists and researchers studying not yet established fundamental transformation mechanisms of IASs and relevant materials is growing as well. Thus, synergic, nanochemical, mechanochemical, nanostructural, and other transformations of IASs' components have been studied not enough [1–3]. These transformations in inorganic systems and compositions with bio-originated materials have not yet found their generalized solution.

Thus, the mentioned considerations show the significant actuality of the questions and the necessity of their solution by conducting relevant systematic experimental, model, and theoretical research of disperse iron-aluminosilicate systems and materials for further generalization of the mechanisms of their transformation into new compositions and ore materials.

4.2   Materials and Methods

Preliminary investigations showed that as a result of the influence on microdisperse and nanodisperse IASs, various interactions between their components are possible [3–6, 12, 13]. Such interactions give new properties and change characteristics of IASs. Concerning the said above, the choice of study materials was based on samples with typical colloid-chemical properties usual for most IASs. Earlier [1–6] there were chosen some examples of iron-aluminosilicate materials: different soils and clays; polymineral iron-aluminosilicate compositions extracted from iron ores; pelagic shallow-water and deep-water sediments of the Black Sea and the Azov Sea as model objects for studying the oceanic basins. The chemical composition of general materials used in the study is given in Table 4.1. Materials and compositions were purified by standard methods [7] and powdered up to particle sizes of 63 μm. XRD and X-ray fluorescence investigations of polymineral disperse systems and compositions [1, 13] showed that their structure includes minerals of kaolinite, illite, montmorillonite, glauconite, saponite, goethite, and others. The composition of fine fractions has a lower content of mixed layer formations of montmorillonite-illite and glauconite types.

Table 4.1 Chemical composition of iron-aluminosilicate materials

Oxide content wt%	Polymineral iron-aluminosilicate compositions			Saponite-goethite composition	The Black Sea ooze	River sand	Montmorillonite
SiO$_2$	18.34	18.31	19.46	46.73	54.57	98.83	49.52
Al$_2$O$_3$	2.09	1.76	1.93	5.12	11.35	0.06	21.06
Fe$_2$O$_3$	3.18	8.34	2.79	2.76	5.54	1.05	2.72
FeO	56.15	49.23	51.16	23.21	–	–	–
CaO	2.17	1.65	1.98	3.87	8.87	0.01	5.7
MgO	0.73	0.61	0.56	11.43	1.80	–	1.61
MnO	2.48	3.24	7.87	0.35	0.04	–	–
Na$_2$O	0.45	0.31	0.24	0.82	1.19	–	0.37
K$_2$O	0.33	0.25	0.26	0.36	1.86	–	0.28
LOI	14.21	16.26	13.67	8.57	13.03	–	17.98

LOI—loss of ignition

Investigations of IASs included using theoretical modeling methods and experimental methods: chemical, rheological, XRD, thermogravimetric, SEM, and biomedical methods [3, 4, 6, 8, 9, 13]. Chemical and X-ray fluorescence analysis used in sample tests was done by the known methodology of qualitative and quantitative methods of analysis of iron-aluminosilicate rocks. X-ray diffraction (XRD) sample analysis was done using diffractometer Dron-UM-1 with CoK$_\alpha$ emission and nickel filter at room temperature. The diffractometer was connected to a computer for diffraction pattern recording. The recording was conducted at 1 degree per minute speed. Registration of X-ray emission was done by scintillation counter BDS-6. Electron microscopy of tested samples: Electron microscopic images were received on electron microscope Selmi PEMU in light field mode. There were also used scanning electron microscopes TESLA BN, JEOL NeoScope JCM-5000, and JEOL JSM6490 LV with INCA ENERGY-450 (Oxford) energy-dispersion device. Thermogravimetric analysis (TGA) was done on thermogravimetric analyzer MOM Q-1500 D (Hungary). Rheological characteristics of investigated systems and materials were determined also by a rotational viscometer with coaxial cylinders Rheotest-2 connected to a computer.

4.3 Results and Discussion

4.3.1 Current Status of Iron-Aluminosilicate System (IASs) Studies

Studying the laws of complex processes in IASs and IASs is the primary source of information about mechanisms of transformation of such systems and materials in natural and technogenic conditions. Substantiated ideas concerning this subject also allow the prediction of the behavior of natural rocks [1, 3–15] as the main compounds of relevant systems and materials in natural, technological, biomedical, and other processes. Thus, such researches of IASs are actual for further development of fundamental ideas concerning their natural transformations under the action of external factors and for the creation of modern technological processes.

Widespread in the earth's crust iron-aluminosilicate materials and marine and lake disperse and ultradisperse systems on their basis take an important place among natural dense nanostructural but at the same time porous on nano- and microlevel rocks and technogenic products of their technological processing. Their physicochemical, physicomechanical, and chemical transformations in the earth's crust and reservoirs, generally in seas and lakes, lead to the formation of disperse nano- and microstructured sedimentary materials of polymineral composition [15]. Their main components are oxides of iron, silicon, and aluminum also containing in iron-aluminosilicates of peloids (Fig. 4.1), but there are many other important compounds contained in clays and oozes as well (Table 4.2). Magnetite and other oxide-hydroxide iron-containing minerals are the most common and present in the most valuable sediments [3, 9–16].

Such sediment minerals have a common effect on the properties of IASs, both in fine-disperse and in dense-fine, and nanocrystalline states. The data in Table 4.3 show that the amount of SiO_2 in sediment samples is the highest and, e.g., reaches 53.93% in red clays, 24.23 and 67.36% in limestone and silica ooze, respectively. A significant amount of Al_2O_3 also shows that the three mentioned oxides (Fe_2O_3, SiO_2, Al_2O_3) play a general role in structural transformations of sediments and MnO_2 (Table 4.1)—in the formation of iron-manganese nodules. Limestone ooze, which contains up to 57% of $CaCO_3$, also has a significant biocolloidal and colloid-chemical effect of calcium minerals [4]. Therefore, the disclosure of the mechanisms of these effects to clarify them requires an additional theoretical, model, and experimental studies.

The distribution of different sediments is presented in Table 4.3. Sizes of nanoparticles in the composition of most distributed red clays are 27.0–86.7 nm [15]. That is why red clays as most important in marine sediments can be attributed to nanostructural materials. However, the nanoparticles' specific role in the deep-sea oozes' composition had almost no research [3, 14, 15]. Shallow-water oozes (diatomic and shelf ones) have a highly disperse microstructure, and the size of ultradisperse particles of about 170–190 nm. Interestingly, the most widespread clays in oceans are red ones containing about 9% of iron oxides (Table 4.2). Their distribution in the World
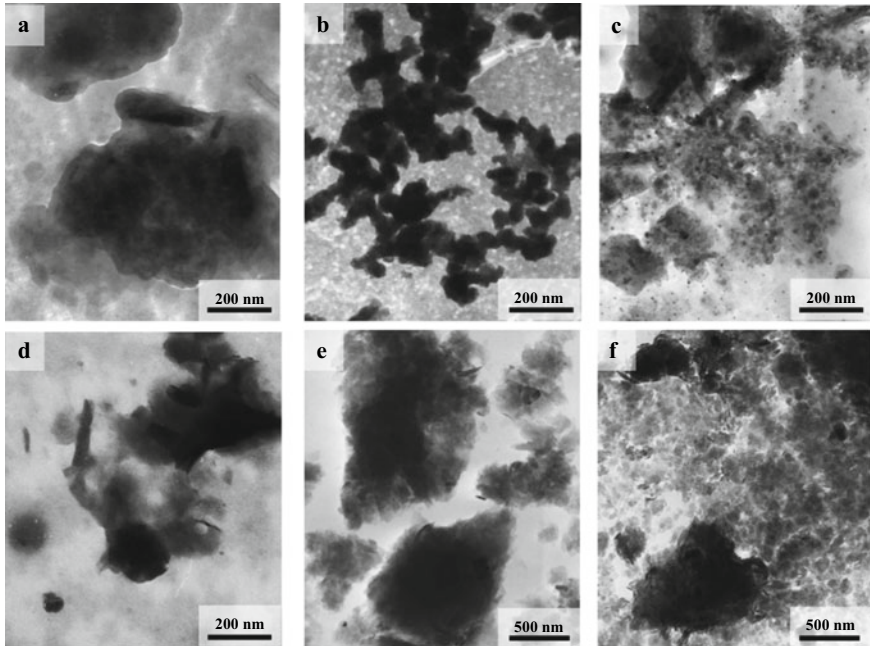
Fig. 4.1 SEM images of peloid sediments and clays: **a** Black Sea sediment. **b** Kuyalnik sediment. **c** Azov-black sea sediment. **d** Bentonitic clay. **e** Glauconite. **f** Hydromica

ocean is the biggest and reaches 540×10^6 km^2, including pelitic and terrigenous oozes [3]. Therefore, nanostructural–nanochemical phenomena in IASs, modeling the behavior of red clays without and with the participation of biogeocenoses and their influence on geomechanical, usual, and critical phenomena accompanying mechanodispersive deformations in IASs both on the earth's surface, and in the ocean depths were considered in the first place.

4.3.2 Analysis of Experimental Data Using Theoretical and Model Conceptions

For this analysis, it is important the ideas about the mechanical and nanochemical or (auto-) self-dispersion of IASs in the presence of aqueous mineralized aqueous solutions, as well as natural or anthropogenic surfactants of various origins.

The mechanism of hydrolytic destruction of siloxane bonds of silicate materials [3] is the basis of abiotic mechanical and nanochemical self-dispersion [18] with the aid of water:

Table 4.2 Chemical composition of some usual samples of marine peloid sediments [3, 14–16]

Component	Red clay (%)	Limestone ooze (%)	Silica ooze (%)
SiO_2	53.93	24.23	67.36
TiO_2	0.96	0.25	0.59
Al_2O_3	17.46	6.60	11.33
Fe_2O_3	8.53	2.43	3.40
FeO	0.45	0.64	1.42
MnO	0.78	0.31	0.19
CaO	1.34	0.20	0.89
MgO	4.35	1.07	1.71
Na_2O	1.27	0.75	1.64
K_2O	3.65	1.40	2.15
P_2O_5	0.09	0.10	0.10
H_2O	6.30	3.31	6.33
$CaCO_3$	0.39	56.73	1.52
$MgCO_3$	0.44	1.78	1.21
C_{org}	0.13	0.30	0.26
N_{org}	0.016	0.017	–
Total	100.20	100.17	100.10
Total Fe_2O_3	9.02	3.14	4.98

Table 4.3 Area (in 10^6 km^2) of dissemination of pelitic sediments [3, 14–16]

	Atlantic Ocean		Pacific Ocean		Indian Ocean		Total	
	Surface	%	Surface	%	Surface	%	%	Surface
Limestone oozes	41.6	67.5	51.9	36.2	34.4	54.3	127.9	47.7
Silica oozes	4.1	6.7	21.0	14.7	12.9	20.4	38.0	14.2
Red clay	15.9	25.3	70.3	49.1	16.0	25.3	102.2	38.1
Total	61.6	100.0	143.2	100.0	63.3	100.0	268.1	100.0

$$\text{(structural scheme: } A + B \rightarrow \dots \rightarrow \dots + 2H_2O) \tag{4.1}$$

interphase space
(nanocrack)

nanocluster
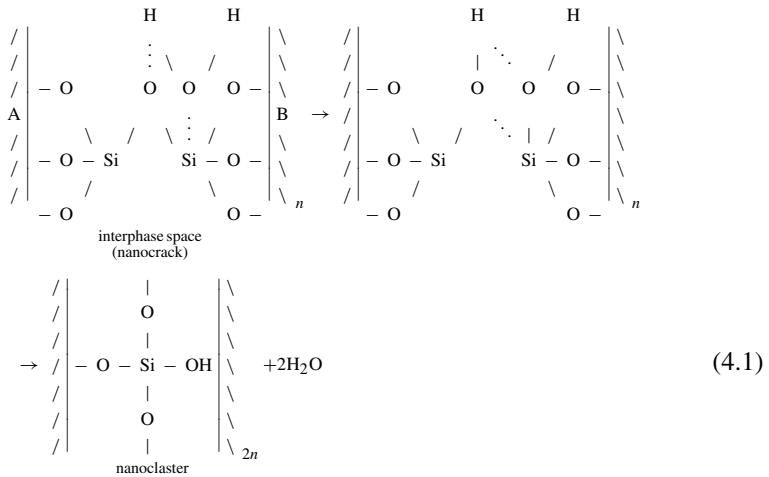
where ⟋⟋⟋—surface of micro- and macroparticles; n—the number of siloxane groups in the phase contacts in the interphase space.

According to the Gibbs–Smith condition, the intergranular boundaries between the microcrystalline formations A and B can also be supplemented by the formation C (aqueous solution) [18]:

$$\sigma AB > \sigma AC + \sigma BC \tag{4.2}$$

described by the linear-parabolic equation:

$$AL + BL^2 = t, \tag{4.3}$$

where t is the time of penetration of the liquid at a distance L.

The linear part of (4.3) is determined by the kinetics of crystallization pressure increasing P_{cr}:

$$A = \delta RT / D_{SL} C_0 P_{cr} \omega, \tag{4.4}$$

where δ is the average grain size.

The application of the Poiseuille equation gives the following expression for the value of B in (4.4):

$$B = 12\eta / \delta P_{KP} \tag{4.5}$$

where η is the viscosity of the fluid.

Evaluation of $1/B$, as a conditional dispersion factor, gives values at the level of 10^{-3}–10^{-4} cm^2/s, which is many orders of magnitude higher than the diffusion coefficient in solids. Therefore, the dispersion rate should increase synergistically
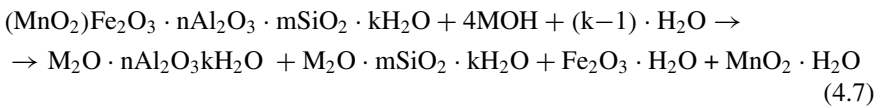
depending on the grain size (δ). That is, (4.5) confirms the importance of the synergism phenomenon influence [2] on the mechanism of self-dispersion. But the mechanism of this phenomenon has not been previously formulated and has not been associated with synergistic processes in the conditions of simultaneous influence of various factors (mineralized water, surfactants presence) on the behavior of IASs.

In addition to the considered processes of IASs' fracturing, there is also a much more intensive natural and technogenic biotic dispersion of porous materials in various surfactants produced by bacteria in biogeocenoses while the process of metabolism. Analysis of the mechanism of such processes, which are also synergistic and symbate, showed that they are being accelerated by many orders of magnitude [1, 3–6, 8–10, 13, 18]. In this case, their kinetics is described by the equation:

$$(S-S_0)^2 = kt, \tag{4.6}$$

where S_0 is the initial specific surface of the porous body.

The processes in (4.2)–(4.6) are only physical. At the same time, the substantiation of the water influence on the dispersion of rocks by (4.1) considers the crystallization pressure in nanopores, which can be created only by nanochemical reactions of mineral nanophase formation on a surface in the form of phase contacts. Therefore, more extensive ideas about the mechanism of volumetric pressure in the nanopores of IASs due to nanochemical reactions of polymineral iron-aluminosilicate, aluminosilicate, and silicate nanophases formation are given. They wedge nanocracks in the conditions of synergetic processes (Fig. 4.2a, b) and are formed, for example, according to the reactions:

$$(MnO_2)Fe_2O_3 \cdot nAl_2O_3 \cdot mSiO_2 \cdot kH_2O + 4MOH + (k-1) \cdot H_2O \rightarrow$$
$$\rightarrow M_2O \cdot nAl_2O_3kH_2O + M_2O \cdot mSiO_2 \cdot kH_2O + Fe_2O_3 \cdot H_2O + MnO_2 \cdot H_2O \tag{4.7}$$

While the reaction products (4.7) react according to the scheme:

$$M_2O \cdot nAl_2O_3 \cdot kH_2O + M_2O \cdot mSiO_2 \cdot kH_2O \rightarrow$$
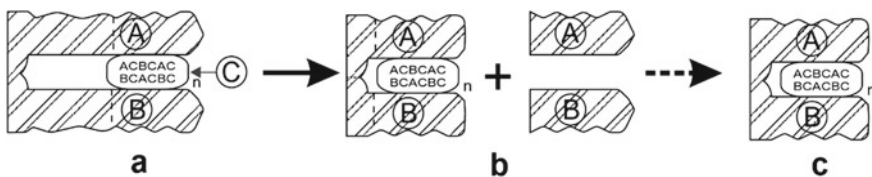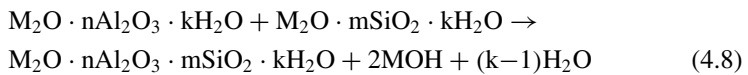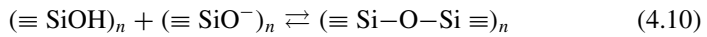$$M_2O \cdot nAl_2O_3 \cdot mSiO_2 \cdot kH_2O + 2MOH + (k-1)H_2O \tag{4.8}$$

Fig. 4.2 Model of self-hydrational [18] dispersion of rocks with the formation of a new phase: **a** and **b** initial products composed of different minerals, **c** solution of surfactants in water (metabolic products), n—nanophase contact capable of dispersion **b** or compaction **c**

Alkaline components and water (4.8) react then according to the scheme (4.7) in cyclic repetitions. That allows almost infinite dispersion with small amounts of alkali and water.

Then, along with $Fe_2O_3 \cdot H_2O$, they take part in nanostructural–nanochemical contact phenomena, which can be of dispersing or compacting nature—depending on the process conditions [3].
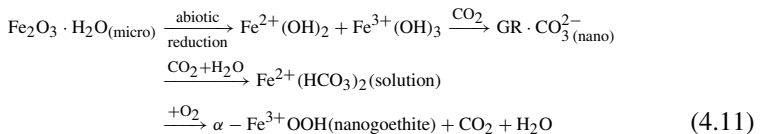
If the products formed by reactions (4.7) and (4.8) have a larger volume than the initial product involved in the reaction (4.7), the resulting pressure breaks (chemically wedges) the crack, which is symbatically facilitated due to the external mechanical load. The water that enters the expanded mouth of the crack hydrolytically breaks up the newly formed secondary nanocracks again by reaction (4.8), and the process of self-dispersion continues with acceleration. The process takes place in the same way as in the case of penetration of liquid phases through intergranular nanoboundaries, but is many orders of magnitude faster and lasts not years, but days or hours. This is also facilitated by other nanochemical interactions in silicate structures, i.e., quartz-like, which complement interactions (4.1), (4.7), and (4.8) and are characterized by the next reactions:

$$(\equiv SiOH)_n + (OH^-)_n \rightleftarrows (\equiv SiO^-)_n + nH_2O \qquad (4.9)$$

$$(\equiv SiOH)_n + (\equiv SiO^-)_n \rightleftarrows (\equiv Si-O-Si \equiv)_n \qquad (4.10)$$

They also give a start to other nanostructural phenomena of opposite compacting transformations of dispersions due to synergetic coagulation–condensation processes (Fig. 4.2c).

Reactions (4.9) and (4.10) not only complement reaction (4.1) but are also intermediate in the processes (4.7) and (4.8) of the transformation of IASs. The process occurs stepwise, which was shown experimentally on the model system of iron-aluminosilicate–alkaline additive [3].

The generalized chemical models (4.11)–(4.14) of interphase contact interactions of surfaces of disperse iron-aluminosilicate minerals in the composition of iron-aluminosilicate (iron-clay) ore sedimentary materials allow to evaluate the nanocluster biocolloidal mechanisms of such interactions in more details. Thus, with the participation of bacteria, the ferrite formed by reaction (4.7) reacts according to the scheme:

$$Fe_2O_3 \cdot H_2O_{(micro)} \xrightarrow[\text{reduction}]{\text{abiotic}} Fe^{2+}(OH)_2 + Fe^{3+}(OH)_3 \xrightarrow{CO_2} GR \cdot CO_{3\,(nano)}^{2-}$$
$$\xrightarrow{CO_2+H_2O} Fe^{2+}(HCO_3)_2 \,(solution)$$
$$\xrightarrow{+O_2} \alpha - Fe^{3+}OOH(nanogoethite) + CO_2 + H_2O \qquad (4.11)$$

Then the following biotic phase interactions occur in the contact zones of microparticles:

$$\left.\begin{matrix} I \\ A \\ S \end{matrix}\right| = \left(Al - O - Fe \overset{\displaystyle OH}{\underset{\displaystyle OH}{\overset{/}{\underset{\backslash}{3+}}}} \right)_{3n} + 3n \left(\overset{\displaystyle HO}{\underset{\displaystyle HO}{\overset{\backslash}{\underset{/}{Fe^{3+} - O}}}} \right) - \left|\begin{matrix} \backslash \\ \backslash \\ \backslash \\ \backslash \\ \backslash \end{matrix}\right| \rightarrow nAl(OH)_3$$

$$+ \underbrace{\left[O = Fe^{3+} - OH \right]_n}_{nanogoethite} + \underbrace{\left[Fe_3^{2+,3+} O_4 \right]_n}_{nanomagnetite} \tag{4.12}$$

$$\left.\begin{matrix} I \\ A \\ S \end{matrix}\right| = \left(Al - O - Fe \overset{\displaystyle OH}{\underset{\displaystyle OH}{\overset{/}{\underset{\backslash}{3+}}}} \right)_{3n} + (HO - Fe^{2+} - OH)_{3n} + 3n[HO - Si] \left|\begin{matrix} \backslash \\ \backslash \\ \backslash \\ \backslash \\ \backslash \end{matrix}\right.$$

$$\rightarrow \quad \equiv nAl(OH)_3 + \underbrace{\left[= Fe^{3+} - O - Fe^{2+} - O - Si \equiv \right]_{2n}}_{nanoironsilicate} + nH_2O \tag{4.13}$$

$$|\equiv (Si - OH)_n + (HO - Fe = O)_n \rightarrow |\equiv (Si - O - FeO)_n + nH_2O \rightarrow \left|\equiv Si - O - Fe \overset{\displaystyle OH}{\underset{\displaystyle OH}{\overset{/}{\underset{\backslash}{}}}} \right)_n \right]$$

$$\left|\equiv Si - O - Fe \overset{\displaystyle OH}{\underset{\displaystyle OH}{\overset{/}{\underset{\backslash}{}}}} \right)_n + \left(\overset{\displaystyle HO}{\underset{\displaystyle HO}{\overset{\backslash}{\underset{/}{Fe - O - Si}}}} \right)_n \equiv \right|$$

$$\rightarrow \left|\equiv Si - O - Fe \overset{\displaystyle O}{\underset{\displaystyle O}{\overset{/\;\backslash}{\underset{\backslash\;/}{Fe - O - Si}}}} \right)_n \equiv \right| + 2nH_2O \tag{4.14}$$
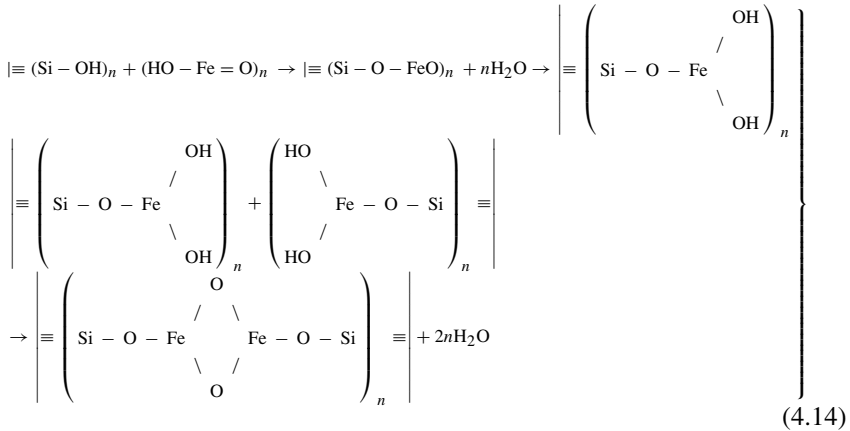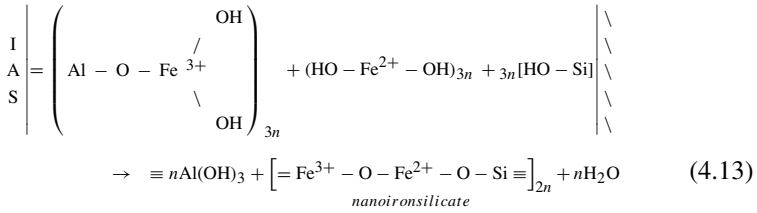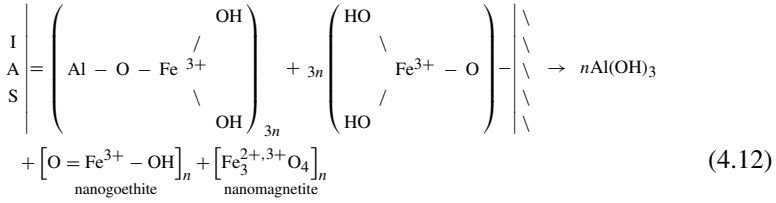
where (…) n—nanocluster.

As can be seen from models (4.12)–(4.14), the interphase biocolloid interactions (Fig. 4.1) are accompanied by the formation of nanocluster coagulation–condensation bonds between the surfaces of the same or different dispersed phases. That leads to the formation of nanophase contacts (Fig. 4.3) in a structure of iron-aluminosilicate materials. Such mechanisms of contact interactions suggest that Fe^{3+} interactions are stronger than Fe^{2+} interactions because in the latter case, which is characteristic for models (4.11) and (4.13), the microbiological oxidation of Fe^{2+} to Fe^{3+}. Thus, and breaking of interfacial bonds are possible. Thus, the biocolloid mechanism aided with biocenosis differs from the inorganic (abacterial) mechanism without bacterial processes by the intermediate formation of iron-layered double hydroxides (LDH) of Green Rust (GR) type, which include Fe (II) and Fe (III) in their structure.

Studies of biocolloid, bacterial, and biochemical processes based on the use of the phenomenon of selective heterocoagulation of minerals with microorganisms have shown that biogeocenosis, or bio-aggregates formed according to the ideas of
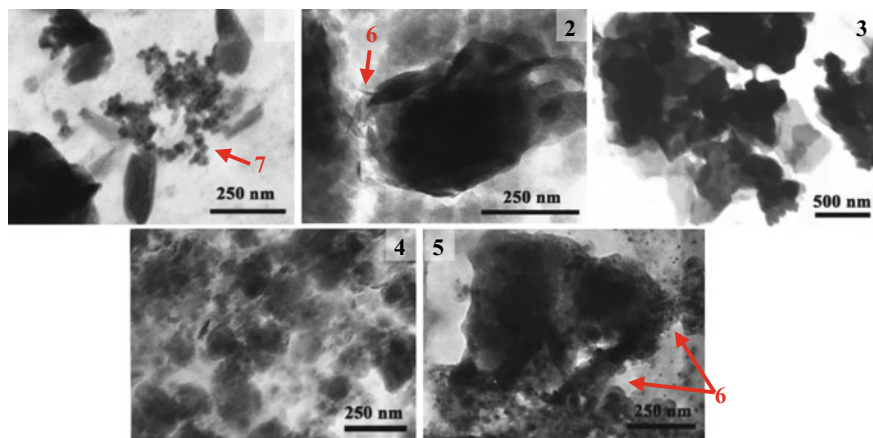
Fig. 4.3 SEM images of montmorillonite (1), hydromica (2), kaolinite (3), glauconite (4), which are the part of typical pelitic sediment (5); zones of phase contacts (6); zone of phase contact formation (7)

biogeochemistry transform into sedimentary deposits and peloids (Tables 4.1, 4.2, 4.3 and 4.4; Figs. 4.1, 4.2, 4.3 and 4.4).

The obtained (Fig. 4.4; Table 4.1) data indicate that bacterial metabolic processes in biocolloidal aggregates lead to the activation of synergetic dispersion of the peloid mineral part according to the mechanisms (4.1), (4.7)–(4.10). Then, upon completion

Table 4.4 Microbiological study of marine peloid samples

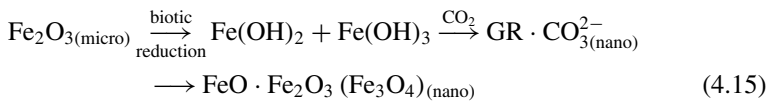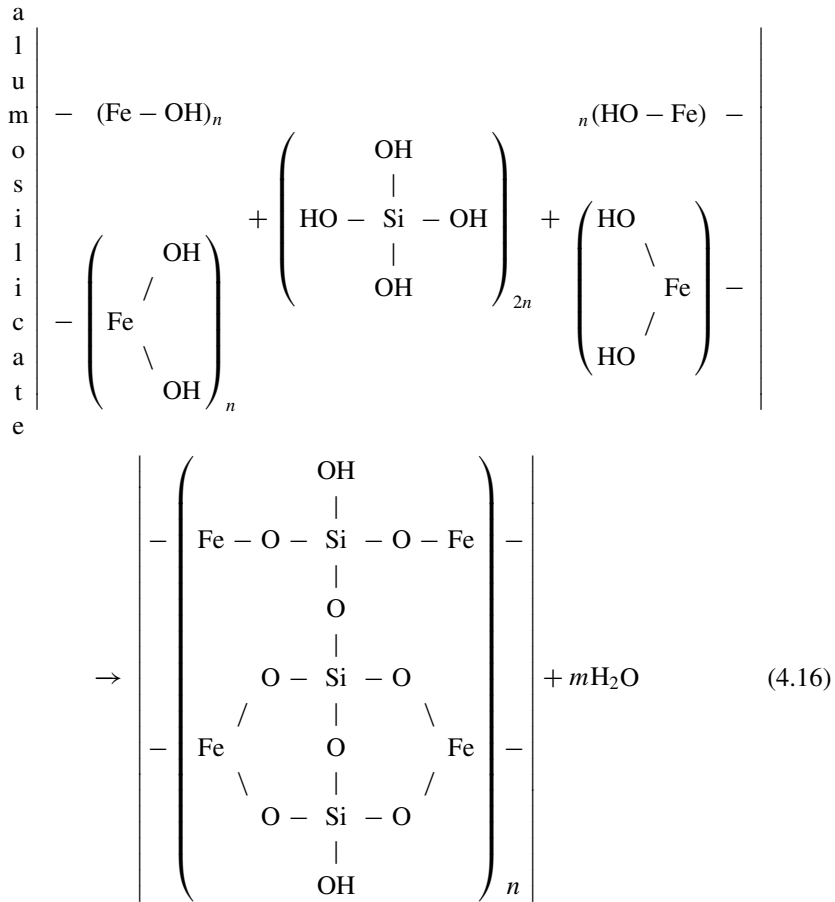| Type of microorganism (bacteria)	CFU/cm^3 in peloids		
	Initial	Used	After activation
Cellulose-fermenting • Aerobic • Anaerobic	10^3 10^1	10^4 10^1	10^3 10^1
Butyric acid	10^4	10^2	10^4
Denitrifying	10^2	10^2	10^2
Sulfate-reducing	10^4	10^2	10^4
Nitrifying	10^6	10^5	10^6
Methane-producing	10^7	10^6	10^7
Iron-oxidizing	$3 \cdot 10^6$	$1 \cdot 10^6$	$3 \cdot 10^6$
Ammonificating • Aerobic • Anaerobic	10^6 10^2	10^2 10^2	10^6 10^2
Fat-decomposing	10^2	10^2	10^2
Sulfur-oxidizing	10^4	10^4	10^4
pH	7.4	6.8	7.3
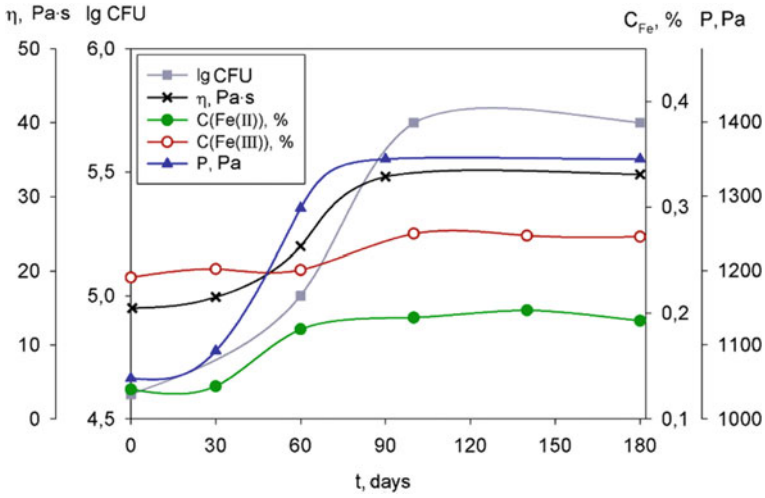
Fig. 4.4 Dependences of viscosity (η), shear stress (P), Fe^{2+} and Fe^{3+} concentration (C, %), and the number of colony-forming organisms (lgCFU) in the Black Sea nanostructured iron-aluminosilicate pelagic sediments of 1800 m depth from the time of their exposure; humidity 46%

of the peloid activation process in 90–100 days—to secondary compaction of pelagic sediments due to the repeated increase in the amount of Fe^{3+} in the composition of rapidly decomposing Green Rust according to models (4.11)–(4.14). The optimal ratio of FeO: Fe_2O_3 is close to 1:1 at that. This ratio corresponds to the formation of magnetite, the mechanical properties of which are the highest among iron oxides of various structures. It follows that due to biocolloidal processes, the contact phase nanofilms in the disperse structure are the strongest at an exposure of sediments in the studied interval of 60–180 days (Fig. 4.4)—the formation of magnetite-type nanostructures. This allows scheme (4.11) to be presented for the biocolloidal process as follows [3]:

$$Fe_2O_{3(micro)} \xrightarrow[\text{reduction}]{\text{biotic}} Fe(OH)_2 + Fe(OH)_3 \xrightarrow{CO_2} GR \cdot CO_{3(nano)}^{2-}$$
$$\longrightarrow FeO \cdot Fe_2O_3 \ (Fe_3O_4)_{(nano)} \tag{4.15}$$

At that, reactions (4.12)–(4.14) transform on the intermediate stage next way:

$$
\text{aluminosilicate}
\begin{vmatrix}
-\ (Fe-OH)_n & & & & {}_n(HO-Fe)\ - \\
\end{vmatrix}
$$

$$
-\left(Fe\begin{smallmatrix} OH \\ / \\ \\ \backslash \\ OH \end{smallmatrix}\right)_n
+\left(HO-\underset{\underset{OH}{|}}{\overset{\overset{OH}{|}}{Si}}-OH\right)_{2n}
+\left(\begin{smallmatrix} HO \\ \backslash \\ Fe \\ / \\ HO \end{smallmatrix}\right)\ -
$$

$$
\rightarrow
\begin{vmatrix}
-\ \Big(Fe-O-\underset{\underset{O}{|}}{\overset{\overset{OH}{|}}{Si}}-O-Fe \\[4pt]
\qquad\qquad\quad O-\underset{|}{Si}-O \\[4pt]
-\ Fe \overset{/}{}\quad O \quad \overset{\backslash}{} Fe \\[4pt]
\qquad\quad O-\underset{|}{Si}-O \\[4pt]
\qquad\qquad\quad OH \Big)_n
\end{vmatrix}
+\ m\,H_2O
\qquad (4.16)
$$

The general model abiotic and biotic scheme of the rock transformation is shown in Fig. 4.5.

According to the data obtained (Tables 4.1, 4.2, 4.3, 4.4 and 4.5; Figs. 4.1, 4.2, 4.3 and 4.4), the greatest influence on the rheological properties of nanostructured IASs has clay minerals, especially montmorillonite, which is a part of bentonite. Therefore, the processes of clay suspension nanostructuring, nanochemical processes of nanoparticle formation in them, including biocolloidal processes, as well as the chemical structure of nanoparticles have a significant impact on the rheological behavior of IAS suspensions. That is shown in Fig. 4.6 for conditions of the viscosity effects of hyper- and ultra-anomaly occurrence.

According to the above curves, hyperanomaly of viscosity is more often characterized by curves 1 and 3, and the previously unknown effect of viscous ultra-anomaly is more usual for curve 2, and sometimes curve 1. Both effects have been experimentally confirmed for numerous rheograms of suspensions for different types of clays, pelitic sediments, and peloids. Therefore, it should be concluded from these data that
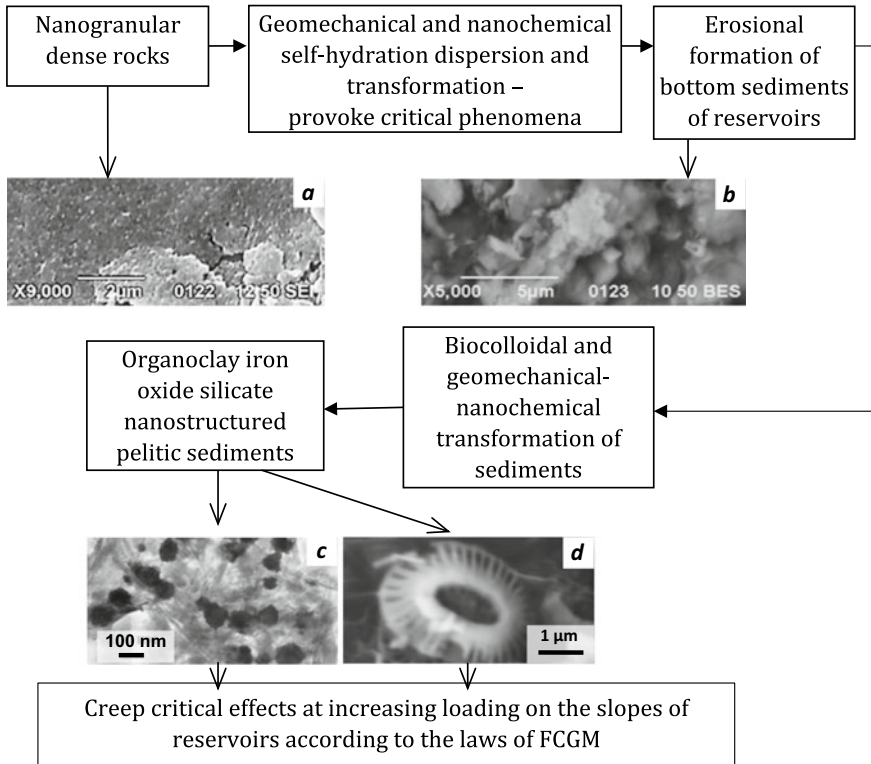
Fig. 4.5 Abiotic and biotic rock transformation general scheme; SEM images of **a** nanogranular rocks; **b** bottom sediments of erosive crushed rocks; **c** pelitic iron-aluminosilicate sediments and peloids; **d** pelitic biotic sediments with carbonate residue of *Foraminifera*

the effect of viscous hyperanomaly is more usual for less concentrated suspensions or with lower iron content in them. On the other hand, the effect of ultra-anomaly of viscosity—for more concentrated suspensions or at lower shear rates with stable other previously mentioned factors. The moisture content of the dispersions (W) changes as follows: $W_{1'-2} < W_{1-2} < W_{1-3}$. If the factors change, i.e., the addition of alkaline additives, the viscosity of iron-aluminosilicate clay sedimentary rock (Figs. 4.4 and 4.7) decreases sharply.

The established regularities allow substantiating the methods of controlling the physicomechanical properties of barrier structures, soils, and rocks with the help of various active environments of natural and technogenic origin.

Thus, theoretical studies and obtained experimental data allowed to consider the thermodynamic basis, kinetics, and mechanisms of transformation of rocks due to their self-hydration spontaneous dispersion [18] aided with nanochemical and bacterial processes with the formation of new disperse structures with thermodynamically stable mineral phases; to develop an idea of the mechanisms of rocks creeping due to

Table 4.5 Physicochemical characteristics of the bottom sediment samples

| Index	Saltwater storage pond (Kryvyi Rih)	Kuyalnik Estuary
1. pH of liquid phase	7.7	7.20
2. Redox potential	–	−227
3. Moisture (wt%)	56	58.1
4. Volume weight (g/cm^3)	1.33	1.47
5. Adhesiveness (Pa)	–	833
6. Shear stress limit (Pa)	770	491
7. Concentration of particles > 250 µm (%)	1.2	0.61
8. Specific heat capacity (kJ/kg K)	–	0.59
9. Concentration of H$_2$S (%)	–	0.17
10. Concentration of C$_{org}$ (%)	–	2.06
11. Concentration of particles (1–5 µm) (%)	3.7	2.65
12. Concentration of particles ≤ 100 nm (%)	0.5	0.34

Fig. 4.6 Load and unload curves (1, 1′ and 2, 2′—respectively) in the conditions of plastic flow of elastic–plastic material; 3—unloading curve in conditions of viscosity hyperanomaly beginning [13]
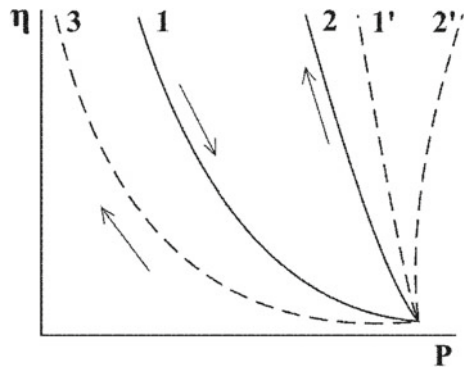
recrystallization of mechanically stressed areas and nanochemical transfer of interfacial boundaries of substances of the liquid phase to other stressed areas of the surface; to reveal the basic global principles of physical–mechanical and nanochemical regulation of structural properties of disperse-porous sediments in natural and technogenic conditions to prevent critical phenomena in them; to outline further ways of developing of these fundamental problems [3].

Analysis of the mechanisms of nanostructured physicochemical transformations of various representatives of IASs and modeling of common and critical creep processes on sea slopes and ocean beds showed that NIASs are generally colloidal oozes and bottom sediments composed of minerals and organic substances that have undergone significant transformations due to geological, geomechanical, chemical, nanochemical, biological, biocolloidal, and other abiotic and biotic processes. They

Fig. 4.7 Influence of the chemical structure of contact silicate nanoclusters on the viscosity of aqueous 50% suspension of iron-aluminosilicate clay pelitic sedimentary rock depending on concentration (*C*) of anionic inorganic nanoclusters of different chemical composition
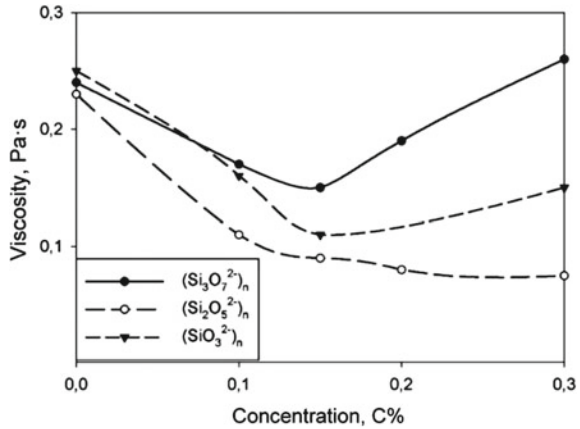
are a homogeneous fine plastic mass. They include natural colloidal, and biocol-loidal formations of various origins, such as iron ore formations with a large amount (40–70%) of iron oxides, and admixtures of aluminosilicates and clay minerals with admixtures of iron oxides, as well as freshwater clay soils, sands, and saltwater iron-containing disperse deposits. Sea oozes (Figs. 4.3 and 4.8) or pelitic deposits of coastal and deep-water origin were studied as the main representatives of the NIASs, the share of which reaches 70–80% among the known NIASs. The finding of nanos-tructural, biocolloidal, physicochemical, and geomechanical mechanisms of their formation was required to answer the system questions of NIASs' participation in usual and critical phenomena, both on the underwater slopes of the seas and oceans, and in the formation processes of ore deposits.

Among the NIASs, the most important from a practical point of view are clays—bounded non-cemented sedimentary rocks of biocolloidal origin with a predominant content of clay minerals with admixtures of iron oxides, sedimentary iron ores, and

Fig. 4.8 Particle size distribution of mud fine-grained fraction: ●●●● mud from the Azov; ■ mud from the Black Sea, sample 1; --- mud from the Black Sea, sample 2
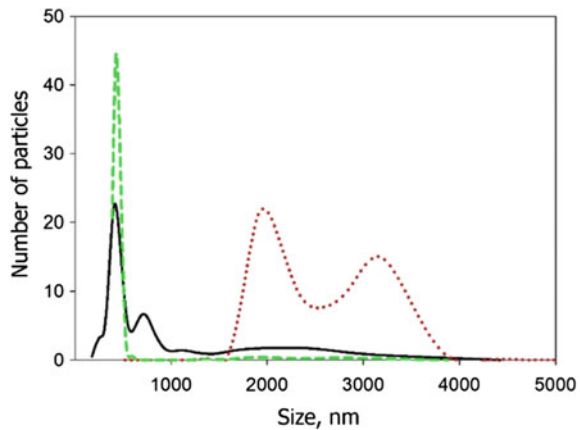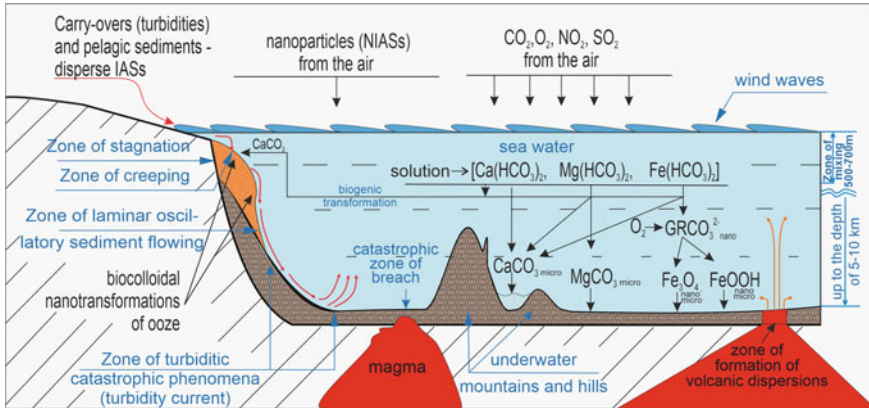
Fig. 4.9 Model of modern nanostructural marine transformations of IASs, pelitic sediments, and turbidites on slopes, gaps, and abyssal plains, accompanied by compacting or ooze flow [1, 3, 14] and stratified sediment separation in processes of ore deposit formation
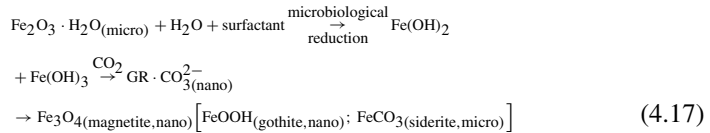
pelitic deposits (peloids)—sediments of lakes, seas, and oceans. They are composed of planktonic organisms rests, fine-disperse mineral particles, space dust, and products of chemical transformations in fresh and saltwater. Their creep or normal and critical behavior in terms of geomechanical and nanochemical processes is most likely related to the destructive work of water waves of various origins and landslides in water reservoirs. The developed model of these processes for marine sediments is given in Fig. 4.9.

Waves that penetrate to a depth of 600–700 m during storms, and sometimes up to several kilometers (while typhoons or tsunami), create the effect of hydraulic shock, which instantly dilutes thixotropic sediments, turning them into a viscous liquid capable of active nanochemical and geomechanical transformations. The resulting suspension flows down the slope without mixing with water due to the higher specific weight. This, in particular, can explain the appearance of chemically transformed (under the influence of pH changes) clay terrigenous sediments at great depths. In addition, on the slopes of seismic zones of the oceans (Fig. 4.9), which can reach lengths up to 2000 m and more, the speed of mudflows weighing up to hundreds of millions tons of rock increases significantly from laminar (up to 0.5 km/h) to normal fast (up to 40 km/h) and catastrophic (up to 100 km/h) current.
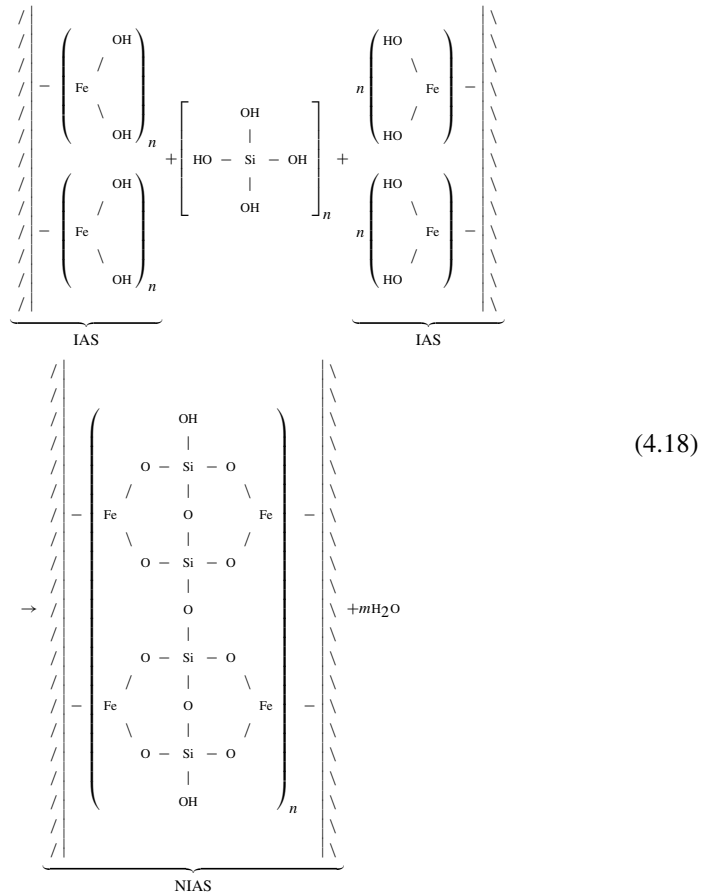
From the process models in Figs. 4.1 and 4.9, and schemes (4.7)–(4.16), it turns out that the interphase biocolloidal interactions are accompanied, with the participation of surface-active products of microorganism metabolism, by the formation of nanocluster coagulation–condensation phase bonds between surfaces of the same or different disperse phases. It leads to the secondary compaction of previously dispersed ferroaluminum silicate materials (Fig. 4.2c). Such mechanisms of contact interactions suggest that Fe^{3+} interfacial interactions are stronger than Fe^{2+}. That is because in the latter case, characteristic for models of surface nanochemical reactions, additional microbiological oxidation of Fe^{2+} to Fe^{3+}, and rupture of interfacial

–O– Fe–O– bonds with the formation of goethite at first, and then magnetite is possible. It coincides with the conclusions of geological science. Thus, the biocolloidal mechanism differs from the previously considered abiotic mechanism by the intermediate formation of Green Rust (GR), which is converted into goethite, magnetite, and siderite or iron-manganese nodules, and other ore minerals. It should be emphasized that the formation of magnetite occurs in anaerobic conditions, but in conditions of the aerobic process, the goethite is formed [3].

It is also possible to provide the scheme for the biocolloidal process in the specified form:

$$Fe_2O_3 \cdot H_2O_{(micro)} + H_2O + surfactant \xrightarrow[\text{reduction}]{\text{microbiological}} Fe(OH)_2$$

$$+ Fe(OH)_3 \xrightarrow{CO_2} GR \cdot CO_{3(nano)}^{2-}$$

$$\rightarrow Fe_3O_{4(magnetite,nano)} \left[FeOOH_{(gothite,nano)}; FeCO_{3(siderite,micro)} \right] \tag{4.17}$$

Reactions (4.12)–(4.14) are transforming as follows:

$$\tag{4.18}$$

The nanostructuring processes of clay suspensions, nanochemical processes of nanoparticle formation in them, including biocolloidal processes, as well as the chemical structure of nanoparticles have an important influence on the rheological behavior of IASs dispersions, especially in conditions of viscous ultra-anomaly (Figs. 4.10 and 4.11).

Systematic analysis of the study results of nanostructural phenomena in the earth's crust and experimental data on the impact of synergistic nanochemical and microbiological processes on these phenomena indicate a scientifically approved ability to achieve shortly a fairly accurate description of nanochemical and rheological mechanisms of many common and critical sediment movement processes occurring in the earth's crust and on its surface, in reservoirs, seas, oceans, and in technogenic conditions. It also gives an ability to develop the ideas of the mechanisms of mineral deposits biocolloidal formation not only in the Archean but also in the Androgenic era (2.588 million years ago and until today).

Based on the analysis of the obtained results, the colloid-chemical ideas about processes on underwater slopes of seas and oceans in the conditions of the gravitational laminar-turbulent flow of sediments according to the laws of physicochemical geomechanics and laws of elastic–plastic change in viscosity was developed too, taking into account the data provided in [1, 3, 14]. The chemical mechanisms of the main processes in such sediments are as follows:

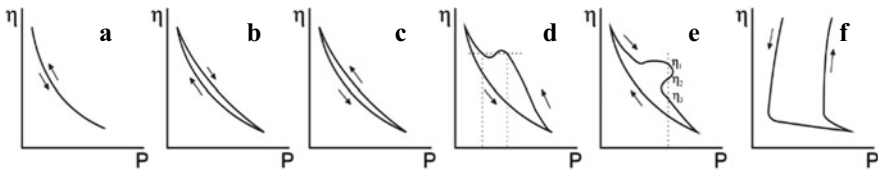1. Contact abiotic phase interactions in conditions of viscosity ultra-anomaly effect:

Fig. 4.10 Rheological curves (general view): **a** non-Newtonian fluid; **b** thixotropy; **c** rheopexy; **d** dilatancy; **e** viscous hyperanomaly; **f** ultra-anomaly of viscosity in the transition area to the Atterberg viscosity limit. Wa > Wb > Wc > Wd > We > Wf, where W is the water content of the dispersion
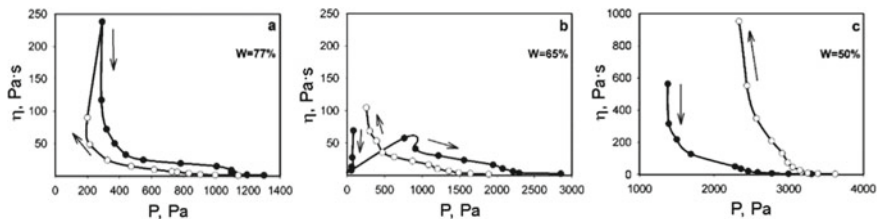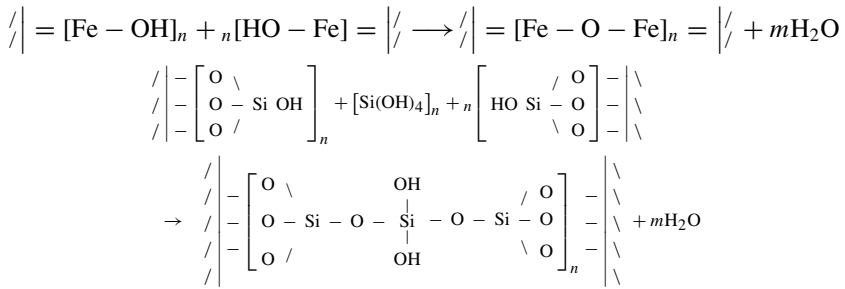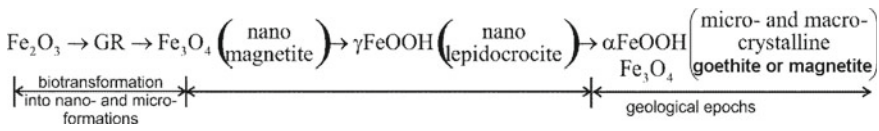

Fig. 4.11 Experimental rheological curves at different humidity (W) for the Black Sea pelitic sediment: **a** thixotropy; **b** ultra- and hyperanomaly of viscosity; **c** ultra-anomaly of viscosity

$$\Big|{/}\atop{/}\Big| = [Fe-OH]_n + {}_n[HO-Fe] = \Big|{/}\atop{/}\Big| \longrightarrow \Big|{/}\atop{/}\Big| = [Fe-O-Fe]_n = \Big|{/}\atop{/}\Big| + mH_2O$$

$$\begin{matrix}/\\/\\/\end{matrix}\Big|{-}\begin{bmatrix}O\ \backslash\\O-Si\ OH\\O\ /\end{bmatrix}_n + [Si(OH)_4]_n + {}_n\begin{bmatrix}/\ O\\HO\ Si-O\\ \backslash\ O\end{bmatrix}{-}\Big|\begin{matrix}\backslash\\\backslash\\\backslash\end{matrix}$$

$$\rightarrow \begin{matrix}/\\/\\/\end{matrix}\Big|{-}\begin{bmatrix}O\ \backslash & OH & /\ O\\O-Si-O-Si-O-Si-O\\O\ / & OH & \backslash\ O\end{bmatrix}_n {-}\Big|\begin{matrix}\backslash\\\backslash\\\backslash\end{matrix} + mH_2O$$

2. Biocolloid nanostructural–nanochemical process:

Preliminary data in Table 4.6 and Figs. 4.12 and 4.13 simulate red clays' behavior in mixing conditions during movements on sea slopes. They give an idea of how the dispersion of various IASs goes, including red clays, under the action of surface-active metabolism products of microorganisms from biogeocenoses (Tables 4.4 and 4.5). Such transformations are accompanied by macrostructures' transition into micro- and nanostructured sedimentary formations with their simultaneous separation into layers with different densities and mineralogical composition. They are forming under the influence of the bacterial metabolism of biogeocenoses. Some stages of such complex phenomena are shown in Figs. 4.1, 4.2, 4.3, 4.4, 4.5, 4.6, 4.7, 4.8, 4.9, 4.10 and 4.11. It can be considered expedient to continue such studies to develop marine biocolloidal geoecology ideas by comprehensively studying the mechanisms of deep-water processes of sediment transportation, their layer-by-layer separation, enrichment of formed ore deposits, and further application.

The mechanisms of nanostructural and microstructural biocolloidal transformations, layer-by-layer separation of iron-aluminosilicate turbidite-pelitic sediments were considered too, taking into account the findings of specialists in various scientific fields [1, 3, 14] and experimental data (Figs. 4.12 and 4.13).

Table 4.6 Geomechanical dispersion of aqueous (NaCl $= 28$ g/dm^3) suspension of iron oxide clayey ore marine sediments under the action of biocolloidal processes

Suspension exposure (days)	Fractions (mm)				
	5–1 mm	1–0.5 mm	0.5–0.05 mm	0.05–0.005 mm	< 0.005 mm
1	21.2	28.7	37.9	8.9	3.3
10	12.3	29.4	40.6	7.9	9.8
15	8.9	25.4	41.3	8.2	13.2
20	7.4	17.7	40.1	14.1	20.7
30	6.8	13.1	37.5	19.3	20.3

Fig. 4.12 Distribution of grain sizes in the most typical iron-aluminosilicate sediments (based on data from [14]): 1—turbidite-pelitic; 2—sand; 3—clays; 4—loess; 5—siltstone; AB—pelitic fractions (lines 1, 3, 4, 5); AC—turbidite fractions (lines 1, 2, 3, 4)
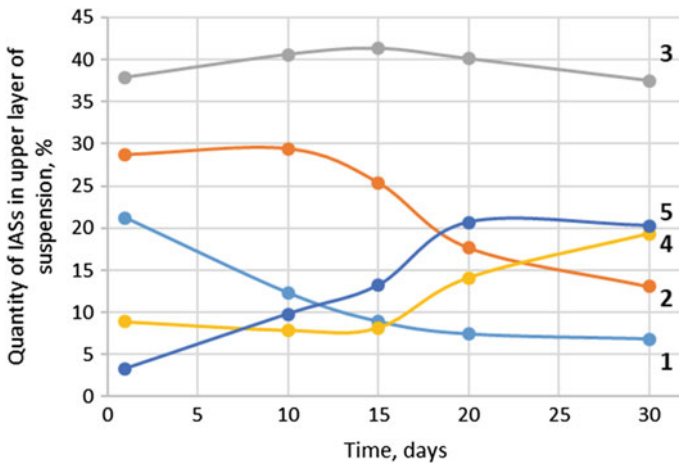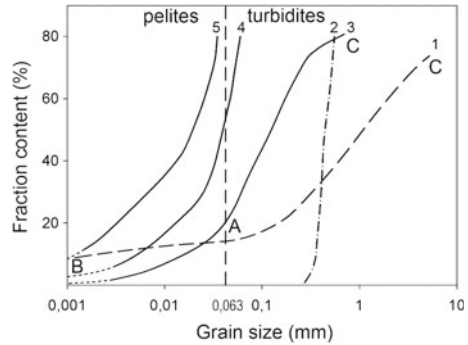
Fig. 4.13 Geomechanical self-dispersion of aqueous suspension (NaCl $= 28$ g/dm^3) of iron-aluminosilicate marine sedimentary red iron ore of biocolloid origin under the action of biocolloidal processes of its activation. Line number for fractions: 1—5–1 mm; 2—1–0.5 mm; 3—0.5–0.1 mm; 4—0.1–0.05 mm; 5—< 0.05 mm

The mentioned processes significantly depend on the biocolloid transformations of sediments. These transformations combine microstructural and nanostructural geomechanical self-hydrational dispersion of sediments with their simultaneous separation into separate layers under the influence of bacterial metabolism as a part of biogeocenoses. The upper layer of such sediment, which forms in conditions of its rapid mixing or displacement (catastrophic processes of underwater sediments flowing at a speed up to 100 km/h), is enriched in natural conditions under the influence of metabolic products with nanostructured iron hydroxides, calcite, and clay minerals—montmorillonite, hydromica, glauconite, kaolinite. Medico-biological studies have shown that such layers, separated from other sediment layers, have different particle sizes and mineral compositions, as well as different biomedical properties. It is shown that the stratification of suspensions into separate layers

occurs during the activation of suspensions with biogeocenoses by nutrient media, i.e., in the conditions of biocolloid and geomechanical processes activation, which last for 5–25 days. Upon completion of these processes, the stratification of suspensions decreases. It was found that the upper layer of suspensions under the brine layer during the activation process hugely enriches with nano- and microparticles of iron and calcium compounds with up to 90–95% purity, and it raises their content in enriched products and increases the therapeutic properties of peloids separated from turbidite-pelagic marine underwater sediments in several times.

It was also established for the first time that the biocolloid treatment of iron-aluminosilicate materials leads to the stratification of suspensions into three layers during the activation process. The middle layer has a higher specific weight than the upper and lower (bottom) layers. The mechanism of such a phenomenon is considered and substantiated.

The results shown in Table 4.7 allow to substantiate the fundamental mechanism of layer-by-layer synergetic [25] separation of ocean red clays with their transition from goethite (tobacco) to red-brown (2′, 2″), and to oolitic (3′, 3″) ores enriched with iron-manganese nodules [15].

4.4   Conclusions

It is shown the interrelation of physical, geomechanical, colloidal, biocolloidal, and other processes in IASs and their complex influence on dispersion, transformation, and subsequent contact interphase nanostructuring, and further chemical transformations of sedimentary deposits of iron-aluminosilicate, and iron oxide-hydroxide materials into ore materials while processes of their self-hydrational separation in several layers.

It is shown and analyzed the generalized physical, nanochemical, mechanochemical, nanostructural, and other transformations of IAS components. It was shown as for separate inorganic iron oxide-hydroxide-silicate systems, first of all, iron oxides and hydroxides, silicate minerals, and quartz and for them in a composition of biocolloidal materials under the action of synergetic phenomena, and processes of symbiosis.

The ideas about complex multifactor mechanisms of IASs transformation are systematized.

An analysis of critical (catastrophic) phenomena and their comparison with usual ones in the earth's crust and on its surface from the viewpoint of colloidal and biocolloidal chemistry is done. That was not done before and is relevant for modern environmental safety.

The effect of ultra-anomalous behavior on marine sediment flow is established. It was explained from the viewpoint of classical mechanics and geomechanics, nanoscience, colloidal and biocolloidal chemistry.

Table 4.7 Results of chemical analysis of biocolloid tobacco (1′, 1″), brown (2′, 2″), and oolitic (3′, 3″) ores of the Azov deposit [15]

Element	Content (%wt)					
	1′	1″	2′	2″	3′	3″
Ag	< 0.01	< 0.01	< 0.01	< 0.01	< 0.01	< 0.01
Al	1.55	1.52	1.46	1.41	1.29	1.29
As	0.12	0.13	0.10	0.11	0.12	0.13
B	< 0.01	< 0.01	< 0.01	< 0.01	0.01	< 0.01
Ba	0.05	0.07	0.14	0.11	0.58	0.62
Be	< 0.01	< 0.01	< 0.01	< 0.01	< 0.01	< 0.01
Bi	< 0.01	< 0.01	< 0.01	< 0.01	< 0.01	< 0.01
Ca	1.62	1.53	1.12	1.18	1.29	1.00
Cd	< 0.01	< 0.01	< 0.01	< 0.01	< 0.01	< 0.01
Co	< 0.01	< 0.01	< 0.01	< 0.01	0.04	0.04
Cr	< 0.01	< 0.01	< 0.01	< 0.01	< 0.01	< 0.01
Cu	< 0.01	< 0.01	< 0.01	< 0.01	< 0.01	< 0.01
Fe	36.11	37.70	30.01	31.82	29.50	29.33
Ga	< 0.01	< 0.01	< 0.01	< 0.01	< 0.01	< 0.01
K	0.23	0.23	0.29	0.27	0.33	0.31
Li	< 0.01	< 0.01	< 0.01	< 0.01	< 0.01	< 0.01
Mg	0.45	0.45	0.29	0.25	0.36	0.23
Mn	0.56	0.70	7.18	6.09	8.81	9.04
Mo	< 0.01	< 0.01	< 0.01	< 0.01	< 0.01	< 0.01
Na	0.07	0.07	0.13	0.12	0.22	0.20
Ni	0.02	0.02	0.11	0.11	0.11	0.12
P	2.01	2.03	0.76	0.79	1.39	0.94
Pb	0.02	0.02	0.01	0.01	0.02	0.02
S	0.04	0.04	0.07	0.09	0.13	0.12
Si	8.31	7.44	7.74	8.07	7.68	8.63
Sn	< 0.01	< 0.01	< 0.01	< 0.01	< 0.01	< 0.01
Sr	0.04	0.04	0.07	0.06	0.11	0.11
Ti	0.12	0.11	0.09	0.08	0.09	0.10
V	0.05	0.05	0.05	0.05	0.05	0.05
W	< 0.01	< 0.01	< 0.01	< 0.01	< 0.01	< 0.01
Zn	0.03	0.03	0.03	0.03	0.03	0.03
Zr	< 0.01	< 0.01	< 0.01	< 0.01	< 0.01	< 0.01

The influence of rheological characteristics of iron-aluminosilicate turbidite-pelitic sediments on the occurrence of their usual and critical flow and the transformation character of the stratified flow is systematized, and the special significance of the phenomena of hyper- and ultra-anomaly is shown.

Research on the interrelated physical, colloid-chemical, biocolloid, nanostructural, and other features of usual and critical transformations of polymineral iron-aluminosilicate estuarine, marine, and oceanic sediments may become a new area of research on their global impact on the flowing of such sediments not only in terms of marine geology but also considering the further pollution of the oceans when the critical phenomena become much greater. On the other hand, colloid-chemical and biocolloid approaches will be able not only to explain more deeply the physical appearances of such flow but also to provide real tools to predict and prevent critical (catastrophic) occurrences with an application of obtained results.

References

1. Gomes C, Carretero M-I, Pozo M, Maraver F et al (2013) Peloids and pelotherapy: historical evolution, classification and glossary. Appl Clay Sci 75–76:28–38
2. Carretero MI (2020) Clays in pelotherapy. A review. Part I: mineralogy, chemistry, physical and physicochemical properties. Appl Clay Sci 189:105526. https://doi.org/10.1016/j.clay.2020.105526
3. Kovzun IG, Prokopenko VA, Panko AV, Tsyganovich OA, Oliinyk VO, Nikipelova OM, Ulberg ZR (2020) Nanochemical, nanostructural and biocolloidal aspects of transformations in dispersions of iron-aluminosilicate minerals. PH "Akademperiodyka", Kyiv. https://doi.org/10.15407/akademperiodyka.416.188
4. Panko AV, Kovzun IG, Ulberg ZR, Oleinik VA, Nikipelova EM, Babov KD (2016) Colloid-chemical modification of peloids with nano- and microparticles of natural minerals and their practical use. In: Fesenko O, Yatsenko L (eds) Nanophysics, nanophotonics, surface studies, and applications. vol 183 Springer PROCEEDINGS IN PHysics, Cham, pp 163–177. https://doi.org/10.1007/978-3-319-30737-4_14
5. Panko AV, Kovzun IG, Nikipelova OM et al (2019) Nanostructural effects in iron oxide silicate materials of the Earth's crust. In: Fesenko O, Yatsenko L (eds) Nanophysics, nanophotonics, surface studies and applications. Springer proceedings in physics, vol 221. Springer, Cham, pp 367–386. https://doi.org/10.1007/978-3-030-17759-1_25
6. Panko AV, Kovzun IG, Nikipelova OM et al (2018) Nanostructural and nanochemical processes in peloid sediments aided with biogeocenosis. In: Fesenko O, Yatsenko L (eds) Nanophysics, nanophotonics, surface studies and applications. NANO 2017. Springer proceedings in physics, vol 214. Springer, Cham, pp 215–230. https://doi.org/10.1007/978-3-319-92567-7_13
7. Tarasevich YuI, Ovcharenko FD (1975) Adsorbtsiya na glinistyih mineralah (Adsorption on clay minerals) (in Russian). Naukova dumka, Kyiv
8. Kovzun IG, Ulberg ZR, Panko AV, Prokopenko VA, Oleinik VA, Nikipelova EM (2015) Colloid-chemical and nanochemical processes in peloids on basis of ferrous clay minerals. In: Fesenko O, Yatsenko L (eds) Nanoplasmonics, nano-optics, nanocomposites, and surface studies. Springer proceedings in physics, vol 167. Springer, Cham, pp 233–243. https://doi.org/10.1007/978-3-319-18543-9_15
9. Panko AV, Kovzun IG, Prokopenko VA, Tsyganovich OA, Oliinyk VO, Nikipelova OM (2017) Nano- and microdisperse structures in processes of metamorphism, reduction sintering, and component separation of iron-oxide-silicate materials. In: Fesenko O, Yatsenko L

(eds) Nanophysics, nanomaterials, interface studies, and applications. NANO 2016. Springer proceedings in physics, vol 195. Springer, Cham, pp 743–755. https://doi.org/10.1007/978-3-319-56422-7_57

10. Ulberg ZR, Pertsov NV, Garbara SV, Nechaev SV, Stepanenko VG (1990) Silikatnyie bakterii v protsessah mikrobiologicheskogo vyischelachivaniya metallov iz rud (Silicate bacteria in the processes of microbiological leaching of metals from ores). Doklady AN USSR, Series B 5:80–83

11. Brierly IA (2007) Biohidrometallyrgy—this microbiologist's perspective. Adv Mater Res 20–21:3–10. https://doi.org/10.4028/www.scientific.net/amr.20-21.3

12. Rozanov AY, Zavarzin GA (1997) Bacterial paleontology. Her Russ Acad Sci 67(6):241–245

13. Panko AV, Kovzun IG, Prokopenko VA, Nikipelova OM, Tsyganovich OA, Oliinyk VO (2021) Catastrophic phenomena on marine slopes and in artificial dams in a presence of nanostructured iron-aluminosilicates. In: Fesenko O, Yatsenko L (eds) Nanomaterials and nanocomposites, nanostructure surfaces, and their applications. Springer proceedings in physics, vol 246. Springer, Cham, pp 381–395. https://doi.org/10.1007/978-3-030-51905-6_28

14. Verhoogen I, Turner FI, Weiss LE, Wahrhaftig C, Fyfe WS (1970) The Earth. An introduction to physical geology. Holt. Rinehart and Winston Inc, New York-Montreal-London-Sydney

15. Sherbak NP, Pavlishin VI, Litvin AL et al (1990) Mineralyi Ukrainyi: Kratkiy spravochnik (Minerals of Ukraine: A Quick Reference). Naukova dumka, Kyiv

16. Weyl PK (1970) An introduction to the marine environment. John Wiley and Sons, New York

17. Kessler YuM, Zaitsev AL (1989) Solvofobnyie effekty (Solvophobic effects). Himiya, Leningrad

18. Yahnin ED (1995) Leading scientists in colloid science of CIS (Vedushie uchenye-kolloidniki stran SNG). Russian Academy of Sciences, Moscow (in Russian)

19. Burkinskii BV, Babov KD, Nikipelova OM et al (2019) Kuyalnytsky estuary: realities and prospects of recreational use (Kuyal′nyts′kyy lyman: realiyi ta perspektyvy rekreatsiynoho vykorystannya) (in Ukrainian). Helgenetika, Odessa

20. Nasibullin BA, Gushcha SG, Nikipelova OM, Nikolenko SI et al (2007) Patofiziolohichni mekhanizmy biolohichnoi aktyvnosti kolorovykh hlyn (Pathophysiological mechanisms of biological activity of colored clays). Kharkiv. ISBN 978-966-400-418-0

21. Gomes CSF, Rautureau M, Gomes JHC, Silva EAF (2021) Interactions of clay and clay minerals with the human health. In: Gomes C, Rautureau M (eds) Minerals latu sensu and human health. Springer, Cham. https://doi.org/10.1007/978-3-030-65706-2_7

22. Gomes CF, Gomes JH, da Silva EF (2020) Bacteriostatic and bactericidal clays: an overview. Environ Geochem Health 42:3507–3527. https://doi.org/10.1007/s10653-020-00628-w

23. Emel'janov VA (2003) Osnovy morskoj geoekologii (Basics of marine geoekology). Kyiv, Naukova dumka

24. Panko AV, Kovzun IG, Nikipelova OM, Prokopenko VA, Tsyganovich OA, Oliinyk, VO, Kosorukov PO (2020) Chemical and geochemical transformations of pelitic (therapeutic) materials under the influence of biocolloid processes. Chem Phys Technol Surface: Proc. Ukr. Conf. Intern. Participation. 21−22 October 2020. Kyiv: ISC: P 136

25. Voitenko YI (2019) Synergetics of geological mediums and its impact on the effectiveness of the exploitation and exploration for mineral deposits. Mineral Res Ukr 3:15–21. https://doi.org/10.31996/mru.2019.3.15-21

Chapter 5
Prospects for the Catalytic Conversion of Plastic Waste

Olena Yanushevska, Tetiana Dontsova, Grygory Krymets, Svitlana Kyrii, Oksana Krasuliak, and Katerina Dorozhko

5.1 Existing Approaches to Plastic Disposal

In recent decades due to the ideal properties of polymers, such as chemical, thermal, and corrosion resistance, as well as low density, the ability to create any product design, the volume of plastic production has increased significantly, and thus plastic has become more applicable as a packaging material compared to wood, aluminum, or other metals [1, 2]. The active use of plastic together with the reluctance of manufacturers to spend resources on its disposal causes a big problem all over the world with a huge amount of plastic waste that is being accumulated in the form of garbage in landfills and in natural habitats.

Plastic can decompose naturally, but the process of natural decomposition cannot solve the problem of plastic pollution in the environment because of the extremely low rate of such decomposition. First, the plastic undergoes photodegradation under the influence of ultraviolet radiation from the sun, which ensures the inclusion of oxygen atoms in the polymer structure, which subsequently leads to the next stage—thermo-oxidative degradation. Due to thermal oxidative degradation, the plastic becomes brittle and breaks down into smaller fragments. This mechanical degradation of the plastic continues until the polymer chains of the individual piece reach a sufficiently low molecular weight that can be metabolized by microorganisms. Microorganisms convert the carbon of polymer chains into carbon dioxide or incorporate it into biomolecules, but this process can take from 50 to 800 years [3].

O. Yanushevska (✉) · T. Dontsova · G. Krymets · S. Kyrii · O. Krasuliak · K. Dorozhko
Kyiv, Ukraine
e-mail: l_rrr@ukr.net

T. Dontsova
e-mail: dontsova@ua.fm

G. Krymets
e-mail: krimets@xtf.kpi.ua

However, it should be taken into account that most commercial plastics are relatively stable in the environment, which makes processes of their destruction and degradation rather difficult. Thus, plastic accumulates in landfills and, what is especially alarming, in water bodies. Considering the fact that plastic can undergo hydrolysis, its micro- and nanoparticles can form in water, which can enter a human or an animal body.

Although the World Health Organization (WHO) [4], which examines the effects of microplastics in drinking water on human health, reported that the facts of such effects are currently unknown, the presence of plastic particles in water can and should cause concern and alarm among environmentalists all over the world. It is also unknown which by-products may appear in the aquatic environment if microplastics are included in the food chain of an aquatic ecosystem.

Burying plastic waste underground also leads to environmental toxicity due to the formation of toxic substances and the ingress of contaminants into groundwater and soil [5].

That is why in recent years the problems of recycling plastic have been tried to be solved in different ways, but on a global scale they can be divided into two main methods: mechanical processing and chemical processing. Plastic disposal methods are selected based on its composition. Polymeric materials can be classified as thermosetting and thermoplastics [6].

Thermoplastics or thermoplastic polymers (thermoplastics, thermoplastics) are called polymers that can be transformed into either a highly elastic or viscous-flow state when being heated. At this stage, plastic is processed into products. Thermoplastics include low-density polyethylene (LDPE) and high-density polyethylene (HDPE), polymethylmethacrylate (PMMA), polypropylene (PP), polyvinyl chloride (PVC), polycarbonate (PC)), polystyrene (PS), polybutylene terephthalate (PBT), polyamide imide (PAI), and other polymers [6].

Thermoplastics are characterized by a linear and branched structure of macromolecules and the absence of three-dimensional cross-linked structures. Such macromolecules can form both amorphous and amorphous-crystalline structures. Macromolecules are linked to each other by physical bonds, the breaking energy of which is small and thus lower than the chemical bond energy. This is the reason for the transition of thermoplastics to a plastic state without any destruction of macromolecules.

However, there are some polymers with linear macromolecules, such as cellulose that are not thermoplastic. This is due to the fact that the temperature of their destruction is below the melting point.

Basically, thermoplastics are dielectrics that are slightly soluble in water, also combustible and resistant to basic and acidic media.

Thermoplastics are divided into filled or homogeneous. Homogeneous thermoplastics, also called resins, are subdivided into natural and synthetic. Depending on the filling, they are distinguished as follows: fiberglass (polymers filled with glass fiber), carbon plastics (polymers filled with carbon fiber), as well as special plastics (polymers filled with various additives—fire retardants, electrically conductive and antifriction additives, antistatic agents, wear-resistant additives, etc.).

Thermosets are polymeric materials that are formed in the process of an irreversible chemical reaction with the formation of macromolecules, which are a cross-linked structural network (hardening).

Thermoset polymers are divided into epoxy plastics (base–epoxy resins), ether plastics (base–acrylic oligomers), phenoplasts (base–phenol–formaldehyde resins), aminoplasts (base–urea and melamine–formaldehyde resins), imidoplasts (base–oligoimides), etc.

Due to the cross-linked three-dimensional structure, thermosets are harder, more brittle, and also have a lower coefficient of thermal expansion. They are more heat-resistant, resistant to organic solvents, as well as to weak acidic and basic medium.

Upon completion of hardening, the products turn into an infusible and insoluble polymer, which practically does not undergo secondary chemical processing and does not melt when heated, but only degrades or ignites.

Thus, the processing of thermosetting plastics is different from the technology of thermoplastics processing waste and includes methods for the production of secondary press powders. At the first stage, thermosetting waste is collected, crushed, and separated into fractions. Due to the fact that thermosetting materials contain a small amount of uncross-linked polymer and after cleaning from metals and dirt, the crushed waste of these materials is used as an active filler—an additive to the main raw materials and other compositions in the amount of 10–20%. The equipment used for the production of secondary press powders includes a vibrating mill with a hopper, a fan, a cyclone, and a mixer, in which the fine fraction of the secondary press powder is mixed in predetermined proportions with the primary press powder.

In 2018, the Manas-Zloczower's Case School engineering laboratory carried out a number of studies related to the processing of thermosetting plastics, which might allow to get the reforming thermosetting plastics and then to convert it into valuable products. The researchers proposed a solvent-based process they called "vitrification". The authors of the process were assured that "vitrification" transforms thermosetting plastics into a new class of materials known as "vitrimer polymers" that could be reformed and recycled. But these works have still been under development and are still far from being implemented on an industrial scale [7].

It should be noted that mechanical type of thermosetting plastics processing is associated with the problem of contamination of the primary material during production processes and, as a result, secondary contamination of the processed materials, which can be of a chemical or microbiological nature. The Food and Drug Administration (FDA) is known to have raised concerns about the use of recycled plastic materials for food [6]. In addition, mechanical methods of processing plastics produce end products with lower thermomechanical properties.

Meanwhile, there is a growing concern among environmentalists about plastics recycling. Researchers estimate that up to 99 million metric tons (Mt) of mismanaged plastic waste (MPW) were produced worldwide in 2015 [8]. By 2060, this figure may increase to 265 Mt per year. Environmental regulations consider plastic recycling by incineration or waste disposal to landfill undesirable, and at the same time, the EU expects 55% recycling of packaging waste by 2030 [9].

The processing of thermoplastics because of their structure and the ability to melt and sublimate is fundamentally different from the processing of thermosets. For thermoplastics, chemical processing is actively used—a process in which polymers, as a result of a chemical reaction, are converted into monomers or oligomers, forming products with a lower molecular weight; in this case, the chemical structure of the polymer changes, which simplifies the process of its processing [10, 11].

Today, the following methods of processing plastic waste can be distinguished:

- hydrolysis—it consists in the splitting of plastic with an aqueous-acid solution at a high temperature;
- glycolysis—treatment with the addition of glycol $(CnH_2n(OH)_2)$ at temperatures above 210–250 ˚C;
- methanolysis—in this case, the decomposition of polymer waste occurs with the help of methanol in reactors under pressure and at high temperatures;
- pyrolysis—based on the method of thermal destruction of plastic, in which air ingress is unacceptable. In this case, the raw material is broken into monomers. With this method, there is no need for careful sorting and cleaning of plastic waste.

5.2 Prospects for Catalytic Thermochemical Conversion in the Recycling of Plastics

The pyrolysis method shows high efficiency in tandem with catalytic methods. Thermochemical conversion in the presence of catalysts is a promising technology for processing plastic waste in order to obtain valuable products. The choice of process conditions and the use of certain types of catalysts to increase the selectivity of the process can make it possible to obtain valuable products for chemical synthesis and also it becomes easier to solve the problem of an environmentally friendly approach to plastic waste processing.

This work [12] has shown the use of catalytic pyrolysis of biomass (cellulose, xylan, or lignin) and polyethylene (PE) using ZSM-5 as a catalyst. It has been shown that the yield of hydrocarbons after catalytic conversion increases, and the formation of coke on the catalyst decreases in comparison with non-catalytic pyrolysis of a mixture of biomass and PE. This indicates the possibility of selective processing of high molecular weight hydrocarbons vapors into the desired products. Further use of ZSM-5 in the process of pyrolysis of various plastics types has shown a decrease in the decomposition temperature of plastics in the following order: PE, PP, PS, and PET.

Works devoted to the use of zeolites as catalysts in polymer processing show that the presence of a controlled pore size in zeolites (9.0 Å for ultrastable zeolite Y (USY), 7.8 Å for HY zeolites compared to 5.6 Å for HZSM -5) promotes the selective synthesis of certain aromatic hydrocarbons. This structure of zeolites facilitates the passage of high molecular weight products into the pores and promotes a mass transfer [13].

The treatment of plastic waste by catalytic pyrolysis using zeolites as catalysts is an important area for the selective formation of aromatic hydrocarbons [14]. Ultrastable Y zeolites (USY) have been used in the conversion of polystyrene (PS) aiming to obtain benzene and ethylbenzene.

Studies have shown [15] that the use of USY, in comparison with HZSM-5, allows not only to reduce the pyrolysis temperature of plastic waste (polypropylene and polyethylene), but also significantly increases the amount of liquid fraction in products containing alkylbenzenes, olefins, and naphthalenes, and moreover, olefins are of much higher quality.

In [16], polymers including polycarbonate (PC), waste tires (WT), polybutadiene rubbers (BR), and polyethylene (PE) were pyrolyzed in the presence of catalysts based on zeolite HY and iron or zirconium. Depending on the type of plastic and the type of catalyst (Fe/HY and Zr/HY), thermal pyrolysis produces various hydrocarbons—from alkanes and alkenes to monocyclic aromatic hydrocarbons (MAHs).

Metal-containing catalysts are widely used in many areas of the chemical industry. The so-called heavy metals are active in many processes due to their ability to exhibit various oxidation states, which causes the interest of scientists in their research [17–19].

The use of iron in the processing of plastics has been proven to be a promising direction [20]. The process of pyrolysis of polystyrene (PS) was studied in the presence of steel slag (SS) as a catalyst. The dehydrogenation of plastic hydrocarbons at 700 °C yielded hydrogen, and pyrolysis in a CO_2 medium yielded CO. Thus, it has been shown that catalytic conversion of PS on iron containing catalyst can be a sustainable method for producing synthesis gas (syngas).

The capabilities of thermochemical catalytic conversion of plastic waste [21] provide much more valuable products than just a wide range of hydrocarbons. The participation of a catalyst in the process leads to an increase in the selectivity of plastic pyrolysis reactions, and the qualitative and quantitative characteristics of the catalyst can be a prerequisite for the synthesis of nanotubes (CNT) and hydrogen. In this work, catalysts based on Fe with the addition of Mn (0, 1, 5, 10 wt.%) for the processing of propylene (PP) at a temperature of 800° C were investigated. With an increase in the Mn content from 0 to 10 wt.%, the yield of CNTs increases (from 23.4 to 32.9 wt.%). The results show that the Fe particles in fresh catalysts are 10–25 nm in size. It is known that the size of catalyst particles affects the formation of CNTs: Larger particles are less catalytically active, while smaller ones in their turn are highly active. The results of the work indicate that Fe is an active center, and Mn prevents sintering of iron particles and stabilizes it in a highly dispersed state.

There are many methods [22] of processing plastics based on alcoholysis (methanolysis, ethanolysis, etc.) using catalysts. The article presents studies of alcoholysis for the destruction of polyethylene terephthalate (PET) in the presence of zinc acetate. In particular, the paper describes examples of the catalytic treatment of biodegradable plastics, especially thermoplastics. It is known that the types of catalysts described for converting polylactic acid (PLA) to methyl lactate also include metal catalysts, organocatalysts, and ionic liquids. It has been shown that the use of

enzymes as biocatalysts for the depolymerization of plastic waste can be an alternative to metal catalysts [22].

5.3   From Traditional Catalysts to Biocatalysts in Plastic Recycling

For example, the lipase enzyme catalyzes two opposite reactions: polymer synthesis and its depolymerization. Researchers have already demonstrated the reversible polymerization-depolymerization of poly (ε-caprolactone) (PCL) using a biocatalyst. The success of using enzymes as biocatalysts lies in the possibility of creating waste-free cyclic processes: first, polymerization, then depolymerization, and then again, polymerization. Therefore, understanding the mechanism of enzymatic reactions will make it possible to use them better as biocatalysts for the treatment of biodegradable polyesters.

Thus, the use of the right modern strategies for the synthesis and decomposition of polymers can make a breakthrough in the implementation of the cyclic and wasteless use of polymers, make them harmless for processing, and, ultimately, increase safety for humans and the environment generally [23]. To do this, the plastics industry needs to focus on the production of biodegradable plastics and study the mechanisms of their biodegradation more actively.

It is worth mentioning that most commercial polymers are not biodegradable. Biodegradable plastics include many of the commonly used plastics such as PVC, PP, PS, PET, PUR, and PE. Moreover, the inertness and resistance of polymers to microbial attack can be reduced by the inclusion of starch and prooxidants to facilitate fragmentation.

Starch (amylopectin and amylase) is one of the cheapest and most widespread materials which often used as a biopolymer for the production of biodegradable plastics that are directly processed by microorganisms (Variovorax paradoxus, Comamonas sp., Aspergillus fumigatus, Acidovorax faecilis, and P. lemoignei) using enzymes in both anaerobic and aerobic conditions. Biodegradable plastics can be of two types: bio-based plastics (polyhydroxyalkanoates (PHA), polylactides (PLA)) and mixed plastics (starch/polyester, starch/polyethylene, starch/polyvinyl alcohol (PVA) blends) [23].

Microorganisms form colonies and attach to the polymer surface (Fig. 5.1). The exoenzyme, or extracellular enzyme, is then released by microorganisms, which, through enzymatic hydrolysis, break down polymer complexes into smaller molecules such as dimers and monomers (Fig. 5.1).

In [24], the authors analyzed in detail the difficulties associated with the biodegradation of polyethylene terephthalate (PET), which ends up in landfills and oceans in large quantities. PET is a polyester that is extremely difficult to hydrolyze due to its high content of terephthalate aromatics, which reduce polymer chain mobility. The natural biodegradation of PET takes hundreds of years, but active PET biocatalysts
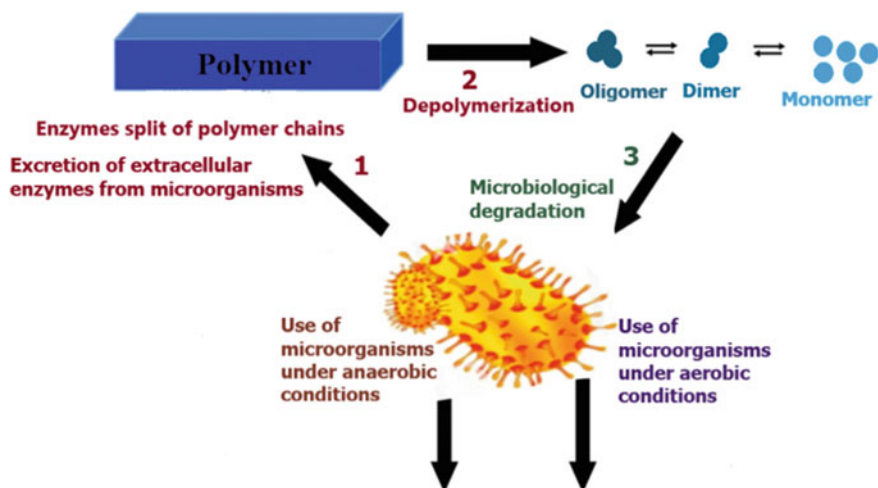
Fig. 5.1 Mechanisms of plastic biodegradation

could open up new possibilities for its bioconversion, including under conditions of high temperatures, pH, and mineralization of the medium.

Scientists have discovered strains of fungal and bacterial microorganisms (TfCut2 from Thermobifida fusca KW3 and LC-cutinase (LCC) isolated from a compost metagenome) that biodegrade PET into low molecular weight oligomers or monomers such as Bis (2-hydroxyethyl) terephthalate (BHET) 2-hydroxyethyl) terephthalate (MHET) [25].

Decomposition of PET based on whole cell biocatalyst [26] has advantages over the use of free enzymes due to the enzymatic activity of metabolites. It is known that whole cells as biocatalysts make it possible to carry out multistep reactions with the regeneration of cofactors and high stereoselectivity, for example, hydroxylation of non-activated carbon atoms. Whole cell biocatalysts are quite effective in multistep reactions because they provide a protective environment for enzymes compared to using free enzymes.

Interesting studies in the field of protein engineering have shown the effectiveness of an improved PET hydrolase that provides of 90% PET depolymerization into monomers during 10 h [27].

An important fact is that enzymatically depolymerized PET waste exhibits the same properties as petrochemical PET, and thus, bioprocessed PET can be reintroduced into the production of plastic products.

The authors [28] consider alternative biodegradable plastics such as polyhydroxyalkanoates (PHAs), which are non-toxic bioplastics and are readily biodegradable by microorganisms with limited carbon and energy sources.

The authors noted the importance [29] of the development of the bioplastics industry, as well as new ways of processing them. New microbial enzymes and their metabolic pathways need to be studied in order to optimize the conditions under

which polymers can be efficiently degraded. The authors paid special attention to the problem of processing polyhydroxyalkanoates (PHA) and polylactic acid (PLA) under aerobic and non-aerobic conditions. The authors assure that biodegradable bioplastics can be recycled using alternative methods that significantly reduces the amount of plastic waste entering the environment. At the same time, bioplastics made from bioplastics can significantly reduce the involvement of natural carbon resources into industry.

5.4   Conclusions

The importance of plastic in human everyday life is very difficult to overestimate. The industrial use of plastics also occupies a huge segment of modern manufacturing, causing an ever-increasing accumulation of plastic waste that is not recyclable. Due to the rapid accumulation and diverse composition of plastic waste, it is impossible to limit ourselves only to their traditional incineration, and the requirements for the state of the environment force the search for more environmentally friendly alternatives.

The existing methods of processing plastic waste imply three main directions: mechanical, chemical, and enzymatic. The main difficulty of the mechanical method is the need to presort and clean up plastic waste. Moreover, it is sometimes impossible to carry out a thorough washing of waste due to the long accumulation of plastic waste in landfills. Methods of chemical processing (hydrolysis, glycolysis, methanolysis, and pyrolysis) are successfully used, which do not require careful washing and sorting of waste, but are quite energy intensive and time consuming. To increase the speed and selectivity of plastics processing, a promising method of catalytic conversion of the vapor phase of pyrolysis is used. The variety of catalysts used makes it possible to obtain target valuable intermediates from thermoplastics. In addition to splitting plastics, pyrolysis plants can also process other organic waste. One of the pyrolysis products is fuel gas, the sale of which can be a source of additional income.

Biological methods of plastics processing are of great interest, as methods that may allow in the future to introduce precisely waste-free technologies for the use of polymers. From this point of view, the development of bio-engineering of microorganisms, capable of including plastic in the chain of their metabolism, is relevant. Biodegradable plastics can also be an effective alternative to petrochemical-based plastics. The production of bioplastics from the decomposition products of the same bioplastics can bring the solution of environmental problems closer to the creation of "green technologies" in the field of synthesis and use of high-polymer compounds.

References

1. Shen L, Worrell E (2014) Plastic recycling. In: Handbook of recycling state-of-the-art for practitioners, analysts, and scientists, pp. 179–190. https://doi.org/10.1016/B978-0-12-396459-5.00013-1
2. Yousef S, Eimontas J, Zakarauskas K, Striūgas N (2021) Microcrystalline paraffin wax, biogas, carbon particles and aluminum recovery from metallised food packaging plastics using pyrolysis, mechanical and chemical. J Clean Prod 290:125878. https://doi.org/10.1016/j.jclepro.2021.125878
3. Francis R (2016) Recycling of polymers: methods, characterization and applications. John Wiley & Sons, Hoboken, NJ, USA, ISBN: 978-3-527-33848-1, 288 Pages
4. WHO publish report on microplastics in drinking water, Written by Tim Newman on August 28, 2019—Fact checked by Jasmin Collier. https://www.medicalnewstoday.com/articles/326144
5. Rudolph N, Kiesel R, Aumnate C (2017) Understanding plastics recycling: economic, ecological, and technical aspects of plastic waste handling. Carl Hanser Verlag GmbH Co. KG: Munich, Germany, eISBN: 978-1-56990-677–4, 131 Pages
6. Grigore ME (2017) Methods of recycling, properties and applications of recycled thermoplastic polymers. Recycling 2(24):2–11. https://doi.org/10.3390/recycling2040024
7. Case Western researchers develop chemical process to recycle thermoset polymers, recycling today. News and information for recycling professionals. https://www.recyclingtoday.com/article/case-western-researchers-develop-technology-recycle-plastic-scrap/
8. Lebreton L, Andrady A (2019) Future scenarios of global plastic waste generation and disposal. Palgrave Commun 5:6. https://doi.org/10.1057/s41599-018-0212-7
9. Schubert T, Lechleitner A, Lehner M, Hofer W (2020) 4-Lump kinetic model of the co-pyrolysis of LDPE and a heavy petroleum fraction. Fuel 262:116597. https://doi.org/10.1016/j.fuel.2019.116597
10. Kasar P, Sharma DK, Ahmaruzzaman M (2020) Thermal and catalytic decomposition of waste plastics and its co-processing with petroleum residue through pyrolysis process. J Clean Prod 265:121639. https://doi.org/10.1016/j.jclepro.2020.121639
11. Jechan L, Eilhann EK, Si SL, Wei-Hsin C, Jörg R, Young-Kwon P (2021) Chemical recycling of plastic waste via thermocatalytic routes. J Clean Prod 321:128989. https://doi.org/10.1016/j.jclepro.2021.128989
12. Xue Y (2017) Thermochemical conversion of organic and plastic waste materials through pyrolysis. Graduate Theses and Dissertations. 16242. https://lib.dr.iastate.edu/etd/16242
13. Kassargy C, Awad S, Burnens G, Kahine K, Tazerout M (2018) Gasoline and diesel-like fuel production by continuous catalytic pyrolysis of waste polyethylene and polypropylene mixtures over USY zeolite. Fuel 224:764–773. https://doi.org/10.1016/j.fuel.2018.03.113
14. Wang J, Jiang J, Sun Y, Zhong Z, Wang X, Xia H, Ragauskas AJ et al (2019) Recycling benzene and ethylbenzene from in-situ catalytic fast pyrolysis of plastic wastes. Energy Convers Manag 200:112088. https://doi.org/10.1016/j.enconman.2019.112088
15. Santos BPS, Almeida DD, Marques MFV et al (2019) Degradation of polypropylene and polyethylene wastes over HZSM-5 and USY Zeolites. Catal Lett 149:798–812. https://doi.org/10.1007/s10562-019-02677-y
16. Wang J, Jiang J, Sun Y, Wang X, Li M, Pang S, Ruan R, Ragauskas AJ, Ok YS, Tsang DCW (2021) Catalytic degradation of waste rubbers and plastics over zeolites to produce aromatic hydrocarbons. J Clean Prod 309:127469. https://doi.org/10.1016/j.jclepro.2021.127469
17. Yanushevska O, Dontsova T, Nahirniak S, Alisova V (2021) TiO$_2$–ZnO nanocomposites for photodegradation of dyes in water bodies conference paper. Springer Proc Phys 246:719–731. https://doi.org/10.1007/978-3-030-51905-6_49
18. Yanushevska OI, Dontsova TA, Aleksyk AI, Didenko OZ, Nypadymka AS et al (2020) Surface and structural properties of clay materials based on natural saponite. Clays Clay Minerals 68(5):465–475. https://doi.org/10.1007/s42860-020-00088-4

19. Litynska M, Dontsova T, Yanushevska O, Tarabaka V (2021) Development of iron-containing sorption materials for water purification from arsenic compounds. Eastern-Euro J Enterprise Technol 2(110):35–42. https://doi.org/10.15587/1729-4061.2021.230216

20. Lee T, Jung S, Park Y-K, Kim T, Wang H, Moon DH, Kwon EE (2020) Catalytic pyrolysis of polystyrene over steel slag under CO_2 environment. J Hazard Mater. https://doi.org/10.1016/j.jhazmat.2020.122576

21. He S, Xu Y, Zhang Y, Bell S, Wu C (2021) Waste plastics recycling for producing high-value carbon nanotubes: investigation of the influence of Manganese content in Fe-based catalysts. J Hazard Mater 402:123726. https://doi.org/10.1016/j.jhazmat.2020.123726

22. Feghali E, Tauk L, Ortiz P, Vanbroekhoven K (2020) Walter Eevers, catalytic chemical recycling of biodegradable polyesters. Polym Degrad Stab 179:109241. https://doi.org/10.1016/j.polymdegradstab.2020.109241

23. Ahmed T, Shahid M, Azeem F et al (2018) Environmental science and pollution research. Environ Sci Pollut Res 25:7287–7298. https://doi.org/10.1007/s11356-018-1234-9

24. Samak NA, Jia Y, Sharshar MM, Mu T, Yang M, Peh S, Xing J (2020) Recent advances in biocatalysts engineering for polyethylene terephthalate plastic waste green recycling. Environ Int 145:106144. https://doi.org/10.1016/j.envint.2020.106144

25. Wei R, Oeser T, Schmidt J, Meier R, Barth M, Then J, Zimmermann W (2016) Engineered bacterial polyester hydrolases efficiently degrade polyethylene terephthalate due to relieved product inhibition. Biotechnol Bioeng 113(8):1658–1665. https://doi.org/10.1002/bit.25941

26. de Carvalho CCCR (2017) Whole cell biocatalysts: essential workers from Nature to the industry. Microb Biotechnol 10(2):250–263. https://doi.org/10.1111/1751-7915.12363

27. Tournier V, Topham CM, Gilles A et al (2020) An engineered PET depolymerase to break down and recycle plastic bottles. Nature 580:216–219. https://doi.org/10.1038/s41586-020-2149-4

28. Ong SY, Chee JY, Sudesh K (2017) Degradation of polyhydroxyalkanoate (PHA): a review. J Sib Fed Univ Biol 10(2):211–225. https://doi.org/10.17516/1997-1389-0024

29. Fredi G, Dorigato A (2021) Recycling of bioplastic waste: a review. Adv Ind Eng Poly Res 4(3):159–177. https://doi.org/10.1016/j.aiepr.2021.06.006

Chapter 6
Antibiotic-Loaded Polyacrylamide-Based Hydrogels for Infected Wound Care

P. Virych, O. Nadtoka, Volodymyr Doroschuk, Sergey Lelyushok, V. Chumachenko, Tetiana Bezugla, Oleg Yeshchenko, and N. Kutsevol

6.1 Introduction

The treatment and preventive care of infected traumatic and burn wounds require powerful antibacterial agents. Among substances with high antimicrobial activity, antibiotics continue to occupy the leading positions, despite the emergence and threatening spread of antibiotic-resistant strains of microorganisms. The therapy of contaminated wounds involves the systemic use of antibiotics, sometimes in large quantities. But in many cases, the systemic administration may not achieve adequate antibiotic concentration in the injury site. The increase of the systemic dose is limited by systemic toxicity. The way out is the topical application of antibiotic-loaded dressings; the hydrogel formulations are rather attractive due to the unique properties of these drug carriers [1].

In recent decades, many antibacterial hydrogels have been created [2, 3]. Such antibiotics as gentamicin, ampicillin, vancomycin, ciprofloxacin, Cefazolin, Cefuroxime, and others are used for the antibiotic-loaded hydrogels [4–9]. Various natural, synthetic, and hybrid hydrogels, obtained by combining natural polymers with synthetic ones, are studied as drug carriers that can deliver the antibiotics directly to the infected area [10–12]. The non-toxicity, biocompatibility, high oxygen permeability, and satisfactory mechanical properties are very important features of such materials [13]. In addition, easy loading with the desired antibiotic is desirable.

The antimicrobial hydrogels used as wound dressings should hydrate the wound, absorb exudates, inhibit microbial growth, and prevent additional contamination [14]. The chemical nature, cross-linking density, and the internal structure of the hydrogels, as well as the properties of antibiotics, must be optimized for delivering

P. Virych (✉) · O. Nadtoka · V. Doroschuk · S. Lelyushok · V. Chumachenko · T. Bezugla · O. Yeshchenko · N. Kutsevol
Taras Shevchenko National University of Kyiv, 64, Volodymyrska Str, Kyiv 01033, Ukraine
e-mail: sphaenodon@ukr.net

drug molecules and killing harmful microorganisms. The antibiotic-loaded hydrogels should gradually release the antibiotic at the target site, thus suppressing infection, inhibiting biofilm formation, and promoting the healing process [15]. The drug release characteristics are very important for wound care. However, studies on the release of various antibiotics from antimicrobial hydrogels are infrequent.

Our idea was to create polyacrylamide-based antimicrobial hydrogels containing different antibiotics. The molecule structure, the side functional groups, and other features of the antibiotics are assumed to influence the drug release from the antimicrobial hydrogel. For the antibiotic release study, the samples of polyacrylamide hydrogel were loaded with five cephalosporin antibiotics by swelling from their concentrated solutions. The local topical application of such antibiotic-loaded hydrogels is a guarantee of overcoming the side effects of a systemic overdose. The influence of hydrogel structure features on antibiotic loading and release was evaluated in experiments with polyacrylamide-based hydrogels synthesized with a small amount of polysaccharides as components affecting the structure. The synthesized antibiotic-loaded hydrogels were tested in vitro against some painful microorganisms and in vivo as antimicrobial dressings.

6.2 Experimental

6.2.1 Reagents

Acrylamide (AA), N,N'-methylene-bis-acrylamide (MBA), dextrans with $M_w = 20\,000$ g/mol (D20), $M_w = 100\,000$ g/mol (D100), and $M_w = 500\,000$ g/mol (D500), as well as cerium (IV) ammonium nitrate (CAN) were supplied by Sigma-Aldrich (USA). Antibiotics Cefuroxime, Cefazolin, Ceftriaxone, Cefoperazone, and Cefotaxime were purchased from a local pharmacy. All reagents were used without additional purification. Deionized water was used for the hydrogel syntheses, and distilled water was used for all experiments.

6.2.2 Syntheses of Hydrogels

Polyacrylamide (PAA) hydrogels were synthesized at 25 ℃ by free radical polymerization in the presence of N,N'-methylene-bis-acrylamide as a cross-linking agent. Before synthesis, a measured volume of distilled water (24 ml) was purged with argon for 20 min to remove dissolved oxygen. Then 1 ml of 0.125 N HNO_3 containing CAN (3×10^{-2} mmol) was added, and the solution was stirred and purged with argon for another 2 min. A mixture of monomer AA (50 mmol) and the cross-linking agent MBA (0.4 g per 100 g of AA) was added to the solution, preventing the access of

atmospheric oxygen. The reaction mixture was kept under argon for 24 h. The synthesized hydrogels were thoroughly washed with distilled water to remove unreacted monomer and all other low molecular weight substances.

To obtain polyacrylamide-based hydrogels with just another internal structure, a small amount of dextran ($5 \cdot 10^{-4}$ mmol) was dissolved in distilled water (24 ml) at the first step of synthesis [16, 17]. All other steps were the same as described above. The interaction of the CAN/HNO$_3$ oxidative system with dextran leads to the formation of the active centers on the polysaccharide macromolecule triggering the growth of polyacrylamide chains The grafted PAA chains have the straightened conformation near the dextran grafting points [18, 19]. As a result, the cross-linked dextran-graft-polyacrylamide (D-g-PAA) has an internal structure quite different compared to the cross-linked PAA sample with the same number of cross-links.

All hydrogels were dried and stored in a desiccator at ambient temperature.

The synthesized hydrogels are designated as PAA-0.4, D20-g-PAA-0.4, D100-g-PAA-0.4, and D500-g-PAA-0.4; the name indicates the presence/absence of the dextran component of different molecular weight in the hydrogel, as well as the cross-linking density (the ratio of MBA to AA in the syntheses).

6.2.3   Preparation of Antibiotic-Loaded Hydrogels

To prepare the antimicrobial hydrogels, cephalosporin antibiotics such as Cefazolin, Cefotaxime, Cefoperazone, Ceftriaxone, and Cefuroxime (Fig. 6.1) were used. Their physicochemical properties and biological activity depend on the structure of the active center and the nature of the functional groups of substituents located in the cephalosporin nucleus. The antibiotic-loaded hydrogels were prepared by swelling in the antibiotic solution (the concentration of this solution, as well as swelling time, was determined by the objectives of the experiment). The names of the antibiotic-loaded hydrogels contain an indication of the antibiotic used.

The concentrated solutions of the antibiotics were used for preparing antibiotic-loaded hydrogels for drug release study (Table 6.1). A piece of dried hydrogel was weighed, placed in an aqueous solution of the antibiotic, and incubated at 25 °C for 18 h. The amount of the antibiotic in the swollen hydrogel sample was estimated by subtracting the amount of the antibiotic remaining in the solution from the initial content. All concentrations were determined by high-performance liquid chromatography with ultraviolet detection (HPLC–UV).

The antibiotic-loaded hydrogels used for antimicrobial testing were prepared by swelling the dry hydrogels in the 1 and 0.1 mg/ml antibiotic solutions. The hydrogel samples were incubated in the antibiotic solution at 25 °C for 24 h.
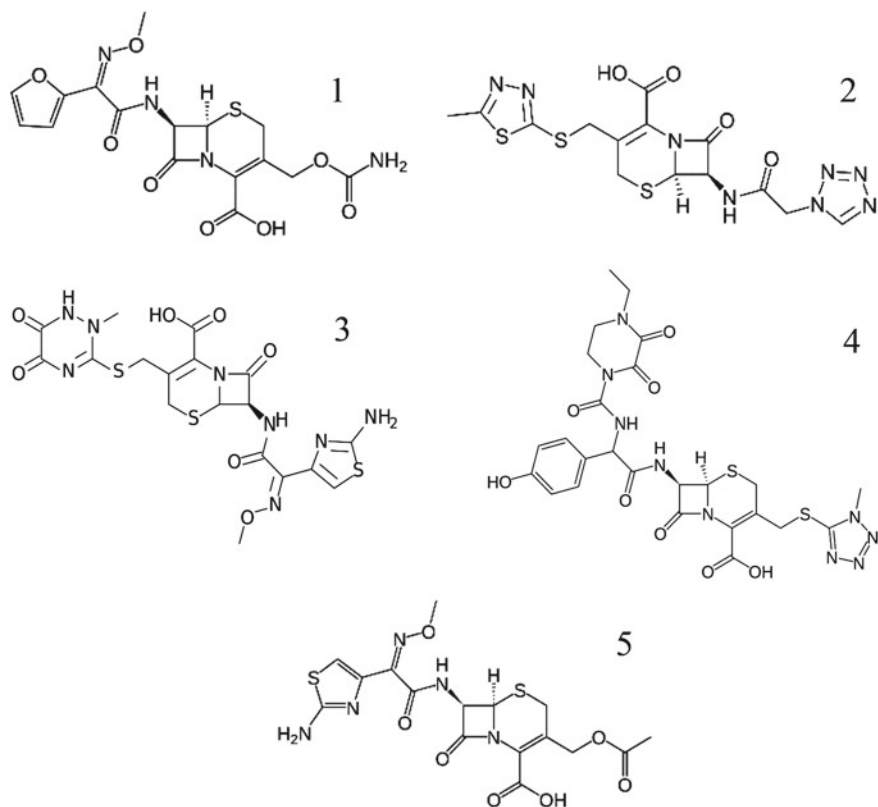
Fig. 6.1 Structural formulas of Cefuroxime (1), Cefazolin (2), Ceftriaxone (3), Cefoperazone (4), and Cefotaxime (5)

Table 6.1 Concentration of the antibiotic solutions used for preparing antibiotic-loaded hydrogels for drug release experiments

	Sample	C (mg/ml)
1	Cefuroxime	167
2	Cefazolin	400
3	Ceftriaxone	400
4	Cefoperazone	335
5	Cefotaxime	286

6.2.4 Antibiotic Release Study

To study the release of the antibiotic into an aqueous solution, the hydrogel samples swollen during 18 h in the concentrated antibiotic solution (Table 6.1) were neatly removed from the container, gently dried with a piece of filter paper, and then placed in 25.0 ml of distilled water. The concentration of the solution was determined at regular

time intervals by the HPLC–UV method. This concentration allowed estimating the part of the antibiotics (in %) that were released from the antibiotic-loaded hydrogels into water.

6.2.5 Antibacterial Activity Testing

The non-resistant to antibiotics wild strains of *Staphylococcus aureus, Escherichia coli,* and *Klebsiella pneumoniae,* as gram-positive and gram-negative bacteria models, were used to test the antibacterial activity of the synthesized antibiotic-loaded hydrogels. The ability to inhibit bacteria growth was evaluated by the disk diffusion method. A Müller–Hinton agar medium was used in the experiments. The tested hydrogel samples were 5 mm in diameter. The measurement of the growth inhibition zone was carried out using a digital caliper Miol 15–240. The contact of the hydrogel samples with the microorganisms occurred within 24 h before recording the diameter of growth inhibition. Statistical data processing was performed using the Shapiro–Wilk test ($p > 0.05$) and the Scheffe ANOVA test ($p < 0.05$). Each in vitro experiment was repeated not less than three times. The antibacterial activity of the hydrogels was assessed by analyzing the diameter of the growth retardation [20].

A rat model was used to evaluate the effectiveness of the synthesized samples in the infected wound treatment. All in vivo experiments were carried out according to the Law of Ukraine "On the Protection of Animals from Cruelty" and the European Convention for the Protection of Vertebrate Animals Used for Research and Other Scientific Purposes. A flesh wound (7–8 mm in diameter) was infected with the mixture of microorganisms *S. aureus, E. coli,* and *K. pneumoniae.* The total amount of pathogens was $1 \cdot 10^8$ CFU/ml. The wounds were covered with the synthesized antibiotic-loaded hydrogels, the unloaded hydrogel, and the standard fabric material (gauze dressing). After 24 h, the bandages were removed, the wounds were wiped with a sterile swab, and wound bacteria were inoculated into the nutrient medium. Yolk-salt agar was used to cultivate gram-positive bacteria, and Endo medium was used for gram-negative bacteria. Wound healing of the rat wounds was assessed visually.

6.3 Results and Discussion

According to the syntheses of hydrogels described above, all samples have the same cross-linking density. The content of the antibiotics in the PAA-0.4 hydrogels is given in Table 6.2; it is determined by the properties of a given antibiotic.

All synthesized hydrogels are very hydrophilic and contain water even when dried [17]; thus, the hydrogel samples swollen in the concentrated antibiotic solution (Table 6.1) were used in drug release experiments immediately after preparation without drying. The drug desorption occurs when the synthesized antibiotic-loaded

Table 6.2 Content of antibiotics in the synthesized hydrogels (g of antibiotic per g of dried hydrogel)

	Sample	Content (g/g)
1	PAA-0.4-Cefuroxime	1.64
2	PAA-0.4-Cefazolin	2.51
3	PAA-0.4-Ceftriaxone	3.72
4	PAA-0.4-Cefoperazone	4.14
5	PAA-0.4-Cefotaxime	7.90

Fig. 6.2 Antibiotic release (in %) versus time for the hydrogels PAA-0.4-Cefazolin (1), PAA-O.4-Cefuroxime (2), PAA-O.4-Cefoperazone (3), PAA-O.4-Cefotaxime (4), and PAA-O.4-Ceftriaxone (5)
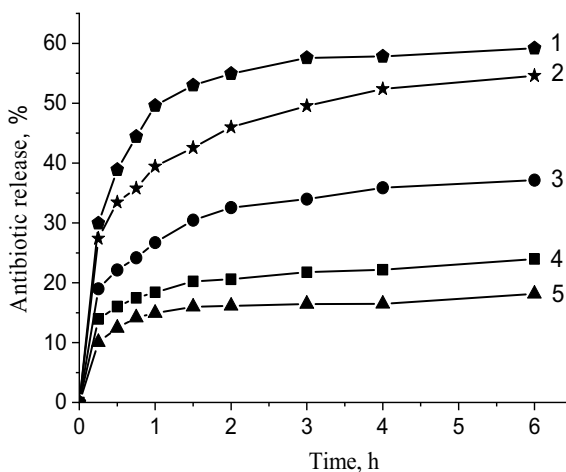
hydrogels are immersed in water. The antibiotic release was estimated by analyzing the concentrations of the antibiotic in the solution at certain intervals. It can be expressed as an amount of the antibiotic (in %) which has passed from the hydrogel into the water solution. The antibiotic release profiles for all antibiotic-loaded PAA-0.4 hydrogels are shown in Fig. 6.2.

According to data obtained, the initial burst of release in the first quarter of an hour is followed by a slowdown in the rate. This is registered for all antibiotic-loaded samples, but the parameters of the drug release process are different for the different antibiotics. As shown in Fig. 6.2, the PAA-0.4-Cefazolin and PAA-0.4-Cefuroxime samples demonstrate the fastest drug release, although the total amount of antibiotic released is less than in the other samples, because the initial concentration is lower here. During this period, other antimicrobial hydrogels release the antibiotics at a much slower rate. A significant decrease in the release rate of all hydrogels occurs after about an hour of contact with the solution. According to data obtained, about 15% of the antibiotic is desorbed from PAA-0.4 hydrogels containing Ceftriaxone or Cefotaxime within the first hour. More than 25% of the drug passes into solution from the Cefoperazone-loaded hydrogel, 40% from Cefuroxime-loaded sample, and almost 50% from Cefazolin-loaded one. So, the drug release rate determines the percentage of antibiotics released into the solution; the total actual

Fig. 6.3 Cefuroxime release (in%) versus time for the Cefuroxime-loaded hydrogels D20-g-PAA-O.4 (1), D100-g-PAA-O.4 (2), and D500-g-PAA-O.4 (3)
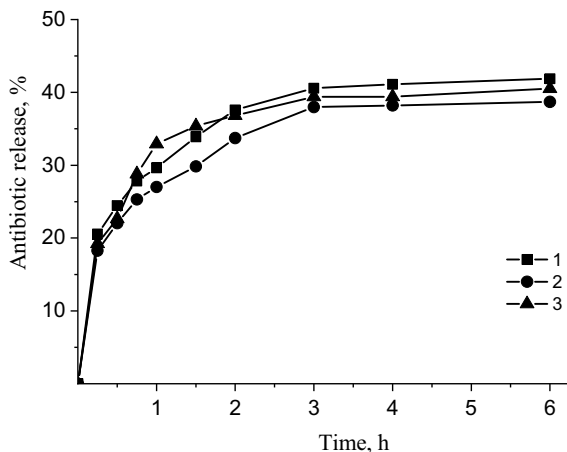
antibiotic concentration also depends on the initial antibiotic content in the hydrogel. These differences, as well as the initial amount of active agent in the hydrogels, must be considered when developing hydrogels for wound care.

As shown earlier, the presence of dextran in the reaction mixture, even in a very small amount, significantly affects the internal structure of the resulting PAA-based hydrogels [16]. The swelling rate of the D-g-PAA hydrogels is noticeably higher than that of PAA hydrogels with the same number of cross-links. The antibiotic-loaded D-g-PAA-0.4 samples prepared under the same conditions contain much more of this drug compared to PAA-0.4. For instance, the content of Cefuroxime is 1.86 g/g in the PAA-0.4-R hydrogel and 3.52, 3.40, and 3.34 g/g in the D20-g-PAA-0.4-R, D100-g-PAA-0.4-R, and D500-g-PAA-0.4-R samples, respectively. According to data obtained, the antibiotic release into water solution (in %) from the D-g-PAA-0.4 hydrogels (Fig. 6.3) is lower compared to the PAA-0.4 sample (Fig. 6.2), although it is undoubtedly more in absolute terms. Such a feature seems advantageous when preparing the antimicrobial dressings with prolonged action.

The antimicrobial activity of the PAA-based antibiotic-loaded hydrogels with different internal structures was tested in vitro on wild strains of *S. aureus, E. coli,* and *K. pneumoniae.* The samples were prepared by swelling in the antibiotic solutions with the concentration of 0.1 and 1 mg/ml. As expected, the antimicrobial activity of the antibiotic-loaded hydrogels is dose dependent, but even at a low dose, all synthesized samples demonstrate high efficacy against harmful microorganisms (Table 6.3).

According to the data on the diameters of the growth inhibition zone of the gram-positive and gram-negative bacteria, the efficacy of the antibiotic-loaded hydrogels mostly depends on the activity of this antibiotic. Along with that, the structure of the hydrogel carrier is also important. Sometimes, the D-g-PAA-based hydrogels, containing antibiotics even in a low dose, are more effective than the PAA ones (Fig. 6.4). And, undoubtedly, in cases when it is necessary to load hydrogels with

Table 6.3 Antimicrobial activity of the antibiotic-loaded hydrogels swollen in the 1 mg/ml (0.1 mg/ml) antibiotic solutions

Hydrogel carrier	Zone retardation (mm)		
	S. aureus	*E. coli*	*K. pneumoniae*
	Cefazolin-loaded hydrogel		
PAA-0.4	30 (21)	17 (9)	19 (10)
D20-PAA-0.4	28 (20)	18 (10)	17 (11)
D100-PAA-0.4	32 (23)	18 (11)	21 (10)
D500-PAA-0.4	31 (23)	16 (8)	19 (11)
	Cefoperazone-loaded hydrogel		
PAA-0.4	23 (13)	24 (19)	18 (13)
D20-PAA-0.4	22 (13)	27 (19)	20 (13)
D100-PAA-0.4	24 (15)	23 (18)	18 (11)
D500-PAA-0.4	25 (15)	24 (17)	20 (11)
	Ceftriaxone-loaded hydrogel		
PAA-0.4	18 (13)	25 (21)	22 (18)
D20-PAA-0.4	22 (12)	25 (20)	24 (19)
D100-PAA-0.4	24 (13)	27 (20)	23 (18)
D500-PAA-0.4	19 (10)	27 (22)	28 (21)
	Cefotaxime-loaded hydrogel		
PAA-0.4	22 (17)	27 (25)	23 (18)
D20-PAA-0.4	25 (16)	28 (25)	24 (19)
D100-PAA-0.4	27 (18)	27 (24)	23 (18)
D500-PAA-0.4	26 (17)	27 (22)	22 (18)
	Cefuroxime-loaded hydrogel		
PAA-0.4	23 (10)	22 (16)	21 (12)
D20-PAA-0.4	24 (12)	23 (15)	20 (11)
D100-PAA-0.4	26 (13)	24 (16)	22(11)
D500-PAA-0.4	26 (11)	24 (16)	22 (12)

high doses of antibiotics, the D-g-PAA-based hydrogels are preferred. For successful wound care, an optimal formulation must be used. A well-chosen hydrogel carrier increases the antibacterial activity of the wound dressing, thus enhancing wound healing.

In vivo experiments were carried out on rat models, which are widely used to test new medicines for living organisms [21, 22]. The synthesized hydrogels were found to be non-irritating to the skin, suggesting that they are safe for use in wound care. Among the most causes of wound infections, *S. aureus, E. coli,* and *K. pneumoniae* are listed [23, 24]; thus, the rat wounds were infected with the mixture of these microorganisms. The rat wounds were dressed with an antibiotic-loaded PAA-based hydrogel and, for comparison, a standard gauze bandage and the unloaded hydrogel. The appearance of an infected wound after a day of care confirms the
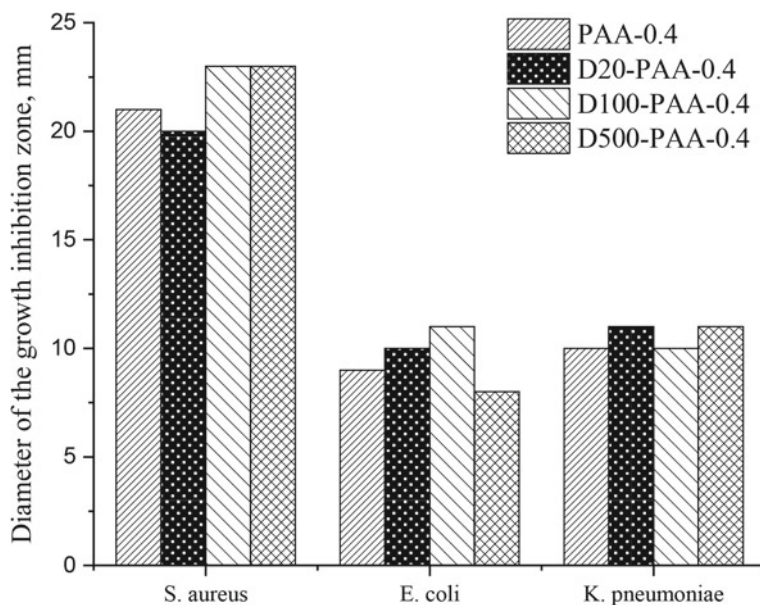
Fig. 6.4 Activity of the Cefazolin-loaded hydrogels swollen in 0.1 mg/ml antibiotic solution against *S. aureus, E. coli,* and *K. pneumoniae*

favorable prospects for using the synthesized antibiotic-loaded hydrogels as antimicrobial dressings (Fig. 6.5). They promote the healing and cleansing of contaminated open wounds without systemic antibiotic overdose.

The isolation of bacteria from wounds covered by a gauze bandage during 24 h revealed a significant amount of *Staphylococcus spp.* including *S. aureus.* The gramnegative bacteria *E. coli* and *K. pneumoniae* are also present in a large amount (Fig. 6.6). The use of the unloaded D20-g-PAA-0.4 hydrogel significantly reduces the number of *Staphylococcus spp.* strains. Only a few colonies of *S. aureus* are registered in the Petri dish. In this case, the growth of *E. coli* and *K. Pneumoniae* strains was not observed. The isolation of the bacteria from wounds covered by
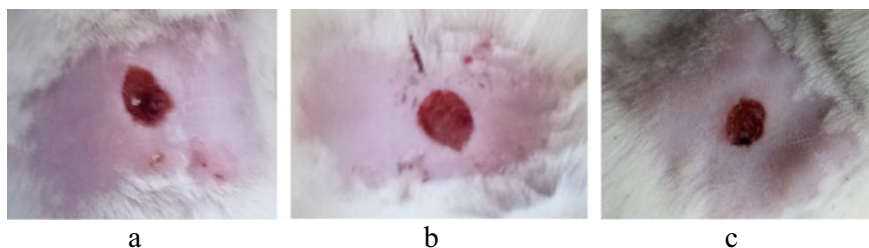
Fig. 6.5 Rat wounds after removal of bandages (24 h): classic gauze dressing (**a**); D20-g-PAA-0.4 hydrogel (**b**), and D20-g-PAA-0.4-Cefotaxime hydrogel (**c**)
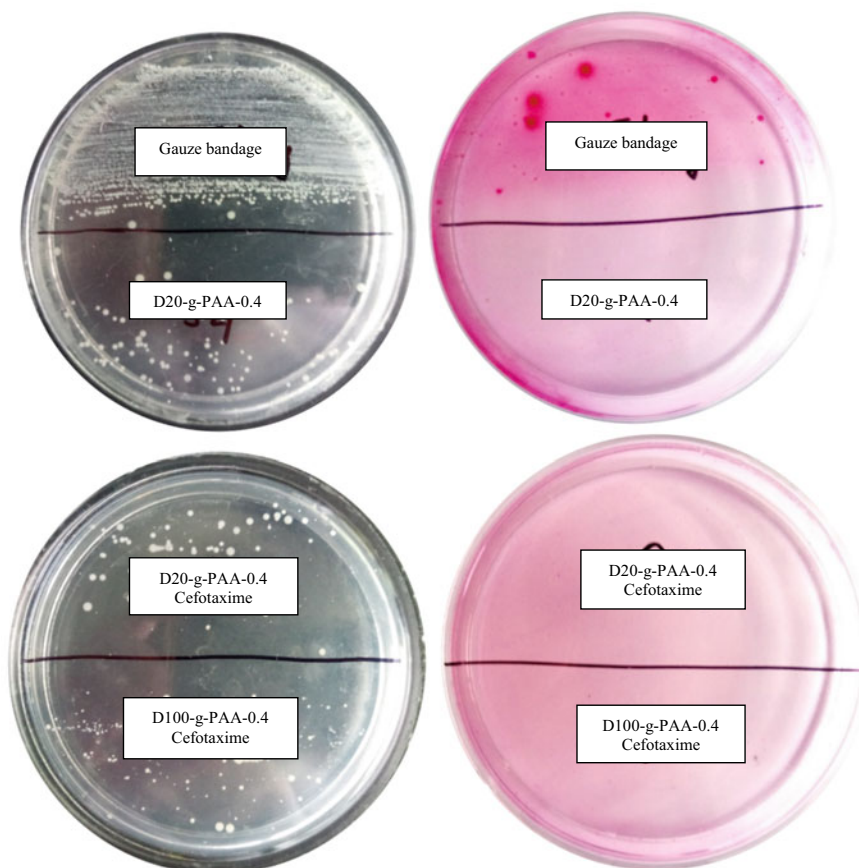
Fig. 6.6 Isolation of *Staphylococcus spp*, *Escherichia colI*, and *Klebsiella pneumoniae* on yolk-salt agar (left) and Endo medium (right) from intentionally infected wounds after bandage removal

the Cefotaxime-loaded hydrogels shows the suppression of *S. aureus* growth. And the antibiotic-loaded D20-g-PAA-0.4 and D100-g-PAA-0.4 samples seem to have somewhat different efficacy (Fig. 6.6). The Petri dish with Endo medium is free of gram-negative bacteria. As a whole, the status of the wounds indicates the promise of using hydrogels as dressings for infected wounds.

6.4 Conclusions

The PAA-based hydrogels are promising carriers for different antibiotics. Their structure can be controlled in the synthesis by the addition of a small amount of polysaccharide. The antibiotic release strongly depends on the antibiotic molecule

characteristics, and for the same antibiotics, it also depends on the internal structure of the PAA-based hydrogel. The synthesized antibiotic-loaded hydrogels demonstrated high efficacy against pathogen microorganisms, indicating their possibility to be used in infected wound care.

References

1. Veiga S, Schneider JP (2013) Antimicrobial hydrogels for the treatment of infection. Biopolymers 100(6):637–644
2. Gupta B, Agarwal R, Alam MS (2011) Hydrogels for wound healing applications. Woodhead Publishing 184–227
3. Yang K, Han Q, Chen B, Zheng Y, Zhang K, Li Q, Wang J (2018) Antimicrobial hydrogels: promising materials for medical application. Int J Nanomed 13:2217–2263
4. Posadowska U, Brzychczy-Włoch M, Drożdż A, Krok-Borkowicz M, Włodarczyk-Biegun M, Dobrzyński P, Chrzanowski W, Pamuła E (2016) Injectable hybrid delivery system composed of gellan gum, nanoparticles and gentamicin for the localized treatment of bone infections. Expert Opin Drug Deliv 13(5):613–620
5. Kamoun EA, Kenawy ERS, Tamer TM, El-Meligy MA, Mohy Eldin MS (2013) Poly (vinyl alcohol)-alginate physically crosslinked hydrogel membranes for wound dressing applications: characterization and bio-evaluation. Arabian J Chem 8:38
6. Gustafson CT, Boakye-Agyeman F, Brinkman CL, Reid JM, Patel R, Bajzer Z, Dadsetan M, Yaszemski MJ (2016) Controlled delivery of vancomycin via charged hydrogels. PLoS ONE 11:e0146401
7. Khalil IA, Saleh B, Ibrahim DM, Jumelle C, Yung A, Dana R, Annabi N (2020) Ciprofloxacin-loaded bioadhesive hydrogels for ocular applications. Biomater Sci 8(18):5196–5209
8. Vigata M, O'Connell CD, Cometta S, Hutmacher DW, Meinert C, Bock N (2021) Gelatin methacryloyl hydrogels for the localized delivery of cefazolin. Polymers 13(22):3960
9. Pawar V, Dhanka M, Srivastava R (2019) Cefuroxime conjugated chitosan hydrogel for treatment of wound infections. Colloids Surf B Biointerfaces 173:776–787
10. Grolman JM, Singh M, Mooney DJ, Eriksson E, Nuutila K (2019) Antibiotic-containing agarose hydrogel for wound and burn care. J Burn Care Res 40(6):900–906
11. Boateng JS, Matthews KH, Stevens HN, Eccleston GM (2008) Wound healing dressings and drug delivery systems: a review. J Pharm Sci 97(8):2892–2923
12. Vasile C, Pamfil D, Stoleru E, Baican M (2020) New developments in medical applications of hybrid hydrogels containing natural polymers. Molecules (Basel, Switzerland) 25(7):1539
13. Li S, Dong S, Xu W, Tu S, Yan L, Zhao C, Ding J, Chen X (2018) Antibacterial hydrogels. Adv Sci (Weinh) 5(5):1700527
14. Alven S, Aderibigbe BA (2020) Chitosan and cellulose-based hydrogels for wound management. Int J Mol Sci 21(24):9656
15. Fu M, Liang Y, Lv X, Li C, Yang YY, Yuan P, Ding X (2021) Recent advances in hydrogel-based anti-infective coatings. J Mater Sci Tech 85:169–183
16. Nadtoka O, Kutsevol N, Krysa V, Krysa B (2018) Hybrid polyacrylamide hydrogels: synthesis, properties and prospects of application. Mol Cryst Liq Cryst 672(1):1–10

17. Virych P, Nadtoka O, Doroschuk V, Lelyushok S, Chumachenko V, Bezugla T, Kutsevol N (2021) Cefuroxime-loaded hydrogels for prevention and treatment of bacterial contamination of open wounds. Int J Polym Sci 2021:4935642
18. Kutsevol N, Bezugla T, Bezuglyi M, Rawiso M (2012) Branched dextran-graft-polyacrylamide copolymers as perspective materials for nanotechnology. Macromol Symp 317–318(1):82–90
19. Kutsevol NV, Bezuglaya TN, Bezuglyi NY (2014) Features of the intramolecular structure of branched polymer systems in solution. J struct chem 55(3):575–587
20. Lehtopolku M, Kotilainen P, Puukka P, Nakari UM, Siitonen A, Eerola E, Huovinen P, Hakanen AJ (2012) Inaccuracy of the disk diffusion method compared with the agar dilution method for susceptibility testing of campylobacter spp. J Clin Microbiol 50(1):52–56
21. Parnell LKS, Volk SW (2019) The evolution of animal models in wound healing research: 1993–2017. Adv Wound Care (New Rochelle) 8(12):692–702
22. Dorsett-Martin WA (2004) Rat models of skin wound healing: a review. Wound Repair Regen 12(6):591–599
23. El Hamzaoui N, Barguigua A, Larouz S, Maouloua M (2020) Epidemiology of burn wound bacterial infections at a Meknes hospital, Morocco. New Microbes New Infect 38:100764
24. Puca V, Marulli RZ, Grande R, Vitale I, Niro A, Molinaro G, Prezioso S, Muraro R, Di Giovanni P (2021) Microbial species isolated from infected wounds and antimicrobial resistance analysis: data emerging from a three-years retrospective study. Antibiotics (Basel) 10(10):1162

Chapter 7
Prediction of Isomorphous Substitutions and Stability of Solid Solutions with β-YF$_3$ Structure in Lu$_{1-x}$Ln$_x$F$_3$, Ln = Sm–Yb Systems

E. I. Get'man, Yu. A. Oleksii, L. I. Ardanova, and S. V. Radio

7.1 Prospects for the Practical Use of Solid Solutions of Lu$_{1-x}$Ln$_x$F$_3$, Ln = Sm–Yb, with β-YF$_3$ Structure

Solid solutions of trifluorides of rare-earth elements (REEs) are being intensively studied since they can find practical application as materials for phosphors, lasers, scintillators, displays, light sources, catalysts, ionic conductors, fiber-optic amplifiers [1–5]. It is possible to use REEs trifluorides for microelectronics, analytical chemistry, technology of separation of elements, regeneration, purification, and disposal of nuclear materials [6]. In recent years, research on their application in the form of nanomaterials in medicine as optical 3D devices and probes for visualizing biological objects [7, 8], for intracellular labels or measurements [9], in biological imaging and immunoassays [10] has become relevant. The use of not individual compounds, but solid solutions is because their properties naturally change depending on the composition.

However, much less attention is paid to the physicochemical foundations for the synthesis of solid solutions (phase diagrams and, in particular, the regions of solubility based on the components of these systems) than the dependences "composition—physical properties". Thus, out of 120 possible diagrams of state (fusibility) of binary systems with the composition LnF$_3$–Ln'F$_3$, consisting of 16 REEs trifluorides, only 34 systems have been studied according to [11]. Moreover, most of the attention is paid to the high-temperature regions directly adjacent to the solidus lines, which, apparently, was due to the interest in growing single crystals. On the website

E. I. Get'man · Yu. A. Oleksii · S. V. Radio (✉)
Vasyl' Stus Donetsk National University, Vinnytsia 21027, Ukraine
e-mail: radio@donnu.edu.ua

L. I. Ardanova
Minnesota State University, Mankato, MN 56001, USA
e-mail: lyudmyla.stackpool@mnsu.edu

[12], only for 6 out of 30 phase diagrams of LnF_3–$Ln'F_3$ the regions of solid solutions are indicated, mainly for systems with non-isostructural components. There is no information on phase relationships below the solidus temperatures for other systems.

At the same time, it is known [13–15] that solid solutions synthesized at high temperatures tend to decompose on cooling, which can lead to the degradation of materials based on them.

In this regard, before synthesizing solid solutions and studying the dependences of their properties on composition, it is desirable to evaluate the limits of isomorphous substitutions as a function of temperature and the stability of solid solutions in the corresponding systems under the conditions of their synthesis, storage, and intended operation. The experimental determination of the limits of substitutions by annealing and quenching is complicated both by the need to use expensive equipment and reagents and by the difficulty of reaching equilibrium at low temperatures due to the low diffusion rate in the solid phase and due to the partial decomposition of the solid solution upon quenching from high temperatures. Therefore, to determine the limits of substitutions, it is rational to use not only experimental but also calculation methods, devoid of the above disadvantages.

It is interesting that earlier the greatest attention was paid to systems involving lanthanum trifluoride with REEs trifluorides of the cerium subgroup with a tysonite structure. This was apparently due to the high concentration of REEs activators in the LaF_3 matrix, which is due to its isostructurality with REEs trifluorides of the cerium subgroup and with trifluorides of other REEs above the temperatures of their transition from the β-YF_3 structural type to the tysonite structural type [6]. Much less attention has been paid to systems containing lutetium trifluoride with the β-YF_3 structure, although a large group of REE trifluorides from Sm to Lu crystallizes in this structural type at temperatures lower than the polymorphic transition temperatures [6].

As far as we know, only the LuF_3–TbF_3 and LuF_3–GdF_3 systems have been studied with isostructural compounds of this structural group [12]. There is also information about the LuF_3–LaF_3 system with non-isostructural components (types of structures β-YF_3 and tysonite, respectively) [16]. Perhaps less attention to the study of systems with LuF_3 is associated with the high cost of lutetium in comparison with other REEs [17].

At the same time, the absorption capacity of LuF_3 is one of the highest among the materials studied in [18]. In addition, LuF_3 has a very high K-absorption edge, equal to 63.3 keV, which will make it possible to use solid solutions based on it when creating emitters for medical devices with higher energies [18].

Considering the above material, the aim of this work was to predict the limits of substitutions and thermodynamic stability of solid solutions with the β-YF_3 structure in a wide range of compositions and temperatures in the $Lu_{1-x}Ln_xF_3$, Ln = Sm–Yb systems.

7.2 Calculation Procedure and Initial Data

In the systems under consideration, the dimensional parameter δ, which we calculated from the volumes of unit cells, did not exceed 0.0375 (Table 7.1), which is significantly less than 0.1. Therefore, in accordance with [13–15], the calculation was carried out in the approximation of regular solid solutions within the framework of the crystal energy theory of isomorphic miscibility.

Mixing energy (Q_{mix}) of solid solutions in the V.S. Urusov crystal energy method, in the general case, consists of three components due to the difference in the sizes of the substituted structural units (Q_δ), the difference in the nature of the chemical bond of the components of the systems (Q_ε) and the difference in their crystal structures, expressed by the change in the enthalpy of the morphotropic transition from the structure of the substituting component to the structure of the substituted component (ΔH_{II-I}):

$$Q_{mix} = Q_\delta + Q_\varepsilon + \Delta H_{II-I}/x_1 = Cmnz_m z_x \delta^2 + 1390 m z_m z_x \alpha (\Delta \varepsilon)^2 /(2R_M) + \Delta H_{II-I}/x_1,$$

where C—constants (see Table 7.1) calculated from the equation $C = 20(2\Delta\chi + 1)$ [13–15], according to the difference between the electronegativities of cations and anion $\Delta\chi$, taken by us from [19]; $\Delta\varepsilon$ is the difference in the degrees of ionicity of the chemical bonds of the components of the systems, which were calculated from the values of electronegativities (χ) of cations and anion (4.368) taken from [19] (determination of the degree of ionicity of the chemical bond in the crystalline components of the systems was carried out according to tables taken from [20]); m is the number of structural units in the components, equal in this case to 4; n is the coordination number of the structural unit being substituted; z_m, z_x are the formal charges of the substituted and common structural units in the components, $z_m = 3$,

Table 7.1 Initial data and results of calculating the critical decomposition temperatures of $Lu_{1-x}Ln_xF_3$, Ln = Sm–Yb solid solutions

Ln	V, Å^3	δ	C, kJ	Q_δ, kJ/mol	Q_ε, kJ/mol	Q_{mix}, kJ/mol	T_{cr}, K
Sm	207.371	0.0375	138.32	20.77	0.60	20.77	1240
Eu	204.325	0.0322	137.40	15.21	0.04	15.21	908
Gd	201.572	0.0276	139.28	11.33	1.48	11.33	677
Tb	198.414	0.0222	138.32	7.28	0.60	7.28	434
Dy	195.225	0.0168	137.68	4.15	0.11	4.15	248
Ho	192.796	0.0124	137.40	2.25	0.04	2.25	134
Er	190.583	0.0085	137.20	1.06	0.01	1.06	63
Tm	188.633	0.0052	136.52	0.39	0.30	0.69	41
Yb	187.033	0.0022	135.56	0.07	0.99	1.06	63
Lu	185.6						

$z_x = 1$; δ—dimensional parameter, calculated for each system by the volumes of unit cells (cell parameters are taken from [6]); α—reduced Madelung constant, $\alpha = 1.6935$ was calculated by the formula of D. Templeton [21]; R_M is the interatomic distance in the structure of the components, equal to ~2.3 Å [6].

Rhombic REEs trifluorides crystallize in the β-YF$_3$ structural type. In this structural type, the cation is surrounded by six fluorine atoms at the vertices of the trigonal prism and three fluorine atoms adjacent to the centers of its side edges. Eight fluorine atoms are at ~2.3 Å from the metal (Y), and the ninth is at ~2.6 Å [6]. Therefore, we used the effective coordination number according to S. Batsanov [22], equal to 8.9.

Since the components in each of the considered systems are isostructural (β-YF$_3$ structural type), in all cases $\Delta H_{\text{II–I}} = 0$ and to determine Q_{mix}, only Q_δ and Q_ε need to be calculated. However, according to [13–15], Q_ε can also be disregarded under conditions if the difference in electronegativities ($\Delta\chi$) of the substituted cations is less than 0.4 or the difference in the degrees of ionicity of the chemical bond in the components of the systems ($\Delta\varepsilon$) is less than 0.05. In this case, the value of Q_ε will be small and it can be assumed that $Q_{\text{mix}} = Q_\delta$. However, if the value of Q_δ is extremely small, then it will be necessary to consider Q_ε [13, 14]. As you can see from the analysis of Table 7.2, the values of $\Delta\varepsilon$ are significantly less than 0.05 (the maximum value is 0.011); therefore, we did not take into account the contribution to the mixing energy due to the difference in the degrees of ionicity in most systems, but it was taken into account for systems with TmF$_3$ and YbF$_3$ for which the values of Q_δ were minimal (0.39 and 0.07 kJ/mol).

Since in all systems the size parameter is less than 0.1 (the range of values is 0.0022–0.0375), then, according to [14], the dependence of the decomposition temperatures of solid solutions on the composition of the systems will be practically symmetric. To calculate the equilibrium substitution limit (x) for a given decomposition temperature of a solid solution (T_d), or the decomposition temperature for a

Table 7.2 Data for calculating the contribution to the mixing energy due to the difference in the degrees of ionicity in the components of the systems

Ln	$\chi(\text{Ln}^{3+})$	$\Delta\chi(\text{Ln}^{3+})$	$\chi(\text{F}^-)-\chi(\text{Ln}^{3+})$	ε_{Ln}	$\Delta\varepsilon$
Sm	1.410	0.021	2.958	0.844	0.007
Eu	1.433	0.002	2.935	0.839	0.002
Gd	1.386	0.045	2.982	0.848	0.011
Tb	1.410	0.021	2.958	0.844	0.007
Dy	1.426	0.005	2.942	0.840	0.003
Ho	1.433	0.002	2.935	0.839	0.002
Er	1.438	0.007	2.930	0.836	0.001
Tm	1.455	0.024	2.913	0.832	0.005
Yb	1.479	0.048	2.889	0.828	0.009
Lu	1.431	–	2.937	0.837	–

given substitution limit x, the Becker equation can be used in the approximation of regular solid solutions [23]:

$$-(1-2x)/\ln[x/(1-x)] = R_g T_d/Q_{mix},$$

where R_g is the universal gas constant.

   The calculation of the critical decomposition temperatures (for $x = 0.50$) was carried out according to the equation [13, 14]:

$$T_{cr} = Q_{mix}/(2kN),$$

where k is the Boltzmann constant, N is the Avogadro number. In these two cases, according to [13, 14], the value of Q_{mix} was taken in cal/mol.

7.3 Calculation Results for $Lu_{1-x}Ln_xF_3$ ($Ln = Sm-Yb$) Solid Solutions with β-YF_3 Structure

Some initial data and calculation results are summarized in Table 7.1. As can be seen from the table, with an increase in the REEs number, the mixing energy naturally decreases (from 20.77 to 0.69–1.06 kJ/mol) and the critical decomposition temperatures T_{cr} of solid solutions (from 1240 to 41–63 K), which is explained by a significant decrease in the differences in the sizes of the substitutional structural units—REEs and Lu^{3+} ions. Thus, ongoing from the $Lu_{1-x}Sm_xF_3$ system to the $Lu_{1-x}Yb_xF_3$ system, the difference between the crystal ionic radii of the substitutional cations (for the coordination number 8 [24]) decreases almost 13 times, from 0.102 Å to 0.008 Å. Such small values of the mixing energies (0.69–1.06 kJ/mol) and critical decomposition temperatures (41–63 K) when substituted by Er, Tm, and Yb are due to the insignificant difference in the values of the ionic radii of lutetium and "heavy" REEs.

   According to the R. Becker equation, the decomposition temperatures of solid solutions were also calculated for the limits of substitutions $x = 0.01, 0.03, 0.05$, and 0.10 (Table 7.3) and plotted their dependences on the nuclear charge of REEs atoms (curves (*a*), (*b*), (*c*), and (*d*), respectively) (Fig. 7.1). These curves can be used to estimate the limit of substitution of lutetium by REEs or the decomposition temperature of a solid solution from the limit of substitution using a given temperature. In the first case, it is necessary to draw an isotherm from a given temperature to the intersection with the vertical line corresponding to the number of the required REE. The intersection point can be used to estimate the range of x values, in which the substitution limit exists. The substitution limit should be clarified by interpolating the vertical segment between the dependences of the decomposition temperatures on the REE number closest to the intersection points.

Table 7.3 Temperatures of decomposition (K) of $Lu_{1-x}Ln_xF_3$ solid solutions for $x = 0.01, 0.03,$ 0.05, 0.10

Ln	Decomposition temperatures of solid solutions for the limits of substitution x			
	0.01	0.03	0.05	0.10
Sm	529	671	758	903
Eu	387	491	555	661
Gd	289	366	414	493
Tb	185	235	266	317
Dy	106	134	151	180
Ho	57	73	82	98
Er	27	34	39	46
Tm	18	22	25	30
Yb	27	34	39	46

Fig. 7.1 Diagram of thermodynamic stability of solid solutions: Dependences of the calculated decomposition temperatures of $Lu_{1-x}Ln_xF_3$ solid solutions ($x = 0.01$, curve (a); $x = 0.03$, curve (b); $x = 0.05$, curve (c); $x = 0.10$, curve (d), and $x = 0.50$, curve (e)) on the REEs atomic number
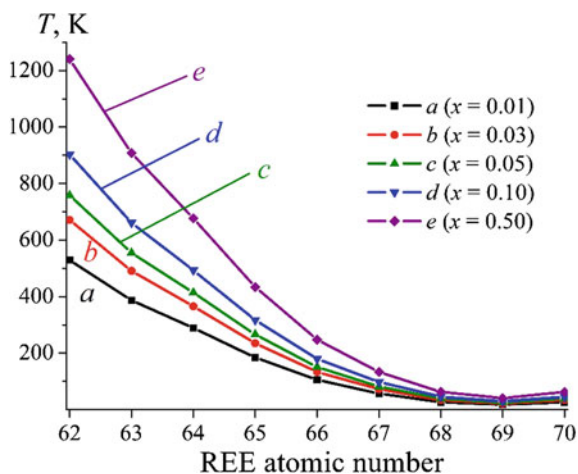
In the second case, according to a given composition, the position of a point on the vertical for a given REE is determined and a horizontal line is drawn up to the intersection with the temperature axis. A large number of dependences at small values of the substitution component in the range from $x = 0$–0.1 (Fig. 7.1) are due to the fact that the results can be used for choosing the amount of activators (dopants).

More precisely these problems are solved by plotting the dependence of the decomposition temperature (stability) of a solid solution on the composition (x) for each system. Since the previously published fusion diagrams [12] did not show the stability regions of solid solutions below the solidus or polymorphic transitions, using the R. Becker equation we calculated the decomposition temperatures for the $Lu_{1-x}Sm_xF_3$, $Lu_{1-x}Eu_xF_3$, $Lu_{1-x}Gd_xF_3$, $Lu_{1-x}Tb_xF_3$, and $Lu_{1-x}Dy_xF_3$ systems in the composition range $1.0 > x > 0$ with an $x = 0.05$ step. And the dependences of the

decomposition temperatures (decomposition domes) on the composition were plotted (see Figs. 7.2 and 7.3). They can be used to graphical determination the equilibrium composition for a given temperature, or the decomposition temperature for a given composition, as well as the stability region of solid solutions.

The decay domes can be used to supplement the fusion diagrams in the low-temperature region previously studied by the methods of physicochemical analysis.

The diagram shown in Fig. 7.1 also makes it possible to estimate the regions of thermodynamic stability of solid solutions in all considered systems. Thus, at $T > T_{cr}$ (in the region above the curve (e)), unlimited solid solutions are thermodynamically stable over the entire concentration range $0 < x < 1$. In the region below the curve (e),

Fig. 7.2 Decay temperature domes for $Lu_{1-x}Gd_xF_3$, $Lu_{1-x}Tb_xF_3$, $Lu_{1-x}Dy_xF_3$, and $Lu_{1-x}Ho_xF_3$ solid solutions with β-YF_3 structure
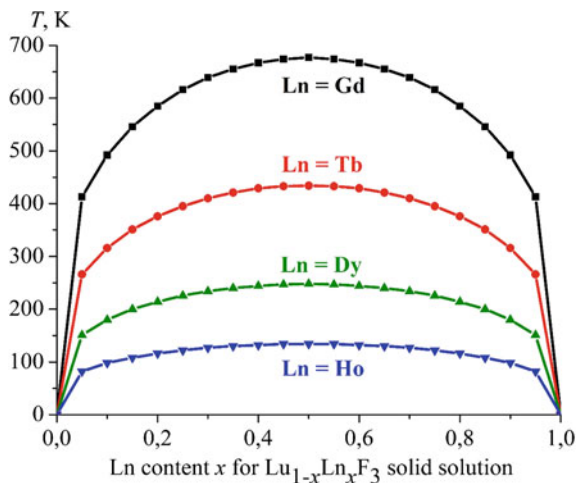
Fig. 7.3 Decay temperature domes for $Lu_{1-x}Sm_xF_3$ and $Lu_{1-x}Eu_xF_3$ solid solutions with β-YF_3 structure
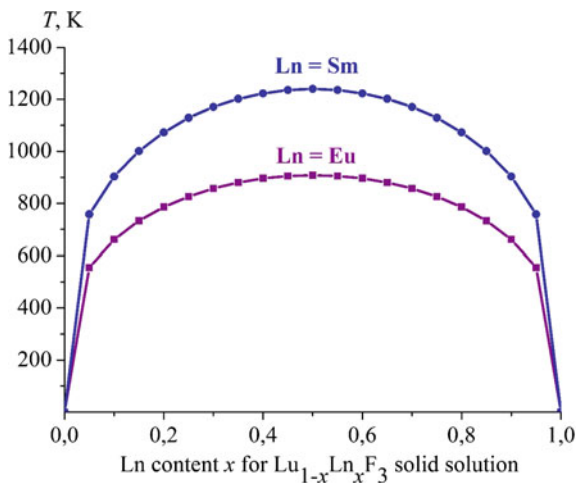
at $T < T_{cr}$, unlimited solid solutions are thermodynamically unstable and can decompose into phases with limited solubility. This occurs if the diffusion rate and time are high enough for stable nuclei of a new phase to arise and begin to grow. Similarly, solid solutions in the regions above curves (*a*), (*b*), (*c*), (*d*) are thermodynamically stable, and below these curves are unstable.

It is known that as the temperature decreases, the mobility of the structural units of a solid solution decreases due to a decrease in the diffusion rate, and the solubility regions become narrower [13–15]. This happens until the diffusion rate becomes so low that the decrease in the solubility regions practically stops, i.e., spontaneous hardening will occur, and solid solutions will become metastable. Earlier, we assumed [25] that the hardening temperature is close to the minimum temperature at which the interaction of the components in the solid phase begins upon heating, leading to the formation of a solid solution. On this basis, and also taking into account the rule of G. Tamman [26], that sintering and interaction in solids upon heating occur at temperatures approximately equal to half the melting temperature, the temperature of spontaneous hardening in related systems based on lanthanum trifluoride LaF_3 was taken equal to ~720 K. This is consistent with the research results on the synthesis of LuF_3 [27], according to which the formation of polycrystalline LuF_3 is accompanied by an exothermic effect at 698 K. Therefore, we will take the temperature of spontaneous quenching of solid solutions based on LuF_3 equal to ~700 K.

Based on the foregoing, it can be assumed that upon cooling, continuous series of solid solutions in systems with Sm and Eu trifluorides in the range from melting temperatures [6] to 1290 and 908 K, respectively, will be thermodynamically stable and unstable at lower temperatures. In the temperature range from 1290 and 908 K to ~700 K, respectively, they will decompose into two rows of limited solid solutions, decreasing in size with a decrease in temperature to ~700 K, upon reaching which they will spontaneously quench.

Continuous series of solid solutions in systems with REE trifluorides of the Tb–Yb series in the range from the melting point to the critical decomposition temperatures will be thermodynamically stable, and below ~700 K they will remain but will become metastable.

The critical decomposition temperature of the $Lu_{1-x}Gd_xF_3$ system, equal to 677 K, differs from the spontaneous quenching temperature (~700 K) by only 23 K, which is significantly less than the error limit of the calculation method (13%). Therefore, it is difficult to predict the state of the system in this temperature range.

7.4   Comparison of the Results Obtained with the Literature Data

As far as we know, among the systems with isostructure components based on LuF_3, only LuF_3–EuF_3, LuF_3–GdF_3, and LuF_3–TbF_3 have been studied. It was previously found that in the LuF_3–GdF_3 and LuF_3–TbF_3 systems, solid solutions crystallize from

the melt with discontinuity due to the non-isostructural nature of the components [12, 16, 28, 29]. Then, upon further cooling, due to polymorphic transitions of components into a structure of the β-YF_3 type at temperatures below ~1223 and 1118 K [6], continuous series of solid solutions are formed in the systems. This agrees with our results, according to which continuous series of solid solutions are possible in the region of thermodynamic stability determined by us above the critical temperatures of 677 and 434 K for the LuF_3–GdF_3 and LuF_3–TbF_3 systems, respectively.

As far as we know, there are practically no data in the literature on the mixing energies and the limits of substitution of REE for lutetium in systems for solid solutions of REE trifluorides $Lu_{1-x}Ln_xF_3$ with limited miscibility of the components. This, of course, makes it difficult to assess the reliability of the calculations. There are only data for the $Lu_{1-x}Eu_xF_3$ system, in which a solid solution of the composition $Lu_{0.8}Eu_{0.2}F_3$ was obtained by calcining at 673 K [18]. The latter is in satisfactory agreement with the results of calculating the decomposition temperature for this composition (786 K), taking into account its accuracy of 13% [14], as well as the presence of some experimental error in the synthesis in [18].

7.5   Conclusions

Using the V.S. Urusov crystal-chemical method in the approximation of regular solid solutions, the mixing energies, critical temperatures, and decomposition temperatures for solid solutions with the β-YF_3 structure of the compositions $Lu_{1-x}Ln_xF_3$, where Ln = Sm–Yb with $x = 0.01, 0.03, 0.05, 0.10$, and 0.50, were calculated. With an increase in the nuclear charge of REE, the mixing energies and decomposition temperatures of solid solutions regularly decrease from 20.77 to 0.69–1.06 kJ/mol and from 1240 to 41–63 K, respectively, which is due to a decrease in the ionic radii of REE in the series from Sm to Yb.

It is shown that the values of the mixing energy of the systems under study are mainly determined by the component due to the difference in the sizes of the substituted structural units. The presented diagram for the $Lu_{1-x}Ln_xF_3$ systems, where Ln = Sm–Yb, makes it possible to estimate the thermodynamic stability of solid solutions in a wide range of compositions and temperatures, and to predict the limits of substitution for limited series of solid solutions at a given decomposition temperature, or their decomposition temperature at a given limit of substitution x.

The calculation results for the LuF_3–GdF_3 and LuF_3–TbF_3 systems do not contradict the literature data obtained earlier by instrumental research methods in the sense that continuous series of solid solutions in these systems are in the predicted region of thermodynamic stability. The calculated decomposition temperature of the solid solution of the composition $Lu_{0.8}Eu_{0.2}F_3$, equal to 786 K, is in satisfactory agreement with the experimentally found one (673 K).

The decay domes of solid solutions for $Lu_{1-x}Sm_xF_3$, $Lu_{1-x}Eu_xF_3$, $Lu_{1-x}Gd_xF_3$, $Lu_{1-x}Tb_xF_3$, $Lu_{1-x}Dy_xF_3$, and $Lu_{1-x}Ho_xF_3$ systems are presented. They can be

used to supplement the previously studied melting diagrams of systems in the low-temperature range, obtained using the methods of physicochemical analysis.

References

1. Mayakova MN (2019) Fazoobrazovaniye pri sinteze neorganicheskikh nanoftoridov shchelochnozemel'nykh i redkozemel'nykh elementov iz vodnykh rastvorov [Phase formation in the synthesis of inorganic nanofluorides of alkaline earth and rare earth elements from aqueous solutions. Dissertation for the degree of candidate of chemical sciences]. PGPI RAS, Moscow, 141p. Available at https://diss.muctr.ru/media/dissertations/2019/05/%D0%9C%D0%B0%D1%8F%D0%BA%D0%BE%D0%B2%D0%B0_%D0%9C.%D0%9D.pdf. Accessed 1 Dec 2021 (in Russian)
2. Sorokin NI, Krivandina EA, Zhmurova ZI, Lyamina OI, Sobolev BP (2000) Growth of single crystals and optimization of anionic transport in $La_{1-x}Nd_xF_3$ solid solutions with tysonite-type structure by isovalent substitutions. Crystallogr Rep 45:695–697
3. Glynn TJ, Laulicht I, Lou L, Silversmith AJ, Yen WM (1984) Trapping of optical excitation by two types of acceptors in $La_{0.72}Pr_{0.25}Nd_{0.03}F_3$. Phys Rev B 29:4852–4858
4. Collings BC, Silversmith AJ (1994) Avalanche upconversion in $LaF_3:Tm^{3+}$. J Lumin 62:271–279
5. Chen F, Wang Z-Y, Zhang Y-Y, Yu K-H, Weng L-X, Wei W (2017) Synthesis of poly(acrylic acid)-functionalized $La_{1-x}Eu_xF_3$ nanocrystals with high photoluminescence for cellular imaging. Acta Phys-Chim Sin 33:1446–14526
6. Batsanova LR (1971) Rare-earth fluorides. Russ Chem Rev 40:465–484
7. Shen J, Sun L-D, Yan C-H (2008) Luminescent rare earth nanomaterials for bioprobe applications. Dalton Trans 5687–5697
8. Li F, Li C, Liu X, Bai T, Dong W, Zhang X, Shi Z, Feng S (2013) Microwave-assisted synthesis and up-down conversion luminescent properties of multicolor hydrophilic $LaF_3:Ln^{3+}$ nanocrystals. Dalton Trans 42:2015–2022
9. Wang F, Zhang Y, Fan X, Wang M (2006) One-pot synthesis of chitosan/$LaF_3:Eu^{3+}$ nanocrystals for bio-applications. Nanotechnology 17:1527–1532
10. Zhang W, Hua R, Shao W, Zhao J, Na L (2014) Bioconjugations of polyethylenimine-capped LaF_3:Ce, Tb nanoparticles with bovine serum albumin and photoluminescent properties. J Nanosci Nanotechnol 14:3690–3695
11. Sobolev BP (2020) Rare-earth-element (REE) trifluorides in the RF_3–$R'F_3$ (R, R' = REEs) systems: 1. Classification of the systems by chemical proximity of components. Russ J Inorg Chem 65:395–404
12. Personal site of Pavel Pavlovich Fedorov. Phase diagrams of fluoride systems RF_3-$R''F_3$. Available at http://ppfedorov.narod.ru/index/phase_diagrams_of_fluoride_systems_rf3_r_f3/0-73. Accessed 1 Dec 2021
13. Urusov VS (1975) Energetic theory of miscibility gaps in mineral solid solutions. Fortschr Mineral 52:141–150
14. Urusov VS (1977) Teoriia izomorfnoi smesimosti [Theory of isomorphous miscibility]. Nauka, Moscow, 251p (in Russian)
15. Urusov VS, Tauson VL, Akimov VV (1997) Geokhimiya tverdogo tela [Geochemistry of solid state]. GEOS, Moscow, 500p (in Russian)
16. Korshunov BG, Safonov VV (1984) Galogenidnyye sistemy: Spravochnik [Halide systems: a handbook]. Metallurgy, Moscow, 304p (in Russian)

17. Głowacki MM (2012) Właściwości optyczne i strukturalne krzemianow ziem rzadkich i ich roztworow stałych. Praca doktorska [Optical and structural properties of rare earth silicates and their solid solutions. PhD thesis]. Instytut Fizyki Polskiej Akademii Nauk. Warszawa, 102p. Available at http://www.ifpan.edu.pl/rn_ifpan/Glowacki-doktorat.pdf. Accessed 1 Dec 2021 (in Polish)

18. Guy E (2020) Applications of radiation in photodiagnosis and photodynamic therapy. Thesis submitted for the Degree of Doctor of Philosophy in the University of Hull. The University of Hull. 269p. Available at https://hydra.hull.ac.uk/assets/hull:17799a/content. Accessed 1 Dec 2021

19. Li K, Xue D (2006) Estimation of electronegativity values of elements in different valence states. J Phys Chem A 110:11332–11337

20. Batsanov SS (1968) The concept of electronegativity. Conclusions and prospects. Russ Chem Rev 37:332–351

21. Templeton DH (1953) Madelung constants and coordination. J Chem Phys 21:2097–2098

22. Batsanov SS (1977) Ob effektivnom koordinatsionnom chisle atomov v kristallakh [About the effective coordination number of atoms in crystals]. Zhurn Neorgan Khimii 22:1155–1159 (in Russian)

23. Becker R (1937) Über den Aufbau binarer Legierungen. Z Metallkunde 29:245–249 (in German)

24. Shannon RD (1976) Revised effective ionic radii and systematic studies of interatomic distances in halides and chalcogenides. Acta Cryst A32:751–767

25. Get'man SV, Radio SV, (2019) Predicting the substitution of rare-earth elements with cerium in the solid solutions based on nanoscale Ln_2SiO_5 (Ln=Tb–Lu, Y). Nanosistemi, Nanomateriali, Nanotehnologii 17:701–710

26. Mikhalkina OG (2013) Polucheniye i kharakteristiki soyedineniy LnF$_3$, LnSF v mikro- i nanosostoyaniyakh. Fazovyye ravnovesiya v sistemakh BaF_2–LnF_3–Ln_2S_3–BaS (Ln = La–Nd, Sm, Gd) [Preparation and characteristics of LnF$_3$, LnSF compounds in micro- and nanostates. Phase equilibria in systems BaF_2–LnF_3–Ln_2S_3–BaS (Ln = La–Nd, Sm, Gd)]. Abstract of dissertation for the degree of candidate of chemical sciences. Tyumen State University, Tyumen. Available at https://elib.utmn.ru/jspui/handle/ru-tsu/13533. Accessed 1 Dec 2021 (in Russian)

27. Andrrev OV, Razumkova IA, Boiko AN (2018) Synthesis and thermal stability of rare earth compounds REF_3, $REF_3 \cdot nH_2O$ and (H_3O) $RE_3F_{10} \cdot nH_2O$ (RE=Tb−Lu, Y), obtained from sulphide precursors. J Fluorine Chem 207:77–83

28. Ranieria IM, Baldochia SL, Klimm D (2008) The phase diagram GdF_3–LuF_3. J Solid State Chem 181:1070–1074

29. Sobolev BP (2020) Polymorphism, isomorphism, and morphotropy in trifluorides of rare-earth elements (R) and RF_3–$R'F_3$ systems. Crystallogr Rep 65:521–533

Chapter 8
Viability of Deconserved Sheep Sperm for Adding Nanomaterial of Ultrafine Silica

O. V. Shcherbak, O. Yu Lyzogub, and S. I. Kovtun

8.1 Introduction

According to the main target parameters of sheep breeding development in Ukraine, it was planned to increase the total number of sheep to 1,097,000 in 2020 [1–3]. Currently, in our country, this figure does not exceed 750 thousand heads. Tasks for the development of sheep breeding include the creation of an effective system selection in sheep breeding. An integral part of it is to ensure the preservation of the gene pool of aboriginal and small breeds and the creation of sperm banks of outstanding breeders. Significant progress has been made in the development of methods for cryopreservation of sheep semen, thanks to which this method is becoming widespread in sheep breeding practice and opens up new opportunities to improve breeding work through the rational use of genetic potential of breeding animals, transportation, and extensive exchange of genetic material [4]. However, as practice shows, in sheep breeding the potential of this progressive method is not fully realized, the main reason for which is the low fertility of sheep after artificial insemination with thawed semen not above 40–50% [5]. Therefore, an important and relevant aspect of modern biotechnology is the development and improvement of protective media for sperm dilution and technology of cryopreservation and deconservation of sheep sperm.

In 1990, Professor Nedava with colleagues showed that the addition to cryoenvironments of ultrafine silica (UFS) during cryopreservation prolongs the survival of sperm after their deconservation [6]. It should be noted that UFS nanomaterial due to its unique physicochemical and medicobiological properties (extremely developed surface, chemical purity, hydrophilicity, significant adsorption capacity) is used as a sorbent and carrier of drugs in many fields of medicine, pharmacology, veterinary

O. V. Shcherbak · O. Y. Lyzogub (✉) · S. I. Kovtun
Institute of Animals Breeding and Genetics nd.a. M.V. Zubets, National Academy of Agrarian Sciences of Ukraine, 1, v. Chubinsky, Pogrebnjaka Boryspil District 08321, Kyiv Region, Ukraine
e-mail: oksanalyzohub@gmail.com

107

medicine, and more. Depending on the method of use, it may interact with various saline solutions, such as blood plasma or gastric acid [7–12]. For more efficient use of silica, it is necessary to understand the mechanism of its interaction with the components of physiological solutions. Therefore, it is important to study the mechanism of action of UFS on body cells during direct contact.

The purpose of study is to investigate the vital signs (activity, viability, survival) of deconserved sheep sperm by adding different concentrations of UFS nanomaterial and evaluate the effectiveness of its use [13–17].

8.2 Materials and Methods of Study

The study was conducted in the laboratory of biotechnology of reproduction of the Institute of Animal Breeding and Genetics nd.a. M.V. Zubets of the National Academy of Sciences of Ukraine. Cryopreserved ejaculated sperm of Sokolska breed sheep were used in the experiments to evaluate the biological activity of the nanomaterial (№ 80–4016, №55–06,535, №044–05,828). The choice of sperm of these sheep is due to the fact that they are stored in the Bank of Animal Genetic Resources of the M.V. Zubets Institute of Animal Breeding and Genetics of the National Academy of Sciences of Ukraine since 1988 and is a valuable genetic material for reproduction and selection work with this breed.

The experiments examined the effect of 0.1%, 0.01 and 0.001% of UFS nanomaterial (brand A-300, Spit $= 285$ m^2/g, treated for 2 h at $+200$ °C) on deconserved sheep sperm after addition to the medium (2.9% sodium citrate solution) with sperm in concentration (experimental groups). The effect of UFS on sheep sperm (each separately and on average) was analyzed for their activity in percent and for viability in hours. The complex absolute survival rate (S_a) was determined by the formula:

$$S_a = a_1 + \sum (at),$$

where: Σ—is amount;
  a—sperm motility for each subsequent time interval, points;
  a_1—sperm motility after thawing, scores;
  t—time between semen checks [18].

8.3 Results and Discussion

It is known that deconserved semen with sperm activity of at least 40% and survival of at least 3 h is used for artificial insemination of sheep [4, 18]. Therefore, the first stage of our research was to evaluate the activity and survival of deconserved sheep sperm (control). We found that the shelf life of cryopreserved sperm of the studied sheep did

Table 8.1 Indicators of viability of deconserved sperm of sokolska breed sheep

Individual №	Activity after thawing, %	Survival after thawing, hours
80–4016	40.0 ± 2.87	2.5 ± 0.29
55–06,535	45.0 ± 2.87	2.5 ± 0.29
044–05,828	40.0 ± 5.77	3.5 ± 0.29
Average figure	41.7 ± 2.21	2.8 ± 0.22

not have a negative impact on the viability of gametes after deconservation, because even after 32 years in liquid nitrogen, their activity averaged 41.7% ± 2.21 (Table 8.1). It was found that the activity of sheep sperm was higher by 5% №55–06.535, compared with the sperm of other sheep. During the analysis of sperm viability after deconservation, it was found that their average survival is about 2.8 h.

The next stage of our study was to evaluate the effect of different concentrations of UFS nanomaterial on the vital signs of deconserved sheep sperm. We found that after 30 min of culturing deconserved ejaculated sheep sperm, the activity of sperm activity in the control decreased to 33.3% ± 1.67 (Fig. 8.1, the average value of vital indicators of sheep sperm). Sperm that were in a medium with 0.001% concentration of UFS showed activity at the level of 45.0% ± 2.87, which is 11.7% higher compared to the control and 3.3% higher compared to the initial activity.

After the presence of sperm in the medium containing 0.1% concentration of UFS, there was a decrease in gamete activity by 10.8% compared to the control and by 19.2% compared to the initial activity.

It should be noted that the sperm that were for 30 min in the environment with 0.01% concentration of UFS showed activity at the level of 38.3% ± 1.67, which is 5.0 and 15.8% higher, compared with the control and 0.1% concentration of UFS and 3.4% lower than the initial activity.

Analysis of sperm activity in the experimental groups showed that after 30 min the highest activity was observed in the case of cultivation with 0.001% concentration of UFS. Thus, in this group the activity was 45.0% ± 2.87, which is 6.7% higher compared to 0.01% concentration of UFS and 22.5% compared to 0.1% concentration of UFS.
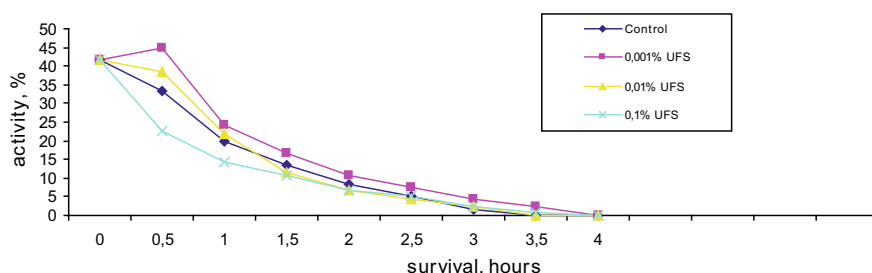
Fig. 8.1 Influence of UFS on the viability of deconserved sheep sperm

Table 8.2 Indicators of viability of deconserved sperm of sheep using different concentrations of UFS

Vital indicators of deconserved sheep sperm	Study groups			
	Control	0.1% UFS	0.01% UFS	0.001% UFS
Activity * after 30 min of cultivation, %	33.3 ± 1.67	22.5 ± 3.82	38.3 ± 1.67	45.0 ± 2.87
Survival, h	2.8 ± 0.22	3.5 ± 0.29	3.0 ± 0.29	3.5 ± 0.29
Absolute survival rate, st. units	7.2 ± 0.60	6.5 ± 0.23	7.3 ± 0.39	8.1 ± 1.56

*sperm activity immediately after deconservation– $41.7 \pm 1.67\%$

It was found that one hour after the start of the study, the activity of sperm in the control was 20.0%, and in the experimental groups for this period of time, there was an increase in activity to 24.3% with 0.001% concentration of UFS and up to 21.7% with 0,01% and a decrease to 14.2% with a 0.1% concentration of UFS.

During the next hour, we observed a tendency to reduce the activity of gametes almost twice, namely in the control for this period of time (two hours from the beginning of the experiment) -8.3% and in the experimental groups activity at 10.8% from 0.001% concentration of UFS, till 6.7% with 0.01 and 0.1% UFS concentrations was noted.

The total survival time of sperm in the control reached three hours, and in the experimental group with 0.01%, it did not exceed three hours; for sperm with 0.1 and 0.001% concentrations, this figure was 3.5 h.

It should be noted that the main physiological parameters such as sperm activity and survival in a medium with 0.001% concentration of UFS were significantly higher compared to the control and other experimental groups (Table 8.2). Analysis of the obtained data on the addition of different concentrations of UDS to the culture medium of deconserved sheep sperm showed that the activity and absolute survival rate of sperm with 0.1% UFS concentration were at the level of 22.5% and 6.5 st. units, which is much lower than the norm [4, 18] and indicators, both in the control and other experimental groups.

At the same time, the survival of sperm in the control and with 0.01% concentration of UFS did not differ significantly, which indicates the passive effect of such a concentration. However, sperm with a 0.001% UFS concentration showed the highest activity, survival, and absolute survival rates. We observed this tendency due to the fact that there is a high concentration of silanol (hydroxyl) groups on the surface of UFS particles, which ensure the hydrophilicity of this nanomaterial with complete safety of even its high concentrations.

Therefore, as a result of the comparative evaluation, the dose-dependent effect of UFS during gamete cultivation was established. During the cultivation of sperm with 0.01% concentration, the main vital indicators of sperm almost did not differ from the control, with increasing its concentration—decreased significantly. In our opinion, we observed this effect due to the interaction of UFS with proteins of

sperm membranes; i.e., this nanomaterial in lower concentrations causes only structural rearrangements of membranes and in case of increasing concentration removes proteins from it, violating the integrity of the bilipid layer. We modeled the in vitro interaction of UFS and deconserved sheep sperm. The obtained results can be taken into account during biotechnological manipulations with cryopreserved reproductive material of farm animals, namely during artificial insemination of females and obtaining embryos outside the body. The effectiveness of such approaches will increase due to the combination of nanotechnology and reproductive biotechnology and will ensure the rational use of genetic material.

8.4 Conclusions

It was found that the application of 0.001% concentration of UFS to deconserved sheep sperm leads to an increase of 11.7% in sperm activity after 30 min of cultivation.

It was found that the vital signs of deconserved sheep sperm depend on the concentration of UFS added to deconserved sheep sperm.

It is proved that the survival of deconserved sperm of sheep is 3.5 h in the case of using 0.001% concentration of UFS in the culture medium.

Prospects for further studies are a comprehensive assessment of the peculiarities of the use of nanomaterials, taking into account its dose-dependent action for specific cell types. Taking into account the obtained results will provide a basis for the development of recommendations for optimizing the technology of gamete cultivation and formation of in vitro embryos of live-stock animals.

References

1. Livestock of Ukraine: state, problems, ways of development (1991–2017–2030) (2017)/edited by Academician of the NAAS MI Bashchenko. К.: Agrarian Science pp 160. [in Ukrainian]
2. Hladiy MV, Polupan YP, Kovtun SI, Kuzebnij SV, Vyshnevskiy LV, Kopylov KV, Shcherbak OV (2018) Scientific and organizational aspects of generation, genetics, reproduction biotechnology and protection of the genofonds in livestock breeding. Animal Breeding and Genetics 56:5–14. [in Ukrainian] https://doi.org/10.31073/abg.56.01
3. Adamchuk VV, Ie HO, Kuz'mins'kyy VV (2020) Report on the activities of the national academy of Agrarian sciences of Ukraine for 2016–2020 and 2020. Nat Acad Agrarian Sci Ukraine; Order. Kyiv: Ahrarna nauka, 2021. pp 765. [in Ukrainian]
4. Program for the development of the sheep industry of Ukraine for 2012–2020 (2013) responsible for the issue Vdovychenko Yu.V. Nova Kakhovka: "Piel" pp 60. [in Ukrainian]
5. Hrymak K (2019) Fertilizing ability of oxford-down ram-sires deep-frozen semen depending on their mode of use and seasonal activity. Scient Techn Bulletin of State Scientif Res Control Instit Veterinary Med Pro Fodder Additives and Instit of Animal Biol 20(1):152–156 [in Ukrainian]
6. Nedava VE (1990) Ispolzovanie aerosilov v praktike iskusstvennogo osemeneniya—using aerosil in practice artificial insemination. Zootechniya 8:63–65
7. Poole CP, Owens FJ (2006) Nanotechnology: study guide: translation from English. 2nd supplemented publishing house—M.: Tekhnosfera, pp 336. [in Russian]

8. Belous AM, Kriobiologija, Grishhenko VI (1994) Monografija. Pod redakciej Kalugina Ju. V. i Nikitina I. I. – K.: «Naukova dumka», pp 432. [in Ukrainian]

9. Pentyuk OO, Chyujko OO, Trahtenberg IM, Shtatko OI, Verbilovsky YP (2004) Problems of toxicity of crystalic and amorphe silica forms. mechanisms of interaction of silicium particles with cell. "Ukrainian J Modern Problems of Toxicol 3:4–16. [in Ukrainian]

10. Kazak LI, Moskalyuk OV, Chekman IS, Voronin EP (2006) Physico-chemical aspects of pharmacological activity of highly dispersed silica preparations. Scient Bulletin of National O. Bogomoletz Med Univer 7:129–134 [in Ukrainian]

11. Galagan NP, Patej LM, Nastasiyenko NS (2006) Nanokompozỳtỳ na osnovi vỳsokodỳspersnogo kremnezemu i biomolekul ta yix termichni peretvorennya—Nanosỳstemỳ, nanomaterialỳ, nanotexnologiyi : Zb. nauk. pr. 4(3):599–612. [in Ukrainian]

12. Rosenfeld LG, Moskalenko VF, Checkman IS, Movchan BA (2008) Nanotechnology, nanomedicine: prospects for scientific investigations and implementation of their results into clinical practice. Scientific and Pract General Med J "Ukrainian Med J" 5(67):63–68. [in Ukrainian]

13. Kovtun SI, Galagan NP, Shherbak OV, Troczkỳj PA (2015) Metodỳchni rekomendaciyi z kriokonservaciyi spermatozoyidiv ta oocỳtiv siìškogospodarškỳx tvarỳn i formuvannya embrioniv in vitro—Chubỳnške pp 17. [in Ukrainian]

14. Zyuzyun AB, Shherbak OV, Osỳpchuk OS, Kovtun SI, Dzicyuk VV (2015) Zastosuvannya nanomaterialu v embriogenetỳchnij sỳstemi in vitro otrỳmannya embrioniv svỳnej—Faktorỳ eksperỳmentaìnoyi evolyuciyi organizmiv: Zb. nauk. pr. Nacionaìna akademiya nauk Ukrayinỳ—K.: "Logos" 17:164–168 [in Ukrainian]

15. Novichkova DA, Kuz'mina TI, Shherbak OV, Galagan NP, Epishko OA (2017) Vlijanie nanochastic vysokodispersnogo kremnezema na morfologiju i intracitoplazmaticheskuju lokalizaciju lipidnyh kapel' v oocitah svinej – Rozvedennja i genetika tvarin. 53:284–292. https://doi.org/10.31073/abg.53.40

16. Shherbak OV, Galagan NP, Troczkỳj PA, Kovtun SI (2017) Zastosuvannya nanochastỳnok dioksỳdu kremniyu v texnologiyi formuvannya embrioniv svỳnej in vitro–Nanosỳstemỳ, nanomaterialỳ, nanotexnologiyi Nanosistemi, Nanomateriali, Nanotehnologii–15:381–388 (Instỳtut metalofizỳkỳ im. G. V. Kurdyumova NAN Ukrayinỳ). https://doi.org/10.15407/nnn.15.02.0381

17. Shherbak OV, Zyuzyun AB, Osỳpchuk OS, Kovtun SI, Galagan NP, Troczkỳj PA (2017) Vỳvchennya biologichnoyi aktỳvnosti nanomaterialu v umovax kuìtỳvuvannya spermatozoyidiv ta oocỳtiv svỳnej in vitro – Faktorỳ eksperỳmentaìnoyi evolyuciyi organizmiv: Zb. nauk. pr. Nacionaìna akademiya nauk Ukrayinỳ –K.: "Logos" 20:256–259. [in Ukrainian]

18. Instruction on artificial insemination of sheep and goats (2003) Responsible for the issue Yu.F. Mel′nyk. - K.: Agrarian Science, pp 40. [in Ukrainian]

Chapter 9
The Effect of Stirring on the Electrodeposition of [(Cu–Zn)$_{base}$/(Cu–Zn)$_{add}$]$_n$ Coatings from Pyrophosphate-Citrate Electrolyte

A. Maizelis

9.1 Introduction

Cu–Zn alloy coatings are widely used in industry [1]. These alloys are known as decorative [2, 3], and they are used for increase in protection against aggressive environments [4], protection of steel from corrosion and as a sublayer against the deposition of metal, ceramic, or plastic coatings [5], as well as for promotion of rubber adhesion with steel busbars [2], and as electrodes for batteries [1].

Due to the large difference between the standard potentials of copper and zinc, only complex electrolytes are used to obtain Cu–Zn alloy coatings. Typically, a cyanide-based electrolyte is used for brass electrodeposition [2]. Due to the high risk to the environment and the hazards associated with cyanide electrolytes, other electrolytes are being developed. Among the electrolytes that do not contain cyanides, electrolytes based on EDTA, tartrate, gluconate, glycine [6], ammonia [3], pyrophosphate [4, 5], and citrate [1, 3, 7] electrolytes are mostly used.

The properties of alloy coatings, particularly microhardness, largely depend on their phase composition. XRD of electrodeposited Cu–Zn alloy coatings obtained from different electrolytes often detected several phases simultaneously. For example, on the XRD plots of coatings obtained from sulfate electrolytes [8] peaks corresponding to the β- and γ-phases of the alloy were determined. The formation of these phases in coatings deposited from pyrophosphate electrolyte was investigated [4] in order to use electrochemically deposited β-brass as an alloy with shape memory. For the same purpose, the parameters of Cu–Zn alloy films deposition from citrate [7] and cyanide [9] electrolytes were studied.

A. Maizelis (✉)

National Technical University «Kharkiv Polytechnic Institute», Kyrpychova Street 2, Kharkiv 61002, Ukraine

e-mail: a.maizelis@gmail.com

113

In recent decades, the properties of multilayer coatings consisting of periodically alternating layers of metals or alloys have been actively studied. Multilayer coatings can exhibit properties superior to the properties of single-layer coatings of the alloys of which they consist. Along with physical methods, they can be obtained by electrochemical methods, e.g., using two electrolytes. However, it is necessary to use one electrolyte when changing the electrolysis conditions for different layers in different ways to obtain coatings consisting of thin films up to 100 nm thick. The most actively studied are multilayer nanoscale coatings such as "ferromagnetic/diamagnetic", in which layers of copper alternate with nickel or cobalt [10]. Much attention is paid to multilayer coatings based on Zn-Ni alloys [11]. However, much less attention is paid to the electrodeposition of multilayer coatings based on other alloys [12–17]. Particularly, layered coatings are obtained using pulsed current in a pyrophosphate electrolyte [18]. A number of alloys corresponding to the phase diagram of copperzinc alloys were obtained in the modified Hull cell, except γ-phase (Cu_5Zn_8 intermetallide). In the complex electrolyte containing ligands in the form of ammonium chloride and EDTA, the effect of current density on the composition of coatings and their microstructure at a pulse and pause duration of 5 ms was studied [19]; Cu, CuZn, and Cu_5Zn_8 phases were detected. Thicker layers of the alloy are deposited by a two-pulse potentiostatic method in glycerol-NaOH-based electrolyte [20]. The deposition of a periodically structured Cu–Zn alloy was studied in a pyrophosphate electrolyte [21]. The duration of deposition of layers using this two-pulse galvanostatic method is from 2 to 15 min; i.e., the coating consists of fairly thick layers of alloy. Cu–Zn films are microheterogeneous: They include metallic copper and a solid solution of Zn in Cu or Cu_5Zn_8. In the films deposited in the mode of periodic change of current density, all phases which are formed in the galvanostatic mode at both current densities are present at the same time.

The results of the study of the effect of stirring on the electrodeposition of multilayer coatings based on Cu–Zn alloys from polyligand pyrophosphate-citrate electrolyte are presented. Layers of alloys periodically alternate due to their deposition under conditions of periodic changes in current density. The composition of the "base" layers corresponds to the composition of single-layer coatings of Cu–Zn alloy composition of yellow brass. Another phase composition of the "additional" layers is designed to ensure the emerging of new conditions for nucleation during the alternate deposition of layers.

9.2   Experimental

The films of Cu–Zn alloy of 80–150 nm thicknesses were deposited from polyligand pyrophosphate-citrate electrolyte. Composition of electrolyte is 0.08 mol L^{-1} $CuSO_4 \cdot 5H_2O$, 0.17 mol L^{-1} $ZnSO_4 \cdot 7H_2O$, 0.5 mol L^{-1} $K_4P_2O_7$, and 0.13 mol L^{-1} $K_3C_6H_5O_7$. The Cu–Zn alloy films were electrochemically dissolved under potentiodynamic conditions in solution of 0.3 mol L^{-1} Na_2SO_4 [4].

Cyclic voltammograms (CVA) and anodic linear sweep voltammograms (ALSV) were obtained using Elins P-45X potentiostat. XRF and XRD method [22] was used to verify ALSV method. Working and counter electrodes in a form of plates were made of platinum. Surface area of working electrode was 1 cm^2, and 5 cm^2 in the case of counter electrode. Saturated silver-silver chloride reference electrode was used in measurements. All the potentials are presented *vs.* this reference electrode. It was connected to the electrolyte by a salt bridge.

9.3   Experimental Results and Discussion

Figure 9.1 shows the cyclic voltammograms (CVA) on inert boron-rich pyrocarbon (PBC) electrode in pyrophosphate-citrate electrolyte containing copper and zinc ions. Active zinc codeposition with more positive copper begins at potential of about −1.1 V (inset in Fig. 9.1). Electrodeposition of the alloy is accompanied by intense hydrogen evolution after a peak at potential of about −1.5 V. A significant decrease in the peak height on the backward branch of the CVA indicates a significant contribution of diffusion inhibition during electrodeposition.

Moderate stirring (52.3 rad s^{-1}) during Cu–Zn alloy electrodeposition (curve 2, Fig. 9.1) leads to coincidence of the beginning of the forward cathode branch of the curve of CVA with cathode branch of CVA without stirring (curve 1). But the limiting current increases almost twice showing partial reduction in diffusion inhibition under alloy deposition. The backward cathode branch initially coincides
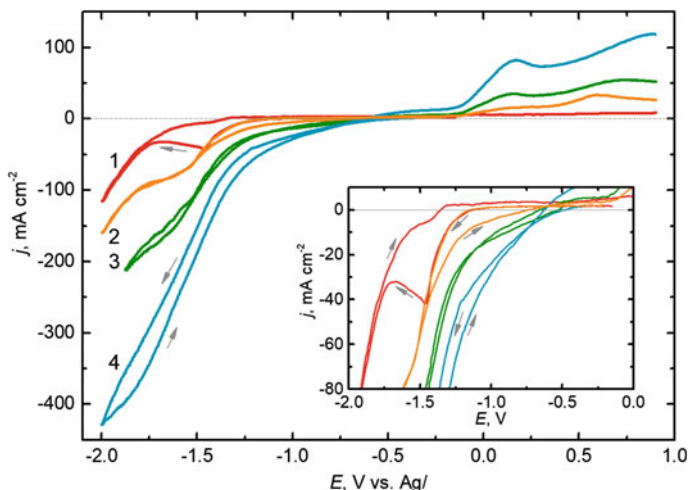
Fig. 9.1 CVA on a PBC rotating disk electrode in a pyrophosphate-citrate electrolyte for Cu–Zn alloy deposition. Electrode rotation rate: 1—0 rad s^{-1}; 2—52.3 rad s^{-1}; 3—104.7 rad s^{-1}; and 4—209.3 rad s^{-1}. The potential scan rate is 50 mV s^{-1}

with the forward cathode branch. At less polarization, the current value is greater, in contrast to backward curve of CVA without stirring (curve 1). It may indicate both the facilitation of zinc discharge and increase the area surface occurred before in the conditions of over-limited current densities. Increasing the rate of rotation of the disk electrode (curves 3 and 4) leads to even greater facilitation of the alloy deposition or the formation of a more developed surface. The main peak (at a potential of 0.2 V) on the anode branches of CVA belongs to the dissolution of copper and α-phase of solid solution of zinc in copper. It increases with increasing in rate of disk electrode rotation, but the deposit does not dissolve completely and continues to oxidize at more positive potentials in a semi-passive state. The anode branches of CVA begin at different potentials that show the presence of different numbers of zinc-enriched phases in the coatings.

For the multilayer coatings formation by two-pulse galvanostatic method, two values of current density were chosen: (1) current density below the limiting current of the backward branch of CVA (7 mA cm^2, curve 2, Fig. 9.2) and (2) current density above this limiting current (12 mA cm^{-2}, curve 4). In the case of electrodeposition on a steel electrode (smaller ohmic potential drop than in the case of PBC rotating disk electrode), the potential values are smaller in absolute value. However, using magnetic stirrer (curves 1 and 3) leads to depolarization of deposition process (curves 1 and 2, 3 and 4, Fig. 9.2) too. Thick coatings are more zinc-enriched under conditions of stirring in comparison with coatings obtained in stationary conditions; their microhardness is reduced (Table 9.1).

Fig. 9.2 Chronopotentiograms of Cu–Zn alloy deposition on electrodes made of steel of "Steel 3" grade (curves 1 and 3) with stirring and (curves 2 and 4) without stirring at current density of (1, 2) 5 mA cm^{-2} and (3, 4) 7 mA cm^{-2}
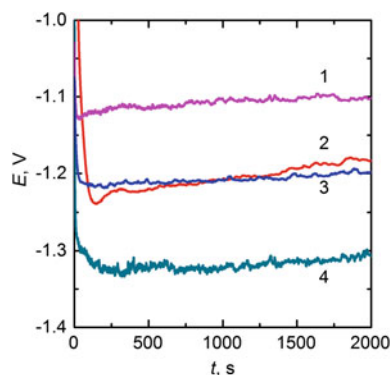
Table 9.1 Zn content and microhardness of coatings deposited with and without stirring

Parameter	Stirring	j, mA cm^{-2}	
		7.0	12.0
Zn content in coating, %	–	13.6	19.1
	+	19.2	29.8
Microhardness, HV	–	156	246
	+	126	161
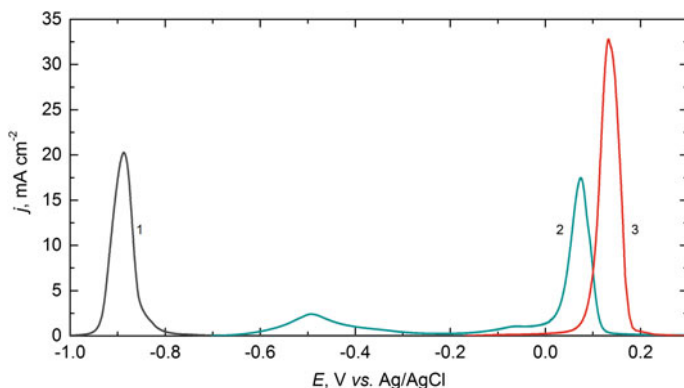
Fig. 9.3 Anode voltammograms of dissolution of films in 0.3 mol dm^{-3} Na$_2$SO$_4$ solution. Films were obtained in pyrophosphate-citrate electrolytes with [Cu^{2+}]: [Zn^{2+}] ratio of 0:1 (1), 1:2 (2), and 1:0 (3). Current density of deposition: 20 mA cm^{-2} (1, 3) and 40 mA cm^{-2} (2). Charge for deposition is $Q_k = 0.4$ C cm^{-2}. The potential scan rate is 5 mV s^{-1}

Stripping voltammetry of the alloy film obtained at current density that is significantly higher than the limiting current showed that it does not contain free zinc (curve 2, Fig. 9.3) as peak on the curve 1 of zinc dissolution is at lower potential values. The third peak of dissolution of the film is located at lower potentials than the peak of copper dissolution (curve 3) due to the formation of solid solution of zinc in copper (α-phase). The low second peak (in fact the shoulder of the third peak) is the dissolution peak of intermetallic compound CuZn (β-phase) [23, 24].

Now, we consider the first peaks of the anodic dependences of film dissolution (Fig. 9.4), in which zinc-enriched alloy phases dissolve [23]. All voltammograms have peaks of α-phase dissolution (last rise in current on curves; see also the 3rd peak on curve 2, Fig. 9.3) and peaks of dissolution of the β-phase of the alloy (-0.05 V). The proportion of the peaks of α-phase dissolution with stirring decreases due to an increase in the height and area of the peaks of β-phase dissolution (compare curves 1 with 2; curves 3 and 4 with curves 5 and 6). It should be mentioned that the first peak of voltammograms of films obtained with stirring at all values of the current density is located at more negative potentials than of films obtained without stirring. It indicates a decrease in the content of the γ-phase (intermetallide Cu$_5$Zn$_8$) and an increase in the content of the ε-phase (CuZn$_5$) [23]. Additionally, this peak is larger in height and area. The difference in the content of the γ- and ε-phases increases with a decrease in the current density of film deposition (Fig. 9.4b). The area of the first peak in the voltammogram of film dissolution obtained with stirring at a current density of 40 mA cm^{-2} (curve 1, Fig. 9.4a) is no more than 2 times larger than the area of the first peak of the voltammogram of dissolution of film obtained at the same current density without stirring (curve 2, Fig. 9.4a). However, in the case of film deposition at 7 mA cm^{-2} (curve 4, Fig. 9.4b), the area of the first peak is three times greater than the area of the peak obtained even at a current density of 10 mA cm^{-2} without stirring (curve 5, Fig. 9.4b).
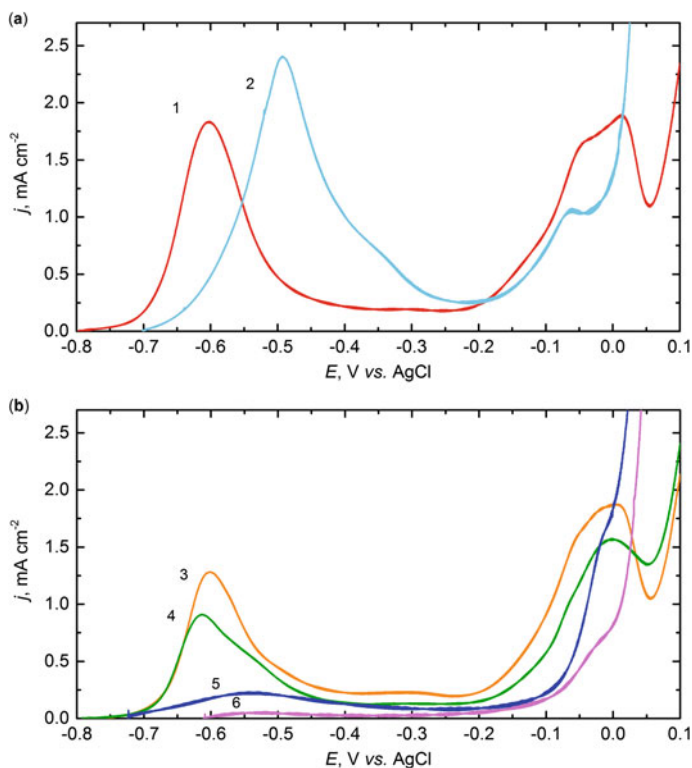
Fig. 9.4 Anode voltammograms of dissolution in a solution of 0.3 mol dm^{-3} Na$_2$SO$_4$ films obtained in pyrophosphate-citrate electrolyte with the ratio [Cu^{2+}]: [Zn^{2+}] = 1:2 under stationary conditions (2, 5, 6) and with stirring (1, 3, 4). The charge for deposition is $Q_k = 0.4$ C cm^{-2}. The potential scan rate is 5 mV s^{-1}. Current density for film deposition: **a** 40 mA cm^{-2}, **b** 12 mA cm^{-2} (3), 7 mA cm^2 (4), 10 mA cm^{-2} (5), and 5 mA cm^{-2} (6)

Thus, the zinc content in the deposit obtained both at higher current density and with stirring increases as compared with those obtained without stirring due to increase in the proportion of β-phase and the replacement of γ-phase with the ε-phase, which is more zinc-enriched. The same change in phase composition was observed with increasing polarization and in the case of deposition of Cu–Zn alloy coatings from ionic liquid [25].

Apparently, this is also associated with a decrease in the microhardness of the coatings obtained with stirring (Table 9.1).

Formation of [(Cu–Zn)$_{base}$/(Cu–Zn)$_{add}$]$_n$ multilayer coating (curve 2, Fig. 9.5) from such films (curves 1 and 3) with stirring leads to the shift of the corresponding sections of the chronopotentiograms by 20–50 mV toward lower potentials. Periodic change in the current density leads to appearance of additional interphase boundaries. The microhardness of the multilayer coating (240 HV) exceeds the microhardness of both corresponding coatings: coating obtained at current density of 7 mA cm^{-2} which
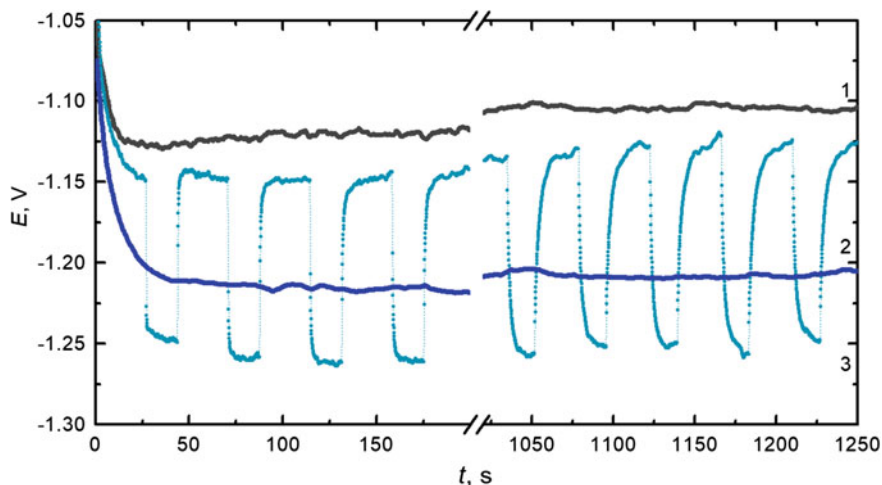
Fig. 9.5 Chronoamperograms of deposition of Cu–Zn alloy coatings (1, 3) and [(Cu–Zn)$_{base}$/(Cu–Zn)$_{add}$]$_n$ coating (2) with stirring. Deposition regime: (1) $j = 7$ mA cm^{-2}; (3) 12 mA cm^{-2}; (2) $j = 7$ mA cm^{-2} for 26.7 s (for (Cu–Zn)$_{base}$ layers) and $j = 12$ mA cm^{-2} for 16.7 s (for (Cu–Zn)$_{add}$ layers)

corresponds to the base layers (126 HV) and coating obtained at current density of 12 mA cm^{-2} which corresponds to the addition layers (161 HV).

It was supposed that the action of two factors of increasing in the β-phase content and replacement of γ-phase by ε-phase leads to a decrease in the microhardness of the coatings. The fact that it decreases during the formation of additional layers of multilayer coatings at a higher current density (Fig. 9.6), i.e., in conditions of intensification of the action of mentioned factors, is the confirmation of above assumption. So, increase in the current density of the deposition of additional layers to 20 mA cm^{-2} leads to decrease in microhardness to 217 HV; further increase to 40 mA cm^{-2} leads to microhardness value of 165 HV. It should be noted that the shape of the chronopotentiogram changes significantly over time. In the first minutes, the areas of chronopotentiogram of the base layer deposition are stable (the left side of Fig. 9.6), as well as along the entire length of curve 2 in Fig. 9.5. In the case of long-term electrolysis (right side of Fig. 9.6), stable deposition is not observed.

When the deposition current of the layers (Cu–Zn)$_{base}$ increases from 7 mA cm^{-2} (curve 1, Fig. 9.7) to 10 mA cm^{-2} (curve 2), the microhardness also decreases from 217 to 161 HV.

It should be noted that the microhardness of [(Cu–Zn)$_{base}$/(Cu–Zn)$_{add}$]$_n$ coatings, depending on the parameters of electrolysis in pyrophosphate-citrate electrolyte without stirring, reaches 397–428 HV, wherein the microhardness of single-layer coatings of "yellow brass" does not exceed 200–250 HV [5, 26], and microhardness of multilayer coating obtained by two-pulse potentiostatic method is 337 HV [20]. This, however, does not mean that it is not possible to obtain harder coatings using
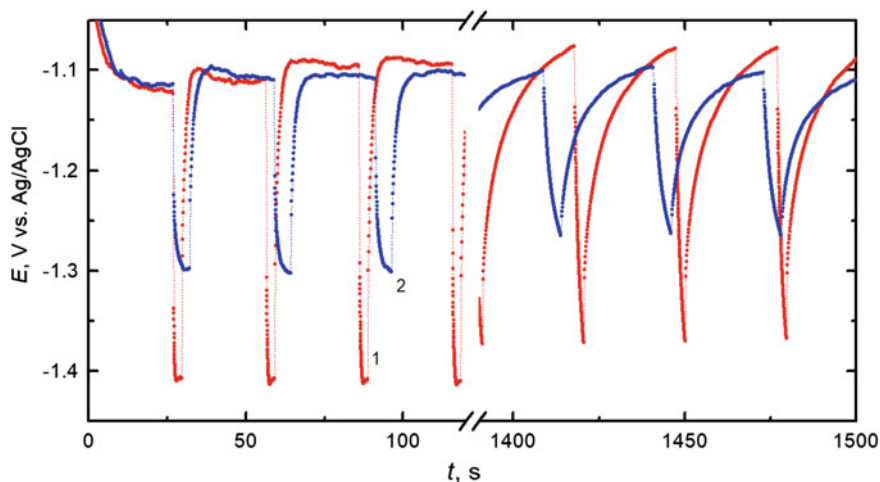
Fig. 9.6 Chronoamperograms of deposition of multilayer coatings $[(Cu-Zn)_{base}/(Cu-Zn)_{add}]_n$ with stirring. Deposition regime: 7 mA cm^{-2} for 26.7 s for $(Cu-Zn)_{base}$ sublayers; (1) at 20 mA cm^{-2} for 5 s or (2) at 40 mA cm^{-2} for 2.5 s for $(Cu-Zn)_{add}$ sublayers
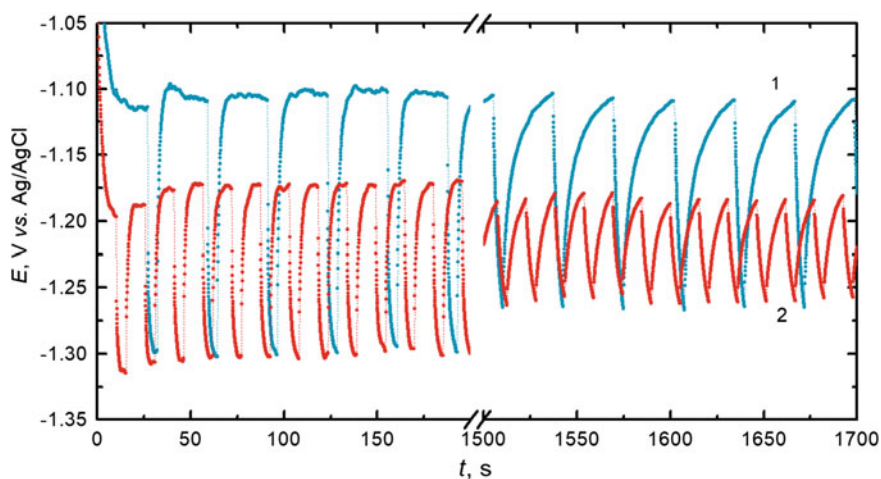
Fig. 9.7 Chronoamperograms of $[(Cu-Zn)_{base}/(Cu-Zn)_{add}]_n$ multilayer coatings deposition with stirring. Deposition regime: 7 mA cm^{-2} for 26.7 s (1) and 10 mA cm^{-2} for 10 s (2) for $(Cu-Zn)_{base}$ sublayers; (1) at 20 mA cm^{-2} for 5 s or (2) at 40 mA cm^{-2} for 2.5 s for $(Cu-Zn)_{add}$ sublayers

stirring when under other conditions of electrolysis and adjusting the composition of the electrolyte.

9.4   Conclusions

The effect of stirring during the deposition of $[(Cu–Zn)_{base}/(Cu–Zn)_{add}]_n$ multilayer coatings from pyrophosphate-citrate electrolyte by a two-pulse galvanostatic method has been investigated. It is shown that the value of the limiting current on the cathode branch of the CVA increases, and zinc content in single-layer coatings increases when stirring is used. Coatings obtained at the same current density with and without stirring have a lower microhardness in the case of stirring.

It was shown by the method of stripping voltammetry that using stirring leads to increase in content of $β$- and $ε$-phases of the Cu–Zn alloy and decrease in content of the $γ$-phase in thin films. It is assumed that this is associated with decrease in microhardness when stirring is used. The advantage of a multilayer coating is shown. When stirring of electrolyte is used, the multilayer coating has higher microhardness than single-layer coatings, which are obtained at the same current density as the layers constituting the multilayer coating.

Further research will be aimed at optimizing the conditions of electrolysis with stirring, since it has a beneficial effect on the anticorrosive properties of multilayer coatings obtained in this pyrophosphate-citrate electrolyte.

References

1. Özdemir R, Karahan İH, Karabulut O (2016) A study on the electrodeposited Cu-Zn alloy thin films. Metall and Mater Trans A 47(11):5609–5617. https://doi.org/10.1007/s11661-016-3715-0
2. Fujiwara Y, Enomoto H (2000) Electrodeposition of β′-brass from cyanide baths with accumulative underpotential deposition of Zn. J Electrochem Soc 147(5):1840. https://doi.org/10.1149/1.1393444
3. Ibrahim MA, Bakdash RS (2015) New cyanide-free ammonia bath for brass alloy coatings on steel substrate by electrodeposition. Int J Electrochem Sci 10(2105):9666
4. Haciibrahimoglu M, Yavuz A, Oztas M, Bedir M (2016) Electrochemical and structural study of zinc-rich brass deposited from pyrophosphate electrolyte onto the carbon steel Dig. J Nanomater Biostruct 11:251–262
5. Senna LF, Díaz SL, Sathler L (2005) Hardness analysis and morphological characterization of copper-zinc alloys produced in pyrophosphate-based electrolytes. Mater Res 8(3):275–279. https://doi.org/10.1590/S1516-14392005000300009
6. Ballesteros JC, Gómez-Solís C, Torres-Martínez LM, Juárez-Ramírez I (2015) Electrodeposition of Cu-Zn intermetallic compounds for its application as electrocatalyst in the hydrogen evolution reaction. Int J Electrochem Sci 10:2892–2903
7. Yurdal K, Karahan İH (2017) Phase formation in electrodeposited Cu-Zn alloy films produced from ultrasonicated solutions. Acta Physica Polonica A 132(3):1091–1094. https://doi.org/10.12693/APhysPolA.132.1091
8. Kopeli NIZS (2014) Electrodeposition and characterization of Cu-Zn alloy films obtained from a sulfate bath. Materiali in tehnologije. 48(2):221–226
9. Fujiwara Y, Enomoto H (2004) Intermetallic phase formation in electrochemical alloy deposition. J Solid State Electrochem 8(3):167–173. https://doi.org/10.1007/s10008-003-0441-5

10. Bakonyi I, Péter L (2010) Electrodeposited multilayer films with giant magnetoresistance (GMR): progress and problems. Prog Mater Sci 55(3):107–245. https://doi.org/10.1016/j.pmatsci.2009.07.001

11. Lotfi N, Aliofkhazraei M, Rahmani H, Darband GB (2018) Zinc-nickel alloy electrodeposition: characterization, properties, multilayers and composites. Prot Met Phys Chem Surf 54(6):1102–1140. https://doi.org/10.1134/S2070205118060187

12. Maizelis A, Bairachniy B (2017) Copper nucleation on nickel from pyrophosphate-based polyligand electrolyte. In: International conference on nanotechnology and nanomaterials, Springer, Cham. pp 443–457. https://doi.org/10.1007/978-3-319-92567-7_28

13. Maizelis AA (2019) Multilayer nickel-copper anode for direct glucose fuel cell. J Electrochem Energy Convers and Storage 16:041003. https://doi.org/10.1115/1.4042986

14. Maizelis A, Bairachniy B (2019) Formation of multilayer metal-hydroxide electrode with developed surface for alkaline water electrolysis. Mater Today: Proc 6:226–230. https://doi.org/10.1016/j.matpr.2018.10.098

15. Maizelis A, Bairachniy B (2019) Protection of NdFeB magnets by multilayer coating. In: IEEE 39th international conference on electronics and nanotechnology (ELNANO). pp. 596–599. https://doi.org/10.1109/ELNANO.2019.8783526

16. Maizelis A, Kolupaieva Z (2021) Quantitative analysis of chemical and phase composition of Zn−Ni alloy coating by Potentiodynamic stripping. Electroanalysis 33(2):515–525. https://doi.org/10.1002/elan.202060195

17. Maizelis A (2021) Stripping voltammetry of nanoscale films of Zn–Ni alloy. Appl Nanosci 1−6. https://doi.org/10.1007/s13204-021-01723-9

18. Beattie SD, Dahn JR (2003) Comparison of electrodeposited copper-zinc alloys prepared individually and combinatorially. J Electrochem Soc 150(11):C802. https://doi.org/10.1149/1.1615998

19. Kartal M, Alp A, Akbulut H (2017) Pulse electrodeposition of copper-zinc coatings from an alkaline bath. Acta Physica Polonica A 132(3):801–803. https://doi.org/10.12693/APhysPolA.132.801

20. Das S, Jena S, Banthia S, Mitra A, Das S, Das K (2019) Novel pulse potentiostatic electrodeposition route for obtaining pure intermetallic Cu_5Zn_8-CuZn composite coating using glycerol-NaOH based electrolyte with advanced scratch resistance and anti-corrosive properties. J Alloy Compd 792:770–779

21. Reva OV, Vorob'eva TN, Sviridov VV (1999) Depositing nanostructured composition-modulated Cu-Sn and Cu-Zn coatings while periodically varying the current density. Russ J Electrochem 35(9):942–947

22. Mikhailov IF, Baturin AA, Mikhailov AI, Fomina LP (2016) Perspectives of development of X-ray analysis for materials compoisiton. Funct Mater 23(1):5–14. https://doi.org/10.1016/j.jallcom.2019.04.068

23. Maizelis A (2020) Stripping voltammetry of nanoscale films of Cu–Zn, Cu–Sn, Zn–Ni alloys. In: International conference on nanotechnology and nanomaterials. Springer, Cham, pp 323–336. https://doi.org/10.1007/978-3-030-74741-1_22

24. Stevanović J, Skibina LJ, Stefanović M, Despić A, Jović VD (1992) Phase-structure analysis of brass by anodic linear-sweep voltammetry. J Appl Electrochem 22(2):172–178. https://doi.org/10.1007/BF01023820

25. Xie X, Zou X, Lu X, Lu C, Cheng H, Xu Q, Zhou Z (2016) Electrodeposition of Zn and Cu–Zn alloy from ZnO/CuO precursors in deep eutectic solvent. Appl Surf Sci 385:481–489. https://doi.org/10.1016/j.apsusc.2016.05.138

26. Krishnan RM, Muralidharan VS, Natarajan SR (1996) A non-cyanide brass plating bath. Bull Electrochem 12(5–6):274–277

Chapter 10
Features of Plasma-Electrolyte Synthesis of Heterooxide Nanocomposites on Multicomponent Alloys of Valve Metals

Hanna V. Karakurkchi, Nikolay D. Sakhnenko[ID]**, Alla N. Korohodska**[ID]**,
Gulmira Sh. Yar-Mukhamedova**[ID]**, Iryna I. Stepanova,
and Svitlana I. Zyubanova**[ID]

Heterooxide (metal oxide) systems formed by the method of PEO on valve metals, in particular aluminum and titanium, are one of the most common classes of catalytic materials (catalysts) for eco-technologies [1, 2].

The nature of the carrier (substrate) is an important aspect of the technology of catalytic systems because it serves as a platform for the catalytic layer. The composition and physicochemical characteristics of the carrier of the catalytic layer will depend on the technology of its processing, obtaining the catalytic layer, the scope, and performance characteristics [3]. Therefore, a significant place in the research of scientists around the world is occupied by research to develop effective methods and technologies for the formation of catalytic systems with the optimal composition of the catalytic layer [4, 5].

Physico-mechanical and physicochemical properties of multicomponent alloys, significantly depend on the composition and ratio of alloying elements. However, the presence of a significant number of alloying elements and their compounds in the surface layers and in the structure of the material causes chemical inhomogeneity and heterogeneity of the surface. This is due to the presence of intermetallic compounds

H. V. Karakurkchi (✉)
National Defence University of Ukraine Named After Ivan Cherniakhovskyi, Povitroflotskyi Avenue, 28, Kyiv 31049, Ukraine
e-mail: anyutikukr@gmail.com

N. D. Sakhnenko · A. N. Korohodska · I. I. Stepanova · S. I. Zyubanova
National Technical University «Kharkiv Polytechnic Institute», Kyrpychova Street 2, Kharkiv 61002, Ukraine

G. Sh. Yar-Mukhamedova
Institute of Experimental and Theoretical Physics, Al-Farabi Kazakh National University, Al-Farabi Avenue, 71, Almaty 050040, Kazakhstan

of different quantitative and qualitative composition in multicomponent alloys [6]. They occupy a certain part of the surface, and their properties are different from the characteristics of the base metal.

That is why electrochemical surface treatment on multicomponent alloys is complicated. This also applies to the formation of heterooxide coatings by plasma electrolytic oxidation. Heteroresistance of the treated surface reduces the duration of thermochemical reactions in the spark zones. In such conditions, uneven PEO coatings of insignificant thickness are formed [7].

It has been carefully investigated [8, 9] that the oxidation of pure valve metals, in particular aluminum and titanium, occurs with the formation of phase oxide and the subsequent increase in the thickness of the oxide layer. The forming monoxide matrix will serve as a platform for the incorporation of catalytically active components. The thickness and structure of this oxide matrix for pure metals will depend only on the selected electrolyte and oxidation regime.

It should be noted that the peculiarity of plasma-electrolytic oxidation is the course of the electrochemical oxidation process at the electrode and thermochemical reactions in a growing oxide matrix and a rather narrow electrode layer, which are simultaneous. Moreover, during these reactions, not only oxidation but also reduction is possible [10]. An example of this is the thermolysis of water with the formation of hydrogen.

Based on the available results of research [11, 12], it is possible to solve this technological problem if we minimize the content of alloying elements in the surface layers without changing the physical and mechanical characteristics of the carrier metal as a whole. This goal is achieved by combining the capabilities of plasma-electrolyte treatment and scientifically sound selection of the composition of the working electrolyte. Establishing common patterns and trends in PEO-treatment of alloys of different chemical composition will provide a systematic approach and the ability to control the process for a wide range of processed materials.

We hypothesized that the efficiency of plasma-electrolyte treatment of alloyed alloys will be much higher if during oxidation conditions are created for the parallel course of partial reactions of base metal oxide matrix formation and oxidation and removal of alloying elements and intermetallic compounds from the surface.

Taking into account the conditions of PEO, the implementation of the outlined approach will consist in adding to the composition of the electrolyte ligand L, which would meet a number of requirements. The main ones are thermal and chemical stability, the ability to form strong complexes $(M_xL_y)L$ with elements of the intermetallic compounds of processed alloy, high solubility of the ligand and the complexes formed by it. It must also not form insoluble compounds with other components of the working electrolyte.

The diphosphate ion was selected on the basis of a comprehensive analysis of possible options in accordance with the outlined requirements, taking into account the results of previous studies [13]. This ion has different degrees of protonation L $\in \{P_2O_7^{4-}, HP_2O_7^{3-},\dots\}$ depending on the acidity of the electrolyte:

$$H_4P_2O_7 \rightarrow H_3P_2O_7^- + H^+, \; pK_{a1} = 0.92 \qquad (10.1)$$

$$H_3P_2O_7^- \rightarrow H_2P_2O_7^{2-} + H^+, pK_{a2} = 2.10 \qquad (10.2)$$

$$H_2P_2O_7^{2-} \rightarrow HP_2O_7^{3-} + H^+, pK_{a3} = 6.70 \qquad (10.3)$$

$$HP_2O_7^{3-} \rightarrow P_2O_7^{4-} + H^+, pK_{a4} = 9.32 \qquad (10.4)$$
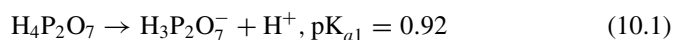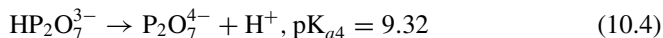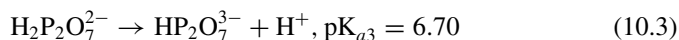
An additional aspect of the choice of this ligand was the value of the instability constants of diphosphate complexes [14] with the main alloying elements of multicomponent alloys of aluminum and titanium (copper, magnesium, nickel, zinc, etc.).

The strength of diphosphate complexes, as a rule, decreases as they protonate. Therefore, plasma-electrolyte treatment of multicomponent alloys should be carried out at pH values ≥ 9.0, when this anion is present in a completely deprotonated form. To control the strength of the formed complexes with the ligand and therefore the form of existence of the ligand in solution can be done by varying the pH of the solution [15]. It allows forming oxide coatings by PEO on alloys with another contain of alloying components.

10.1 Experimental

10.1.1 The Materials, Electrolytes, and Modes

The samples of aluminum (D16, AMn, AL25) and titanium (VT1-0, OT4-1) alloys were selected for research. Rectangular plates and cylindrical specimens of various sizes and thicknesses were used.

Preparation of working electrolytes (Table 10.1) was carried out using reagents qualified "ch.p." and "p.f.a.". Potassium diphosphate solutions were used for plasma electrolytic oxidation and heterooxide coating formation. Monoxide coatings were formed from electrolytes with concentration 0.5–1.0 mol/dm^3 $K_4P_2O_7$. The dopant metal salts (manganese—$MnSO_4$ and $KMnO_4$, cobalt—$CoSO_4$) were added to the working electrolytes for the synthesis of heterooxide.

For PEO model samples used a laboratory equipment, which included a stabilized current source B5-50, electrolytic cell with cooling and stirring of the electrolyte, temperature sensor, working electrodes, and devices for control (registration) of PEO process parameters (ammeter and voltmeter or recorder MTech ADC-UI18).

The PEO modes were used according to the processed material (Table 10.2).

Table 10.1 Composition of electrolytes for the formation of heterooxide PEO coatings on aluminum (titanium) alloys

Metal carrier (substrate)	The composition of the electrolyte	Concentration of components, mol/dm^3	Coating
Al/Ti	$K_4P_2O_7$	0.5–1.0	Al_2O_3 (TiO_2)
Al	$KMnO_4$	0.005	$Al_2O_3 \cdot MnO_x$
	KOH	0.05	
Al	$CoSO_4$	0.05–0.2	$Al_2O_3 \cdot CoO_y$
	$K_4P_2O_7$	0.2–0.6	
Ti	$K_4P_2O_7$	1.0	$TiO_2 \cdot MnO_x$
	$MnSO_4$	0.3	
Ti	$K_4P_2O_7$	0.3	$TiO_2 \cdot CoO_y$
	$CoSO_4$	0.1	
	$Na_3C_6H_5O_7$	0.1	

Table 10.2 Modes of plasma-electrolyte treatment of model samples

Parameter	Material	
	Al alloys	Ti alloys
Current density, i, A/dm^2	2–20	1–5
Voltage U, V:		
Sparking	110–140	65–85
Maximum	160–240	140
PEO time, min	up to 60 min	
Electrolyte temperature, °C	20–25	

10.1.2 The Research Methods

The thickness of the formed oxide systems was set gravimetrically by weight gain of the samples and verified using a micrometer. Surface morphology was analyzed using a scanning electron microscope ZEISS EVO 40XVP. The chemical composition of the coatings was investigated using an energy-dispersion spectrometer Oxford INCA Energy 350. The topography of the surface layers was studied by the contact method using the atomic force microscope NT-206. X-ray phase analysis was performed on a DRON-2 diffractometer in monochromatized Co-Kα radiation (α = 1.7902A). Adhesion strength was controlled by qualitative methods (ISO 2819: 2017). The microhardness of materials and coatings was determined using a microhardness tester PMT-3 in accordance with ISO 2819: 2017. Catalytic properties were evaluated by the parameters of the model conversion reaction CO to CO_2.

10.2 Surface Homogenization of Valve Metals

10.2.1 Surface Homogenization of Aluminum Alloys

The analysis of kinetic regularities of PEO is carried out by registration of change of pressure during oxidation and the analysis of forming dependences $(U-t)$ [16].

Characteristic parameters of plasma-electrolyte treatment of aluminum alloys (spark voltage, voltage of microarc, and arc modes) were determined in accordance with the generally accepted notions of changing the shape of the dependences $U-t$ of the processed alloys.

According to the analysis of the forming dependences (Fig. 10.1) of aluminum alloys, it is established that the spark start voltage U_i during PEO is 90–95 V for the AMn alloy, 80–85 V, for the D16 alloy and 95–105 V for the AL25. The PEO arc mode is set in the voltage range of 150–200 V. For comparison, the dependence for pure A99 aluminum is given.

The formation of the barrier monoxide layer occurs in the characteristic area I (Fig. 10.1). Monoxide coating is formed better on an alloy without alloying elements (pure aluminum A99, Fig. 10.1, dependence 1). The beginning of sparking (Fig. 10.1, area II) and entering the mode of microarc oxidation (Fig. 10.1, area III) for multi-component alloys (AMn, D16, AL25) occur over long time (Fig. 10.1, dependence 2–4). This can be explained by the presence in their composition of alloying elements and intermetallic compounds of different nature [17], as noted above. Therefore, part of the anode current is spent on partial oxidation processes. As a result, this leads to the removal or minimization of the content of alloying elements and the formation of a homogeneous composition of the equipotential surface of the substrate monoxide matrix Al_2O_3 [18].

Given the obtained results, it can be noted that at the initial stage of plasma-electrolyte treatment the homogenization of the surface layer of the treated material is carried out due to the removal of alloying elements from its surface layers [19]. The process of homogenization of the surface of multicomponent alloys during PEO

Fig. 10.1 Forming dependences of PEO for aluminum alloys in 1.0 mol/dm^3 solution K$_4$P$_2$O$_7$, current density 5.0 A/dm^2: A99 (1), AMn (2), D16 (3), AL25 (4)
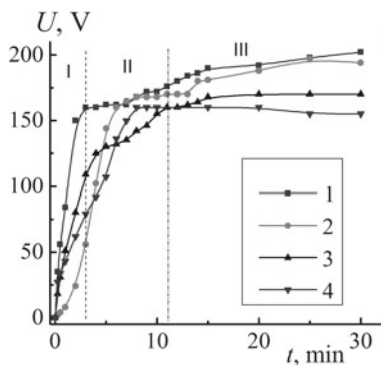
is confirmed by the transformation of morphology and changes in the composition of surface layers.

It is proved that PEO of AMn and D16 alloys in diphosphate solution allows to completely remove such elements as Mn and Cu from the surface of the processed samples [20]. For AL25 alloy, complete removal of copper and reduction of silicon content by 3 times compared to untreated material was established [21]. This is a confirmation of the effectiveness of diphosphate electrolytes for homogenization of the surface of aluminum alloys during PEO.

The confirmations of structural changes during PEO are the results of X-ray analysis of the studied systems (on the example of alloy AL25) (Fig. 10.2).

Peaks of the main components of the alloy are visualized on the untreated surface (Fig. 10.2, dependence 1). After PEO, the number and intensity of aluminum and silicon peaks decrease, and α-Al_2O_3 (corundum) peaks appear (Fig. 10.2, dependence 2). This indicates that PEO is carried out in microarc mode (Fig. 10.1, area III). In the discharge channels, the temperature reaches up to 2000 K, which causes melting of the base metal elements [22].

Therefore, uniform monoxide coatings of Al_2O_3 are formed on the investigated alloys (D16, AMn, and AL25) during PEO in a solution of 1.0 mol/dm^3 of $K_4P_2O_7$ at a current density of 5.0 A/dm^2. The morphology of the treated surface layer during plasma electrolytic oxidation is also transformed (Fig. 10.3).

The morphology of the surface layer of the studied materials during plasma electrolytic oxidation in a solution of $K_4P_2O_7$ varies from non-uniform and rough (Fig. 10.3a–c) to microporous globular which belongs to the monoxide matrix Al_2O_3 (Fig. 10.3d–f). The formed monoxide coating evenly covers the entire surface of the samples. The oxidized surface is characterized by the presence of a significant number of micropores, which are mainly interconnected.

The formed aluminum monoxide matrix is a three-dimensional porous structure like a grid. The porosity of such a system is differentiated: The outer layer has a larger number of pores with a larger size, and the depth of the oxide layer, the degree

Fig. 10.2 X-rays diffraction patterns of the AL25 surface: untreated surface (**a**), after PEO in solution of 1.0 mol/dm^3 $K_4P_2O_7$ (**b**)

a   b   c

untreated surface

d   e   f

treated surface in solution of $K_4P_2O_7$
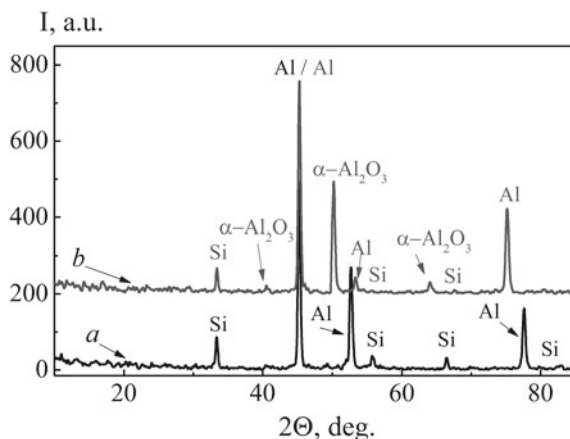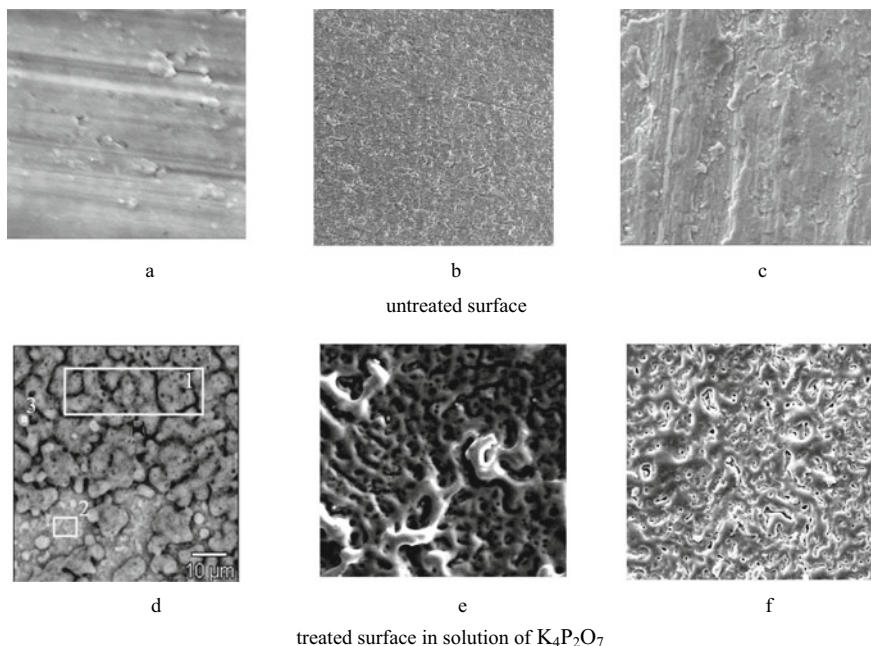
Fig. 10.3 Surface morphology of multicomponent alloys D16 (a, d), AMn (b, e), AL25 (c, f) before PEO (**a–c**) and after 15 min PEO in solution of 1.0 mol/dm^3 $K_4P_2O_7$ (**d–f**). Magnification × 500

of porosity decreases. This correlates both with the general ideas about the course of PEO [23] and with the results obtained by other authors [24].

The total porosity of a conversion layer is relatively low (about 5%) and occurs due to the release of oxygen during PEO according to the model PEO ideas. The high local temperatures and pressures in the spark zones cause a significant content of dissolved oxygen in the molten oxides and closed pores. This creates the conditions for "healing" of defects in contact with the electrolyte and provides increased corrosion resistance of the oxidized surface. On the other hand, porosity helps to obtain a coating of greater thickness by facilitating the electric discharge between the electrolyte and the substrate.

The high degree of development of the surface layer is a prerequisite for increasing the specific surface area of the catalytic material (catalyst). Therefore, the formed structure of the porous monoxide matrix enhances the catalytic properties of the obtained oxide platform when incorporating the target active components is carried out [25].

10.2.2 Features of Surface Homogenization of Titanium Alloys

According to the available results of valve metals PEO-treatment, it is noted that the oxidation of titanium is a more complex process compared to other materials, in particular aluminum. This is due to the formation during PEO of lower oxidation states oxides with different composition TiO_x ($0.75 \leq x < 1.3$), Ti_2O_3, TiO_2. These oxides differ in structure, chemical, and physical properties.

Features of the anodic behavior of multicomponent alloys, in particular OT4-1, due to the manganese content up to 2 wt% and the presence in its composition of intermetallic compounds (γ-TiAl, α-2-Ti_3Al, $TiAl_3$, TiMn, $TiMn_2$) [26]. Therefore, the oxidation reactions of alloying elements and intermetallic compounds take place on the surface of the electrode along different routes, taking into account the qualitative and quantitative composition of the working electrolyte.

Given the different nature of the material for titanium alloys are characterized by lower values of both the processing current density (up to 5.0 A/dm^2) and voltage (up to 100 V) during plasma electrolytic oxidation [27].

During the plasma-electrolyte treatment of titanium alloys (on the example of VT1-0), it was found that the voltage chronograms also have a classical form with a division into characteristic regions (Fig. 10.4). The areas of the formation dependences corresponding to the prespark region of the coating formation (2–4 min) are practically linear, which is explained by the increase in the thickness of the oxide film and, accordingly, its resistance.

The time to the beginning of sparking at $i = 2.5$–5.0 A/dm^2 in the electrolyte 1.0 mol/dm^3 $K_4P_2O_7$ is 1–2 min. As the oxidation current density increases, the characteristic parameters of the process increase accordingly (the spark voltage U_i and the final stress U_f of the formation), as well as the rate of voltage change dU/dt.

Fig. 10.4 Forming dependences (**a**) and rate of voltage change for PEO of titanium alloy VT1-0 in 1.0 mol/dm^3 of $K_4P_2O_7$ and (**b**) voltage change rate dU/dt at current density i, A/dm^2: 1.0 (1), 2.5 (2), 4.0 (3), 5.0 (4)
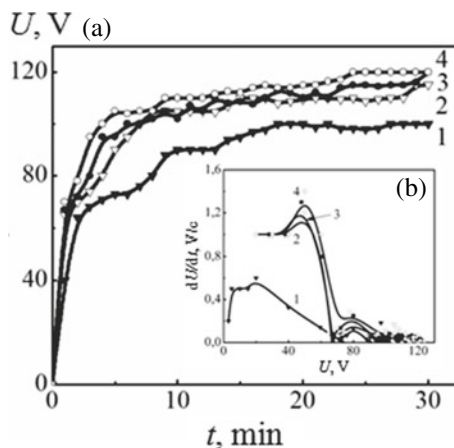
The dynamics of change of differential dependences $dU/dt - U$ in general correlates with the regularities defined for aluminum alloys. Increasing the rate of dU/dt (Fig. 10.4b) from the voltage in the sparking region, including with increasing current density of PEO, occurs due to thermolysis of water with a local increase in temperature to 700–2000 °C in the breakdown zone of the phase oxide [28]. There is also a thermal decomposition of the components of the electrolyte and their inclusion in the formed oxide layer simultaneously with the remelting of the mineral phase of the electrolyte, which contributes to the "healing" of the defects of the composite layer.

The transition voltage of PEO to microarc mode for titanium alloys is significantly lower than for aluminum alloys and is 90–95 V. After reaching during PEO these indicators U, the oxidation process is stabilized, which is affected by a decrease in the intensity and number of oscillations on the dependences $dU/dt - U$ is stabilized. At the same time, the specified course of plasma-electrolyte treatment determines the linear dependence of the thickness of the formed monoxide coatings on the current density of PEO (Fig. 10.5).

For multicomponent alloy, OT4-1 technological parameters of plasma-electrolyte treatment differ insignificantly (within 3–5%) [27, 29], which can be explained by the low content of alloying elements in its composition. In particular, a decrease in the concentration of diphosphate in the working electrolyte to 0.5 mol/dm³ causes an increase in the final oxidation voltage to 130–140 V and an increase in the thickness of the synthesized coatings to 60–65 µm.

Studies of the morphology and chemical composition of the modified surface indicate the inclusion of remelts of electrolyte components in the composition of the surface layers (Fig. 10.6). This allows giving the modified surface extended functional properties.

At the same time, the homogenization of the monoxide matrix surface TiO_2 was proved for the OT4-1 alloy. The analysis of the chemical composition of manganese in the surface layer of the formed coating did not reveal [30], although there are trace amounts of other alloying elements.

Fig. 10.5 Dependence of the thickness of the monoxide coating on the alloy VT1-0 on the density current in solution 1.0 mol/dm³ $K_4P_2O_7$. The time PEO 30 min
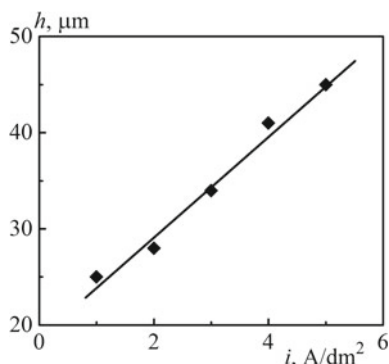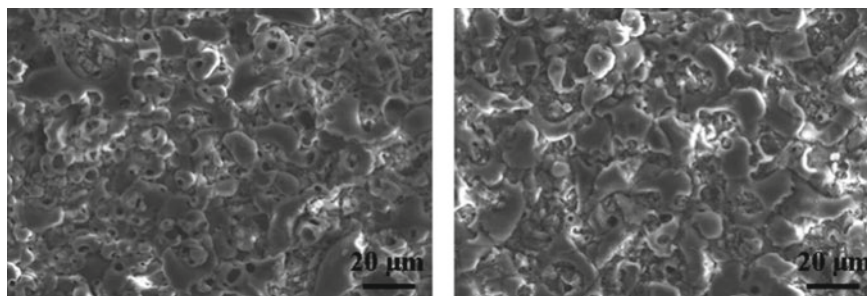
The content of elements excluding oxygen, at.%:

Ti – 56.15; P – 34.0; K – 9.35;   Ti – 50.72; P – 33.76; K – 11.37;

Al – 0.5   Al – 0.24; Si – 0.83; Fe – 2.06;

Zn – 1.02

a   b

Fig. 10.6 Morphology and composition of monoxide coatings on alloys VT1-0 (**a**) and OT4-1 (**b**), formed by PEO in electrolyte 1,0 mol/dm^3 $K_4P_2O_7$ at $i = 4$ A/dm^2. Magnification × 1500

The obtained results are evidence of the efficiency of using diphosphate solutions for homogenization of the surface of multicomponent alloys, both aluminum [31, 32] and titanium [33].

The formed monoxide coatings are characterized by a globular structure, with titanium oxide predominating in the pores, and oxides of phosphorus and potassium on the toroidal structures. Variation of PEO current density contributes to the alignment of the surface relief and the formation of a more uniform and microglobular structure (Fig. 10.7).

The synthesized coating consists of many needle grains and contains more titanium dioxide in the surface layer. The potassium content in the coating is slightly lower, and the phosphorus concentration remains unchanged.

Fig. 10.7 Morphology and composition of the coating on titanium, formed by the method of PEO in a solution of 1.0 mol/dm^3 $K_4P_2O_7$: at $i = 1$ A/dm^2. Magnification × 1500
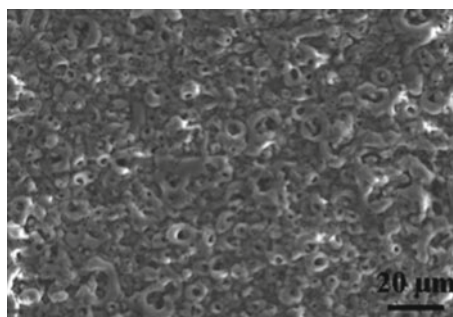
Ti – 61.39; P – 34.86; K – 3.75

Fig. 10.8 X-ray diffraction pattern of monoxide coating on a titanium alloy formed by PEO in a solution of 1.0 mol/dm^3 K$_4$P$_2$O$_7$ for 30 min
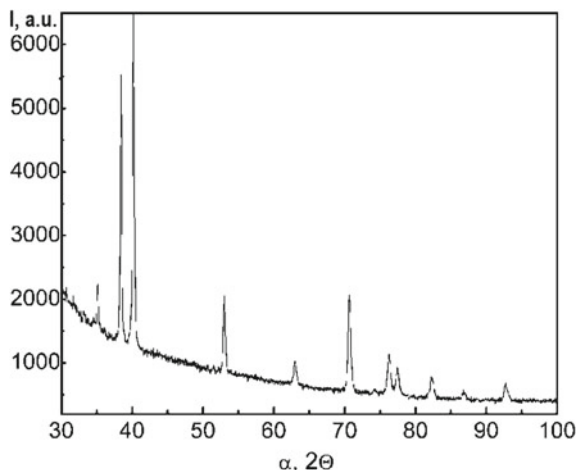
The formation of the monoxide matrix of the substrate metal during PEO of titanium alloys in solutions of diphosphate is confirmed by the results of the analysis of the phase composition of the synthesized oxide layers (Fig. 10.8).

The study of the spectra on the X-ray pattern (Fig. 10.8) revealed the presence of different phases, namely titanium oxides TiO, TiO$_2$, Ti$_3$O$_5$, which correlates with the results obtained by other authors [33].

Thus, it is proved that plasma-electrolyte treatment of titanium alloys in diphosphate electrolytes with a concentration of 0.5–1.0 mol/dm^3 at a current density of 1–4 A/dm^2 can form monoxide coatings for 10–30 min.

Voltage and current density of plasma-electrolyte treatment of titanium alloys are lower than aluminum alloys. This is due to the difference in the resistivity of the monoxide matrices of these metals. Predicted variation in the composition of the electrolyte and PEO parameters will influence the control of the morphology, composition, thickness, and functional properties of the synthesized oxide coatings.

10.2.3   Rationalization of Electrolyte Composition and Modes for Surface Homogenization of Multicomponent Alloys

The established regularities confirm the possibility of homogenization of the surface of multicomponent alloys in diphosphate solutions by the classical mechanism of PEO. They also expand the idea of the stages of the process of their plasma-electrolyte treatment [20].

It is also confirmed that the PEO voltage is the main indicator of the oxidation process. It can determine the mechanism of surface homogenization of multicomponent alloys in working electrolytes based on the analysis of chronograms of voltage

Fig. 10.9 Effect of $K_4P_2O_7$ concentration on the PEO voltage during Al treatment of D16 alloy for, min: 5 (1), 20 (2), 30 (3)
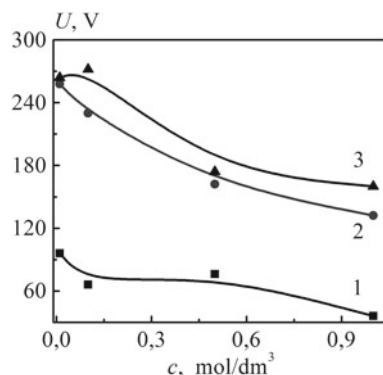
$U-t$ (Figs. 10.1 and 10.4a) and the rate of voltage change from oxidation time $dU/dt-U$ (Fig. 10.4b) [34].

The factors influencing the voltage indicators of PEO and the course of the oxidation process will be the concentration of diphosphate, current density, and time of plasma-electrolyte treatment.

According to the results of experimental studies, it was found that the oxidation voltage of the multicomponent alloy (e.g., D16) increases with the dilution of the diphosphate solution (Fig. 10.9) due to the decrease its electrical conductivity.

The effective plasma electrolytic oxidation of the alloy will be provided at the lower limit of the diphosphate content in the electrolyte (0.5 mol/dm^3) given the previously established voltage range of PEO for the process in microarc mode (160–200 V). The upper limit of $K_4P_2O_7$ content should not exceed 1.0 mol/dm^3.

At the same time, it is shown that the PEO voltage naturally increases with increasing oxidation time, which correlates with the kinetic regularities of the plasma-electrolyte treatment process (see Fig. 10.1). This is also evidence of a more complete removal of alloying elements from the surface layers and the formation of a uniform matrix of the base metal oxide (aluminum/titanium) during longer processing of the material. The rational time for PEO should be 10–30 min [35].

Another important parameter of the influence on the homogenization of the surface layers of the multicomponent alloy is the current density of the plasma electrolytic oxidation. Stabilization of PEO operating voltage in the range corresponding to the microarc mode (160–200 V) occurs at an oxidation current density of 5.0–7.0 A/dm^2 (Fig. 10.10) in electrolytes with $c(K_4P_2O_7) = 0.5$–1.0 mol/dm^3.

The use of a higher PEO current density is impractical due to the rapid achievement of the arc voltage and the sharp degradation of the quality of the formed oxide layer. At the same time, when the diphosphate content in the solution increases by more than 1.0 mol/dm^3 (Fig. 10.10, dependence 3), it is impossible to carry out the process at certain current densities. This is due to the fact that the spark voltage at PEO in solution with $c(K_4P_2O_7) = 2.0$ mol/dm^3 is achieved only at much higher current densities ($i = 10.0$ A/dm^2). Under these conditions, the etching processes of the surface of the processed alloy will prevail over the formation of the oxide coating.

Fig. 10.10 Effect of current
density on the voltage of
PEO during processing of Al
alloy D16 in electrolytes
with $c(K_4P_2O_7)$, mol/dm^3:
0.5 (1); 1.0 (2); 2.0 (3)
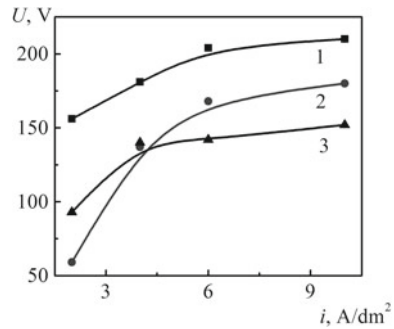
The efficiency of plasma-electrolyte treatment of multicomponent alloys, in addition to estimating the content of alloying elements in the surface layers, can also be performed by analyzing the thickness h of the formed oxide layer. It is considered a technological parameter of the oxide coating forming process [36]. The study of the influence of PEO current density on h (Fig. 10.11) confirms the validity of the choice of the operating range i for plasma-electrolyte treatment of alloyed valve metal alloys (aluminum and titanium).

It is shown (on the example of aluminum alloys) that the increase of PEO current density and diphosphate concentration in the electrolyte composition causes acceleration of the oxide layer thickness increase on the treated surface. From the dependences h–i (Fig. 10.11), it is established that under the same conditions (diphosphate concentration, treatment current density) on an substrate with a higher content of alloying elements (AL25) an oxide layer of smaller thickness is formed compared to an alloy of simpler composition (D16).

On the one hand, this is a reflection of the kinetic patterns and mechanism of plasma-electrolyte treatment of these materials (Fig. 10.1). On the other hand, it
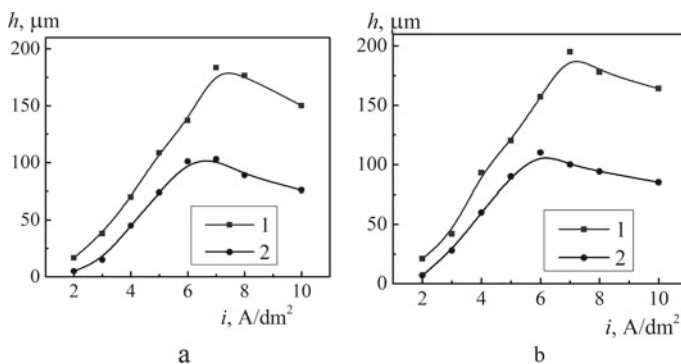
Fig. 10.11 Influence of oxidation current density on the thickness of the monoxide layer Al_2O_3 during PEO alloys D16 (1) and AL25 (2) in a solution of $K_4P_2O_7$ composition, mol/dm^3: 0.5 (**a**); 1.0 (**b**). PEO time 10 min

is evidence of the peculiarities of homogenization of the treated surface and transformations of morphology and chemical composition of the surface layers of the studied alloys. So, plasma electrolytic oxidation of multicomponent alloys (Al/Ti) of different composition and nature in solutions of diphosphates promotes the formation on their surface of monoxide coatings (Al_2O_3/TiO_2) of considerable thickness.

Thus, the complex of studies allows us to conclude that the homogenization of the surface of multicomponent alloys (aluminum/titanium) and the formation of a developed monoxide matrix up to 100–200 μm are carried out in a solution of 0.5–1.0 mol/dm^3 $K_4P_2O_7$ at current densities of 5.0–7.0 A/dm^2 for 20–30 min. The revealed regularities allow defining ways of management of process of homogenization of a surface of the processed materials by PEO method in solutions of diphosphates.

10.3   Formation of Heterooxide Nanocomposites on Multicomponent Aluminum and Titanium Alloys

The developed concept of surface homogenization of alloyed aluminum (titanium) alloys became the basis of the hypothesis that the formation of strongly adhesive composite heterooxide coatings with a wide range of functional properties on multicomponent aluminum and titanium alloys is realized in one technological process by plasma electrolytic oxidation in alkaline solutions of diphosphates in the presence of dopant metals.

A feature of the proposed technological approach to plasma-electrolyte treatment of multicomponent valve metal alloys is a combination of partial processes of homogenization of surface layers and formation of a developed oxide matrix of carrier (substrate) metal, which includes incorporated oxides of doped components. As a result, it will provide the obtaining of multifunctional material in which the characteristic properties of the oxide matrix and doped components are synergistically combined [37].

The proposed hypothesis can be realized by adding doped components into the base electrolyte and their incorporation into the formed oxide layer in the microarc mode. This will provide a comprehensive solution to the scientific and practical problem. The surface layer of the processed material will be homogenized. The dopant metals will be incorporated into the oxide matrix of the base metal. In general, a continuous oxide layer will be formed on the treated surface with a uniform distribution of the target components on the surface and the thickness of the obtained heterooxide coating.

It is necessary to solve some of technological problems for the selection of qualitative and quantitative composition of the electrolyte, the mode of plasma-electrolyte treatment, and adaptation of the developed method to PEO alloys of different types and compositions.

The manganese and cobalt were selected for doping of monoxide matrices. The dopants were added into the electrolytes in the form of $KMnO_4$ ($MnSO_4$) and $CoSO_4$, respectively. The multicomponent aluminum (titanium) alloys (AL25 and OT4-1) were selected as model objects for research. Testing the concept of formation of heterooxide coatings on more complex objects, allowed the transfer of technology to alloys with a lower content of alloying elements.

The use of the proposed concept will provide a comprehensive unified approach to plasma-electrolyte synthesis of heterooxide coatings on aluminum (titanium) alloys of different composition using variable technological schemes, which will form the basis of a new paradigm of surface engineering for forming functional heterooxide layers on multicomponent alloys.

During the formation of oxide coatings on aluminum and titanium alloys in these electrolytes, the chronograms of PEO voltages have a classical form with a division into characteristic areas: prespark, spark, microarc (as shown in Fig. 10.1). The shape of the dependences and the parameters of the characteristic areas, in particular the angle of inclination, and hence the rate of formation of the heterooxide layer, are influenced by the composition of the carrier material and the ratio of the electrolyte components.

The dependence of $U-t$ in the prespark region is almost linear due to the formation of a barrier oxide of the parent metal (aluminum/titanium) with increasing thickness and, accordingly, resistance. At the onset of sparking, the voltage rise is inhibited due to breakdown competition and barrier oxide regeneration, but at the same time thermochemical reactions take place, which ensures the incorporation of electrolyte components. Therefore, the characteristics of the initial stage of PEO—the time before the start of the spark Ti and the initial spark voltage Ui should depend on the nature of the material being processed.

Indeed, at PEO OT4-1 in electrolytes with the addition of Mn and Co salts at the specified current densities (Table 10.1) Ti is 1–2 min, and U_i does not exceed 65 V. Sparking at PEO AL25 in electrolytes 1 and 2 1) begins after 5–8 min, and U_i is 110–120 V. This is significantly explained, firstly, by the higher resistivity of aluminum oxides compared to titanium oxides, and, secondly, the presence of a significant amount of alloying impurities, in particular silicon, as a part of AL25.

Stabilization of the plasma-electrolyte treatment process takes place in the region of stable sparking, the sparking voltage U_i for titanium alloys is in the range of 120–130 V, and for aluminum alloy U_i reaches 140–180 V depending on the electrolyte type. The incorporation of electrolyte components into the surface layers is visualized by the appearance of areas of arbitrary shape of black (for manganese) and purple (for cobalt) color.

In the microarc mode, the number of inclusions of dopants in the composition of the formed covers increases significantly, and gradually they cover the entire surface of the treated sample. Under these conditions, the process voltage hardly changes, although for all electrolytes and processing modes, both aluminum and titanium, there are slight voltage fluctuations, which can be explained by the formation of oxide systems with different resistivity and thermal stability. At the same time, the

most powerful microarcs can break the surface and destroy the oxide layer, so it is necessary to support the PEO process within sections II-IV.

A "falling power" mode has been developed for processing multicomponent alloys (on the example of AL25). Experimental studies have shown that the use of a higher initial current density i_1 accelerates the formation of a barrier oxide film. After entering the mode of stable sparking, the current density is reduced to stabilize the process in the voltage range, which corresponds to sections II-III and the formation of a uniform mixed oxide (composite coating). For cobalt-diphosphate solutions, the current density of PEO of the first stage i_1 does not exceed 10 A/dm^2. In alkaline-permanganate solution oxidation is more effectively realized at $i_1 = 15-25$ A/dm^2. The second stage of PEO in cobalt-containing electrolyte should be carried out at $i_2 = 2-5$ A/dm^2, in manganese-containing electrolyte $i_2 = 5-15$ A/dm^2.

The characteristic voltage indicators of the PEO process of aluminum alloy also depend on the type and composition of the electrolyte. The sparking voltage U_i in cobalt-containing electrolytes is 115–120 V, and the final (maximum) voltage in the arc mode $U_f = 140–160$ V. For manganese-containing electrolytes, these indicators are slightly higher—$U_i = 150-160$ V and $U_f = 220-240$ V. These differences are explained by the peculiarities of the course of electrochemical and thermochemical processes involving Co^{2+} and MnO^{4-}.

In general, the revealed regularities testify to the creation of conditions for the course of electrochemical and thermochemical reactions and transformations that determine the synthesis of heterooxide oxide composites strongly adhered to the metal carrier. The stages of the plasma-electrolyte treatment process are similar to those discussed earlier [34] and take into account the formation in the microarc mode of the oxide matrix of aluminum (titanium), which incorporates of dopant metals oxides.

Thus, it is proved that the formation of manganese-containing coatings on multi-component aluminum alloys (AMn, D16, AL25) should be carried out from alkaline-permanganate electrolyte. The synthesis of manganese-enriched (up to 40.0 at.%) heterooxide layers with a uniform distribution of the active component is provided in the mode of "decreasing power" at a polarization current density of 10–20 A/dm^2 for 20–40 min. Higher values of i at the initial stage provide the formation of a monoxide matrix of the carrier metal (Al_2O_3) and the removal of alloying elements from the surface layers. The further reduction of i after achieving stable sparking allows to form strongly adhered heterooxide layers up to 50 microns thick.

Incorporation of MnOx during PEO occurs in the microarc mode due to the flow in the spark zone of the reaction of thermal intramolecular oxidation–reduction of permanganate ions [38].

$$2MnO_4^- \xrightarrow{T} MnO_4^{2-} + MnO_2 + O_2, \qquad (10.5)$$
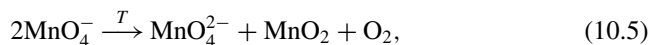
disproportionation of unstable anions $MnO_4{}^{2-}$:
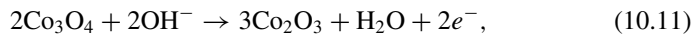
$$3MnO_4^{2-} + 2H_2O \rightarrow 2MnO_4^- + MnO_2 + 4OH^-. \qquad (10.6)$$

and high-temperature transformations

$$MnO_2 \xrightarrow{900K} Mn_2O_3 \xrightarrow{1300K} Mn_3O_4. \tag{10.7}$$
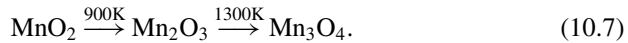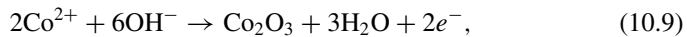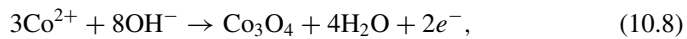
The results of the analysis of the chemical composition of the synthesized coatings indicate that manganese oxides MnO_x are not only embedded in the monoxide matrix Al_2O_3, but also form an outer coating layer.

It was found that the formation of $TiO_2·MnO_x$ coatings with a thickness of 15–50 μm on an alloy OT4-1 with ω(Mn) up to 3.0 at.% is carried out in one stage at i 1–5 A/dm² from the electrolyte (mol/dm³) 1.0 $K_4P_2O_7$ + 0.1−0.3 $KMnO_4$, which is due to the peculiarities of plasma-electrolyte treatment of titanium alloys.

Partial oxidation reactions of aluminum (titanium) and Co (II) can simultaneously run in cobalt (II)-containing electrolytes in the anodic polarization of aluminum (titanium) alloys in the prespark mode. These reactions occur in several stages along different routes, depending on the potential.

$$3Co^{2+} + 8OH^- \rightarrow Co_3O_4 + 4H_2O + 2e^-, \tag{10.8}$$

$$2Co^{2+} + 6OH^- \rightarrow Co_2O_3 + 3H_2O + 2e^-, \tag{10.9}$$

$$Co^{2+} + 4OH^- \rightarrow CoO_2 + 2H_2O + 2e^-, \tag{10.10}$$

$$2Co_3O_4 + 2OH^- \rightarrow 3Co_2O_3 + H_2O + 2e^-, \tag{10.11}$$

$$Co_2O_3 + 2OH^- \rightarrow 2CoO_2 + H_2O + 2e^-. \tag{10.12}$$
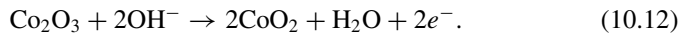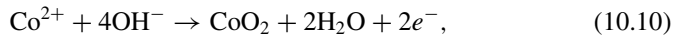
Moreover, oxides of Co_2O_3 and CoO_2 are not thermodynamically stable and tend to spontaneously decompose with the release of oxygen under standard conditions with the formation of stable cobalt oxide Co_3O_4 of variable oxidation ($CoO·Co_2O_3$), which crystallizes in the spinel lattice:

$$CoO_2 \xrightarrow{-O_2} Co_2O_3 \xrightarrow{-O_2} Co_3O_4 \tag{10.13}$$
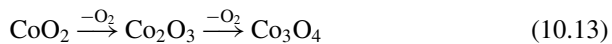
Given the high temperature in the discharge channel during PEO for aluminum alloys, it is likely that the process of high-temperature interaction of oxides with the formation of cobalt spinel

$$CoO + Al_2O_3 \xrightarrow{1400K} CoAl_2O_4. \tag{10.14}$$
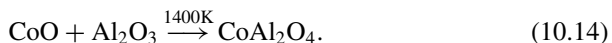
Formation of CoO oxide in the discharge channel at temperatures 1200–1230 K occurs by endothermic reaction:

Table 10.3 Technological modes of plasma-electrolyte formation of heterooxide coatings

Substrate	Coating	i, A/dm^2	Voltage	
			U_s	U_f
Manganese-containing heterooxide nanocomposites				
Al alloys (AL25, D16, AMn)	Al|Al$_2$O$_3$·MnO$_x$	10–20	140–160	180–240
Ti alloys (VT1-0, OT-4)	Ti|TiO$_2$·MnO$_x$	1–5	65–85	120–140
Cobalt-containing heterooxide nanocomposites				
Al alloys (AL25, D16, AMn)	Al|Al$_2$O$_3$·CoO$_y$	2–5	110–120	140–160
Ti alloys (VT1-0, OT-4)	Ti|TiO$_2$·CoO$_y$	1–5	80–85	130–140

$$2Co_3O_4 \rightarrow 6CoO + O_2 \quad \Delta G = 322.8 \text{ kJ}. \tag{10.15}$$
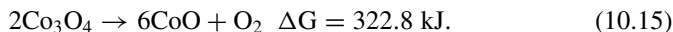
Under these conditions, a heterooxide conversion layer with a cobalt content of up to 10.0 at.% is formed on the aluminum alloys and up to 5.0 at.% on titanium. Varying the ratio of electrolyte components allows to increase the content of additional components by 2.0–3.0 at.%, which allowed to clarify the composition of the working solutions for further research.

As a result of a complex of experimental studies, the technological parameters for the formation of heterooxide nanocomposites on alloyed aluminum and titanium alloys are generalized (Table 10.3).

The qualitative and quantitative composition of the electrolyte and the starting density of the oxidation current are factors influencing on the operating voltage of PEO (Table 10.3). Increasing the operating current density and the use of the "decreasing power" mode allows to accelerate the process of incorporation of the dopant metal into the matrix of the base metal oxide during PEO of multicomponent alloys, in particular aluminum.

Increasing the oxidation time to 20–30 min contributes to the enrichment of the surface layers of the target component and minimizes the content of alloying elements of the alloy. Thus, due to the variation of the component composition of the electrolyte and technological parameters (i, U, t), it is possible to flexibly control the process of formation of heterooxide coatings.

The surface morphology of the synthesized heterooxide layers changes with the incorporation of dopant metals into the matrix of the carrier metal oxide. The inclusion of manganese ensures the formation of a uniform brown-black oxide layer on aluminum alloys. The surface of the coatings is fine, a significant number of conglomerates formed by small spheroids (Fig. 10.12a) with a uniform distribution of the active component on the surface is visualized on it.

Incorporation of cobalt occurs in the form of spheroidal island structures of blue-violet color. The coating is characterized by a "spheroidal-mosaic" morphology of the surface, the protrusions of which are enriched with the active component (Fig. 10.12b). Given the possible mechanism of coating formation, spheroids are impregnations of CoAl$_2$O4, and their distribution on the surface reflects the distribution of spark and the trajectory of microarc discharges during PEO.
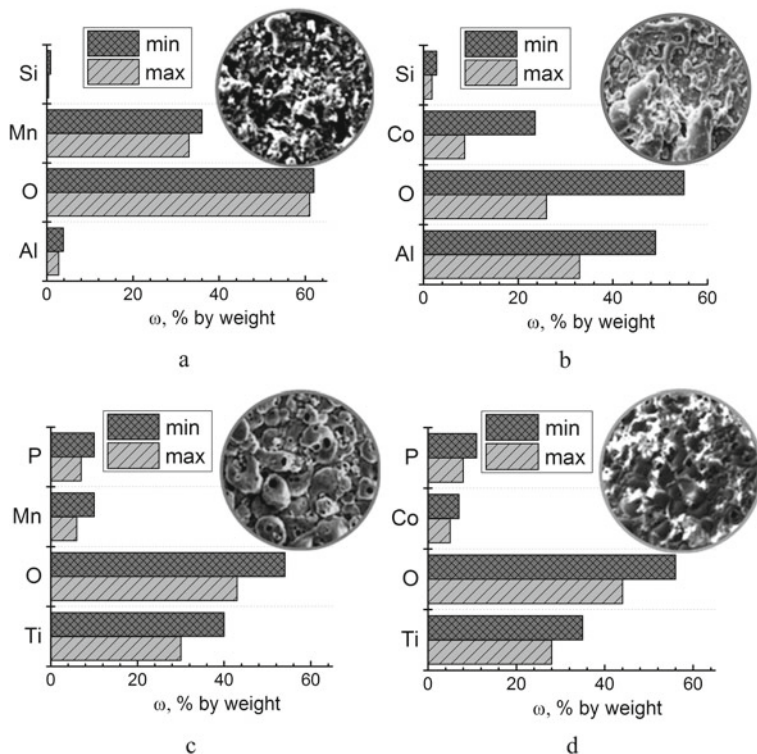
Fig. 10.12 Morphology and composition of heterooxide nanocomposites on aluminum (titanium) alloys

During PEO of titanium alloys in manganese and cobalt-containing electrolytes, an enamel-like developed surface is formed, which consists of spheroidal grains (Fig. 10.12c and d). Also under these conditions, the tubular microporous structure characteristic of titanium oxides is shown.

According to the results of AFM scan, it was found that heterooxide coatings on aluminum (titanium) multicomponent alloys have a smoother spheroidal surface compared to monoxide matrices. Thus, the incorporation of manganese into titanium oxide coatings OT4-1 contributes to the smoothing of the relief of the oxidized surface due to the formation of spheroidal crystallites (Fig. 10.13). The heterooxide layer becomes more uniform, and the difference in height of the crystallites on the surface of the coating is reduced.

The results of X-ray diffraction analysis of the obtained systems confirm the formation of composites. The structure of the oxide matrix of the carrier metal (substrate) is transformed due to the incorporation of oxides of the target components (MnO_x, CoO_y). Peculiarities of the formation of oxide PEO structures in non-equilibrium conditions reflect the amorphous halo at angles of $2\theta \sim 20°$ on the diffractograms of the formed heterooxide systems (on the example of aluminum

Fig. 10.13 2D-surface map (**a**) and cross-sectional profile between markers 1 and 2 (**b**) of the heterooxide coating $TiO_2 \cdot MnO_x$. Scanning area 10×10 μm

a

b
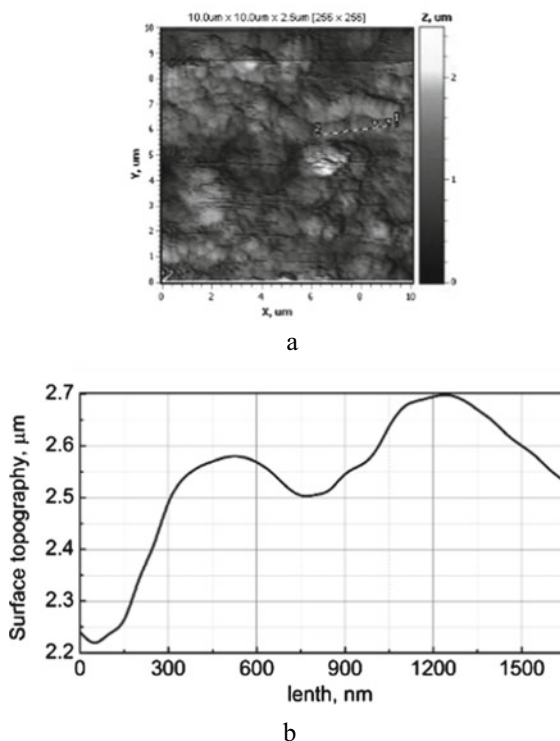
alloys) (Fig. 10.14). The quantitative composition of the formed heterooxide layer can be indirectly determined by the intensity of the detected lines of oxides of dopant metals [39].

After heat treatment, the formed coating crystallizes. This is evidenced by the absence of diffraction patterns of the amorphous halo after calcination of coatings at 600 °C. The number of peaks of the corresponding high-temperature oxides of manganese and cobalt also increases. This increases the catalytic activity of the synthesized composite materials.

For heterooxide coatings on titanium on diffractograms, the presence of oxides of manganese and cobalt of variable valence (MnO, MnO_2, Mn_2O_3, CoO, Co_3O_4) along with titanium oxides Ti_3O_5, TiO_2, and TiO [40].

Features of the phase structure of the formed oxide coatings in combination with the developed surface and a significant content of target active components are a prerequisite for improving the functional properties of the synthesized materials.

The results of metallographic studies have shown that the formed mono- and heterooxide coatings have high adhesion to the substrate (aluminum and titanium alloys). On the modified surface of alloys, there are no peelings, fractures and chips of a covering, in particular at polishing, grinding, other types of machining. Heating the samples to 200 °C does not change the morphology of the oxide layer, does not

Fig. 10.14 X-ray diffraction patterns of the heterooxide nanocomposites on aluminum alloys: $Al_2O_3 \cdot MnO_x$ (**a**); $Al_2O_3 \cdot CoO_y$ (**b**)

a

b
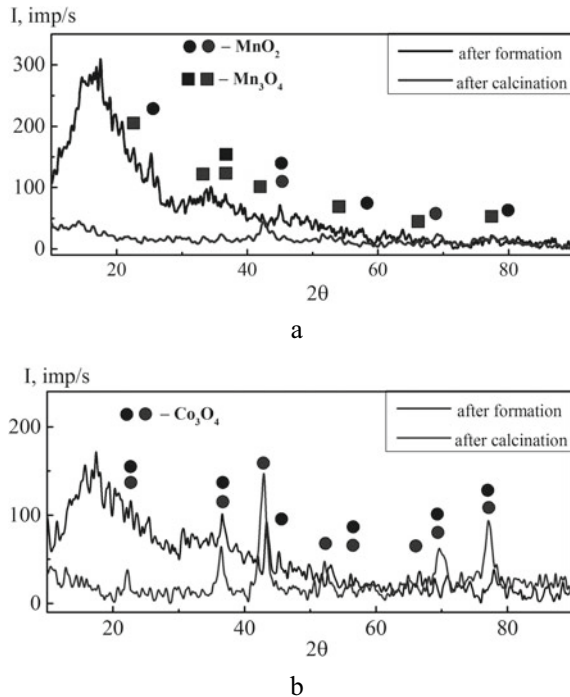
cause cracking of the coatings, and does not affect the strength of its adhesion to the carrier metal.

The incorporation of the dopant metals into the synthesized oxide matrix, along with the transformation of its morphology, topography, and chemical composition, leads to the strengthening of the surface. The microhardness of the studied systems increases in the series $Al < Al_2O_3 \cdot MnO_x < Al_2O_3 \cdot CoO_y < Al_2O_3$. The identified patterns are explained by the structural features of the synthesized heterooxide layers. Coatings on multicomponent alloys, given the presence of alloying elements in their composition, are characterized by higher microhardness than unalloyed alloys. The increase in the microhardness of the synthesized coatings is explained by the formation of the structure of corundum (α-Al_2O_3), which is the basis of the oxide matrix. Higher values for cobalt-containing systems compared to coatings doped with manganese are due to the formation during PEO of the structure of cobalt spinel $CoAl_2O_4$, which also has high strength characteristics.

Heterooxide nanocomposites doped with transition metals are of practical interest as catalytic materials for electrochemical and heterophase processes. [41]. Determination of the catalytic activity of heterooxide coatings on aluminum and titanium alloys was performed in a model oxidation reaction of carbon monoxide (II). The intervals of temperatures for the effective operation of the obtained catalytic materials are defined. They are 170–230 K for heterooxide coatings synthesized on aluminum

alloys and 250–280 K for coatings synthesized on titanium alloys. For manganese-containing systems, the degree of CO conversion is 70–100%. For cobalt-containing coatings, the conversion rate is 68–81%.

The set of properties of the obtained heterooxide composites allows us to consider them as promising materials for ecocatalysis, chemical energy, engine building and the automotive industry in general, and so on. Prospects for further research are related to the adaptation of the proposed technology to the plasma-electrolyte treatment of other structural materials, expanding the range of dopant metals. This will increase the efficiency and increase the use of heterooxide nanocomposites.

The practical value of the results lies in their application in the creation of a wide range of *smart*-materials for the needs of the industrial complex (ecocatalysis, chemical energy and automotive industry, microelectronics, photovoltaics, sensors, utilities, and others).

10.4 Conclusions

1. The concept of plasma-electrolyte treatment of aluminum (titanium) alloys of different chemical composition in alkaline solutions of diphosphates is developed. It is shown that plasma electrolytic oxidation allows to combine in one technological process of the stages of homogenization of the surface layer, its development and formation of monoxide coating. It is proved that PEO in a solution of 0.5–1.0 mol/dm^3 K$_4$P$_2$O$_7$ at a current density to 7 A/dm^2 allows to minimize the content of alloying elements in the surface layers of multi-component alloys and to form a developed monoxide matrix of the valve metal (aluminum/titanium alloy).
2. It is shown that by PEO of multicomponent aluminum (titanium) alloys in diphosphate solutions monoxide coatings are formed. The control of surface morphology, chemical, and phase composition can be carried out by varying the concentration of electrolyte components and PEO modes, in particular current density.
3. A technological approach in surface engineering of multicomponent alloys of valve metals has been developed. According it, the heterooxide coatings doped by oxides of transition metals are formed by PEO from complex diphosphates electrolytes in one technological process with minimization of alloying components and homogenization of treated surface.

Conflicts of Interest The authors certify that they have no conflicts of interest.

References

1. Simchen F, Sieber M, Kopp A, Lampke T (2020) Introduction to plasma electrolytic oxidation—an overview of the process and applications. Coat 10(628):1–19. https://doi.org/10.3390/coatings10070628

2. Rudnev V (2013) Micro- and nano-formations on the surface of plasma electrolytic oxide coatings on aluminum and titanium. Surf Coat Technol 235:134–143

3. Meille V (2006) Review on methods to deposit catalysts on structured surfaces. Appl Catal A: Gen 315:1–17. https://doi.org/10.1016/j.apcata.2006.08.031

4. Lukiyanchuk I, Rudnev V, Tyrina L (2016) Plasma electrolytic oxide layers as promising systems for catalysis. Surf Coat Technol 307:1183–1193

5. Mohedano M, Lu X, Matykina E, Blawert C, Arrabal R, Zheludkevich ML (2017) Plasma electrolytic oxidation (PEO) of metals and alloys. In: Reference module in chemistry, molecular sciences and chemical engineering, pp 432–437. https://doi.org/10.1016/B978-0-12-409547-2.13398-0

6. Wang P, Li JP, Guo YC, Yang Z, Wang JL (2016) Ceramic coating formation on high Si containing Al alloy by PEO process. Surf Engin 32(6):428–434. https://doi.org/10.1179/1743294415y.0000000003

7. Fangtao X, Yuan X, Guang L (2009) The mechanism of PEO process on Al–Si alloys with the bulk primary silicon. Appl Surf Sci 255:9531–9538. https://doi.org/10.1016/j.apsusc.2009.07.090

8. Shin KR, Ko YG, Shin DH (2011) Effect of electrolyte on surface properties of pure titanium coated by plasma electrolytic oxidation. J Alloys Comp 509(1):S478–S481

9. Ayday A, Durman M (2015) Growth characteristics of plasma electrolytic oxidation coatings on aluminum alloys. Acta Phys Polon A 127(4):886–887. https://doi.org/10.12693/aphyspola.127.886

10. Yerokhin A, Snishko L, Gurevina N, Leyland A, Pilkington A, Matthews A (2003) Discharge characterization in plasma electrolytic oxidation of aluminium. J Phys: Appl Phys 36(17):2110–2120. https://doi.org/10.1088/0022-3727/36/17/314

11. Cheng YL, Xue ZG, Wang Q, Wu XQ, Matykina E, Skeldon P, Thompson GE (2013) New findings on properties of plasma electrolytic oxidation coatings from study of an Al–Cu–Li alloy. Electrochim Act 107:358–378

12. Ma C, Lu Y, Sun P, Yuan Y, Jing X, Zhang M (2011) Characterization of plasma electrolytic oxidation coatings formed on Mg-Li alloy in an alkaline polyphosphate electrolyte. Surf Coat Technol 206(2–3):287–294. https://doi.org/10.1016/j.surfcoat.2011.07.019

13. Sakhnenko MD, Ved MV, Karakurkchi A (2017) Morphology and properties of coatings obtained by plasma-electrolytic oxidation of titanium alloys in pyrophosphate electrolytes. Prot Met Phys Chem Surf 53(6):1082–1090. https://doi.org/10.1134/S207020511706020X

14. Sillen L, Martell A (1971) Stability constants of metal–ion complexes. Special publ. No. 25. London.

15. Yermolenko IYu, Ved MV, Karakurkchi AV, Sakhnenko ND, Kolupayeva ZI (2017) The electrochemical behavior of Fe^{3+}-WO_4^{2-}-Cit^{3-} and Fe^{3+}-MoO_4^{2-}-WO_4^{2-}-Cit^3 systems. Iss Chem Chem Technol 2(111):4–14

16. Rudnev V, Gordienko P, Kurnosova A, Orlova T (1990) Kinetics of the galvanostatic formation of spark-discharge films on aluminum-alloys. Sov Electrochem 26(7):756–762

17. Clyne TW, Troughton SC (2018) A review of recent work on discharge characteristics during plasma electrolytic oxidation of various metals. Intern Mater Rev, pp 127−162

18. Wong YH, Affendy MG, Lau SK (2017) Effects of anodisation parameters on thin film properties: a review. Mater Sci Tech 33:699–711

19. Zin IM, Mardarevych RS, Bilyi LM, Korniy SA, Duryagina ZA (2019) Influence of the surface chemical treatment of D16T alloy on the protective properties of alkyd coatings. Mater Sci 55(4):284–290. https://doi.org/10.1007/s11003-019-00301-3

20. Slonova AI, Terleeva OP (2008) Morphology, structure, and phase composition of microplasma coatings formed on Al-Cu-Mg alloy. Prot Met 44:65–75

21. Karakurkchi A, Sakhnenko M, Ved M, Horokhivskyi A, Galak A (2017) Study into formation of cobalt containing PEO-coatings on AK12M2MgN from a pyrophosphate electrolyte. East-Eur J Enterp Technol 6(12):19–27. https://doi.org/10.15587/1729-4061.2017.118028
22. Gebarowski W, Pietrzyk S (2014) Growth characteristics of the oxide layer on aluminium in the process of plasma electrolytic oxidation. Arch Metall Mater 59:407–411
23. Hryniewicz T (2018) Plasma electrolytic oxidation of metals and alloys. Metals 8(12):1058. https://doi.org/10.3390/met8121058
24. Patcas F, Krysmann W (2007) Efficient catalyst with controlled porous structure obtained by anodic oxidation. Appl Catal A: Gen 316:240–249. https://doi.org/10.1016/j.apcata.2006.09.028
25. Erfanifar E, Aliofkhazraei M, Fakhr Nabavi H, Sabour Rouh Aghdam A (2017) Growth kinetics and morphology of plasma electrolytic oxidation coating on aluminum. Mater Chem Phys 185:162–175. https://doi.org/10.1016/j.matchemphys.2016.10.019
26. Protsenko VS, Tsurkan AV, Vasil'eva EA, Baskevich AS, Korniy SA, Cheipesh TO, Danilov FI (2018) Fabrication and characterization of multifunctional Fe/TiO$_2$ composite coatings. Mater Res Bull 100:32–41. https://doi.org/10.1016/j.materresbull.2017.11.051
27. Sakhnenko M, Ved MV, Karakurkchi A (2017) Nanoscale oxide PEO coatings forming from diphosphate electrolytes. Nanophis Nanomater Interf Stud Appl 195:507–531. https://doi.org/10.1007/978-3-319-56422-7_38
28. Sakhnenko M, Ved MV, Mayba MV, Karakurkchi AV, Galak A (2018) Mixed oxide films formed on titanium alloy by plasma electrolytic oxidation. Surf Eng Appl Electrochem 54(2):203–209. https://doi.org/10.3103/S1068375518020102
29. Liu X, Chu PK, Ding C (2004) Surface modification of titanium, titanium alloys, and related materials for biomedical applications. Mater Sci Eng: R: Rep 47(3–4):49–121. https://doi.org/10.1016/j.mser.2004.11.001
30. Rakoch AG, Bardin IS (2013) Microarc oxidation of light constructional alloys: part 1. Main notions on the microarc oxidation of light constructional alloys. Russ J Non-ferr Met 54(5):341–344
31. He J, Cai QZ, Luo HH (2009) Influence of silicon on growth process of plasma electrolytic oxidation coating on Al-Si alloy. J Alloy Compd 471:395–399
32. Karakurkchi A, Sakhnenko M, Ved M, Yermolenko I, Pavlenko S, Yevsieiev V, Pavlov Y, Yemanov V (2019) Determining features of application of functional electrochemical coatings in technologies of surface treatment. East-Eur J Enterp Technol 3(12):29–38. https://doi.org/10.15587/1729-4061.2019.171787
33. Rokosz K, Hryniewicz T, Raaen S, Chapon P, Dudek L (2017) GDOES, XPS, and SEM with EDS analysis of porous coatings obtained on titanium after plasma electrolytic oxidation. Surf Interf Anal 49(4):303–315. https://doi.org/10.1002/sia.6136
34. Karakurkchi AV, Sakhnenko ND, Ved MV, Luhovskyi IS, Drobakha HA, Mayba MV (2019) Features of plasma electrolytic formation of manganese- and cobalt-containing composites on aluminum alloys. Adv Mater Sci Eng 2019:6381291. https://doi.org/10.1155/2019/6381291
35. Karakurkchi AV, Sakhnenko MD, Ved MV, Tulenko MV, Dzheniuk AV (2020) Analysis of technological approaches to electrochemical surface treatment of aluminum alloys. East-Eur J Enterp Technol 3(12):44–55. https://doi.org/10.15587/1729-4061.2020.206014
36. Hussein RO, Nie X, Northwood DO (2010) Influence of process parameters on electrolytic plasma discharging behaviour and aluminum oxide coating microstructure. Surf Coat Technol 205:1659–1667. https://doi.org/10.1016/j.surfcoat.2010.08.059
37. Sakhnenko M, Karakurkchi A, Galak A, Menshov S, Matykin O (2017) Examining the formation and properties of TiO$_2$ oxide coatings with metals of iron triad. East-Eur J Enterp Technol 2(11):4–10. https://doi.org/10.15587/1729-4061.2017.97550
38. Vasilyeva MS, Rudnev VS (2018) Manganese-containing nanostructured oxide coatings on titanium formed by plasma electrolytic oxidation. Def Diff Forum 386:349–352
39. D'Ippolito V, Andreozzi GB, Bosi F, Hålenius U (2012) Blue spinel crystals in the MgAl2O4-CoAl2O4 series: part I. Flux growth and chemical characterization. Am Mineral 97:1828–1833. https://doi.org/10.2138/am.2012.4138

40. Sakhnenko ND, Ved MV, Karakurkchi AV (2018) Effect of doping metals on the structure of PEO coatings on titanium. Int J Chem Eng 2018:4608485. https://doi.org/10.1155/2018/460 8485
41. Parsadanov IV, Sakhnenko ND, Ved MV, Rykova IV, Khyzhniak VA, Karakurkchi AV, Gorokhivskiy ASA (2017) Increasing the efficiency of intra-cylinder catalysis in diesel engines. Iss Chem Chem Technol 6:75–81

Chapter 11
Deterioration of Crack Growth Resistance Characteristics of a Fine-Grained YSZ–NiO(Ni) Anode Material During Its Degradation in a Hydrogen Sulfide Containing Atmosphere

B. D. Vasyliv, V. V. Kulyk, Z. A. Duriagina, T. M. Kovbasiuk, I. A. Lemishka, and V. V. Vira

11.1 Introduction

A solid oxide fuel cell (SOFC) is an environmentally friendly and highly efficient electrochemical conversion device producing electricity directly from oxidizing a fuel [1–3]. It is promising thus for solving issues of climate change. SOFCs may be fueled by hydrogen or a variety of fuels such as synthesis gases from coal and biomass gasification, oil-derived gases and liquids, natural gas, and pure ammonia [4–11].

According to the work [12], in biogas of the composition $CH_4:CO_2$ corresponding to 60:40, H_2S was found to vary between 70 and 700 ppm. It was shown in the work [13] that the area-specific resistance lowered by 22% when an H_2S concentration of

B. D. Vasyliv (✉)
Department of Hydrogen Technologies and Alternative Energy Materials, Karpenko Physico-Mechanical Institute of the NAS of Ukraine, 5 Naukova Str., Lviv 79060, Ukraine
e-mail: mechengin1111@gmail.com

V. V. Kulyk · Z. A. Duriagina · T. M. Kovbasiuk · I. A. Lemishka
Department of Materials Science and Engineering, Lviv Polytechnic National University, 12 S. Bandera Str., Lviv 79013, Ukraine

Z. A. Duriagina
Department of Materials Engineering, The John Paul II Catholic University of Lublin, 14 Racławickie Al., 20-950 Lublin, Poland

V. V. Vira
Department of Strength of Materials and Structural Mechanics, Lviv Polytechnic National University, 12 S. Bandera Str., Lviv 79013, Ukraine

1.34 ppmv was added to the main biogas flow to feed the SOFC cell at 800 °C. It is well known [14] that sulfur affects Ni-catalysts by chemisorption. Such a poisoning effect is reversible, and a temperature-dependent threshold exists [15]. Below a certain sulfur concentration, no effect is noted. At 700 °C, the threshold is about 1 ppm, whereas at 1000 °C it is about 50 ppm.

It was suggested by the authors of the work [16] three general approaches to solve the sulfur problem in the molten carbonate fuel cell (MCFC) which are also related to SOFCs: (1) favoring conditions that inhibit hydrogen sulfide production during fermentation, i.e., preventing the formation of hydrogen sulfide at the source; (2) identifying the sulfur tolerance levels of the fuel cell components currently in use and developing sulfur-tolerant components that show long-term electrochemical performance and corrosion stability; (3) removing the generated sulfur species to very low levels before the gas enters the fuel cell.

In the works [4, 5], poisoning effects by various fuel impurities, including H_2S, CH_3SH, etc., to ScSZ–Ni cermet anodes were studied. The authors measured cell voltage and anode polarization at a constant current density of 0.2 A·cm^{-2} for humidified H_2 and CH_4 fuels to characterize degradation of cell performance caused by these impurities. In the cases of hydrogen-based fuels containing 5 ppm sulfur compounds, H_2S, and CH_3SH, an initial cell voltage drop of 15 mV was observed at 1000 °C. Such an initial voltage drop was similar for the most cases independently of the sulfur compounds used. The only exception was the case of poisoning by CH_3SH, when an additional gradual decrease in cell voltage occurred.

Scientists of several research laboratories [17–19] studied the poisoning of YSZ–Ni cermet anodes by sulfur in hydrogen with the addition of 3% H_2O. It was found about two times increase in polarization resistance when sulfur amounts changed from 5 to 105 ppm. In the work [17, 18], the poisoning effect of sulfur on porous Ni anode materials and YSZ–Ni cermets was found to be reversible at 35 ppm, and to be constant in a temperature range of 700–1000 °C. However, the effect was not reversible at 105 ppm [19]. The effect of 69 ppm sulfur was found to result in 5% reduction of the voltage of a full SOFC at 1000 °C, whereas 10 ppm sulfur at 800 °C causes 2% reduction of the SOFC voltage [18].

The YSZ–Ni cermet is the most common material used for manufacturing anode substrates, since it has high catalytic activity and satisfactory electrical conductivity [1, 20–24]. It was shown in a number of works that physical and mechanical properties of this material significantly depend on the nickel content and porosity [3, 25–35].

There are lots of papers aimed at studying mechanical behavior and physical properties of materials for fuel cell electrodes [2, 8, 36–47]. In particular, biaxial strength of as-sintered YSZ–NiO ceramics and corresponding YSZ–Ni cermets reduced in hydrogen-containing atmospheres as materials for SOFC anodes was studied in a wide range of porosity [48, 49]. The average limit value of the strength of the fuel cell on the anode substrate is 200–300 MPa at 20 °C and 150–250 MPa at 800 °C [39, 50, 51]. Therefore, it is considered [44, 52–56] that the minimum value of the strength of an anode substrate is to be at least 100 MPa at 20 °C. Recently, a redox treatment technique has been developed [20, 57–61] implementing intermediate degassing between reduction and oxidation stages at 600 °C and providing a

significant increase in strength and electrical conductivity of the YSZ–NiO ceramics due to the microstructural transformation of the nickel phase particles. It was reached bend strength values (of about 100–110 MPa) for the reduced YSZ–Ni cermet close to those for the as-sintered YSZ–NiO ceramics (105–125 MPa). However, there is a lack of microstructure-related research works aimed at studying the effect of high-temperature reduction atmospheres with different contaminants on mechanical and physical properties of SOFC anode materials preconditioned in various treatment modes [62–66].

Due to a current tendency to develop anode-supported SOFC with a thick (over 500 μm) anode substrate layer, the operating temperature of the SOFC may be lowered to 500–600 °C [50, 67–70]. Therefore, there is a need to investigate behavior of Ni-containing SOFC anode substrates in a hydrogenous atmosphere with admixtures of H_2S, CO, CO_2, etc.

This work is aimed at studying the effect of hydrogen sulfide content in a high-temperature (600 °C) hydrogenous atmosphere on the microstructure, strength, microhardness, and crack growth resistance of a fine-grained YSZ–NiO(Ni) anode materials for solid oxide fuel cells.

11.2 Materials and Methods

We studied the behavior of the YSZ–NiO anode substrate ceramics (ZrO_2 stabilized by 8 mol% Y_2O_3 with the addition of 50 wt% NiO) manufactured by tape casting. The material was sintered at a temperature of 1450 °C. The average grain size of the ceramics was in the range of 1–2 μm, and the porosity was about 29%.

A series of as-sintered beam ceramic specimens (of mode 1, see Table 11.1) of 1 × 5 × 25 mm in size were processed (preconditioned) in a hydrogenous atmosphere (Ar–5 vol% H_2 mixture) for 4 h at 600 °C under a pressure of 0.15 MPa (Fig. 11.1) in order to obtain the corresponding YSZ–NiO(Ni) cermet structure (mode 2). A part of the specimens of this series was then aged in "H_2S in Ar–5 vol% H_2 mixture" atmosphere for 4 h at 600 °C under a pressure of 0.15 MPa [71]. According to a test mode, the atmosphere contained 7 or 18 vol% H_2S (modes 3 and 4, respectively). To reach a pressure of 0.15 MPa, the test chamber was degassed and filled with hydrogen sulfide of certain volume. After that, the chamber was filled with Ar–5 vol% H_2 mixture up to a pressure of 0.15 MPa.

The three-point bend test of beam specimens was carried out in air at 20 °C to estimate mechanical behavior of the material. As a result of the test, the "load–flexure" diagrams were constructed and the fracture stresses for the as-sintered material (σ_{f0}) and after the corresponding processing or aging (σ_f) were calculated [71]. Five samples of each series were tested to calculate the average values of the fracture stresses. The error margins were about ±5% of the corresponding values.

Besides, the relative stiffness E/E_0, where E_0 and E are values of Young's modulus for the material in as-sintered state and after corresponding processing or aging [71, 72], was estimated to characterize material behavior (Table 11.1). The E/E_0

Table 11.1 Physical and mechanical properties of tested materials

Mode marking	Mode (mixture composition in vol%; processing and aging at 600 °C)		Mean values of the characteristics		
	Preconditioning for 4 h	Aging for 4 h	$\sigma_f / \sigma_{f\,0}$ (%)	E/E_0	Conductivity σ (S/m)
1	As-sintered		100	100	(*)
2	Processing in Ar–5% H_2	–	86	82	$(5.5–6.5) \times 10^5$
3	Processing in Ar–5% H_2	Aging in Ar–5% H_2 with 7% H_2S	82	76	$(5.5–6.5) \times 10^5$
4	Processing in Ar–5% H_2	Aging in Ar–5% H_2 with 18% H_2S	61	75	$(5.5–6.5) \times 10^5$

Comment (*) Electrical conductivity is very low

Fig. 11.1 Schematic of a processing/aging mode for the materials tested
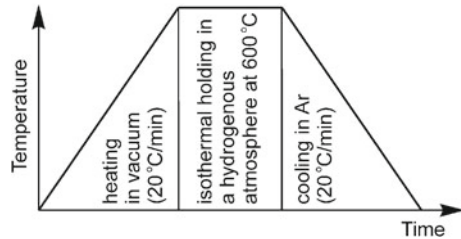
characteristic was calculated according to the technique proposed in the works [22, 73]. This technique was based on the slopes of the "stress–flexure" diagram linear sections for the processed and as-sintered materials.

Vickers microhardness of the material was measured according to the relevant standards [74, 75] with a NOVOTEST TC-MKB1 microhardness tester. The following set of indentation loads was used: 0.49, 0.98, 1.96, 2.94, 4.91, and 9.81 N. At least 10 indentations for each level of the indentation load were made to determine microhardness of each material variant.

Fracture toughness of material was estimated due to calculating the critical stress intensity factor (SIF) K_{Ic}. In particular, this parameter characterizes the propensity of materials to brittle fracture [2, 72, 76–84]. Recently [73, 85], we examined the formulas for estimating the fracture toughness of materials under Vickers pyramid indentation proposed in a number of works [8, 84, 86–99]. Due to the comparison of the K_{Ic} values calculated by these formulas with those obtained by conventional methods of fracture mechanics [92–94, 100–103], we concluded that the following formula presented by the authors of the work [95] fits the best for the characterization of YSZ ceramics:

$$K_{\mathrm{Ic}} = 0.016 \left(\frac{E}{H} \right)^{1/2} \left(\frac{P}{c^{3/2}} \right) \qquad (11.1)$$

where E is Young's modulus [GPa], H is microhardness [GPa], P is the indentation load [N], and c is the radial crack length [m].

Therefore, we used this formula to estimate the fracture toughness of the materials under study.

The specific electrical conductivity σ of materials (Table 11.1) was measured at 20 °C in air using the four-probe method [104].

The X-ray diffraction (XRD) analysis was performed using a DRON-3.0 diffractometer in CuKα monochromatic irradiation.

The studies of material microstructure and fracture surface morphology were carried out with a Carl Zeiss EVO-40XVP scanning electron microscope (SEM). An INCA Energy 350 system was used for an energy-dispersive X-ray (EDX) microanalysis.

11.3 Results and Discussion

The microstructure, mechanical properties, and fracture surface morphology of specimens of the YSZ–NiO anode ceramics in as-sintered state and corresponding YSZ–NiO(Ni) cermet specimens after processing in Ar–5 vol% H_2 gas atmosphere, after aging in Ar–5 vol% H_2 gas atmosphere with an admixture of 7 vol% H_2S, and after aging in the same atmosphere with an admixture of 18 vol% H_2S at a temperature of 600 °C have been studied.

The XRD analysis of the as-sintered YSZ–NiO ceramics and corresponding YSZ–NiO(Ni) cermet after processing in Ar–5 vol% H_2 gas atmosphere was performed. The XRD pattern for the as-sintered ceramics exhibited peaks of the YSZ and NiO phases (Fig. 11.2, line 1). The diffraction pattern of the preconditioned cermet contained, along with both the peaks of the YSZ and NiO phases, peaks of the Ni phase (Fig. 11.2, line 2). Besides, some differences in the line shapes for both material variants were observed. In particular, the peaks of the NiO phase corresponding to line 2 are much lower than for line 1, especially at the larger angles (Fig. 11.2).

As-sintered YSZ–NiO anode material exhibited much higher values of Vickers microhardness in the whole range of the indentation load compared to other material variants (Fig. 11.3a). At levels of the indentation load above 4.91 N, the microhardness becomes invariant and for this material is about 2.3 GPa.

In contrast to this, we observe significantly lower levels of microhardness for the rest of the studied material variants when the dependences yield the plateau. These dependences are almost superimposed. The exception is the material aged in Ar–5 vol% H_2 gas atmosphere with an admixture of 18 vol% H_2S, which has the lowest microhardness (Fig. 11.3a). A similar trend is observed for fracture toughness of material variants measured by the Vickers method. Here, at the plateau, i.e., at the indentation load above 4.91 N, the fracture toughness of the as-sintered ceramics is
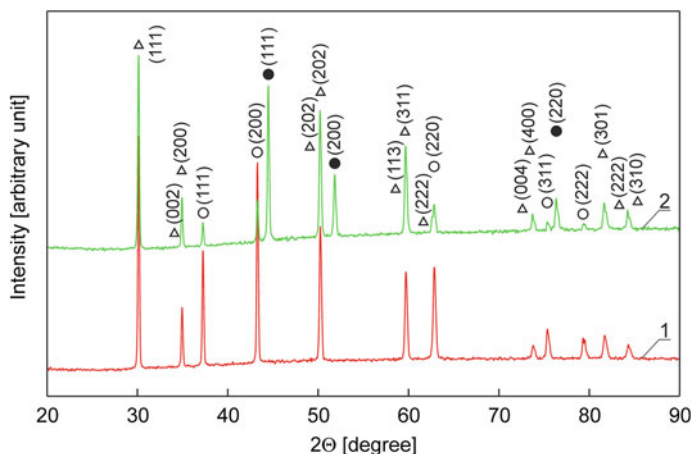
Fig. 11.2 XRD patterns of as-sintered YSZ–NiO ceramics (of mode 1) and the preconditioned one according to mode 2 (Table 11.1) showing corresponding peaks for the YSZ (light triangles), NiO (light circles), and Ni phases (dark circles) and corresponding Miller indices (in parentheses)

Fig. 11.3 Changes in mechanical characteristics of YSZ–NiO(Ni) anode materials (Table 11.1) depending on the indentation load: **a** Vickers microhardness; **b** fracture toughness measured by the Vickers method
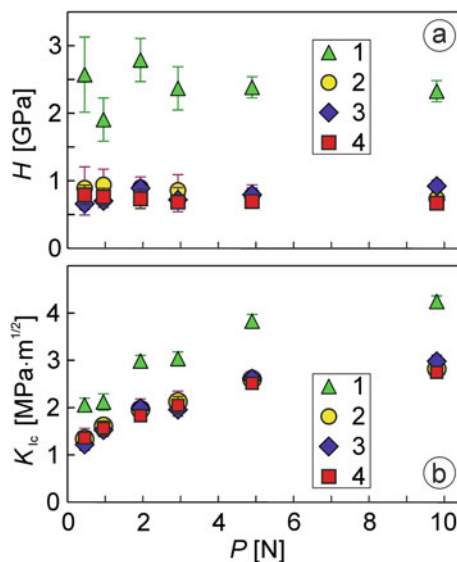
about 4.1 MPa·m$^{1/2}$ (Fig. 11.3b). For YSZ–NiO(Ni) cermet after the preconditioning, we observe quite low level of fracture toughness (of about 2.8 MPa·m$^{1/2}$). As in the case of microhardness, the values of fracture toughness for preconditioned and aged materials are similar except in the case of aging in Ar–5 vol% H$_2$ gas atmosphere with an admixture of 18 vol% H$_2$S. For the last one, fracture toughness was found of about 2.5 MPa·m$^{1/2}$ (Fig. 11.3b) which is lower by about 10% compared to both

the materials preconditioned and aged in Ar–5 vol% H$_2$ gas atmosphere with an admixture of 7 vol% H$_2$S.

Such changes in mechanical characteristics of YSZ–NiO(Ni) anode material depending on the indentation load can be explained by taking into account material microstructure. For YSZ–NiO(Ni) cermet after processing in Ar–5 vol% H$_2$ gas atmosphere, we observe at a low magnification a homogeneous microstructure of NiO(Ni) particles in the YSZ skeleton with quite uniformly distributed micropores (Fig. 11.4a). Pores of sizes in a range of 3–10 μm dominate here.

At low magnifications, there is no distinct difference between microstructure images of the preconditioned YSZ–NiO(Ni) cermet (Fig. 11.4a) and aged ones in Ar–5 vol% H$_2$ gas atmosphere with an admixture of 7 vol% H$_2$S (Fig. 11.4c) and 18 vol% H$_2$S (Fig. 11.4e). Similarly, there is no difference in fracture patterns of the
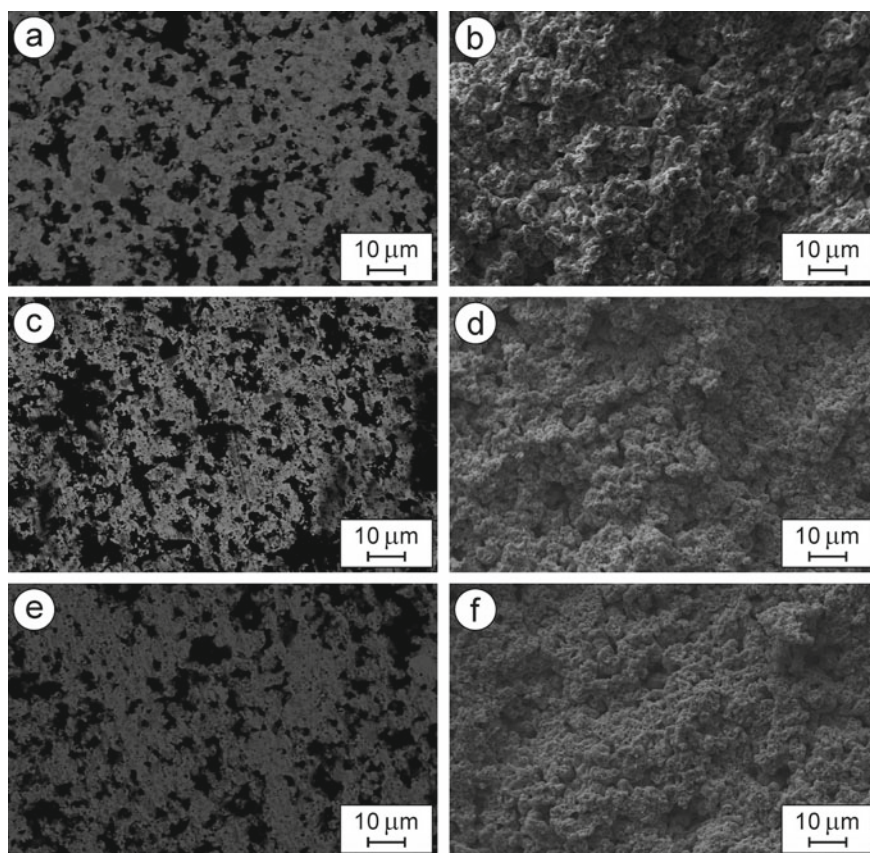
Fig. 11.4 SEM (**a, c, e**) microstructures (BSD images at low magnifications) and (**b, d, f**) fractography (SE images at low magnifications) of YSZ–NiO(Ni) cermet specimens after processing in Ar–5 vol% H$_2$ gas atmosphere (**a, b**) and after aging in Ar–5 vol% H$_2$ gas atmosphere with an admixture of 7 vol% H$_2$S (**c, d**) and 18 vol% H$_2$S (**e, f**) (Table 11.1)

preconditioned YSZ–NiO(Ni) cermet (Fig. 11.4b) and aged one in Ar–5 vol% H_2 gas atmosphere with an admixture of 7 vol% H_2S (Fig. 11.4d). However, the fracture surface of a specimen of the material aged in Ar–5 vol% H_2 gas atmosphere with an admixture of 18 vol% H_2S is slightly smoother (Fig. 11.4f).

At higher magnifications, we can clearly observe nickel phase particles distributed in the YSZ skeleton for materials after processing and aging (Fig. 11.5a, c, e). The particles are of round shape and appear like dark-gray grains with light-gray fringes. The dark-gray areas correspond to unreduced NiO, whereas light-gray ones are metallic Ni fringes formed during reduction in a hydrogenous atmosphere.

It was found that the atmosphere containing 7 vol% H_2S had a slight effect on the electrical conductivity and strength of the YSZ–NiO(Ni) cermet (Table 11.1). In contrast to this, discernible microstructure changes in the YSZ–NiO(Ni) cermet
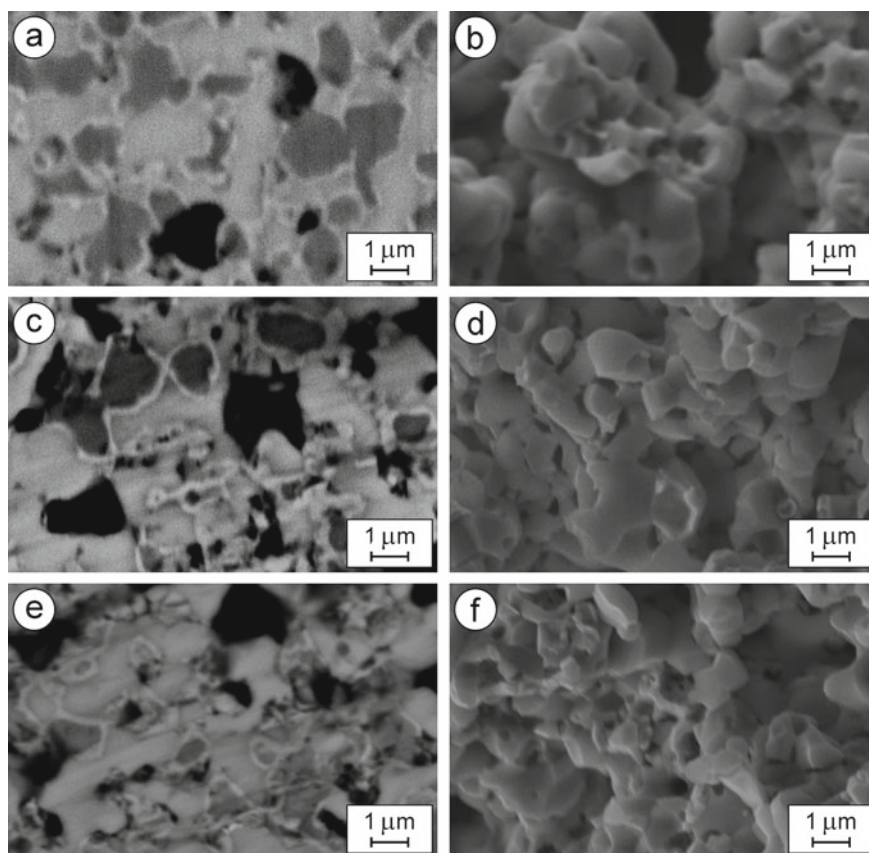
Fig. 11.5 SEM (**a, c, e**) microstructures (BSD images at intermediate magnifications) and (**b, d, f**) fractography (SE images at intermediate magnifications) of YSZ–NiO(Ni) cermet specimens after processing in Ar–5 vol% H_2 gas atmosphere (**a, b**) and after aging in Ar–5 vol% H_2 gas atmosphere with an admixture of 7 vol% H_2S (**c, d**) and 18 vol% H_2S (**e, f**) (Table 11.1)

occurred with increasing hydrogen sulfide content up to 18 vol% H_2S. In particular, the zirconia-nickel bonds weakened and the structural integrity of microareas of the bulk material was partially lost (Fig. 11.5e) as compared to the YSZ–NiO(Ni) cermet after processing (Fig. 11.5a). As a result, strength of the cermet decreased by almost 30% as compared to the one-time reduced ceramics (Table 11.1). In contrast to this, microhardness and fracture toughness of the cermet were only lowered by about 10% (Fig. 11.3a, b).

Such a difference in mechanical behavior can be analyzed from the point of view of fracture micromechanisms. The localization of stresses in the crack tip vicinity (so-called process zone) during indentation with a Vickers pyramid promotes further crack growth until touching a "material–pore" interface in the case when a pore size is comparable with a process zone size. Then, stress relaxation occurs at the interface causing crack retardation. Such a fracture micromechanism is supposed to be implemented in the case of indentation of materials in modes 2, 3, and 4 (i.e., the YSZ–NiO(Ni) cermet specimens after processing in Ar–5 vol% H_2 gas atmosphere, after aging in Ar–5 vol% H_2 gas atmosphere with an admixture of 7 vol% H_2S, and after aging in the same atmosphere with an admixture of 18 vol% H_2S). This is a reason of a little difference between values of fracture toughness of these material variants.

In the case of strength test, ultimate stress zone expands at larger scale surrounding integrally pores in the material bulk. Such a decrease in the integral cross-sectional area due to pores results in a sharp decrease in strength of the YSZ–NiO(Ni) cermet aged in Ar–5 vol% H_2 gas atmosphere with an admixture of 18 vol% H_2S compared to the cermet preconditioned in Ar–5 vol% H_2 gas atmosphere. Such different mechanical behaviors of material variants are consistent with differences in fracture surface morphology of the corresponding specimens (Figs. 11.4b, d, f and 11.5b, d, f). As it was mentioned above, fracture surface of a specimen of the material in mode 4 at a low magnification is smoother than those of other material variants (Fig. 11.4b, d, f).

At high magnifications, we can clearly observe the morphology of particles of both the nickel phase and YSZ phase (Fig. 11.6a, c): the dark-gray cores (unreduced NiO) and light-gray fringes (metallic Ni) of nickel phase particles as well as smooth monochrome YSZ areas. For the material in mode 4, nanopores in Ni fringes are found (Fig. 11.6c).

At the intermediate (Fig. 11.5b, d, f) and high magnifications (Fig. 11.6), signs of fracture of separate microstructural components can be observed.

In particular, a mixed fracture micromechanism comprising cleavage facets (brittle fracture) and crowns of plastic elongation of nickel fringes surrounding nickel phase particles (ductile fracture) was observed in the YSZ–NiO(Ni) cermet specimen aged in Ar–5 vol% H_2 gas atmosphere with an admixture of 7 vol% H_2S (Fig. 11.6b). The same fracture micromechanism was noted in the YSZ–NiO(Ni) cermet specimen preconditioned in Ar–5 vol% H_2 gas atmosphere. In contrast to this, only intergranular fracture along boundaries of both the nickel and zirconia phase grains can be seen on the fracture surface of the YSZ–NiO(Ni) cermet specimen aged in Ar–5 vol% H_2 gas atmosphere with an admixture of 18 vol% H_2S (Fig. 11.6d). The reason for such a low-energy fracture may probably be the segregation of sulfur along grain
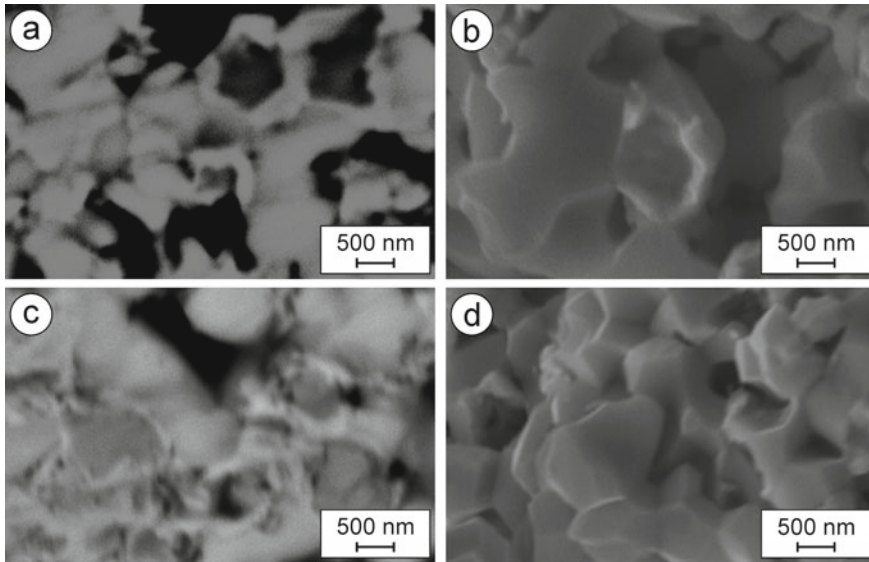
Fig. 11.6 SEM (**a, c**) microstructures (BSD images at high magnifications) and (**b, d**) fractography (SE images at high magnifications) of YSZ–NiO(Ni) cermet specimens after aging in Ar–5 vol% H$_2$ gas atmosphere with an admixture of 7 vol% H$_2$S (**a, b**) and 18 vol% H$_2$S (**c, d**) (Table 11.1)

boundaries or weakening the "zirconia–nickel" bonds due to the acceleration of a reaction of nickel oxide reduction with high-temperature hydrogen sulfide gas.

Using the line scan EDX chemical analysis, some amount of sulfur (about 0.07 wt%) was detected in the material in mode 4 (Fig. 11.7 and Table 11.2), whereas in the material in mode 3 no sulfur was found.

Therefore, we can conclude that the high-temperature hydrogen sulfide gas only affects the surfaces of nickel particles due to the acceleration of a reaction of nickel oxide reduction weakening thus the "zirconia–nickel" bonds.

11.4 Conclusions

In this work, the YSZ–NiO ceramics for SOFC anode substrates in as-sintered state and after corresponding processing and aging in a hydrogenous gas atmosphere with admixtures of 7 and 18 vol% H$_2$S have been studied.

1. It was shown that hydrogen sulfide gas at a temperature of 600 °C affects the surfaces of nickel particles in the YSZ–NiO(Ni) cermet due to the acceleration of a reaction of nickel oxide reduction. No sulfur was detected by EDX chemical analysis in the YSZ–NiO(Ni) cermet aged in Ar–5 vol% H$_2$ gas atmosphere with an admixture of 7 vol% H$_2$S, whereas some amount of sulfur (about
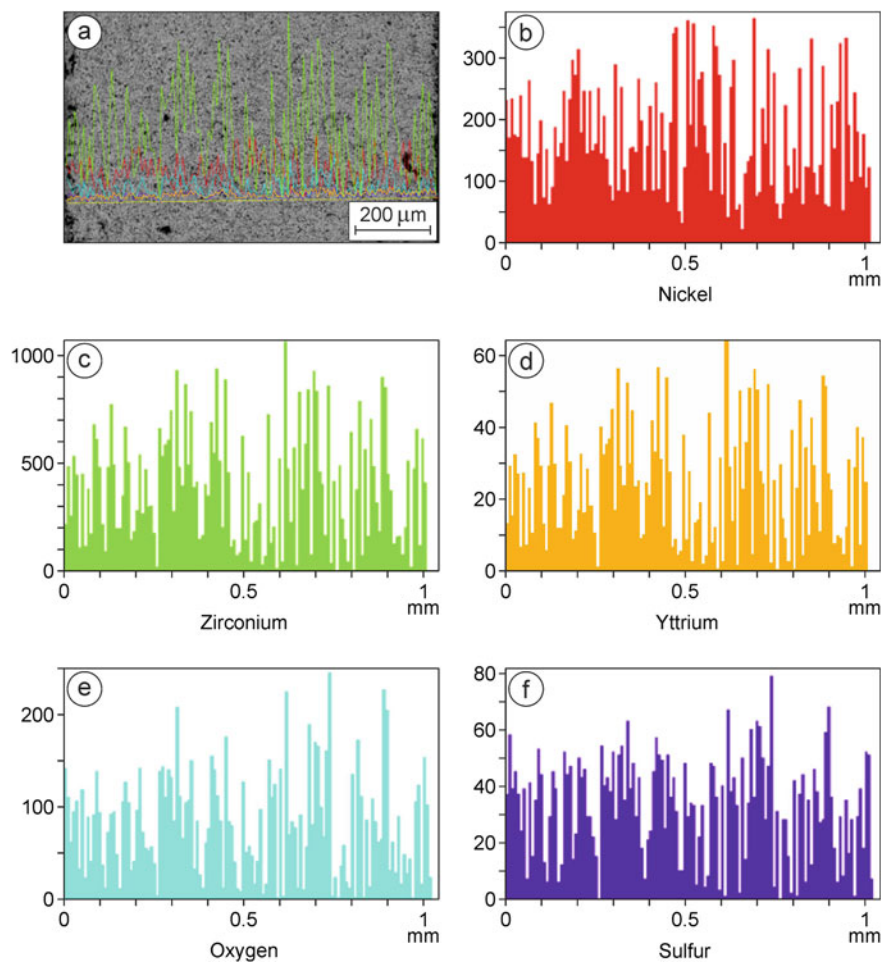
Fig. 11.7 SEM image of the cermet microstructure after aging in Ar–5 vol% H_2 gas atmosphere with an admixture of 18 vol% H_2S (mode 4) with the line scan EDX chemical analysis **a** and corresponding spectra of **b** nickel, **c** zirconium, **d** yttrium, **e** oxygen, and **f** sulfur

Chemical element and X-ray series	EDX spectrum	
	wt%	at%
O K	14.41	42.71
S K	0.07	0.11
Ni K	43.88	35.43
Y L	4.50	2.40
Zr L	37.14	19.35

Table 11.2 Data of the line scan EDX chemical analysis (Fig. 11.7) of a YSZ–NiO(Ni) cermet specimen after aging in Ar–5 vol% H_2 gas atmosphere with an admixture of 18 vol% H_2S

0.07 wt%) was detected in the cermet aged in Ar–5 vol% H_2 gas atmosphere with an admixture of 18 vol% H_2S.

2. The hydrogenous environment containing up to 7 vol% H_2S does not affect the fracture toughness and strength of the YSZ–NiO(Ni) cermet. In the case of increased content of H_2S (18 vol%) in a hydrogenous atmosphere, microstructure degradation due to the weakening of the "zirconia–nickel" bonds occurs promoting low-energy fracture, i.e., intergranular fracture along boundaries of both the nickel and zirconia phase grains. This results in lowering strength and fracture toughness of the cermet by 30% and 10%, respectively, as compared to the YSZ–NiO(Ni) cermet preconditioned in Ar–5 vol% H_2 gas atmosphere.

References

1. Zhu WZ, Deevi SC (2003) A review on the status of anode materials for solid oxide fuel cells. Mater Sci Eng A 36(1–2):228–239. https://doi.org/10.1016/S0921-5093(03)00620-8
2. Shabri HA, Othman MHD, Mohamed MA et al (2021) Recent progress in metal-ceramic anode of solid oxide fuel cell for direct hydrocarbon fuel utilization: a review. Fuel Process Technol 212:106626. https://doi.org/10.1016/j.fuproc.2020.106626
3. Budzianowski WM, Milewski J (2011) Solid-oxide fuel cells in power generation applications: a review. Recent Patents Eng 5(3):165–189. https://doi.org/10.2174/187221211797636926
4. Shiratori Y, Oshima T, Sasaki K (2008) Feasibility of direct-biogas SOFC. Int J Hydrog Energy 33(21):6316–6321. https://doi.org/10.1016/j.ijhydene.2008.07.101
5. Haga A, Adachi S, Shiratori Y et al (2008) Poisoning of SOFC anodes by various fuel impurities. Solid State Ionics 179(27–32):1427–1431. https://doi.org/10.1016/j.ssi.2008.02.062
6. Yi Y, Rao AD, Brouwer J et al (2005) Fuel flexibility study of an integrated 25 kW SOFC reformer system. J Power Sources 144(1):67–76. https://doi.org/10.1016/j.jpowsour.2004.11.068
7. Milewski J, Lewandowski J, Miller A (2008) Reducing CO_2 emissions from a coal fired power plant by using a molten carbonate fuel cell. In: Proceedings of the ASME Turbo Expo 2:389–395. https://doi.org/10.1115/GT2008-50100
8. Zhang P, Yang Z, Jin Y et al (2021) Progress report on the catalyst layers for hydrocarbon-fueled SOFCs. Int J Hydrog Energy 46(79):39369–39386. https://doi.org/10.1016/j.ijhydene.2021.09.198
9. Lanzini A, Leone P (2010) Experimental investigation of direct internal reforming of biogas in solid oxide fuel cells. Int J Hydrog Energy 35(6):2463–2476. https://doi.org/10.1016/j.ijhydene.2009.12.146
10. Wongchanapai S, Iwai H, Saito M et al (2013) Performance evaluation of a direct-biogas solid oxide fuel cell-micro gas turbine (SOFC-MGT) hybrid combined heat and power (CHP) system. J Power Sources 223:9–17. https://doi.org/10.1016/j.jpowsour.2012.09.037
11. Milewski J, Lewandowski J (2009) Solid oxide fuel cell fuelled by biogases. Arch Thermodynamics 30(4):3–12. https://www.imp.gda.pl/fileadmin/doc/imp_publishing/wimp/archives%20of%20thermodynamics/C_09_4.pdf
12. Van herle J, Membrez Y, Bucheli O (2004) Biogas as a fuel source for SOFC co-generators. J Power Sources 127:300–312. https://doi.org/10.1016/j.jpowsour.2003.09.027
13. Papurello D, Lanzini A, Smeacetto F et al (2013) Effect of sulfur and carbon contaminants on a solid oxide fuel cell (SOFC) fed with anaerobic digestion biogas. In: Proceedings of the 3rd international conference on microgeneration and related technologies. Naples, Italy, 15–17 Apr 2013, pp 1–9

14. Alstrup I, Rostrup-Nielsen JR, Roen S (1981) High temperature hydrogen sulfide chemisorption on nickel catalysts. Appl Catalysis 1:303–314
15. Twigg MV (1996) Catalyst handbook, 2nd edn. Manson Publishing Ltd., London
16. Ciccoli R, Cigolotti V, Lo Presti R (2010) Molten carbonate fuel cells fed with biogas: combating H_2S. Waste Manage 30(6):1018–1024. https://doi.org/10.1016/j.wasman.2010.02.022
17. Primdahl S (1999) Nickel/yttria-stabilised zirconia cermet anodes for solid oxide fuel cells. Dissertation, Riso National Laboratory, Materials Research Department, Denmark. https://core.ac.uk/download/pdf/11461938.pdf
18. Norheim A, Wærnhus I, Broström M et al (2007) Experimental studies on the influence of H_2S on solid oxide fuel cell performance at 800 °C. Energy Fuels 21(2):1098–1101. https://doi.org/10.1021/ef060532m
19. Dees DW, Balachandran U, Dorris SE et al (1989) Interfacial effects in monolithic solid oxide fuel cells. In: SOFC I: the electrochemical society proceedings series. Pennington, NJ, pp 317–321. https://www.electrochem.org/sofc/Solid_Oxide_Fuel_Cells_PV89-11.pdf
20. Vasyliv BD (2010) Improvement of the electric conductivity of the material of anode in a fuel cell by the cyclic redox thermal treatment. Mater Sci 46(2):260–264. https://doi.org/10.1007/s11003-010-9282-4
21. Ettler M, Blaβ G, Menzler NH (2007) Characterization of Ni–YSZ-cermets with respect to redox stability. Fuel Cells 7(5):349–355. https://doi.org/10.1002/fuce.200700007
22. Podhurs'ka VY, Vasyliv BD, Ostash OP et al (2014) Structural transformations in the NiO-containing anode of ceramic fuel cells in the course of its reduction and oxidation. Mater Sci 49(6):805–811. https://doi.org/10.1007/s11003-014-9677-8
23. Wincewicz KC, Cooper JS (2005) Taxonomies of SOFC material and manufacturing alternatives. J Power Sources 140(2):280–296. https://doi.org/10.1016/j.jpowsour.2004.08.032
24. Podhurska V, Vasyliv B, Ostash O et al (2016) Influence of treatment temperature on microstructure and properties of YSZ–NiO anode materials. Nanoscale Res Lett 11:93. https://doi.org/10.1186/s11671-016-1306-z
25. Clemmer RMC, Corbin SF (2009) The influence of pore and Ni morphology on the electrical conductivity of porous Ni/YSZ composite anodes for use in solid oxide fuel cell applications. Solid State Ionics 180:721–730. https://doi.org/10.1016/j.ssi.2009.02.030
26. Lin C-K, Chen T-T, Chyou Y-P et al (2007) Thermal stress analysis of a planar SOFC stack. J Power Sources 164(1):238–251. https://doi.org/10.1016/j.jpowsour.2006.10.089
27. Chiang L-K, Liu H-C, Shiu Y-H et al (2008) Thermo-electrochemical and thermal stress analysis for an anode-supported SOFC cell. Renew Energy 33(12):2580–2588. https://doi.org/10.1016/j.renene.2008.02.023
28. Vasyliv BD (2009) A procedure for the investigation of mechanical and physical properties of ceramics under the conditions of biaxial bending of a disk specimen according to the ring–ring scheme. Mater Sci 45(4):571–575. https://doi.org/10.1007/s11003-010-9215-2
29. Chiang L-K, Liu H-C, Shiu Y-H et al (2010) Thermal stress and thermo-electrochemical analysis of a planar anode-supported solid oxide fuel cell: effects of anode porosity. J Power Sources 195(7):1895–1904. https://doi.org/10.1016/j.jpowsour.2009.10.011
30. Posuvailo VM, Kulyk VV, Duriagina ZA et al (2020) The effect of electrolyte composition on the plasma electrolyte oxidation and phase composition of oxide ceramic coatings formed on 2024 aluminium alloy. Arch Mater Sci Eng 105(2):49–55. https://doi.org/10.5604/01.3001.0014.5761
31. Fischer W, Malzbender J, Blass G et al (2005) Residual stresses in planar solid oxide fuel cells. J Power Sources 150:73–77. https://doi.org/10.1016/j.jpowsour.2005.02.014
32. Andrzejczuk M, Vasylyev O, Brodnikovskyi I et al (2014) Microstructural changes in NiO–ScSZ composite following reduction processes in pure and diluted hydrogen. Mater Charact 87:159–165. https://doi.org/10.1016/j.matchar.2013.11.011
33. Weil KS, Koeppel BJ (2008) Thermal stress analysis of the planar SOFC bonded compliant seal design. Int J Hydrog Energy 33(14):3976–3990. https://doi.org/10.1016/j.ijhydene.2007.11.008

34. Jin HM, Shen MS (2009) Study of integrity of NiO oxide film by acoustic emission method. In: Proceedings of the 5th international conference on natural computation (ICNC-2009), Tianjin, China, 14–16 Aug 2009, pp 252–256. https://doi.org/10.1109/ICNC.2009.133

35. Lin C-K, Huang L-H, Chiang L-K et al (2009) Thermal stress analysis of planar solid oxide fuel cell stacks: effects of sealing design. J Power Sources 192(2):515–524. https://doi.org/10.1016/j.jpowsour.2009.03.010

36. Zhang Y, Liu B, Tu B et al (2009) Understanding of redox behavior of Ni–YSZ cermets. Solid State Ionics 180:1580–1586. https://doi.org/10.1016/j.ssi.2009.10.011

37. Mori M, Yamamoto T, Itoh H et al (1998) Thermal expansion of nickel-zirconia anodes in solid oxide fuel cells during fabrication and operation. J Electrochem Soc 145(4):1374–1381. https://doi.org/10.1149/1.1838468

38. Duriagina Z, Kulyk V, Kovbasiuk T et al (2021) Synthesis of functional surface layers on stainless steels by laser alloying. Metals 11(3):434. https://doi.org/10.3390/met11030434

39. Sciazko A, Shimura T, Komatsu Y et al (2021) Ni-GDC and Ni-YSZ electrodes operated in solid oxide electrolysis and fuel cell modes. J Therm Sci Technol 16(1):JTST0013. https://doi.org/10.1299/jtst.2021jtst0013

40. Kulyk VV, Vasyliv BD, Duriagina ZA et al (2021) The effect of water vapor containing hydrogenous atmospheres on the microstructure and tendency to brittle fracture of anode materials of YSZ–NiO(Ni) system. Arch Mater Sci Eng 108(2):49–67. https://doi.org/10.5604/01.3001.0015.0254

41. Komatsu Y, Sciazko A, Shikazono N (2021) Isostatic pressing of screen printed nickel-gadolinium doped ceria anodes on electrolyte-supported solid oxide fuel cells. J Power Sources 485:229317. https://doi.org/10.1016/j.jpowsour.2020.229317

42. Milewski J, Kupecki J, Szczęśniak A et al (2021) Hydrogen production in solid oxide electrolyzers coupled with nuclear reactors. Int J Hydrog Energy 46(72):35765–35776. https://doi.org/10.1016/j.ijhydene.2020.11.217

43. Khajavi P, Hendriksen PV, Chevalier J et al (2020) Improving the fracture toughness of stabilized zirconia-based solid oxide cells fuel electrode supports: effects of type and concentration of stabilizer(s). J Eur Ceram Soc 40(15):5670–5682. https://doi.org/10.1016/j.jeurceramsoc.2020.05.042

44. Serbenyuk TB, Prikhna TO, Sverdun VB et al (2018) Effect of the additive of Y_2O_3 on the structure formation and properties of composite materials based on AlN–SiC. J Superhard Mater 40(1):8–15. https://doi.org/10.3103/S1063457618010021

45. Buchaniec S, Sciazko A, Mozdzierz M et al (2019) A novel approach to the optimization of a solid oxide fuel cell anode using evolutionary algorithms. IEEE Access 7:34361–34372. https://doi.org/10.1109/ACCESS.2019.2904327

46. Hassan N (2021) Catalytic performance of nanostructured materials recently used for developing fuel cells' electrodes. Int J Hydrog Energy 46(79):39315–39368. https://doi.org/10.1016/j.ijhydene.2021.09.177

47. Smyrnova-Zamkova MY, Ruban OK, Bykov OI et al (2018) Physico-chemical properties of fine-grained powder in Al_2O_3–ZrO_2–Y_2O_3–CeO_2 system produced by combined method. Comp Theory Practice 18(4):234–240. https://kompozyty.ptmk.net/pliczki/pliki/1290_2018t04_maria-y-smyrnova-zamkova-.pdf

48. Radovic M, Lara-Curzio E (2004) Mechanical properties of tape cast nickel-based anode materials for solid oxide fuel cells before and after reduction in hydrogen. Acta Mater 52(20):5747–5756. https://doi.org/10.1016/j.actamat.2004.08.023

49. Wang Y, Walter ME, Sabolsky K et al (2006) Effects of powder sizes and reduction parameters on the strength of Ni–YSZ anodes. Solid State Ionics 177:1517–1527. https://doi.org/10.1016/j.ssi.2006.07.010

50. Weil KS, Koeppel BJ (2008) Comparative finite element analysis of the stress-strain states in three different bonded solid oxide fuel cell seal designs. J Power Sources 180(1):343–353. https://doi.org/10.1016/j.jpowsour.2008.01.093

51. Romaniv OM, Vasyliv BD (1998) Some features of formation of the structural strength of ceramic materials. Mater Sci 34(2):149–161. https://doi.org/10.1007/BF02355530

52. Zhang T, Zhu Q, Huang WL et al (2008) Stress field and failure probability analysis for the single cell of planar solid oxide fuel cells. J Power Sources 182(2):540–545. https://doi.org/10.1016/j.jpowsour.2008.04.027

53. Danilenko I, Lasko G, Brykhanova I et al (2017) The peculiarities of structure formation and properties of zirconia-based nanocomposites with addition of Al_2O_3 and NiO. Nanoscale Res Lett 12:125. https://doi.org/10.1186/s11671-017-1901-7

54. Smyrnova-Zamkova MY, Red'ko VP, Ruban OK et al (2017) The properties of nanocrystalline powder of 90% Al_2O_3–10% ZrO_2 (wt.%) obtained via the hydrothermal synthesis/mechanical mixing. Nanosistemi Nanomater Nanotehnol 15(2):309–317. https://doi.org/10.15407/nnn.15.02.0309

55. Podhurska V, Vasyliv B (2012) Influence of NiO reduction on microstructure and properties of porous Ni–ZrO_2 substrates. In: Proceedings of the 3rd international conference on oxide materials for electronic engineering (OMEE-2012), Lviv, Ukraine, 3–7 Sept 2012, pp 293–294. https://doi.org/10.1109/OMEE.2012.6464761

56. Smyrnova-Zamkova MY, Ruban OK, Bykov OI et al (2021) The influence of the ZrO_2 solid solution amount on the physicochemical properties of Al_2O_3–ZrO_2–Y_2O_3–CeO_2 powders. Powder Metall Met Ceram 60(3–4):129–141. https://doi.org/10.1007/s11106-021-00222-4

57. Ettler M, Timmermann H, Malzbender J et al (2010) Durability of Ni anodes during reoxidation cycles. J Power Sources 195(17):5452–5467. https://doi.org/10.1016/j.jpowsour.2010.03.049

58. Tikekar N, Armstrong T, Virkar A (2006) Reduction and reoxidation kinetics of Ni-based SOFC anodes. J Electrochem Soc 153(4):A654–A663. https://doi.org/10.1149/1.2167949

59. Ostash OP, Vasyliv BD, Podhurs'ka VY et al (2011) Optimization of the properties of 10Sc1CeSZ-NiO composite by the redox treatment. Mater Sci 46(5):653–658. https://doi.org/10.1007/s11003-011-9337-1

60. Vasyliv B, Podhurska V, Ostash O (2017) Preconditioning of the YSZ–NiO fuel cell anode in hydrogenous atmospheres containing water vapor. Nanoscale Res Lett 12:265. https://doi.org/10.1186/s11671-017-2038-4

61. Vasyliv B, Milewski J, Podhurska V et al (2022) Study of the degradation of a fine-grained YSZ–NiO anode material during reduction in hydrogen and reoxidation in air. Appl Nanosci 12:965–975. https://doi.org/10.1007/s13204-021-01768-w

62. Zhang Y, Liu B, Tu B et al (2005) Redox cycling of Ni–YSZ anode investigated by TPR technique. Solid State Ionics 176:2193–2199. https://doi.org/10.1016/j.ssi.2005.06.016

63. Vedarsi V, Young JL, Birss VI (2010) A possible solution to the mechanical degradation of Ni-yttria stabilized zirconia anode-supported solid oxide fuel cells due to redox cycling. J Power Sources 195(17):5534–5542. https://doi.org/10.1016/j.jpowsour.2010.03.043

64. Sarantaridis D, Atkinson A (2007) Redox cycling of Ni-based solid oxide fuel cell anodes: a review. Fuel Cells 7(3):246–258. https://doi.org/10.1002/fuce.200600028

65. Waldbillig D, Wood A, Ivey DG (2005) Electrochemical and microstructural characterization of the redox tolerance of solid oxide fuel cell anodes. J Power Sources 145(2):206–215. https://doi.org/10.1016/j.jpowsour.2004.12.071

66. Savka SS, Popovych DI, Serednytski AS (2017) Molecular dynamics simulations of the formation processes of zinc oxide nanoclusters in oxygen environment. In: Nanophysics, nanomaterials, interface studies, and applications. Springer Proceedings in Physics, vol 195, pp 145–156. https://doi.org/10.1007/978-3-319-56422-7_11

67. Panteix PJ, Baco-Carles V, Tailhades P et al (2009) Elaboration of metallic compacts with high porosity for mechanical supports of SOFC. Solid State Sci 11:444–450. https://doi.org/10.1016/j.solidstatesciences.2008.09.006

68. Kwak BH, Youn HK, Chung JS (2008) Ni and metal aluminate mixtures for solid oxide fuel cell anode supports. J Power Sources 185(2):633–640. https://doi.org/10.1016/j.jpowsour.2008.09.009

69. Park HC, Virkar AV (2009) Bimetallic (Ni–Fe) anode-supported solid oxide fuel cells with gadolinia-doped ceria electrolyte. J Power Sources 186(1):133–137. https://doi.org/10.1016/j.jpowsour.2008.09.080

70. Tucker MC, Lau GY, Jacobson CP et al (2007) Performance of metal-supported SOFCs with infiltrated electrodes. J Power Sources 171(2):477–482. https://doi.org/10.1016/j.jpowsour.2007.06.076

71. Vasyliv BD, Podhurska VY, Ostash OP et al (2018) Effect of a hydrogen sulfide-containing atmosphere on the physical and mechanical properties of solid oxide fuel cell materials. In: Nanochemistry, biotechnology, nanomaterials, and their applications. Springer Proceedings in Physics, vol 214, pp 475–485. https://doi.org/10.1007/978-3-319-92567-7_30

72. Vasyliv BD (2002) Initiation of a crack from the edge of a notch with oblique front in specimens of brittle materials. Mater Sci 38(5):724–728. https://doi.org/10.1023/A:1024222709514

73. Vasyliv B, Kulyk V, Duriagina Z et al (2020) Estimation of the effect of redox treatment on microstructure and tendency to brittle fracture of anode materials of YSZ-NiO(Ni) system. Eastern-Eur J Enterp Technol 108/6(12):67–77. https://doi.org/10.15587/1729-4061.2020.218291

74. ASTM E 384-11 (2011) Standard test method for Knoop and Vickers hardness of materials. ASTM International. https://doi.org/10.1520/E0384-11

75. ASTM C 1327-03 (2003) Standard test method for Vickers indentation hardness of advanced ceramics. ASTM International. https://doi.org/10.1520/C1327-03

76. Cook RF, Pharr GM (1990) Direct observation and analysis of indentation cracking in glasses and ceramics. J Am Ceram Soc 73(4):787–817. https://doi.org/10.1111/j.1151-2916.1990.tb05119.x

77. Ostash OP, Andreiko IM, Kulyk VV et al (2013) Influence of braking on the microstructure and mechanical behavior of steels of railroad wheel. Mater Sci 48(5):569–574. https://doi.org/10.1007/s11003-013-9539-9

78. Nastic A, Merati A, Bielawski M et al (2015) Instrumented and Vickers indentation for the characterization of stiffness, hardness and toughness of zirconia toughened Al_2O_3 and SiC armor. J Mater Sci Technol 31(8):773–783. https://doi.org/10.1016/j.jmst.2015.06.005

79. Adams JW, Ruh R, Mazdiyasni KS (1997) Young's modulus, flexural strength, and fracture of yttria-stabilized zirconia versus temperature. J Am Ceram Soc 80(4):903–908. https://doi.org/10.1111/j.1151-2916.1997.tb02920.x

80. Andreiko IM, Kulyk VV, Ostash OP (2012) Resistance of steels of railroad wheels to corrosion-fatigue fracture. Mater Sci 47(5):608–612. https://doi.org/10.1007/s11003-012-9434-9

81. Kharchenko YV, Blikharskyy ZY, Vira VV et al (2019) Study of structural changes in a nickel oxide containing anode material during reduction and oxidation at 600 °C. In: Nanocomposites, nanostructures, and their applications. Springer Proceedings in Physics, vol 221, pp 595–604. https://doi.org/10.1007/978-3-030-17759-1_42

82. Lawn BR (1993) Fracture of brittle solids, 2nd edn. Cambridge. https://doi.org/10.1017/CBO9780511623127

83. Ivasyshyn AD, Vasyliv BD (2001) Effect of the size and form of specimens on the diagram of growth rates of fatigue cracks. Mater Sci 37(6):1002–1004. https://doi.org/10.1023/A:1015669913601

84. Lawn BR, Swain MV (1975) Microfracture beneath point indentations in brittle solids. J Mater Sci 10(1):113–122. https://doi.org/10.1007/BF00541038

85. Kulyk VV, Duriagina ZA, Vasyliv BD et al (2021) Effects of yttria content and sintering temperature on the microstructure and tendency to brittle fracture of yttria-stabilized zirconia. Arch Mater Sci Eng 109(2):65–79. https://doi.org/10.5604/01.3001.0015.2625

86. Lawn BR, Fuller ER (1975) Equilibrium penny-like cracks in indentation fracture. J Mater Sci 10(12):2016–2024. https://doi.org/10.1007/BF00557479

87. Evans AG, Charles EA (1976) Fracture toughness determinations by indentation. J Am Ceram Soc 59(7–8):371–372. https://doi.org/10.1111/j.1151-2916.1976.tb10991.x

88. Tanaka K (1987) Elastic/plastic indentation hardness and indentation fracture toughness: the inclusion core model. J Mater Sci 22(4):1501–1508. https://doi.org/10.1007/BF01233154

89. Niihara K, Morena R, Hasselman DPH (1982) Evaluation of K_{Ic} of brittle solids by the indentation method with low crack-to-indent ratios. J Mater Sci Lett 1(1):13–16. https://doi.org/10.1007/BF00724706

90. Niihara K (1983) A fracture mechanics analysis of indentation-induced Palmqvist crack in ceramics. J Mater Sci Lett 2(5):221–223. https://doi.org/10.1007/BF00725625

91. Danilenko I, Glazunov F, Konstantinova T et al (2014) Effect of Ni/NiO particles on structure and crack propagation in Zirconia based composites. Adv Mater Lett 5(8):465–471. https://doi.org/10.5185/amlett.2014.amwc1040II

92. Grigoriev ON, Vinokurov VB, Mosina TV et al (2017) Kinetics of shrinkage, structurization, and the mechanical characteristics of zirconium boride sintered in the presence of activating additives. Powder Metall Met Ceram 55(11–12):676–688. https://doi.org/10.1007/s11106-017-9855-y

93. Gogotsi GA, Dub SN, Lomonova EE et al (1995) Vickers and Knoop indentation behaviour of cubic and partially stabilized zirconia crystals. J Eur Ceram Soc 15(5):405–413. https://doi.org/10.1016/0955-2219(95)91431-M

94. Aswad MA (2014) Comparison of the fracture toughness of high temperature ceramic measured by digital image correlation and indentation method. J Univ Babylon 22(4):927–937. https://www.iasj.net/iasj?func=article&aId=99010

95. Anstis GR, Chantikul P, Lawn BR et al (1981) A critical evaluation of indentation techniques for measuring fracture toughness: I, direct crack measurement. J Am Ceram Soc 64(9):533–538. https://doi.org/10.1111/j.1151-2916.1981.tb10320.x

96. Lawn BR, Evans AG, Marshall DB (1980) Elastic/plastic indentation damage in ceramics: the median/radial crack system. J Am Ceram Soc 63(9–10):574–581. https://doi.org/10.1111/j.1151-2916.1980.tb10768.x

97. Blendell JE (1979) The origins of internal stresses in polycrystalline alumina and their effects on mechanical properties. Cambridge. http://hdl.handle.net/1721.1/44234

98. Lankford J (1982) Indentation microfracture in the Palmqvist crack regime: implications for fracture toughness evaluation by the indentation method. J Mater Sci Lett 1(11):493–495. https://doi.org/10.1007/BF00721938

99. Ropyak LY, Shatskyi IP, Makoviichuk MV (2017) Influence of the oxide-layer thickness on the ceramic-aluminium coating resistance to indentation. Metallofiz Noveishie Tekhnol 39(4):517–524. https://doi.org/10.15407/mfint.39.04.0517

100. ASTM E 399-20a (2020) Standard test method for linear-elastic plane-strain fracture toughness of metallic materials. ASTM International. https://doi.org/10.1520/E0399-20A

101. ASTM C 1421-18 (2018) Standard test methods for determination of fracture toughness of advanced ceramics at ambient temperature. ASTM International. https://doi.org/10.1520/C1421-18

102. Kübler J (2002) Fracture toughness of ceramics using the SEVNB method: from a preliminary study to a standard test method. In: Salem J et al. (ed) Fracture resistance testing of monolithic and composite brittle materials. ASTM International, pp 93–106. https://doi.org/10.1520/STP10473S

103. Romaniv OM, Zalite IV, Simin'kovych VM et al (1996) Effect of the concentration of zirconium dioxide on the fracture resistance of Al_2O_3–ZrO_2 ceramics. Mater Sci 31(5):588–594. https://doi.org/10.1007/BF00558793

104. ASTM F 43-99 (2005) Test methods for resistivity of semiconductor materials. CA, SEMI. https://www.scribd.com/document/228100659/astm-F43-99

Chapter 12
Synthesis and Characterization of Deca-Quinoline Bearing Pillar[5]arene Macrocycle

Ahmed Nuri Kursunlu and Ersin Güler

12.1 Introduction

Quinolines and their derivatives have antimalarial (e.g., quinine or chloroquine), showed many biological activities such as analgesic, antibacterial, antifungal, anti-inflammatory, anthelmintic, and anticancer antineoplastic effects [1–3]. Many quinolines and their derivatives are present in many natural products and have been found to have applications as agrochemicals as well as general synthetic building blocks. There are several known methods for synthesizing quinolines in the literature, and the development of new synthetic methods continues as an area of active research because of their great importance.

In light of all this information, in this study, it was aimed to combine the antimicrobial properties of quinoline-derived compound with pillar arene compound, which have yet to be discovered in the field of biochemical application [3]. All the elements selected as the title of the study (quinoline, pillar[5]arene) were designed to form an antimicrobial agent of new origin. The macrocycles and their complexes to be prepared both add originality to the targeted work and draw a profile that can serve the purpose.

A. N. Kursunlu · E. Güler (✉)
"Faculty of Science, Department of Chemistry", University of Selcuk, Konya, Turkey
e-mail: eguler66@gmail.com

167

Pillar[n]arenes are a macrocyclyle that Ogoshi and co-workers developed the host–guest chemistry of pillar[5]arene molecules using in their simple one-step synthesis. Pillar[n]arene macrocycles are actually a derivative prepared by using hydroquinone groups bound by methylene bridges at the 1,4-positions of benzene. The donor dialkoxybenzene fragments of pillar[n]arene compounds led to the host–guest interactions with various small molecules such as including alkylnitriles alkanediamines, sensors, organogels, and viologens [4].

In 2008, Tomoki Ogoshi published an efficient synthesis for hydroquinolic derivatives connected by methylene bridges at the para positions (Scheme 4). Owing to their pillar-like structure, Ogoshi named these macrocyclic structures "pillar[n]arenes", where n corresponds to the number of aromatic repeat units. The efficient, one-step synthesis of the cyclopentamer ($n = 5$) involved the reaction of commercially available 1,4-dimethoxybenzene with paraformaldehyde in the presence of a Lewis acid catalyst in dichloromethane and 1,2-dichloroethane. Under these reaction conditions, they obtained exclusively pillar[5]arene in 22% yield.

The yield was improved to 71% upon reaction of one equivalent of the 1,4-dimethoxybenzene with three equivalents of paraformaldehyde. As a result of their facile and high-yielding synthesis from commercially available starting materials, the chemistry of pillar[5]arenes received significant attention within the scientific community [5].

12.2 Experiment Details

All chemicals used 8-aminoquinoline, copper sulfate, propargyl bromide, sodium ascorbate, 1,3-dibromopropane, hydroquinone, potassium carbonate, sodium azide. Different solvents (petroleum ether (40–60%) dimethylformamide, dichloromethane, ethyl acetate, 1,2-dichloroethane, n-hexane, deutero chloroform, acetone, chloroform, acetonitrile) were used in characterization, synthesis, and purification. processes.

Elemental analysis of the compounds was performed on the TRUSPEC elemental analyzer to determine the percent amount of C, N, and H atoms in the molecule. The spectra of ^{13}C-NMR and ^{1}H-NMR were obtained from a Varian 400 MHz spectrometer.

12.2.1 The Synthesis of 1,4-bis(3-bromopropoxy)benzene (Compound 3)
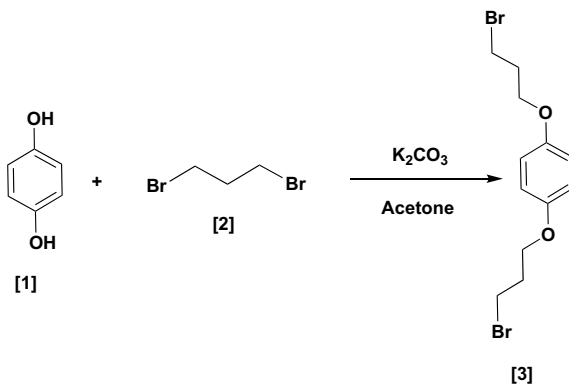
Hydroquinone (2 mmol, 0.22 g), 1,3-dibromopropane (1 mmol, 0.2 g), and K_2CO_3 (3 equiv) were dissolved in 20 mL of N,N'-dimethylformamide and refluxed at 100 °C. It was refluxed for 24 h. The cold water was added to the resulting mixture, and the precipitated product was washed for several times with cyclohexane/water to obtain compound 3. Yield is 68%; 0.24 g.

12.2.2 The Synthesis of deca(3-bromopropane) Pillar[5]arene (Compound 4)
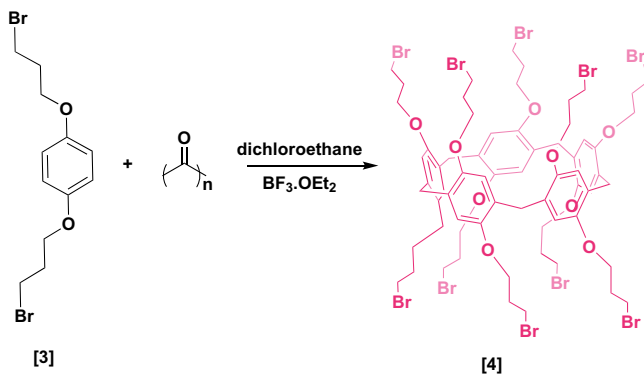
Paraformaldehyde (10 mmol) and 1,4-bis(3-bromopropoxy)benzene (10 mmol, 3.24 g) (12.4 mmol) will be dissolved in 100 mL of 1,2-dichloroethane under an argon atmosphere, and then, 6 mL of BF$_3$.OEt$_2$ is added to the mixture by syringe. The solution was stirred for 4 h at room temperature, and 100 mL of cyclohexane was added and filtrated. After a conventional extraction process, the solvent was removed in the evaporator and the raw product was purified on the column using a cyclohexane/ethyl acetate (5:1) mixture [6, 7]. Yield is 28%; 0.509 g.

12.2.3   The Synthesis of deca(3-azidopropane) Pillar[5]arene (Compound 5)
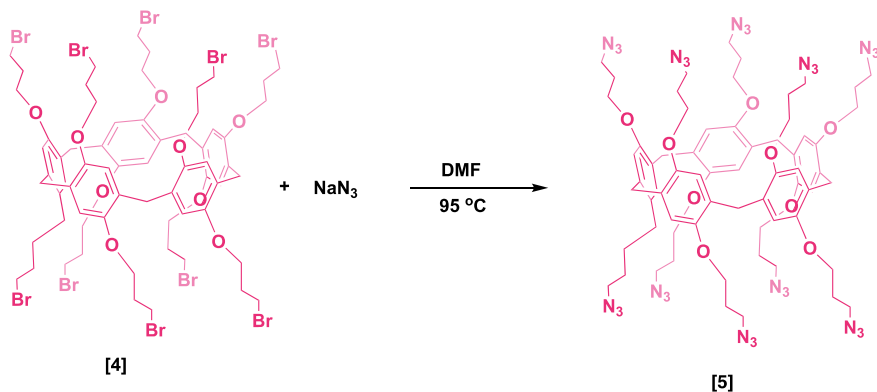
Compound 4 (0.5 mmol, 0.91 g) and NaN$_3$ (5 mmol, 0.325 g) were refluxed at 95 °C for overnight in 20 mL of DMF. After, the resulting mixture was cooled, it poured to water. The precipitated product was filtrated with a funnel and washed with water for several times. The white product was dried in vacuum. Yield: 81%, 0.583 g.

12.2.4   The Synthesis of N-(prop-2-yn-1-yl)quinolin-8-amine (Compound 8)
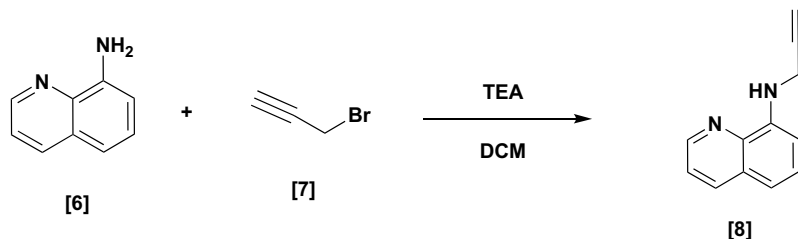
Propargyl bromide (1 mmol, 0.12 g) and 8-aminoquinoline (1 mmol, 0.145 g) were solved in dichloromethane. After the mixture was cooled in salt-ice bath, triethylamine was dropped to this solution. The reaction was stirred for overnight at room temperature. After the reaction completed, the solvent was evaporated under vacuum and purified in column (petroleum ether/dichloromethane 8:1 to obtain as a colorless oil. Yield is 78%; 0.14 g.

12.2.5   The Synthesis of Q-Pillar[5]arene

Compound 8 (1 mmol, 0.182 g) and Compound 5 (0.1 mmol, 0.144 g), $CuSO_4$ (0.021 mmol) and sodium ascorbate (0.076 mmol) were stirred for 72 h by a magnetic stirrer in a mixture of dichloromethane, water and ethanol (5:1:1). The raw product was purified in column (ethylacetate/petroleum ether: 1:5) to give a brown solid. Yield is 65%; 0.211 g.
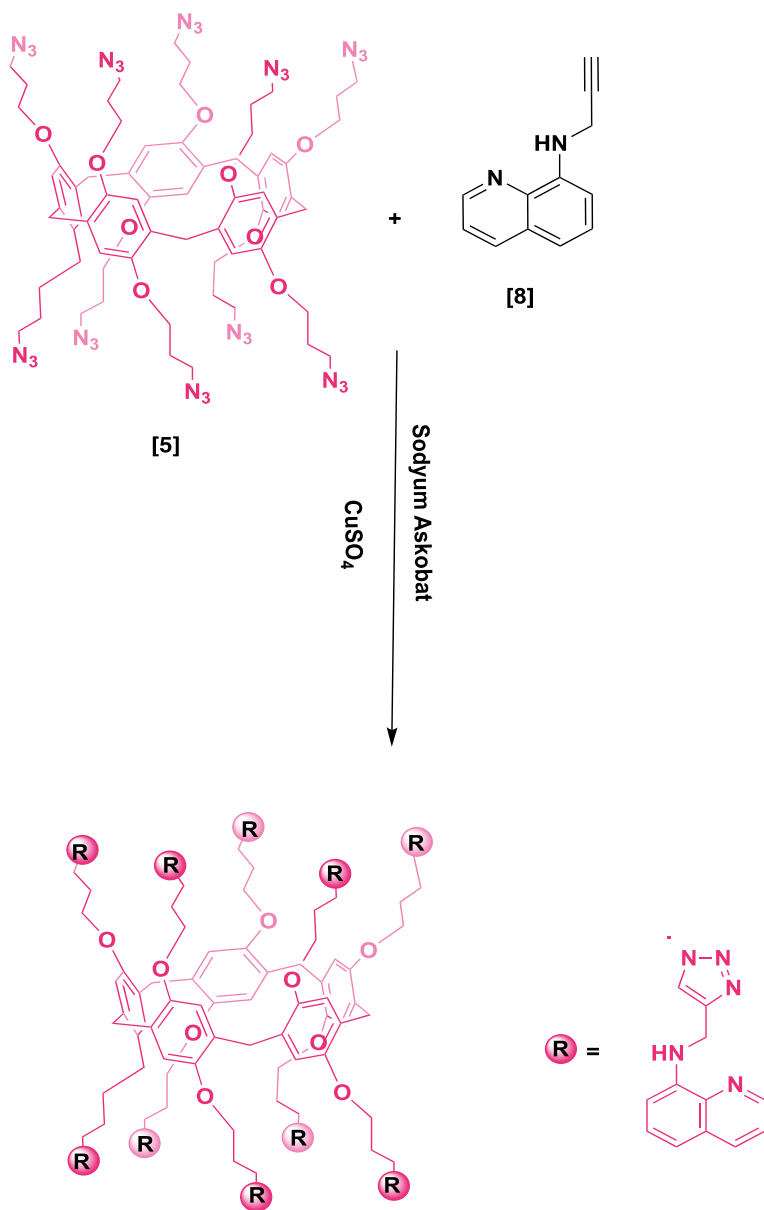
12.3   Results and Discussion

When the FT-IR spectrum of 1,4-bis(3-bromopropoxy)benzene is examined, the most characteristic change can be shown by the disappearance of the broad O–H band located at hydroquinone around 3430 cm^{-1}. In addition, the C-O stretching vibration observed at 1100 cm^{-1} in hydroquinone shifted toward 1200 cm^{-1} in the FT-IR spectrum of 1,4-bis(3-bromopropoxy)benzene. Again, the peaks of C = C and C–H stretching vibrations were seen as multiple vibrations in the range of 1570–1405 cm^{-1} and 2800–3050 cm^{-1}, respectively. Here, alkyne C–H stresses are included in vibrations around 2800 cm^{-1}. All these vibrational changes confirmed the synthesis of the structure.

When the FT-IR spectrum of the deca(3-bromopropane) pillar[5]arene terminals is examined, due to the five repeating 1,4-bis(3-bromopropoxy)benzene structures of the pillar[5]arene, no significant difference was observed in the FT-IR spectrum, although small shifts in vibration were detected. The pillar[5]arene was also supported by FT-IR spectrum as well as melting point comparison and other methods (NMR et al.).

When the FT-IR spectrum of the target macroring deca(3-azidoopropane) pillar[5]arene is examined, small band observed around 1700 cm^{-1} indicated C = N vibration in Bodipy structures, multiple peaks in the range of 1555–1405 cm^{-1} indicated C = C stretching, and aliphatic and aromatic C–H stretches between 2800 and 3050 cm^{-1}. In addition, the most significant difference is deca(3-azidoopropane) pillar[5]arene. The N = N stretch at 2070 cm^{-1} in the IR spectrum disappeared in the FT-IR spectrum of deca(3-azidoopropane) pillar[5]arene.

When the ^{1}H-NMR spectrum of 1,4-bis(3-bromopropoxy)benzene is examined, benzene hydrogens were observed as singlet at 7.01 ppm. -CH$_2$ hydrogens were observed around 3.5–2 ppm in triplet or pentet forms. All peaks in the spectrum were detected in singlet form. The characterization data of this compound, which were also prepared in other literatures, were compared and the structure was confirmed.

When the 1H-NMR spectrum of the pillar[5]arene containing ten 3-bromopropoxy terminals is examined, due to the five repeating 1,4-bis(3-bromopropoxy)benzene structures of pillar[5]arene, the reactive compound has a spectrum similar to 1,4-bis(3-bromopropoxy)benzene graph is obtained. The most significant difference was observed at 3.76 ppm as the peak singlet pointing to the bridging CH$_2$ hydrogens in the macroring. Although the other peaks gave similar results, a shift to the upper area was detected with the expansion. This may be attributed to the bridging CH$_2$ providing electrons to the ring.

12.4   Conclusions

Pillar[n]arene compounds, the new class of supramolecular chemistry, are cheap and easily synthesized, new generation macrocyclic compounds that can contain multiple

functional groups and are waiting to be discovered in many new areas of the scientific world. Pillar[5]arene, a 5-membered macroring as a new generation compound, is conformationally stable and is part of the parasilaphone macroring family due to the coupling between the 2 and 5 positions of the aromatic rings. These compounds continue to expand rapidly due to their cyclic structure and stability. These are: gas sensor, polymer, membrane studies, enzymatic applications, and anion/cation molecule carriers are used. In particular, these compounds are investigated for their usability through guest–host complexation due to the molecular gaps they have.

In here, we synthesized a macrocycle based on pillar[5]arene including ten quinoline units. The compounds was characterized with NMR, FT-IR, elemental analysis, melting point, etc. The prepared macrocycle can be used in a lot of scientific areas such as material chemistry, biochemistry, pharmacology, medicine.

References

1. Eissa SI, Farrag AM, Abbas SY, Shehry MFE, Ragab A, Fayed EA, Ammar YA (2021) Novel structural hybrids of quinoline and thiazole moieties: synthesis and evaluation of antibacterial and antifungal activities with molecular modeling studies. Bioorg Chem 110:104803
2. Hu Y-Q, Zhang S, Xu Z, Lv Z-S, Liu M-L, Feng L-S (2017) 4-Quinolone hybrids and their antibacterial activities. Eur J Med Chem 141:335–345
3. Kursunlu AN, Acikbas Y, Ozmen M, Erdogan M, Capan R (2020) Fabrication of LB thin film of pillar[5]arene-2-amino-3-hydroxypyridine for the sensing of vapors. Mater Lett 267:127538
4. Ogoshi T, Kanai S, Fujinami S, Yamagishi T, Nakamoto Y (2008) para-Bridged symmetrical pillar[5]arenes: their lewis acid catalyzed synthesis and host–guest property. J Am Chem Soc 130(15):5022–5023
5. Atacan K, Kursunlu AN, Ozmen M (2019) Preparation of pillar[5]arene immobilized trypsin and its application in microwave-assisted digestion of Cytochrome c. Mater Sci Eng: C 94:886–893
6. Bastug E, Kursunlu AN, Guler E (2020) A fluorescent clever macrocycle: Deca-bodipy bearing a pillar[5]arene and its selective binding of asparagine in half-aqueous medium. J Luminescence 225:117343
7. Kursunlu AN, Acikbas Y, Ozmen M, Erdogan M, Capan R (2019) Haloalkanes and aromatic hydrocarbons sensing using Langmuir–Blodgett thin film of pillar[5]arene-biphenylcarboxylic acid. Coll Surfaces A: Physicochem Eng Asp 565:108–117

Chapter 13
Synthesis and Photochemical Properties of Benzylidene-Containing Polymers

Vitaliy Smokal, Oksana Kharchenko, and Oleksiy Kolendo

13.1 Introduction

The development of modern technologies enables us to create polymer materials with a number of properties, which would be impossible to realize in a single polymer [1–3]. Compounds with benzylidene fragment are known for their biological properties [4]. Benzene oxazolones have exhibited antibacterial as well as antifungal activities. Thiazolidinones have shown a wide range of pharmaceutical properties [5]. These molecules are promising due to their photophysical properties [6, 7]. In the present work, we chose oxazolone, thiohydantoin, thiazolidinone derivatives, synthesized the methacrylic monomers containing these fragments, polymers, co-polymers with methylmethacrylate, and investigated their spectral characteristics.

13.2 Experimental

13.2.1 Methods

N,N-dimethylformamide (DMF) were vacuum—distilled from calcium hydride just prior to use. 2,2-Azobis(isobutyronitrile) (AIBN) was recrystallized twice from absolute methanol. Methacrylic anhydride and methacryloyl chloride were vacuum—distilled, immediately before use. Methylmethacrylate (MMA) was dried by distillation under argon. All other reagents and solvents were commercially available and used as received.^{1}H NMR (400 MHz) spectra were recorded by a "Mercury-400" spectrometer using DMSO-d_6 as solvent. Chemical shifts are in ppm from the

V. Smokal · O. Kharchenko (✉) · O. Kolendo
Kyiv Taras Shevchenko National University, Volodymyrska 60, Kyiv 01033, Ukraine
e-mail: oksana_kharchenko@ukr.net

Fig. 13.1 Chemical
structures of thiazolidinone,
oxazolone, and
thiohydantoin derivatives

R_1O—⬡—R_2

R_1= H (1), CH_3CO (2), $CH_2C(CH_3)CO$ (3)

R_2 =

R   ,   O   ,   T
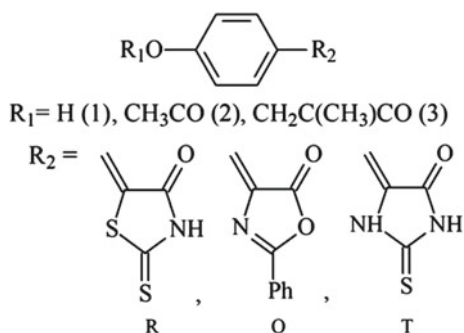
tetramethylsilane internal standard (TMS). UV measurements in the 210–600 nm
spectral areas were performed at room temperature in ethanol in quartz cuve (C =
10^{-5} mol/L) with a PerkinElmer UV/VIS/NIR Lambda 19 spectrometer. The general
structures of benzylidene-containing derivatives are shown in Fig. 13.1.

13.2.2 Materials

(4-Hydroxyphenyl)methylene-2-thioxo-4-thiazolidinone (1-R) 0.91 g of 4-hydroxy
benzaldehyde were added to a solution of 2-thiox o-4-thiazolidinone 1 g, in isopropyl
alcohol.

The reaction mixture was heated for 2 h on a steam bath at 80–90 ℃ and then
poured into water. The resultant solid product was collected, washed with cold
ethanol, hot water, ethanol, and then small amount of hexane, and then dried to
afford compound 1-R as yellow solid, melting point (mp). 283–285 ℃, yield 80%.
1H NMR (400 MHz, DMSO-d6), % (ppm): 7.49 (s, 1H, -CH=), 10.26 (s, 1H,
OH), 13.52 (s,1H, NH), 6.87–7.70 (m, 4H, Ph-H). UV–Vis (ethanol) λ_{max}: 242, 292,
395 nm.

(4-Acetyloxyphenyl)methylene-2-thioxo-4-thiazolidinone (2-R) One gram (1-R)
in acetic anhydride 3 ml was heated on a steam bath at 80–90 ℃. After 2 h, the mixture
was cooled and then poured into water. The resultant solid product that formed was
filtered off, washed with water and dried. Crystallization from ethanol alcohol gave
yellow crystals m.p. 238–240 ℃, yield 70%. ^{1}H NMR (400 MHz, DMSO-d6), %
(ppm): 7.61 (s, 1H, -CH=), 2.29 (s, 3H, CH_3), 13.75 (s, 1H, NH), 7.25–7.50 (m,
4H, Ph-H). UV vis (ethanol) λ_{max}: 240, 266, 377 nm.

4-(Methacryloyloxy)benzaldehyde. A solution containing 4.9 g of 4-
hydroxybenzaldehyde and 11.4 ml of triethylamine in 150 ml of diethyl ether was
cooled to 0 ℃. To the solution 8.4 g of methacryloyl, chloride in 8 ml of diethyl ether
was added dropwise in 40 min while stirring. The precipitated triethylammonium
chloride was filtered off and the filtrate was allowed to stand for 12 h at 4 ℃. The

suspended matter formed in the solution was separated by filtration. Then the solvent was evaporated, and the residue was dried to give 7.0 g (90%) of a pale yellow solid.

4-(Methacryloyloxyphenyl)methylene-2-thioxo-4-thiazolidinone (3-R).

A solution containing 2 g of 4-(methacryloyloxy)benzaldehyde, 2.5 g of 2-thioxo-4-thiazolidinone, and 0.3 g of anhydrous sodium acetate in 50 ml isopropanol was heated on a steam bath at 80–90 ºC. After 2 h, the mixture was cooled and then was poured on ice. The resultant solid product that formed was filtered off, washed with water and dried. Crystallization from ethanol alcohol gave yellow crystals m.p. 195 ºC, 65%. ^{1}H NMR (400 MHz, DMSO-d6), % (ppm): 5.86 (s, 1H, CH2=), 6.31 (s, 1H, CH2=), 2.04 (s, 3H, CH3), 7.28–7.66 (m, 4H, Ph-H), 7.62 (s, 1H, -CH=), 13.69 (s, 1H, NH).

Oxazolone derivatives were prepared by condensation of m- and p-arylaldehydes with hippuric acid in acetic anhydride, in the presence of anhydrous sodium acetate as a homogeneous basic catalyst. The synthesis procedure was described previously [2].

2-Phenyl-4-[(4-hydroxyphenyl)methylene]-5(4H)-oxazolone (1-O): m.p. is 220 ºC, the yield is 35%.^{1}H NMR (400 MHz, DMSO-d6), (ppm): 7.22 (s, 1H, -CH=), 10.27 (s, 1H, -OH), 6.88–8.14 (m, 4H, Ph-H), 7.60–8.13 (m, 5H, Ph-H). UV (ethanol) λmax: 258, 383 nm.

2-Phenyl-4-[[4-acetyloxyphenyl]methylene]-5(4H)-oxazolone (2-O): m.p. is 168 ºC, the yield is 80%. ^{1}H NMR (400 MHz, DMSO-d6), (ppm): 7.36 (s, 1H, -CH=), 2.44 (s, 3H, CH3), 8.26–8.18 (m, 4H, Ph-H), 7.3–7.65 (m, 5H, Ph-H). UV (ethanol) λ max: 225, 261, 366 nm.

2-Phenyl-4-[(4-methacryloyloxyphenyl)methylene]-5(4H)-oxazolone (3-O): mp is 170 ºC, the yield is 55%. ^{1}H NMR (400 MHz, DMSO-d6), (ppm): 5.89 (s, 1H, -CH2=), 6.34 (s, 1H, CH2=), 2.06 (s, 3H, -CH3), 7.28–8.18 (m, 4H, Ph-H), 7.70–8.35 (m, 5H, Ph-H).

The polymerization ability of the new monomers was investigated kinetically for radical homopolymerization using the dilatometric method. The process was conducted in 10% DMF solution at 80 ºC (argon atmosphere, initiator. AIBN 1%); contractions were measured by KM-6 cathetometer. Monomers conversion during the homopolymerization process of (3-R) was 67% in 240 min with homopolymer (h3-R), for (3-O) was 60% in 240 min with homopolymer (h3-O) and for (3-T) was 53% in 240 min. The parameters of polymerization such as conversion, speed of polymerization (V_{gr}), total constant of polymerization's speed (K_{sum}) were calculated (Table 13.1).

13.3 Results and Discussion

As expected, for all novel monomers, the speed of polymerization was slowly than for MMA and phenylmethacrylate (PhMA) due to influences benzylidene-containing moiety. The kinetic curves of the radical homopolymerization for monomers 3-R, 3-O, 3-T are shown in Fig. 13.2.

Table 13.1 Kinetic's parameters of 3-R, 3-O, 3-T, MMA and PhMA

Monomer	Yield for 4 h, %	$V_{gr} \times 10^4$, mol/l $\times$ s	$K_\Sigma \times 10^3$, mol/l $\times$ s
3-R	67	0.33	1.25
3-O	60	0.36	1.27
3-T	53	0.56	1.9
MMA	33	1.08	0.51
PhMA	–	0.52	1.10

^{1}H NMR (400 MHz) spectra for new polymers were recorded on a Mercury-400 spectrometer using DMSO-d$_6$ as solvent. Chemical shifts are in ppm from the internal standard tetramethylsilane (TMS)

Fig. 13.2 Kinetic curves of the radical polymerization of 10% methacrylic monomers in DMF at 80 ℃ (argon atmosphere, 1% of AIBN initiator). 1—3-R; 2—3-O; 3—3-T; 4—MMA
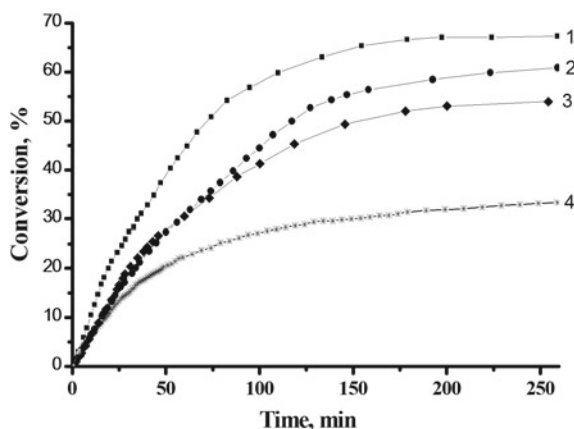
Photochemical investigation

UV vis measurements in the 210–500 nm spectral region were performed at room temperature in ethanol in quartz cell (C $=10^{-5}$ mol/L) with a PerkinElmer UV/vis/NIR Lambda 19 spectrometer. In order to determine the role of electron-withdrawing heterocyclic fragments on photoisomerization reactions, we used acetyl derivatives as modeling compounds of methacrilic monomers. The absorption spectra of compounds, 2-R, 2-O recorded during UV irradiation clearly indicate that this compound undergoes the photoisomerization process (Figs. 13.3 and 13.4). The observable results are typical of the cis–trans isomerization process for compounds with benzylidene fragment [8, 9]. The stable state of the molecule with benzylidene fragment is the cis-isomeric configuration [10]. The absorption in the visible range of a photon induces the transition to the trans-isomer. This state is metastable with the reverse transition to the cis-state taking place through photo activation. Therefore, a molecule absorbing of a photon undergoes a complete cis–trans-cis isomerization cycle [11]. From the trans form, molecules come back to the cis form by two mechanisms, spontaneous thermal reactions and trans–cis photoisomerization.

Fig. 13.3 Changes in absorbance spectra 2-R in in ethanol (C = 10^{-5} mol/L): before—1 and after every 5 min periods of irradiation(λ = 365 nm) at room temperature
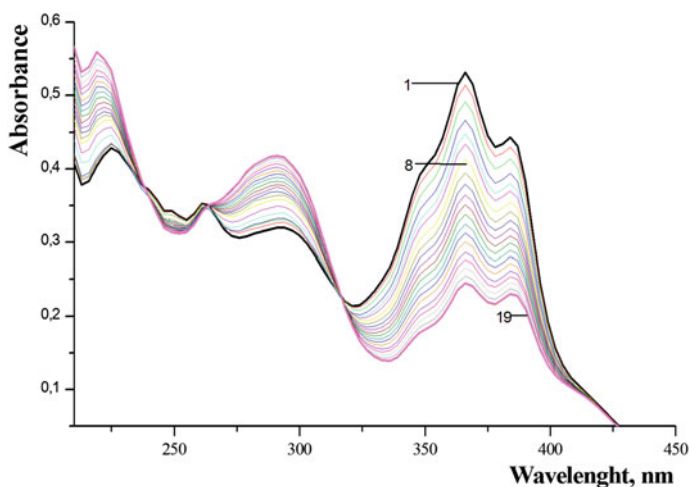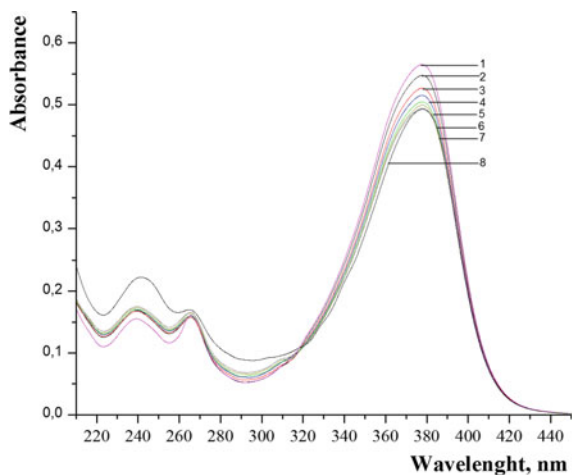
Fig. 13.4 Changes in absorbance spectra 2-O in in ethanol (C = 10^{-5} mol/L): before—1 and after every 5 min periods of irradiation(λ = 365 nm) at room temperature

In the spectrum of absorption the ethanol solutions of compounds, 2-R, 2-O, have two bands with vibrational structure, i.e., an intensive long-wave band with approximate maximum of 320–420 nm and a medium-intensity absorption band with its maximum about 240–260 nm. Spectral changes take place during UV irradiation of the solution of 2-R in ethanol with maximum of 380. During the 2-O solution irradiation process, the decolouration is observed accompanied with a drop of the long-wave maximum intensity, as well as an increase of absorption intensity at 291 nm with isosbestic point at 316 nm.
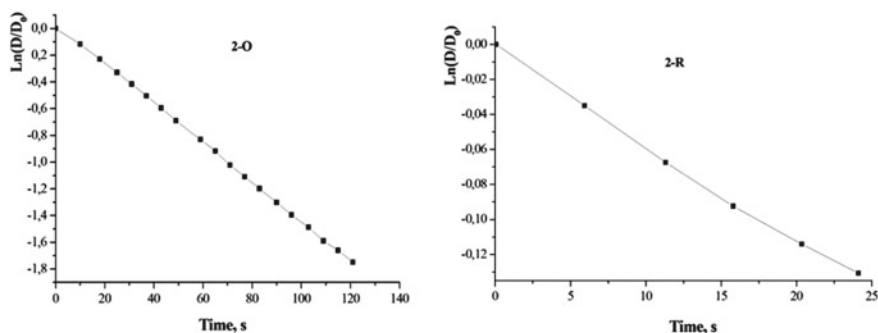
Fig. 13.5 Graphic dependence ln(Dt/D0) at wavelength 360 nm for 2-O and 380 nm for 2-R

Table 13.2 Constant's values of speed cis–trans-photoisomerization and times of half-reaction

Compound	λ_{abs}, nm		$k_{cis\text{-}trans} \times 10^2$, s^{-1}	$\tau_{0,5}$, s
2-R	240	380	0.91	7617
2-O	292	366	2.45	2829

The obtained benzylidene-containing compounds in vitro have cis-conformation along the double bond [11]. The cis–trans-photoisomerization with strong spectral changes took place during UV irradiation at 365 nm of the solution 2-O, 2-R in ethanol. The time of half-reaction ($\tau_{0,5}$) and rate constants ($k_{cis\text{-}trans}$) of the photo cis–trans-photoisomerization were obtained by the calculation of tgα for curve ln(D/D_0) in the time of irradiation (Fig. 13.5). The $k_{cis\text{-}trans}$ for 2-O and 2-R have been determined, and the times of half-reaction for cis–trans-photoisomerization have been calculated by the equation $\tau_{0,5} = \ln2/k_{cis\text{-}trans}$ (Table 13.2).

We suppose that k and half-reaction period of photoisomerization are not a constant speed of elementary photoprocesses. These constants characterized the speed of "disappearing" for cis-isomer under these experimental conditions (intensity of irradiation, temperature, and wavelength of irradiation). The results of our research confirmed that the nature of benzylidene moiety influences on parameters of cis-trans-photoisomerization ($k_{cis\text{-}trans}$, $\tau_{0,5}$) for benzylidene-containing derivatives. It was found that the values of speed cis-trans-photoisomerization decrease for electron-withdrawing heterocyclic fragments.

13.4 Conclusion

New modeling compounds and their polymers were synthesized, characterized, and their photochemical properties were studied. The polymerization ability of the new monomers 3-R, 3-O, 3-T was investigated kinetically for radical homopolymerization. These products were characterized by spectroscopic measurements. Absorption

spectroscopic properties for modeling compounds in ethanol solutions were investigated with UV–visible spectrophotometry. In all cases, we notice that irradiation of acyloxy derivatives with benzylidene fragment leads to photoinduced cis-trans-isomerization. It was found that presence of electron with-drawing heterocyclic fragment influences on photoisomerization process. Extensive studies of new thiazolidone derivatives have shown favorable photophysical and photochemical properties for applications requiring photosensitivity in certain of range of wavelength.

References

1. Krupka O, Yu KA, Kushnir K, Blazejowski J (2005) Synthesis and Investigation of a Methacrylic Monomer Based on 4-[4-(Phthalimido)-Phenylsulphamido]-2,6-Dimethoxypyrimidine Mol. Cryst Liq Cryst 427:235–243. https://doi.org/10.1080/15421400590892316
2. Smokal V, Czaplicki R, Derkowska B, Krupka O, Kolendo A, Sahraoui B (2007) Synthesis and study of nonlinear optical properties of oxazolone containing polymers. Synth Met 157(18–20):708–712. https://doi.org/10.1016/j.synthmet.2007.07.006
3. Fritz A, Schonhals A, Sapich B, Stumpe J (1999) Dynamic and photochemical behavior of amorphous comb-like copolymers with photochromic azobenzene side groups Macromol. Chem Phys 200:2213. https://doi.org/10.1002/(SICI)1521-3935(19991001)200:10%3c2213::AID-MACP2213%3e3.0.CO;2-G
4. Mesaik MA, Rahat S, Khan KM, Choudhary MI, Shahnaz M, Ismaeil Z (2004) Synthesis and immunomodulatory properties of selected oxazolone derivatives Bioorg. Med Chem 12:2049–2057. https://doi.org/10.1016/j.bmc.2004.02.034
5. Cetenko W, Connor D, Sorenson R, Unangst P, Stabler S (1989) Preparation of (arylmethylenyl) thiazolidinones,-imidazolidinones and -oxazolidinones as anti-inflammatory agents and antiallergy agents. Eur Pat. Appl. Warner-Lambert Co., USA
6. Koczan G, Csik G, Csampai A, Balog E, Bosze S, Sohar P, Hudecz F (2001) Synthesis and characterization of 4-ethoxymethylene-2-naphthyl-5-oxazolone and its fluorescent amino acid derivatives. Tetrahedron 57:4589–4598. https://doi.org/10.1016/S0040-4020(01)00332-5
7. Icli S, Icli H, Koc H, McKillop A (1994) NMR, absorption and fluorescence parameters of azlactones. Spectrosc Lett 27:1115–1128. https://doi.org/10.1080/00387019408006969
8. Ullman EF, Baumann N (1970) Unsaturated lactone photochemistry. Effect of wavelength and sensitizer structure on selective population of specific excited states. J Am Chem Soc 192:5892–5899. https://doi.org/10.1021/ja00723a013
9. Brocklehurst K, Williamson K (1974) Electronic spectra of the isomeric 4-benzylidene-2-phenyl-Δ2-oxazolin-5-ones and the products of their reaction with nucleophiles including α-chymotrypsin: kinetics of the hydrolysis of the isomeric enzyme derivatives. Tetrahedron 30:351. https://doi.org/10.1016/S0040-4020(01)91470-X
10. Baumann N, Ullman EF (1968) Photosensitization of wavelength-dependent lactones. Influence of orbital symmetries on triplet energy transfer. J Am Chem Soc 90:4158–4160. https://doi.org/10.1021/ja01017a044

11. Rao YS (1976) Reactions in polyphosphoric acid. I. New stereospecific synthesis of the E isomers of 2-phenyl-4-arylmethylene-2-oxazolin-5-ones. J Org Chem 41:722–725. https://doi. org/10.1021/jo00866a037

Chapter 14
POSS-Containing Nanocomposites Based on Polyurethane/Poly(Hydroxypropyl Methacrylate) Semi-IPN Matrix

L. V. Karabanova and L. A. Honcharova

14.1 Introduction

Nanocomposites are known as class of materials in which a small amount of nanofillers could greatly improve their properties [1–5]. Among the matrixes for the nanocomposites, preparation polyurethanes (PUs) are successfully used due to their wide variety of physical and chemical properties [6–9]. The creation of the nanocomposites based on polyurethane matrix and polyhedral oligomeric silsesquioxane (POSS) macromer was found could essentially improve, in compare with native matrix, the permeability of gas transport [10], to increase of the permittivity and conduction [11]. The addition of POSS into the PU's polymers leads to reinforcement effect of the nanoparticles and, as result, to improving of the mechanical properties of the nanocomposites, also leads to enhancement of their thermal stability [12–16]. The incorporation of POSS into the systems results in increasing of resistance to oxidation of the nanocomposites [14, 16]. These favorable effects are evident mainly when the functionalized POSS particles are integrated into a polymer's chains via a chemical reaction.

The nanocomposites based on polyurethane matrix and 1,2-propandiolisobutyl-POSS (POSS), used as functionalized nanofiller, were created and analyzed in our previous investigations [17, 18]. The presence of two reactive hydroxy groups in peripheral substituent's of POSS allows it to react with diisocyanates results in embedding of the POSS particles into the main polymer chain of the nanocomposites [19–21]. By these investigations, it was shown that incorporation of the POSS nanoparticles into PU matrix leads to the formation of more ordered structure [18] and also significantly affects the thermal stability of the nanocomposites [17].

L. V. Karabanova (✉) · L. A. Honcharova
Institute of Macromolecular Chemistry of National Academy of Sciences of Ukraine, Kyiv, Ukraine
e-mail: lyudmyla_karaban@ukr.net

The essential interest for the creation of the nanocomposites could be the using of the multicomponent polymer matrices obtained by the method of interpenetrating polymer networks (IPNs) [22, 23], where polyurethane selected as one of the polymer components of IPNs. The existence of several levels of chemical and structural heterogeneities in such matrices could provide additional opportunities for regulation of nanocomposites' properties [22, 24, 25]. The successful attempts of the nanofillers introduction into interpenetrating polymer networks were described in articles [3, 25, 26].
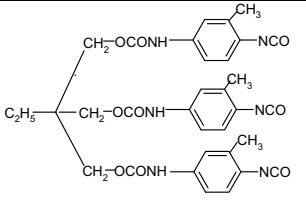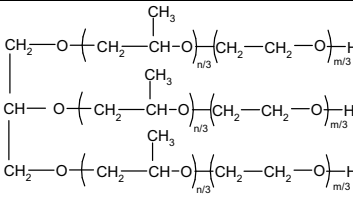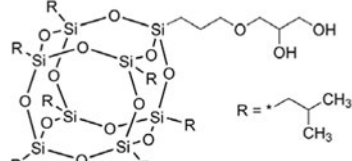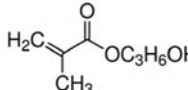
The objective of the present study was the creation of the nanocomposites based on polymer matrix made by method of interpenetrating polymer networks (IPN), consisting of polyurethane and poly(hydroxypropyl methacrylate), and contains 1,2-propanediolisobutyl polyhedral oligomeric silsesquioxanes (1,2-propandiolisobutyl-POSS) as functionalized nanofiller, and investigation of the effects induced by the POSS content on the thermodynamic properties, thermal properties, porosity, and morphology of the nanocomposites.

14.2   Materials and Testing Methods

14.2.1   Materials

The chemicals used in the nanocomposites preparation were obtained from commercial sources. Toluene 2,4-diisocyanate (TDI) and trimethylolpropane (TMP) were obtained from Merck. 1,2-propanediolisobutyl polyhedral oligomeric silsesquioxanes (POSS) was purchased from Sigma-Aldrich Inc. Hydroxypropyl methacrylate was obtained from Acros organics. The oligoetherglycol with Mw = 5.000 g/mol^{-1} (Laprol 5003) obtained from commercial sources was additionally dried with liquid nitrogen under vacuum at 75–80 °C for 5 h before use.

The molecular structures of chemicals used in the nanocomposites preparation are presented below.

CH$_3$ CH$_2$—OCONH——NCO CH$_3$ C$_2$H$_5$—CH$_2$—OCONH——NCO CH$_3$ CH$_2$—OCONH——NCO	CH$_3$ CH$_2$—O—(CH$_2$—CH—O)$_{n/3}$(CH$_2$—CH$_2$—O)$_{m/3}$H CH$_3$ CH—O—(CH$_2$—CH—O)$_{n/3}$(CH$_2$—CH$_2$—O)$_{m/3}$H CH$_3$ CH$_2$—O—(CH$_2$—CH—O)$_{n/3}$(CH$_2$—CH$_2$—O)$_{m/3}$H n=69÷81, m=10÷12
Adduct TMP-TDI	Laprol 5003
R = ·CH$_2$—CH(CH$_3$)—CH$_3$	H$_2$C=C(CH$_3$)—C(=O)—OC$_3$H$_6$OH
1,2-propanediolisobutyl-POSS	Hydroxypropyl methacrylate

14.2.1.1 Preparation of POSS-Containing Nanocomposites

First, the PU network was synthesized by two-step method. In the first stage, the adduct of trimethylolpropane with toluene 2,4-diisocyanate (the adduct TMP-TDI) was obtained as described in previous articles [17, 26]. Next step was the three-dimensional polyurethane synthesis. Polyurethane network was synthesized from a mixture of Laprol 5003 and adduct TMP/TDI (ratio 1:2 g-eq.) at 80 °C in nitrogen atmosphere. 1,2-propanediolisobutyl-POSS was added at the second stage of PU network synthesis as a functionalized nanofiller with amount of 1, 3, 5 and 10 wt. %. The mixture of Laprol 5003 and adduct TMP/TDI was poured out on Petri dishes and cured at 70 °C for 2 h and post-cured at 80 °C for 24 h. The obtained films were post-cured for 2 h at 100 °C and then were held at 80 °C for 36 h in vacuum 10^{-5} Pa to remove residual solvent. The nanocomposites were prepared by swelling of POSS-containing polyurethane with monomer hydroxypropyl methacrylate in controlled conditions and by subsequent radical polymerization of monomer using UV irradiation. For radical polymerization, the initiator Irgacure 651, $\lambda = 340$ nm^{-1} was used. The polymer matrixes with ratio of PU/PHPMA = 85/15 and PU/PHPMA = 70/30 (the semi-IPN-15 and semi-IPN-30) were used for preparation of the nanocomposites.

14.2.2 Testing Methods

14.2.2.1 Fourier Transform Infrared Spectroscopy (FTIR)

FTIR spectra of the neat POSS, neat adduct TMP-TDI, and model adduct + POSS were recorded using a TENSOR 37 FTIR spectrometer (BRUKER, USA, Germany) in the spectral range of 4000–400 cm^{-1} (with resolution of 0.8 cm^{-1}). The samples (thin films) of PU, PHPMA, PU/PHPMA semi-IPNs, and nanocomposites were presented in the ATR module.

14.2.2.2 Vapor Sorption and Thermodynamic Calculations

The methylene chloride vapor sorption by PU samples and by nanocomposite's samples was studied using a vacuum installation and a McBain balance [25]. The changes in partial free energy of methylene chloride by sorption (dissolution) were determined from the experimental data using (14.1):

$$\Delta\mu_1 = (1/M)RT \ln(P/P_0), \tag{14.1}$$

where M is the molecular mass of methylene chloride and P/P_0 is the relative vapor pressure. The value $\Delta\mu_1$ changes with solution concentration from 0 to$-\infty$.

To calculate the free energy of mixing of the polymer components with the solvent, the changes in partial free energy of the polymers (native PU, nanocomposites) need to be determined. This requires the calculation of the difference between the polymer chemical potential in the solution of a given concentration and in pure polymer under the same conditions ($\Delta\mu_2$). $\Delta\mu_2$ for the polymer components were calculated using the Gibbs–Duhem equation:

$$\omega_1 d(\Delta\mu_1)/d\omega_1 + \omega_2 d(\Delta\mu_2)/d\omega_1 = 0 \tag{14.2}$$

where ω_1 and ω_2 are the weight fractions of a solvent and of a polymer. This can be rearranged to give (14.3):

$$\int d(\Delta\mu_2) = -\int (\omega_1/\omega_2)d(\Delta\mu_1) \tag{14.3}$$

Equation 14.3 allows the determination of $\Delta\mu_2$ for each polymer from the experimental data by integration over definite limits. The average free energy of mixing of solvent with the individual PU and nanocomposites of various compositions for the solutions of different concentration was then estimated using (14.4) and using computational analysis.

$$\Delta g^m = \omega_1 \Delta\mu_1 + \omega_2 \Delta\mu_2 \tag{14.4}$$

14.2.2.3 Different Scanning Calorimetry (DSC)

DSC was undertaken using a TA Instruments Q1000, on samples (cut thin film samples) of 10–15 mg in hermetically sealed aluminum pans. Experiments were conducted at the heating rate of 20 °C min^{-1} in the temperature range –90 to 200 °C under nitrogen. The glass transition temperature (Tg) was taken as the midpoint of the curve at the change in heat capacity.

14.2.2.4 Thermogravimetric Analysis (TGA)

TGA was undertaken using a TA Instruments Q500 in hermetically sealed aluminum pans. In a dry nitrogen atmosphere, the samples (about 5–6 mg) were heated from ambient temperature to 700 °C at the heating rate of 20 °C min^{-1}. The initial thermal degradation temperature was taken as the onset temperature at which a mass loss of 5 wt. % occurs.

14.2.2.5 Porosity of the Nanocomposites by BET Method

To estimate the porosity of the synthesized nanocomposites, the classical sorption method was chosen [27]. It consists in determining of the amount of vapors of low molecular weight liquid, which adsorbed by the sample at different vapor pressures, building of the sorption–desorption isotherms and subsequent calculations based on isotherms of the specific surface area, total pore volume and average pore size of the nanocomposites. The adsorption of the methanol vapors by samples of semi-IPNs and POSS-containing nanocomposites based on them was investigated at a temperature of 20 °C using a vacuum installation with McBain balances using molybdenum spirals with a sensitivity of 3–4 mg/mm [24, 25].

The specific surface area S_{spec} of the samples was calculated by the Brunauer, Emmet, and Teller method (BET method) [27]. The BET equation was used as:

$$\frac{P/P_0}{a \cdot (1 - P/P_0)} = \frac{1}{C \cdot a_M} + \frac{C - 1}{C \cdot a_M} \cdot \frac{P}{P_0} \tag{14.5}$$

where P/P_0 is the relative vapor pressure of the sorbate;

a—the amount of adsorbed substance, mmol/g;

a_m—the amount of adsorbed substance in the monomolecular layer, mmol/g;

C—is a constant.

Experimental data were presented as a dependence:

$$\frac{P/P_0}{a \cdot (1 - P/P_0)} = f \frac{P}{P_0} \tag{14.6}$$

The tilt angle of the line and the length on the *y*-axis allowed to calculate *C* and *am*.

The specific surface area of the samples was calculated by the equation:

$$S_{\text{spec}} = a_M \omega N_a 10^{-7}, \tag{14.7}$$

where N_a—is the Avogadro's number; ω—is the area occupied by one molecule of sorbate.

The value of ω was calculated by the formula:

$$\omega = 4 \cdot 0.866 \cdot (M/4 \cdot \sqrt{2} \cdot d \cdot N_a)^{\frac{2}{3}} \tag{14.8}$$

where *M*—is the molecular weight of the sorbate;

d—is the density of the sorbate.

The total pore volume in samples W_0 was evaluated using the maximum amount of methanol adsorbed by samples according to the formula [27]:

$$W_0 = aV, \tag{14.9}$$

where *a*—is the maximum amount of sorbate, absorbed by 1 g of sorbent, mol/g;

V—is the volume of one mole of sorbate.

The average pore radius of the samples was calculated by equation [27]:

$$r_{\text{av}} = \left(2W_0/S_{\text{spec}}\right) \cdot 10^4 \left(\overset{\circ}{A}\right) \tag{14.10}$$

14.2.2.6   Scanning Electron Microscopy (SEM)

Scanning electron microscopy (SEM) was performed on a JEOL JSM 6060 LA (Tokyo, Japan) at an accelerating voltage of 30 kV and using a detector of secondary electrons. The samples were cut into the strips, before being submerged in liquid nitrogen for 5 min and then fractured. The samples were warmed to room temperature and fixed to an SEM stub. The fracture surface of samples was coated with gold in a vacuum to prevent accumulation of static charge and to increase the resolution. All measurements were done at 20 °C and at magnification of 15,000 times.

14.3   Results and Discussion

14.3.1   Fourier Transform Infrared Spectroscopy (FTIR)

The chemical structures of all synthesized samples were investigated using the infrared spectroscopy analysis. The FTIR-ATR spectra of a neat semi-IPN-15 and semi-IPN-15 nanocomposites with different POSS content are presented in Fig. 14.1.

The absence of NCO peak at 2270 cm^{-1} in all spectra indicates that the isocyanate groups conversion were complete. The characteristic absorption peaks for semi-IPN based on PU network (urethane units peaks) (Fig. 14.1, curve 1) are in the spectral range of 3400–3300 cm^{-1} (N–H stretching, slightly weaker signal; free and hydrogen-bonded, respectively), 1728–1707 cm^{-1} (C = O stretching, mainly H-bonded, first amide band), 1535 cm^{-1} (N–H bending, second amide band), and 1223 cm^{-1} (N–CO–O asymmetric stretching, third amide band) [28, 29]. Other characteristic band present in semi-IPN can be found in the range around 1040–1150 cm^{-1} (N–CO–O symmetric stretching and C–O–C asymmetric stretching). The broad bands in the range from 2870 to 2970 cm^{-1} are assigned to the saturated C–H symmetric and asymmetric stretching vibrations of methylene groups [28].

The occurrence of POSS-cage structures in semi-IPN-15 nanocomposites was confirmed by the presence of bands at 1108 and 743 cm^{-1} for Si–O–Si and Si–C stretching vibrations and corresponding bending modes at 839 and 1233 cm^{-1},
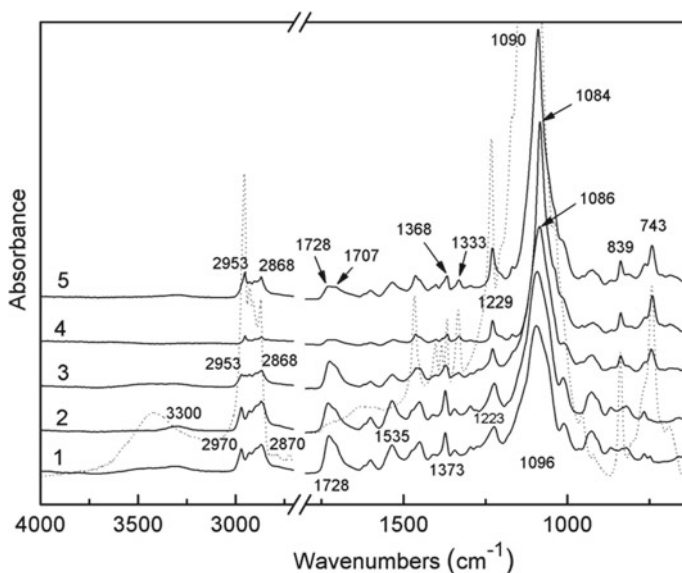
Fig. 14.1 FTIR spectrum of POSS (drop line). FTIR-ATR spectra of a neat semi-IPN-15 (1) and semi-IPN-15 nanocomposites with different POSS content: 1 (2); 3 (3); 5 (4); and 10 (5) wt.%. (FTIR spectrum of POSS (dot line) is given for comparison)

respectively [30]. More detailed, the band at 743 cm^{-1} is attributed to the stretching vibration in the Si–CH2- isobutyl groups of POSS and accompanied by CH2 (2871 and 2926 cm^{-1}) and CH3 (2908 and 2955 cm^{-1}) stretching and corresponding deformational modes (1465, 1402, 1384, 1230, and 839 cm^{-1}) [31]. From FTIR spectra of semi-IPN-15 nanocomposites is evident that the intensity of those bands increases with the increase of the POSS content in the semi-IPN-15 nanocomposite structure. This is especially visible in the FTIR spectrum of semi-IPN-15-10 (Fig. 14.1, curve 5), where the increase in the CH3 stretching with an increase in the POSS content was clearly observed at the peak position at 2953 cm^{-1}.

The next region, where the POSS content influence on nanocomposite's structure was clearly observed, is located in the area 1040–1150 cm^{-1}. From literature, it is known that hydrogen bonds are formed in the polyurethanes between the active hydrogen atom in the urethane N–H group and the oxygen atom of the carbonyl C = O group in the hard segments or the ether oxygens in the soft segments [32]. In Fig. 14.1 (curves 3–5), the asymmetric stretching band of C–O–C groups shifts significantly toward lower wavenumbers from 1096 cm^{-1} for neat semi-IPN-15 to 1084 cm^{-1} in semi-IPN-15-5 that may be due to an increase of the participation of C–O–C groups in the formation of hydrogen bonds [33] Moreover as we see from FTIR spectra in the range of 1728–1707 cm^{-1}, the neat semi-IPN-15 has a wide peak centered near 1728 cm^{-1}, which characterizes the hydrogen bonds in disordered domains [29]. In the semi-IPN-15-10, it is clearly visible the decrease and redistribution of the intensities of this peak in favor of the growth of the peak shoulder at 1707 cm^{-1} corresponding to the ordered hydrogen-bonded carbonyl groups. It demonstrates that the addition of POSS nanoparticles influences the formation of hydrogen bonds in the structure of the semi-IPN-15 nanocomposites, and they become more ordered with increases of POSS content. Thus, FTIR-ATR spectra clearly demonstrated the existence of POSS in the semi-IPN-15 nanocomposites and the POSS content effect on their structure.

14.3.2   Thermodynamics of Polymer-Filler Interactions in the Nanocomposites

The aim of the study was to evaluate the effect of the nanofiller on the Gibbs energy, i.e., on the free energy mixing of the polymer components during formation of the semi-IPNs.

The basis for the thermodynamic parameters calculation was the experimental isotherms of vapor solvent sorption by the samples. Sorption of methylene chloride vapors by samples of native polymers, semi-IPNs, nanocomposites, and nanofiller was investigated at 25 °C using a vacuum installation with McBain balance with molybdenum spirals with a sensitivity of 3–4 mg/mm [34, 35].
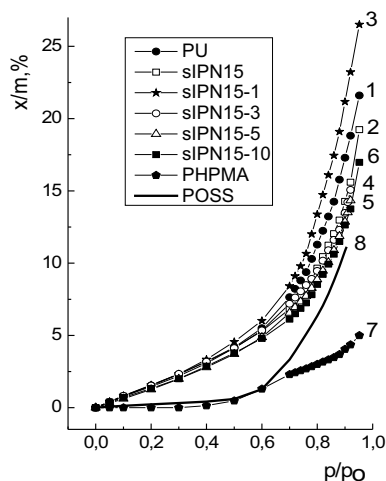
Fig. 14.2 Isotherms of methylene chloride vapor sorption at 25 °C by samples of semi-IPNs and nanocomposites containing hydroxy-POSS: 1—PU; 2—semi-IPNs PU/PHPMA 85/15; 3—semi-IPNs PU/PHPMA 85/15 + 1% hydroxy-POSS; 4—semi-IPNs PU/PHPMA 85/15 + 3% hydroxy-POSS; 5—semi-IPNs PU/PHPMA 85/15 + 5% hydroxy-POSS; 6—semi-IPNs PU/PHPMA 85/15 + 10% hydroxy-POSS; 7—PHPMA; 8—hydroxy-POSS

Figure 14.2 shows the isotherms of methylene chloride vapors sorption by samples of polyurethane, polyhydroxypropyl methacrylate, semi-IPN of composition PU/PHPMA = 85/15, and nanocomposites based on them.

The isotherm of methylene chloride vapor sorption by polyurethane (curve 1) has a typical form for elastomers. It could be seen that the sorption capacity of polyurethane (curve 1) is much higher than the sorption capacity of polyhydroxypropyl methacrylate (curve 7). The sorption of methylene chloride vapor by the PHPMA sample (curve 7) was very low in the region of the relative vapor pressure up to 0.4, then it increases. This behavior is typical for polymers in the glassy state [36]. With increasing relative vapor pressure of methylene chloride, the amount of solvent in the sample reaches a critical value for the transition of PHPMA from glassy to elastic state. From this moment, there is an increase in the sorption of methylene chloride vapors by this polymer.

For semi-IPNs based on PU and PHPMA (curve 2), the sorption capacity of methylene chloride vapor decreases relative to polyurethane. The introduction of nanofiller hydroxy-POSS with the amount of 1% to the matrix of semi-IPNs composition PU/PHPMA = 85/15 leads to an increase in the sorption of methylene chloride vapor, and a further increase in the amount of nanofiller to 3–10 wt% results in a decrease in the sorption capacity of the nanocomposites in comparison with an unfilled semi-IPNs. The latter could indicate the formation of a more dense structure of nanocomposites in comparison with the matrix.

Fig. 14.3 Isotherms of methylene chloride vapor sorption at 25 °C by samples of semi-IPNs and nanocomposites containing hydroxy-POSS: 1—PU; 2—semi-IPNs PU/PHPMA 70/30; 3—semi-IPNs PU/PHPMA 70/30 + 1% hydroxy-POSS; 4—semi-IPNs PU/PHPMA 70/30 + 3% hydroxy-POSS; 5—semi-IPNs PU/PHPMA 70/30 + 5% hydroxy-POSS; 6—semi-IPNs PU/PHPMA 70/30 + 10% hydroxy-POSS; 7—PHPMA; 8—hydroxy-POSS
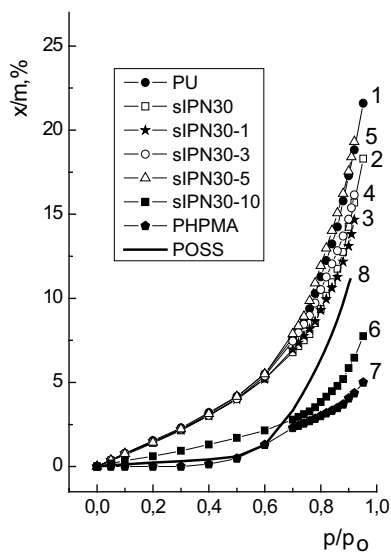

Figure 14.3 shows the isotherms of methylene chloride vapors sorption by samples of polyurethane, polyhydroxypropyl methacrylate, semi-IPNs of composition PU/PHPMA = 70/30, and nanocomposites based on them.

Comparison of the sorption capacity of semi-IPNs PU/PHPMA 85/15 (Fig. 14.2, curve 2) and semi-IPNs PU/PHPMA 70/30 (Fig. 14.3, curve 2) shows that the increasing of PHPMA amount in the system leads to a decrease in sorption of methylene chloride vapors by the samples of semi-IPNs. Unlike semi-IPNs PU/PHPMA 85/15, nanocomposites based on the matrix of semi-IPNs PU/PHPMA 70/30 have a lower sorption capacity at all concentrations of nanofiller hydroxy-POSS (Fig. 14.3).

This is especially refers to the nanocomposite sample, which contains 10% of nanofiller hydroxy-POSS (Fig. 14.3, curve 6), where the sorption capacity is twice lower compared to the nanocomposites containing 1–5% of nanofiller (Fig. 14.3, curves 2–5). This may indicate the formation of a dense package of polymers during formation of this nanocomposite.

Experimental data of the methylene chloride vapor sorption by samples of native polymers, samples of semi-IPNs, and samples of nanocomposites were used to calculate the thermodynamic parameters of polymer mixing during the semi-IPNs formation and the effect of nanofiller on the free energy mixing of polymer components. The calculations were carried out in according to the description in the experimental part (2.2.2).

The change in the partial free energy of methylene chloride $\Delta\mu_1$ was calculated using (14.1).

Fig. 14.4 Free energy of mixing Δg^m of the native polymers and nanocomposites based on the matrix semi-IPNs PU/PHPMA 85/15 with methylene chloride: 1—PU; 2—semi-IPNs PU/PHPMA 85/15; 3—semi-IPNs PU/PHPMA 85/15 + 1% hydroxy-POSS; 4—semi-IPNs PU/PHPMA 85/15 + 3% hydroxy-POSS; 5—semi-IPNs PU/PHPMA 85/15 + 5% hydroxy-POSS; 6—semi-IPNs PU/PHPMA 85/15 + 10% hydroxy-POSS; 7—PHPMA; 8—hydroxy-POSS
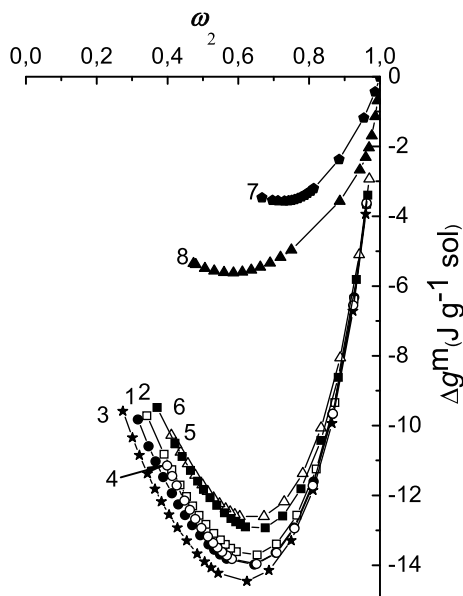
The change in the partial free energy of the individual polymer components and the semi-IPNs during sorption $\Delta \mu_2$ were determined in accordance with Gibbs–Dughem (14.2). The free energy of mixing of individual polymers and semi-IPNs with solvent Δg^m was determined in accordance with (14.4).

Figures 14.4 and 14.5 show the concentration dependences of the calculated values of the average free energy of mixing of solvent Δg^m with individual polymers and semi-IPNs. As could be seen, all systems under investigation: polyurethane—methylene chloride, PHPMA—methylene chloride, semi-IPNs—methylene chloride are thermodynamically stable ($d^2\Delta g^m/\mathrm{d}W_2^2 > 0$).

It is evident that the thermodynamic affinity of methylene chloride to polyurethane is significantly higher (Fig. 14.4, curve 1) than to PHPMA (Fig. 14.4, curve 7). The thermodynamic affinity of methylene chloride to semi-IPNs samples (Fig. 14.4, curve 2, Fig. 14.5, curve 2) increases with increasing amount of polyurethane in the systems. For the nanocomposites, both on the basis of the matrix of semi-IPNs PU/PHPMA 85/15 and on the basis of the matrix of semi-IPNs PU/PHPMA 70/30, with increasing amount of nanofiller, the affinity of methylene chloride to the nanocomposites decreases (Figs. 14.4 and 14.5).

Based on concentration dependences of the calculated values of the average free energy of mixing of solvent Δg^m with individual polymers and semi-IPNs, using the thermodynamic cycles proposed by AA Tager [37], the values of free mixing energy of polymers Δg^x during formation of semi-IPNs were calculated. The calculated data are presented in Table 14.1.

Fig. 14.5 Free energy of
mixing Δg^m of the native
polymers and
nanocomposites based on the
matrix semi-IPNs
PU/PHPMA 70/30 with
methylene chloride: 1—PU;
2—semi-IPNs PU/PHPMA
70/30; 3—semi-IPNs
PU/PHPMA 70/30 + 1%
hydroxy-POSS;
4—semi-IPNs PU/PHPMA
70/30 + 3% hydroxy-POSS;
5—semi-IPNs PU/PHPMA
70/30 + 5% hydroxy-POSS;
6—semi-IPNs PU/PHPMA
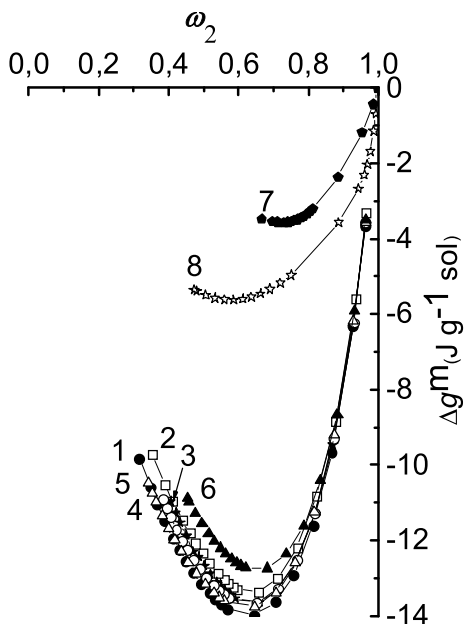70/30 + 10%
hydroxy-POSS;
7—PHPMA;
8—hydroxy-POSS

Table 14.1 demonstrates that the values of free mixing energy Δg^x are positive for both semi-IPNs, which are the matrixes for the nanocomposites (semi-IPNs PU/PHPMA 85/15, semi-IPNs PU/PHPMA 70/30). This means that polymer components polyurethane and polyhydroxypropyl methacrylate are thermodynamically incompatible [38], and synthesized semi-IPNs have a structure with incomplete phase separation, because the phase separation process was stopped at a certain stage due to the formation of a three-dimensional structure [39].

The introduction of hydroxy-POSS into the matrix of semi-IPNs PU/PHPMA 85/15 with the amount of 1–3 wt% leads to a further phase separation between the polymer components of the semi-IPNs (Table 14.1), apparently due to the concentration of hydroxy-POSS particles in the polyurethane component of the systems. Studies by FTIR spectroscopy have shown that the particles of hydroxy-POSS are embedded into the structure of the PU due to chemical binding [17].

A further increase in the amount of hydroxy-POSS in the nanocomposites based on the matrix of semi-IPNs PU/PHPMA 85/15 to 5–10 wt% leads to a change in the sign of the free mixing energy from positive to negative. This means that in the nanocomposites of these concentrations, the hydroxy-POSS play the role of compatibilizer; result is that the hydroxy-POSS leads to thermodynamic compatibility of polyurethane and polyhydroxypropyl methacrylate. This could mean that the particles of hydroxy-POSS at their concentration 5–10 wt% are concentrated not only in the domains of polyurethane but also in the interfacial region of IPNs, and this leads to compatibilization.

Table 14.1 Free mixing energy of polyurethane with polyhydroxypropyl methacrylate during the formation of nanocomposites depending on the content of hydroxy-POSS

Matrix	Amount of hydroxy-POSS, %	Free mixing energy, Δg^x, J/g of polymer
Semi-IPNs PU/PHPMA = 85/15	0	+1.07
Semi-IPNs PU/PHPMA = 85/15	1	+7.62
Semi-IPNs PU/PHPMA = 85/15	3	+0.74
Semi-IPNs PU/PHPMA = 85/15	5	−2.03
Semi-IPNs PU/PHPMA = 85/15	10	−1.58
Semi-IPNs PU/PHPMA = 70/30	0	+4.68
Semi-IPNs PU/PHPMA = 70/30	1	+3.96
Semi-IPNs PU/PHPMA = 70/30	3	+5.29
Semi-IPNs PU/PHPMA = 70/30	5	−7.55
Semi-IPNs PU/PHPMA = 70/30	10	−11.53

This situation is possible in case of that not all particles of hydroxy-POSS are embedded in the structure of polyurethane, and some of them remain as a nanofiller in the system, and they are distributed in the interfacial region of semi-IPNs and in the nanodomains of PHPMA.

As for the semi-IPNs PU/PHPMA 70/30, the PU and PHPMA in this system are more incompatible compared to the semi-IPNs PU/PHPMA 85/15 (Table 14.1). The introduction of hydroxy-POSS particles in the matrix of semi-IPNs PU/PHPMA 70/30 with the amount of 1–3 wt% does not change the situation; the polymer components remain the thermodynamically incompatible. Only the introduction of 5–10 wt.% particles of hydroxy-POSS leads to compatibility in the semi-IPNs; we observe a change in the sign of the free mixing energy from positive to negative (Table 14.1).

14.3.3 Thermal Properties of the Nanocomposites

Thermal properties of the nanocomposites were studied by using dynamic scanning calorimetry (DSC) and thermogravimetric analysis (TGA). It was found that introduction of POSS nanofiller into the matrix results in increased thermal stability of the created nanocomposites. Figure 14.6 shows the DSC scans of the native matrix semi-IPNs PU/PHPMA 85/15 and of the nanocomposites based on this matrix. From the DSC data (second scans), the glass transition temperature (Tg) of the nanocomposite was found to be increased with increasing of POSS content: from Tg = −60.98 °C (native sIPN-15) to Tg = −60.01 °C, Tg = −57.82 °C, Tg = −58.60 °C and Tg = −59.01 °C (sIPN-15-1, sIPN-15-3, sIPN-15-5 and sIPN-15-10, with 1, 3, 5 and 10 wt% of POSS, respectively).

The thermal nature of the nanocomposites was observed by using TGA and presented in Fig. 14.7a, b. The TGA curves for all the samples displayed similar degradation profiles, which suggest that the amount of POSS did not significantly alter the degradation mechanism of the nanocomposites. For all the samples, degradation was observed in two steps, around 280–300 °C and above 380 °C, which is indicative of the soft and hard segments in polyurethane. Maximum values of the thermal decomposition temperatures, $T_{d(\max)}$, defined as the second maximum of the TGA curves for PU/POSS, shift toward higher temperatures with increasing POSS content: from 376 °C for pure PU to 379 °C and 382 °C for PU/POSS with 1 and 10 wt.%, respectively. $T_{d(\max)}$ for semi-IPN-15 shifted to higher values, comparing with PU and PU/POSS: 387.69 °C. However, $T_{d(\max)}$ semi-IPN-15-1 decreases and then, the thermal decomposition temperatures semi-IPN-15-10 increases back to the values of native semi-IPN-15: 387 °C. The initial degradation temperature, T_{onset}, of the nanocomposites shifted to a significantly higher temperature: from 269.98 °C for pure PU to 294.04 °C and 291.39 °C for PU/POSS-1 and PU/POSS-10; and 323.36 °C for semi-IPN-15. When the hydroxy-POSS loading from 1 to 10 wt.% in semi-IPN-15, T_{onset} was decreased to 312.24 °C and 317.73 °C, respectively.

Fig. 14.6 DSC thermograms of the matrix semi-IPNs PU/PHPMA 85/15 (1) and nanocomposites with POSS content 1 (2), 3 (3), 5(4) and 10% (5) under inert atmosphere (N₂) at the heating rate of 20 °C/min
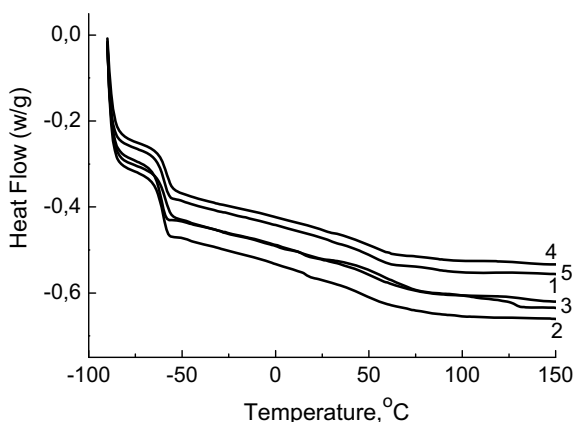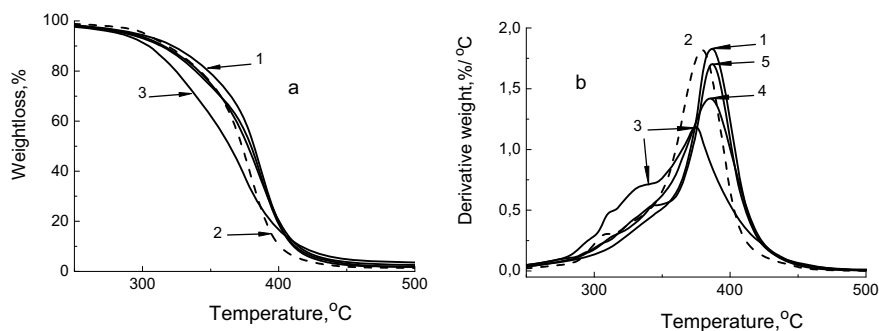
Fig. 14.7   TGA **a**, **b** thermograms of the matrix semi-IPNs PU/PHPMA 85/15 (1) and nanocomposites with POSS content 1 (2), 3 (3), 5 (4) and 10% (5) under inert atmosphere (N_2) at the heating rate of 20 °C/min

Overall, the results of thermal properties investigation of nanocomposite based on PU/POSS and semi-IPNs demonstrate that the obtained nanocomposites are significantly more thermally stable than the native PU network and native semi-IPN-15.

14.3.4   Porosity of Native Matrix and Nanocomposites

In Figs. 14.8 and 14.9, the isotherms of methanol vapors adsorption by samples of semi-IPNs of different composition and POSS-containing nanocomposites based on them are presented. As could be seen, the adsorption isotherms of all samples have the form of curves concave to the abscissa. The maximum value of methanol adsorption for semi-IPN-15 and for the nanocomposites based on them is in the range of 0.75–0.90 mmol/g, and for a series of semi-IPN-30 and for the nanocomposites based on semi-IPN-30, the maximum value of methanol adsorption is slightly higher– in the range of 0.80–0.95 mmol/g. According to the classification of Brunauer, Emmett and Teller (BET) [40], such adsorption isotherms belong to the third type. This means that the BET equation could be applied to the obtained isotherms in the region of low vapor pressures [27].

Therefore, the isotherms were rearranged according to the BET equation. In Fig. 14.10, the following experimental data for matrix of semi-IPN-15 and POSS-containing nanocomposites based on them are presented.

From Fig. 14.10, it is clear that in the region of low relative pressures of methanol vapors, the curves have linear sections. The tangents of the angles of these linear sections and the cutoffs on the *y*-axis allowed to obtain the amount of sorbed substance in the monomolecular layer. Using formulas (14.7, 14.8, 14.9 and 14.10) in Experimental part 2.2.5, the specific surface area, total pore volume, and average pore radius of the synthesized materials were calculated. The results of the calculations are presented in Table 14.2.

Fig. 14.8 Isotherms of
methanol vapor adsorption
by samples of semi-IPN15
and nanocomposites based
on them with different
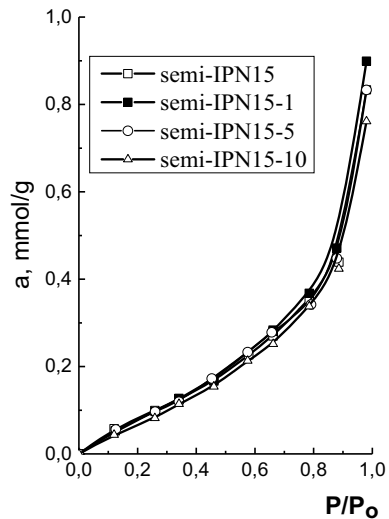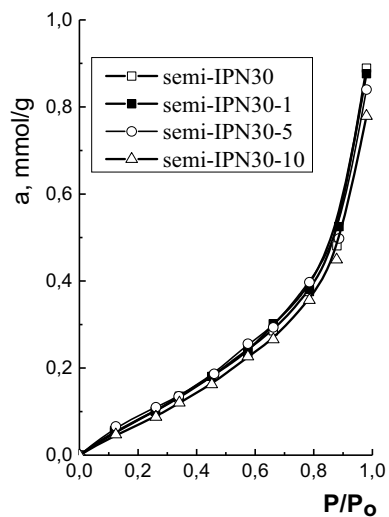content of POSS: 0 (1), 1%
(2), 5% (3)), 10% (4)

Fig. 14.9 Isotherms of
methanol vapor adsorption
by samples of semi-IPN30
and nanocomposites based
on them with different
content of POSS: 0 (1), 1%
(2), 5% (3)), 10% (4)

From the Table 14.2, it could be seen that the specific surface area of the samples
of POSS-containing nanocomposites S_{spec} varies from 10.6 to 13.2 m^2/g. The specific
surface area of the semi-IPNs samples increases with the amount of the linear compo-
nent of the semi-IPN PHPMA from 11.3 to 12.2 m^2/g. With the introduction of POSS
nanoparticles with the amount of 1 wt. %, specific surface area of the nanocompos-
ites increases regardless of the type of semi-IPNs. However, with a further increase
in the amount of POSS in the nanocomposites to 5–10 wt. %, their specific surface
area regularly decreases.

Fig. 14.10 Experimental data on isothermal adsorption of methanol vapors by samples of semi-IPN-15 and nanocomposites based on them with different content of POSS: 0 (1), 1% (2), 5% (3), 10% (4), presented within the BET equation
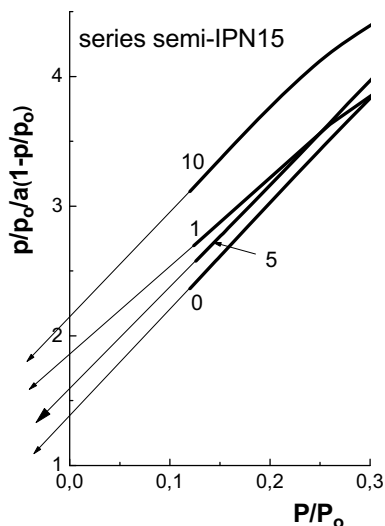
Table 14.2 Specific surface area and porosity of POSS-containing nanocomposites

Sample	a_M, mmol/g	S_{spec}, m^2/g	a_{max}, mol/g	W_0, sm^3/g	r_{av}, Å
Semi-IPN-15	0.10408	11.3	8.34×10^{-4}	3.38×10^{-2}	59.8
Semi-IPN-15-1	0.11726	12.7	8.99×10^{-4}	3.64×10^{-2}	57.3
Semi-IPN-15-5	0.10753	11.7	8.33×10^{-4}	3.38×10^{-2}	57.8
Semi-IPN-15-10	0.09824	10.6	7.62×10^{-4}	3.09×10^{-2}	58.3
Semi-IPN-30	0.11261	12.2	8.89×10^{-4}	3.60×10^{-2}	59.0
Semi-IPN-30-1	0.12225	13.2	8.76×10^{-4}	3.55×10^{-2}	53.8
Semi-IPN-30-5	0.11204	12.1	8.40×10^{-4}	3.40×10^{-2}	56.2
Semi-IPN-30-10	0.10683	11.6	7.79×10^{-4}	3.16×10^{-2}	54.5

According to Table 14.2, the value of the total pore volume W_0 for the matrix of semi-IPN-15 is less in compare with the semi-IPN-30. However, when 1 wt. % of POSS nanoparticles is adding, the total pore volume in the nanocomposite based on semi-IPN-15 increases and in the nanocomposite based on semi-IPN-30 remains almost at the same level as in the matrix. With a further increase in the amount of POSS nanoparticles to 5–10 wt. %, a decrease in the value of the total pore volume in the nanocomposites based on both matrices is observed.

The average pore size r_{av} of the obtained samples was also calculated from the isotherms of methanol vapor adsorption. From the results of calculations given in Table 14.2, it could be seen that the average pore size in the studied samples of POSS-containing nanocomposites ranged from 50 to 60 Å. According to the Dubinin's classification [41], materials with pore size up to 20 Å are microporous, and those with pore size larger than 200 Å are considered as macroporous. According to this

classification, the studied samples with existing pores ranging in size from 20 to 200 Å are the materials with transition pores.

From Table 14.2, it also could be seen that with the introduction of POSS nanoparticles into the semi-IPN matrix, the average pore size is slightly reduced. The essential decrease in the values r_{av} was observed with the introduction of the minimum amount of nanofiller in the semi-IPN-30: from 59 to 54 Å. Obviously, the chemical incorporation of POSS nanoparticles into the PU chain [17] leads to the compaction of the structure of the semi-IPN, which is reflected in the reduction of size of the pores. In this case, the total pore volume is also reduced with the introduction of POSS nanoparticles with the amount of 5–10% in the matrix of semi-IPN-15 and semi-IPN-30.

14.3.5 Morphology of Native Matrix and Nanocomposites

Figure 14.11 shows the SEM cross-sectional images of semi-IPNs (fractured surfaces) based on PU and PHPMA with content of PHPMA 15% (semi-IPN15) (a) and 30% (semi-IPN30) (b).

We could observe that the semi-IPN with 15% PHPMA has the comparatively homogeneous structure. Increasing amount of PHPMA up to 30% results in the changes of semi-IPN's structure. Heterogeneity with size about 50 nm appeared in the structure of the semi-IPN30. These changes are in accordance with thermodynamic investigations (part 3.2) and the DMA measurements [42]: with increasing amount of PHPMA in the system, the phase separation in the semi-IPN became more obvious. It is also in agreement with the degree of polymer component's segregation [42]. This parameter indicates that in semi-IPN with 15% of PHPMA, the phase separation is stopped at an earlier stage, and in the semi-IPN with 30% of PHPMA, the phase separation is more advanced.
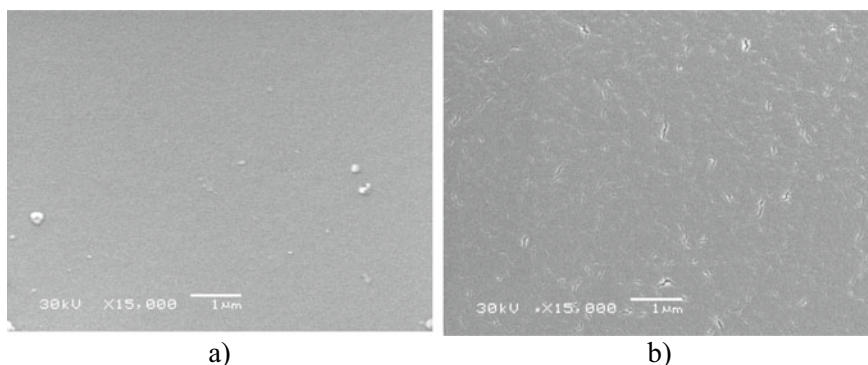

a)   b)

Fig. 14.11 SEM cross-sectional images of neat semi-IPN-15 (**a**) and semi-IPN-30 (**b**) (at magnification of 15,000 times)

From Fig. 14.12, it could be seen that introduction of nanofiller 1,2-propanediolisobutyl-POSS into the matrix with 15% of PHPMA leads to the formation of nano- and microdomains (Fig. 14.12a, b), especially it is more obvious at concentrations of 5 and 10% nanofiller. We could observe the POSS particles aggregation in the form of rectangular nano (Fig. 14.12c) and microdomains (Fig. 14.12d).

Regarding the matrix with 30% of PHPMA, introduction of 1,2-propanediolisobutyl-POSS into the matrix also leads to increasing of materials' heterogeneity (Fig. 14.13a–c). The amount of 1–3% of 1,2-propanediolisobutyl-POSS in the semi-IPN30 results in formation of the nanodomains with size of 50–100 nm. Increasing amount of 1,2-propanediolisobutyl-POSS in the semi-IPN30 up to 5–10% leads to formation of microdomains with size about 1 μm (Fig. 14.13d) and with size of 2–3 μm (Fig. 14.13c).

Obviously, the 1,2-propanediolisobutyl-POSS, introduced into the semi-IPN based on PU and PHPMA on the stage of polyurethane synthesis, acts as nanostructuring agent in the system. As a result, the nanocomposites with more ordered structure are formed so leading to obtaining of materials with improved storage

a)   b)

c)   d)
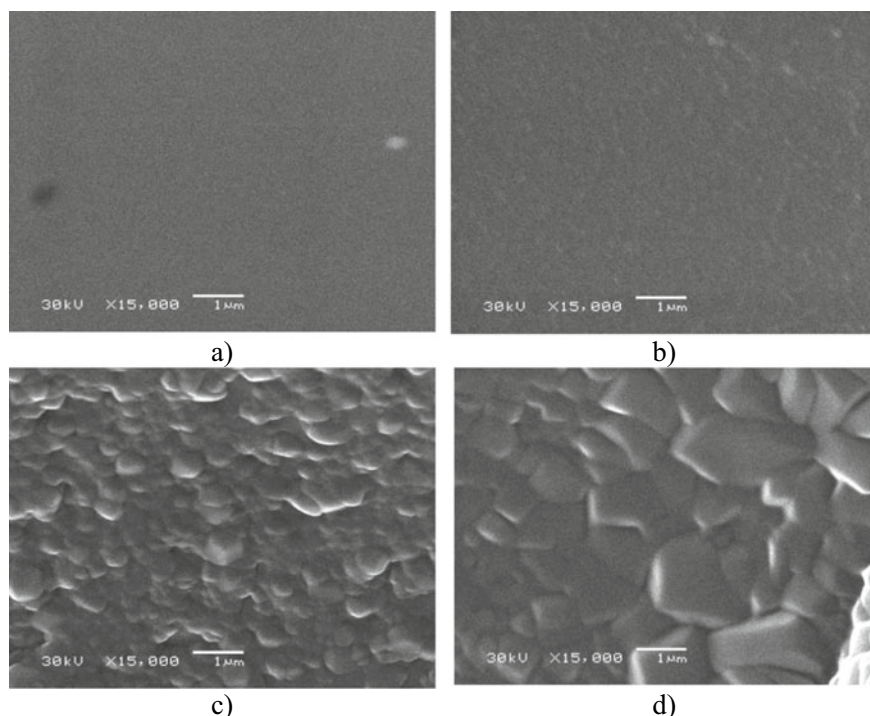
Fig. 14.12 SEM cross-sectional images of semi-IPN-15 nanocomposites with different POSS content: 1% (**a**), 3% (**b**), 5% (**c**), 10% (**d**) (at magnification 15,000 times)
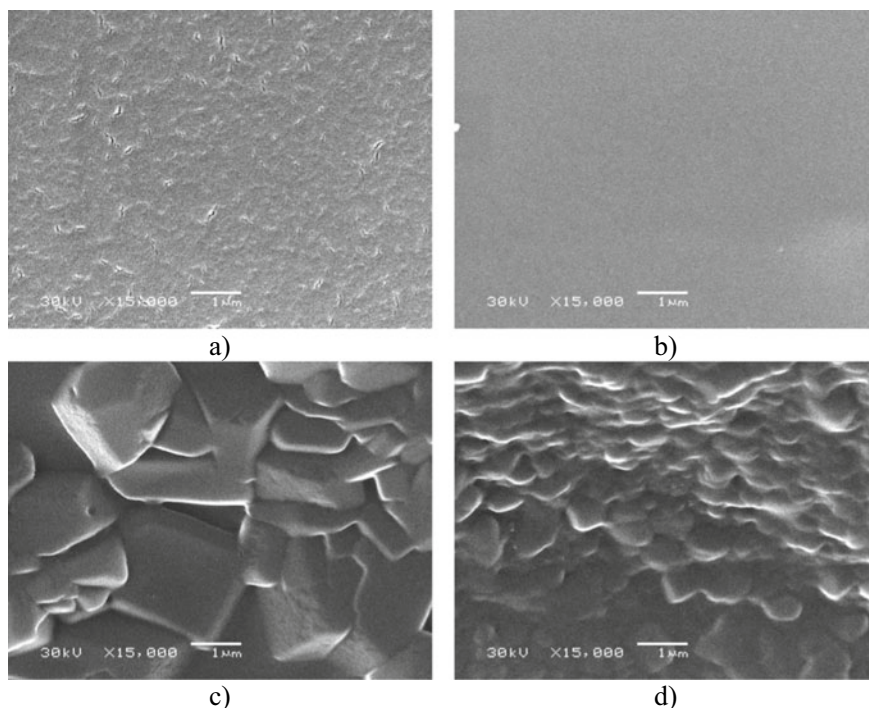
Fig. 14.13 SEM cross-sectional images of semi-IPN-30 nanocomposites with different POSS content: 1% (**a**), 3% (**b**), 5% (**c**), 10% (**d**) (at magnification 15,000 times)

moduli [42]. The increasing of the storage moduli of nanocomposites to 1.5–3 times was found depend on amount of 1,2-propanediolisobutyl-POSS in the systems [42].

Investigation of the nanocomposites by SEM has shown that POSS-diol, introduced into the semi-IPN based on PU and PHPMA on the stage of polyurethane synthesis, acts as nanostructuring agent in the system. As a result, the nanocomposites with more ordered structure are formed so leading to obtaining materials with improved storage moduli.

14.4 Conclusion

A series of nanocomposites based on matrix consisting of polyurethane and poly(hydroxypropyl methacrylate), and 1,2-propanediolisobutyl polyhedral oligomeric silsesquioxanes (1,2-propandiolisobutyl-POSS), used as functionalized nanofiller, have been synthesized. The chemical structures of all samples by FTIR method were investigated. The thermodynamics of polymer-filler interactions in the nanocomposites, the morphology, thermal properties, and porosity of the created

nanocomposites, were studied. FTIR-ATR spectra of the constituents and nanocomposites clearly demonstrated the existence of POSS in the semi-IPN nanocomposites and the POSS content effect on their structure. By thermodynamic investigations, it was shown that the values of free mixing energy of polymer components Δg^x are positive for both semi-IPNs, which are the matrixes for the nanocomposites (semi-IPNs PU/PHPMA 85/15, semi-IPNs PU/PHPMA 70/30). This means that polymer components polyurethane and polyhydroxypropyl methacrylate are thermodynamically incompatible. The introduction of hydroxy-POSS to the matrix of semi-IPNs PU/PHPMA 85/15 with the amount of 1–3 wt% leads to a further phase separation between the polymer components of the semi-IPNs, apparently due to the concentration of hydroxy-POSS particles in the polyurethane component of the systems. A further increase in the amount of hydroxy-POSS in the nanocomposites based on the matrix of semi-IPNs PU/PHPMA 85/15 to 5–10 wt% leads to a change in the sign of the free mixing energy from positive to negative. This means that in the nanocomposites of these concentrations, the hydroxy-POSS play the role of compatibilizer, which leads to thermodynamic compatibility of polyurethane and polyhydroxypropyl methacrylate. This could be in case when the particles of hydroxy-POSS at their concentration 5–10 wt% are concentrated not only in the domains of polyurethane but also in the interfacial region of IPNs, and this leads to compatibilization.

SEM investigations have shown that POSS-diol, introduced into the semi-IPN based on PU and PHPMA on the stage of polyurethane synthesis acts as nanostructuring agent in the system. As a result, the nanocomposites with more ordered structure are formed so leading to obtaining materials with improved storage moduli.

Porosity investigation of the nanocomposites has shown that created materials have the transition pores ranged from 50 to 60 Å and could be used as gas barrier systems.

References

1. Ray SS, Okamoto M (2003) Polymer/layered silicate nanocomposites: a review from preparation to processing. Prog Polym Sci 28(11):1539–1561. https://doi.org/10.1016/j.progpolymsci.2003.08.002
2. Shaffer MSP, Sandler JKW (2006) Carbon nanotube/nanofibre polymer composites. In: Advani SG (ed) Processing and properties of nanocomposites. World Scientific, Singapore
3. Bershtein VA, Gun'ko VM, Karabanova LV, Sukhanova TE, Yakushev PN, Egorova LM, Turova AA, Zarko VI, Pakhlov EM, Vylegzhanina ME, Mikhalovsky SV (2013) Polyurethane-poly(2-hydroxyethyl methacrylate) semi-IPN-nanooxide composites. RSC Adv 3:14560–14570. https://doi.org/10.1039/c3ra40295a
4. Karabanova LV, Bershtein VA, Sukhanova TE, Yakushev PN, Egorova LM, Lutsyk ED, Svyatyna AV, Vylegzhanina ME (2008) 3D diamond-containing nanocomposites based on hybrid polyurethane–poly(2-hydroxyethyl methacrylate) semi-IPNs: composition-nanostructure-segmental dynamics-elastic properties relationships. J Pol Sci B 46(16):1696–1712. https://doi.org/10.1002/polb.21506
5. Moniruzzaman M, Winey KI (2006) Polymer nanocomposites containing carbon nanotubes. Macromolecules 39(16):5194–5205. https://doi.org/10.1021/ma060733p

6. Wolinska-Grabczyk A, Jankowski A (2007) Gas transport properties of segmented polyurethanes varying in the kind of soft segments. Sep Pur Tech 57(3):413–417. https://doi.org/10.1016/j.seppur.2006.03.025

7. Gumenna MA, Shevchuk AV, Klimenko NS, Shevchenko VV (2007) Polyurethanes on the base of polyhedral oligosilsesquioxanes (POSS). Polym J 29(3):177–185 [in Russian]

8. Karabanova LV, Whitby RLD, Bershtein VA, Korobeinyk AV, Yakushev PN, Bondaruk OM, Lloyd AW, Mikhalovsky SV (2013) The role of interfacial chemistry and interactions in the dynamics of thermosetting polyurethane-multi-walled carbon nanotube composites with low filler content. Colloid Polym Sci 291(3):573–583. https://doi.org/10.1007/s00396-012-2745-4

9. Karabanova LV, Whitby RL, Bershtein VA, Korobeinyk AV, Yakushev PN, Bondaruk OM, Lloyd AW, Mikhalovsky SV (2012) Microstructure changes of polyurethane by inclusion of chemically modified carbon nanotubes at low filler contents. Comp Sci Tech 72(8):865–872. https://doi.org/10.1016/j.compscitech.2012.02.008

10. Madhavan K, Reddy BSR (2009) Structure–gas transport property relationships of poly(dimethylsiloxane–urethane) nanocomposite membranes. J Mem Sci 342(1–2):291–299. https://doi.org/10.1016/j.memsci.2009.07.002

11. Fomenko AA, Gomza YuP, Klepko VV, Gumenna MA, Klimenko NS, Shevchenko VV (2009) Dielectric properties, conductivity and structure of urethane composites based on polyethylene glycol and polyhedral silsesquioxane. Polym J 31(2):137–143 [in Ukrainian]

12. Mahapatra SS, Yadav SK, Cho JW (2012) Nanostructured hyperbranched polyurethane elastomer hybrids that incorporate polyhedral oligosilsesquioxane. React Funct Polym 72(4):227–232. https://doi.org/10.1016/j.reactfunctpolym.2012.02.001

13. Lewicki JP, Pielichowski K, Jancia M, Hebda E, Albo RLF, Maxwell RS (2014) Degradative and morphological characterization of POSS modified nanohybrid polyurethane elastomers. Polym Degrad Stab 104:50–56. https://doi.org/10.1016/j.polymdegradstab.2014.03.025

14. Wei K, Wang L, Zheng S (2013) Organic–inorganic polyurethanes with 3, 13-dihydroxypropyloctaphenyl double-decker silsesquioxane chain extender. Polym Chem 4:1491–1501. https://doi.org/10.1039/c2py20930f

15. Bourbigot S, Turf T, Bellayer S, Duquesne S (2009) Polyhedral oligomeric silsesquioxane as flame retardant for thermoplastic polyurethane. Polym Degrad Stab 94:1230–1237. https://doi.org/10.1016/j.polymdegradstab.2009.04.016

16. Huang J, Jiang P, Li X, Huang Y (2016) Synthesis and characterization of sustainable polyurethane based on epoxy soybean oil and modified by double-decker silsesquioxane. J Mater Sci 51(5):2443–2452. https://doi.org/10.1007/s10853-015-9557-0

17. Karabanova LV, Honcharova LA, Sapsay VI, Klymchuk DO (2016) Synthesis, morphology and thermal properties of the POSS-containing polyurethane nanocomposites. Chem Phys Tech Surf 7(4):413–420. https://doi.org/10.15407/hftp07.04.413

18. Karabanova LV, Honcharova LA, Shtompel VI (2020) Structure and properties of the POSS-containing nanocomposites based on polyurethane matrix. In: Nanomaterials and nanocomposites, nanostructure, surfaces, and their applications. Springer Proceedings in Physics, vol. 246, pp. 485–505. https://doi.org/10.1007/978-3-030-51905-6_34

19. Wang W, Guo Y, Otaigbe JU (2009) The synthesis, characterization and biocompatibility of poly(ester urethane)/polyhedral oligomeric silesquioxane nanocomposites. Polymer 50(24):5749–5757. https://doi.org/10.1016/j.polymer.2009.05.037

20. Lai YS, Tsai CW, Yang HW, Wang GP, Wu KH (2009) Structural and electrochemical properties of polyurethanes/polyhedral oligomeric silsesquioxanes (PU/POSS) hybrid coatings on aluminum alloys. Mater Chem Phys 117(1):91–98. https://doi.org/10.1016/j.matchemphys.2009.05.006

21. Huitron-Rattinger E, Ishida K, Romo-Uribe A, Mather PT (2013) Thermally modulated nanostructure of poly(ε–caprolactone)–POSS multiblock thermoplastic polyurethanes. Polymer 54(13):3350–3362. https://doi.org/10.1016/j.polymer.2013.04.015

22. Lipatov YS et al (1995) Polymer reinforcement. ChemTech, Toronto. ISBN-10: 1895198089, ISBN-13: 978-1895198089

23. Lipatov YS, Karabanova LV (1994) Gradient interpenetrating polymer networks. In: Advances in interpenetrating polymer networks. Technomic, Lancaster, PA, vol. 4, pp 191–212. ISBN-10: 0877627088, ISBN-13: 978-0877627081

24. Karabanova LV, Sergeeva LM, Boiteux G (2001) Filler effect on formation and properties of reinforced interpenetrating polymer networks. Compos Interfaces 8(3–4):207–219. https://doi.org/10.1163/15685540152594677

25. Karabanova LV, Gomza YuP, Nesin SD, Bondaruk OM, Voronin EP, Nosach LV (2016) Nanocomposites based on multicomponent polymer matrices and nanofiller densil for biomedical application. In: Nanophysics, nanophotonics, surface studies and application. Springer Proceedings in Physics, vol. 183, pp. 451–475. https://doi.org/10.1007/978-3-319-30737-4_38

26. Karabanova LV, Bershtein VA, Gomza YuP, Kirilenko DA, Nesin SD, Yakushev PN (2016) Nanostructure, dynamics, and mechanical properties of nanocomposites based on polyurethane-poly(2-hydroxyethyl methacrylate) semi-interpenetrating polymer network with ultra-low MWCNT contents. Polym Compos 39(1):263–273. https://doi.org/10.1002/pc.23926

27. Gregg SJ, Sing KS (1970) Adsorption, specific surface area, porosity. Mir, Moscow, p. 408 [in Russian]

28. Bellamy LJ (1980) The infrared spectra of complex molecules, v. II. In: Advances in infrared group frequencies, 2nd edn. Chapman and Hall, London, pp 1–299. https://trove.nla.gov.au/version/12064222

29. Mattia J, Painter P (2007) A comparison of hydrogen bonding and order in a polyurethane and poly(urethane-urea) and their blends with poly(ethylene glycol). Macromolecules 40(5):1546–1554. https://doi.org/10.1021/ma0626362

30. Wamke A, Dopierała R, Prochaska K, Maciejewski H, Biadasz A, Dudkowiak A (2015) Characterization of Langmuir monolayer, Langmuir-Blodgett and Langmuir-Schaefer films formed by POSS compounds. Col Surf A 464:110–120. https://doi.org/10.1016/j.colsurfa.2014.10.022

31. Xue M, Zhang X, Wu Z, Wang H, Ding X, Tian X (2013) Preparation and flame retardancy of polyurethane/POSS nanocomposites. Chin J Chem Phys 26(4):445–450. https://doi.org/10.1063/1674-0068/26/04/445-450

32. Chang Z, Zhang M, Hudson AG, Orler EB, Moore RB, Wilkes GL, Turner SR (2013) Synthesis and properties of segmented polyurethanes with triptycene units in the hard segment. Polymer 54(26):6910–6917. https://doi.org/10.1016/j.polymer.2013.10.02

33. Pielichowski K, Njuguna J, Janowski B, Pielichowski J (2006) Polyhedral oligomeric silsesquioxanes (POSS)-containing nanohybrid polymers. Adv Polym Sci 201(1):225–296. https://doi.org/10.1007/12_077

34. Karabanova LV, Lloyd AW, Mikhalovsky SV, Helias M, Philips GJ, Rose SF, Mikhalovska L, Boiteux G, Sergeeva LM, Lutsyk ED, Svyatyna A (2006) Polyurethane/poly(hydroxyethyl methacrylate) semi-interpenetrating polymer networks for biomedical applications. J Mater Sci: Mater Med 17(12):1283–1296. https://doi.org/10.1007/s10856-006-0603-y

35. Karabanova LV, Gorbach LA, Skiba SI (1991) Thermodynamic study of interactions in filled interpenetrating networks. Kompozitsionnyye polimernyye materialy 49:35–39 [in Russian]

36. Tager AA (1978) Physicochemistry of polymers. Moscow, Khimiya, p. 544 [in Russian]

37. Tager AA (1972) Thermodynamic stability of polymer–solvent and polymer–polymer systems. Visokomol Soed Ser A 14(12):2690–2698 [in Russian]

38. Tager AA (1977) Thermodynamics of polymer mixing and thermodynamic stability of polymer compositions. Visokomol Soed Ser A 19(7):1659–1669 [in Russian]

39. Karabanova LV (2012) Phase processes in semi-IPN of sequential curing. In: Phase processes in heterogeneous polymer systems. Naukova dumka, Kyiv, pp. 297–329 [in Russian]

40. Brunauer S, Emmett PH, Teller E (1938) Adsorption of gases in multimolecular layers. JACS 60(2):309–319. https://doi.org/10.1021/ja01269a023

41. Dubinin MM (1960) The potential theory of adsorbtion of gases and vapors for adsorbents with energetically nonuniform surfaces. Chem Rev 60(2):235–241

42. Karabanova LV, Honcharova LA, Babkina NV, Sapsay VI, Klymchuk VO (2018) Poss-containing nanocomposites based on polyurethane/poly(hydroxypropyl methacrylate) polymer matrix: dynamic mechanical properties and morphology. Polym Testing 69:556–562

Chapter 15
Iron Oxide Nanomaterials for Bacterial Inactivation and Biomedical Applications

Tetiana Tatarchuk, Ostap Olkhovyy, Ivanna Lapchuk, and Roman Dmytryshyn

15.1 Introduction

In recent years, more and more attention is being paid to the development of various synthesis methods of magnetic nanostructures and the study of their physicochemical properties. The use of nanomaterials with magnetic properties in medicine and pharmacology is a priority area of research, which allows to solve current problems related to the diagnosis and treatment of various diseases, including cancer. The use of magnetic nanoparticles simplifies the detection of affected areas of the tissue at an early stage, targeted drug delivery, as well as the therapy of pathological areas with the latest promising techniques.

Among the many magnetic nanoparticles obtained today, oxide nanoparticles are of particular interest to medicine, due to having stable magnetic properties, being more resistant to oxidation than metal nanoparticles, and having low toxicity. Modified by various functional groups, magnetic oxide nanoparticles are used in medicine as carriers of biologically active and medicinal substances, as contrast materials for

T. Tatarchuk · I. Lapchuk (✉)
Department of Chemistry, Vasyl Stefanyk Precarpathian National University,
Ivano-Frankivsk 76018, Ukraine
e-mail: ivannalapchyk@gmail.com

T. Tatarchuk
Faculty of Chemistry, Jagiellonian University, 30-387 Kraków, Poland

O. Olkhovyy
Faculty of Pharmacy, Jagiellonian University Medical College, Medyczna, 9, 30-688 Kraków, Poland

R. Dmytryshyn
Faculty of Mathematics and Computer Science, Vasyl Stefanyk Precarpathian National University, 57 Shevchenko Street, Ivano-Frankivsk 76018, Ukraine
e-mail: roman.dmytryshyn@pnu.edu.ua

magnetic resonance imaging, as biosensors, as media for targeted delivery. Additionally, magnetic nanoparticles have been used in thermal therapy (magnetic hyperthermia), which involves heating with ultrahigh-frequency radiation to the temperatures, in which the cancer-affected tissue is destroyed, in combination with a magnetic field that delivers the particles to the pathological area of the body.

For the application of magnetic nanoparticles in medicine, it is important to choose a synthesis method that will provide small particles, with a narrow size distribution, high magnetic characteristics, stable composition, and physical parameters, the particles must be biodegradable or excreted to avoid accumulation in excess.

Infectious diseases spread quickly and easily in the environment. Microbiological organisms have different ways of spreading, water in particular. Every year the demand for water consumption increases, so purified water is currently sought after. Economic constraints and poor water bodies' treatment from microbiological contaminants such as bacteria and viruses are the cause of the rapid spread of infectious agents. Thus, the presence of pathogenic organisms in the water becomes a threat to the environment and the population [1].

There is a wide range of materials that exhibit antimicrobial properties. For example, such substances as silver and copper are the most studied for the inactivation of biological microorganisms [2]. ZnO [3], TiO_2 [4], Al_2O_3 [5], and CuO [6] oxides also play an important role in treating water bodies, as well as various surfaces [7]. However, the abovementioned materials, in addition to having high biocidal activity, can be somewhat toxic, which is their main disadvantage. Iron is one of the most common elements on Earth. Due to this, and also low toxicity, Fe has recently been the subject of active research, in particular its antibacterial properties [7–9].

Iron oxide nanoparticles at the highest concentration of 3 mg/ml inhibited bacterial cells of *Staphylococcus aureus* in the water [10]. Cell destruction occurred within 4, 12 and 24 h, according to the results of the analysis to determine live/dead bacteria. Fernández et al. [11] showed high inhibition efficiency of bacteria at neutral pH value, which is the main advantage for industrial applications in wastewater treatment. They evaluated the use of magnetite with an additional coating for the destruction of *Escherichia coli* bacteria. PEI (polyethyleneimine) coating reduced the negative charge of Fe_3O_4, thereby improving the adsorption of *E. coli* cells (gram-negative bacteria). Effective magnetic photocatalyst based on iron, Fe@Al-ZnO, after 5 h interaction with bacteria and visible irradiation showed inactivation of *E. coli* in the amount of 7-log (dose of nanocomposite was equal to 40 mg). High stability and resilience of the material was confirmed after photocatalysis, allowing multiple use of Fe@Al-ZnO for water disinfection [11]. An additional advantage is the magnetism of Fe-based materials, which simplifies the technological conditions in use.

As a result, iron oxides are particularly interesting due to their antibacterial properties as well as a variety of applications in medicine.

15.2   Bacterial Inactivation with Iron Oxides

Iron is known as one of the most common elements on Earth. It is an essential component for the functioning of hemoglobin, and is also a cofactor of enzymes [7]. However, it has recently become known that Fe nanoparticles; namely, iron oxides (Fe_3O_4 magnetite, Fe_2O_3 hematite) are good biocidal materials. The antibacterial properties of such compounds are caused by the damage to the bacterial DNA, as well as the destruction of such structural materials as proteins, lipids, polysaccharides. Inactivation of microorganisms can occur due to the Fenton reaction, which leads to the generation of radicals with strong oxidizing ability [7]. Usually, the antimicrobial ability of Fe-containing materials is related to the morphology of nanoparticles, size, shape and depends on other physicochemical properties [7, 9]. Nanosize of the particles is an advantage in inhibiting bacterial cells, and it facilitates the material to penetrate the cell walls of bacteria, causing it to break down and leak cell contents.

Hematite nanoparticles have proven to possess a better antibacterial ability in inhibiting gram-positive bacteria *S. aureus,* compared to the destruction of gram-negative *E. coli* bacteria [12]. The authors also note that this trend is due to the fact that the surface of *E. coli* is hard and negatively charged.

In order to improve the reusability of nanocomposite based on iron oxide and carbon nanotubes [1], washing with $CaCl_2$ and distilled water takes place. Such method improved the productivity of the material in subsequent cycles of inactivation of *E. coli* bacteria. The effect of the nanocomposite on the structure of bacterial cells is demonstrated by scanning electron microscopy (Fig. 15.1). It is noted that the inactivation of *E. coli* was significantly dependent on the oxidative stress.

γ-Fe_2O_3 maghemite with a particle size of 10 nm was investigated in vitro and in vivo [13]. Maghemite nanoparticles have shown an effective result in vitro with human endothelial cells. Despite γ-Fe_2O_3 can be rapidly eliminated from the body, the toxicity is still observed in organs such as the kidneys, liver, and lungs, so further clinical studies need to address low toxicity issues. Bhushan et al. [14] obtained α-Fe_2O_3/Co_3O_4 nanocomposites, which damaged bacterial cells of *Bacillus subtilis*, *Salmonella typhi*, *S. aureus,* and *E. coli* and at the same time had high biocompatibility and non-toxicity toward MCF7 cells.

15.2.1   *The Effect of the Synthesis Method on the Antibacterial Properties of Iron Oxides*

Various types of nanomaterials, as well as the iron oxide nanoparticles can be obtained via following methods: sol-gel, co-precipitation, electrochemical method, hydrothermal method, "green" method, sonochemical method [7, 15]. To improve the biocidal properties, Fe oxides can be modified with additional compounds [1, 9, 11]. As an example, a nanocomposite of iron and cobalt oxides was obtained by co-precipitation [14]. Inactivation of pathogenic strains of *B. subtilis*,
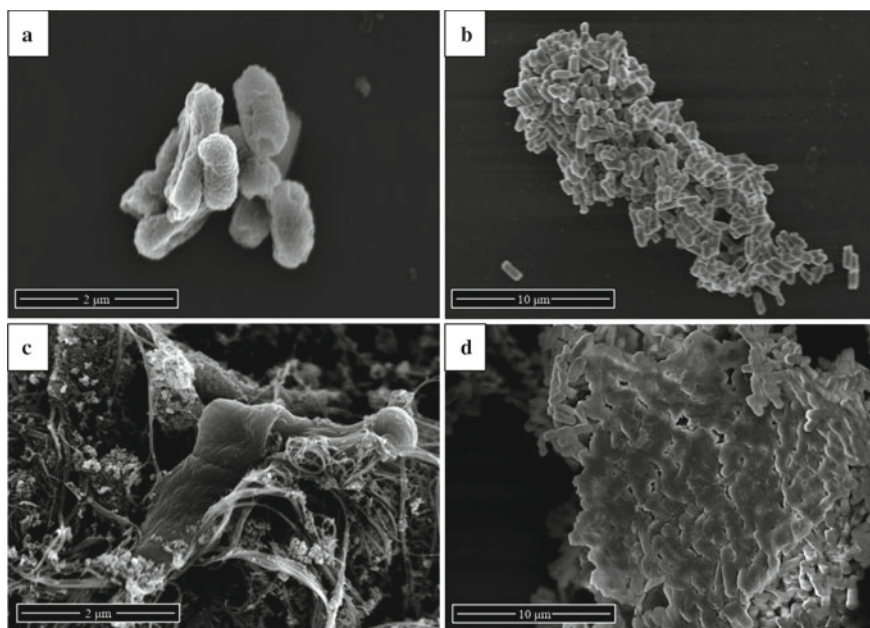
Fig. 15.1 SEM of *E. coli* cells before (**a**, **b**) and after (**c**, **d**) being subject to the nanocomposite material (Reprinted from [1], with permission from Royal Society of Chemistry)

S. typhi, S. aureus, E. coli is observed due to the synergistic action of α-Fe$_2$O$_3$ and Co$_3$O$_4$. In contrast, these oxides showed weaker antibacterial properties separately.

Sathishkumar et al. [16] synthesized nanoparticles of Fe$_3$O$_4$ magnetite using an extract of C. guianensis (CGFE). Nanoparticles obtained by the "green" method expressed strong biocidal activity against *E. coli, S. typhi, K. renumoniae, S. aureus*. However, in vitro they demonstrate cytotoxicity at a dose of 44.5 mg·ml^{-1} against HepG2 cells. Fe$_3$O$_4$, synthesized via low-temperature method from ferric chloride and sulfate, had the ability to damage and destroy *P. aeruginosa, Serratia marcescens, E. coli,* and *Listeria monocytogenes* [17]. Magnetite suppressed the biofilm of bacteria up to 88%. The minimum inhibitory concentrations were 128 μg/ml, 64 μg/ml, and 32 μg/ml for *P. aeruginosa, E. coli,* and *S. marcescens*, respectively.

15.2.2 Iron Oxides and Their Bacterial Inactivation Mechanism

According to the literature, the main mechanism of bacterial inactivation is the generation of reactive oxygen species (ROS) [1, 9]. The action of reactive oxygen species is to damage DNA, proteins, and lipids, which are destroyed due to the oxidative stress. Magnetite with chitosan molecules as a coating exhibited significantly higher

antibacterial properties than sole Fe_3O_4 [9]. The coating provided a positive surface potential of the material (p-IONP), which was used for 100% bacterial inactivation (magnetite concentration was 50 μM). Fluorescence analysis demonstrates the difference between n-IONP (with a negative surface potential) and p-IONP during the destruction of bacteria (Fig. 15.2a and b). The authors indicated that the chitosan coating increased the production of reactive oxygen species, which provided a high biocidality of the magnetic material (Fig. 15.2c and d).

Oxidative stress was also observed by Behera et al. [18]. The generation of ROS, namely radicals O^{2-}, OH^-, and $^1O_2$, damages the proteins and DNA of bacteria. In this case, iron oxide nanoparticles inhibited six gram-positive and four gram-negative bacteria. Hematite showed good inhibitory activity against
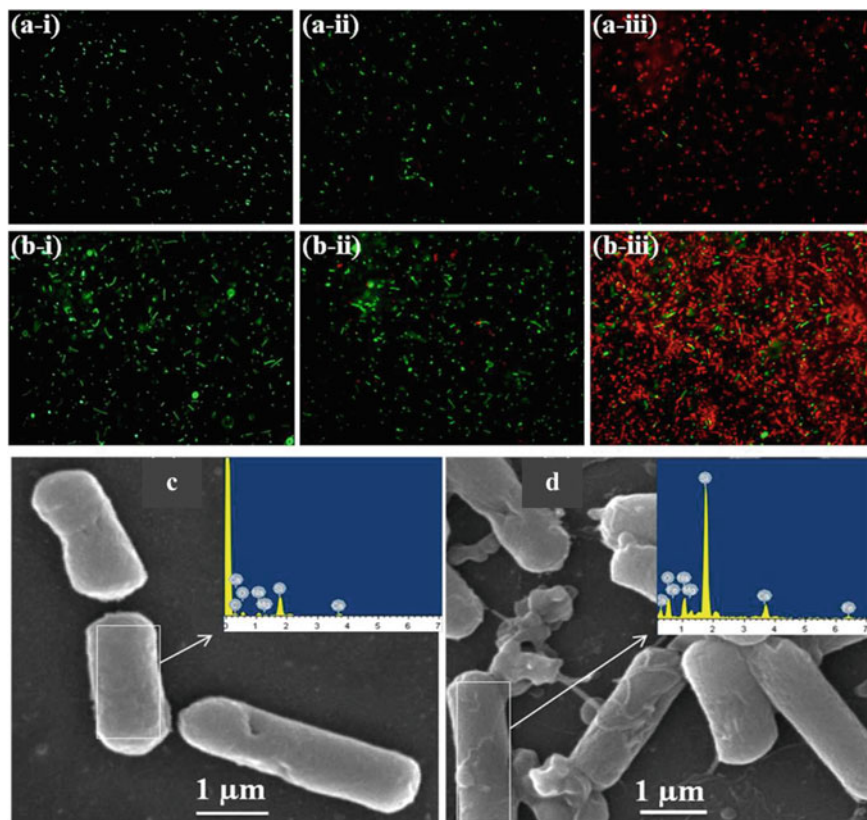
Fig. 15.2 Fluorescent microscopy of *B. subtilis* (**a-i**) in the presence of 50 μM of iron oxide nanoparticles with negative surface potential (n-IONP) (**a-ii**) and 50 μM of nanoparticles with positive surface potential (p-IONP) (**a-iii**); *E. coli* (**b-i**) subjected to 50 μM of n-IONP (**b-ii**) and 50 μM of p-IONP (**b-iii**); SEM of deformations of *B. subtilis* membranes before (**c**) and after (**d**) treatment with p-IONP, as well as the EDX spectra of the surface of bacterial cells (Reprinted from [9], with permission from Springer Nature)

S. aureus, P. vulgaris, P. aeruginosa pathogens [19]. Measurement of reactive oxygen species proved the destruction of mitochondrial membranes of *S. aureus*, which confirms effective bactericidal action of iron oxide. The effect of magnetite nanoparticles on *S. aureus* damaged the cell walls of bacteria, as per scanning electron microscopy [20]. There are also known cases when iron oxides, due to their nanosize, penetrated and destroyed the cell walls of microbes, which led to their death.

15.3 Iron Oxides as Drug Carriers

15.3.1 The Use of Iron Oxides in Medicine

Magnetic nanoparticles are known to bind pathogenic substances on the surface, most importantly those of high molecular weight that are poorly eliminated by classical blood purification techniques, such as hemodialysis (Fig. 15.3) [21], and remove them from blood by magnetic separation. A wide range of compounds, including heavy metal ions (cadmium [22], lead [23–25], uranyl [26], drugs (digoxin [24, 25, 27], diazepam [28], proteins (cytokines [24, 27]), and bacteria [29]) had been efficiently removed from blood over the years. However, because of arguable and limited applicability of the nanoparticles due to the need of pathogen-specific capturing agents, a safe and fast alternative to in vivo administration of MNPs without accumulation in the organism was proposed. Extracorporeal magnetic separation-based blood purification may be used for selective rapid removal of toxic compounds from blood, once it is confirmed to be efficient and lack safety issues [30].

Fe$_3$O$_4$ magnetic nanoparticles (MNPs) were synthesized using Massart procedure, coated with polyethyleneimine (PEI), polystyrene sulfonate (PSS), polyethylene glycol (PEG) [31], and loaded with doxorubicin (DOX) [31]. The release study
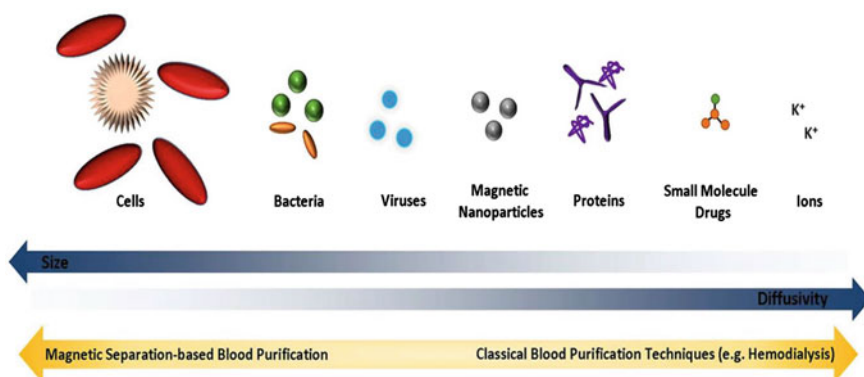
Fig. 15.3 Size and diffusivity of various biologically relevant target compounds for blood purification (Reprinted from [30], with permission from Springer Nature)

of DOX is examined in three conditions: at 37 °C (healthy body temperature), at 42 °C in a thermostatic bath, and at 42° with simultaneous hyperthermia and states that the results are similar in three situations. Therefore, this polymer-coated system is suitable for cancer treatment due to extended DOX release with simultaneous hyperthermia [32].

In the article by Zou et al. [31] mesoporous magnetic nanoparticles (MMNP) were prepared using solvothermal method, loaded with doxorubicin (DOX) using incubation method and coated with chitosan. Drug release study of DOX from chitosan-coated mesoporous magnetic nanoparticles (CMMNP) was performed in two media: phosphate buffered saline (PBS) at pH 7.4 and acetate buffered saline (ABS) at pH 5.5. It was observed that drug release is most efficient in ABS (~100% over 48 h) than in PBS (~60% over 48 h). This explains the fact that DOX has better solubility in acidic medium. Cytotoxicity of DOX and DOX-CMMNP in MCF-7 breast cancer cells was evaluated based on methyl thiazolyl tetrazolium (MTT) assay, resulting in a superior cytotoxic effect of the latter compared to free DOX, due to polymer coating of MNPs. Appliance of alternating current magnetic field (ACMF) improves synergistic effect of both free DOX and DOX-CMMNP over the time of exposure. To sum up, modification of MNPs through polymer coating has great potential for breast cancer treatment, possessing such advantages as prevention from premature release of the drug, high loading capacity, lack of toxicity, excellent biocompatibility with high cell viability, biodegradability [33].

15.3.2 The Use of Magnetic Materials for Drug Delivery

Superparamagnetic iron oxide nanoparticles (SPIONs) have a wide range of biomedical applications due to their great biocompatibility and biodegradability [34]. In order to improve magnetic properties, such as molecular imaging, iron oxides enhanced with metal (Mn^{2+}, Fe^{2+}, Co^{2+} or Ni^{2+}) have been synthesized with following compositions: $MnFe_2O_4$, $FeFe_2O_4$, $CoFe_2O_4$, $NiFe_2O_4$, providing higher magnetic susceptibility than magnetite NPs [35]. Coating with polymer prevents nanoparticle agglomeration. For in vivo applications, such polymers as polysaccharide dextran, which forms dextran-coated iron oxide nanoparticles also known as monocrystalline iron oxide nanoparticles (MION) [36] or polyethylene glycol (PEG), which increases time of circulation of NPs in blood [37], are used.

Feng et al. [38] reported that drug-loaded magnetic Janus particles (DMJPs) consisting of three compartments containing Paclitaxel (for cancer cells apoptosis), rhodamine B (for fluorescent tracing), and Fe_3O_4 nanoparticles (for DMJPs guidance) were synthesized using electrohydrodynamic (EHD) technique, with poly(lactic-co-glycolic acid) (PLGA) being the substrate due to its good biocompatibility and degradability. The morphology of the DMJPs was characterized by scanning electron microscope (SEM) (Fig. 15.4a), which shows DMJPs as spherical shapes with the diameters of 3.7–4.2 μm, prepared at the concentration of ~6 wt% of PLGA solution. Paclitaxel release studies were performed in the phosphate-buffered saline

(PBS) solution as a medium, and the peak area of paclitaxel was confirmed using high-performance liquid chromatography (HPLC). The DMJPs were selected at a certain ratio of paclitaxel: PLGA = 1:5, due to their sufficiently high drug-loading efficiency (DE%) and reasonable encapsulation efficiency (EE%). Release curve of DMJPs was examined in two media: (1) PBS and (2) Tween-80(0.1%)/PBS (Fig. 15.4b). The release of paclitaxel from DMJPs was faster in Tween-80/PBS solution (71%) than that of paclitaxel in PBS solution (61%) over the course of 32 days. The anti-cancer effect of DMJPs was observed, indicating a significant inhibitory effect on cell growth of MDA-MB-231. Magnetic field application enables the DMJPs to be delivered quickly and accurately to the desired location, allowing DMJPs to achieve an efficient anticancer effect through adherence and aggregation onto cellular surface in large quantities (Fig. 15.4c). In conclusion, suggested multifunctional drug delivery system of PLGA drug-loaded Janus particles may offer a safer, more accurate, and controllable alternative for cancer treatment compared with traditional chemotherapy drugs.

In a study performed by Gautier et al. [39], DOX-loaded PEGylated SPIONs (DLPS) were prepared by synthesizing superparamagnetic iron oxide nanoparticles (SPIONs), coating them with activated polyethylene glycol (aPEG) [40] and finally loading them with doxorubicin (DOX) [41]. DLPS turn out to be compatible with in vivo administration due to their physical and chemical characteristics, such as small size, neutral pH of the surface and good colloidal stability [42]. Furthermore, process of PEGylation of nanoparticles preserves cytotoxicity of the drug. In conclusion, PEG
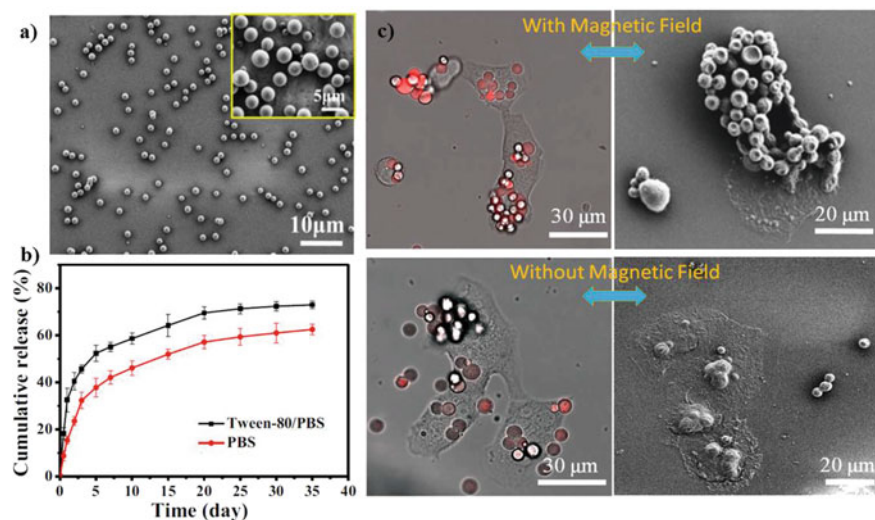
Fig. 15.4 a SEM images of the DMJPs; **b** Release curve of DMJPs in PBS and Tween-80/PBS media; **c** Fluorescence and SEM images of the cancer cells and DMJPs before and after magnetic field application (Reprinted from [38], with permission from Elsevier)

coating of nanoparticles has an important effect on drug loading and release, as well as on the distribution of nanoparticles into the cell.

L-cysteine-coated $CoFe_2O_4$ nanoparticles were synthesized by ultrasonic-assisted chemical co-precipitation method. In vitro cytotoxicity on HeLa cells was investigated using methyl thiazolyl tetrazolium (MTT) assays, resulting in slight cytotoxicity at a high concentration over 24 h incubation period. The drug release study of doxorubicin (DOX) from Lys-$CoFe_2O_4$ was performed in acidic (pH 4.0) and neutral (pH 7.4) media. The results show sensitivity to pH, reducing drug loss in the blood circulation due to lower release rate at pH 7.4, while also enabling active release of the drug on cancerous tissues at pH 4.0, which is highly beneficial for using Lys-$CoFe_2O_4$ as anti-cancer drug carriers [43].

Nano-sized magnetic graphene oxide (mGO) was prepared using chemical co-precipitation of Fe_3O_4 magnetic nanoparticles (MNPs) on GO nano-platelets, modified with chitosan (mGOC) and polyethylene glycol (PEG) in order to achieve non-toxic, biocompatible mGOC-PEG which prolongs circulation of the drug in the blood [44]. U87 human glioblastoma cells were used to determine drug release of doxorubicin (DOX) loaded onto mGOC-PEG. Drug release experiment was performed at pH 7.4 (physiological medium) and pH 5.4 (acidic pH of cancer cells), and showed that the release rate of drug at pH 5.4 is higher than at pH 7.4. In vitro cytotoxicity study confirmed that magnetic targeting can be used to enhance toxic effect on U87 cancer cells, which proves mGOC-PEG nanocarriers to be efficient for in vivo drug delivery in cancer treatment.

Superparamagnetic iron oxide nanoparticles (SPIONs) were synthesized and coated with chitosan [45], placed on the surface of previously synthesized graphene oxide (GO) sheets [46] and coated with polyvinyl alcohol (PVA) as the final step to obtain PVA-SPION-GO nanocomposite [47]. To evaluate drug loading, 5-Fluorouracil (5-Fu) was added to the nanocomposite. The drug loading showed the result of 35.91% and drug entrapment efficiency was 88.9%, which confirmed that PVA-SPION-GO can be used as carriers of the drug. The release study showed that release of 5-Fu from PVA-SPION-GO nanocomposite is pH-dependent, with 91.1% of drug released in pH 5.8 and 80.6% in pH 7.4. In conclusion, because of a large specific surface area and many functional groups, GO has a potential for wide biomedical applications, such as imaging and drug delivery [48].

Magnetic Fe-based nanofluid was synthesized through Massart method, using oleic acid as surfactant and four different cephalosporins: Cephoperazone, Cefotaxime, Ceftriaxone, and Cephaclor for adsorption-coating. The bacteriostatic effect of coated nanofluid on the bacteria *E. coli* and *S. aureus* was proved through observation, having lower inhibition zone diameters over the same time interval than sole cephalosporins [49]. In experiment by Wang et al. [50], $MnFe_2O_4$ nanoparticles were synthesized, coated with polyvinylpyrrolidone (PVP) using sonochemical mechanism and loaded with doxorubicin (DOX). Polymer coating prevents aggregation of MNPs, proving them to have good dispersion, homogeneous shape, and narrow particle size distribution. Such modified $MnFe_2O_4$ nanoparticles have low cytotoxicity, which allows for different biomedical applications [51]. Drug loading capacity of PVP-$MnFe_2O_4$ gradually increases with increasing concentration of DOX, making
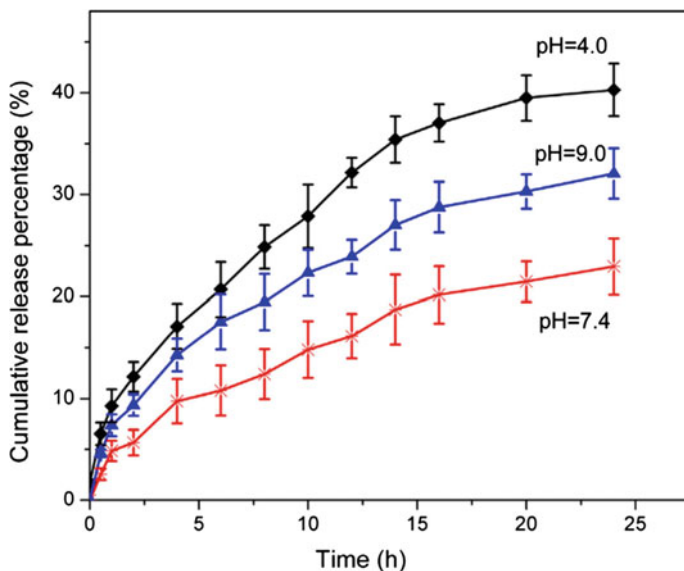
Fig. 15.5 Cumulative release (%) of DOX from drug-loaded PVP-MnFe$_2$O$_4$ in media with different pH (Reprinted from [50], with permission from Elsevier)

them similar or even more acceptable than other nanocarriers [35, 52]. Drug release study showed that DOX is being better released in acidic (40.3% over 24 h) and alkaline (32.1% over 24 h) media than in neutral conditions (22.9% over 24 h), which prevents quick release of DOX into blood, instead speeds up release of the drug on acidic cancer cells (Fig. 15.5).

Co$_{1-X}$Zn$_X$Fe$_2$O$_4$ (x = 0; 0.4; 0.6; 0.8; 1) nanoparticles were synthesized by thermal-treatment method and loaded with curcumin (CUR), which has several beneficial properties such as anti-cancer, anti-bacterial, and anti-inflammatory [53]. In vitro release study was performed at pH 7.4 and 5.5 as a simulation of normal and tumor tissue environment. The results showed that Co-0.4 and Co-0.6 have natural pH in neutral media, while also having positive pH in acidic media, which can be helpful in controlling CUR release [54, 55]. The amount of released drug from nanocarriers (NCs) increases alongside with decrease of pH from 7.4 to 5.5, which proves pH sensitivity. Cytotoxicity of NCs on normal (HEK-293) and cancer (MCF-7) cells was evaluated using MTT assay test. Cell viability in Co-0.6 was 61.6% in neutral media, decreasing to 37% at the highest dose in acidic media, making them the most suitable NCs for drug delivery. Acute toxicity in vivo experiment was performed on mice, administrating 2000 mg/kg of CUR-coated NCs (for 24 h and one week) and measuring the weight. Throughout the experiment, all mice survived. Furthermore, the changes in weight were normal after 24 h and 7 days, which proves that all NCs are safe. In conclusion, synthesized Co$_{1-X}$Zn$_X$Fe$_2$O$_4$ nanoparticles have great potential for delivery of anti-cancer drugs.

Magnetic nanoparticles (MNPs) can have different composition, morphology, and properties depending on the process of their preparation [56]. One of these processes is co-precipitation technique, with main advantage being the ability to synthesize large amount of MNPs [57] Magnetite (Fe_3O_4) nanoparticles (MNPs) were synthesized through chemical co-precipitation [58], coated with gelatin (GMNPs) [59, 60] and loaded with anti-cancer drug mercaptopurine (Mer) [61]. Polymer coating prevents MNPs from aggregation and reduces their size through weakening magnetic interaction between Fe_3O_4 particles [60, 62]. Suitable pH for loading the drug onto GMNPs is 10, based on the experiments to obtain small size without particle aggregation [58, 63–66]. Mer-GMNPs exhibit superparamagnetic behavior, making them acceptable for potential drug delivery [67].

15.4 Conclusions

Magnetic materials belong to a field of research that is being actively studied and developed. Their physicochemical properties are attracting researchers more and more, due to one of their predominant features—the presence of magnetic characteristics. This is verified by a large number of studies aimed at studying the methods of synthesis of iron-containing materials, in particular Fe oxides. Regulation of the properties of iron oxides by choosing a proper production method makes it possible to create a material that could be used in medicine and pharmacology. It is magnetic oxides that solve the problems associated with the diagnosis and treatment of various diseases, particularly cancer. Delivery of drugs using iron oxides has promising widespread medical use. Their antibacterial properties and low toxicity increase the range of use, since the search for disinfectants is a currently important issue. Therefore, this review focuses on the biocidal properties of magnetic oxides, the influence of the synthesis method and morphological characteristics on the inhibition of bacteria in the aquatic environment, as well as determining the mechanism of pathogen damage. Oxide nanoparticles modified by different functional groups are considered as carriers of biologically active and medicinal substances, materials for magnetic resonance imaging, as biosensors and carriers for target delivery. Thus, iron oxides are a priority area of research and a way to address many medical issues.

References

1. Engel M, Hadar Y, Belkin S, Lu X, Elimelech M, Chefetz B (2018) Bacterial inactivation by a carbon nanotube-iron oxide nanocomposite: a mechanistic study using *E. coli* mutants. https://doi.org/10.1039/c7en00865a
2. Kim JS, Kuk E, Yu KN, Kim JH, Park SJ, Lee HJ, Kim SH, Park YK, Park YH, Hwang CY, Kim YK, Lee YS, Jeong DH, Cho MH (2007) Antimicrobial effects of silver nanoparticles. Nanomed Nanotechnol Biol Med 3:95–101. https://doi.org/10.1016/j.nano.2006.12.001
3. Saliani M, Jalal R, Goharshadi EK (2015) Effects of pH and temperature on antibacterial activity of zinc oxide nanofluid against Escherichia coli O157: H7 and staphylococcus aureus, Jundishapur. J Microbiol 8:1–6. https://doi.org/10.5812/jjm.17115
4. Allahverdiyev AM, Abamor ES, Bagirova M, Rafailovich M (2011) Antimicrobial effects of TiO$_2$ and Ag$_2$O nanoparticles against drug-resistant bacteria and leishmania parasites. Future Microbiol 6:933–940. https://doi.org/10.2217/fmb.11.78
5. Chen H, Tian W, Ding W (2018) Preparation of meso-Ag/Al$_2$O$_3$ and synergistic water disinfection of metallic silver and ROS under visible light. Sol Energy 173:1065–1072. https://doi.org/10.1016/j.solener.2018.08.047
6. George A, Raj DMA, Raj AD, Irudayaraj AA, Arumugam J, Senthil kumar M, Prabu HJ, Sundaram SJ, Al-Dhabi NA, Arasu MV, Maaza M, Kaviyarasu K (2020) Temperature effect on CuO nanoparticles: antimicrobial activity towards bacterial strains. Surf. Interfaces 21:100761. https://doi.org/10.1016/j.surfin.2020.100761
7. Gudkov SV, Burmistrov DE, Serov DA, Rebezov MB, Semenova AA, Lisitsyn AB (2021) Do iron oxide nanoparticles have significant antibacterial properties? Antibiotics 10:1–23. https://doi.org/10.3390/antibiotics10070884
8. Wang D, Zhu B, He X, Zhu Z, Hutchins G, Xu P, Wang WN (2018) Iron oxide nanowire-based filter for inactivation of airborne bacteria. Environ Sci Nano 5:1096–1106. https://doi.org/10.1039/c8en00133b
9. Arakha M, Pal S, Samantarrai D, Panigrahi TK, Mallick BC, Pramanik K, Mallick B, Jha S (2015) Antimicrobial activity of iron oxide nanoparticle upon modulation of nanoparticle-bacteria interface. Sci Rep 5:1–12. https://doi.org/10.1038/srep14813
10. Tran N, Mir A, Mallik D, Sinha A, Nayar S, Webster TJ (2010) Bactericidal effect of iron oxide nanoparticles on *Staphylococcus aureus*. Int J Nanomed 5:277–283. https://doi.org/10.2147/ijn.s9220
11. Fernández L, González-Rodríguez J, Gamallo M, Vargas-Osorio Z, Vázquez-Vázquez C, Piñeiro Y, Rivas J, Feijoo G, Moreira MT (2020) Iron oxide-mediated photo-Fenton catalysis in the inactivation of enteric bacteria present in wastewater effluents at neutral pH. Environ Pollut 266. https://doi.org/10.1016/j.envpol.2020.115181
12. Rufus A, Sreeju N, Philip D (2016) Synthesis of biogenic hematite (α-Fe$_2$O$_3$) nanoparticles for antibacterial and nanofluid applications. RSC Adv 6:94206–94217. https://doi.org/10.1039/c6ra20240c
13. Hanini A, Schmitt A, Kacem K, Chau F, Ammar S, Gavard J (2011) Evaluation of iron oxide nanoparticle biocompatibility. Int J Nanomed 787. https://doi.org/10.2147/ijn.s17574
14. Bhushan M, Kumar Y, Periyasamy L, Viswanath AK (2018) Antibacterial applications of α-Fe$_2$O$_3$/Co$_3$O$_4$ nanocomposites and study of their structural, optical, magnetic and cytotoxic characteristics. Appl Nanosci 8:137–153. https://doi.org/10.1007/s13204-018-0656-5
15. Tatarchuk T, Myslin M, Lapchuk I, Olkhovyy O, Danyliuk N, Mandzyuk V. (2021) Synthesis, structure and morphology of magnesium ferrite nanoparticles, synthesized via "Green" method. Phys. Chem. Solid State 2:195–203. https://doi.org/10.15330/pcss.22.2.195-203
16. Sathishkumar G, Logeshwaran V, Sarathbabu S, Jha PK, Jeyaraj M, Rajkuberan C, Senthilkumar N, Sivaramakrishnan S (2018) Green synthesis of magnetic Fe$_3$O$_4$ nanoparticles using Couroupita guianensis Aubl. fruit extract for their antibacterial and cytotoxicity activities. Artif Cells Nanomed Biotechnol 46:589–598. https://doi.org/10.1080/21691401.2017.1332635

17. Arshad M, Alyousef A, Ahmad I, Khan JM, Shahzad SA (2018) Low temperature synthesis of superparamagnetic iron oxide (Fe_3O_4) nanoparticles and their ROS mediated inhibition of biofilm formed by food-associated bacteria. Front Microbiol 9:1–10. https://doi.org/10.3389/fmicb.2018.02567

18. Behera SS, Patra JK, Pramanik K, Panda N, Thatoi H (2012) Characterization and evaluation of antibacterial activities of chemically synthesized iron oxide nanoparticles. World J Nano Sci Eng 02:196–200. https://doi.org/10.4236/wjnse.2012.24026

19. Das S, Diyali S, Vinothini G, Perumalsamy B, Balakrishnan G, Ramasamy T, Dharumadurai D, Biswas B (2020) Synthesis, morphological analysis, antibacterial activity of iron oxide nanoparticles and the cytotoxic effect on lung cancer cell line. Heliyon 6:e04953. https://doi.org/10.1016/j.heliyon.2020.e04953

20. Sousa C, Sequeira D, Kolen'ko YV, Pinto IM, Petrovykh DY (2015) Analytical protocols for separation and electron microscopy of nanoparticles interacting with bacterial cells. Anal Chem 87:4641–4648. https://doi.org/10.1021/ac503835a

21. Vanholder R, Baurmeister U, Brunet P, Cohen G, Glorieux G, Jankowski J (2008) A bench to bedside view of uremic toxins. J Am Soc Nephrol 19:863–870. https://doi.org/10.1681/ASN.2007121377

22. Jin J, Yang F, Zhang F, Hu W, Sun SB, Ma J (2012) 2, 2′-(phenylazanediyl) diacetic acid modified Fe_3O_4@PEI for selective removal of cadmium ions from blood. Nanoscale 4:733–736. https://doi.org/10.1039/c2nr11481j

23. Lee HY, Bae DR, Park JC, Song H, Han WS, Jung JH (2009) A selective fluoroionophore based On bODIPY-Functionalized magnetic silica nanoparticles: Removal of Pb^{2+} from human blood. Angew Chem—Int Ed 48: 1239–1243. https://doi.org/10.1002/anie.200804714.

24. Herrmann IK, Urner M, Koehler FM, Hasler M, Roth-Z'Graggen B, Grass RN, Ziegler U, Beck-Schimmer B, Stark WJ (2010) Blood purification using functionalized core/shell nanomagnets. Small 6:1388–1392. https://doi.org/10.1002/smll.201000438

25. Herrmann IK, Schlegel A, Graf R, Schumacher CM, Senn N, Hasler M, Gschwind S, Hirt AM, Günther D, Clavien PA, Stark WJ, Beck-Schimmer B (2013) Nanomagnet-based removal of lead and digoxin from living rats. Nanoscale 5:8718–8723. https://doi.org/10.1039/c3nr02468g

26. Wang L, Yang Z, Gao J, Xu K, Gu H, Zhang B, Zhang X, Xu B (2006) A biocompatible method of decorporation: bisphosphonate-modified. pp 13358–13359

27. Herrmann IK, Bernabei RE, Urner M, Grass RN, Beck-Schimmer B, Stark WJ (2011) Device for continuous extracorporeal blood purification using target-specific metal nanomagnets. Nephrol Dial Transplant 26:2948–2954. https://doi.org/10.1093/ndt/gfq846

28. Cai K, Li J, Luo Z, Hu Y, Hou Y, Ding X (2011) β-Cyclodextrin conjugated magnetic nanoparticles for diazepam removal from blood. Chem Commun 47:7719–7721. https://doi.org/10.1039/c1cc11855b

29. Herrmann IK, Urner M, Graf S, Schumacher CM, Roth-Z'graggen B, Hasler M, Stark WJ, Beck-Schimmer B (2013) Endotoxin removal by magnetic separation-based blood purification. Adv Healthc Mater 2:829–835. https://doi.org/10.1002/adhm.201200358

30. Herrmann IK, Schlegel AA, Graf R, Stark WJ, Beck-Schimmer B (2015) Magnetic separation-based blood purification: a promising new approach for the removal of disease-causing compounds? J Nanobiotechnol 13:1–4. https://doi.org/10.1186/s12951-015-0110-8

31. Zou Y, Liu P, Liu CH, Zhi XT (2015) Doxorubicin-loaded mesoporous magnetic nanoparticles to induce apoptosis in breast cancer cells. Biomed Pharmacother 69:355–360. https://doi.org/10.1016/j.biopha.2014.12.012

32. Iglesias GR, Delgado AV, González-Caballero F, Ramos-Tejada MM (2017) Simultaneous hyperthermia and doxorubicin delivery from polymer-coated magnetite nanoparticles. J Magn Magn Mater 431:294–296. https://doi.org/10.1016/j.jmmm.2016.08.023

33. Javid A, Ahmadian S, Saboury AA, Kalantar SM, Rezaei-Zarchi S (2013) Chitosan-coated superparamagnetic iron oxide nanoparticles for doxorubicin delivery: synthesis and anticancer effect against human ovarian cancer cells. Chem Biol Drug Des 82:296–306. https://doi.org/10.1111/cbdd.12145

34. Sun C, Lee JSH, Zhang M (2008) Magnetic nanoparticles in MR imaging and drug delivery. Adv Drug Deliv Rev 60:1252–1265. https://doi.org/10.1016/j.addr.2008.03.018

35. Rana VK, Choi MC, Kong JY, Kim GY, Kim MJ, Kim SH, Mishra S, Singh RP, Ha CS (2011) Synthesis and drug-delivery behavior of chitosan-functionalized graphene oxide hybrid nanosheets. Macromol Mater Eng 296:131–140. https://doi.org/10.1002/mame.201000307

36. Shen T, Weissleder R, Papisov M, Bogdanov A, Brady TJ (1993) Monocrystalline iron oxide nanocompounds (MION): physicochemical properties. Magn Reson Med 29:599–604. https://doi.org/10.1002/mrm.1910290504

37. Theunis CH, Pierson ES, Cresti M, Plant Reprod S, Kranz E, Bautor J, Lorz H, Faure J, Mogensen HL, Dumas C, Lbrz H, Claude Bernard U, The F (1994) Biodegradable long-circulating polymeric nanospheres. Science (80) 263:1600. www.sciencemag.org

38. Feng ZQ, Yan K, Li J, Xu X, Yuan T, Wang T, Zheng J (2019) Magnetic Janus particles as a multifunctional drug delivery system for paclitaxel in efficient cancer treatment. Mater Sci Eng C 104:110001. https://doi.org/10.1016/j.msec.2019.110001

39. Gautier J, Munnier E, Paillard A, Hervé K, Douziech-Eyrolles L, Soucé M, Dubois P, Chourpa I (2012) A pharmaceutical study of doxorubicin-loaded PEGylated nanoparticles for magnetic drug targeting. Int J Pharm 423:16–25. https://doi.org/10.1016/j.ijpharm.2011.06.010

40. Herve K, Douziech-Eyrolles L, Munnier E, Cohen-Jonathan S, Souce M, Marchais H, Limelette P, Warmont F, Saboungi ML, Dubois P, Chourpa I (2008) The development of stable aqueous suspensions of PEGylated SPIONs for biomedical applications. Nanotechnology. 19. https://doi.org/10.1088/0957-4484/19/46/465608

41. Munnier E, Cohen-Jonathan S, Linassier C, Douziech-Eyrolles L, Marchais H, Soucé M, Hervé K, Dubois P, Chourpa I (2008) Novel method of doxorubicin-SPION reversible association for magnetic drug targeting. Int J Pharm 363:170–176. https://doi.org/10.1016/j.ijpharm.2008.07.006

42. Veiseh O, Gunn JW, Zhang M (2010) Design and fabrication of magnetic nanoparticles for targeted drug delivery and imaging. Adv Drug Deliv Rev 62:284–304. https://doi.org/10.1016/j.addr.2009.11.002

43. Wang G, Zhou F, Li X, Li J, Ma Y, Mu J, Zhang Z, Che H, Zhang X (2018) Controlled synthesis of L-cysteine coated cobalt ferrite nanoparticles for drug delivery. Ceram Int 44:13588–13594. https://doi.org/10.1016/j.ceramint.2018.04.193

44. Huang YS, Lu YJ, Chen JP (2017) Magnetic graphene oxide as a carrier for targeted delivery of chemotherapy drugs in cancer therapy. J Magn Magn Mater 427:34–40. https://doi.org/10.1016/j.jmmm.2016.10.042

45. Shagholani H, Ghoreishi SM, Mousazadeh M (2015) Improvement of interaction between PVA and chitosan via magnetite nanoparticles for drug delivery application. Int J Biol Macromol 78:130–136. https://doi.org/10.1016/j.ijbiomac.2015.02.042

46. Zhao J, Pei S, Ren W, Gao L, Cheng HM (2010) Efficient preparation of large-area graphene oxide sheets for transparent conductive films. ACS Nano 4:5245–5252. https://doi.org/10.1021/nn1015506

47. Aliabadi M, Shagholani H, Yunessnia lehi A (2017) Synthesis of a novel biocompatible nanocomposite of graphene oxide and magnetic nanoparticles for drug delivery. Int J Biol Macromol 98:287–291. https://doi.org/10.1016/j.ijbiomac.2017.02.012

48. Yao K, Tan P, Luo Y, Feng L, Xu L, Liu Z, Li Y, Peng R (2015) Graphene oxide selectively enhances thermostability of trypsin. ACS Appl Mater Interfaces 7:12270–12277. https://doi.org/10.1021/acsami.5b03118

49. Buteică AS, Mihaiescu DE, Grumezescu AM, Vasile BŞ, Popescu A, Mihaiescu OM, Cristescu R (2010) The anti-bacterial activity of magnetic nanofluid: Fe_3O_4/oleic acid/cephalosporins core/shell/adsorption-shell proved on *S. Aureus* and *E. Coli* and possible applications as drug delivery systems. Dig J Nanomater Biostruct 5:927–932

50. Wang G, Zhao D, Ma Y, Zhang Z, Che H, Mu J, Zhang X, Zhang Z (2018) Synthesis and characterization of polymer-coated manganese ferrite nanoparticles as controlled drug delivery. Appl Surf Sci 428:258–263. https://doi.org/10.1016/j.apsusc.2017.09.096

51. Peng E, Choo ESG, Chandrasekharan P, Yang CT, Ding J, Chuang KH, Xue JM (2012) Synthesis of manganese ferrite/graphene oxide nanocomposites for biomedical applications. Small 8:3620–3630. https://doi.org/10.1002/smll.201201427
52. Santos MC, Seabra AB, Pelegrino MT, Haddad PS (2016) Synthesis, characterization and cyto-toxicity of glutathione- and PEG-glutathione-superparamagnetic iron oxide nanoparticles for nitric oxide delivery. Appl Surf Sci 367:26–35. https://doi.org/10.1016/j.apsusc.2016.01.039
53. Zamani M, Naderi E, Aghajanzadeh M, Naseri M, Sharafi A, Danafar H (2019) $Co_{1-X}Zn_xFe_2O_4$ based nanocarriers for dual-targeted anticancer drug delivery: Synthesis, characterization and in vivo and in vitro biocompatibility study. J Mol Liq 274:60–67. https://doi.org/10.1016/j.molliq.2018.10.083
54. Bohara RA, Thorat ND, Yadav HM, Pawar SH (2014) One-step synthesis of uniform and biocompatible amine functionalized cobalt ferrite nanoparticles: a potential carrier for biomedical applications. New J Chem 38:2979–2986. https://doi.org/10.1039/c4nj00344f
55. Li J, Ng DHL, Song P, Song Y, Kong C (2015) Bio-inspired synthesis and characterization of mesoporous $ZnFe_2O_4$ hollow fibers with enhancement of adsorption capacity for acid dye. J Ind Eng Chem 23:290–298. https://doi.org/10.1016/j.jiec.2014.08.031
56. Lima-Tenorio MK, Pineda EA, Ahmad NM, Fessi H, Elaissari A (2015) Magnetic nanoparti-cles: in vivo cancer diagnosis and therapy. Int J Pharm 493:313–327. https://doi.org/10.1016/j.ijpharm.2015.07.059
57. Ockwig NW, Nenoff TM, Separation H, Rev C, Chem E, Laurent S, Forge D, Port M, Roch A, Robic C, Vander Elst L, Muller RN (2010) Additions and corrections. 110:2573–2574
58. Mascolo MC, Pei Y, Ring TA (2013) Room temperature co-precipitation synthesis of magnetite nanoparticles in a large pH window with different bases. Mater (Basel) 6:5549–5567. https://doi.org/10.3390/ma6125549
59. Lee BH, Shirahama H, Cho NJ, Tan LP (2015) Efficient and controllable synthesis of highly substituted gelatin methacrylamide for mechanically stiff hydrogels. RSC Adv 5:106094–106097. https://doi.org/10.1039/c5ra22028a
60. Silva VAJ, Andrade PL, Silva MPC, Bustamante AD, De Los Santos Valladares L, Albino Aguiar J (2013) Synthesis and characterization of Fe_3O_4 nanoparticles coated with fucan polysaccharides. J Magn Magn Mater 343:138–143. https://doi.org/10.1016/j.jmmm.2013.04.062
61. Dorniani D, Zobir M, Shaari AH, Ahmad Z (2013) Dorniani-2013-Preparation and char.pdf
62. Mahdavi M, Ahmad MB, Haron MJ, Namvar F, Nadi B, Ab Rahman MZ, Amin J (2013) Synthesis, surface modification and characterisation of biocompatible magnetic iron oxide nanoparticles for biomedical applications. Molecules 18:7533–7548. https://doi.org/10.3390/molecules18077533
63. Feng J, Mao J, Wen X, Tu M (2011) Ultrasonic-assisted in situ synthesis and characterization of superparamagnetic Fe_3O_4 nanoparticles. J Alloys Compd 509:9093–9097. https://doi.org/10.1016/j.jallcom.2011.06.053
64. Andrade ÂL, Souza DM, Pereira MC, Fabris JD, Domingues RZ (2010) pH effect on the synthesis of magnetite nanoparticles by the chemical reduction-precipitation method. Quim Nova 33:524–527. https://doi.org/10.1590/S0100-40422010000300006
65. Palagiri B, Chintaparty R, Nagireddy RR, Imma Reddy VSR (2017) Influence of synthesis conditions on structural, optical and magnetic properties of iron oxide nanoparticles prepared by hydrothermal method. Phase Transitions 90:578–589. https://doi.org/10.1080/01411594.2016.1237636
66. Dorniani D, Bin Hussein MZ, Kura AU, Fakurazi S, Shaari AH, Ahmad Z (2012) Preparation of Fe_3O_4 magnetic nanoparticles coated with gallic acid for drug delivery. Int J Nanomed 7:5745–5756. https://doi.org/10.2147/IJN.S35746
67. Sirivat A, Paradee N (2019) Facile synthesis of gelatin-coated Fe_3O_4 nanoparticle: effect of pH in single-step co-precipitation for cancer drug loading. Mater Des 181:107942. https://doi.org/10.1016/j.matdes.2019.107942

Chapter 16
Proliferative Activity of Ehrlich Carcinoma Cells After Use of Nanocomplexes

A. Goltsev ⓘ**, Natalia M. Babenko** ⓘ**, Yuliia O. Gaevska** ⓘ**,
Mykola O. Bondarovych** ⓘ**, Tetiana G. Dubrava** ⓘ**, Maksym V. Ostankov** ⓘ**,
and Vladimir K. Klochkov** ⓘ

16.1 Introduction

The search for the methods capable of selective recognition and inactivation of cancer stem cells (CSCs) with an increased tumorigenic activity is an urgent task of modern oncology. The CSCs are known to be a small population of tumor cells with a unique ability to self-maintenance as part of a heterogeneous tumor pool [1–4]. Studies of different types of tumors have shown that the CSCs multiply slowly, but give rise to more differentiated offspring with a high proliferative activity and provide a rapid increase in tumor size.

The CSCs were first identified in 1997 among a heterogeneous population of bone marrow cells [1]. The authors investigated acute myelogenous leukemia and proved that the $CD34^+CD38^-$ subpopulation, being about 0.01–1% of the total bone marrow cell population, was able to cause leukemia when transplanted into immune deficient NOD/SCID mice. In 2003, it became possible to identify the CSCs in a solid human breast cancer [2]. The same team showed that the $CD44^+CD24^{-/low}$ subpopulation had increased tumorigenic capacity, demonstrating tumor formation

A. Goltsev (✉) · N. M. Babenko · Y. O. Gaevska · M. O. Bondarovych · T. G. Dubrava ·
M. V. Ostankov
Department of Cryopathophysiology and Immunology, Institute for Problems of Cryobiology and
Cryomedicine of the National Academy of Sciences of Ukraine, Pereyaslavska Street 23,
Kharkiv 61016, Ukraine
e-mail: cryopato@gmail.com

V. K. Klochkov
Nanostructured Materials Department Named By Yu.V. Malyukin, Institute for Scintillation
Materials of the National Academy of Sciences of Ukraine, 60 Nauki Ave, Kharkiv 61001,
Ukraine
e-mail: klochkov@isma.kharkov.ua

223

in 100% of cases with the introduction of 10^3 cells/mouse. The unfractionated population of primary breast tumor showed tumorigenic potential at a much higher dose, i.e., 5×10^4 cells/mouse when administered to NOD/SCID mice. The obtained results showed that during the breast cancer development there is a hierarchy of tumorigenic properties of tumor cells because of which only some subpopulations, in particular $CD44^+CD24^{-/low}$, are able to proliferate, while most cells ($CD44^+CD24^+$, $CD44^-CD24^+$) have limited proliferative potential in vivo [2].

These studies have been continued by Ponti et al., who demonstrated that only 7 of 16 biopsy specimens derived from breast cancer patients formed the mammospheres in vitro [5]. Most cells of the formed mammospheres had the $CD44^+CD24^{-/low}$ phenotype and almost 1000 times greater tumorigenic potential in vivo when administered to SCID mice than the total population of MCF7 breast cancer cells [5]. Cells of total MCF7 population formed new tumors only when 10^6 cells were injected into an animal, whereas the injection of lower concentrations of 10^5 cells/animal to experimental animals did not cause cancer.

On the contrary, the $CD44^+CD24^{-/low}$ fraction isolated from the total MCF7 cell population formed tumors in 80%, 60%, and 60% of cases if 10^5, 10^4, and 10^3 cells were introduced per animal, respectively. This fact can be explained by the heterogeneity of MCF7 composition with the presence of subpopulations having additional markers (ESA, ALDH), which determine the self-maintenance function of tumor cells.

One of the mechanisms of tumor transformation and progression is a disordered cell cycle regulation with apoptosis inhibition and proliferation activation [6, 7]. A known marker of cell proliferative activity is the Ki-67 antigen that is nuclear non-histone protein, expressed in all phases of the cell cycle: G1, S, G2, M except the G0 phase. This protein is involved in the synthesis of ribosomes, organization of heterochromatin, and separation of chromosomes during mitosis [8].

The topography of Ki-67 distribution in a cell depends on the cell cycle phase, which determines the different intensity of its binding to the corresponding monoclonal antibodies [9]. At the very beginning of the G1 phase, Ki-67 is localized in the nucleoplasm of satellite DNA in the centromeres and telomeres of chromosomes (the most condensed parts of DNA), with that a low intensity of its binding to monoclonal antibodies is associated. In the middle of the G1 phase, the Ki-67 protein begins to appear in the nucleoli and, then, in the G2 phase, both in the nucleoli and in the karyoplasm. In the phase of mitosis, the amount of Ki-67 protein increases rapidly, already in the prophase of mitosis, the protein passes to the surface of chromosomes and looks like a smart network surrounding the condensed chromatin. In metaphase, this reticular structure already surrounds individual chromosomes. After destruction of the nuclear membrane, part of Ki-67 is diffusely distributed in cytoplasm. During this period, the protein is found in the cells in the largest amount with the highest fluorescence intensity. In mitosis anaphase and telophase, the amount of Ki-67 in cells begins to decline rapidly, and during the transition of cells to phase G0, this protein is quickly proteasome-catabolized and ceases to be found in the nuclei of interphase cells [10].

The rate of Ki-67 expression changes during the cell cycle, and an increased rate of its expression correlates with a rise in the average fluorescence intensity (AFI) of cells. The most highly proliferating cells have the highest values of Ki-67 protein, and the increase in its AFI occurs mainly in cells being in the mitosis phase [11]. Thus, determining the number of Ki-67^{+}—cells and the expression rate of this marker by the intensity of staining with appropriate MAB allows to determine the proliferative activity of cells, indicating their distribution in relevant phases of the cell cycle, indicating the growth rate of tumor, the risk of metastasis and potential tumor response to therapeutic measures.

The expression rate of the CD44 marker is of significant importance in implementing the oncogenic potential by tumor cells. Thus, it has been proven that the CSCs with a high rate of expression of the marker CD44 (CD44^{high}) has the greatest tumorigenic activity [3, 12]. During an orthotopic implantation of 5×10^5 RAS-transformed CD44^{high}- or CD44^{low}- cells to NOD/SCID mice, it was found that the CD44^{low}—subpopulation had a low tumorigenicity (tumor was formed in 30% of cases), while CD44^{high}-cells were able to form tumors in 100% of cases [3].

The more "stem-like" CD44^{+}CD24^{−/low} cell phenotype is thought to be related to the functions performed by these surface molecules. In particular, it is known that the standard isoform of the CD44 receptor is expressed on almost all cells, while some variants of alternative splicing of this molecule are detected only in the during cancer development [13]. The interaction of the CD44 receptor with its ligand, hyaluronic acid has been shown to enhance the translocation and transcription of the twist regulatory molecule, which promotes epithelial-mesenchymal transition (EMT) [14]. During EMT, tumor epithelial cells acquire mesenchymal-like properties with the ability to proliferate indefinitely, and the reverse process is defined as a mesenchymal-epithelial transition (MET). Previous studies indicate that the CD24 receptor is involved in regulation of the EMT-MET transitions in breast cancer [15]. Thus, the absence of this marker in the CD44^{+}CD24^{−}—population determines their mesenchymal phenotype [16, 17], while CD44^{+}CD24^{+}—cells with the presence of the CD24 receptor possess more differentiated epithelial features [18].

EMT is thought to be controlled by the activity of a number of genes, including the pluripotency of the *oct-4* and *nanog* genes [19]. On the other hand, high CD44 expression has been found to correlate with the EMT, thereby contributing to tumor invasion, metastasis, recurrence, and chemoresistance [20]. Thus, surface markers of tumor cells can act as regulators of the "stem" properties of CSCs, therefore this connection realized by changing gene expression.

Ehrlich ascites carcinoma (EAC) cell line, obtained from spontaneous mouse breast cancer [21] is a convenient model to study the effect of various factors and therapeutic agents directly on functional activity of cancer cells. Evaluation of the phenotypic characteristics and functional potential of the EAC demonstrated the presence of a heterogeneous pool of cells with high and low potent tumor-inducing precursors [22].

Higher tumorigenic activity of CD44 positive EAC cells was demonstrated compared to the CD44^{−}—fraction [22]. After introduction of the same number of cells (3×10^6) into peritoneal cavity, the intensity of tumor growth initiated by

CD44$^+$—cells was 23 times higher than the tumorigenic potential of total population of EAC cells and this was 105 times higher than the CD44$^-$—cell fraction. At the same time, the changes of not only quantitative, but also qualitative structure of the formed tumor at its induction by cells of the total EAC population in comparison with CD44$^+$—and CD44$^-$—fractions were noted [22]. Thus, cells of the CD44$^+$—fraction formed ascites, which mainly contained CD44 positive EAC cells, i.e., CD44^{high}, CD44$^+$CD24$^-$,—and CD44$^+$CD24$^+$ subpopulations. The concentration of CD44^{high} cells in this ascites was 2 times higher than in the tumor, which was initiated by total EAC population and if it was initiated by CD44$^-$—fraction that concentration was 16 times higher. It is notable that the initiation of oncology pathology by cells of the CD44$^-$—fraction caused the formation of tumors with a predominant content of mature cells with the CD44$^-$CD24$^+$ phenotype. Obviously, this redistribution of the subpopulation composition of the EAC formed by the CD44$^-$—fraction determined the minimal intensity of tumor growth in animals of this experimental group [22].

The main disadvantage of modern methods for treating the malignant neoplasms, which include surgery, radiation, and chemotherapy, is the lack of their targeted action on CSCs, the manifestation of oncology pathology. Many therapeutic agents can affect the pathology proceeding via inhibiting proliferative activity of tumor cells. Therefore, the search for methodological approaches and compounds capable of purposefully affecting the most tumorigenic precursors is undergoing.

Promising in this regard is the use of vanadium derivatives. Previous studies have shown that vanadium salts can inhibit the progression of various types of tumor lines derived from different organs, including those of brain tissues (neuroblastoma SH-SY5Y line) [23], those of lungs (A549 cell line) [24] and prostate (cells of line DU145 and PC-3) [25]. Günther et al. reported that sodium orthovanadate is able to inhibit the proliferation of EAC cells and increase the survival of tumor-bearing mice [26]. This is consistent with the data of our previous studies [27], which indicate the possibility to inhibit EAC growth under the influence of spherical, spindle-shaped, and rod-shaped nanoparticles (NPs) of rare earth metals of orthovanadates. In addition, it was previously demonstrated that nanocomplexes (NCs), containing spherical NPs of orthovanadates of rare earth metals GdYEuVO$_4$ and cholesterol, were selectively accumulated in the cells of the most tumorigenic CD44$^+$—fraction [28] and inhibit the development of oncopathology in the experiment [22, 29]. It is shown that the effective implementation of the antitumor effect of NCs involves their penetration and accumulation inside cells, mitochondrial dysfunction with subsequent induction of apoptotic and necrotic processes in tumor cells [28]. There is a high probability that the implementation mechanism of the antitumor effect of NCs may be associated with the formation of reactive oxygen species and subsequent DNA damage [30, 31]. In particular, it is known that metal complexes are able to act as artificial nucleases and cleave the DNA of actively proliferating cells that prevents their replication [32]. Such developments may likely affect the function of pluripotency genes in tumor cells.

Based on the above, this study was aimed to comparatively analyze the ability of NCs to change the proliferative status of tumors formed by cells of total EAC

population and CD44$^+$—fraction to determine the expression rate of *nanog*, *oct4*, *sox2* genes and relevant transcription factors.

16.2 Synthesis of Nanocomplexes

Obtaining nanoparticles (NPs). For the synthesis of aqueous colloidal solutions of NPs by the method [33], we used rare earth metal chlorides ("Acros organics", Belgium), sodium citrate ("Acros organics", Belgium), sodium methavanadate ("Acros organics", Belgium), distilled water. Chlorides of rare earth elements (99.9%), sodium citrate $Na_3C_6H_5O_7 \cdot 2H_2O$ (>99%), and anhydrous sodium metavanadate (96%) were obtained from Acros organics (USA). Sodium hydroxide (99%) was purchased from JSC Macrokhem (Ukraine). Sodium orthovanadate Na_3VO_4 solution was obtained by adding a 1 M solution of NaOH in aqueous solution $NaVO_3$ to pH = 13. Particle morphology and size distribution were analyzed using transmission electron microscopy (TEM). Samples were prepared by placing a drop of a colloidal solution onto a 200-mesh holey carbon copper grid. The grid was air dried under dust-free conditions and examined in TEM 125 K (JSC, Ukraine) electron microscope at 100 kV electron beam. The size of NPs in colloidal solutions before and after addition of the dyes was determined by dynamic light scattering (DLS). The hydrodynamic diameter and ζ-potential of NPs were measured with a ZetaPALS analyzer (Brookhaven Instruments Corp., USA). Before the measurements, the test solutions were incubated at 25 °C. Colloidal solutions containing spherical particles were prepared by the method described earlier using sodium citrate as a stabilizing agent. At this stage of the synthesis, the lanthanide chelator contributes to a slow formation of a heterogeneous system as thermal degradation of the complex. On the other hand, citrate molecules as the components of chelate complexes with cations on the surface of the solid phase, form protective layers, preventing coagulation of the colloidal system. Briefly, 10 mL of aqueous solution of rare-earth chlorides (0.01 mol/L) was mixed with 8 mL of sodium citrate solution (0.01 mol/L). Then, the obtained solution of 8 mL Na_3VO_4 (0.01 mol/L) was dropwise (pH = 13). The mixture was intensively stirred by using a magnetic stirrer until yellowish transparent solution was formed. The solution was heated at 90 °C on a water bath for 30–90 min. According to the TEM, solid phase of colloidal solution represents spherical NPs with average size of 2 ± 0.2 nm. Through DLS measurements, the average intensity-weighted hydrodynamic diameter of NPs was determined to be 15.2 nm. The average value of ζ-potential was (-36 ± 2 mV). The solutions were purified by dialysis with "Cellu Sep H1" 3.5 kDa membrane. The solution is transparent in transmitted light and opalescent in lateral light (Tyndall cone). Colloidal particles pass easily through nitrocellulose ultrafilters with a pore diameter of 100 nm. The solid-phase concentration was 1 g/L, pH is 7.4–7.6. The solutions were stored in sealed ampoules without changing their properties for more than 2 months at normal conditions.

Obtaining nanocomplexes (NCs). Nanocomplexes were synthesized at the Institute for Scintillation Materials of the National Academy of Sciences of Ukraine (Kharkiv), as reported [34]. Nanocomplexes represent an aqueous dispersion of cholesterol (0.55 g/l) ("Acros organics", Belgium) using as a stabilizer of nanoparticles (NPs) of orthovanadates of rare earth metals $GdYEuVO_4$ at a concentration of 1.30 g/l. The method of NCs obtaining includes dissolving cholesterol in ethyl alcohol and adding sterile aqueous solution of NPs to the sterilized in insulated ampoules at 120 °C with further vacuum removal of alcohol with adding sterile isotonic 5% glucose solution ("Infusion", Ukraine). The size of the NPs did not exceed 3 nm in diameter, because the use of larger diameters reduces the probability of their localization on the surface of cholesterol dispersed particles and does not provide a sufficient value of electrokinetic potential (charge) on the surface of cholesterol dispersed particles for electrostatic repulsion in solution, therefore, do not contribute to their aggregative stabilization in solution. In the NCs, negatively charged NPs are localized on the periphery of cholesterol particles due to Van der Waals and hydrophobic interactions. The dimensions of the synthesized NCs do not exceed 100 nm.

16.3 Proliferative Activity of Ehrlich Ascites Carcinoma Cells After Use of Nanocomplexes

The possibility of nanocomplexes (NCs) containing nanoparticles (NPs) of rare earth orthovanadates $GdYEuVO_4$ and cholesterol to identify and specifically inhibited the tumor-inducing cells should, first of all, be adequately assessed in experiments. A convenient model for performing such experimental research is the inoculated tumor cell line of Ehrlich ascites carcinoma (EAC), which was obtained from spontaneous breast cancer in mice [21]. The EAC was induced in 7-month-old female BALB/c mice by intraperitoneal injection of tumor cells at a dose of 5×10^6 cells/mouse in 0.3 ml of saline in the left lower quadrant of abdominal wall. The EAC cells were cultured in peritoneal cavity of mice for 7 days.

The CD44$^+$ fraction was isolated from total population of EAC cells by magnetic sorting (BDTM Imagnet, USA). To obtain it, we applied a positive selection using primary monoclonal antibodies CD44 MicroBeads ("BD", USA, 558739) and secondary IgG1 Magnetic Particles ("BD", USA, 557983) according to the manufacturer's protocol. Magnetic sorting of 2×10^7 of EAC cells allows to obtain about 6×10^5 cells of CD44$^+$—fraction, which is not less than $2.8 \pm 0.1\%$ of the total population of tumor cells. The purity of the CD44$^+$ fraction was $87.0 \pm 0.3\%$, as evidenced by flow cytometry.

Total population of EAC cells and the isolated CD44$^+$—fraction with NCs were incubated in vitro at the ratio of 100 µl of aqueous solution of NCs per 900 µl of EAC cells (10^7 cells/ml in saline) at room temperature for 3 h. The incubation time of 3 h was previously determined as optimal for the penetration of NCs into the cells, which was confirmed by confocal microscopy [35]. Then, the EAC cells were

washed once with 5% glucose solution by centrifugation (300 g). The controls were the cells of total EAC population and CD44+—fractions, which were incubated in a 5% glucose solution for 3 h without NCs treatment. Treated and untreated EAC cells were injected into the peritoneal cavity of mice as described above to initiate oncology pathology.

After 7 days of in vivo culturing of the EAC cells of all the groups, inhibitory effect of NCs was observed on an absolute number of EAC cells in peritoneal cavity (Table 16.1). Incubation of NCs with EACs cells led to significant decrease in an absolute number of EAC cells in peritoneal cavity ($18.27 \pm 1.23\%$ in the total EAC population and $91.40 \pm 4.87\%$ in the CD44+—fraction) compared to the control (52.25 ± 4.27 and $826.5 \pm 6.53\%$, respectively).

Comparative evaluation of the intensity growth rate of tumor, induced by total population of EAC cells or isolated from it CD44+—fraction, allowed to establish the dependence of the intensity of EAC development on functional activity of CD44+ cells. As Table 16.1 shows, the tumor-inducing activity of CD44+—fraction cells was 15 times higher than in total EAC population.

Our previous studies have shown that the NCs based on spherical NPs of ortho-vanadates of rare earth metals GdYEuVO$_4$ (1.3 g/l) and cholesterol are accumulated most intensively only in $1.20 \pm 0.13\%$ of cells of the total EAC pool, which also highly express CD44 marker [28]. This confirms our previously suggested assumption that the antitumor activity of NCs is implemented by inhibiting the activity of

Table 16.1 Tumor growth of EAC cells on day 7 of in vivo cultivation of total population and CD44+—fractions untreated and treated by NCs

Group	Absolute number of EAC cells in peritoneal cavity ($\times 10^7$)	Intensity of growth rate (%)	Inhibition of growth rate (%)
Total EAC population (Control 1)	52.25 ± 4.27	100	–
Total EAC population + NCs	$18.27 \pm 1.23^*$	$34.96 \pm 4.67^*$	65.03 ± 4.50
CD44+—fraction (Control 2)	826.5 ± 6.53	100	–
CD44+—fraction + NCs	$91.40 \pm 4.87^*$	$11.05 \pm 0.81^*$	88.95 ± 5.78

Notes Absolute number of cells (ANC) calculated by the formula: ANC = Vol * Conc, where Vol is the volume of ascitic fluid in the peritoneal cavity of animals (ml), Conc is the concentration of tumor cells, counted in the Goryaev chamber ($\times 10^7$ cells/ml). Intensity growth rate (IGR) of the EAC was calculated by the formula: IGR = (ANC$_{exp}$/ANC$_{control}$) $\times$ 100%, where ANC$_{exp}$ is the absolute number of cells in the peritoneal cavity of animals with EAC, which was initiated by NCs—treated cells; ANC$_{control}$—the absolute number of cells in peritoneal cavity of animals with EAC, which was initiated untreated cells. Inhibition growth rate (IGR) was calculated by the formula: IGR = ((ANC$_{control}$−ANC$_{exp}$)/ANC$_{control}$) $\times$ 100%. *—difference is significant in comparison with the corresponding indices of untreated EAC cells (Control 1 and 2); $p < 0.05$

CD44^{+} cells—subpopulations having higher tumorigenic potential compared to total EAC population [22].

This is evidenced by the fact that treatment with NCs of the cells of total EAC population led to inhibition by 65.04% of intensity growth rate of tumor on day 7 of cultivation in vivo (Table 16.1), while after similar treatment of CD44^{+}—fraction, this value reached almost 90% compared to the corresponding indices of the control groups.

Such features of EAC growth after treatment with NCs are to some extent confirmed by the data of determining the proliferative activity of tumor cells by the Ki-67 marker. Proliferative activity of tumor cells was determined by the number of Ki-67^{+}—cells using "PE Mouse Anti-Ki-67 Set" ("BD Pharmingen", USA, 556027) according to the manufacturer's instructions with flow cytometer "FACS Calibur" ("BD", USA). The average number was quantitatively assessed and density of antigens per cell was determined using the average fluorescence intensity (AFI) in the "WinMDi 2.9" software ("Joseph Trotter, La Jolla", USA).

It was found that in tumors formed on day 7 of cultivation of both total EAC population of cells and the CD44^{+}—fraction, the number of cells expressing Ki-67 protein was at the level of $95.6 \pm 7.4\%$ and $99.04 \pm 8.5\%$, respectively (Fig. 16.1). However, Ki-67^{+} cells derived from the CD44^{+} fraction had significantly higher average fluorescence intensity (AFI) compared to cells derived from the total EAC population (3710 ± 210.00 and 2661 ± 120.37, respectively).

Moreover, in the cells formed by the CD44^{+} fraction, a larger number of cells with a high expression of the marker Ki-67 was detected: Ki-67^{high} was equal to $69.24 \pm 7.40\%$ and its AFI was equal to 3732 ± 183.00 arb.units in comparison with the similar index of cells of total EAC population: Ki-67^{high} made $53.10 \pm 4.87\%$, AFI was 2232 ± 125.45 arb.units (Fig. 16.1, Table 16.2). This is evidence that the CD44^{+}—EAC fraction comprises the cells with higher proliferative activity. The most informative index of the phenotypic identification of CSCs is the expression of the CD44 molecule, which alone or in combination with other surface markers is used to determine this population of cells in different types of tumors, including EAC [2, 22, 36]. The most important role in tumorigenesis implementing is this molecule expression rate. Subpopulation of CD44^{high} cells has previously been found to have an increased potential for self-maintenance and is able to support the EAC development [22]. Therefore, it is quite natural that the number of CD44^{+}CD24^{−} and CD44^{high} cells in ascites formed by CD44^{+}—fraction was significantly higher than in total EAC population (Table 16.2).

Highly proliferating Ki-67[highs] are thought to be more sensitive and vulnerable to chemotherapeutic drugs than those with low values of this marker [37]. The search for therapeutic agents capable of inhibiting tumor growth is based on these principles. One such agent may be nanosized vanadium compounds, in particular NCs. Indeed, after treatment with NCs of the cells of total EAC population, the number of Ki-67^{+} cells in the peritoneal cavity decreased from $95.6 \pm 7.40\%$ to $61.84 \pm 5.67\%$, i.e. 1.6 times. (Fig. 16.1). The effect of NCs on the cells of total EAC population to the same extent (1.3 times) led to a decrease in both the percentage of Ki-67^{high}—cells and its AFI (Table 16.2). A much larger decrease in the total number of Ki-67^{+} and
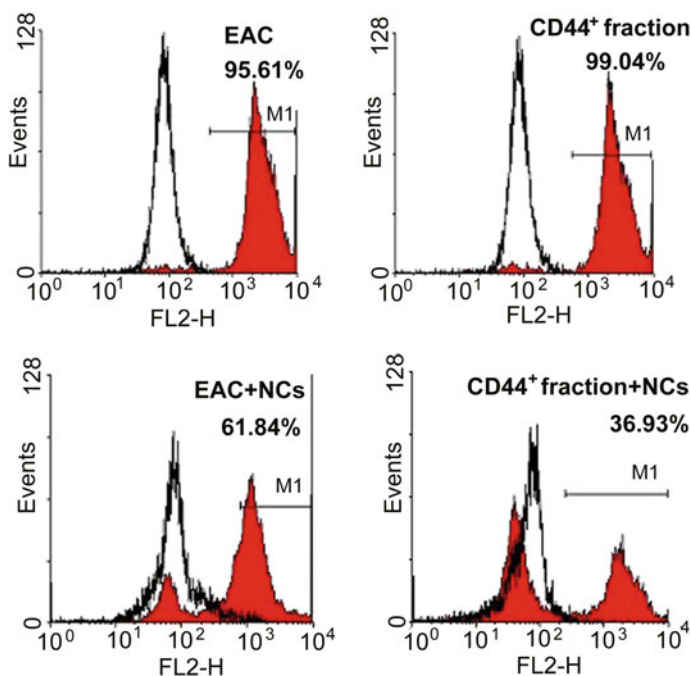
Fig. 16.1 Number of Ki-67$^+$—cells on day 7 of in vivo cultivation of total EAC population and CD44$^+$—fraction untreated and treated by NCs

highly proliferating Ki-67^{high} cells under the action of NCs was found in CD44$^+$—fraction—formed ascites (Table 16.2). Treatment of these cells with NCs decreased the number of Ki-67$^+$ and their AFI by about 2 times, and that of Ki-67^{high} and their AFI did by 4 and 3.5 times compared to similar CD44$^+$—fractions—untreated with NCs.

Confirmation that NCs mediate its effect on tumor by decreasing the number of CD44$^+$—cells is the fact that treatment of cells of total EAC population with NCs resulted in the formation of ascites with a reduced (18.5 times) number of CD44^{high}—cells and almost sixfold decreased content of CD44$^+$CD24$^-$—cells in comparison with the corresponding controls (Table 16.2). An even more impressive effect of NCs was observed with respect to the CD44$^+$ fraction. Thus, the coefficient of reduction in the content of the most tumorogenic CD44^{high} cells under the influence of NCs in this group reached 24.4 times, and the number of CD44$^+$CD24$^-$—cells made 11.3 times. In addition, there was not only a decrease in the number of CD44^{high} cells, but also their fluorescence degree by almost 3 times (Table 16.2).

Thus, it was found that ascites formed by CD44$^+$—cells fraction was more "aggressive" growth and had the ability to more rapidly expand the tumor, judging by the increased content of Ki-67^{high}- and CD44^{high}—cells (Table 16.2). The results obtained accept the ability of NCs to the greatest extent to inhibit the proliferative

Table 16.2 Phenotypic characteristics of EAC cells on day 7 of in vivo cultivation of total population and CD44$^+$—fractions before and after their treatment with NCs

Index	Total EAC population		CD44$^+$ —fraction	
	Control 1	+ NCs	Control 2	+ NCs
Number of Ki-67$^+$ cells, %	95.6 ± 7.4	61.8 ± 5.7*	99.0 ± 8.5	36.93 ± 3.7*#
AFI of Ki-67$^+$ cells, arb. units	2661 ± 120.4	1570 ± 97.0*	3710 ± 210.0#	1813 ± 85.2*#
Number of Ki-67^{high} cells, %	53.1 ± 4.9	38.6 ± 4.6*	69.2 ± 7.4#	16.9 ± 3.5*#
AFI of Ki-67^{high} cells, arb. units	2232 ± 125.5	1,744 ± 79.3*	3732 ± 183.0#	1043 ± 96.3*#
Number of CD44^{high} cells, %	0.37 ± 0.03	0.02 ± 0.04*	1.22 ± 0.05*#	0.05 ± 0.02*
AFI of CD44^{high} cells, arb. units	7465 ± 525	3554 ± 312*	9110 ± 637#	3114 ± 269*
Number of CD44$^+$CD24$^-$ cells, %	3.8 ± 0.5	0.6 ± 0.01*	5.65 ± 0.73#	0.50 ± 0.04*

Notes AFI—average fluorescence intensity; *—difference is significant in comparison with the corresponding indices of untreated EAC cells (Control 1 and 2); $p < 0.5$, #—difference is significant in comparison with the corresponding indices of total EAC population, $p < 0.05$

activity of the fraction of CD44+—cells. These data are to some extent consistent with the findings of Fasching PA et al., who found that cells that express Ki-67 to an increased degree were more sensitive to chemotherapeutic agents [37].

The reduced number of the most potent CD44^{high}—and highly proliferating Ki-67^{high}—cells under the influence of NCs clearly coincides with the decrease in absolute number of cells in the peritoneal cavity (see Table 16.2), which indicates the inhibition of tumor growth rate. It should be noted that the lowest number of CD44^{high} and Ki-67^{high} -cells in the growing pool of EAC after treatment with NCs was observed in the CD44+—fraction, which led to almost 90% inhibition of tumor growth rate (see Table 16.1).

The antitumor activity of vanadium compounds is known to be implemented by various mechanisms, including activating or suppressing a number of pluripotency genes, in particular *oct4*, *nanog* and *sox2*, which mutually regulate each other through a chain of relevant transcription factors [38–40]. Almost half of all transcription factors in the human genome are expressed in any cell type [41]. At the same time, abnormally high expression of *oct3/4*, *nanog* and *sox2*, even in highly differentiated cells, can induce their ability to pluripotency [42, 43]. Moreover, *oct4* and *sox2* transcription factors are components of Yamanaka ones [42, 44]. The authors showed that mouse and human fibroblasts can be reprogrammed into induced pluripotent stem cells by virus-mediated transduction of factors: Klf4, *oct3/4*, *sox2*, and c-Myc.

The mechanism of implementing the cooperative interaction of *oct3/4*, *nanog* and *sox2* transcription factors, assumes that they bind to each other's promoter and support or limit each other's expression, forming a regulatory network of autoregulation to maintain pluripotency of both cancer and embryonic stem cells. *sox2-oct4* transcription factors have been shown to be at the top of the hierarchical pyramid of pluripotent regulatory networks, with *sox2* transcription factor acting as a cofactor that regulates *oct4* gene activity [45]. In the *nanog* gene promoter, there is a binding site for the *oct4-sox2* complex, the successful interaction of which determines the functioning of the *nanog* and underlying target genes. There are preconditions to believe that cancer cells are genetically and epigenetically plastic [46]. This suggests that they have the potential for "reprogramming" by modulating the expression of the major pluripotency genes and the transcription factors they encode.

Because nanosized vanadium compounds have antitumor activity [28, 40], in this research we comparatively analyzed the expression rate of *nanog*, *oct4*, *sox2* pluripotency genes and the corresponding transcription factors in total EAC population and CD44+ cells—fractions untreated and treated by NCs as well as after subsequent cultivation in mice peritoneal cavity.

The rate of expression of *nanog, oct4, sox2* genes in EAC cells was determined by real-time polymerase chain reaction (PCR). For PCR, total RNA was isolated from 5×10^5 EC cells using the Thermo Scientific Gene Set PCR Purification Kit ("Thermo Fisher Scientific", USA). All samples were treated with DNase ("NeoFroxx", Germany). The reverse transcription reaction was performed using the appropriate Thermo Scientific First Standard cDNA Synthesis Kit ("Thermo Fisher Scientific", USA). The obtained cDNA was immediately used for PCR. All manipulations were performed according to the manufacturer's instructions. All TaqMan

PCR primers and probes were designed and synthesized by Metabion, Germany. Table 16.3 presents the sequence numbers in GenBank, nucleotide sequences of primers and probes, as well as the length of the corresponding amplification product. Real-time PCR was performed with ANK-16 ("Sintol", Russia) using a reaction mixture for real-time PCR One Taq (2X) with standard buffer, M04825 ("New England Biolab", Germany). Amplification was performed as follows: The first stage consisted of denaturation for 180 s at 95 °C, the second one involved denaturation at 95 °C for 20 s and annealing of primers at 60 °C for 50 s (Number of cycles was 40). Gene expression was analyzed using the method of ΔCt [47]. The results of the expression of *nanog, oct-4, sox-2* genes in EAC cells after treatment with NCs are presented as relative values, while "1" is the expression of the corresponding genes in untreated EAC cells (control). Data were normalized on the expression of the Rn18s "house-keeping" gene.

It was found that the treatment with NCs of the cells of total EAC population led to the formation of ascites with a significant decrease in the expression of all genes in comparison with similar indices of the corresponding control group (Fig. 16.2). In tumor, formed by the CD44^{+}—fraction, after treatment with NCs, a similar pattern of gene expression was observed, but the degree of their reduction was almost twice as large.

One possible explanation for this is the reported data of Petanidis et al. on the ability of vanadium-based NCs to inhibit tumor growth in vitro by impeding the TGF-β-mediated EMT of cells, which plays a key role in tumor progression and metastasis [48]. The authors showed that treatment of tumor cells with vanadium compounds decreased the expression of a number of CSCs markers, in particular CD44. According to other authors, it is the CD44 receptor and the increased activity of the functionally related *nanog* gene that contribute to the induction of EMT [19, 49]. Thus, we can assume that the effect of our NCs can be realized by preventing EMT, which is evidenced by the greatest inhibition of pluripotency gene expression in CD44^{+} fraction cells (Fig. 16.2) against the background of the strongest decrease in CD44^{+}—cells (see Table 16.2).

In both groups (induction of oncology pathology by cells of total EAC population and CD44^{+}—fraction) under NCs effect, the maximum inhibition of *nanog* gene expression was found (Fig. 16.2). Hamazaki et al. [39] also revealed that the addition of sodium vanadate to mouse embryonic stem cell culture selectively inhibited *nanog* gene transcription without any significant changes in *oct3/4* and *sox2* expression. The authors attribute this to the fact that vanadium compounds in the form of V^{5+} can act as tyrosine phosphatase inhibitors, controlling the activity of pluripotency genes.

Excessive expression of *nanog* is known to promote malignant transformation of cells, enhancing their proliferation and acquisition of malignant properties such as clonogenic growth, oncogenicity, invasiveness, and drug resistance [50, 51]. However, other authors reports about the contraversal role of *nanog* in carcinogenesis induction. Thus, in contrast to models of transgenic mice, in which hyperexpression of *oct4* caused dysplastic and aggressive tumor-like tumors in a relatively short time in the epithelium of skin and gastrointestinal tract [52], overexpression of *nanog* induced by following intraperitoneal injection of doxycycline and dexamethasone to

Table 16.3 Primers and probes sequences used in the research

Gene name, number in GenBank	Forward (F) and reverse (R) primers	Probe	Product length
oct4 (Pou5f1), NM_013633.3	F: GTGGAGGAAGCCGACAACAAT R: GCTTCGGGCACTTCAGAAACA	(ROX)AGACTCCACCTCACACGGTTCTCAATG(BHQ2)	142
nanog, NM_028016.2	F: GAACAACCAGACCTGGACCAA R: GAGTCACAGAGTAGTTCAGGAA	(ROX)AACTTGGAGCAGCCAGGCCTGGAC(BHQ2)	248
sox2, NM_011443.3	F: ACAGCTACGCGCACATGAAC R: TGCGAGCTGGTCATGGAGTT	(ROX)TGGAGCAACGGCAGCTACAGCATGAT(BHQ2)	169
Rn18s, NR_003278.3	F: ATTGCAATTATTCCCCATGAACGA R: CACTAAACCATCCAATCGGTAG	(R6G)TAAGTGCGGGTCATAAGCTTGCGTTG(BHQ2)	121
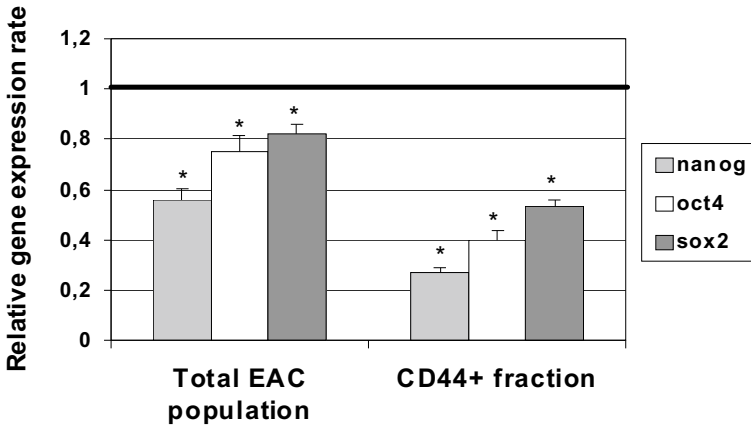
Fig. 16.2 Relative expression rate of *nanog, oct4, sox2* genes in culture cells initiated by NCs treated cells of total EAC population and CD44⁺ fraction. Note. "1" denotes the rate of gene expression in untreated EAC cells; normalized to the house-keeping gene (18s rRNA); *—difference is significant in comparison with similar indices of untreated cells; $p < 0.05$

transgenic mice, contributed to the formation of only moderate hyperplastic changes in the small and large intestine cells [53] as well as stratified epithelium of the anterior stomach and esophagus [54].

The trigger for cancer development in human mammary gland is hyperexpression of the *sox2* gene, which is characteristic of tumors at the early stages of their development, and causes the formation of mammospheres in vitro even without increasing the *nanog* and *oct4* genes expression [55]. The data of Lu et al. are in agreement that overexpression of *nanog* alone in breast epithelial cells is insufficient to induce cancer [56].

Based on this, there is every reason to believe that *nanog* does not function as a classic oncogene, unlike the *sox2* and *oct4* genes. Therefore, it should be emphasized that although in our experiments the use of NCs was more conducive to inhibition of *nanog* gene expression in cells of total EAC population and CD44⁺—fraction (see Fig. 16.2), but for complete inhibition of tumor growth this was not enough, judging by the absolute number of cells in peritoneal cavity of tumor-bearing mice (see Table 16.1), that requires coordinated activity of other transcription factors.

It should be noted that a variety of extra- and intracellular stimuli of the CSCs microenvironment, including hypoxia, low pH, lack of trophic substances, oxidative stress which, incidentally, vanadium compounds are capable of this can cause significant posttranslational modifications of transcription factors [57]. Thus, the most common of them the *oct4* includes phosphorylation, ubiquitination, sumoylation, and glycosylation, which are important regulatory mechanisms of cell pluripotency [58, 59]. By regulating target genes, post-translationally altered proteins can promote the induction or inhibition of stem cell properties of CSCs (self-maintenance, unrestricted proliferation, ability to metastasize, drug resistance).
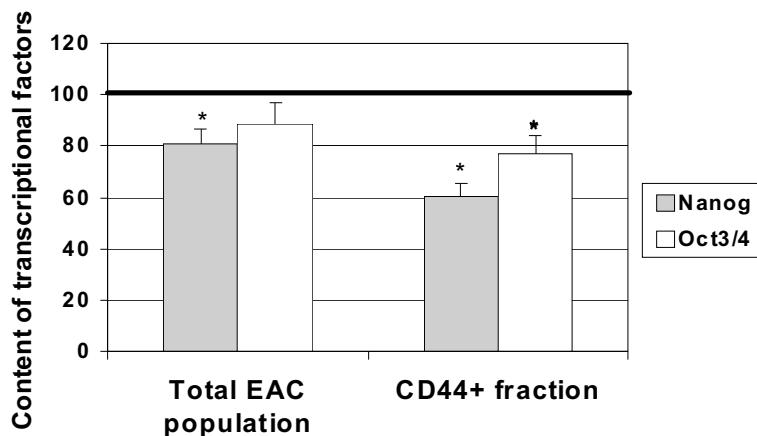
Fig. 16.3 Expression of *nanog* and *oct3/4* transcription factors in tumor cells, formed by total EAC population and CD44^{+}—fraction before and after treatment of NCs. *Notes* The values of the content of transcription factors in the cells of untreated total EAC population (Control 1) and untreated CD44^{+}—fractions (Control 2) were assumed as 100%. *—difference is significant in comparison with the corresponding indices of untreated EAC cells; $p < 0.05$

Therefore, at the next stage of research, the change in the degree of activity of transcriptional factors of pluripotency (*nanog* and *oct3/4*) as products of functional activity of these genes under the influence of NCs in different forms of EC cells was determined (Fig. 16.3). The content of transcriptional factors of pluripotency *oct3/4* and *nanog* in EAC cells was examined with a flow cytometer "FACS Calibur" ("BD", USA) using monoclonal antibodies ("BD Biosciences", USA) *oct3/4* (PE, №560,186), *nanog* (Alexa Fluor, №560,278) by means of "CellQuestPro" software ("BD", USA).

It was found that under the influence of NCs in all experimental groups there were formed tumors with reduced expression of transcription factors (*nanog* and *oct3/4*) in comparison with the similar indices control groups (Fig. 16.3). Judging by the changes in the expression rate, the transcription factors (*nanog* and *oct3/4*) in the tumor cells formed by the CD44^{+}—fraction were much more sensitive to the action of NCs. These data are clearly consistent with the above results on the strong reduction under the influence of NCs content of CD44^{high} cells and Ki-67^{high} cells in ascites formed by the CD44^{+}—fraction (see Table 16.2). Thus, we can assume that the antitumor effect of NCs can be implemented by inhibiting the expression of pluripotency genes and the corresponding transcription factors in highly proliferating CD44^{+}—cells.

The lifespan of animals injected with a total EAC population of cells to induce tumor was 21 days (Fig. 16.4), while in those with injected CD44^{+}—fraction, this time did not exceed 11 days. Treatment with NCs of total EAC population prolonged a life expectancy of animals in this group by 4 days (up to 25 days compared with 21 days in animals with EAC). It was found that up to 20 days after the application

Fig. 16.4 Lifespan of mice with EAC, determined by the Kaplan–Meier method
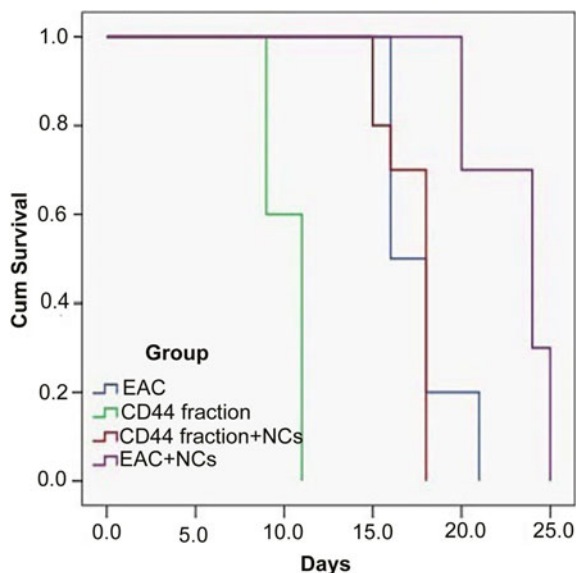
of NCs 70% of mice and up to 24 days about 30% survived. That is, the treatment of total EAC cell population with NCs caused a prolongation of life expectancy of tumor-bearing animals by 19%.

Treatment with NCs of the most actively proliferating cells of CD44+—fraction with a high expression rate of pluripotency genes and the corresponding transcription factors led to a prolongation of life expectancy of tumor-bearing animals by 30% compared with the corresponding control. Thus, the total life expectancy of animals in this group after their treatment with NCs was 28 days with their predominant death (70%) only at the end of the observation period (Fig. 16.4).

That is, treatment with NCs of cells of total EAC population increased a lifespan of animals in average by 4 days, and similar treatment of more tumorigenic cells CD44+—fraction contributed to a rise in this value per week. This suggests that NCs can selectively inhibit the functional activity of CSCs by synergistically reducing the activity of genes that regulate pluripotency and the content of corresponding transcription factors that stipulates the in vivo formation of pool of EAC cells with reduced proliferative activity, judging by the content of Ki-67+—cells (see Table 16.2). In clinical practice, this marker expression rate correlates with the severity of different cancer types [37, 60]. The results of our study suggest that the action of NCs causes the modification of genomic and post-genomic cell activities, generally resulting in inhibition of the proliferative ability of EAC cells. This is evidenced by the inhibiting the expression rate of Ki-67 protein and the following decrease in the intensity of tumor growth. It is possible that NCs may inhibit tumor development by several alternative mechanisms, namely by dissociating the integrative interaction of pluripotency genes to trigger a proliferative signal to the translation apparatus due to vanadium induction of DNA breaks [31], mitochondrial dysfunction with

subsequent induction of apoptotic and necrotic changes in cells [28], due to the ability of vanadium compounds to act as artificial nucleases and to cleave the DNA of actively proliferating cells, preventing their replication, etc. [31]. Jointly, all these processes significantly inhibit the tumor expansion, which was manifested by a rise of life expectancy of tumor-bearing animals. An in-depth study of the action of NCs with the specifying the mechanism of their antitumor action is the purpose of further research. However, the obtained data already allow us to consider the NCs based on NPs of orthovanadates of rare earth metals and cholesterol as promising drugs for antitumor therapy.

16.4 Conclusions

1. The ability of nanocomplexes consisting of nanoparticles of orthovanadates of rare earth metals GdYEuVO$_4$ and cholesterol to inhibit the proliferative activity of EAC has been established.
2. Nanocomplexes are to a greater extent able to inhibit the growth rate of tumor, initiated by the CD44$^+$ -fraction compared to similar index for total EAC population.
3. The antitumor effect of nanocomplexes is implemented at the genomic and postgenomic levels by synergistically reducing the expression rate of *nanog*, *oct4*, *sox2* pluripotency genes and the corresponding transcription factors in cells.
4. Treatment of cells of total EAC population with nanocomplexes increased the life expectancy of tumor-bearing animals by an average of 19%, and similar treatment of more tumorigenic cells of CD44$^+$—fraction did it by an average of 30%.
5. The ability of nanocomplexes to selectively inhibit functional activity of the most potent CD44^{high} when reducing the content of highly proliferating Ki-67^{high}—cells indicates their possible use as an antitumor agent in treating the most malignant tumors.

References

1. Bonnet D, Dick JE (1997) Human acute myeloid leukemia is organized as a hierarchy that originates from a primitive hematopoietic cell. Nat Med 3(7):730–737. https://doi.org/10.1038/nm0797-730
2. Al-Hajj M, Wicha MS, Benito-Hernandez A, Morrison SJ, Clarke MF (2003) Prospective identification of tumorigenic breast cancer cells. Proc Natl Acad Sci USA 100(7):3983–3988. https://doi.org/10.1073/pnas.0530291100
3. Ghebeh H, Sleiman GM, Manogaran PS et al (2013) Profiling of normal and malignant breast tissue show CD44high/CD24low phenotype as a predominant stem/progenitor marker when used in combination with Ep-CAM/CD49f markers. BMC Cancer 13:289. https://doi.org/10.1186/1471-2407-13-289

4. Nassar D, Blanpain C (2016) Cancer stem cells: basic concepts and therapeutic implications. Annu Rev Pathol 11:47–76. https://doi.org/10.1146/annurev-pathol-012615-044438
5. Ponti D, Costa A, Zaffaroni N et al (2005) Isolation and in vitro propagation of tumorigenic breast cancer cells with stem/progenitor cell properties. Cancer Res 65:5506–5511. https://doi.org/10.1158/0008-5472.CAN-05-0626
6. Wang R-A, Li Q-L, Li Z-S et al (2013) Apoptosis drives cancer cells proliferate and metastasize. J Cell Mol Med 17(1):205–211. https://doi.org/10.1111/j.1582-4934.2012.01663.x
7. Burz C, Berindan-Neagoe I, Balacescu O, Irimie A (2009) Apoptosis in cancer: key molecular signaling pathways and therapy targets. Acta Oncol 48(6):811–821. https://doi.org/10.1080/02841860902974175
8. Sun X, Kaufman PD (2018) Ki-67: more than a proliferation marker. Chromosoma 127(2):175–186. https://doi.org/10.1007/s00412-018-0659-8
9. Endl E, Gerdes J (2000) The Ki-67 protein: fascinating forms and an unknown function. Exp Cell Res 257(2):231–237. https://doi.org/10.1006/excr.2000.4888
10. Kreipe H (2018) Ki67: biological intertumor variance versus variance of assay. Pathologe 39(Suppl 2):272–277. https://doi.org/10.1007/s00292-018-0502-2
11. Graefe C, Eichhorn L, Wurst P et al (2019) Optimized Ki-67 staining in murine cells: a tool to determine cell proliferation. Mol Biol Rep 46(4):4631–4643. https://doi.org/10.1007/s11033-019-04851-2
12. Jaggupilli A, Elkord E (2012) Significance of CD44 and CD24 as cancer stem cell markers: an enduring ambiguity. Clin Dev Immunol 2012:708036. https://doi.org/10.1155/2012/708036
13. Ortiz-Montero P, Liu-Bordes W-Y, Londoño-Vallejo A et al (2018) CD24 expression and stem-associated features define tumor cell heterogeneity and tumorigenic capacities in a model of carcinogenesis. Cancer Manag Res 10:5767–5784. https://doi.org/10.2147/CMAR.S176654
14. Morel AP, Lièvre M, Thomas C et al (2008) Generation of breast cancer stem cells through epithelial-mesenchymal transition. PLoS ONE 3(8):e2888. https://doi.org/10.1371/journal.pone.0002888
15. Deng X, Apple S, Zhao H et al (2017) CD24 Expression and differential resistance to chemotherapy in triple-negative breast cancer. Oncotarget 8(24):38294–308. https://doi.org/10.18632/oncotarget.16203
16. Blick T, Hugo H, Widodo E et al (2010) Epithelial mesenchymal transition traits in human breast cancer cell lines parallel the CD44(hi/)CD24 (lo/-) stem cell phenotype in human breast cancer. J Mammary Gland Biol Neoplasia 15:235–252. https://doi.org/10.1007/s10911-010-9175-z
17. Liu S, Cong Y, Wang D et al (2014) Breast cancer stem cells transition between epithelial and mesenchymal states reflective of their normal counterparts. Stem Cell Rep 2:78–91. https://doi.org/10.1016/j.stemcr.2013.11.009
18. Park SY, Lee HE, Li H et al (2010) Heterogeneity for stem cell-related markers according to tumor subtype and histologic stage in breast cancer. Clin Cancer Res 16:876–887. https://doi.org/10.1158/1078-0432.CCR-09-1532
19. Wang D, Lu P, Zhang H et al (2014) Oct-4 and Nanog promote the epithelial-mesenchymal transition of breast cancer stem cells and are associated with poor prognosis in breast cancer patients. Oncotarget 5(21):10803–10815. https://doi.org/10.18632/oncotarget.2506
20. Xu H, Tian Y, Yuan X et al (2015) The role of CD44 in epithelial–mesenchymal transition and cancer development. Onco Targets Ther 8:3783–92. https://doi.org/10.2147/OTT.S95470
21. Ozaslan M, Karagoz ID, Kilic IH, Guldur ME (2011) Ehrlich ascites carcinoma. Afr J Biotechnol 10(13):2375–2378
22. Goltsev AN, Babenko NN, Gaevskaya YA et al (2017) Nanotechniques inactivate cancer stem cells. Nanoscale Res Lett 12(1):415. https://doi.org/10.1186/s11671-017-2175-9
23. Tian X, Fan J, Hou W et al (2016) Sodium orthovanadate induces the apoptosis of SH-SY5Y cells by inhibiting PIWIL2. Mol Med Rep 13:874–880. https://doi.org/10.3892/mmr.2015.4616
24. Klein A, Holko P, Ligeza J, Kordowiak AM (2008) Sodium orthovanadate affects growth of some human epithelial cancer cells (A549, HTB44, DU145). Folia Biol (Krakow) 56(3–4):115–121. https://doi.org/10.3409/fb.56_3-4.115-121

25. Liu TT, Liu YJ, Wang Q, Yang X-G, Wang K (2012) Reactive-oxygen-species-mediated Cdc25C degradation results in differential antiproliferative activities of vanadate, tungstate, and molybdate in the PC-3 human prostate cancer cell line. J Biol Inorg Chem 17(2):311–320. https://doi.org/10.1007/s00775-011-0852-1

26. Günther TMF, Kviecinski MR, Baron CC et al (2013) Sodium orthovanadate associated with pharmacological doses of ascorbate causes an increased generation of ROS in tumor cells that inhibits proliferation and triggers apoptosis. Biochem Biophys Res Commun 430(3):883–888. https://doi.org/10.1016/j.bbrc.2012.12.061

27. Goltsev AN, Babenko NN, Gaevskaya YuA, et al (2015) Application of nanoparticles based on rare Earth orthovanadates to inactivate Ehrlich carcinoma growth. Biotechnologia Acta 8(4):113–121. https://doi.org/10.15407/biotech8.04.113

28. Goltsev A, Malyukin Yu, Babenko N, et al (2020) Mechanisms of antitumor effect of nanomaterials based on rare earth orthovanadates. In: Fesenko O, Yatsenko L (eds) Nanooptics and photonics, nanochemistry and nanobiotechnology, and their applications. Springer Proceedings in Physics, vol 247. Springer, Cham. https://doi.org/10.1007/978-3-030-52268-1_1

29. Goltsev AN, Malyukin YuV, Dubrava TG et al (2016) Nanocomposites specifically penetrate and inhibit tumor cells. Mat-wiss u Werkstofftech 47(2–3):156–165. https://doi.org/10.1002/mawe.201600457

30. Leyn IE, Butenko N, Di Virgilio AL et al (2014) Vanadium and cancer treatment: antitumoral mechanisms of three oxidovanadium (IV) complexes on a human osteosarcoma cell line. J Inorg Biochem 134:106–117. https://doi.org/10.1016/j.jinorgbio.2013.10.009

31. Kowalski S, Wyrzykowski D, Inkielewicz-Stępniak I (2020) Molecular and cellular mechanisms of cytotoxic activity of vanadium compounds against cancer cells. Molecules 25(7):1757. https://doi.org/10.3390/molecules25071757

32. Saha U, Mukherjea KK (2014) DNA binding and nuclease activity of an oxovanadium valinato-Schiff base complex. Int J Biol Macromol 66:166–171. https://doi.org/10.1016/j.ijbiomac.2014.02.033

33. Klochkov VK (2009) Aqueous colloid solutions of nanoluminophores nReVO4:Eu3+ (Re = Y, Gd, La). Mater Sci Nanostruct 2:3–8 [Ukrainian]

34. Klochkov VK (2015) Method for producing water dispersion of cholesterol. Patent of Ukraine 108011 [Ukrainian]

35. Goltsev AM, Malyukin YV, Babenko NM et al (2020) Antitumor activity of spherical nanoparticles GdYVO$_4$:Eu^{3+} depends on pre-incubation time. Appl Nanosci 10:2749–2758. https://doi.org/10.1007/s13204-020-01284-3

36. Schatton T, Murphy GF, Frank NY et al (2008) Identification of cells initiating human melanomas. Nature 451(7176):345–349. https://doi.org/10.1038/nature06489

37. Fasching PA, Heusinger K, Haeberle L et al (2011) Ki67, chemotherapy response, and prognosis in breast cancer patients receiving neoadjuvant treatment. BMC Cancer 11:486–498. https://doi.org/10.1186/1471-2407-11-486

38. Evangelou AM (2002) Vanadium in cancer treatment. Crit Rev Oncol Hematol 42(3):249–265. https://doi.org/10.1016/S1040-8428(01)00221-9

39. Hamazaki T, Kehoe SM, Nakano T, Terada N (2006) The Grb2/Mek pathway represses Nanog in murine embryonic stem cells. Mol Cell Biol 26:7539–7549. https://doi.org/10.1128/MCB.00508-06

40. Ivankovic S, Music S, Gotic M, Ljubesic N (2006) Cytotoxicity of nanosize V2O5 particles to selected fibroblast and tumor cells. Toxicol In Vitro 20:286–294

41. Vaquerizas JM, Kummerfeld SK, Teichmann SA, Luscombe NM (2009) A census of human transcription factors: function, expression and evolution. Nat Rev Genet 10:252–263. https://doi.org/10.1038/nrg2538

42. Takahashi K, Tanabe K, Ohnuki M et al (2007) Induction of pluripotent stem cells from adult human fibroblasts by defined factors. Cell 131(5):861–872. https://doi.org/10.1016/j.cell.2007.11.019

43. Pan G, Thomson JA (2007) Nanog and transcriptional networks in embryonic stem cell pluripotency. Cell Res 17:42–49. https://doi.org/10.1038/sj.cr.7310125

44. Takahashi K, Yamanaka S (2006) Induction of pluripotent stem cells from mouse embryonic and adult fibroblast cultures by defined factors. Cell 26(4):663–676. https://doi.org/10.1016/j.cell.2006.07.024

45. Rodda DJ, Chew JL, Lim LH et al (2005) Transcriptional regulation of nanog by OCT4 and SOX2. J Biol Chem 280(26):24731–24737. https://doi.org/10.1074/jbc.M502573200

46. Meacham CE, Morrison SJ (2013) Tumour heterogeneity and cancer cell plasticity. Nature 501(7467):328–337. https://doi.org/10.1038/nature12624

47. Livak KJ, Schmittgen ThD (2001) Analysis of relative gene expression data using real-time quantitative PCR and the the 2(-Delta Delta C(T)) method. Methods 25:402–408. https://doi.org/10.1006/meth.2001.1262

48. Petanidis S, Kioseoglou E, Domvri K et al (2016) In vitro and ex vivo vanadium antitumor activity in (TGF-в)-induced EMT. Synergistic activity with carboplatin and correlation with tumor metastasis in cancer patients. Int J Biochem Cell Biol 74:121–134. https://doi.org/10.1016/j.biocel.2016.02.015

49. Strouhalova D, Macejova D, Lastovickova M et al (2020) CD44 and vimentin, markers involved with epithelial-mesenchymal transition: a proteomic analysis of sequential proteins extraction of triple-negative breast cancer cells after treatment with all-trans retinoic acid. Gen Physiol Biophys 39(4):399–405. https://doi.org/10.4149/gpb_2020026

50. Zhang J, Wang X, Chen B et al (2005) Expression of Nanog gene promotes NIH3T3 cell proliferation. Biochem Biophys Res Commun 338:1098–1102. https://doi.org/10.1016/j.bbrc.2005.10.071

51. Lin YL, Han ZB, Xiong FY et al (2011) Malignant transformation of 293 cells induced by ectopic expression of human Nanog. Mol Cell Biochem 351(1–2):109–116. https://doi.org/10.1007/s11010-011-0717-5

52. Hochedlinger K, Yamada Y, Beard C et al (2005) Ectopic expression of Oct-4 blocks progenitor-cell differentiation and causes dysplasia in epithelial tissues. Cell 121:465–477. https://doi.org/10.1016/j.cell.2005.02.018

53. Fischedick G, Wu G, Adachi K et al (2014) Nanog induces hyperplasia without initiating tumors. Stem Cell Res 13(2):300–315. https://doi.org/10.1016/j.scr.2014.08.001

54. Piazzolla D, Palla AR, Pantoja C et al (2014) Lineage-restricted function of the pluripotency factor NANOG in stratified epithelia. Nat Commun 5:4226. https://doi.org/10.1038/ncomms5226

55. Leis O, Eguiara A, Lopez-Arribillaga E, Alberdi MJ et al (2012) Sox2 expression in breast tumours and activation in breast cancer stem cells. Oncogene 31:1354–1365. https://doi.org/10.1038/onc.2011.338

56. Lu X, Mazur SJ, Lin T, Appella E, Xu Y (2014) The pluripotency factor NANOG promotes breast cancer tumorigenesis and metastasis. Oncogene 33:2655–3266. https://doi.org/10.1038/onc.2013.209

57. Clevers H (2011) The cancer stem cell: premises, promises and challenges. Nat Med 17:313–319. https://doi.org/10.1038/nm.2304

58. Fessler E, Dijkgraaf FE, De Sousa EMF, Medema JP (2013) Cancer stem cell dynamics in tumor progression and metastasis: is the microenvironment to blame? Cancer Lett 341(1):97–104. https://doi.org/10.1016/j.canlet.2012.10.015

59. Cai N, Li M, Qu J et al (2012) Post-translational modulation of pluripotency. J Mol Cell Biol 4:262–265. https://doi.org/10.1093/jmcb/mjs031

60. Zhu X, Chen L, Huang B et al (2020) The prognostic and predictive potential of Ki-67 in triple-negative breast cancer. Sci Rep 10(1):225. https://doi.org/10.1038/s41598-019-57094-3

Chapter 17
Extraction and Properties of Nanocellulose from Hemp Fibers

V. A. Barbash, O. V. Yashchenko, O. S. Yakymenko, and R. M. Zakharko

17.1 Introduction

Recent scientific and technological advances in the production of new materials emphasize the importance of using renewable sources of raw materials to replace products from depleted oil and gas resources. In the context of sustainable development, the reuse and recycling of agricultural plants can minimize the environmental problems. Cellulose-containing fibers attract the attention of scientists and manufacturers due to the high availability and demand for renewable raw materials for the production of products with unique physical, chemical, and physiological properties. Such products include nanocellulose, which has mechanical properties with high values of the Young's modulus and tensile strength at the level of Kevlar, transparency at the level of quartz glass, low weight and a large absolute surface, potential compatibility with other materials such as polymers, proteins, and living cells [1–3].

Cellulose is the most common organic compound in the world, which is produced annually through photosynthesis in significant quantities. Cellulose, as the main structural component of the cell walls of plant raw materials, is a promising material for the production of various consumer goods, in particular, nanocellulose.

Nanocellulose as a biodegradable material is widely used in the production of flexible electronics [4, 5], to increase the mechanical strength and improve the surface

V. A. Barbash (✉) · O. V. Yashchenko · O. S. Yakymenko · R. M. Zakharko
National Technical University of Ukraine "Igor Sikorsky Kyiv Polytechnic Institute", Kyiv, Ukraine
e-mail: v.barbash@kpi.ua

O. V. Yashchenko
e-mail: voliav@ukr.net

O. S. Yakymenko
e-mail: olgayakymenko@i.ua

243

properties of paper and paperboard [6, 7], in the composition of polymer and cement materials [8, 9], in pharmaceuticals and medicine [10, 11].

Qualitative indicators of nanocellulose depend on the quality of raw materials and the method of obtaining nanocellulose [12]. Nanocellulose is obtained by various methods, usually from wood pulp or cotton pulp for chemical processing. Such pulp by chemical composition should have a high content of α-cellulose (97.5–99%) and a low residual content of non-cellulosic components, not more than 0.3% lignin, organic and mineral substances [13]. The main raw materials for pulp production in world practice are coniferous and deciduous wood species. Countries with limited timber resources consider non-wood plant raw materials as a potential source of pulp. The following types of non-wood plant raw materials are suitable for pulp production: cereal stalks and fibers of industrial crops, in particular fibers of hash-free industrial hemp [14–17].

Hash-free industrial hemp is an annual plant in the cannabis bast fiber family that is grown for fiber and seeds. Hemp stems are widely used in the automotive, paper, chemical, furniture, construction industries [18, 19]. Hemp fiber in section has a round shape, its walls are thick, and the channel is narrow. In terms of chemical composition, hemp fibers contain up to 80–90% of α-cellulose and a significant amount of hemicelluloses. Due to this, the fibers are easily fibrillated during grinding, forming a fatty mass, which is important for the production of thin types of paper such as cigarette, copy, condenser, which are characterized by high mechanical strength and elasticity [20].

Among the existing traditional methods of obtaining pulp, the most common are sulfate method, which belongs to alkaline methods, and sulfite method, which refers to acid methods [21]. In the process of cooking pulp by these methods, sulfur-containing by-products are formed, which are harmful to the environment. An alternative to these methods is non-traditional methods of delignification of plant raw materials. An example of environmentally safer methods are the various options for producing pulp using organic solvents, in particular a solution of peracetic acid [22]. The advantages of this method are to carry out the process in one stage at temperatures up to 100 °C in a relatively short time to obtain pulp, which does not require an additional bleaching process [23].

The aim of the work is to obtain pulp from hemp fibers for chemical processing by environmentally friendly organosolv method of delignification and obtaining nanocellulose by hydrolysis using sulfuric acid and study of its properties.

17.2 Experiment

17.2.1 Materials

Hemp grown in the Zhytomyr region of Ukraine was used for experiments. To obtain pulp, hemp fibers were sorted from stems and leaves, ground to a size of 5–10 mm

and stored in a desiccator to maintain constant humidity. According to standard methods [24], the chemical composition of hemp fibers was determined, which in comparison with the chemical composition of the most common representatives of wood and bast fibers of flax. The analysis of the chemical composition of hemp fibers and the process of cellulose hydrolysis were carried out using chemically pure substances.

17.2.2 Methods

To obtain hemp, pulp used methods of alkaline extraction and cooking in flasks at atmospheric pressure under reflux. The consumption of NaOH solution was 5% by weight of hemp fibers, at a ratio of liquid to solid 10:1. Alkaline extraction was performed at a temperature about 100 °C for 60, 120, and 180 min. The washed pulp was sent for cooking in a mixture of glacial acetic acid and hydrogen peroxide at a ratio of 70:30 by volume at a temperature of 98 ± 2 °C for 60, 120, and 180 min. The obtained organosolv hemp pulp (OHP) thoroughly washed with hot distilled water and stored moist in airtight containers to obtain nanocellulose. Such values of temperature and duration of thermochemical treatment were taken on the basis of our previous research for other non-wood plant raw materials [25–28].

To obtain nanocellulose used the method of acid hydrolysis of OHP followed by its sonication. The OHP hydrolysis process was carried out using sulfuric acid solutions with a concentration of 40, 45, and 50% at a temperature of 40, 50, and 60 °C for 60, 75, and 90 min. The resulting nanocellulose was thoroughly washed with distilled water using a laboratory centrifuge to achieve a neutral pH value. Then, the nanocellulose suspension was treated with ultrasound using an ultrasonic dispersant UZDN—2t for 60 min to disperse the particles. Due to cavitation, the clots of nanocellulose particles are destroyed, which leads to a stable gel of evenly dispersed particles. Gels were used to make films by casting nanocellulose suspension in Petri dishes and drying them in air for several days. The obtained films were used to determine the physical and mechanical parameters.

The scanning electron microscopy (SEM) method was used to perform morphological studies using a PEM—106I microscope (SELMI, Ukraine). Samples for research were coated with a layer of gold by spraying. The transparency of nanocellulose films was determined by the method of studying electron absorption spectra in the range from 200 to 1100 nm. The spectra of the films in the UV, visible, and near-infrared regions were recorded using a two-beam spectrophotometer 4802 (UNICO, USA) with a resolution of 1 nm. The density of nanocellulose films was determined in accordance with ISO 534:1988. Transmission electron microscopy (TEM) method used to determine the size of nanocellulose particles using an electron microscope TEM125K (SELMI, Ukraine). To do this, a dissolved nanocellulose suspension of 0.1 wt% was applied on a thin copper frame Lacey Formvar/Carbon, 400 mesh (TED PELLA, Inc, USA).

17.3   Results and Discussion

17.3.1   Chemical Composition

To determine the optimal values of technological parameters for obtaining cellulose from hemp fibers, it is necessary to know the content of its main components. For this, a comparative analysis of the chemical composition of hemp fibers with the most common representatives of coniferous and deciduous woods and bast fibers of flax was carried out (Table 17.1).

From the data in Table 17.1, it is seen that hemp fibers in terms of cellulose, lignin, and minerals are similar to fibers of flax, but differ from their content in wood. The content of cellulose in hemp fibers significantly exceeds the content of cellulose in coniferous and deciduous species of wood and has several times lower lignin content compared to wood. The content of other components of hemp fibers are within their content in other representatives of plant raw materials, with the exception of minerals. This specific content of the main components of hemp fibers must be taken into account in the processes of their delignification and a priori indicate the need for lower consumption of chemicals in obtaining pulp from them compared to obtaining pulp from wood [30].

The dependence of the quality indicators of hemp pulp on the duration of alkaline extraction and peracetic cooking is shown in Figs. 17.1, 17.2 and 17.3.

As can be seen from Figs. 17.1 and 17.2 data, with increasing duration of the process of alkaline treatment and peracetic cooking residual content of lignin and minerals decreases, which allows to obtain cellulose of the required quality for further chemical processing into cellulose-containing products, in particular to obtain nanocellulose. The yield of hemp pulp after alkaline extraction relative to the weight of dry material (Fig. 17.3a) and the yield of hemp pulp after peracetic cooking relative to the weight of pulp after alkaline extraction (Fig. 17.3b) naturally decreases with an increase in the duration of thermochemical treatments due to the transfer of lignin, organic and mineral substances (ash) from plant materials into the cooking

Table 17.1 Composition of the main components of hemp fibers and other representatives of plant raw materials, % relative to the weight of dry material

Component	Hemp fibers	Spruce [21]	Poplar [21]	Flax fibers [29]
Cellulose	73.9	46.1	51.0	69.5
Lignin	8.8	28.5	21.9	6.1
Extraction in H_2O	4.2	7.3	2.8	3.7
NaOH	20.2	18.3	22.2	13.4
RFW[a]	1.9	2.9	2.7	3.6
Ash	1.6	0.2	0.9	1.5

[a]RFW—resins, fats, waxes
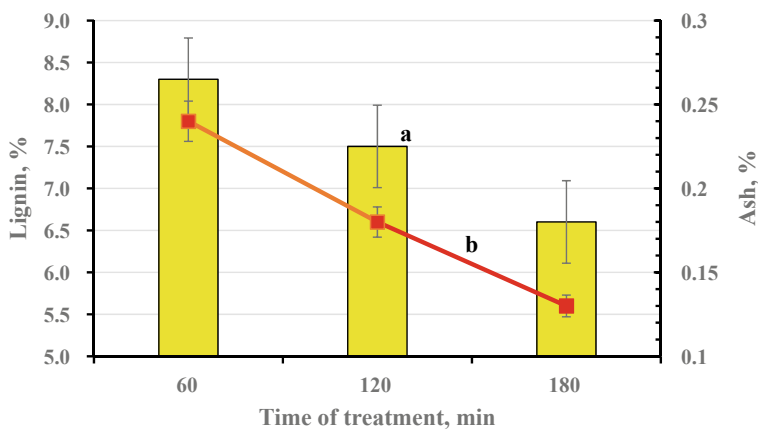
Fig. 17.1 Dependence of the content of residual lignin (**a**) and ash (**b**) after alkaline extraction on the duration of processing
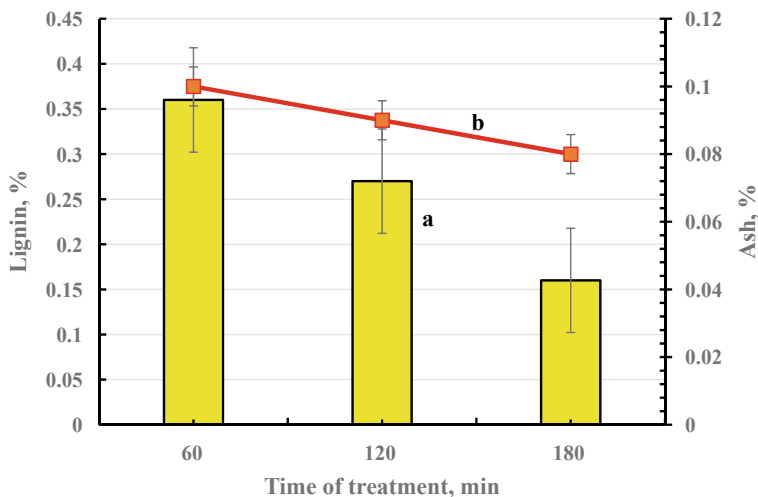
Fig. 17.2 Dependence of the content of residual lignin (**a**) and minerals (**b**) after peracetic cooking on the duration of processing

solution. To obtain nanocellulose, we used OHP obtained after coarse cooking for 180 min with a residual lignin content of 0.16% and ash 0.08%.
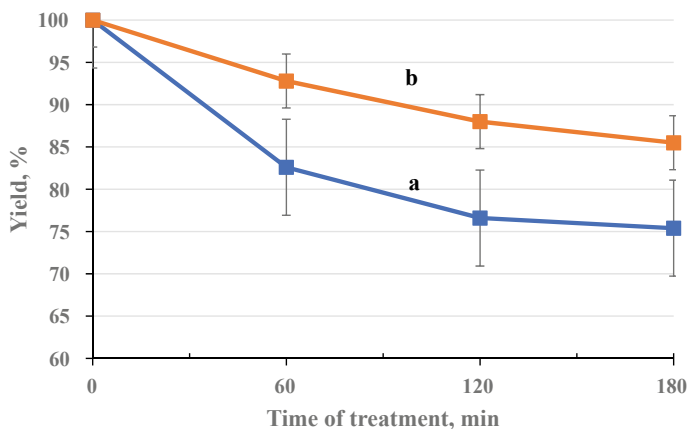
Fig. 17.3 Dependence of the yield of hemp pulp after alkaline extraction (**a**) and after peracetic cooking (**b**) on the duration of processing

17.3.2 Morphology

Morphological changes in the structure of plant material were observed by scanning electron microscopy (Fig. 17.4). As can be seen from Fig. 17.4a, the raw material has densely arranged fibers, which as a result of alkaline extraction are divided into individual fibers and smaller than in the raw material content of hemicelluloses and minerals. There is a partial removal of lignin, which bound the fibers in the raw material (Fig. 17.4b). Figure 17.4c shows parts of hemp fibers with small residues of lignin and extractives. Due to the action of the cooking solution of peracetic acid, there is a partial destruction of the fibers with a decrease from length to 20–250 μm (Fig. 17.4c). Due to the action of sulfuric acid in the process of hydrolysis of OHP, there is a destruction of 1–4 glycosidic bonds between glucopyranose units of cellulose macromolecules, dissolution of the amorphous part of cellulose and reducing the size of fibers to nanoparticles (Fig. 17.4d).

17.3.3 Mathematical Modeling

In order to determine the regression equations describing the dependence of the quality indicators of hemp nanocellulose on the technological parameters of the hydrolysis process, the mathematical modeling of the process was carried out using the method of a full factorial experiment of type 2^3 [31]. Previous laboratory studies have identified three significant factors and intervals of their variation (Table 17.2).

The following indicators are selected as optimization parameters (Y_i): Y_1—density, g/cm^3; Y_2—tensile strength, MPa and Y_3—transparency, %. The working planning matrix with the results of experiments at eight points of the plan 2^3 and three points in the middle of the plan is given in Table 17.3.
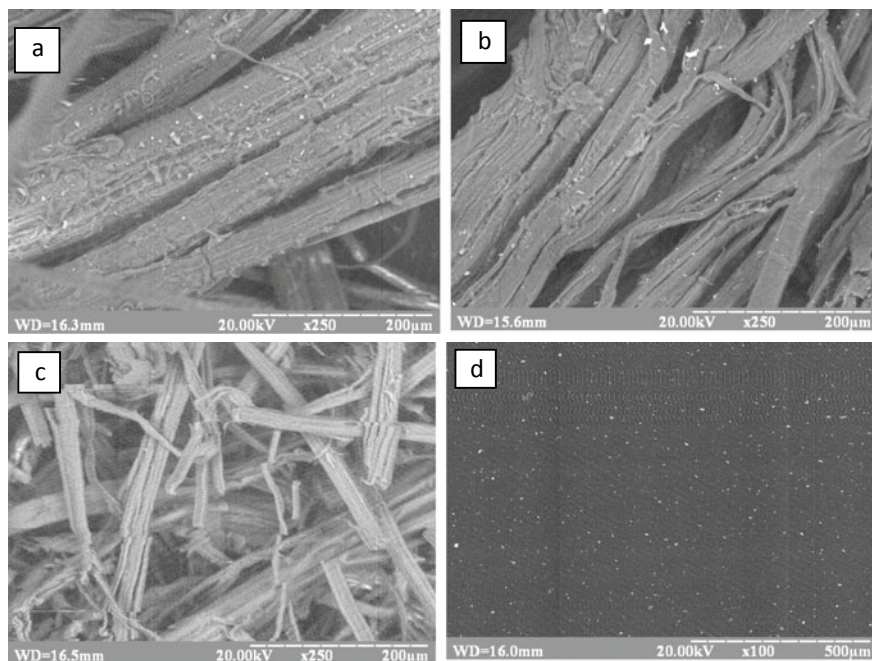
Fig. 17.4 SEM images of hemp fibers (**a**); pulp after alkaline extraction (**b**); pulp after peracetic cooking (**c**) and nanocellulose (**d**)

Table 17.2 Factors (X_i) and ranges of their values

Range of variation factors	Sulfuric acid concentration, % X_1	Duration of hydrolysis, min X_2	Hydrolysis temperature, °C X_3
Low (−1)	40.0	60.0	40.0
Standard (0)	45.0	75.0	50.0
High (+1)	50.0	90.0	60.0
Variation interval (Δ_i)	5.0	15.0	10.0

The following mathematical models of the process of hydrolysis of organosolv hemp pulp were determined by statistical processing of the obtained results [31]. For the nanocellulose film density (Y_1), the regression equation in coded form is as follows:

$$Y_1 = 1.2475 + 0.065 * x_1 + 0.065 * x_2 + 0.2325 * x_3$$
$$-0.0125 * x_1 x_2 - 0.7125 * x_1 x_3 - 1.0125 * x_2 x_3,$$

where $x_{i,\text{coded}} = (X_{i\,\text{natural}} - X_{\text{standard}})/\Delta_i$.

Table 17.3 Working matrix of planning of the full factor plan 2^3

No	Consent-ration of H_2SO_4, % (X_1)	Duration of hydro-lysis, min (X_2)	Hydrolysis temperature °C (X_3)	Density, g/cm^3 (Y_1)	Tensile strength, MPa (Y_2)	Transpa-rency, % (Y_3)
1	50	90	60	1.50	66.7	81.3
2	40	90	60	1.42	55.0	83.0
3	50	60	60	1.54	60.0	85.5
4	40	60	60	1.46	52.0	82.0
5	50	90	40	1.26	34.1	80.0
6	40	90	40	1.07	23.0	72.1
7	50	60	40	0.95	27.0	74.8
8	40	60	40	0.78	15.0	58.2
9	45	75	50	1.28	56.0	77.0
10	45	75	50	1.25	57.0	78.9
11	45	75	50	1.23	58.0	78.5

For the tensile strength of nanocellulose films (Y_2), the regression equation has the form:

$$Y_2 = 41.6 + 5.350 * x_1 + 3.1 * x_2 + 16.825 * x_3$$
$$-0.013 * x_1 x_2 - 0.713 * x_1 x_3 - 1.013 * x_2 x_3$$

For the indicator of transparency of nanocellulose films (Y_3), the equation has the form:

$$Y_3 = 77.1 + 3.3 * x_1 + 1.975 * x_2 + 5.85 * x_3$$
$$-0.013 * x_1 x_2 - 0.713 * x_1 x_3 - 1.013 * x_2 x_3$$

As a result of mathematical processing of the obtained regression equations, the following optimal conditions for the hydrolysis process were determined: concentration of sulfuric acid—50%, temperature—60 °C, duration—90 min.

17.3.4 Nanosize

Figure 17.5 shows the dependence of the transparency of nanocellulose suspensions on the concentration of sulfate acid and the duration of the hydrolysis process.

As can be seen from the induced data, an increase in the acid concentration and the duration of the hydrolysis process leads to an increase in the transparency of nanocellulose suspensions. This phenomenon is explained by a decrease in the particle size
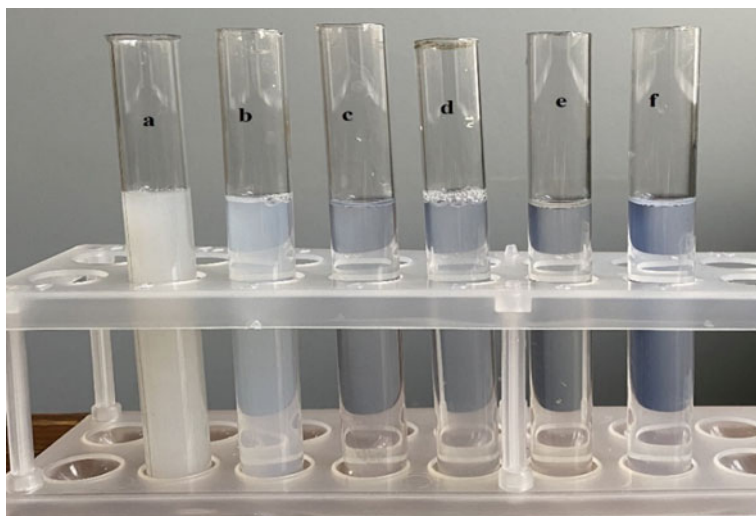
Fig. 17.5 Dependence of the transparency of hemp nanocellulose suspensions on the duration of acid hydrolysis: 30 min (**a** and **d**), 60 min (**b** and **e**), 90 min (**c** and **f**) for sulfate acid concentration of 40% (**a**, **b**, **c**) and 50% (**d**, **e**, **f**)

of hemp nanocellulose under the increasing effect of acid, primarily on the amorphous regions of the cellulose macromolecule, and the rupture of 1–4 glycosidic bonds between glucopyranose units of cellulose. This statement is confirmed by the results of transmission electron microscopy (TEM).

Figure 17.6 shows a TEM image of a sample of hemp nanocellulose after hydrolysis of organosolv hemp pulp with 50% sulfuric acid at a temperature of 60 °C for 90 min and ultrasonic treatment for 60 min. Figure 17.6 shows that the process of hydrolysis of OHP leads to the formation of a network of nanocellulose particles having a transverse size in the range of 15–50 nm.

Analysis of TEM micrographs showed that the aqueous suspension of nanocellulose consists of rod-shaped nanoparticles, in which some nanoparticles agglomerated in the form of beams, some of them were well separated. Agglomeration individual nanoparticles led to the formation of dense-layered structure.

Formation agglomerates probably due to the strong interaction between nanoparticles induced by chemical modifications of cellulose macromolecules during acid hydrolysis and due to the hydrogen bond between the nanoparticles. A similar morphology of nanocellulose was obtained as a result of acid hydrolysis by the authors [32, 33]. It should also be noted that as a result of hydrolysis of organosolv hemp pulp with sulfuric acid solutions followed by sonication, a transparent suspension of nanocellulose was obtained, which remained stable for several months.
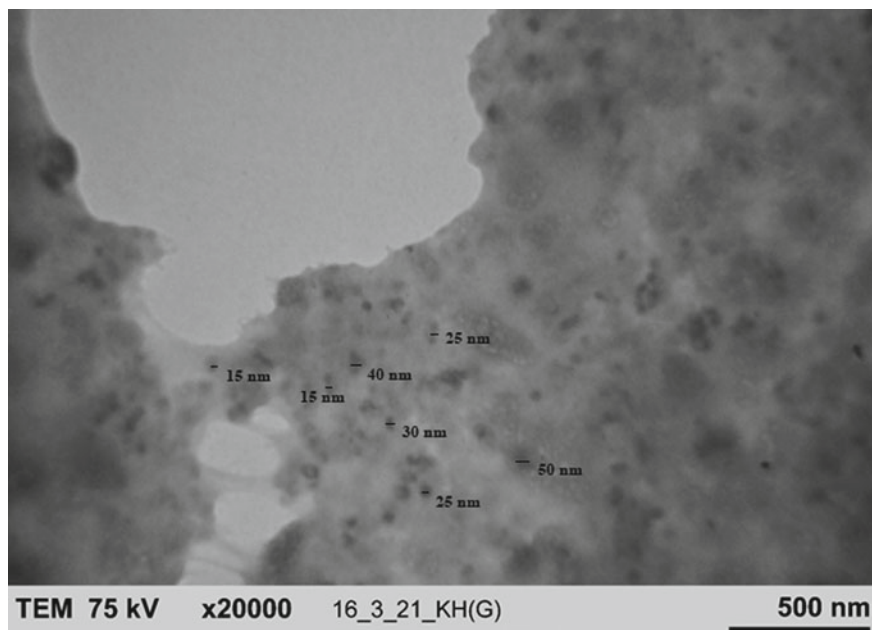
Fig. 17.6 TEM images of a hemp nanocellulose sample after hydrolysis of organosolv hemp pulp and its ultrasonic treatment

17.4 Conclusion

1. It is shown that an increase in the duration of the process of thermochemical treatment of hemp fibers leads to a decrease in the yield of organosolv hemp pulp and the residual content of lignin and minerals.
2. By the method of a full factorial experiment, regression equations were obtained that adequately describe the influence sulfuric acid concentrations, temperature and duration of hydrolysis on the quality indicators of hemp nanocellulose. It was found that the optimal conditions for the production of nanocellulose are 50% sulfuric acid at a temperature of 60 °C for 90 min and ultrasonic treatment for 60 min.
3. It was found by TEM that an aqueous suspension of nanocellulose consists of rod-shaped nanoparticles with a transverse size in the range of 15–50 nm. The resulting transparent suspension of nanocellulose maintains the stability of the gel for several months.
4. Hemp nanocellulose can be used as a transparent base for the production of flexible electronics, as a hardening additive in the production of paper and cardboard, cement, and other composite materials.

References

1. Dufresne A (2019) Nanocellulose processing properties and potential applications. Curr For Rep 5:76–89. https://doi.org/10.1007/s40725-019-00088-1
2. Jasmani L, Thielemans W (2018) Preparation of nanocellulose and its potential application. For Res 7:1–8. https://doi.org/10.4172/2168-9776.1000222
3. Ioelovich M (2017) Characterization of various kinds of nanocellulose. In: Kargarzadeh H, Ahmad I, Thomas S, Dufresne A (eds) Handbook of nanocellulose and cellulose nanocomposites. Wiley. https://doi.org/10.1002/9783527689972.ch2
4. Reshmy R, Philip E, Paul SA, Madhavan A, Sindhu R, Binod P, Pandey A, Sirohi R (2020) Nanocellulose-based products for sustainable applications: recent trends and possibilities. Rev Environ Sci Biotechnol. https://doi.org/10.1007/s11157-020-09551-z
5. Zhanga Y, Haoa N, Lina X, Nie S (2020) Emerging challenges in the thermal management of cellulose nanofibrilbased supercapacitors, lithium-ion batteries and solar cells: a review. Carbohydr Polym 234 (2020) 115888. https://doi.org/10.1016/j.carbpol.2020.115888
6. Charani PR, Moradian MH (2019) Utilization of cellulose nanofibers and cationic polymers to improve breaking length of paper. Cellul Chem Technol 53(7–8):767–774
7. Iriani ES, Permana AW, Yuliani S, Kailaku SI, Sulaiman AA (2019) The effect of agricultural waste nanocellulose on the properties of bioplastic for fresh fruit packaging. In: 2nd international conference on agriculture postharvest handling and processing. IOP Conf Ser: Earth Environ Sci 309:012035. https://doi.org/10.1088/1755-1315/309/1/012035
8. Baghban MH, Mahjoub R (2020) Natural kenaf fiber and LC^3 binder for sustainable fiber-reinforced cementitious composite: a review. Appl Sci 357:1–15. https://doi.org/10.3390/app10010357
9. Brodin M, Vallejos M, Opedal MT, Cristina M, Area MC (2017) Lignocellulosics as sustainable resources for production of bioplastics—a review. J Clean Prod. https://doi.org/10.1016/j.jclepro.2017.05.209
10. Chaker A, Boufi S (2015) Cationic nanofibrillar cellulose with high antibacterial properties. Carbohyd Polym. https://doi.org/10.1016/j.carbpol.2015.06.00
11. Alavi M (2019) Modifications of microcrystalline cellulose (MCC), nanofibrillated cellulose (NFC), and nanocrystalline cellulose (NCC) for antimicrobial and wound healing applications. E-Polymers 19:103–119
12. Yang Y, Chen Z, Zhang J, Wang G, Zhang R, Suo D (2019) Preparation and applications of the cellulose nanocrystals. Int J Polym Sci. https://doi.org/10.1155/2019/1767028
13. Trache D, Tarchoun AF, Derradji M, Hamidon TS, Masruchin N, Brosse N, Hussin MH (2020) Nanocellulose: from fundamentals to advanced applications. Front Chem 8:392. https://doi.org/10.3389/fchem.2020.00392
14. Sheltami RM, Abdullah I, Ahmad I, Dufresne A, Kargarzadeh H (2012) Extraction of cellulose nanocrystals from mengkuang leaves (Pandanus tectorius). Carbohyd Polym 88(2):772–779. https://doi.org/10.1016/j.carbpol.2012.01.062
15. Alila S, Besbes I, Vilar MR, Mutjéc P, Boufi S (2013) Non-woody plants as raw materials for production of microfibrillated cellulose (MFC): a comparative study. Ind Crops Prod 41:250–259. https://doi.org/10.1016/j.indcrop.2012.04.028
16. Liu ZM, Xie C (2012) Preparation and morphology of nanocrystalline cellulose from bamboo pulp. In: Proceedings of the 55th International Convention of Society of Wood Science and Technology, Beijing, China, PS-30, 27–31 Aug 2012, pp 1–6
17. Sánchez R, Espinosa E, Domínguez-Robles J, Loaiza JM, Rodríguez A (2016) Isolation and characterization of lignocellulose nanofibers from different wheat straw pulps. Int J Biol Macromol 92:1025–1033. https://doi.org/10.1016/j.ijbiomac.2016.08.019
18. Ranalli P, Venturi G (2004) Hemp as a raw material for industrial applications. Euphytica 140(1):1–6. https://doi.org/10.1007/s10681-004-4749-8
19. Small E, Marcus D, McElroy A (2002) Hemp: a new crop with new uses for North America. American Society for Horticultural Science, pp 284–326

20. Paulapuro H (2000) Paper and board grades. Papermaking Science and Technology, vol 18. Fapet Oy, Finland, p 114. ISBN 978-952-5216-18-9
21. Smook GA (2003) Handbook for pulp & paper technologists, 3rd edn. Angus Wilde Publications, Inc., TAPPI Test Methods, TAPPI Press, Atlanta, Georgia, 425p
22. Deykun I, Halysh V, Barbash V (2018) Rapeseed straw as an alternative for pulping and papermaking. Cellul Chem Technol 52(9–10):833–839
23. Esmaeil MHK, Talaeipour M, Bazyar B, Mirshokraei SA, Eslam HK (2019) Two-step delignification of peracetic acid and alkali from sugar cane bagasse. BioResources 14(4):9994–10003
24. TAPPI Test Methods, Tappi Press, Atlanta, Georgia (2004)
25. Barbash VA, Yaschenko OV, Shniruk OM (2017) Preparation and properties of nanocellulose from organosolv straw pulp. Nanoscale Res Lett 12(1):241
26. Barbash VA, Yashchenko OV, Opolsky VO (2018) Effect of hydrolysis conditions of organosolv pulp from kenaf fibers on the physicochemical properties of the obtained nanocellulose. Theor Exp Chem 54:193–198. https://doi.org/10.1007/s11237-018-9561-y
27. Barbash V, Yashchenko O (2020) Preparation, properties and use of nanocellulose from non-wood plant materials. In: Krishnamoorthy K (ed) Novel nanomaterials. IntechOpen, London
28. Barbash VA, Yashchenko OV, Gondovska AS, Deykun IM (2021) Preparation and characterization of nanocellulose obtained by TEMPO-mediated oxidation of organosolv pulp from reed stalks. Appl Nanosci. https://doi.org/10.1007/s13204-021-01749-z
29. Ramamoorthy SK, Skrifvars M, Persson A (2015) A review of natural fibers used in biocomposites: plant, animal and regenerated cellulose fibers. Polym Rev 55:107–162. https://doi.org/10.1080/15583724.2014.971124
30. Azeez MA (2018) Pulping of non-woody biomass. In: Pulp and paper processing. https://doi.org/10.5772/intechopen.79749
31. NIST/SEMATECH e-Handbook of statistical methods. http://www.itl.nist.gov/div898/handbook/
32. Lani NS, Ngadi N, Johari A, Jusoh M (2014) Isolation, characterization, and application of nanocellulose from oil palm empty fruit bunch fiber as nanocomposites. Hindawi Publishing Corporation J Nanomater. https://doi.org/10.1155/2014/702538
33. Gopakumar DA, Arumughan V, Pasquini D, (Ben) Leu SY, Thomas S (2019) Nanocellulose-based membranes for water purification. In: Nanoscale materials in water purification, pp 59–85. https://doi.org/10.1016/b978-0-12-813926-4.00004-5

Chapter 18
Impact of Gold Nanoparticles on Metabolic and Antioxidant Status of Cryopreserved Mesenchymal Stem Cells from Adipose Tissue

Nataliia Volkova, Mariia Yukhta, Larisa Sokil, Ludmila Chernyshenko, Ludmila Stepanyuk, and A. Goltsev

18.1 Introduction

Stem cell technology rapidly developed since discovery of hematopoietic stem cells in the 1960s. Now we know that stem cells are also present in bone marrow, umbilical cord blood and tissue, amniotic fluid, placenta, adipose tissue, skin, cartilage, tendon, teeth, human embryos [1–3], and many more which continue to open until now. Today, stem cells are classified into embryonic stem cells, adult stem cells, and induced pluripotent stem cells. They are key players in the fields of tissue engineering and regenerative medicine due to ability to proliferate and direct differentiate into different lineages [4]. Cells that undergo terminal differentiation are derived from proliferating stem cells known as progenitors that stop division cycle and simultaneously activate cell-type-specific transcriptional programs. Among the known stem cells mesenchymal stem cells (MSCs), which can be readily obtained from various sources without raising ethical concerns, have shown great promise for regenerative medicine in the treatment of arthritis, cartilage defects, tissue wounds, stroke, graft versus host disease, myocardial infarction, traumatic brain injury, and even cancer due to their special biological properties such as significant self-renewability, low immunogenicity, and ability to differentiate into variety types of specialized cells, control inflammation, modify the proliferation, and cytokine production by immune cells [5].

In parallel with the development of tissue and regenerative medicine, there have been significant changes in the field of nanotechnologies that allow improving of

N. Volkova (✉) · M. Yukhta · L. Sokil · L. Chernyshenko · L. Stepanyuk · A. Goltsev
Institute for Problems of Cryobiology and Cryomedicine, National Academy of Sciences of Ukraine, Kharkiv, Ukraine
e-mail: volkovana781@gmail.com

255

stem cell application. Today, various types of nanomaterials are applied in tissue engineering but nanoparticles of noble metals have been studied with growing interest, since they exhibit particular physical, chemical, and biological properties [6]. Among them, gold nanoparticles (AuNPs) are one of the most widely used due to valuable optical, electronic, catalytic, biocompatible specifications, and potentially high surface reactivity [7]. The nanoscale size of AuNPs, wide range of easy preparation techniques, high surface area, and broad opportunities of surface functionalization make AuNPs attractive to fit the requirements of tissue engineering [8]. Moreover, AuNPs are found to be nontoxic according to the numerous reports [9–11] that makes them favorable materials for directing stem cell fate and tissue regeneration. There are a lot of studies showing the link between AuNPs and the osteogenic differentiation of stem cells. So, Heo and co-workers demonstrated that adipose-derived MSCs cultured on gelatin-AuNPs composite hydrogel exhibited increased proliferation, osteogenic differentiation, and maturation. The authors further demonstrated that these composite hydrogels assisted in bone formation in vivo in a time- and dose-dependent manners [12]. The potential use of AuNPs embedded scaffolds for cardiogenic differentiation has also been shown. Baei and colleagues have shown that AuNPs-chitosan composite hydrogels accelerated the differentiation of mesenchymal stem cells toward the cardiac lineage and increased the expression of the cardiac markers Nkx-2-5 and α-MHC [13].

One of the promising directions in nanomedicine is the use of AuNP for wound healing. In the authors' work, better effect of wound healing was observed in AuNPs containing wet silk fibroin by the electrospinning method [14]. It also shows [15] that application of loaded by AuNPs cells promoted the activation of regenerative processes in the burns that manifested in accelerated contraction, restoration of the skin histological structure, and types I and III collagen content on post-treatment day 21. In our previous studies [16], we studied the influence of AuNPs on viability, proliferative capacity, and apoptosis/necrosis processes of the human fibroblast cells before and after cryopreservation. Besides, we have shown that some concentrations of AuNPs (6–9 μg/mL) affected the phenotype, synthesis of type I collagen, ability to direct adipogenic and chondrogenic differentiation of rat bone marrow MSCs [17]. Summarizing the above, AuNPs are capable to modulate MSCs differentiation and proliferation, which highlights their potential for regenerative therapy. However, further efforts are required to obtain good quality results by finding the best design and optimal exposure conditions with minimal toxicity for AuNPs. This will allow innovative use of stem cells for the treatment of incurable human diseases.

The influence of Au nanoparticles (AuNPs) on phenotypic characteristics, metabolic activity, and antioxidant status of cryopreserved mesenchymal stem cells (CrMSCs) from adipose tissue was investigated.

18.2   Materials and Methods

Outbreed white sexually immature male rats were used in the study. All the manipulations were carried out in accordance with the Euroconvention for the protection of vertebrate animals used for experimental and other scientific purposes (Strasbourg, 18.03.1986). The study protocols were approved by the Bioethics Committee of Institute for Problems of Cryobiology and Cryomedicine of the NAS of Ukraine (Permit No 2016-05).

Primary suspension of cells from biopsies of adipose tissues of rats (n = 15) was obtained by enzymatic digestion [18]. To do this, tissue samples were washed with Hanks' solution (PAA, Austria) with gentamicin (150 µg/mL) (Farmak, Ukraine) and incubated in a type II collagenase solution (1.5 mg/mL) (PanEco, Russia) at 4 °C for 18 h. Then cells were isolated from biopsies by resuspension followed by centrifugation at 1500 rpm for 3 min. Supernatant was removed, culture medium was added to the precipitate, and the cell suspension was placed on culture plastic. The seeding density of the cells was 1×10^4 per 1 cm^2 of culture flasks. The culture medium in all cases contained: IMDM medium (PAA, Austria), 10% fetal bovine serum (HyClone, USA), kanamycin (150 µg/mL) (Farmak, Ukraine), and amphotericin B (5 µg/mL) (PAA, Austria). The culture medium was changed every 3 days. The standard culturing conditions at 37 °C in an atmosphere of 5% CO_2 in an incubator (Sanyo, Japan) were used. Upon reaching a monolayer, cell cultures were subcultured using a 0.25% solution of trypsin (PAA, Austria) and Versene (PanEco, Russia) in a ratio of 1:1.

Cryopreservation of MSCs cultures was carried out under the protection of 10% dimethyl sulfoxide (PanEco, Russia) with an addition of 20% fetal bovine serum. The cryoprotectant solution was prepared on the culture medium. The resulting suspension was placed in Nunc CryoTubes (Sigma-Aldrich, USA) to 1 mL. The cooling rate was 1 °C/min to −80 °C followed by immersion in liquid nitrogen [19]. Warming was carried out in a water bath at 40 °C until the liquid phase. Removal of the cryoprotectant was performed by adding Hanks' solution (PAA, Austria) 1: 9 followed by centrifugation at 1500 rpm for 5 min.

The AuNPs (Sigma-Aldrich, USA) were obtained by citrate synthesis. The average size of the particles was 15 nm. The MSCs after freezing-thawing were incubated in Hank's solution supplemented with AuNPs at final concentrations of 4, 6, 10, or 20 µg/mL for 1 h. The samples of CrMSCs incubated under the same conditions without AuNPs were taken as a control. A scheme of the experiment is shown in Fig. 18.1.

The total metabolic activity of CrMSCs after interaction with AuNPs was investigated by MTT test (Fluka, Germany). The MTT was added to the samples of CrMSCs at final concentration of 0.5 mg/mL; after 3 h incubation at 37 °C, the medium was removed and 100% dimethyl sulfoxide was added to each sample of cells to solubilize the formazan. Absorbance was read at 570 nm (CHEM 7, ERBA, Czech Republic) and normalized to 1 mg of protein.

Fig. 18.1 Experimental
scheme
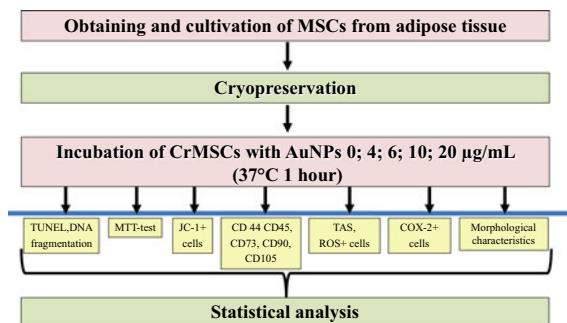
For biochemical tests, the samples of CrMSCs were lysed in RIPA buffer (Millipore, Germany), filtered, and centrifugated (1000 g for 10 min). A total protein level and total antioxidant status (TAS) were quantitatively estimated in supernatant by the method of UV spectrophotometry (CHEM 7) using test kits (Randox, UK) according to the manufacturer's instructions.

Cells after 1 h incubation with AuNPs were investigated by cytofluorimetric method using mouse–antirat monoclonal antibodies to CD45-FITC, CD44-FITC, CD73-FITC, CD90-FITC, and CD105-PE (BD Biosciences, USA), ROS (Sigma-Aldrich, USA), and JC-1 (Becton Dickinson, USA) assay kits according to the manufacturer's instructions. DNA fragmentation was evaluated by TUNEL-method on preparations of CrMSCs using a set of reagents from the company "BiVision" (USA) according to the manufacturer's instructions. FACS Calibur (Becton Dickinson, USA) was used for this test. Data were analyzed using WinMDI v.2.8.

The CrMSCs after incubation with AuNPs were cultured using the same conditions as for primary cultures. On the 10th day, the cells were fixed in a 4% solution of paraformaldehyde followed by azure-II and eosin staining by Romanowsky–Giemsa. ZEISS Primo Star light microscope (Carl Zeiss Microscopy GmbH, Germany) was used for the analysis of preparations.

Immunocytochemical staining of CrMSCs after culturing was performed using monoclonal antibodies to cyclooxygenase-2 (COX-2) at a titer of 1:100 (Thermo Fisher Scientific, USA). Staining was performed according to the protocol recommended for the peroxidase detection system UltraVision Quantro HRP DAB (Thermo Fisher Scientific, USA). COX-2 positively stained cells (brown color) were counted using the ZEISS ZEN 2 (blue edition) program (Carl Zeiss Microscopy GmbH, Germany), and their percentage was determined as the ratio of the number of stained cells to the total number of one's (per 1 mm^2) taken as 100%. For negative control of COX-2, cell staining was performed according to the same protocol using the mouse IgG isotype instead of monoclonal antibodies.

Kruskal–Wallis test and Student–Newman–Keuls multiple comparison tests were applied to compare the difference between the groups using Statistica 8 (StatSoft, USA) software.

18.3   Results and Discussion

The first stage of the work was to determine the total metabolic activity (by MTT test) of CrMSCs after incubation in the media with the addition of AuNPs. The obtained results indicated (Fig. 18.2a) that the use of low doses of AuNPs (final concentrations of 4 and 6 μg/mL) did not lead to the significant changes in metabolic activity of CrMSCs. At the same time, 1.52-fold decrease of the considered index was observed in the samples incubated with 10 μg/mL AuNPs relative to the control. With an increase in AuNP dose to 20 μg/mL, the metabolic activity index for the samples was 1.95-fold lower relative to the control. As known, the MTT assay reflects mitochondria function, and, in particular, mitochondrial redox metabolism in live cells and tissues [20]. Yellow tetrazolium salt of MTT is one of the most widely used dyes to assess the cytotoxicity of various compounds, including nanoparticles and interaction of cells with them [21].

The present study has shown that the cell metabolic activity is inversely related to the concentration of AuNPs. The best results were obtained using 4 and 6 μg/mL AuNPs. Many papers have shown size-dependent nanoparticle uptake, and particles with a size of 40–70 nm have higher rates of endocytosis than smaller ones (14 nm) [22]. Overall, 15 nm AuNP exposure had a statistically significant effect on CrMSC metabolism, but its decrease was moderate compared to the control.

To address the issue of activation of the process of DNA fragmentation in adipose-derived CrMSCs, as an early reaction to the interaction with nanoparticles, the cell suspension was incubated with AuNPs for 1 h (Fig. 18.3b). Analysis of the obtained data of immunocytochemical reaction to detect DNA fragmentation showed that the severity of the process was low in all studied groups. But under the conditions of using of AuNPs at concentrations of 10 and 20 μg/mL, there was an increase in the relative number of cells with signs of DNA fragmentation in 1.3 and 1.4 times, respectively, compared to the control. Because DNA fragmentation is considered to be the hallmark of apoptosis, the occurrence of this process was detected by two factors, reduced and shrunken cells, and DNA fragmentation. The research of authors
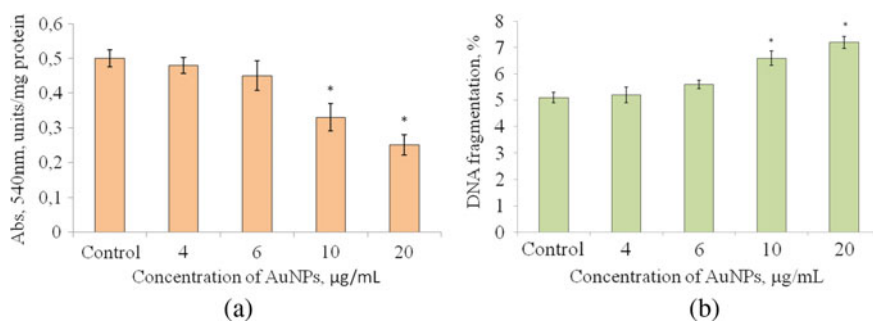
Fig. 18.2   Effect of AuNPs on metabolic activity (**a**) and DNA fragmentation (**b**) in adipose-derived CrMSCs. *Note* *—the difference is statistically significant compared to the control ($p < 0.05$)
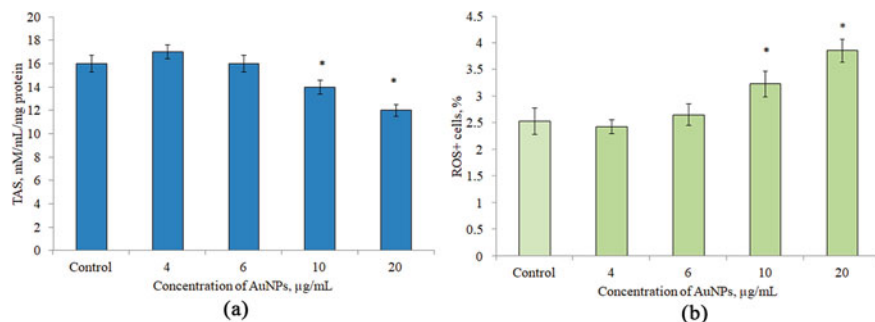
Fig. 18.3 Effect of AuNPs on total activity of antioxidant systems (TAS) and number of ROS positive cells in adipose-derived CrMSCs. *Note* *—the difference is statistically significant compared to the control ($p < 0.05$)

[23] obtained results was shown that the AuNPs induce apoptosis through increased hydrophobicity as compared with untreated cell DNA.

TAS activity and ROS$^+$ cell content were also determined in adipose-derived CrMSCs after incubation in investigated media. The obtained results are graphically presented in Fig. 18.3.

The use of 4 µg/mL as well as 6 µg/mL AuNPs did not lead to the significant changes in TAS activity (Fig. 18.3a). The incubation of CrMSCs in media containing AuNPs in concentrations of 10 and 20 µg/mL decreased investigated parameter in 1.15 and 1.33 times, respectively, relative to the control.

Both 4 and 6 µg/mL AuNPs did not significantly affect the relative number of ROS positive cells (Fig. 18.3b). The addition of AuNPs at concentration of 10 µg/mL led to an increase of the considered parameter by 1.27 times relative to the control. In the case using of 20 µg/mL AuNPs the considered index was decreased by 1.52 times, respectively, compared to the control.

Thus, the results of TAS activity and ROS formation study in CrMSCs showed that the use of AuNPs on concentration of 4 and 6 µg/mL did not affect significantly investigated parameters. At the same time, the using AuNPs concentrations of 10 µg/mL and more led to significant changes of antioxidant system parameters. The increased levels of ROS are discussed to be the underlying mechanism for the observed variations in the genome-wide expression profile induced by AuNPs. It is known that oxidative stress occurs in response to damage caused when the antioxidant activity and absorption capacity of a biological object cannot neutralize ROS. Oxidative stress in cells contained molecular damage, proteins denaturation, DNA damage, disbalance in energy and metabolic activity [24].

Mitochondria play important role in cell survival, providing cellular energy as ATP, and in apoptotic pathway. Therefore, we assessed whether AuNPs caused changes in mitochondrial activity of CrMSCs from adipose tissue by detecting the number of JC-1 positive cells. The obtained results are graphically presented in Fig. 18.4.

Fig. 18.4 Effect of incubation of adipose-derived CrMSCs in media with AuNPs on the number of JC-1 positive cells. *Note* *—the difference is statistically significant compared to the control (p < 0.05)
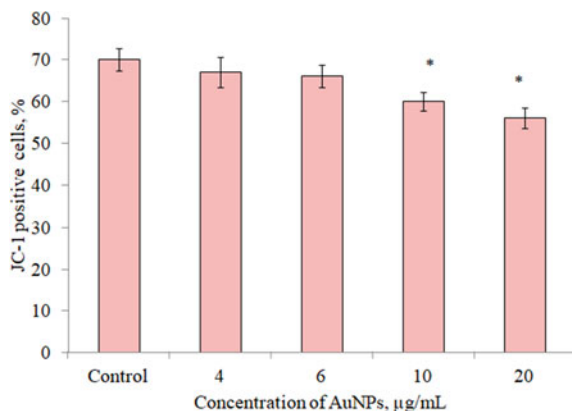
The analysis obtained data showed that in the case of addition of 4 and 6 µg/mL AuNPs to incubation medium did not lead to significant changes in JC-1$^+$ cell content. The use of AuNPs at concentrations of 10 and 20 µg/mL caused, respectively, 1.16- and 1.25-fold decreases in the indicator of mitochondrial activity relative to the control.

Cells with high mitochondria membrane potential (healthy) promote the formation of dye aggregates that fluorescence orange, whereas cells with low mitochondria membrane potential (damaged) remain monomeric JC-1 that fluoresces green. As a result, the decrease of the red/green intensity ratio provides an indication of the damage of mitochondria membrane function. Our results showed concentration dependence in the activity of mitochondria caused by the AuNPs: the larger concentration of nanoparticles, the higher toxicity, as evidenced by a decrease in the content cells with orange fluorescence [25].

The results of cytofluorometric analysis of adipose-derived CrMSCs phenotype are presented in the Table 18.1. A high expression degree of CD73, CD90, CD105 and low expression of the hematopoietic marker CD45 were observed in all studied groups of cells, that is, cells after incubation with AuNPs retained generally the phenotype typical for mesenchymal stem cells. Nevertheless, the use of 10 and 20 µg/mL AuNP led to a decrease in number of CD44$^+$ cells by 12% and 18%, respectively, and the content of CD105$^+$ cells decreased by 9% after incubation with 20 µg/mL AuNP compared to the control. Expression level of CD45, CD73, and CD90 did not change even when cells were exposed to AuNPs at a concentration of 20 µg/mL. Such a change in the expression of CD44 and CD105 in adipose-derived CrMSCs may be associated with a violation in the morphological and functional state of cells when interacting with nanoparticles.

These observed changes in the phenotype of interacted with AuNPs adipose-derived CrMSCs give the prerequisites for the detection and correction of imbalance in their proliferation and differentiation potentials.

Table 18.1 Phenotype of adipose-derived CrMSCs after 1 h incubation with AuNPs

Samples	Expression level (%)				
	CD 44	CD 45	CD 73	CD 90	CD 105
Control	97.71 ± 0.22	1.12 ± 0.11	92.04 ± 0.82	97.78 ± 1.21	94.64 ± 0.45
AuNPs 4 µg/mL	97.23 ± 0.41	1.09 ± 0.12	92.30 ± 0.41	97.47 ± 0.51	94.48 ± 0.36
AuNPs 6 µg/mL	97.15 ± 0.36	1.06 ± 0.13	92.88 ± 0.31	97.62 ± 0.35	94.14 ± 0.45
AuNPs 10 µg/mL	85.98 ± 0.42*	1.08 ± 0.08	92.92 ± 0.32	97.51 ± 0.24	93.17 ± 0.51
AuNPs 20 µg/mL	82.52 ± 0.31*	1.10 ± 0.15	92.26 ± 0.65	97.86 ± 0.11	86.12 ± 0.44*

Note *—the difference is statistically significant compared to the control ($p < 0.05$)

The next stage of the study was to determine the morphological characteristics of the CrMSCs from adipose tissue after incubation in the media with the addition of AuNPs. The obtained results are shown in the microphotographs (Fig. 18.5).

The maximum proliferative activity of CrMSCs was observed for 10 days of cultivation. Addition of AuNPs at concentrations of 4 and 6 µg/mL to CrMSCs did not change the morphological characteristics of the control samples, namely sail-, star- and spindle-shaped cell elements were observed. The use of AuNPs at concentrations of 10 and 20 µg/mL led to changes in the morphological characteristics of CrMSCs from adipose tissue in relation to control samples, namely signs of cytoskeletal dystrophy, cytoplasmatic granularity, and vacuolization of nuclei.
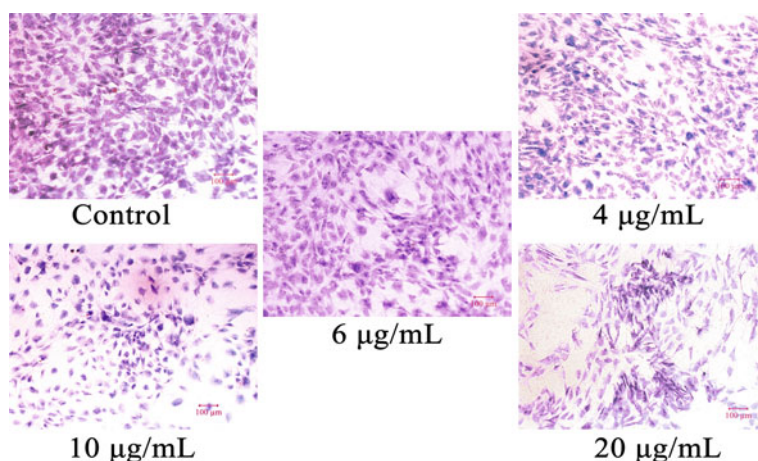
Fig. 18.5 Influence of AuNPs on morphological characteristics of CrMSCs from adipose tissue, 10 days of cultivation. Light microscopy. Azure and eosin staining

Fig. 18.6 Effect of incubation of adipose-derived CrMSCs in the media with AuNPs on the relative number of COX-2 positive cells. *Note* *—the difference is statistically significant compared to the control (p < 0.05)
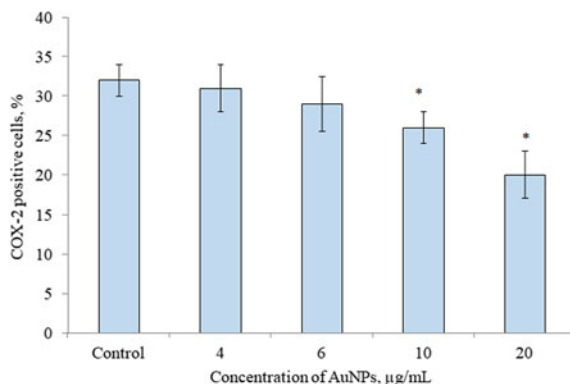
The last stage of the work was to determine the relative number of adipose-derived CrMSCs positively stained to cyclooxygenase-2 (COX-2) after incubation with AuNPs. The obtained results are shown in Fig. 18.6. In the control group (32.4 ± 3.7) % of cells expressed COX-2 and the use of AuNPs at concentrations of 4 and 6 µg/mL did not affect the studied indicator. The use of AuNPs in the concentrations of 10 and 20 µg/mL led, respectively, to 1.2- and 1.6-fold decreases in the relative amount of positively stained to COX-2 CrMSCs compared to the control.

The authors [26] showed that the activation of lipoxygenase (LOX) and COX-2 enzymes leads to a significant increase in the cytotoxic effect of zinc oxide on cultured cells. It should be noted that the metabolism of arachidonic acid between neuroblastoma cells and MSCs of the human bone marrow during the inflammatory process, which is induced by zinc oxide, may be different depending on the cell type. Thus, the cytotoxic effect of NPs may involve the simultaneous activation of the enzymes COX-2 and LOX, triggering casp-3/7-mediated apoptosis against the background of mitochondrial dysfunction in MSCs under culture conditions.

At present, there is provided a plurality of hypotheses regarding how AuNPs interact with cellular components after endocytosis [27]. Thus, it has been suggested that endosomal release may lead to physical interactions between AuNPs and biological components [28]. In other studies, it is expected to release gold ions due to the decomposition of the particles caused by the acidic lysosomal environment [29].

MSCs involved in tissue regeneration can be obtained from the various sources mentioned above. In the present study, we selected adipose-derived CrMSCs of rats as a model object for investigating the effect of AuNPs on stem cells. Furthermore, due to their high immunomodulatory and reparative activity, these cells represent an excellent cellular object for analysis of a possible influence of AuNPs on cell function. As it has been reported [30], AuNPs have a size-dependent cytotoxicity and particles less than 15 nm are only considered to be toxic.

This research was aimed at comprehensive studying of the effect of different concentrations of AuNPs on the antioxidant capacity, total metabolic activity, and morphological characteristics of CrMSCs. The obtained data showed that in the case of addition of 4 and 6 µg/mL AuNPs to incubation medium did not lead to significant

changes in the phenotype, metabolic, mitochondrial, and antioxidant activity as well as morphological and proliferative potential compared to the control. In this work, we also encountered the fact that the increase of the concentration of AuNPs up to 10 and 20 µg/mL had a destructive effect on the metabolic activity and morphological structure of CrMSCs. We associate such impact with toxic effect of AuNPs in this dose on cells and their partial death that follows from the results of MTT test, antioxidant activity, and morphological examination.

NPs of metals, such as gold interacting with cells, are able to affect their enzymatic activity, exhibit antioxidant and antimicrobial properties. The use of nanoparticles as a component can significantly improve therapy, and although the potential is significant, there are still many issues that need to be addressed before accepting them for clinical use. Therefore, it is especially important to involve modern nanobiotechnologies based on the combined use of cryopreserved MSCs and nanoparticles to ensure the effectiveness of treatment of experimental arthritis.

18.4 Conclusion

Using of investigated concentrations of AuNPs did not lead to changes in the content of CD45$^+$, CD73$^+$, and CD90$^+$ cells. Adding of 10 and 20 µg/mL AuNPs resulted in reduction of CD44$^+$ cells by 12% and 18% accordingly compared to the control. Content of CD105$^+$ cells was decreased by 9% under use of 20 µg/mL AuNPs. Incubation with 4 and 6 µg/mL AuNPs did not affect mitochondrial and TAS activities, level of DNA fragmentation, morphological characteristics, ROS formation, and COX-2 expression of adipose-derived CrMSCs. AuNPs at concentrations of 10 and 20 µg/mL decreased the TAS index (in 1.15 and 1.33 times, respectively), JC-1$^+$ (in 1.16 and 1.25 times, respectively), and COX-2$^+$ (in 1.2 and 1.6 times, respectively) cell content as well as increase the DNA fragmentation (in 1.3 and 1.4 times, respectively) and number of ROS positive cells (in 1.15 and 1.33 times, respectively) compare with the control samples. It was found that AuNPs in concentrations of 4 and 6 µg/mL are safe for CrMSCs from adipose tissue, while increase up to 10 µg/mL has a destructive effect expressed by the change of phenotype, mitochondrial, and antioxidant activities. In sum, the presented results are related to the field of applied nanobiotechnology and spread to regenerative medicine, particularly in the development of drug delivery to target cells or organs.

References

1. Macrin D, Joseph JP, Pillai AA et al (2017) Eminent sources of adult mesenchymal stem cells and their therapeutic imminence. Stem Cell Rev Rep 13:741–756. https://doi.org/10.1007/s12015-017-9759-8

2. Zakrzewski W, Dobrzyński M, Szymonowicz M et al (2019) Stem cells: past, present, and future. Stem Cell Res Ther 10:68. https://doi.org/10.1186/s13287-019-1165-5

3. Mushahary D, Spittler A, Kasper C et al (2018) Isolation, cultivation, and characterization of human mesenchymal stem cells. Cytometry Part A: J Int Soc Anal Cytol 93(1):19–31. https://doi.org/10.1002/cyto.a.23242

4. Yadid M, Feiner R, Dvir T (2019) Gold nanoparticle-integrated scaffolds for tissue engineering and regenerative medicine. Nano Lett 9(4):2198–2206. https://doi.org/10.1021/acs.nanolett.9b00472

5. Liu X, Yang Z, Sun J et al (2019) A brief review of cytotoxicity of nanoparticles on mesenchymal stem cells in regenerative medicine. Int J Nanomed 14:3875–3892. https://doi.org/10.2147/IJN.S205574

6. Yaqoob AA, Ahmad H, Parveen T et al (2020) Recent advances in metal decorated nanomaterials and their various biological applications: a review. Front Chem 8:341. https://doi.org/10.3389/fchem.2020.00341

7. Elahi N, Kamali M, Baghersad MH (2018) Recent biomedical applications of gold nanoparticles: a review. Talanta 184:537–556. https://doi.org/10.1016/j.talanta.2018.02.088

8. Nejati K, Dadashpour M, Gharibi T et al (2021) Biomedical applications of functionalized gold nanoparticles: a review. J Clust Sci. https://doi.org/10.1007/s10876-020-01955-9

9. Iram F, Yasmeen A, Massey S et al (2021) Synthesis of gold and silver nanoparticles by use of arabinoglucan from Lallemantia royleana. Int J Biol Macromol 191:1137–1150. https://doi.org/10.1016/j.ijbiomac.2021.09.096

10. Singh N, Das MK, Ansari A et al (2021) Biogenic nanosized gold particles: physico-chemical characterization and its anticancer response against breast cancer. Biotechnol Rep (Amst) 30:e00612. https://doi.org/10.1016/j.btre.2021.e00612

11. Adewale OB, Davids H, Cairncross L et al (2019) Toxicological behavior of gold nanoparticles on various models: influence of physicochemical properties and other factors. Int J Toxicol 38(5):357–384. https://doi.org/10.1177/1091581819863130

12. Heo DN, Ko WK, Bae MS et al (2014) Enhanced bone regeneration with a gold nanoparticle-hydrogel complex. J Mater Chem B 2(11):1584–1593. https://doi.org/10.1039/C3TB21246G

13. Baei P, Jalili-Firoozinezhad S, Rajabi-Zeleti S et al (2016) Electrically conductive gold nanoparticle-chitosan thermosensitive hydrogels for cardiac tissue engineering. Mater Sci Eng C 63:131–141. https://doi.org/10.1016/j.msec.2016.02.056

14. Fathi-Achachelouei M, Knopf-Marques H, Ribeiro da Silva CE et al (2019) Use of nanoparticles in tissue engineering and regenerative medicine. Front Bioeng Biotechnol 7:113. https://doi.org/10.3389/fbioe.2019.00113

15. Volkova N, Yukhta M, Pavlovich O et al (2016) Application of cryopreserved fibroblast culture with Au nanoparticles to treat burns. Nanoscale Res Lett 11(1):1–6. https://doi.org/10.1186/s11671-016-1242-y

16. Pavlovich EV, Volkova NA (2015) Influence of gold nanoparticles on human fibroblast before and after cryopreservation. In: Nanoplasmonics, nano-optics, nanocomposites, and surface studies. Springer, Cham, pp 413–420. https://doi.org/10.1007/978-3-319-18543-9_28

17. Volkova N, Pavlovich O, Fesenko O et al (2017) Studies of the influence of gold nanoparticles on characteristics of mesenchymal stem cells. J Nanomater. https://doi.org/10.1155/2017/6934757

18. Volkova NA, Yukhta MS, Goltsev AN (2016) Morphological and functional characteristics of cryopreserved multipotent mesenchymal stromal cells from bone marrow, adipose tissue and tendons. Cell Organ Transplantology 4(2):200–205. https://doi.org/10.22494/cot.v4i2.64

19. Volkova NA, Goltsev AN (2015) Cryopreservation effect on proliferation and differentiation potential of cultured chorion cells. CryoLetters 36(1):25–29

20. Monteiro-Riviere NA, Inman AO, Zhang LW (2009) Limitation sand relative utility of screen in gassaystoassess engineered nanoparticle toxicity in a human cell line. Toxicol Appl Pharmacol 234(2):222–235. https://doi.org/10.1016/j.taap.2008.09.030
21. Bahadar H, Maqbool F, Niaz K et al (2016) Toxicity of nanoparticles and an overview of current experimental models. Iran Biomed J 20(1):1–11. https://doi.org/10.7508/ibj.2016.01.001
22. Chithrani BD, Ghazani AA, Chan WCW (2006) Determining the size and shape dependence of gold nanoparticle uptake into mammalian cells. Nano Lett 6:662–668. https://doi.org/10.1021/nl052396o
23. Muthukumarasamyvel T, Rajendran G, Santhana Panneer D et al (2017) Role of surface hydrophobicity of dicationic amphiphile-stabilized gold nanoparticles on A549 lung cancer cells. ACS Omega 2(7):3527–3538. https://doi.org/10.1021/acsomega.7b00353
24. Naha PC, Davoren M, Lyng FM et al (2010) Reactive oxygen species (ROS) induced cytokine production and cytotoxicity of PAMAM dendrimers in J774A.1 cells. Toxicol Appl Pharmacol 246(1–2):91–99. https://doi.org/10.1016/j.taap.2010.04.014
25. Yao M, He L, McClements DJ et al (2015) Uptake of gold nanoparticles by intestinal epithelial cells: impact of particle size on their absorption, accumulation, and toxicity. J Agric Food Chem 63(36):8044–8049. https://doi.org/10.1021/acs.jafc.5b03242
26. Kim JH, Jeong MS, Kim DY et al (2015) Zinc oxide nanoparticles induce lipoxygenase-mediated apoptosis and necrosis in human neuroblastoma SH-SY5Y cells. Neurochem Int 90:204–214. https://doi.org/10.1016/j.neuint.2015.09.002
27. Khlebtsov N, Dykman L (2011) Biodistribution and toxicity of engineered gold nanoparticles: a review of in vitro and in vivo studies. Chem Soc Rev 40(3):1647–1671. https://doi.org/10.1039/c0cs00018c
28. Soenen SJ, Manshian B, Montenegro JM et al (2012) Cytotoxic effects of gold nanoparticles: a multiparametric study. ACS Nano 6:5767–5783. https://doi.org/10.1021/nn301714n
29. Kang B, Mackey MA, El-Sayed MA (2010) Nuclear targeting of gold nanoparticles in cancer cells induces DNA damage, causing cytokinesis arrest and apoptosis. J Am Chem Soc 132:1517–1519. https://doi.org/10.1021/ja9102698
30. Pan Y, Neuss S, Leifert A et al (2007) Size-dependent cytotoxicity of gold nanoparticles. Small 3(11):1941–1949. https://doi.org/10.1002/smll.200700378

Chapter 19
Chemical Transformations of Phosphoric Acid on Hydrated Anatase Surface: A Quantum Chemical Simulation

O. V. Filonenko, M. I. Terebinska, E. M. Demianenko, A. Grebenyuk, and V. V. Lobanov

19.1 Introduction

Titanium dioxide (TiO_2) is widely used in many fields, including medicine, pharmacology, and photocatalysis, due to its properties such as chemical and optical stability, non-toxicity, and low cost. At the nanoscale, the most stable polymorph of TiO_2 is anatase, which is also widely used in catalysis, photo-, and electrochemistry [1–3]. It is extremely important for medicine to elucidate the nature of the interaction between anatase surface groups and functional groups of biological objects. It is known [4] that phosphorus esters and anhydrides are widespread in wildlife. DNA and RNA molecules that carry genetic information are phosphodiesters. Molecules-reservoirs of biochemical energy (adenosine triphosphate, creatine phosphate, phosphoenolpyruvate), as well as most enzymes—esters of phosphoric or pyrophosphoric acids. The surface of titanium metal used to make implants is usually covered with a layer of its dioxides. This layer is in direct contact and interacts with biological fluids

O. V. Filonenko (✉) · M. I. Terebinska · E. M. Demianenko · A. Grebenyuk · V. V. Lobanov
Chuiko Institute of Surface Chemistry of National Academy of Sciences of Ukraine, 17 General Naumov Street, Kyiv 03164, Ukraine
e-mail: oksana.filonenko@isc.gov.ua; filonenko_ov@ukr.net

M. I. Terebinska
e-mail: terebinska@ukr.net

E. M. Demianenko
e-mail: demianenko_en@ukr.net

A. Grebenyuk
e-mail: grebenyuk_ag@ukr.net

V. V. Lobanov
e-mail: natbu@ukr.net

where the concentration of phosphates is high enough, what actualizes the examination of the interaction between phosphates and the hydrated surface of titanium dioxide.

There is a small amount of theoretical works in the literature on the study of phosphate adsorption on the anatase surface. Thus, the adsorption of organophosphorus compounds, namely phosphonates and phosphonic acids, was considered in [5–8]. Phosphonates are shown to bind to the anatase surface by coordinating the phosphoryl oxygen atom to a five-coordinated surface titanium atom with the formation of the TiO–P bond, i.e., adsorption involves the formation of intraspherical complexes. In the mentioned works, the calculations were performed for vacuum conditions of pure anatase surfaces, i.e., without taking into account hydroxyl groups and coordination-bound water molecules. To approach the experimental conditions, it is desirable to examine the interaction of phosphates with the hydroxylated surface of titania, taking into account the effect of the solvent.

A complex is considered intraspherical when the sorbed anion is directly bound to a surface atom. And if a layer of anion-bound water or surface ions is kept between the anion and the surface, the complex is external-spherical and exists due to electrostatic forces. Outer-sphere complexes are analogs of ion pairs [9].

The adsorption of KH_2PO_4, $KH_3P_2O_7$, and $KH_4P_3O_{10}$ salts on hydrated (100) and (101) faces of anatase with direct inclusion of H_2O molecules in the calculation model to take into account the effect of solvent was examined by molecular dynamics and electron density functional methods with periodicity conditions [10]. In this paper, various variants of phosphate coordination are considered, namely the formation of mono-, bi-, and tridendate intraspherical complexes with the formation of the appropriate number of Ti–O–P bonds. Comparing their own theoretically obtained data with the experimental results of NMR spectroscopy, the authors concluded that the anion $H_2PO_4{}^-$ should be chemisorbed on the hydrated (100) and (101) faces of anatase mainly with the formation of bidentate complexes. The coexistence of bidentate and tridentate complexes (their formation is thermodynamically advantageous) cannot be excluded.

The adsorption of inorganic phosphates, which contain from one to three phosphorus atoms in their chains, has been experimentally studied [4] as dependent on the pH and ionic strength of the solution on the surface of nanocrystalline titanium dioxide. The interaction between phosphates and oxide is presented as the formation of adsorption complexes in accordance with the provisions of the theory of complexation on the surface [11]. It is shown that the adsorption of inorganic phosphates on the surface of nanocrystalline titanium dioxide can be interpreted as the formation of external and intraspherical adsorption complexes due to two types of interaction: electrostatic and covalent. In this case, all intraspherical complexes were considered as monodentate, because the formation of bidentate bridging structures is believed to be unlikely by the authors, because the distance between oxygen atoms of neighboring hydroxyl groups of phosphate anion is 0.255 nm, whereas the distance between neighboring titanium atoms in anatase is 0.38–0.39 nm [4].

The data available in the literature [5–11], both experimental and theoretical, are quite ambiguous and do not provide an accurate answer to the question on the bonding nature in the complexes formed on the anatase surface.

Therefore, the aim of this work is to examine by means of quantum chemistry the probable paths of phosphoric acid adsorption on the hydrated anatase (001) surface as well as to clarify what anatase face is dominant, along with (101) one, for its nanoparticles.

19.2 Research Methods and Objects

The calculations were performed by the method of density functional theory using the exchange-correlation functional PBE0 [12] and the valence-split base set 6-31G (d, p). As shown in [13], this technique for systems such as anatase and rutile provides theoretically calculated structural and energy characteristics that are in good agreement with the experimental ones. The influence of the aqueous medium was taken into account in the framework of the continuous model of solvent (PCM) [14, 15]. The equilibrium spatial structures of starting materials and those of reaction products were found by minimizing the norm of the total energy gradient vector. The stationarity of the points corresponding to the energy minima of the optimized structures was proved by the absence of negative eigenvalues of the Hesse matrices. All calculations were performed using software packages PC GAMESS by A. Granovsky (FireFly version 8.2.0) and USGAMESS [16].

The energy effect (ΔE_{react}) and free Gibbs energy (ΔG_{react}) values of the reactions at 298 K were determined according to the formulas:

$$\Delta E_{\text{react}} = E_{\text{tot}}(\text{reaction products}) - E_{\text{tot}}(\text{reagents}),$$

$$\Delta G_{\text{react}} = G^0_{298}(\text{reaction products}) - G^0_{298}(\text{reagents}),$$

where $G^0_{298} = E_{\text{tot}} + \text{ZPE} + G_{0 \to 298\,\text{K}}$; E_{tot} is the total energy of the corresponding optimized structure, and the zero oscillation energy (ZPE) and the correction value $G_{0 \to 298\,\text{K}}$ were found from the diagonalized Hesse matrices of normal vibration frequencies for reaction products and reagents.

The face (001) was chosen to model the interaction between H_3PO_4 molecules with the anatase surface, because it is more reactive than the face (101). As in [17], the cluster $Ti(OH)_4(H_2O)_2$ was chosen as a model of the hydrated anatase surface (001) (Fig. 19.1d). In the mentioned work, it was shown that such a cluster is thermodynamically the most advantageous; its energy is 60.2 kJ/mol lower than the energy of the complex shown in Fig. 19.1c.

When designing the model, X-ray structural data of the unit cell of the bulk phase of anatase were used (Fig. 19.1a). As known, the structural unit of the crystal lattice of anatase is distorted TiO_6 octahedra united by common edges.
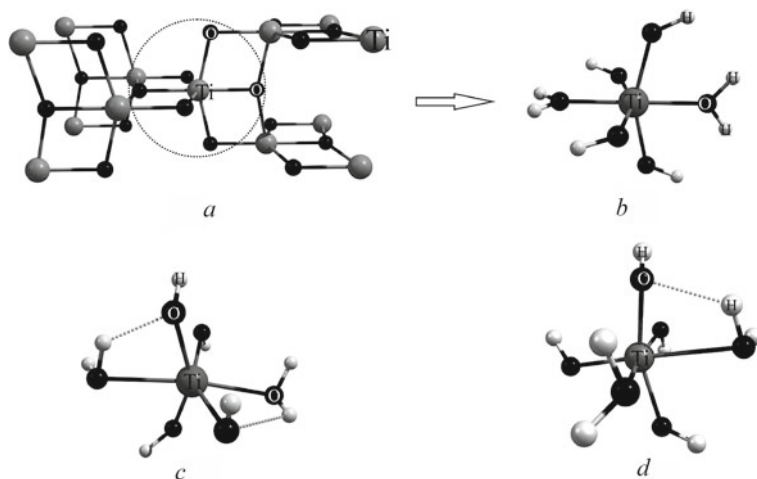
Fig. 19.1 Elementary cell of anatase (**a**), the initial structure of the cluster $Ti(OH)_4(H_2O)_2$ (**b**), the optimized structure of the $Ti(OH)_4(H_2O)_2$ cluster with axial arrangement of water molecules relative to the titanium atom (**c**), an alternative optimized structure $Ti(OH)_4(H_2O)_2$ clusters with equatorial arrangement of water molecules (**d**)

Each octahedron has four common edges with neighbors that form zigzag chains. There are four valence electrons in the titanium atom, and it is hexa-coordinated in anatase, i.e., surrounded by 6 oxygen atoms, four of which are in the equatorial position and two in the axial position. There are two types of Ti–O bonds in bulk anatase crystals: equatorial—short (1.93 Å) and axial—long (1.98 Å). Ti–O bonds are considered as a superposition of four covalent and two dative bonds. In the cluster $Ti(OH)_4(H_2O)_2$ (Fig. 19.1d), two datively bound water molecules are placed at the angle of $79.52°$, while for bulk samples of anatase this value is close to $180°$.

In [17], using the methods of quantum chemical modeling, the structural and energy characteristics were studied of intermolecular complexes of the cluster $Ti(OH)_4(H_2O)_2$ with a orthophosphoric acid molecule formed due to hydrogen bonds between them. The results of analysis of the obtained characteristics for all the calculated complexes show that the highest interaction energy is inherent in the intermolecular complex of orthophosphoric acid and cluster $Ti(OH)_4(H_2O)_2$, where the oxygen atom of the phosphoryl group (O=P≡) forms a hydrogen bond with the hydrogen atom of the coordinated water molecule of the $Ti(OH)_4(H_2O)_2$ cluster, whereas two hydrogen atoms of the hydroxyl groups of the orthophosphoric acid molecule form two hydrogen bonds with two oxygen atoms of the titanol groups (Fig. 19.2a). The formation of intermolecular complexes with separated charges due to proton transfer from the H_3PO_4 molecule to the $Ti(OH)_4(H_2O)_2$ cluster with formation of a dihydrogen phosphate anion, and a protonated form of the titanol group ($\equiv TiOH_2^+$) is thermodynamically less advantageous. The difference in the energy effects of the formation of these complexes is insignificant (about 4 kJ/mol) (Fig. 19.2b). Therefore, we can assume that the processes of their formation compete with each other.
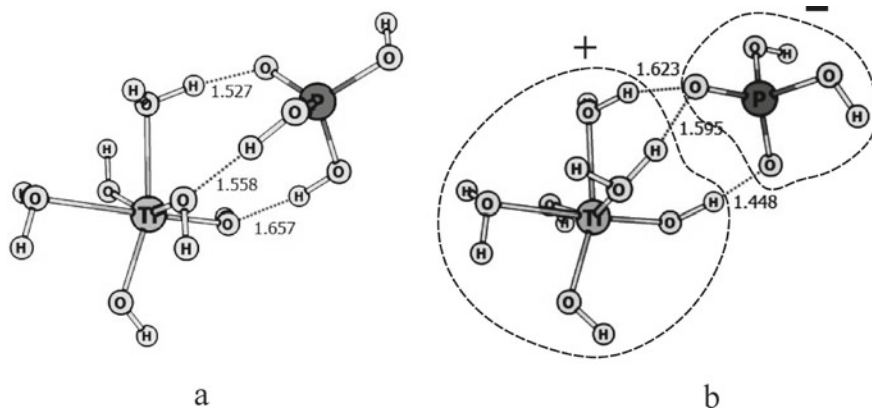
Fig. 19.2 Equilibrium structure of intermolecular complexes: hydrogen-bound complex (**a**) and complex with separated charges (**b**)

19.3 Results and Discussion

The chemical interaction between the phosphoric acid molecule and the $Ti(OH)_4(H_2O)_2$ cluster can occur with the formation of covalent and coordination-bound complexes [5, 6, 10].

In covalent bonding, the interaction between the starting materials occurs with the formation of a Ti–O–P link and with the cleavage of a water molecule. The hydroxyl groups of the $Ti(OH)_4(H_2O)_2$ cluster and the phosphoric acid (1) molecules are involved in the formation of the covalent bond.

$$\equiv Ti - O - H \ + \ H - O - \underset{\underset{OH}{|}}{\overset{\overset{O}{\|}}{P}} - OH \ \longrightarrow \ \equiv Ti - O - \underset{\underset{OH}{|}}{\overset{\overset{O}{\|}}{P}} - OH \ + \ H - O - H \qquad (1)$$
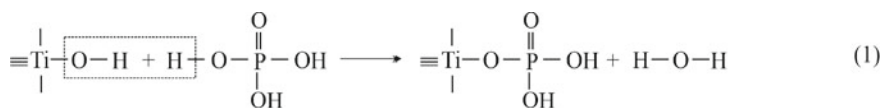
Taking into account the data known from the literature [4, 18] on the dissociation constants of the H_3PO_4 molecule and hydroxyl groups of anatase (2.2 and 7.8, respectively), we can assume that the condensation of a water molecule occurs due to cleavage of a hydrogen atom from the phosphoric acid molecule and hydroxyl groups from the Ti cluster. Indeed, among the models of hydrogen-bound complexes of the H_3PO_4 molecule with the $Ti(OH)_4(H_2O)_2$ cluster considered in the previous work [17], the more energetically advantageous structures are those containing the fragment shown in Fig. 19.3a, not 19.3b.

In order to determine the reaction mechanism, the energies and spatial structure of possible participants in the process and the activation barriers of several reaction routes are calculated.

The first step for each route involves the formation of a prereaction complex between the $Ti(OH)_4(H_2O)_2$ cluster and the H_3PO_4 molecule. For its consideration,
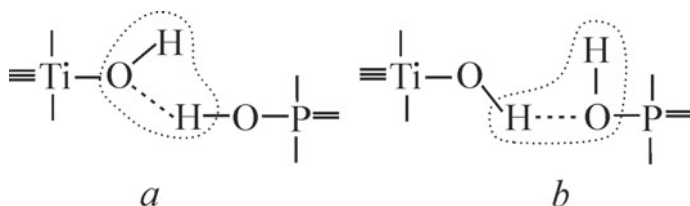
Fig. 19.3 Schemes of hydrogen bond formation between hydroxyl groups of a phosphoric acid molecule and a Ti(OH)$_4$(H$_2$O)$_2$ cluster

the intermolecular complex shown in Fig. 19.2a is selected, because, as shown in [17], it is the most thermodynamically stable. The hydrogen bonds formed between the Ti–OH groups and the hydroxyl groups of the acid molecule stabilize this prereaction complex.

We can assume two different routes of this reaction:

The first is a synchronous approach of one ligand (in our case, phosphoric acid molecules) and the removal of the hydroxyl group from the coordination sphere of the titanium atom (Fig. 19.4). This route assumes the existence of a transition state with a hepta-coordinated Ti atom. Since it is known [19] that the most optimal coordination number for the Ti atom in the environment of oxygen atoms is 6 (this is also true for anatase), this complex must be very unstable. The point corresponding to this structure (Fig. 19.4) could not be localized on the surface of potential energy (PES).

Figure 19.5 shows the energy profile of the second mechanism; the sum of the total energies of the starting substances, namely those of the cluster Ti(OH)$_4$(H$_2$O)$_2$ and of the molecule H$_3$PO$_4$, is taken as zero on the energy scale. This two-stage mechanism involves the formation of an intermediate with a pentacoordinated titanium atom in the first stage due to the release of a molecule of datively bound water from its coordination sphere (Fig. 19.5c). The activation energy of the formation of this

Fig. 19.4 Schematic structure of a hypothetical transition state with a seven-coordinated Ti atom
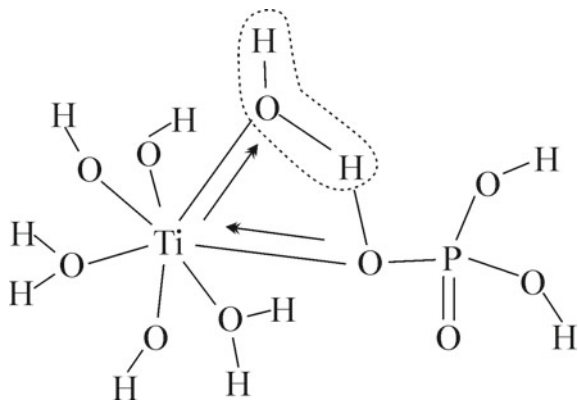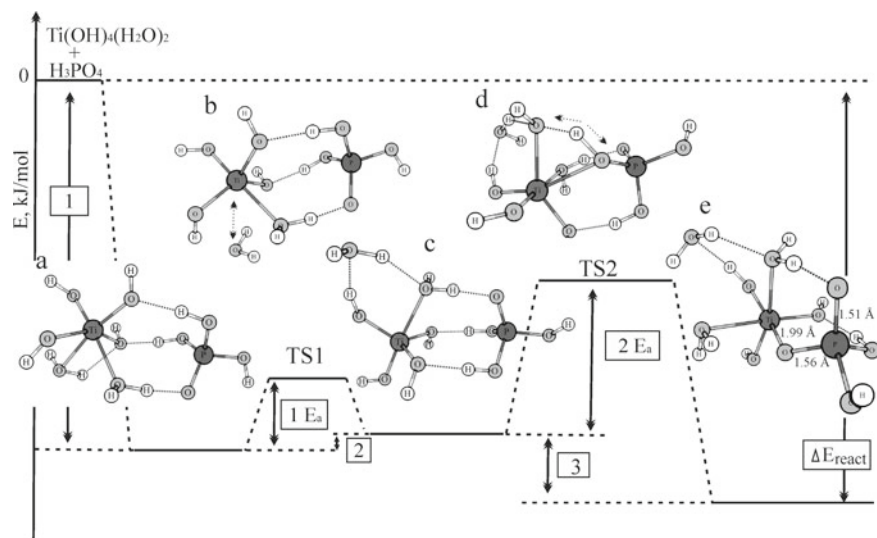
Fig. 19.5 Energy profile of the reaction of covalent binding between the cluster of $Ti(OH)_4(H_2O)_2$ with the molecule H_3PO_4 and the configurations of the prereaction complex (**a**), the transition state TS1 (**b**), the intermediate with the five-coordinated atom Ti (**c**), the transition state TS2 (**d**), and reaction product (**e**)

intermediate, based on the prereaction complex, is 7.6 kJ/mol. This value indicates the ease of this stage of the reaction, almost regardless of the medium temperature.

The energy effect of the first stage of the reaction is $+ 1.0$ kJ/mol. In the second stage, the oxygen atom of the $\equiv$P–O–H the group is coordinated with the titanium atom, and the coordination number of the latter is restored to 6. At the same time, proton is transferred from the group $\equiv$P–O–H to the group $\equiv$Ti–O–H with the formation of a coordinated to the atom Ti water molecule. The activation energy of the second stage of the reaction is 28.6 kJ/mol, and the energy effect is 13.1 kJ/mol. The total energy effect of the covalent binding between the H_3PO_4 molecule and the $Ti(OH)_4(H_2O)_2$ cluster is 156.1 kJ/mol (Table 19.1). The spatial structure of the reaction product is shown in Fig. 19.5e, which shows that the Ti–O and O–P bond lengths in the Ti–O–P chain are 1.99 and 1.56 Å, respectively. The first value corresponds to the length of the covalent bonds in anatase [3], and the second to the length of the O–P bond in the P–OH groups of the phosphoric acid molecule. This indicates that in the formed link Ti–O–P, the bonds are single. The structure of the formed complex is additionally stabilized by two hydrogen bonds between the oxygen atom of the phosphoryl group and the hydrogen atom of $\equiv$Ti–OH$_2$ group of anatase cluster $(d(OH) = 1.53$ Å) as well as by that between the H atom of the $\equiv$P–O–H—group and the O atom of the titanol group $(d(OH) = 1.77$ Å).

As can be seen from the energy profile of the reaction of covalent binding between the cluster $Ti(OH)_4(H_2O)_2$ and the molecule H_3PO_4, the real transformation path does not correspond to the simple scheme (1) above: namely the water molecule is

Table 19.1 Energy parameters (kJ/mol) of covalent binding between the H_3PO_4 molecule and the $Ti(OH)_4(H_2O)_2$ cluster (see Fig. 19.5)

		1	1 E_a	2	2 E_a	3	E_{react}
ΔE	Vacuum	−143.8	+7.6	+1.0	+28.6	−13.1	−156.1
	PCM	−121.3	+19.9	+9.6	+31.8	−27.0	−138.6
$\Delta G^0{}_{298}$	Vacuum	−81.2	+11.1	+0.2	+30.1	−3.9	−85.1
	PCM	−56.1	+24.5	+11.1	+32.0	−18.6	−62.8

not formed due to condensation of hydroxyl groups $Ti(OH)_4(H_2O)_2$ and phosphoric acid molecules; instead it merely leaves the coordination sphere of the Ti atom at the first stage of the reaction. And at the second stage, proton is transferred from the H_3PO_4 molecule to the $Ti(OH)_4(H_2O)_2$ cluster, with the simultaneous formation of a covalent bond (Ti–O–P) between them.

In the formation of coordination-bound complexes, the phosphoric acid molecule should take the place of the datively bound water molecule in the cluster structure, i.e., form a coordination bond between the phosphoryl oxygen atom of the H_3PO_4 molecule and the titanium atom in the $Ti(OH)_4(H_2O)_2$ cluster, according to reaction (2).

$$\equiv Ti-O\overset{H}{\underset{H}{\cdot}} \; + \; \underset{OH}{\overset{OH}{O=P-OH}} \longrightarrow \equiv Ti-O-\underset{OH}{\overset{OH}{P-OH}} + \; H-O-H \tag{2}$$
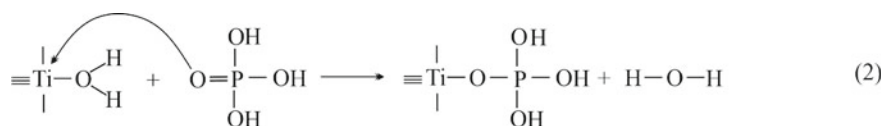
As the formation of a covalently bound complex, this reaction can occur by a two-stage mechanism. The PES localizes stationary points that correspond to the prereaction complex (Fig. 19.6a), transition state 1 (TS1) (Fig. 19.6b), intermediate (Fig. 19.6c), transition state 2 (TS2) (Fig. 19.6d), and the reaction product (Fig. 19.6e).

Scanning of PES allowed us to locate a point corresponding to the prereaction complex, the spatial structure of which is shown in Fig. 19.6a, where the oxygen atom of the phosphoryl group (O=P≡) forms a hydrogen bond with the hydrogen atom Ti–OH of the $Ti(OH)_4(H_2O)_2$ cluster group, and the two hydrogen atoms of the hydroxyl groups of the orthophosphoric acid molecule form two hydrogen bonds with the two oxygen atoms of the titanol groups. As can be seen from Tables 19.1 and 19.2, although the total energy effect of the reaction in the case of coordination binding is greater, the formation of the corresponding prereaction complex is energetically less beneficial.

The spatial structure of the species, related to the intermediate with the five-coordinated Ti atom, formed due to the cleavage of the datively bound water molecule from the cluster $Ti(OH)_4(H_2O)_2$, is shown in Fig. 19.6c. This water molecule forms three hydrogen bonds: between H atoms and O atoms of titanol groups and between an O atom with a phosphoric acid ≡P–OH group. In addition, the formed complex
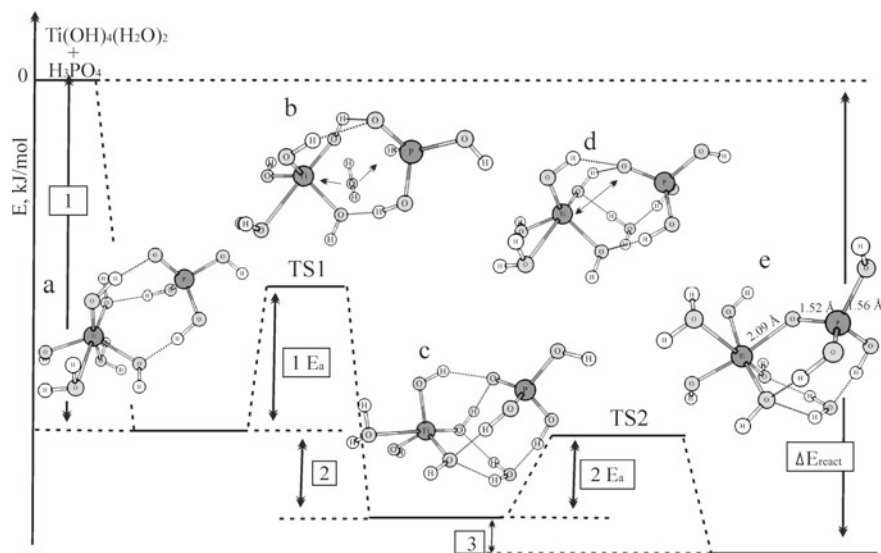
Fig. 19.6 Energy profile of the reaction of coordination binding of the cluster $Ti(OH)_4(H_2O)_2$ with the molecule H_3PO_4 and the configuration before the reaction complex (**a**), transition state TS1 (**b**), intermediate with a five-coordinated atom Ti (**c**), transition state TS2 (**d**) and reaction products (**e**)

Table 19.2 Energy parameters of the of formation (kJ/mol) of the coordination complex between the H_3PO_4 molecule and the $Ti(OH)_4(H_2O)_2$ cluster (see Fig. 19.6)

		1	1 E_a	2	2 E_a	3	E_{react}
ΔE	Vacuum	−126.2	+26.5	−27.5	+3.15	−6.3	−160.1
	PCM	−108.9	+29.9	−5.0	+13.1	−30.2	−144.1
$\Delta G^0{}_{298}$	Vacuum	−61.5	+24.9	−25.6	+7.5	−6.5	−93.6
	PCM	−33.8	+23.5	−6.9	+7.9	−32.3	−73.0

is stabilized due to the formation of two hydrogen bonds between the oxygen atom of the phosphoryl group (O=P≡) and the hydrogen atoms of the Ti–OH groups of the $Ti(OH)_4(H_2O)_2$ cluster as well as one hydrogen bond between Ti–OH and ≡P–OH groups. Figures 19.6b and 19.6d show the spatial structures of the prereaction complexes TS1 and TS2, respectively.

The equilibrium spatial structure of the product of the coordination binding of the cluster $Ti(OH)_4(H_2O)_2$ with the molecule H_3PO_4 is shown in Fig. 19.6e, which shows that the Ti–O bond length in the Ti–O–P chain increases as compared to the case of covalent binding and is 2.09 Å. On the contrary, the length of the O–P bond in the Ti–O–P chain decreases (1.52 Å) and corresponds to the length of the phosphoryl bond in the phosphoric acid molecule (1.51 Å). Such changes in the lengths of Ti–O and O–P bonds indicate the coordinating nature of the binding. The total energy effect of the coordination binding reaction (Fig. 19.6e) is −160.0 kJ/mol. Energy

characteristics of all the stages of the considered reaction route are given in Table 19.2.

The use of the polarization continuum model in the calculations (as can be seen from Tables 19.1 and 19.2) does not significantly change the energy characteristics of the chemical binding reaction mechanisms discussed above. The energy profiles of all considered reaction mechanisms remain practically unchanged.

An analysis of the obtained energy data (Tables 19.1 and 19.2) shows that regardless of the chosen method of calculation (in the gas phase or using the polarization continuum model), the chemical binding reaction between the H_3PO_4 molecule and the $Ti(OH)_4(H_2O)_2$ cluster occurs due to the second route. Thus, coordination binding is thermodynamically more likely at both 0 and 298 K.

19.4   Conclusions

An analysis of the results of calculations shows a possibility of a chemical bonding reaction between the $Ti(OH)_4(H_2O)_2$ cluster and the H_3PO_4 molecule by different mechanisms, but both are two-stage. Among the participants of the process, there were found intermediates in which the titanium atom turns into a pentacoordinated state. Thus, the binding of the H_3PO_4 molecule on the surface of real anatase crystals occurs at defective sites. However, in the second route, the activation energy of the first stage is higher than that for the first route.

Comparing the values of the total energy effect of the considered reaction routes, it has been found that regardless of the chosen method (gas phase or PCM), the course of the II route (coordination binding) is thermodynamically more probable both at 0 K and at 298 K. An analysis of the highest values barriers (which are limiting) of the considered reaction routes indicates that the second mechanism is kinetically more probable.

The results obtained indicate that the chemical binding of orthophophoric acid on the anatase surface occurs mainly due to the formation of a coordination bond between the phosphoryl group of the H_3PO_4 molecule and the incompletely coordinated surface titanium atom.

References

1. Carp O, Huisman CL, Reller A (2004) Photo induced reactivity of titanium dioxide. Prog Solid State Chem 32(1–2):33
2. Diebold U (2003) The surface science of titanium dioxide. Surf Sci Rep 48(5–8):53
3. Blagojevic V, Chen YR, Steigerwald M, Brus R, Friesner A (2009) Quantum chemical investigation of cluster models for TiO_2 nanoparticles with water-derived ligand passivation: studies of excess electron states and implications for charge transport in the gratzel cell. J Phys Chem C 113:19806

4. Vlasova NN, Markitan OV (2020) Adsorption of inorganic phosphateson the surface of titanium dioxide. Colloid J 82(3):292 (in Russian)
5. Bermudez VM (2010) Ab Initio Study of the Interaction of Dimethyl Methyl phosphonate with Rutile (110) and Anatase (101) TiO_2 Surfaces. J Phys Chem C 114:3063
6. Valentin C, Costa D (2012) Anatase TiO_2 surface functionalization by alkylphosphonic acid: a DFT+D study. J Phys Chem C 116:2819
7. Pang CL, Watkins M, Cabailh G, Ferrero S, Ngo L, Chen Q, Thornton G (2010) Bonding of methyl phosphonate to TiO_2 (110). J Phys Chem C 114(40):16983
8. Pawsey S, Yach K, Reven L (2002) Self-assembly of carboxyalkylphosphonic acids on metal oxide powders. Langmuir 18(13):5205
9. Pechenyuk SI, Kuzmich LF (2008) On the nature of the sorption complex on the surface of metal oxyhydroxides. Sorb Chromatogr Process 8(5):779 (in Russian)
10. Tielens F, Gervais C, Dero G, Jaber M, Stievano L, Diogo C, Lambert JF (2016) Characterization of phosphate species on hydrated anatase TiO_2 surfaces. Langmuir 32(4):997
11. Davis JA, Kent DB (1990) Surface complexation modeling in aqueous geochemistry. Rev Miner 23(1):177
12. Adamo C, Barone V (1999) Toward reliable density functional methods without adjustable parameters: the PBE0 model. J Chem Phys 110(13):6158
13. Labat F, Baranek P, Domain C, Minot C, Adamo C (2007) Density functional theory analysis of the structural and electronic properties of TiO_2 rutile and anatase polytypes: performances of different exchange-correlation functionals. J Chem Phys 126(15):154703
14. Tomasi J, Mennucci B, Cammi R (2005) Quantum mechanical continuum solvation models. Chem Rev 105(8):2999
15. Cossi M, Barone V, Cammi R, Tomasi J (1996) Ab initio study of solvated molecules: a new implementation of the polarizable continuum model. Chem Phys Lett 255(4–6):327
16. Schmidt MW, Baldridge KK, Boatz JA, Elbert ST, Gordon MS, Jensen JH, Koseki S, Matsunaga N, Windus L, Dupuis M, Montgomery JA (1993) General atomic and molecular electronic structure system. J Comp Chem 14:1347
17. Filonenko OV, Demianenko EM, Lobanov VV (2020) Quantum chemical modeling of orthophosphoric acid adsorption sites on hydrated anatase surface. SURFACE 12(27):20–35 (in Ukrainian)
18. Chung SH, Bajue S, Greenbaum SG (2000) Mass transport of phosphoric acid in water: a 1H and 31P pulsed gradient spin-echo nuclear magnetic resonance study. J Chem Phys 112(19):8515–8521
19. Reznitsky LA (1991) Chemical bond and transformation of oxides. Publishing house of MSU, p 168

Chapter 20
Structural Functionalization of the Polymer Matrix in PVC-MWCNT Nanocomposites

T. M. Pinchuk-Rugal, V. M. Popruzhko, O. P. Dmytrenko, M. P. Kulish, M. A. Alieksandrov, A. I. Misiura, A. P. Onanko, A. I. Momot, T. O. Busko, and O. F. Kolomys

20.1 Introduction

Polymeric materials are widely used in various science-intensive industries. At the same time, they have low mechanical, thermally conductive, and electrically conductive characteristics, so it is important to improve these characteristics by filling polymer matrices with conductive dopants, including carbon nanostructures [1–4].

Carbon nanotubes (CNTs) have unique electrically conductive, thermally conductive, and mechanical properties, and aspect ratio of length to diameter (~ 1000) can significantly change electrically conductive, optical, and mechanical characteristics of polymer composites even at low concentrations [5–9].

Modification of polymers by conjugate systems can also dramatically change their physical and mechanical properties. Polyvinyl chloride (PVC) is a polymer, in the matrix of which already in the initial state there is a developed system of polyene structures due to dehydrochlorination. By filling the PVC matrix with multiwall carbon nanotubes, which are also conjugate systems, the role of the matrix can be significantly enhanced and the electrical and mechanical properties of composites can be improved even at low filler content under the condition of dispersed distribution in the matrix [10–12].

However, the mechanisms of influence of polyene structures on the electrically conductive and mechanical characteristics of PVC-MWCNT composites have not been established.

T. M. Pinchuk-Rugal · V. M. Popruzhko · O. P. Dmytrenko · M. P. Kulish ·
M. A. Alieksandrov (✉) · A. I. Misiura · A. P. Onanko · A. I. Momot · T. O. Busko
Taras Shevchenko National University of Kyiv, Kyiv, Ukraine
e-mail: mrmarafon@gmail.com

O. F. Kolomys
V.E. Lashkaryov Institute of Semiconductor Physics NAS of Ukraine, Kyiv, Ukraine

The aim of this work is to establish the mechanisms of influence of polyenes on the change of electrical and mechanical properties, as a result of modification of polyene structures in PVC-MWCNT nanocomposites due to mechanochemical action.

20.2   Experimental Studies

For production of PVC-MWCNT composites was used powder C-7058 with $M_{\mathrm{w}} = 157*10^3$ (Ukraine). MWCNT was synthesized by the method of temperature catalytic conversion. The catalyst used fine powder of Fe particles; the temperature in the reactor was 1000–1300 K. Due to the reaction of chemical precipitation on the catalysts was obtained MWCNT with an outer diameter of $d \sim 100$ nm. The nanotubes were purified from impurities by etching in a solution of NH_4F HF: H_2O: HCl.

Volumetric PVC samples with the addition of MWCNT were made by hot pressing. The polymer and filler components were weighed to the nearest of 0.0001 g. Then, they were poured into a glass vessel and filled with a small amount of alcohol. After that, the flask was placed for 5 min in an ultrasonic bath with warm water, 40–60 °C until the alcohol evaporated. After that, the resulting mixture was again mixed mechanically and poured into a mold. This mold was heated to 115°; the temperature was controlled by a thermocouple, the contact of which was in a special hole in the mold. After reaching the desired temperature, the mold was placed under the press, with an overload of 100 bar (107 PA; 98.69 atmospheres) and began to cool with a fan. The load and air flow were kept constant throughout the cooling process to room temperature. The obtained PVC-MWCNT composites had the form of disks with a diameter of 30 mm. The concentrations of BVNT in the polymer matrix were 0–0.0025 vol. part.

The crystal structure of PVC-MWCNT nanocomposites was determined using an X-ray diffractometer (DRON-3 M, Russia) using monochromatic CoKα ($\lambda = 0.1790$ nm) radiation. Radiographs were taken at a tube voltage of 40 kV and a current of 25 mA. The measurement was performed in Bragg–Brentano geometry. The division of diffraction patterns into crystalline and amorphous components was carried out using the software package Peak Fit 4.12. The accuracy of the partition was $\sim 98\%$.

Using teraohmmeter E6-13A (Latvia) was obtained the percolation dependence of PVC-MWCNT composites. Measurements were performed at room temperature. The dependence was constructed using the scaling equation:

$$\sigma = \sigma_0(\varphi - \varphi_{\mathrm{c}})^t \qquad (20.1)$$

where σ_0 is the conductivity of the dispersed filler in the composite; φ is the concentration of the filler; φ_{c} is the percolation threshold; and t is the critical index.

Investigation of mechanical properties of PVC-MWCNT nanocomposites used ultrasonic computer speed meter KERN-4 (Ukraine).

The dynamic modulus of elasticity of Jung was determined by the formula:

$$E' = \rho V_l^2 \tag{20.2}$$

where ρ is the density of the sample, and V_1 is the velocity of quasi longitudinal ultrasonic elastic waves.

The dynamic shear modulus was determined by the formula:

$$G' = \rho V_{tr}^2 \tag{20.3}$$

where V_{tr} is the velocity of quasitransverse ultrasonic elastic waves. The ultrasound frequency was (~ 1 MHz).

The Raman spectra of pure PVC and PVC-BVNT composites were measured at room temperature on a Horiba Jobin Yvon T64000 triple spectrometer (Japan). The spectra were excited by a He–Cd laser with a wavelength $\lambda_L = 532$ nm.

20.3 Results and Discussion

PVC belongs to the polymers in which the degree of crystallinity is insignificant. This can be seen from the behavior of the X-ray diffraction pattern for unfilled PVC, Fig. 20.1 (insert). The presence of blurred halos with maxima near $2\theta = 20$ and $2\theta = 28°$, the presence of which indicates an amorphous structure of PVC. At the same time, there are separate interference maxima, which allows to decompose into crystalline and amorphous components to obtain the degree of crystallinity in this polymer. It was equal to 21%, which really confirms the low degree of packaging of PVC macromolecules.

It is important to note that the crystalline phase can be realized by two spatial conformations of PVC macromolecules—syndiotactic and isotactic. Depending on the content of nanotubes, a non-monotonic dependence of the degree of crystallinity is observed. It is seen that at concentrations of nanotubes (0–0.0020 vol. part.), there is an increase in the degree of crystallinity from 21 to 27%. At the maximum content of MWCNT (0.0025 vol. part), the degree of crystallinity decreases to 26%, which is a manifestation of insignificant aggregation of nanotubes. However, even in the presence of artificial nucleation centers, which are nanotubes, the degree of crystallinity in nanocomposites remains small.

In Fig. 20.2 are shown mechanical modules of PVC-MWCNT composites.

Concentration dependences of dynamic modulus of elasticity and shear are similar and are characterized by non-monotonic dependences. The presence of a minimum of about 0.0002 vol. part., their further growth at a concentration of 0.0005 vol. part., output, "on the shelf" to 0.002 vol. part., and decline at a maximum of 0.0025 vol. part. MWCNT concentration. The depth of the minimum for the modulus of elasticity
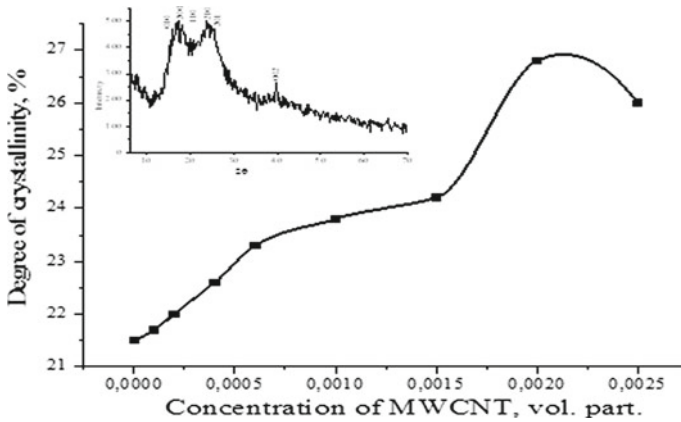
Fig. 20.1 Dependence of the degree of crystallinity of PVC on the content of MWCNT (the insert shows an X-ray diffraction pattern of pure PVC, $\lambda_{K\alpha Co} = 0.1790$ nm, $T = 293$ K)
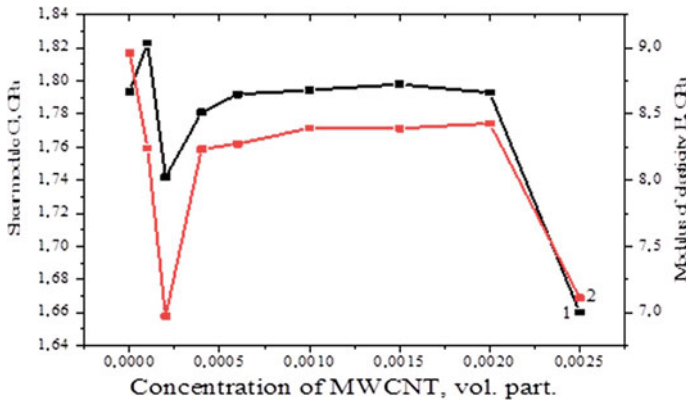
Fig. 20.2 Concentration dependences of the dynamic shear modulus G' (1) and the modulus of elasticity E' of PVC-MWCNT nanocomposites

is higher. It can be assumed that the drop in modulus at low concentrations of carbon nanotubes is due to the destruction of macromolecules. Instead, with an increase in the concentration of MWCNT in the range of 0.0005–0.002 vol. part. Two processes are competing: On the one hand, carbon nanotubes act as centers of nucleation, and on the other—at high concentrations of MWCNT 0.002–0.0025 vol. part., there is a decrease in the centers of nucleation and aggregation of tubes, which leads to the fall of the modules.

Obviously, depending on the concentration and distribution of carbon nanotubes in the polymer matrix is the formation of a leading cluster [13, 14].

In Fig. 20.3 is shown the scaling behavior of electrical conductivity in PVC-MWCNT nanocomposites.
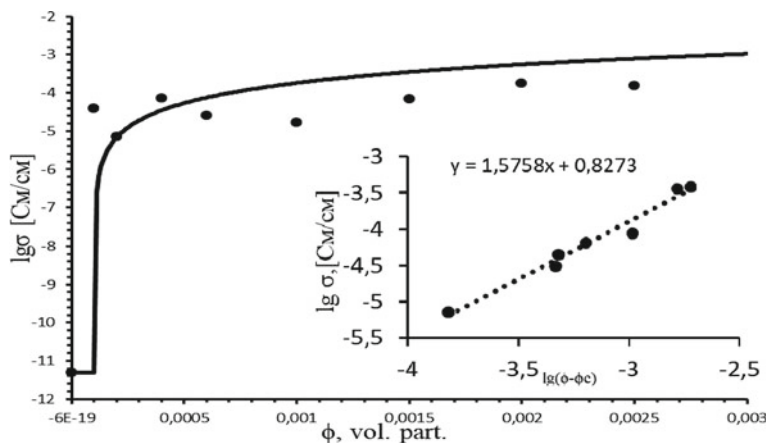
Fig. 20.3 Percolation curve of electrical conductivity of PVC-MWCNT nanocomposite. The insert presents the logarithmic dependence $\sigma \sim (\varphi - \varphi_c)$; φ_c—percolation threshold

Adjustment of experimental data was performed in accordance with the scaling (20.1).

It should be noted that as a result of the segregated structure of the distribution of nanotubes, there is a very low value of the percolation threshold $\varphi_c = 0.0001$. At the same time, the critical index $t = 1.5$ remains close to the theoretical value obtained for the statistical distribution of the filler. Thus, the fabrication of nanocomposites with segregated nanotube distribution is an effective method of improving electrical conductivity with a small value of the percolation threshold. However, the problem of obtaining high values of electrical conductivity due to the strong influence of contact resistance remains unsolved. It is seen that after the percolation threshold, the segregated structure is not preserved due to the transition of nanotubes into the volume of the polymer matrix. It can be assumed that in this case a polymer layer is deposited on the nanotubes, which prevents the existence of ohmic contact between the filler particles.

Figure 20.4 shows the dependences of $\log (\sigma_c/\sigma_m)$, which reflect the ratio of static electrical conductivity σ_c for PVC-MWCNT nanocomposites with different content of nanotubes, to its maximum value of σ_m from φ, vol. part.

The experimental data of the ratio σ_c/σ_m were adjusted in accordance with the following equation [15]:

$$\log\left(\frac{\sigma_c}{\sigma_m}\right) = A(1 - e^{-\alpha\varphi})^n \tag{20.4}$$

As a result, the following parameter values were obtained for nanocomposites:

$$A = 7; n = 2; \varphi_c = 0.0001 \text{ vol. part.}$$
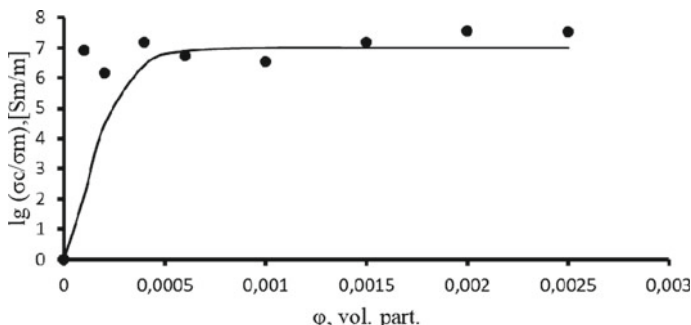
Fig. 20.4 Dependence of the electrical conductivity ratio of PVC-MWCNT nanocomposites on the content of nanotubes

That is, the experimental and calculated percolation thresholds coincide.

Under the formation of a conductive cluster in PVC-BVNT nanocomposites, polyene structures are generated, which can affect the value of electrical conductivity in the percolation region.

Effective study of existing polyconjugated sequences in PVC is possible in the case of resonant Raman spectroscopy.

The DFT calculations were performed for the PVC molecule containing 9 carbon atoms. The M06-2X exchange–correlation functional with 6-31G $+ (d, p)$ basis set was used in calculations. The optimized geometry is presented in Fig. 20.5.

Vibrational frequencies of the molecule were calculated. The absence of imaginary frequencies proves that the optimized geometry is local minima. Figure 20.6 shows the calculated Raman spectra that was scaled by the factor 0.94 [16].

High-frequency bands in the range 2874–2984 cm^{-1} correspond to hydrogen valence vibrations, 1384 cm^{-1} hydrogen scissoring vibrations There are also peaks in the low-frequency range near 300–600 cm^{-1}.

Experimental Raman spectra show the presence in PVC of a developed system of polyene structures.

In Fig. 20.7 is shown the Raman spectrum of unfilled PVC.

It is seen that in the spectrum of unfilled PVC there is a set of bands associated with vibrational modes of non-degraded PVC near 362, 636, 696, 2920, and 2960 cm^{-1},
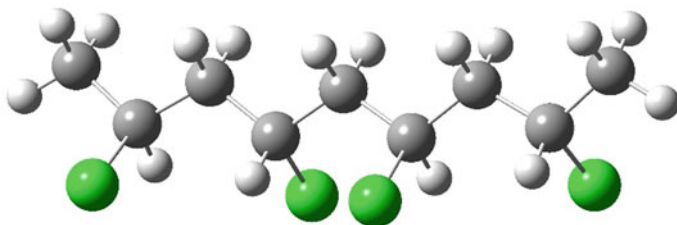
Fig. 20.5 Optimized geometry of PVC molecule
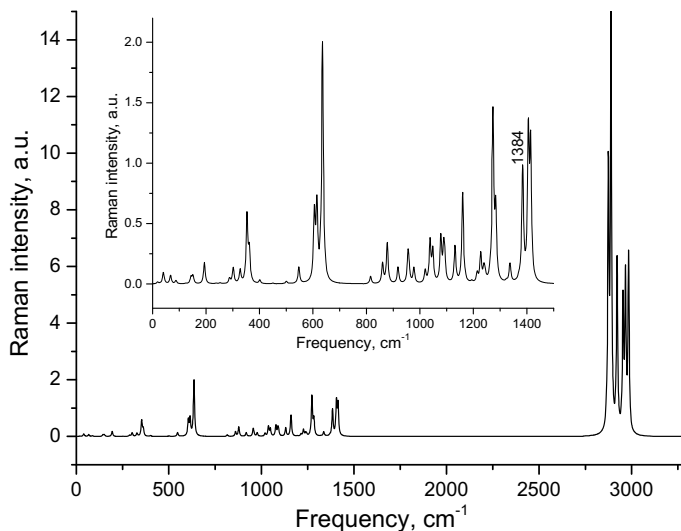
Fig. 20.6 Calculated Raman spectra of PVC molecule
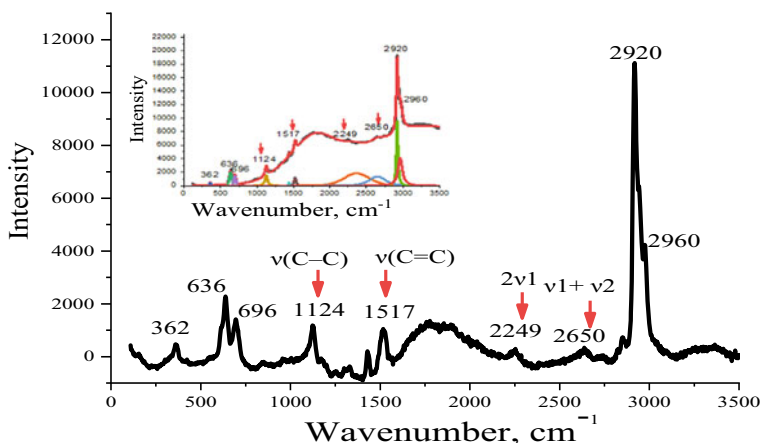
Fig. 20.7 Raman spectra of unfilled PVC (λex = 532 nm)

as well as cattle lines due to the structure of polyenes, $\nu\,(C-C)$ near $\nu_1 = 1124\ cm^{-1}$, and $\nu\,(C=C)$ near $\nu_2 = 1517\ cm^{-1}$. In addition to these lines, higher harmonics and compound modes are observed for $C-C$ and $C=C$ bonds in polyconjugate systems. Thus, the second harmonic of valence oscillations of CC bonds appears at about $2\nu_1 = 2249\ cm^{-1}$. A compound oscillating mode with a frequency of $\nu_1 + \nu_2$ leads to a band of about $2650\ cm^{-1}$. To find the length of conjugate fragments, you can use an empirical expression that represents the relationship between the frequency ν_2 and the number n of conjugate double bonds $C=C$ in the polyene sequence [11]:

$$\nu_2 = 1461 + 151.24\exp(-0.07808n) \tag{20.5}$$

Thus, for unfilled unradiated PVC, the value of n for different sequences can be obtained. Near $\nu_2 = 1517$ cm^{-1}, the number of conjugate links $n = 13$.

With the filling of PVC with the minimum concentration of MWCNT (0.0001 vol. part.), there is a sharp increase in the intensities of the main polyene bands ν (C – C) near $\nu_1 = 1123$ cm^{-1} and ν (C = C) near $\nu_2 = 1511$ cm^{-1}, Fig. 20.8.

In addition to polyene strips, there are still peaks from PVC around 361, 634, 698, and 2917–2977 cm^{-1}, which are slightly shifted compared to pure PVC. In this case, $n = 6$.

At the concentration of MWCNT (0.0002 vol. part.) in PVC continue to generate polyene structures, Fig. 20.9.
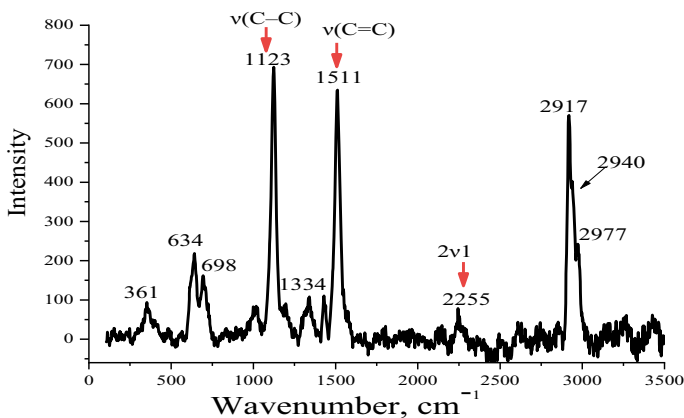
Fig. 20.8 Raman spectrum of PVC with 0.0001 vol. part. MWCNT (λex = 532 nm)
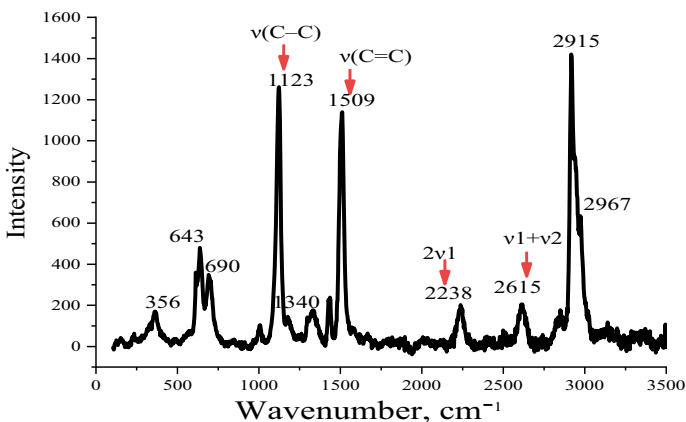
Fig. 20.9 Raman spectrum of PVC with 0.0002 vol. part. MWCNT (λex = 532 nm)
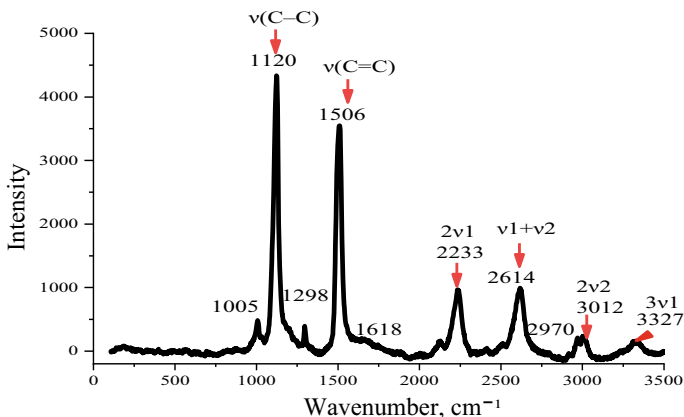
Fig. 20.10 Raman spectrum of PVC with 0.0004 vol. part. MWCNT (λex = 532 nm)

In addition to polyene bands v (C – C) near $v1 = 1123$ cm^{-1} and v (C = C) near $v_2 = 1509$ cm^{-1}, their overtones $2v_1$ appear near 2238 cm^{-1}, composed modes $v_1 + v_2$ about 2615 cm^{-1}. In addition, the band characteristic of non-degraded PVC around 356, 643, 690, and 2715–2767 still remains quite intense. In this case, $n = 10$.

With increasing concentration of carbon nanotubes to 0.0004 vol. part, the formation of polyene structures continues, Fig. 20.10.

Peaks characteristic of PVC in the low-frequency region is absent, while the bands v (C – C) near $v_1 = 1120$ cm^{-1} and v (C = C) near $v_2 = 1506$ cm^{-1} and $2v_1 = 2233$ cm^{-1} remain intense; $v_1 + v_2 = 2614$ cm^{-1} and overtones $2v_2 = 3012$ cm^{-1} and $3v_1 = 3327$ cm^{-1} also appear. The predominant length of polyenes is $n = 15$.

This means that in the area of percolation (0.0002–0.0004 vol. part. MWCNT) under the conditions of the percolation cluster is the generation of polyene structures, the length of which varies slightly, but their number increases significantly. These polyene structures can affect the amount of electrical conductivity in the percolation region.

There is a significant restructuring of the main bands, in the region of significant concentrations of MWCNT (0.0006–0.001 vol. part.), in the Raman spectrum, Fig. 20.11.

At a concentration of MWCNT 0.0006 vol. part., the main polyene bands v (C – C) $v_1 = 1123$ cm^{-1} and v (C = C) near $v_2 = 1509$ cm^{-1} are still quite intense, but their overtones $2v_1$, $2v_2$, and $3v_1$ and the composite modes $v_1 + v_2$ are absent, and more and more peaks from PVC appear around 365, 643, 695, 1325, 2920, and 2967 cm^{-1} (Fig. 20.11a). With increasing concentration of MWCNT to 0.001 vol. part., even the main polyene peaks become less intense, and polymer modes are manifested to a greater extent (Fig. 20.11b). That is, at significant concentrations of MWCNT, the formation of new polyene structures is stopped due to tube aggregation.
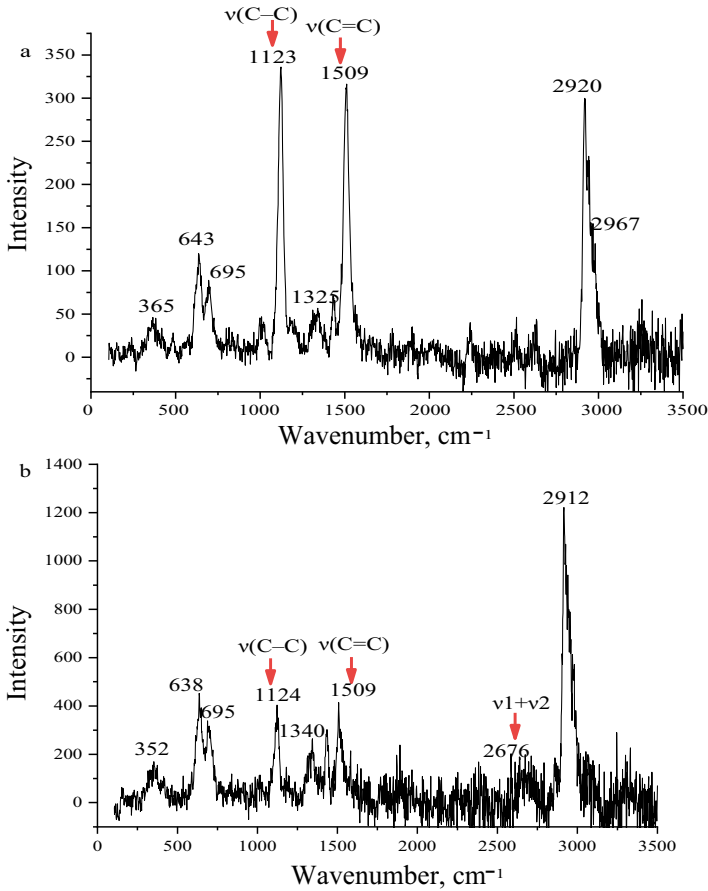
Fig. 20.11 Raman spectrum of PVC with 0.0006 (**a**) and 0.001 (**b**) vol. part. of MWCNT (λex = 532 nm)

20.4   Conclusion

1. It is shown that in PVC there is a low value of the degree of crystallinity (21%). With the filling of PVC with carbon nanotubes, which act as centers of nucleation of crystallites with isotactic and syndiotactic conformations of macromolecules, with a low content of nanotubes (0–0.002 vol. part.), there is an increase in the degree of crystallinity to ~ 27%. At higher concentrations of MWCNT (0.0025 vol. part.), the degree of crystallinity due to aggregation of nanotubes decreases to ~ 26%.

2. It is established that the non-monotonic dependence of dynamic modulus of elasticity and shear in PVC-MWCNT composites is due to the destruction of

MWCNT at low concentrations of filler, increasing the role of tubes as nucleation centers and their aggregation at large (0.0025 vol. part.).

3. The percolation character of electrical conductivity in PVC-MWCNT nanocomposites ($\varphi_c = 0.0001$ vol. part.) is determined, which is due to the formation of a leading cluster in composites. Under the conditions of formation of the conductive cluster (0.0002–0.0004 vol. part.), the generation of polyene structures in composites occurs simultaneously, which can affect the value of electrical conductivity in the percolation region.

4. It is shown that already in the initial state in PVC there are polyconjugated systems. With the filling of PVC with carbon nanotubes in the percolation region (0.0002–0.0004 vol. part.), the most intensive is the generation of polyene structures, as evidenced by the appearance in the Raman spectrum intense bands ν_1 (C – C), ν_2 (C = C), overtones $2\nu_1$, $2\nu_2$, and $3\nu_1$, and compound modes $\nu_1 + \nu_2$. The length of the conjugate links in the sequences varies from $n = 6$ to $n = 15$, but the values $n = 13$ and $n = 15$ are preferred. At high concentrations of MWCNT (0.0006–0.001 vol. part.), the formation of new polyene structures is stopped due to aggregation of tubes.

References

1. Shi J-H, Yang B-X, Pramoda KP (2007) 1. Enhancement of the mechanical performance of poly(vinyl chloride) using poly(n-butyl methacrylate)-grafted multi-walled carbon nanotubes. Nanotechnology. 18:375704
2. Lisunova MO, Mamunya YP, Lebovka NI, Melezhyk AV (2007) Percolation behaviour of ultra-high molecular weight polyethylene/multi-walled carbon nanotubes composites. Eur Polymer J 43(3):949–958
3. O'Connor I, Hayden H, O'Connor S et al (2008) Kevlar coated carbon nanotubes for reinforcement of polyvilnylchloride. J Mater Chem 18(46):5585–5588
4. Wu XL (2010) Poly(vinyl chloride)-grafted multi-walled carbon nanotubes via friedel-crafts alkylation. Polymer Lett 14(11):723–728
5. Harris PJ (2004) Carbon nanotube composites. Internat Mat Rev 49(1):31–43
6. Yung R (2007) Multiwalled carbon nanotube-reinforced PVC. Macromol Symp 249–250:259–264
7. Broza G, Piszczek K, Schulte K, Sterzynski T, Nanocomposites of poly(vinyl chloride) with carbon nanotubes (CNT). Compos Sci Technol 67:890–894
8. Елецкий АВ (2010) Холодные полевые эмиттеры на основе углеродных нанотрубок. УФН 180(9):897–930
9. Елецкий АВ (2015) Электрические характеристики полимерных композитов, содержащих углеродные нанотрубки. УФН 185(3):225–270
10. Pinchuk-Rugal TM, Dmytrenko OP, Kulish MP, Nychyporenko OS, Grabovskyy YY, Strelchuk VV, Nikolenko AS, Shut MI, Shlapatska VV (2015) Structure and electronic properties of nanocomposites of polyvinylchloride with carbon nanotubes under an irradiation. Nanosyst Nanomater Mamotechnol 13(2):325–336
11. Pinchuk-Rugal TM, Dmytrenko OP, Kulish MP, Prylutskyy YuI, Nychyporenko OS, Shut MI, Tkach VM, Shlapatska VV (2017) The electron radiation effect on polyvinylchloride (PVC) nanocomposites with multiwalled carbon nanotubes. Springer Proc Phys 195:757–770

12. Pinchuk-Rugal TM, Dmytrenko OP, Kulish MP, Alieksandrov MA, Pavlenko OL, Onanko AP, Grabovskiy YuE, Strelchuk VV, Kolomys OF (2021) Mechanisms of stack interaction in polymer composites of polyvinylchloride with methylene blue. Springer Proc Phys 247:245–254
13. Pinchuk-Rugal TM, Alexandrov MA, Kulish MP, Dmitrenko OP, Mamunya CP, Strelchuk VV, Electrical and optical properties of polyethylene composites with multiwall carbon nanotubes and dyes. Nanosistemi Nanomateriali Nanotehnologii 16(4):737–744
14. Pinchuk-Rugal TM, Alieksandrov MA, Misiura AI, Grabovskii YuE, Onanko AP, Dmytrenko OP, Kulish MP, Pavlenko EL, Busko TO, Pundyk IP, Gaponov AM, Lesiuk AI (2020) Structural features of polymer nanocomposite LDPE–MWCNT in the percolation transition region of electrical conductivity. Nanosistemi Nanomateriali Nanotehnologii 18(2):299–310
15. Lesenkov EA (2016) Features of percolation transition in nanocomposites based on polyetheres and carbon nanotubes. J Phys Stud 20(3):3702–3706
16. Alecu IM, Zheng J, Zhao Y, Truhlar DG (2010) Computational thermochemistry: scale factor databases and scale factors for vibrational frequencies obtained from electronic model chemistries. J Chem Theory Comput 6(9):2872–2887

Chapter 21
Hydrogel Materials for Biomedical Application: A Review

O. Nadtoka, P. Virych, V. Krysa, V. Chumachenko, and N. Kutsevol

21.1 Introduction

Hydrogels in biomedical applications have been used for decades, and their engineering potential grows with discoveries in chemistry and biology. New approaches in diagnostic and treatment methods have led to the demand for "smart" hydrogels capable of responding to the environmental changes.

Progressive developments in this field have established promising approaches to the development of biologically significant hybrid hydrogel materials that include nano/microstructures. These materials are promising in the treatment of wounds of various genesis, drug/gene delivery, regenerative medicine, etc.

Hydrogels properties and their application are caused by their main characteristics, namely cross-linking density, mechanical strength, swelling degree, elasticity, permeability, as well as biocompatibility and sorption/sorption of drugs.

The gel is a three-dimensional polymer mesh consisting of cross-linked long chain molecules capable of absorbing large amounts of solvent, causing macroscopic changes in size. The hydrogel network can be stabilized as a giant single molecule

O. Nadtoka (✉) · P. Virych · V. Chumachenko · N. Kutsevol
Taras Shevchenko National University of Kyiv, 64, Volodymyrska Street, Kyiv 01033, Ukraine
e-mail: oksananadtoka@ukr.net

P. Virych
e-mail: sphaenodon@ukr.net

V. Chumachenko
e-mail: chumachenko_va@ukr.net

N. Kutsevol
e-mail: kutsevol@ukr.net

V. Krysa
Ivano-Frankivsk National Medical University, 2, Galytska Street, Ivano-Frankivsk 76000, Ukraine
e-mail: kwm5@ukr.net

by chemical (covalent bonds) and/or physical (ionic bonds, weaves, crystallites, complexes, hydrogen bonds, van der Waals or hydrophobic interactions) cross-links.

Special properties of hydrogels, such as high sensitivity to the physiological environment, hydrophilic nature, high content of water or biological fluids, sufficient flexibility, soft and rubbery consistency, make them similar to living tissues [1, 2].

Our works devoted to modeling the structure of chemically cross-linked hydrogels based on branched graft copolymers of dextran-polyacrylamide and studying their physicochemical properties.

Hydrogel synthesis requires the integral presence of three components: monomer, initiator, and cross-linker [3]. Solvents such as water are required to control the heat of polymerization and other properties of the hydrogels. To increase the applicability of hydrogels, it is necessary to reduce and remove by-products of reactions, in particular, unreacted monomer, initiator, and cross-linker [4]. Various hydrophilic polymers or their precursors are also used for the synthesis of hydrogels. The main classes of constituents are represented by natural polymers and their derivatives (polysaccharides and proteins), as well as synthetic polymers containing the following hydrophilic functional groups: –COOH, –OH, –CONH$_2$, –SO$_3$H, amines, and ethers [1].

Grafted copolymerization is an attractive technique for modifying the chemical and physical properties of polymers to expand their practical use. The properties of the obtained graft copolymers are controlled by the characteristics of the side chains, including molecular structure, length, and number. By covalently grafting on a polysaccharide base (chitosan, dextran, etc.), the desired functional properties of the hydrogels can be introduced.

There are three most common methods of synthesis of grafted copolymers [5–7]: grafting pre-synthesized chains to the main chain ("grafting onto" method); macromonomer synthesis ("grafting through" method), which involves the synthesis of side macrochains, and then their copolymerization with monomers, the formation of active centers along the main chain (macroinitiator synthesis) and the growth of side chains from these centers by polymerization ("grafting from" method).

Grafting can be carried out by chemical, photochemical, and γ-initiation methods. It was observed that UV initiation leads to much smaller amounts of grafts compared to other methods, while γ-radiation provides a very large number of grafts and is accompanied by the destruction of macromolecules. Grafted copolymerization is also initiated by enzymes, gamma irradiation [8], and microwave irradiation [9].

Free radical-initiated grafting is the most promising method of chemical modification, which allows the use of a wide range of synthetic polymers and natural polysaccharides and the creation of new types of hybrid hydrogels through a variety of molecular architectures.

Various redox systems are used to initiate graft copolymerization: ammonium persulfates [10], potassium [11], as well as salts of metals of variable valence, such as Fe (III), Co (III), V (V), and Ce (IV) [12–14]. The role of reducing agent is played by a polymer, such as cellulose, chitosan, and polyvinyl alcohol. Today, cerium (IV) salts are considered to be the most promising for initiating graft copolymerization,

Fig. 21.1 Schematic representation of nonionic and ionic grafted copolymers

because homopolymerization of the monomer practically does not occur during their use [15].

In our previous works [16], the intramolecular structure of dextran-polyacrylamide copolymers depending on the length of the main macrochain and the distance between the grafted chains was studied. At a constant concentration of initiator, monomer, polysaccharide, reaction time, and temperature, dextrans of different weight average molecular weights were used: 20,000, 70,000, 500,000 (denoted as D20, D70, D500), as well as dextran sodium sulfate with a weight average molecular weight of 500,000 (DSS500). It is known that macromolecules of dextrans form coils in aqueous solutions, and during polymerization on their surface-active centers, they are formed due to the presence of hydroxyl groups [17]. By "grafting from" polymerization, side chains grow from these centers. It was shown that in graft copolymers of dextran-polyacrylamide, star models are realized, and dextran sulfate–polyacrylamide spherical polymer brushes are formed [16] (Fig. 21.1).

It has been shown [16] that branched polymers form a more compact structure than linear ones. It was proved that the compactness of the macromolecular coil of star-shaped dextran-polyacrylamide copolymers is determined by the original architecture of macromolecules caused by the distance between the grafts and the length of the grafted PAA chains.

21.2   Synthesis and Characteristic of Chemically Cross-Linked Hydrogels Dextran-Polyacrylamide

To improve the hydrogels properties, the concept of creating a mesh structure based on branched polymers was used. This allows to obtain a more orderly and compact network and regulate the properties by the internal architecture of the cross-linked macromolecules.

21.2.1 Synthesis of Chemically Cross-Linked Hydrogels

Chemically cross-linked hydrogels based on grafted dextran-polyacrylamide were synthesized [18] by radical copolymerization of dextrans of different molecular weight with acrylamide (AA) using cerium (IV) ammonium nitrate (CAN) as an initiator (Fig. 21.1). Dextrans D20, D100, D500 and DS500 were used. A cross-linked polymer based on polyacrylamide was also synthesized for comparison. In the process of copolymerization, branched water-soluble copolymers of different macromolecular architecture were formed which was cross-linked by N, N-methylene-bis-acrylamide to form a 3D network. Thus, polysaccharides of different molecular weights were mesh-modeling factors. At the same time, the cross-linking density was adjusted by changing the cross-linker concentration during polymerization. The cross-linker concentration was 0.1; 0.2; 0.4; 0.6; 0.8% by weight of acrylamide to obtain hydrogels with different cross-linking densities. The obtained samples were designated as D20-PAA-x, D100-PAA-x, D500-PAA-x, and DS500-PAA-x, where x is the concentration of the cross-linker during the reaction (Fig. 21.2).

Cross-linked hydrogels based on linear polyacrylamide were obtained by a similar method without the addition of dextran. These samples were designated as PAA-x.

Copolymers based on PAA-x and D-PAA-x in anionic form were obtained by alkaline hydrolysis (Fig. 21.3).
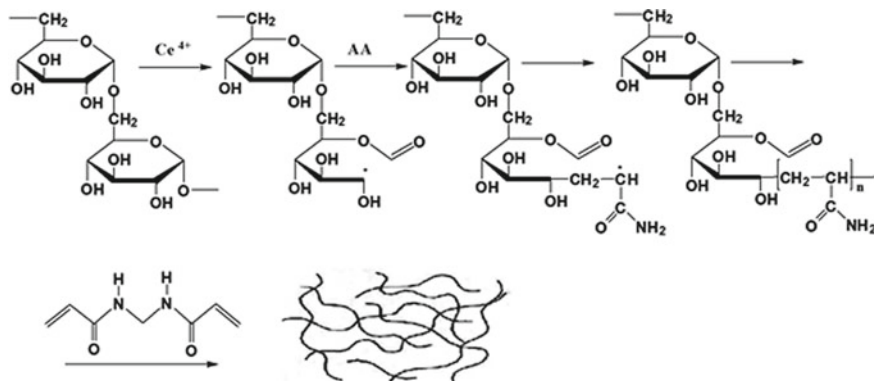
Fig. 21.2 Scheme of synthesis of chemically cross-linked hydrogels D-PAA-x
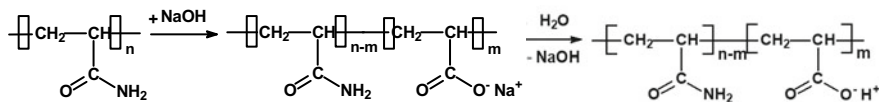
Fig. 21.3 Scheme of alkaline hydrolysis of chemically cross-linked hydrogels based on PAA-x
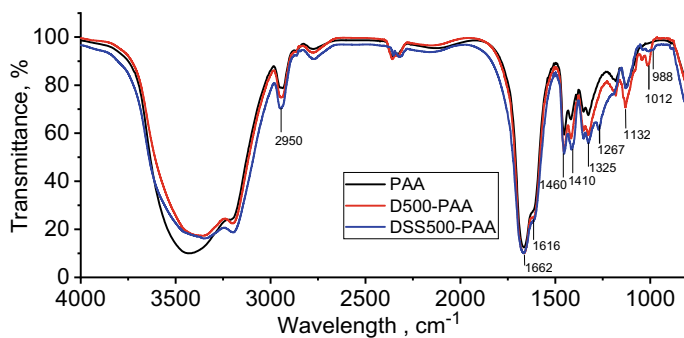
Fig. 21.4 FTIR spectra of hydrogels

21.2.2 FTIR Spectroscopy

The structure of cross-linked hydrogels in nonionic and anionic form was confirmed by FTIR spectroscopy [19].

IR spectra of PAA, D500-PAA, and DS500-PAA are shown in Fig. 21.4.

Characteristic peaks of the PAA component for all hydrogels were recorded at 1665 cm^{-1} (ν (C $=$ O), amide I) and 1615 cm^{-1} (δ (N–H), amide II). The peak at 1450 cm^{-1} can be attributed to the valence vibrations in the functional amide groups (ν (C-N), amide III) [20].

Only the area below 1400 cm-1 is specific for dextrans [21]. The range from 1480 to 1130 cm^{-1} contains five peaks, which are at 1460, 1410, 1350, 1325 and 1132 cm^{-1}. As is known, this region contains vibrations of the deformation components in the plane of the associated and monomer alcohols and groups CH and CH$_2$. For aliphatic alcohols, the bands 1410 and 1350 cm^{-1} correspond to deformation vibrations in the plane of hydrogen bonds of alcohols ("association bands"). The bands at 1410 cm^{-1} correspond to both deformations of C–OH groups and deformations of CH and CH$_2$ groups. The strong peak at 1267 cm^{-1} has a high intensity in samples with a higher degree of hydration, such as ionized samples. In the DSS500-PAA spectrum, the presence of a sulfo group (SO$_2$) can be determined by the presence of absorption bands at approximately 1267 and 988 cm^{-1} belonging to ν_{as} (S $=$ O) and ν_s (S $=$ O) vibrations, respectively.

21.2.3 Morphological Characterization

The study of the microstructure of cross-linked hydrogels using a scanning electron microscope (SEM) shows that hydrogels based on linear and branched PAA differ in the shape of the pores. As shown in Fig. 21.5, the mesh size does not exceed 1000 nm for all hydrogels, which allows the penetration of gases, but retains microorganisms.
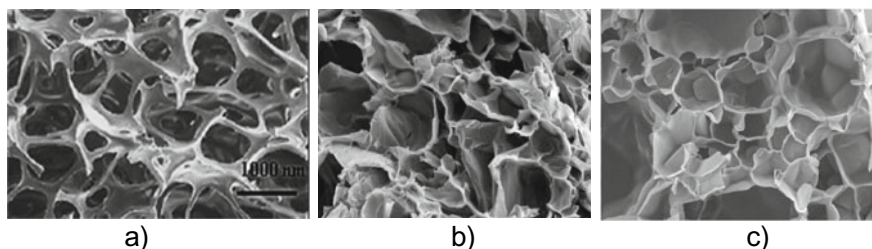
Fig. 21.5 SEM image of hydrogels based on cross-linked PAA **a**, D500-PAA **b**, and DSS500-PAA **c** (SEM Model Stereoscan 440 (LEO), Cambridge, UK)

The three-dimensional internal structure of the grafted copolymers-based hydrogels is characterized by conical pores, and this pore structure differs from the PAA-based hydrogel, which is less ordered. More enlarged pores were obtained for hydrogels based on DSS500-PAA.

For hydrogels with different cross-linking degrees, pores were obtained of differed sizes, but their characteristics were similar for a certain class of polymers. Thus, the SEM results confirm the possibility of influencing the internal structure of the hydrogel by grafting PAA onto dextran or dextran sulfate.

21.2.4 Swelling

The hydrogel as a cross-linked polymer network is able to retain water in its porous structure. Determining the amount of absorbed water is an important characteristic of the hydrogel for biomedical applications and is often described as the *swelling degree* (*S,%*) [22]. The swelling degree affects the diffusion of soluble substances passing through the hydrogel. In general, the higher the swelling degree, the greater the amount of absorbed water and the higher the rate of diffusion of the solute. Other factors, such as the microarchitecture of the polymer chain, can also play an important role. Experimentally, the swelling degree *S,%* can be determined by the following equation:

$$S_t\% = \frac{m_t - m_0}{m_o} \times 100 \tag{21.1}$$

where m_t is the mass of the hydrogel in the swollen state at time t and m_0 is the mass of the dry hydrogel.

As mentioned above, star-shaped branched copolymers of dextran-polyacrylamide (D-PAA) have advantages over linear polyacrylamide (PAA) due to the ability to regulate their internal structure during synthesis. In addition, for higher diffusion of water in the hydrogels of the PAA unit was converted into a polyelectrolyte.

Fig. 21.6 Equilibrium
swelling degree S_{eq}, % of
hydrogels based on dextrans
with different Mw
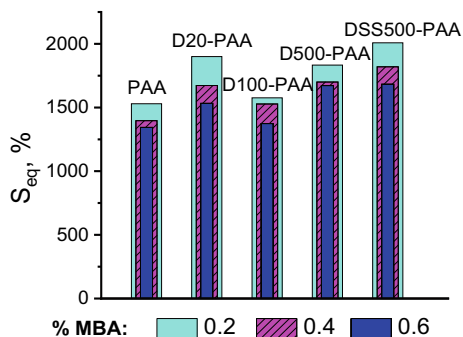
The behavior of hydrogels of different compositions during swelling at different cross-linking densities is shown in Fig. 21.6.

The decrease in the swelling degree of the gels decreases with increasing concentration of the cross-linker N,N'-methylene-bisacrylamide. This pattern is caused by an increase in the density of polymer chains, a decrease in pores, and an increase in the rigidity of the polymer network.

It was shown that dextrans of different molecular weights as mesh-modeling components affect the swelling ability of hydrogels in distilled water. As shown in our work [23], the internal macromolecular structure of grafted polymers depends on the size of the polysaccharide and after cross-linking leads to the formation of a more compact polymer network. In this case, the formed networks have higher porosity and a better ability to absorb water. The swelling degrees in the equilibrium state (S_{eq},%) of cross-linked polymers based on PAA, D20-PAA, D100-PAA, D500-PAA, and DS500-PAA are presented in Fig. 21.6.

In water, polyelectrolyte hydrogels dissociate and form charged macromolecules and counterions. In a three-dimensional polymer network, the charged chains are repelled from each other, and as a result, network cells begin to stretch. At the same time, the sample begins to actively absorb water and swells. Conversion of cross-linked polymers into polyelectrolytes polyacrylamide-co-polyacrylic acid (PAA-PAAc) and dextran-(polyacrylamide-co-polyacrylic acid) (D-(PAA-PAAc)) significantly increases the swelling ability (Fig. 21.7). The increase in water absorption after hydrolysis is explained by the presence of carboxyl groups in polymer matrices, and their concentration is directly proportional to the hydrolysis time.

The study of swelling of cross-linked hydrogels PAA and D-PAA in salt solutions, in particular sodium chloride, is interesting because of the possibility of using hydrogels as coatings for wounds, where diffusion processes occur in the presence of dissolved low molecular weight compounds. In addition, the saturation of the hydrogel with saline (0.8% NaCl solution) makes the material close to the natural intercellular environment of living tissues and does not irritate the wound surface. The effect of ionic force on the swelling ability of the synthesized hydrogels is shown
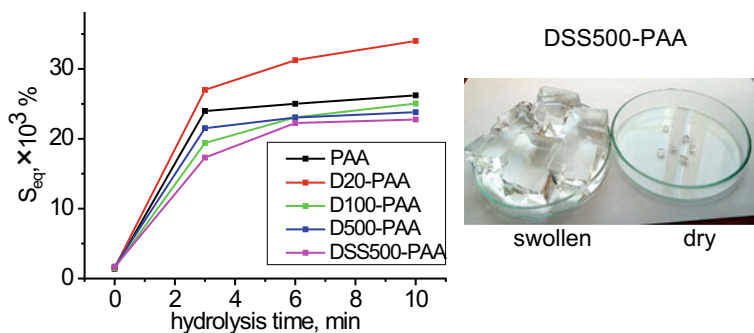
Fig. 21.7 Influence of hydrolysis time on the equilibrium swelling degree

in Fig. 21.8. It is obvious that the increase in ionic strength in the range of 0.01–1 M salt concentrations leads to a significant decrease in the swelling coefficient of hydrogels.

The high swelling sensitivity of anionic hydrogels PAA-PAAc and D-(PAA-PAAc) to ionic strength is caused by the change in charge distribution on the surface of the gel network. An increase in the concentration of Na+ ions in solution leads to a stronger "charge shielding effect" of additional cations and anion–anion electrostatic repulsion appearing [24]. Due to the reduction of the osmotic pressure difference between the polymer mesh and the external solution, the swelling of the hydrolyzed hydrogels is significantly reduced in 1 M NaCl solution.

Thus, the ability of the hydrogels to swell in the salt solution decreases compared to the swelling in distilled water. This feature is important for understanding the swelling behavior of hydrogels in physiological solutions or fluids that mimic plasma blood.
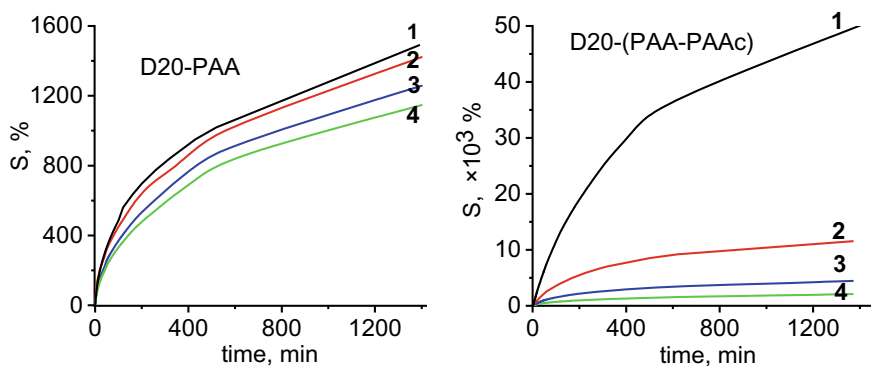
Fig. 21.8 Influence of the ionic strength of the solution on the swelling kinetics of cross-linked hydrogels (at 0.4% MBA, 10 min of hydrolysis): (1) distilled water, (2)—0.01 M, (3)—0.1 M, and (4)—1 M NaCl

21.2.5   Sorption Properties

Sorption capacity is an important characteristic of hydrogels used to remove contaminants from wounds. On the other hand, the ability to gradually release the absorbed substances can be used for the long-term delivery of drugs to the surface of the affected tissue.

The sorption capacity of hydrogels in the presence of an ionic dye is usually determined as the residual concentration of the dye in aqueous solution by spectrophotometry, where the concentration of the substance is determined by the calibration curve. The sorption degrees (Q) and sorbate release (R) are expressed by (21.2) and (21.3), respectively:

$$Q_{eq} = \frac{(C_0 - C_{eq}) \times V_1}{V_2}, \text{ mg/cm}^3 \tag{21.2}$$

$$R = \frac{(Q_{abs} - Q_{des}) \times 100}{Q_{des}}, \% \tag{21.3}$$

where C_0 and C_{eq}—initial and final concentrations of sorbate, respectively, V_1—the volume of aqueous phase (L), V_2—the volume of hydrogel without sorbate in the swollen state (cm^3), and Q_{abs} and Q_{des}—degree of absorption and desorption at equilibrium.

A pseudo-first-order kinetic model was used to determine the rate constant k of the interaction between the hydrogels and the dye in solution. The pseudo-first-order equation proposed by Lagergren [25] is often used to model fluid sorption [26]. The mathematical equation is the following

$$\frac{dQ_t}{dt} = k(Q_{eq} - Q_t) \tag{21.4}$$

where Q_{eq} and Q_t are the sorption degree ($mol\ cm^{-3}$) at equilibrium and time, t, respectively, and k is the rate constant for the equation of the pseudo-first order (min^{-1}).

As was mentioned above, branched grafted polymers have greater advantages for the sorption of charged organic molecules. Polymer networks of hybrid D-PAA form relatively structured hydrogel matrices [27] and, therefore, possess more controlled physical properties than hydrogels based on PAA. It is known that some dyes, such as diamond green ($\lambda_{max} = 625$ nm), methylene blue ($\lambda_{max} = 668$ nm), and basic fuchsin ($\lambda_{max} = 540$ nm), are also used as disinfectants for the skin or for the treatment of wounds and burns [28]. Such dyes are photosensitizers and are able to produce free radical oxygen in the presence of light sources to immobilize bacterial activity [29]. These biologically active dyes loaded into the structure of highly porous hydrogels can enter the target tissues or wound surface.

Among the studied hydrogels based on branched copolymers of D-PAA, hydrogels based on ionized branched macromolecules DS500-PAA have the best sorption

properties (Table 21.1). In ionized hydrogels, the groups $-SO_3Na$ dissociate to form stationary ionized groups $-SO_3^-$. This generates electrostatic repulsion forces inside the polymer network and induces pore expansion. The formation of an ionic complex between dye molecules and ionized polymer chains promotes the absorption of a positively charged dye [30].

Studying the processes of *desorption* of methylene blue (MB) from the polymer matrix of hybrid hydrogels has shown that the release of dye occurs gradually, which provides a prolonged delivery of the biologically active substance into the environment. As can be seen from Table 21.1 and Fig. 21.9, the desorption of MB from hydrogels has significant differences in the case of non-ionized and ionized hydrogels. In hydrogels based on nonionic PAA and D500-PAA, desorption of MB is faster and caused by the presence of positively charged amide groups [31], which push out positively charged molecules MB.

Due to the presence of anionic sulfo groups, the ionized DSS500-PAA hydrogel is able to form cationic–anionic complexes with dyes, which causes a slow release of MB, as evidenced by the deeper color of the hydrogel (Fig. 21.9).

Table 21.1 Absorption–desorption characteristics of hydrogels relative to methylene blue

Sample	Absorption		Desorption		R, %
	Q_{eq}, $\times 10^{-8}$ mol cm^{-3}	k_1, min^{-1}	Q_{eq}, $\times 10^{-8}$ mol cm^{-3}	k_2, min^{-1}	
PAA-0.2	42.05	0.32	33.65	0.50	20
PAA-0.4	21.46	0.30	17.50	0.40	19
PAA-0.6	20.88	0.28	17.20	0.27	18
D500-PAA-0.2	14.79	0.27	10.07	0.36	31
D500-PAA-0.4	13.75	0.25	9.91	0.35	28
D500-ПAA-0.6	12.85	0.22	9.45	0.30	25
DSS500-PAA-0.2	127.89	0.56	126.49	0.56	1
DSS500-PAA-0.4	127.31	0.51	126.43	0.33	0.7
DSS500-PAA-0.6	127.02	0.45	126.26	0.28	0.6

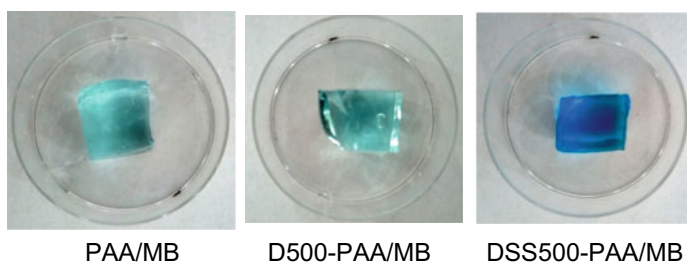PAA/MB   D500-PAA/MB   DSS500-PAA/MB

Fig. 21.9 Photo of hydrogel samples after desorption of methylene blue

As shown in our work, the sorption and desorption of diamond green and basic fuchsin occur in a similar manner, because these dyes are cationic too.

21.3 Hydrogels as Matrices for the Synthesis and Stabilization of Nanoparticles

The incorporation of metal nanoparticles (NPs) into the polymer hydrogel network is a very attractive way to develop nanocomposites for a wide range of applications.

AgNPs have many unique functions for biomedical applications due to their antibacterial properties, but high instability and low biocompatibility still remain serious clinical problems.

Hydrogels were used to protect NPs from aggregation and agglomeration. The stabilization of nanoparticles in cross-linked hydrophilic polymers is an expected effect in the production of hydrogel/AgNPs composites. As the free space inside the gel mesh can be used as a nanocontainer for the formation and growth of metal nanoparticles, the porous structures of hydrogels are suitable for the formation of AgNP in situ [32].

The modern method of obtaining silver nanoparticles by irradiation with ultraviolet light is based on the ability of D-PAA to generate free radicals in the presence of UV irradiation and act as a reducing agent against Ag^+. Hydrogel composites with AgNPs were obtained at different doses of UV irradiation (Fig. 21.10). With increasing irradiation time, the color of the samples becomes deeper, which indicates an increase in the concentration of nanoparticles.

As the SEM results show, the main advantage of UV technology is providing of controlled and uniform distribution of nanoparticles inside the hydrogel network without the addition of any other stabilizer (Fig. 21.11).

Analysis of the absorption spectra of composites based on linear and branched polymers PAA/AgNPs and D20-PAA/AgNPs with different cross-linking degrees (Fig. 21.12) shows that all nanocomposites registered a wide peak in the range of 380–850 nm. The presence of this SPR band indicates the presence of AgNPs with a wide particle size distribution.
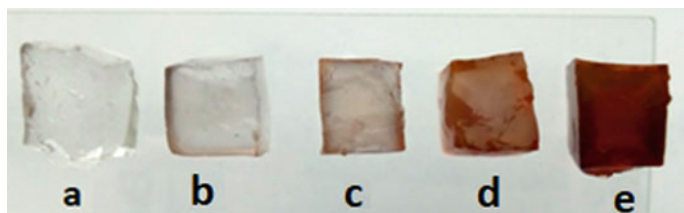

Fig. 21.10 Photo of D-PAA/AgNPs samples at different radiation doses: **a** 0 min, **b** 1 min, **c** 3 min, **d** 5 min, and **e** 10 min
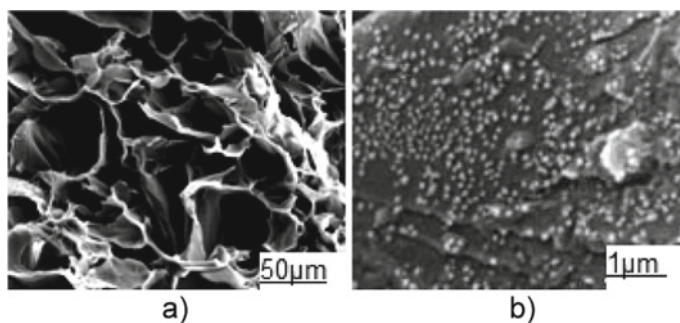
Fig. 21.11 SEM photo of hydrogel composites D20-PAA/AgNPs, obtained by photochemical method: **a** magnification of 7000 times and **b** magnification of 35 000 times
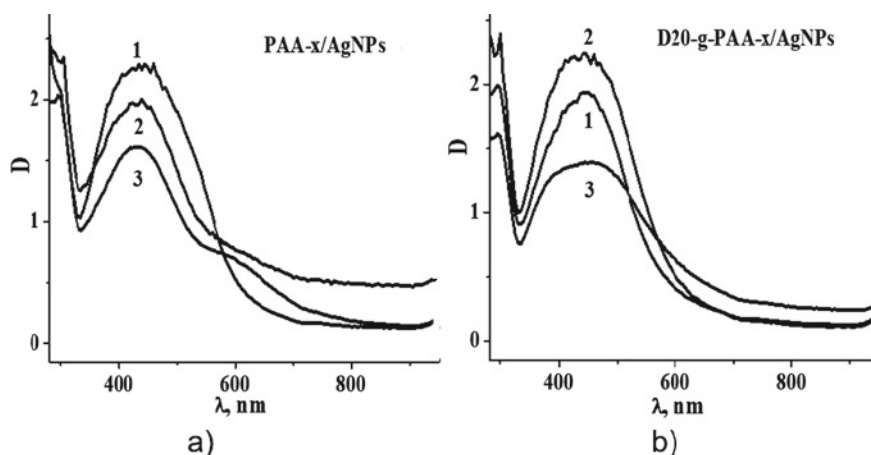

Fig. 21.12 Absorption spectra of composites PAA/AgNPs **a** and D20-PAA/AgNPs **b** at different cross-linking degrees of hydrogels: % MBA = 0.2 (1); 0.4 (2); 0.6 (3). Irradiation time 5 min

It is known that the absorption peak at 298 nm can be registered for $AgNO_3$ solution and corresponds to Ag^+ ions [33]. The procedure for obtaining a hydrogel/AgNPs composite assumes the presence of residual Ag^+ ions in the swollen cross-linked polymer, and the presence of this peak in the absorption spectrum is obvious (Fig. 21.12). All absorption bands have a complex line shape and contain various components that contribute to the overall spectrum. Three regions are well distinguished: about 380, 420, and 535 nm. These bands indicate the formation of polydisperse AgNPs of 20, 50, and 100 nm, respectively [34].

21.4   Hydrogels as Materials for Wound Dressings

Initially, polymer dressings were considered passive materials that play a minimal role in the wound healing process. In the 1960s, the first generation of polymer dressings was introduced, [35] which provided the optimal environment for wound healing. Since then, polymer hydrogels as biomaterials have attracted much attention and interest from scientists for many years.

Wound healing takes place in four stages: homeostasis, inflammation, granulation tissue formation, and reconstruction. Self-healing of the skin is usually accompanied by the formation of scars. Therefore, traditional treatment leads to the loss of the dermis and is therefore unsatisfactory, while the use of polymeric materials to create wound dressings of the new generation provides complete recovery or healing of skin tissues. It has been shown that wound healing with wet dressings is faster than with dry ones! Thus, moisturized or moisturizing dressings should be considered in skin repair and wound healing.

It has been shown that hydrogels as dressings provide all the requirements for wound healing and burns due to the following justifications [36]:

- hydrogels as porous materials are able to absorb and retain water, controlling fluid loss from the body and maintaining wetting and moisture in the wound area;
- small size of hydrogel pores protects the wound from infection and prevents the penetration of microorganisms and bacteria into the wound;
- the elastic property of swollen or hydrated hydrogels provides flexibility and elasticity to adapt to the wound surface and minimizes irritation or damage of surrounding tissues;
- hydrogel can absorb wound exudates, which promotes the processes of fibroblast proliferation and keratinocyte migration, which are necessary for complete epithelialization and wound healing;
- both compositionally and mechanically hydrogels are similar to the natural extracellular matrix; thus, they can serve as an auxiliary material for cells during tissue regeneration and a carrier in the delivery of a therapeutic agent;
- the low interfacial voltage between the surface of the hydrogel and body fluid minimizes protein adsorption and cell adhesion, which reduces the likelihood of a negative immune response;
- the mucoadhesive and bioadhesive properties of many polymers used in hydrogel materials (e.g., polyacrylic acid, polyethylene glycol, and polyvinyl alcohol) increase the time of stay of the drug on the skin/plasma membrane, leading to increased tissue permeability.

Thus, the trend toward research and development of hydrogels as polymeric dressings becomes a commercial goal.

Hybrid hydrogels based on cross-linked branched graft copolymers were converted into composites with biologically active substances that are able to show a bactericidal effect directly or under the action of light.

21.4.1 Antibacterial Wound Dressings with Silver Nanoparticles

The discovery and use of antibiotics have reduced mortality from bacterial wound infections. At the same time, antibiotic-resistant strains of microorganisms have emerged [37], prompting the search for alternative antibacterial agents. One of them was combined hydrogels [38] with silver nanoparticles. It is the structural organization of the hydrogel that determines the size of nanoparticles and effectively stabilizes them [39, 40]. Silver nanoparticles show high bactericidal activity, although the reduced form of Ag^0 silver itself does not show biological activity. In the presence of oxygen and protons in the environment, the following reactions occur:

$$4Ag + O_2 = 2Ag_2O$$
$$2Ag_2O + 4H^+ = 4Ag^+ + 2H_2O$$
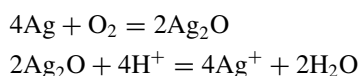
It is the released Ag^+ that cause cytotoxic effects [41]. The mechanism of action of Ag^+ is based on interactions with free hydrogen sulfide groups of proteins of bacterial membranes, which leads to disruption of their function and neutralization of the transmembrane ion gradient and cell necrosis. It is important that resistance to Ag^+ develops slowly compared to antibiotics [42].

Three-dimensional polymer hydrogels loaded with AgNPs are considered to be materials with very high potential for medical therapeutic and diagnostic applications [43]. Loading of the hydrogel structure with silver nanoparticles allows to give the material antibacterial properties, and the high water content and no toxic effects on the surrounding tissues contribute to faster wound healing. Polyacrylamide is a particularly promising polymer because it is similar in peptide structure and promotes skin regeneration. PAA-based hydrogels with bactericidal properties prevent bacterial contamination of damaged tissues and reduce the risk of inflammation and ulcers.

Antibacterial properties were investigated for PAA/AgNPs and D20-g-PAA-x/AgNPs at a cross-linker concentration of 0.2, 0.4, or 0.6% by weight of the monomer.

To test the material for its ability to inhibit the growth of bacterial cultures, wild strains of gram-positive and gram-negative cultures of *Escherichia coli* and *Staphylococcus aureus*, electively obtained on Endo media and yolk-salt agar, were used. The susceptibility of strains of microorganisms was evaluated by the disk-diffusion method (Fig. 21.13).

Due to the widespread use of antibiotic-resistant strains of microorganisms, general antibiotics Cefazolin and Ceftriaxone were used as controls. Measurement of the zone of growth retardation was performed after 24 h.

According to the photos in Fig. 21.13, it was found that the used wild strains of microorganisms *E. coli* and *S. aureus* show resistance to Cefazolin and Ceftriaxone, because after some time the emergence of new colonies of these bacteria in the area of antibiotic action was rerecorded. It is known that this is a global health problem that leads to limited treatment options using antibiotics.
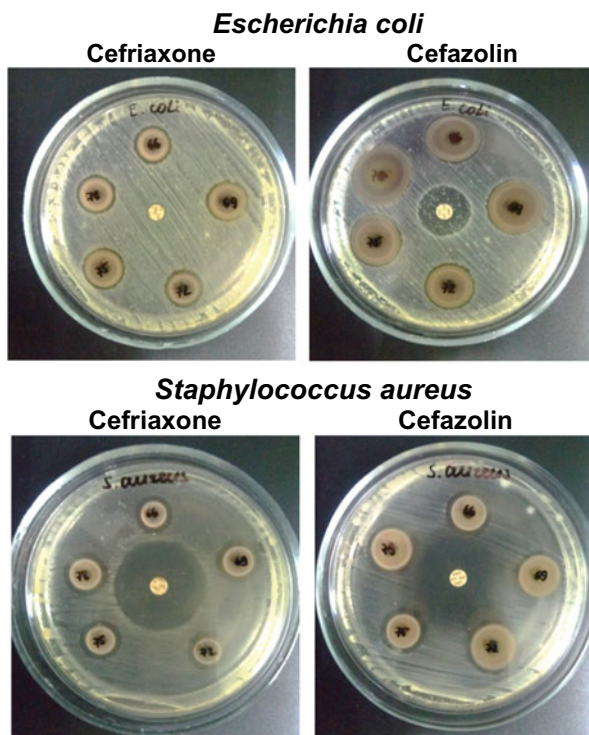
Fig. 21.13 Disk-diffusion tests of antibacterial efficacy of hydrogel/AgNPs nanocomposites against *Escherichia coli* and *Staphylococcus aureus* compared to antibiotics Ceftriaxone and Cefazolin (placed in the center)

Almost equally high sensitivity of *E. coli* and *S. aureus* strains to both antibiotic and hydrogel composites with silver nanoparticles was revealed. Although the antibacterial activity of composites is slightly lower than that of antibiotics, this study is evidence that silver nanoparticles as antibacterial agents are competitive substitutes for antibiotics and have valuable advantages because they do not cause bacterial resistance. Hydrogel composites based on branched polymers, in particular D20-PAA and D100-PAA, show advantages in bactericidal action on strains of both cultures in comparison with linear PAA.

To confirm the relationship between the density of the polymer network and the biological activity of nanoparticles obtained in this network, the sensitivity of *E. coli* to the nanocomposites of different cross-linking densities was studied (Fig. 21.14). As seen from Fig. 21.14, the photo of the disk-diffusion test demonstrates the presence of bacterial resistance to the antibiotic as the appearance of colonies in the area of its initial action. In the presence of hydrogel composites, bacterial resistance is not observed. Figure 21.14b shows an increase in the efficiency of the composite with increasing density of the polymer matrix in which the silver nanoparticles
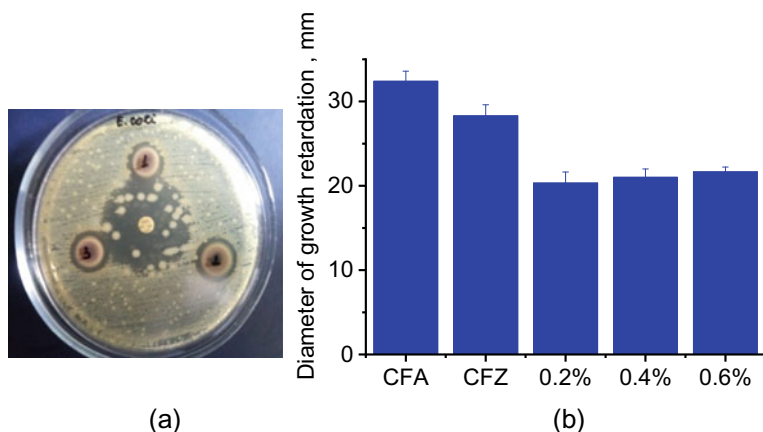
Fig. 21.14 a Disk-diffusion tests of antibacterial efficacy against *Escherichia coli* of hydrogel/AgNPs nanocomposites compared to the antibiotic Cefazolin (inside); **b** the dependence of the diameter of the growth retardation of *Escherichia coli* on the concentration of the cross-linker for composites D20-PAA/AgNPs

were obtained. As mentioned above, the higher the mesh density, the smaller the nanoparticles formed and the greater their bactericidal properties.

21.4.2 Comparison of Antibacterial Efficacy of Composites Hydrogel/AgNPs and Hydrogels/Chlorohexidine

To the comparison of bactericidal activity of composites hydrogel/AgNPs and hydrogels/chlorohexidine (CH), wild strain *Staphylococcus aureus* was used (Fig. 21.15).

Fig. 21.15 Diameter of the growth retardation of *Staphylococcus aureus* for hydrogel composites with CH and AgNPs
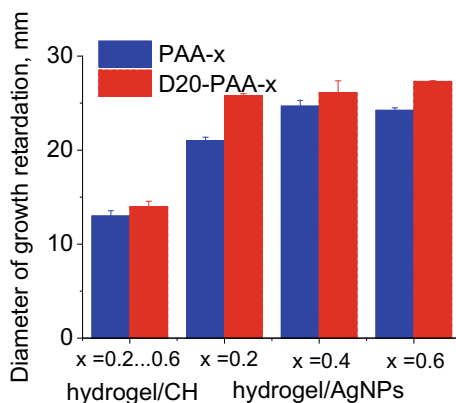
As shown in Fig. 21.15, hydrogels containing silver nanoparticles inhibit the growth of *S. aureus* colonies more actively: The diameters of growth retardation for hydrogel/AgNPs are larger than that for the samples hydrogel/CH and reach 21–27 mm. It should be noted that for both hydrogel composites a larger diameter of growth retardation was obtained when using hydrogels based on branched polymers D20-PAA-x compared to analogs based on linear PAA-x. There was also a tendency to increase the activity of composites with AgNPs with increasing degree of cross-linking. Obviously, this is caused by the smaller size of the formed nanoparticles, as presented above, in which they have greater biological activity.

21.4.3   Testing of Hydrogel Composites with AgNPs on Open Wounds

The obtained hydrogel composites proved to be effective in the treatment of wounds. The therapeutic efficacy of hydrogel materials was investigated in vivo on open wounds with artificial bacterial contamination [44].

White outbred rats were used in the studies. All animal manipulations were performed in accordance with the International Convention on the Treatment of Animals.

Sterile gauze bandages were used as controls. The bandages were on the animals for 48 h. The examination was performed 3 and 5 days after surgery. At the first examination (after 72 h), bacterial culture was performed from the wound on selective Endo media and yolk-salt agar for the presence of appropriate bacterial strains.

Figure 21.16 shows the stages of wound formation and treatment over five days. For comparison, a traditional gauze material (1) was used, as well as a hydrogel sample (2) and a composite hydrogel/AgNPs (3).

The study showed significant advantages in the effectiveness of treatment with the use of hydrogels, namely no colonies of pathogenic bacteria were detected during treatment with hydrogel coatings, while when using a gauze bandage, about 200 colonies of *S. aureus* were recorded. Three days after hydrogel dressing, the wound surface was reduced by approximately 30% without any inflammation or discharge, and five days of treatment showed significant benefits of using hydrogel composites with silver nanoparticles.

The achieved efficiency of composites caused by two main factors: the humid environment of treatment, which is provided by hydrogels, and bactericidal properties due to the presence of silver nanoparticles [45].
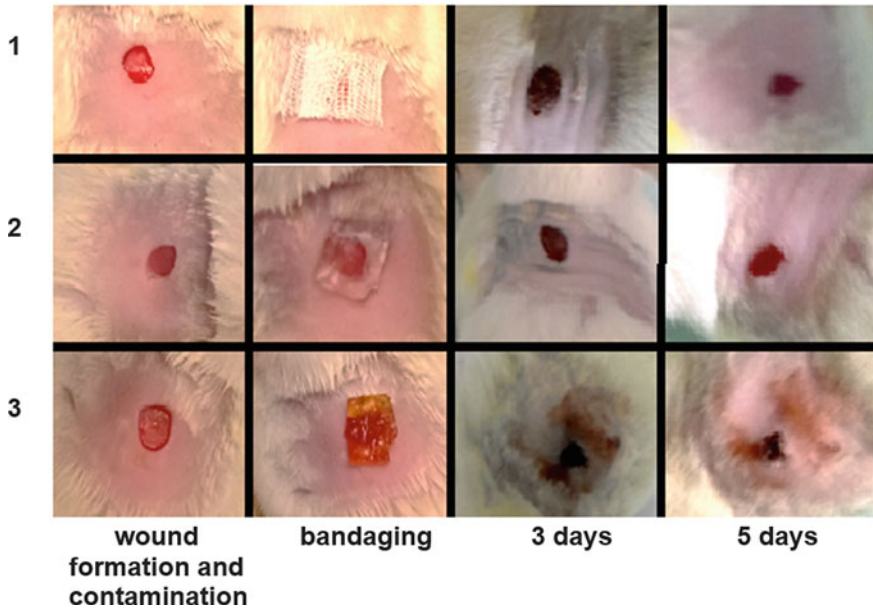
Fig. 21.16 In vivo study of the effectiveness of hydrogel dressings in the treatment of open wounds with artificial bacterial contamination: (1) traditional gauze material, (2) hydrogel sample, and (3) composite hydrogel/AgNPs

21.4.4 Testing of Hydrogel Composites with AgNPs on Open Human Wounds

Hydrogel composites with silver nanoparticles were tested as dressings for the treatment of wounds, in particular, chronic active ulcers (Fig. 21.17).

Fig. 21.17 Efficacy of hydrogel wound dressings with AgNPs in the treatment of trophic human wounds
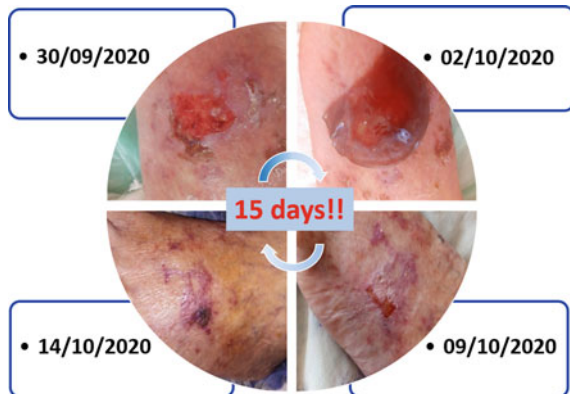
In the previous long-term treatment (more than 2 years) of ulcers by traditional methods using analgesics, anti-inflammatory, and antibacterial drugs, patients complained of an increase in the wound surface of the ulcer, which was accompanied by pain. In a short time, when using the application of hydrogel composites with AgNPs on the same trophic ulcers, doctors proved the high effectiveness of wound healing. Positive signs during treatment were the rapid disappearance of pain, reduction in a short time the size of ulcers, and complete epithelialization of the wound within 14 days.

21.4.5 Hydrogel Materials for Photodynamic Therapy of Open Wounds

In clinical practice, aseptic dressings are used to treat wound processes. It closes the wound surface from infection and at the same time maintains a moist environment on the wound surface, which promotes tissue regeneration. Such conditions also contribute to the reproduction of pathogenic microflora, which is present on the skin. Reproduction of microflora in the wound causes the appearance of pathological processes that interfere with its healing. To prevent such consequences, solutions of antibiotics or antiseptics are used. They have bactericidal or bacteriostatic properties and provide the desired therapeutic effect. However, the rapid development of resistance of microorganisms reduces the effectiveness of antibiotics. Alternatives are agents based on inorganic compounds: ions, metal oxides and their nanoparticles, chelates, etc. They provide non-selective action and, in contrast to the effect of antibiotics on gram-positive and gram-negative microorganisms, have multiple mechanisms of action [38].

One of the promising areas of treatment of wounds and chronic ulcers is photodynamic therapy. Visible light has significant antibacterial properties, although the efficiency is inferior to ultraviolet. Unlike high-energy UV irradiation, visible light is less harmful [46]. When irradiated, it has less risk to body tissues. Bacterial photosensitizers (PS) are important additional enhancers of bactericidal efficiency of visible light. It was found that the interaction of PS with red light (405–470 nm) destroys microorganisms or creates preconditions that disrupt the metabolism of microorganisms [47, 48].

Synthetic photosensitizers are used to increase the bactericidal activity of light irradiation of certain wavelengths. By absorbing light, they are able to generate active radicals or interact with cellular targets, inactivating them. Such substances include dyes that have absorption maxima in the red and green regions of the visible range of electromagnetic oscillations. Among such compounds, the most well-known is methylene blue.

The method of photodynamic therapy (PDT) is based on the interaction of visible light and photosensitizer (PS), which during photoactivation generates short-lived cytotoxic species of radicals. Depending on the formed active particles, PDT is

classified into two types. Type I is the interaction between the excited triplet state of the photosensitizer (3PS*) and the target tissue substrates. As a result of the reaction between the photosensitizer and the substrates, new radicals are formed. They interact with molecular oxygen and other molecules in the environment. According to type II, the interaction of 3PS* and molecular oxygen leads to the formation of singlet highly reactive oxygen [$^1O_2$]. These formed free radicals and singlet oxygen interact with various cellular targets, including membranes, nucleic acids, and enzymatic complexes, disrupting their functioning [49]. Thus, the main components of PDT are as follows: (1) photosensitizer, (2) light source, and (3) molecular oxygen.

Hydrogels based on branched copolymers of D-PAA, loaded with light-sensitive photosensitizer MB (Fig. 21.9), were studied as materials for photodynamic therapy for inactivation of microorganisms under the red light [50].

The LIKA-Led device (Photonics Plus, Cherkasy, Ukraine) with laser emitters of 660 nm was used to generate light. Irradiation with a power of 100 mW for 20, 30, and 40 min leads to an irradiation dose of 21, 31.5 and 42.1 J/cm^3, respectively.

First of all, the antimicrobial activity of D500-PAA/MB ($5 \times 10^{-4}\%$) in suspension of *S. aureus* (10^5 CFU/ml) was studied. Hydrogel samples were placed in a bacteria suspension at mass ratio of hydrogel: suspension = 1:4. After 120 min, the equilibrium concentration of MB in solution was $10^{-4} \pm 2 \times 10^{-5}\%$. The bactericidal effect caused by light irradiation (660 nm, 100 mW) was evaluated as the percentage of deaths from CFU relative to the control sample.

The study of the antibacterial efficacy of red light (660 nm) against *S. aureus* in bacterial suspension indicates the absence of its bactericidal action (Fig. 21.18). It can be explained by the low energy of light quanta and the absence of photosensitizer targets in bacterial cells. Unlike ultraviolet or blue light (380 nm and 490 nm), red light (660 nm) is less aggressive to living tissues and therefore desirable for wound healing. In this case, infrared radiation penetrates deeper into body tissues and causes heating of the entire skin and subcutaneous tissue. The therapeutic effect of infrared radiation is determined by the mechanism of its physiological action, which is to accelerate the reversal of inflammatory processes and increase tissue regeneration, local resistance, and anti-infective protection.

Fig. 21.18 Antibacterial effect of red light (660 nm) (1); MB ($10^{-4}\%$) (2); pure D500-PAA (3); D500-PAA, saturated MB ($5 \times 10^{-4}\%$) and activated by red light (660 nm) (4); MB ($10^{-4}\%$) activated by red light (660 nm) (5) in a suspension of wild strains of *S. aureus*. M $\pm$ SD
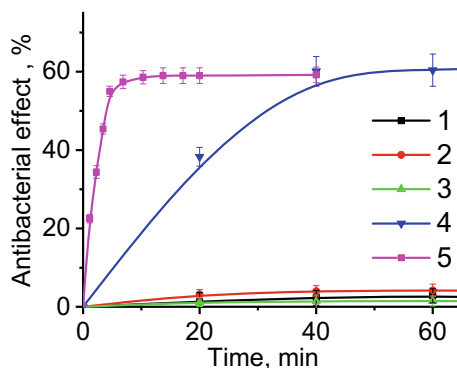
As shown in Fig. 21.18, methylene blue at a concentration of $10^{-4}\%$ has no antibacterial properties in the suspension of *S. aureus*. The combination of red light and MB at $10^{-4}\%$ resulted in a 20% reduction in CFU at a low irradiation dose of about 2 J/cm^3. Increasing the radiation dose to 6 J/cm^3 leads to inactivation of 60% CFU. A further increase in the radiation dose does not lead to an increase in bactericidal activity, which may be associated with the adaptation of the culture of *S. aureus* to the created conditions or lack of oxygen and/or dye in solution.

The study of the diffusion of MB from the hydrogel into the solution showed the gradual release of the dye in a short time. This allows for a long time to provide the required concentration of active substance in a suspension of pathogenic bacteria. Taking into account the obtained results, the antibacterial effect of hydrogel materials saturated with MB in combination with visible light was investigated. D500-PAA of the lowest cross-linking density (at 0.2% MBA), and the highest release ability was selected as the MB container. It was shown that certain components, such as pure hydrogel, light irradiation at 6 J/cm^3, and MB sensitizer, do not have antibacterial activity in the bacterial suspension (Fig. 21.19). The complex action of the hydrogel composite D500-PAA/MB and light irradiation resulted in the loss of 60% of the initial amount of CFU when incubating the hydrogel in suspension for 40 min.

In addition, it should be noted that the time to achieve the maximum bactericidal effect of MB in suspension is shorter than MB contained in the hydrogel and gradually released from it. This indicates that the hydrogels saturated with MB provide a prolonged bactericidal effect.

The disk-diffusion method was used to study the antibacterial activity of hydrogels *on a solid medium*. The antimicrobial activity of MB-saturated hydrogels was evaluated by analyzing the diameter of bacterial growth retardation [51].

D500-PAA was used as a hydrogel matrix at MB concentration of 10^{-3} and $10^{-4}\%$. As can be seen from Fig. 21.19, at MB concentration of $10^{-4}\%$, irradiation of the hydrogel with different energy doses does not lead to appreciable bactericidal activity.

Fig. 21.19 Bactericidal effect of D500-PAA/MB, activated by red light (660 nm) on Mueller–Hinton agar against *S. aureus*. H is the diameter of the hydrogel sample, M ± SD, * p < 0,05
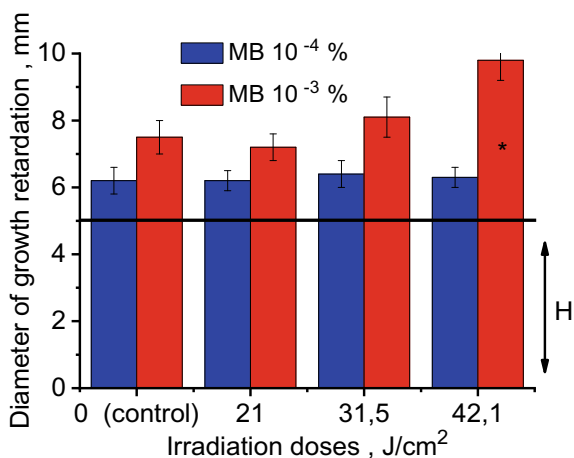
When the concentration of MB in the hydrogel increases to 10^{-3}%, the dependence of the bactericidal activity of the composites on the irradiation doses was observed and the bactericidal effect reaches about 10 mm in the diameter shown as the bacterial growth retardation around the sample.

Thus, hydrogels based on branched copolymers dextran-graft-polyacrylamide as nanocontainers for biologically active substances, in particular photosensitizers, have shown high efficacy for photodynamic antibacterial therapy and can be used in the treatment of wounds. The application of these materials saturated with photosensitizers significantly increases their effectiveness due to long-term maintenance of the required therapeutic concentrations of the substance at the site of injury. Hydrogels with high water content, low toxicity, and high biocompatibility are used to prevent or treat bacterial contamination of wounds. Their structure allows them to keep the required amount of drug substance and release it into the environment at a certain rate.

21.4.6   Hydrogel Materials for Drug Delivery

Among many antibacterial agents, antibiotics are one of the most effective and widely used drugs. However, their widespread and often thoughtless use has provoked the emergence and spread of resistant strains of bacteria. This has led to the problem of antibiotic resistance, which has become a global challenge today.

There are two main ways to overcome antibiotic resistance: the synthesis of new antibiotics and the development of new methods of antibiotic use. Hydrogels of various chemical nature can be used as promising carriers of antibiotics in biotechnology and medicine. Over the last few decades, various antibiotic-loaded hydrogels were developed as antibacterial coatings and dressings for the treatment of superficial traumatic, burn, or diabetic wounds [50, 52]. These materials release antibiotics at the wound site, thus preventing infection and promoting healing [53]. Local wound treatment with antibiotics significantly reduces the unwanted side effects that are often observed with systemic use.

This method of treating wound surfaces requires the creation of hydrogels that contain high concentrations of antibiotics. This is especially important for the care of infected wounds and burns. Antibiotic-loaded hydrogels are tested for both antibiotic-sensitive and antibiotic-resistant bacteria [54].

Because successful anti-inflammatory treatment of wounds is directly dependent on the continuous action of antimicrobials, hydrogels loaded with antibiotics must release the active substance for a long time (prolonged). Controlled and sustained release of the antibiotic in the affected area is an important requirement to prevent the formation of biofilms [53]. In addition, the continuous delivery of the drug to the application site provides a significant increase in the time intervals required to change the dressing on the wound. As noted, the nature of the polymer and the degree of cross-linking are the main factors that regulate the ability of hydrogels to deliver drugs and release them at the target site.

Table 21.2 Content of Cefuroxime in the synthesized hydrogels (g of antibiotic per g of dried hydrogel) and its release into the water

Sample	Content, g/g	Time of contact with water, h		
		0.5	1	6
PAA-0.4-Cef	1.64	28	42	55
D20-PAA-0.4-Cef	3.52	24	30	42
D100-PAA-0.4-Cef	3.40	22	27	38
D500-PAA-0.4-Cef	3.34	19	34	40
DSS500-PAA-0.4-Cef	3.31	27	37	51

Chemically cross-linked hydrogels based on branched copolymers D-PAA were used to create antimicrobial coatings for the treatment of infected wounds. These hydrogels were loaded with the required concentration of antibiotics, and their local drug release was intended to overcome the side effects of systemic overdose. Antibiotic samples were tested in vitro for pathogenic bacteria and in vivo as antimicrobial dressings.

To prepare antibiotic hydrogel samples, dried hydrogel samples were placed in an aqueous solution of Cefuroxime (Cef) (166.6 mg/ml) and incubated at 25 °C for 18 h. The amount of loaded antibiotic in the hydrogel sample was evaluated by subtracting the amount of Cefuroxime remaining in solution from the initial content. All concentrations were determined by high-performance liquid chromatography with ultraviolet detection (HPLC–UV). Swollen hydrogels in this solution were used for further studies of their ability to release the antibiotic. Determination of the concentration of antibiotic released into the solution was performed by HPLC–UV at regular intervals.

As given in Table 21.2, the content of Cefuroxime is the highest for hydrogels that were synthesized using dextran as a structuring component.

Contact of the antibiotic-loaded hydrogels with water leads to desorption of drug molecules into solution. For all samples, the initial release is characterized by a low rate within 3 h. As given in Table 21.2, the sample PAA-0.4-Cef has the highest release rate. The content of Cefuroxime in this hydrogel decreased by 55% after 6 h of contact with water. In contrast, D-PAA-0.4-Cef, being initially more loaded with Cefuroxime, releases the drug into solution more slowly than PAA-0.4-Cef.

Thus, D/DSS-PAA-0.4-Cef hydrogels have some advantages over other studied hydrogels. They are able to provide a prolonged antibacterial effect on the wound surface. It is assumed that they are promising biomaterials for local application as antimicrobial dressings.

Antibacterial activity in vitro was studied by the above-described disk-diffusion method. All synthesized hydrogels loaded with Cefuroxime showed high activity against bacterial strains of *S. aureus*, *E. coli,* and *Klebsiella spp.* (Table 21.3).

The antimicrobial activity of hydrogels depends on the concentration, but even at low doses, antibiotic-loaded hydrogels show high efficacy against harmful microorganisms (Fig. 21.20).

Table 21.3 Antimicrobial activity of Cefuroxime-loaded hydrogels

Sample	Diameter of bacterial growth retardation, mm		
	S. aureus	E. coli	Klebsiella spp.
PAA-0.4-Cef	27	23	20
D20-PAA-0.4-Cef	26	21	20
D100-PAA-0.4-Cef	30	22	20
D500-PAA-0.4-Cef	25	22	23
DSS500-PAA-0.4-Cef	29	21	22

Fig. 21.20 Antimicrobial activity of hydrogels (1) PAA-0,4-Cef; (2) D20-PAA-0.4-Cef; (3) D100-PAA-0.4-Cef; (4) D500-PAA-0.4-Cef, and (5) DSS500-PAA-0.4-Cef against *S. aureus*
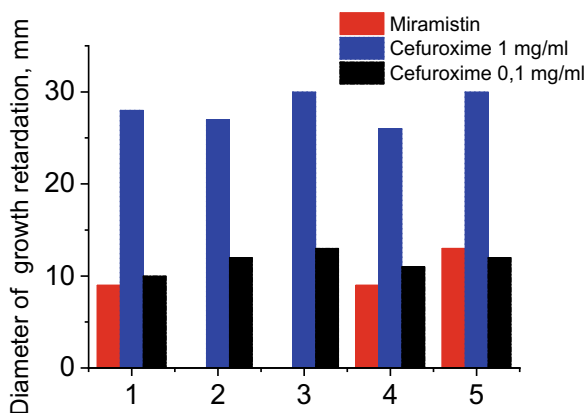
White outbred rats were used to evaluate the therapeutic properties of hydrogel coatings in vivo. The rat wounds were infected with *S. aureus*, *E. coli,* and *Klebsiella spp* (10^8 CFU/ml). The wound was then covered with hydrogels loaded with Cefuroxime (1 mg/ml) or miramistin (0.1 mg/ml) and standard tissue material (gauze bandage) for 24 h. Miramistin was used as an antibacterial agent for control experiments. After the bandage was removed, the wounds were tested for microorganisms. No gram-negative bacteria and very few gram-positive colonies were detected when Cefuroxime-coated hydrogel wounds were applied (Fig. 21.21c). Their efficacy was higher then miramistin-loaded hydrogels (Fig. 21.21b). In the case of classical gauze dressings, a significant number of colonies of bacteria of the studied strains were found (Fig. 21.21a).

Thus, hydrogels based on branched copolymers containing dextran as a structure-forming component can be used as containers for drugs, in particular antibiotics. When locally applied, they have demonstrated their effectiveness against a mixture of pathogenic bacteria, significantly inhibiting the growth of microorganisms on the infected wound surface. In vivo experiments confirm that antimicrobial hydrogels are promising biomaterials that provide rapid healing of superficial wounds.
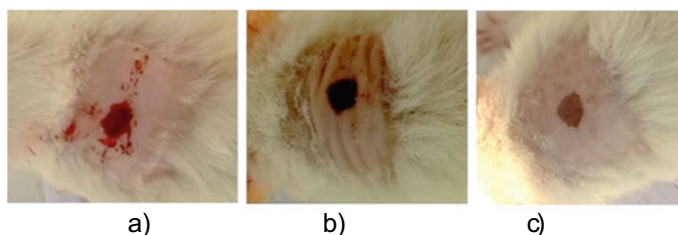
Fig. 21.21 Rats wounds after removal of bandages after 24 h: **a** classic gauze bandage; **b** hydrogel D500-PAA-0.4, saturated with miramistin; and **c** hydrogel D500-PAA-0.4, saturated with Cefuroxime

21.5 Conclusion

Methods of synthesis and prospects of using hydrogels as biomedical materials are shown. Data on the synthesis and characterization of chemically cross-linked hydrogels based on branched copolymers of acrylamide with dextran as a structure-forming component are presented. The synthesis of ionic to nonionic hydrogels due to variation of dextan and its sulfodextran derivative and saponification of polyacrylamide units in the hydrogel are described.

The dependence of physicochemical properties of hydrogels on (a) chemical structure of polymers, (b) cross-linker concentration, and (c) internal structure of the network is shown. The efficiency of sorption properties of the obtained hydrogels for the creation of systems with drugs, silver nanoparticles, and biologically active substances has been proved.

The synthesis and characterization of nanocomposites with silver nanoparticles based on ionic and nonionic hydrogels are described, and the prospects of their use as antibacterial coatings for open wounds are shown. The advantages of the photochemical method of obtaining nanoparticles in hydrogels as nanocontainers are noted. It is proved that such nanosystems are stable and have a nanoparticle of suitable size for use in in vitro experiments.

In experiments with hydrogels saturated with biologically active dyes as photosensitizers, their antibacterial activity under irradiation with light of different wavelengths was shown. The research revealed hydrogel/dye materials effectiveness for antibacterial photodynamic therapy of open wounds of various genesis. Hydrogels based on branched copolymers containing dextran-polyacrylamide can be used as containers for drugs.

References

1. Hoffman AS (2002) Hydrogels for biomedical applications. Adv Drug Deliv Rev 43:3–12
2. Peppas NA, Bures P, Leobandung W, Ichikawa H (2000) Hydrogels in pharmaceutical formulations. Eur J Pharm Biopharm 50:27–46

3. Peppas NA, Huang Y, Torres-Lugo M, Ward JH, Zhang J (2000) Physicochemical foundations and structural design of hydrogels in medicine and biology. Annu Rev Biomed Eng 2:9–29

4. Ahmed EM (2015) Hydrogel: Preparation, characterization, and applications. J Adv Res 6:105–121

5. Hadjichristidis N, Pitsikalis M, Pispas S, Iatrou H (2001) Polymers with complex architecture by living anionic polymerization. Chem Rev 101(12):3747–3792

6. Gao H, Matyjaszewski K (2009) Synthesis of functional polymers with controlled architecture by CRP of monomers in the presence of cross-linkers: from stars to gels. Prog Polym Sci 34(4):317–350

7. Blencowe A, Tan JF, Goh TK, Qiao GG (2009) Core cross-linked star polymers via controlled radical polymerisation. Polymer 50(1):5–32

8. Kumar D, Khan N, Kumar P (2016) Improve the native characteristics of polysaccharides by grafting through the gamma radiation: a review. Green Chem and Tech Lett 2(3):151–159

9. Kumar D, Pandey J, Kumar P (2018) Microwave assisted synthesis of binary grafted psyllium and its utility in anticancer formulation. Carbohydr Polym 179:408–414

10. Xie W, Xu P, Wang W, Liu Q (2002) Preparation and antibacterial activity of a watersoluble chitosan derivative. Carbohydr Polym 50(1):35–40

11. Kaith B, Kumar K (2007) In air synthesis of Psy-cl-poly (AAm) network and its application in water-absorption from oil-water emulsions. Express Polym Lett 1(1):474–480

12. Kumar D, Kumar S (2014) Grafting of acrylic acid on to Plantago psyllium mucilage IOSR. J Appl Chem (IOSR-JAC) 7:76–82

13. Kumar D, Chandra R, Dubey R (2016) Synthesis and characterisation of cross-linked polymers of acrylic acid and psyllium mucilage (Psy-cl-AA). J Technol Adv Scient Res 2:185–189

14. Kumar D, Pandey J, Khan N, Kumar P, Kundu PP (2019) Synthesize and characterization of binary grafted psyllium for removing toxic mercury (II) ions from aqueous solution. Mater Sci Eng 104:109900

15. Kutsevol NV, Chumachenko VA, Rawiso M, Shkodich VF, Stoyanov OV (2015) Star-like dextran-polyacrylamide polymers: prospects of use in nanotechnologies J. Struct Chem 56(5):959–966

16. Kutsevol N, Guenet JM, Melnyk N, Sarazin D, Rochas C (2006) Solution properties of dextran-polyacrylamide graft copolymers. Polymer 47:2061–2068

17. Plieva F, Oknianska A, Degerman E, Galaev IY, Mattiasson B (2006) Novel supermacroporous dextran gels. J Biomat Sci 17(10):1075–1092

18. Nadtoka O, Kutsevol N, Krysa V, Krysa B (2018) Hybrid polyacryamide hydrogels: synthesis, properties and prospects of application. Mol Cryst Liq Cryst 672(1, 2):1–10

19. Nadtoka O, Virych P, Kutsevol N (2020) Hydrogels loaded with methylene blue: sorption-desorption and antimicrobial photoactivation study. Int J Polym Sci 2020:9875290

20. Ye Zh, Qin X, Lai N (2013) Synthesis and performance of an acrylamide copolymer containing nano-SiO_2 as enhanced oil recovery chemical. J Chem ID 437309. https://doi.org/10.1155/2013/437309

21. Nho YC, Park JS, Lim YM (2014) Preparation of poly(acrylic acid) hydrogel by radiation crosslinking and its application for mucoadhesives. Polymers 6:890–898

22. Nadtoka O, Virych P, Kutsevol N (2020) Investigation of swelling behavior of PAA and D-PAA hydrogels. Springer Proc Phys 247:47–60

23. Kutsevol NV, Chumachenko VA, Rawiso M, Shkodich VF, Stoyanov OV (2015) Star-like polymers dextran-polyacrylamide: the prospects *of* application for nanotechnology. J Struct Chem 56(5):1016–1023

24. Zhao Y, Su H, Fang L, Tan T (2005) Superabsorbent hydrogels from poly(asparticacid) with salt, temperature and pH-responsiveness properties. Polymer 46:5368–5376

25. Lagergren S (1898) About the theory of socalled adsorption of soluble substances. Kungl Svenska Vetenskapsakad Handl 24:1–39

26. Demirbas A (2004) Adsorption of lead and cadmium ions aqueous solutions onto modified lignin from alkali glycerol delignication. J Hazard Mater B 109:221–226

27. Nadtoka O, Kutsevol N, Naumenko AP, Virych PA (2019) Photochemical synthesis and characterization of hydrogel–silver nanoparticle composites. Res Chem Intermed. https://doi.org/10.1007/s11164-019-03891-4

28. Cooper R (2004) A review of the evidence for the use of topical antimicrobial agents in wound care World wide wounds 2004:1–11

29. Michielsen S, Churchward G, Bozia J, Stojilokivic I, Anic S (2006) Light activated antiviral materials and devices and methods for decontaminating virus infected environments. US 20070238660A1.

30. Nadtoka O, Virych P, Kutsevol N (2021) Synthesis and absorption properties of hybrid polyacrylamide hydrogels. Mol Cryst Liq Cryst 719(1):84–93

31. Kemnitz CR, Loewen MJ (2007) "Amide resonance" correlates with a breadth of c−n rotation barriers. J Am Chem Soc 129(9):2521–2528

32. Thoniyot P, Tan MJ, Karim AA, Young DJ, Loh XJ (2015) Nanoparticle-hydrogel composites: concept, design and applications of these promising, multi-functional materials. Adv Sci 2(1–2):1400010

33. Varaprasad K, Murali Mohan Y, Ravindra S, Narayana Reddy N, Vimala K, Monika K, Sreedhar B, Mohana Raju K (2010) Hydrogel-silver nanoparticle composites: a new generation of antimicrobials. J App Polymer Sci 115:1199–1207

34. Pradhan N, Jana NR, Mallick K, Pal T (2000) Seed mediated growth: a convenient way for size control in nanoparticle synthesis. J Surface Sci Technol 16:188–199

35. Winter GD (1962) Formation of the scab and the rate of epithelization of superficial wounds in the skin of the young domestic pig. Nature 193:293–294

36. Peppas NA, Bures P, Leobandung W, Ichikawa H (2000) Hydrogels in pharmaceutical formulations. Eur J Pharm Biopharm 50(1):27–46

37. Boehle KE (2017) Utilizing paper-based devices for antimicrobial resistant bacteria detection. Angew Chem 56(24):6886–6890

38. Li S, Dong S, Xu W, Tu S, Yan L, Zhao C, Chen X (2018) Antibacterial hydrogels. Adv Sci 5(5):1700527

39. Liao C, Li Y, Tjong SC (2019) Bactericidal and cytotoxic properties of silver nanoparticles. Int J Mol Sci 20(2):449

40. Nadtoka O, Virych P, Bezugla T, Yeshchenko O, Kutsevol N (2021) Antibacterial hybrid hydrogels loaded with nano silver. Appl. Nanosci. https://doi.org/10.1007/s13204-021-01706-w

41. Xiu ZM, Ma J, Balvarez PJJ (2011) Differential effect of common ligands and molecular oxygen on antimicrobial activity of silver nanoparticles versus silver ions. Environ Sci Technol 45:9003–9008

42. Knetsch MLW, Koole LH (2011) New strategies in the development of antimicrobial coatings: the example of increasing usage of silver and silver nanoparticles. Polymers 3(1):340–366

43. Suresh AK, Pelletier DA, Wang W, Morrell-Falvey JL, Gu B, Doktycz MJ (2012) Cytotoxicity induced by engineered silver nanocrystallites is dependent on surface coatings and cell types. Langmuir 28:2727–2735

44. Virych P, Nadtoka O, Virych P, Martynyuk V, Krysa V, Krysa B, Kutsevol N (2021) Photoinactivation in vitro of Staphylococcus aureus by visible light of different wavelengths. Interdisciplinary Stud Complex Syst 18:40–50

45. Nadtoka O, Kutsevol N, Linnik O, Nikiforov M (2019) Nanocomposite hydrogels containing silver nanoparticles as materials for wound dressings. Springer Proc Phys 222:375–387

46. Ramakrishnan P, Maclean M, MacGregor S, Anderson J, Grant M (2016) Cytotoxic responses to 405 nm light exposure in mammalian and bacterial cells: Involvement of reactive oxygen species Toxicol In Vitro 33:54–62

47. Ashkenazi H, Malik Z, Harth Y, Nitzan Y (2003) Eradication of Propionibacterium acnes by its endogenic porphyrins after illumination with high intensity blue light. FEMS Immunol Med Microbiol 35(1):17–24

48. Guffey J, Wilborn J (2006) In vitro bactericidal effects of 405-nm and 470-nm blue light. Photomed Laser Surg 24(6):684–688

49. Mahmoudi H, Bahador A, Pourhajibagher M, Alikhani M (2018) Antimicrobial photodynamic therapy: an effective alternative approach to control bacterial infections. J Lasers Med Sci 9(3):154–160
50. Li S, Dong S, Xu W (2018) Antibacter Hydrogels Adv Sci 5(5):1700527
51. Lehtopolku M, Kotilainen P, Puukka P (2012) Inaccuracy of the disk diffusion method compared with the agar dilution method for susceptibility testing of *Campylobacter spp.* J Clin Microbiol 50(1):52–56
52. Veiga S, Schneider JP (2013) Antimicrobial hydrogels for the treatment of infection. Biopolymers 100(6):637–644
53. Yang K, Han Q, Chen B (2018) Antimicrobial hydrogels: promising materials for medical application. Int J Nanomed 13:2217–2263
54. Tamahkar E, Özkahraman B, Süloğlu AK, İdil N, Perçin I (2020) A novel multilayer hydrogel wound dressing for antibiotic release. J Drug Deliv Sci Technol 58:101536

Part II
Nanooptics and Photonics

Chapter 22
Properties of Renormalized Spectra of Localized Quasiparticles Interacting with One- and Two-Mode Phonons in Davydov's Model at T = 0K

M. V. Tkach, V. V. Hutiv, Ju. O. Seti, and O. M. Voitsekhivska

22.1 Introduction

In early papers [1–4], the theory of quasiparticles (electrons, holes, excitons, impurity centers, etc.) interacting with phonons in 3D structures (metals, semiconductors, etc.) has been developed within different methods and approaches, the choice of which was determined by magnitudes of coupling constants (weak, intermediate, or strong). To study the effect of the electromagnetic field on these structures, the theory of complex dielectric constant and the field absorption coefficient in the respective energy range for the quasiparticles have been developed too. The main results obtained in the initial period are described in detail in the books [5–8], where the general theory of Kubo about the response of quantum mechanical systems to the external perturbation is presented and the problems of interaction between quasiparticles and quantized fields are solved using the new methods of quantum field theory [6–10].

In the majority of papers, the research was conditioned by a rather narrow range of energies, in the vicinity of the renormalized ground state of quasiparticles interacting with phonons. This interval does not significantly exceed the radiation threshold of one phonon, which allows using only a one-phonon approximation in a mass operator of Green's function. However, to explain some experimental results, in particular, the so-called dielectric modes of the crystals, it is necessary to observe the high-energy bound-to-phonon states of the quasiparticle. In its turn, it demands the accounting of multiphonon processes in the theory at its initial stages of development. The main theoretical results obtained during this period, well correlating with the experimental data, were discussed in the review [8], where the crucial role of multiphonon

M. V. Tkach (✉) · V. V. Hutiv · Ju. O. Seti · O. M. Voitsekhivska
Department of Theoretical Physics and Computer Simulation, Yuriy Fedkovych Chernivtsi National University, 2, Kotsyubinsky Street, Chernivtsi 58012, Ukraine
e-mail: m.tkach@chnu.edu.ua

processes in the formation of the renormalized spectrum in a wide range of energies, containing the main and satellite states were revealed.

The relatively laminar flow of development of the theory of systems of quasiparticles interacting with phonons lasted until there was an urgent need to explain the phenomenon of high-temperature superconductivity, as well as that in the physics of low-dimensional structures. In particular, the intensive development of experimental physics of nanoheterostructures has led to the appearance of unique nanodevices (quantum cascade lasers, detectors, etc.), successfully functioning [11–14] for a long time. However, lack of sufficient understanding of certain phenomena and physical processes in such structures, which are mainly caused by the interaction of actual quasiparticles with phonons, does not yet make it possible to guide purposefully the parameters of these devices in order to optimize their functioning.

In numerous theoretical studies of nanostructures of different dimensions, in particular described in [15–18], it was established that their integral feature is multiband (or multilevel) energy spectra of quasiparticles and multimode phonon spectrum, due to the spatial confinement of the completing parts. These circumstances have sharply complicated the development of a consistent theory of the interaction of quasiparticles with phonons in low-dimensional structures. Although it should be noted that over the past two decades, the new methods of quantum Monte Carlo diagram technique [19–22] and other mathematical approaches [23–26] have been used to solve the problems of spectra of quasiparticles renormalized by multiphonon processes in different models of the systems.

The application of new approaches in the method of Green's functions has recently made it possible to investigate the renormalized spectra of multilevel systems of quasiparticles interacting with phonons and one-level quasiparticles interacting with several phonon modes at $T = 0K$ in Davydov's model without the decay [27–29]. The mentioned papers allow us to hope for the possibility of constructing a consistent general theory of the quasiparticles interacting with phonons. However, this task is still too difficult even for reasons of mathematical cumbersomeness, taking into account non-phonon scattering mechanisms. Thus, the question arises: Does the introduction of phenomenological decay retain the basic properties of the renormalized due to phonons spectrum of quasiparticles in the approach of Green's function method? A positive answer is given in the present research.

22.2 Electromagnetic Field Absorption Coefficient and Fourier Image of Retarded Green's Function

We are going to study the effect of dissipative mechanisms (taken into account by phenomenological decay) on the properties of electromagnetic field absorption coefficient produced by a system of localized quasiparticles interacting with one- and two-mode polarization phonons at $T = 0K$ in Davydov's model. According to Kubo's theory for the response of an isotropic system to external action, the

absorption coefficient of electromagnetic field ($\chi(\tilde{\omega})$) is associated with the Fourier image of the retarded Green's function of quasiparticle ($G(\tilde{\omega})$) within the expression [6]

$$\chi(\omega) = \frac{4\pi\hbar\omega_f^2 d^2}{V\omega v_g} I(\omega); \quad I(\omega) = -\mathrm{Im}G(\tilde{\omega}); \quad (\tilde{\omega} = \omega + i\eta), \quad \eta \to +0.$$

(22.1)

Here $I(\omega)$ is a form-function of the absorption band of electromagnetic field, $d = er$ is a dipole moment, V is a unit cell volume, ω_f is a frequency of dipole transition, ω is electromagnetic field frequency, v_g is a group velocity.

Assuming the smooth frequency dependence of the coefficient near $I(\omega)$ in the actual frequency range, we will further study the form-function of the band absorbed by a system consisting of a localized quasiparticle (exciton, impurity, etc.) which interacts with non-dispersive two-mode polarization phonons at $T = 0$K. Like in [5, 6], in Davydov's model, the Hamiltonian of such system (without dissipative processes) in the representation of second quantization over all variables is written as

$$\hat{H} = \sum_{\vec{k}} E_0 \hat{A}_{\vec{k}}^+ \hat{A}_{\vec{k}} + \sum_{\lambda=1}^{2} \sum_{\vec{q}} \Omega_\lambda \left(\hat{B}_{\lambda\vec{q}}^+ \hat{B}_{\lambda\vec{q}} + \frac{1}{2} \right) + \sum_{\vec{k}\lambda\vec{q}} \varphi_\lambda(\vec{q}) \hat{A}_{\vec{k}}^+ \hat{A}_{\vec{k}} \left(\hat{B}_{\lambda\vec{q}} + \hat{B}_{\lambda-\vec{q}}^+ \right).$$

(22.2)

Here E_0 is an energy of uncoupling quasiparticle, Ω_λ is an energy of λ-th phonon mode, $\phi_\lambda(\vec{q})$ is a quasiparticle binding function with λ-th phonon mode. Quasiparticle $\left(\hat{A}_{\vec{k}}^+, \hat{A}_{\vec{k}} \right)$ and phonon $\left(\hat{B}_{\lambda\vec{q}}^+, \hat{B}_{\lambda\vec{q}} \right)$ operators of second quantization satisfy Bose commutative relationships.

It is well known [5, 6] that Hamiltonian (22.2) is diagonalized exactly by the unitary transformation. It allows obtaining an accurate analytical expression for the retarded Green's function of the quasiparticle

$$G(t) = -i\theta(t) \exp\left\{ -\frac{i\mathbf{E}t}{\hbar} + \sum_{\lambda=1}^{2} \alpha_\lambda \left\{ \exp\left(-\frac{i\Omega_\lambda t}{\hbar} \right) - 1 \right\} \right\}.$$

(22.3)

where

$$\mathbf{E} = E_0 - \sum_{\lambda=1}^{2} \alpha_\lambda \Omega_\lambda; \quad (\alpha_\lambda = \Omega_\lambda^{-2} \sum_{\vec{q}} |\varphi_\lambda(\vec{q})|^2)$$

(22.4)

is the energy of new elementary excitations, expressed through the dimensionless parameter (α_λ), which characterizes the binding energy of the quasiparticle with λ-th phonon mode.

Transition to the Fourier image $G(\omega + i\eta)$ is carried out by integration of function (22.3) using Newton's binomial. As a result, introducing phenomenological decay by replacing small quantity ($\eta \to +0$) by a finite value ($\Gamma > 0$), we get the representation of $G(\omega, \Gamma)$ function in the form

$$G(\omega, \Gamma) = \exp\left[-\sum_{\lambda=1}^{2} \alpha_\lambda\right]\left\{\frac{1}{\hbar\omega - \mathbf{E} + i\Gamma} + \sum_{\lambda=1}^{2}\sum_{n=1}^{\infty} \frac{\alpha_\lambda^{n_\lambda}}{n_\lambda![\hbar\omega - \mathbf{E} - n_\lambda\Omega_\lambda + i\Gamma]}\right.$$
$$\left. + \sum_{n_1,n_2=1}^{\infty} \frac{\alpha_1^{n_1}\alpha_2^{n_2}}{n_1!n_2![\hbar\omega - \mathbf{E} - n_1\Omega_1 - n_2\Omega_2 + i\Gamma]}\right\}. \tag{22.5}$$

Such convenient expression for $G(\omega, \Gamma)$ makes it possible to calculate and analyze the dependences of spectral parameters of the form-function of the absorption band on the frequency of electromagnetic field and energy values, which characterize the system. Introducing dimensionless quantities

$$I(\xi) = \Omega_1 I(\omega); \quad \gamma = \frac{\Gamma}{\Omega_1}; \quad \alpha = \sum_{\lambda=1}^{2} \alpha_\lambda; \quad P_\lambda = \frac{\Omega_\lambda}{\Omega_1}; \quad (\lambda = 1, 2), \tag{22.6}$$

the form-function of the band absorbed by two-mode system gets the following analytical form

$$I(\alpha_1; \alpha_2; \xi) = \gamma e^{-\alpha}\left\{\frac{1}{\xi^2 + \gamma^2} + \sum_{\lambda=1}^{2}\sum_{n=1}^{\infty} \frac{\alpha_\lambda}{n_\lambda![(\xi - n_\lambda P_\lambda)^2 + \gamma^2]}\right.$$
$$\left. + \sum_{n_1,n_2=1}^{\infty} \frac{\alpha_1\alpha_2}{n_1!n_2![(\xi - n_1 - n_2 P_2)^2 + \gamma^2]}\right\}. \tag{22.7}$$

Putting $\alpha_1 = \alpha$, $\alpha_2 = 0$, $P_2 = 0$ in formula (22.7), the expression for the dimensionless form-function of the band absorbed by one-mode system is obtained as

$$I(\alpha, \xi) = \gamma e^{-\alpha}\left\{\frac{1}{\xi^2 + \gamma^2} + \sum_{n=1}^{\infty} \frac{\alpha^n}{n![(\xi - n)^2 + \gamma^2]}\right\}. \tag{22.8}$$

From analytical expressions (22.7) and (22.8), it is clear that both functions ($I(\alpha, \xi)$, $I(\alpha_1, \alpha_2, \xi)$) are the superpositions of an infinite number of quasi-Lorentz functions (peaks) with very small decay ($\gamma << 1$). Quasi-Lorentz peaks are characterized by obvious spectral parameters: heights (h) and half-widths ($\boldsymbol{\gamma}$), which depend on the number of phonon modes of the system. Let us analyze the properties of $I(\alpha, \xi)$ and $I(\alpha_1, \alpha_2, \xi)$ functions for one-and two-mode systems.

22.3 Properties of I(A,ξ) Function for the One-Mode System

The properties of $I(\alpha, \xi)$ form-function are well seen from the analytical expression (22.8), as well as from Figs. 22.1 and 22.2, which show its dependence on the dimensionless frequency (ξ) at different values of α and γ. Function $I(\alpha, \xi)$ is a superposition of an infinite number of quasi-Lorentz peaks. The heights of their maxima ($h_\ell(\alpha)$) are located at $\xi_\ell = \ell = 0, 1, 2, \ldots, \infty$ and are determined by the values

$$h_\ell(\alpha) = \gamma e^{-\alpha} \sum_{n=0}^{\infty} \frac{\alpha^n}{n!} \frac{1}{(\ell - n)^2 + \gamma^2}; \quad \ell = 0, 1, 2, \ldots, \infty. \tag{22.9}$$

As a result, the half-width of $\ell-$th peak ($\boldsymbol{\gamma_\ell}$) is fixed as a difference ($\boldsymbol{\gamma_\ell} = \xi_\ell^> - \xi_\ell^<$) of the quantities $\xi_\ell^>$, $\xi_\ell^<$, which are the solutions of nonlinear equation

$$\sum_{n=0}^{\infty} \frac{\alpha^n}{n!} \left\{ \frac{1}{(\xi_\ell^< - n)^2 + \gamma^2} - \frac{1}{2(n^2 + \gamma^2)} \right\} = 0;$$
$$\ell = 0, 1, 2, \ldots, \infty. \tag{22.10}$$
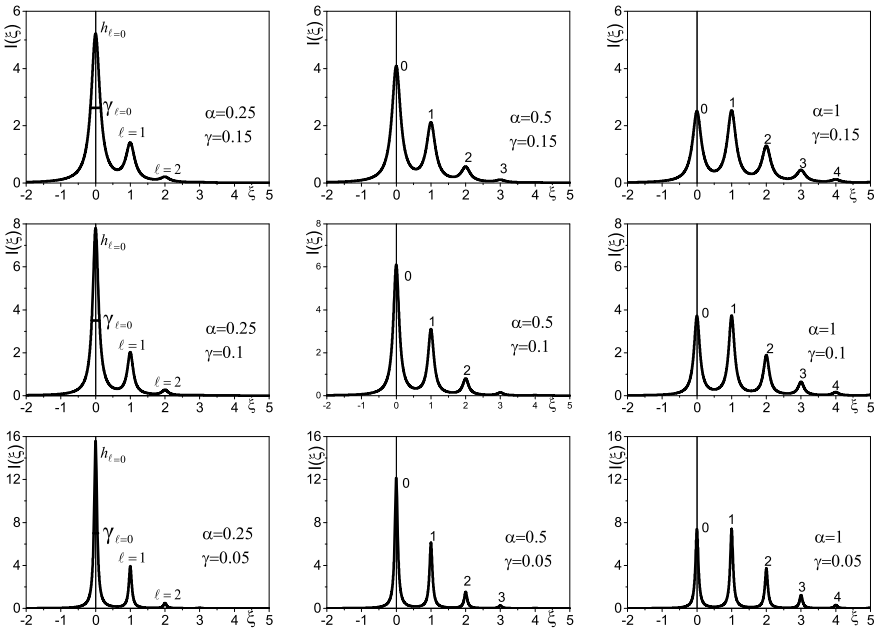
Fig. 22.1 Structure of $I(\xi)$ form-function at different decay ($\gamma = 0.05; 0.1; 0.15$) and small coupling constants ($\alpha = 0.25; 0.5; 1$)
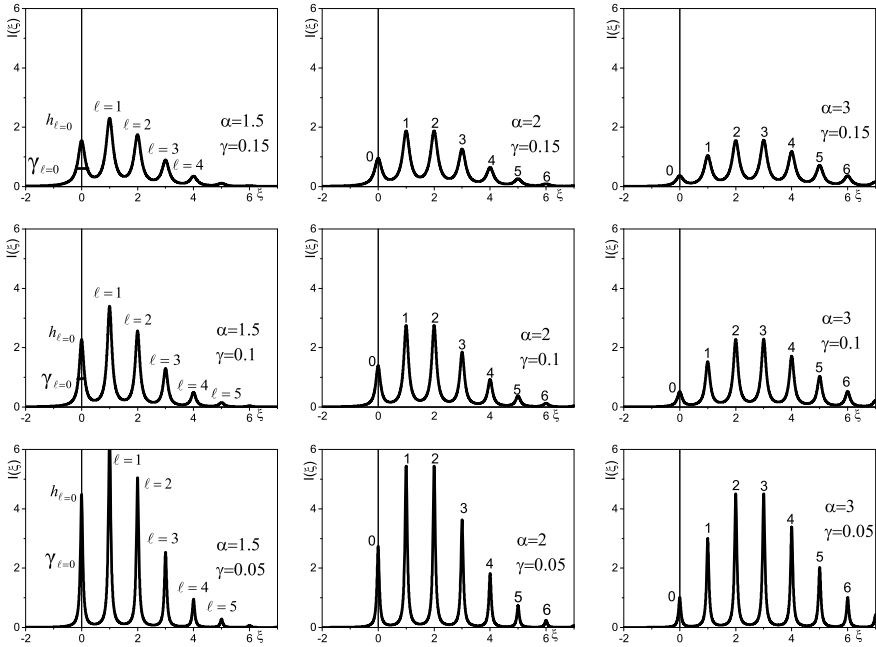
Fig. 22.2 Structure of $I(\xi)$ form-function at different decay ($\gamma = 0.05; 0.1; 0.15$) at intermediate coupling constants ($\alpha = 1.5; 2; 3$)

The lowest energy peak at $\ell = 0$ corresponds to the main non-phonon state. The phonon satellite peaks at $\ell = 1, 2, \ldots$ are produced by bound states of quasiparticles with one, two and the rest of phonons (the so-called phonon repeats). The maxima of the main and phonon satellite peaks are equidistant from each other (at a distance of one-phonon energy). The ratio of the $\ell-$ th peak maximum to the main one is fixed by the expression

$$J_\ell(\alpha, \gamma) = \frac{h_\ell(\alpha, \gamma)}{h_0(\alpha, \gamma)} = \left[\sum_{n=0}^{\infty} \frac{\alpha^n}{n![n^2 + \gamma^2]} \right]^{-1}$$

$$\sum_{n=0}^{\infty} \frac{\alpha^n}{n![(\ell - n)^2 + \gamma^2]}; \quad \ell = 0, 1, 2, \ldots, \infty. \tag{22.11}$$

Taking advantage of small γ from Eq. (22.10), in a linear order over $\alpha\gamma^2$, a simple approximated analytical expression for the half-width of an arbitrary $\ell-$ th peak is obtained

$$\boldsymbol{\gamma}_\ell(\alpha, \gamma) = 2\gamma(1 + \alpha\gamma^2). \tag{22.12}$$

Expressions (22.9, 22.12) and Figs. 22.1 and 22.2 prove that the heights $(h_\ell(\alpha))$ of peaks are more complicated functions than half-widths $(\gamma_\ell(\alpha))$. The heights are sensitive to varying magnitudes of γ, α, and ℓ, that is especially clear from the figures. In particular, the height, as a parameter of the functions that characterize the main state $(I_{\ell=0}(\alpha, \xi))$, only decrease if α increases in the interval $(0 < \alpha < 1)$, while the heights of the respective functions of phonon satellite states $I_{\ell \neq 0}(\alpha, \xi)$ only increase. Herein, according to (22.9), if ℓ increases, the heights $h_{\ell \geq 1}(\alpha, \xi)$ are rapidly decreasing. As a result, the peaks of high-energy satellite states "merge" with a continuous background.

It is worth to note that if $\alpha = 1$, not just the widths $(\gamma_{\ell=0} \cong \gamma_{\ell=1})$, but also the heights $(h_{\ell=0} \cong h_{\ell=1})$ of the peaks of the main and the first phonon satellite (repeat) are almost the same (with accuracy $\leq 1\%$). The revealed properties of functions $I(\alpha, \xi)$ in the interval $0 \leq \alpha \leq 1$ cause such a rapid "immersion" of satellite phonon states into a continuous background, that besides of the main state, only 3–4 bound-to-phonons states of quasiparticle are manifested (Figs. 22.1 and 22.2).

Figure 22.2 shows the results of calculations of $I(\xi)$ function and its parameters at average values of α constants in the interval $1.5 \leq \alpha \leq 3$ at $\gamma = 0.05$. Here one can see some new properties of these functions. If $\alpha = 1$ and the heights of the main and the first phonon repeats become equal $(I_0 = I_1 = 7.38)$, further increase of α magnitude leads only to a decrease of the first satellite peak height, as well as for the main one. Heights of other phonon satellite peaks $(h_{\ell \geq 2})$ continue to grow until coupling constant $\alpha = 2$, at which the heights of the first and second phonon peaks become equal $(h_1 = h_2 = 5.44$ at $\gamma = 0.05)$. If α increases further, the heights of 0, 1, 2 peaks decrease, and that of the rest continue to increase. At $\alpha = 3$, the heights of 2 and 3 peaks are equalized, and that of the rest—increase. This property leads to the fact that the curve, which is an envelope of the maxima of the absorption peaks has a maximum in the field of phonon repeats the further, the stronger is the interaction (α).

22.4 Properties of I(α_1,α_2,ξ) Form-Function for the Two-Mode System

The calculation and analysis of the properties of the spectral parameters of two-mode system were performed on the example of the most typical physical structure in which the quasiparticle is weakly interacting with one mode and intermediately with the other. Figures 22.3 and 22.4 show $I(\alpha_1, \alpha_2, \xi)$ form-function for the two-mode system in a frequency range (ξ), where the main and satellite phonon peaks are fairly well-identified without "merging" into the continuous background.

In contrast to the one-mode, in the two-mode system the structure of $I(\alpha_1, \alpha_2, \xi)$ form-function bands is more complicated because it is produced both by the bound states of the quasiparticle with the phonons of certain modes and with their combinations too. Therefore, $I(\alpha_1, \alpha_2, \xi)$ function is a superposition of the main peak (0,0)
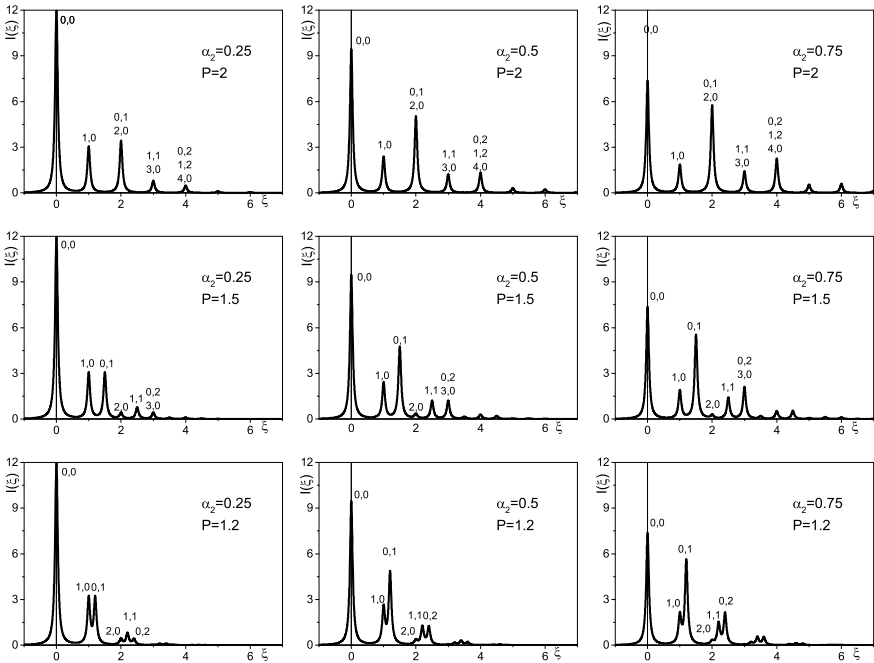
Fig. 22.3 Structure of $I(\alpha_1, \alpha_2; \xi)$ form-function at small values of coupling constants (α_1, α_2). Here $\alpha_1 = 0.25$, $\gamma = 0.05$

of quasi-Lorenz type (with height $h_{0,0}(\alpha_1, \alpha_2)$ and half-width $\gamma_{0,0}(\alpha_1, \alpha_2)$) and three groups of infinite number of phonon satellite peaks produced by bound states of quasiparticle with unmixed phonon modes $(\ell_1 \neq 0, \quad \ell_2 = 0)$; $(\ell_1 = 0, \quad \ell_2 \neq 0)$ and mixed phonon modes $(\ell_1 \neq 0, \quad \ell_2 \neq 0)$.

Figures 22.3 and 22.4 show that the picture of $I(\alpha_1, \alpha_2, \xi)$ formation significantly depends on both the relationships between the values of energies (P_2) of both phonon modes and the values of both coupling constants (α_1, α_2). The height $(h_{0,0})$ and width $(\gamma_{0,0})$ of the main peak are almost independent of P_2 magnitude. If α_2 increases, only its height, which is mainly formed by the stronger interaction of the quasiparticle with the second phonon mode, gradually decreases.

The peaks corresponding to the phonon satellites of certain unmixed $(\ell_1 \neq 0, \quad \ell_2 = 0; \quad \ell_1 = 0, \quad \ell_2 \neq 0)$ modes create a picture of structures that have the same properties as previously described for the respective one-mode structures. Herein, the heights of the peaks formed by a stronger interaction with the second mode significantly dominate over those, formed by a weaker interaction with the first mode. $(h_{0,\ell_2} \gg h_{\ell_1,0})$.

As for the peaks, which correspond to the combined frequencies of the satellite phonon states, at $P_2 = 1.25; \ 1.5; \ 1.75$, they appear either in the form of individual peaks or on the wings of the peaks produced by the second phonon mode, which stronger interacts with the quasiparticle. In the case of multiple frequencies
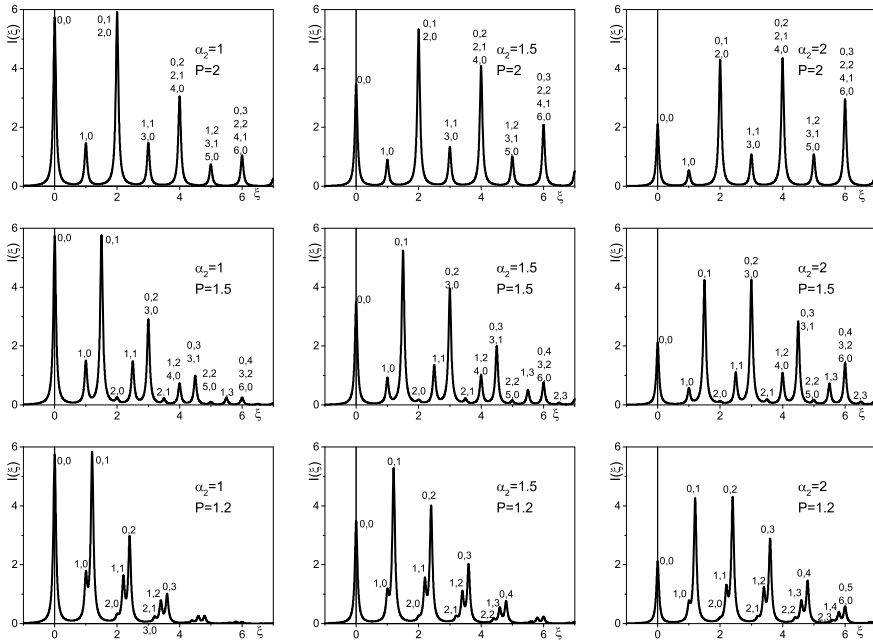
Fig. 22.4 Structure of $I(\alpha_1, \alpha_2; \xi)$ form-function at small (α_1) and intermediate (α_2) coupling constants. Here $\alpha_1 = 0.25$, $\gamma = 0.05$

($P_2 = 2$), as can be seen from Figs. 22.3 and 22.4, all combined peaks, produced by the interaction of quasiparticles with superpositions of both phonon modes, are "absorbed" into the satellite peaks of both separate modes. As a result, the spectrum looks like equidistant, with variable intensity and decay.

22.5   Main Results and Conclusions

1. Based on the Hamiltonian of the Froehlich type, which describes a localized quasiparticle interacting with two-mode non-dispersive phonons in Davydov's model with decay at $T = 0K$, an analytical calculation of Fourier image of retarded Green's function is performed. It gave opportunity to obtain and analyze the frequency dependence of the form-function of absorption band and its spectral parameters in a wide range of energies, which contains the main peak and satellite phonon peaks.

2. The structures of the form-functions are presented for the one- and two-mode system. It is shown that in the limits of physically justified values of decay caused by non-phonon mechanisms at $T = 0K$, the structure does not change

qualitatively, although its evolution depends on the coupling constants, which characterize the interaction between quasiparticle and both phonon modes.

3. It is shown that in the one-mode system the widths of the peaks of the main and phonon satellite peaks vary slightly if α increases. The height of the main peak only decrease significantly, while the heights of the phonon peaks gradually increase, and, reaching the height of the neighbor previous peak, further also decrease. In the most typical interval of coupling constants ($0 \leq \alpha_\lambda < 1$), the heights of the peaks of phonon satellites rapidly decrease. As a result, only 3–4 peaks of the bound-to-phonon states of quasiparticle appear in addition to the main one. The rest of the high-frequency bound states create a weak structure on a continuous background.

4. It is revealed that the two-mode system, which is characterized by a weak binding with the phonon of a smaller mode and an intermediate one with the phonon of a higher mode, has a complicated structure of the form-function. In this structure, one can see the peaks corresponding to both phonon modes and their superpositions. It is clear that the picture of peaks of phonon repeats of a higher phonon mode, with which the quasiparticle interacts stronger, is like the picture of similar one-mode system. The peaks produced by lower mode or combinations of both modes are weak or even absorbed by stronger peaks and general continuous background.

5. It is shown that in the approach of Green's function method, accounting for the non-phonon mechanisms of quasiparticle interaction, the introducing of phenomenological decay at $T = 0$K retains the basic properties of the parameters of the renormalized spectrum of the system without the decay. Herein, the delta-like form-functions are transformed to the quasi-Lorenz peaks with finite height and width.

References

1. Huang К, Rhys A (1950) Theory of light absorption and non-radiative transitions in F-centres. Proc Roy Soc A 204:406–423. https://doi.org/10.1098/rspa.1950.0184
2. Pekar SI (1951) Studies in the electronic theory of crystals. Gostekhizdat, Moscow
3. Toyozawa Y (1958) Theory of line-shapes of the exciton absorption bands. Progress Theoret Phys 20(1):53–81. https://doi.org/10.1143/PTP.20.53
4. Toyozawa Y (1959) On the dynamical behavior of an exciton. Prog Theor Phys Suppl 12:111–140. https://doi.org/10.1143/PTPS.12.111
5. Davydov AS (1968) Theory of molecular excitons. Nauka, Moscow
6. Davydov AS (1976) Theory of solids. Nauka, Moscow
7. Agranovich VM (1968) Theory of exitons. Nauka, Moscow
8. Levinson YB, Rashba EI (1974) Threshold phenomena and bound states in the polaron problem. Sov Phys Usp 16:892–912. https://doi.org/10.1070/PU1974v016n06ABEH004097
9. Mahan GD (1981) Many-particle physics. Plenum, New York
10. Abrikosov AA, Gorkov LP, Dzyaloshinski IE (2012) Methods of quantum field theory in statistical physics. Dover, New York

11. Giorgetta FR, Baumann E, Graf M, Yang Q, Manz C, Kohler K, Beere HE, Ritchie DA, Linfield E, Davies AG, Fedoryshyn Y, Jackel H, Fischer M, Faist J, Hofstetter D (2009) Quantum cascade detectors. IEEE J Quantum Electron 8:1039–1052. https://doi.org/10.1109/JQE.2009.2017929

12. Faist J (2013) Quantum cascade lasers. Oxford University Press, Oxford

13. Belkin MA, Capasso F (2015) New frontiers in quantum cascade lasers: high performance room temperature terahertz sources. Phys Scr 90:118002. https://doi.org/10.1088/0031-8949/90/11/118002

14. Reininger P, Zederbauer T, Schwarz B, Detz H, MacFarland D, Maxwell Andrews A, Schrenk W, Strasser G (2015) InAs/AlAsSb based quantum cascade detector. Appl Phys Lett 107:081107. https://doi.org/10.1063/1.4929501

15. Stroscio MA, Dutta M (2001) In: Phonons in nanostructures. Cambridge University Press, Cambridge

16. Tkach MV, Seti JO, Voitsekhivska OM (2015) Quasiparticles in nanoheterostructures: quantum dots, wires and layers. Books-XXI, Chernivtsi

17. Harrison P, Valavanis A (2016) Quantum wells, wires and dots: theoretical and computational physics of semiconductor nanostructures, 4th edn. Wiley, New York

18. Tkach MV, Seti JO, Voitsekhivska OM (2019) Diagram technique in the method of green's functions of quasiparticles interacting with phonons. Chernivtsi National University, Chernivtsi, p 164

19. Prokof'ev NV, Svistunov BV, Tupitsyn IS (1998) Exact, complete, and universal continuous-time worldline Monte Carlo approach to the statistics of discrete quantum systems. J Exp Theor Phys 87:310. https://doi.org/10.1134/1.558661

20. Mishchenko AS, Prokof'ev NV, Sakamoto A, Svistunov BV (2000) Diagrammatic quantum Monte Carlo study of the Fröhlich polaron. Phys Rev B 62:6317. https://doi.org/10.1103/PhysRevB.62.6317

21. De Filippis G, Cataudella V, Mishchenko AS, Nagaosa N (2012) Optical conductivity of polarons: Double phonon cloudconcept verified by diagrammatic Monte Carlo simulations. Phys Rev B 85:094302. https://doi.org/10.1103/PhysRevB.85.094302

22. Mishchenko AS, Nagaosa N, Prokof'ev N (2014) Diagrammatic Monte Carlo method for many-polaron problems. Phys Rev Lett 113:166402. https://doi.org/10.1103/PhysRevLett.113.166402

23. Berciu M (2006) Green's function of a dressed particle. Phys Rev Lett 97:036402. https://doi.org/10.1103/PhysRevLett.97.036402

24. Covaci L, Berciu M (2007) Holstein polaron: the effect of coupling to multiple-phonon modes. EPL 80:67001. https://doi.org/10.1209/0295-5075/80/67001

25. Kornilovitch PE (2006) Polaron action for multimode dispersive phonon systems. Phys Rev B 73:094305. https://doi.org/10.1103/PhysRevB.73.094305

26. Möller MM, Berciu M (2016) Discontinuous polaron transition in a two-band model. Phys Rev B 93:035130. https://doi.org/10.1103/PhysRevB.93.035130

27. Tkach M, Seti J, Pytiuk O, Voitsekhivska O (2019) Renormalized spectrum of three-level localized quasiparticle interacting with polarization phonons at cryogenic temperature. J Low Temp Phys 195:26–36

28. Tkach MV, Seti JuO, Voitsekhivska OM, Hutiv VV (2021) Renormalized spectrum of quasi-particle in limited number of states, strongly interacting with two-mode polarization phonons at T=0K. Condens Matter Phys 24:13705. https://doi.org/10.5488/CMP.24.13705

29. Tkach MV, Seti JO, Voitsekhivska OM, Hutiv VV (2021) Spectrum of localized quasi-particle interacting with three-mode phonons. In: Fesenko O, Yatsenko L (eds) Nanooptics and photonics, nanochemistry and nanobiotechnology, and their applications, NANO 2020, Springer proceedings in physics, vol 264. Springer, Cham. https://doi.org/10.1007/978-3-030-74800-5_6

Chapter 23
Fluorinated Oligoazomethine with Azo Groups in the Main Chain as Stimuli-Responsive Photoactive Materials

Yu. Kurioz ⓘ**, I. Tkachenko, A. Kovalchuk, Ya. Kobzar, O. Shekera, R. Kravchuk, V. Nazarenko, and V. Shevchenko**

23.1 Introduction

Stimuli-responsive polymers based on photochromic switches (azobenzenes, diarylethenes, spiropyrans, azomethines) have attracted increasing attention due to their possible use in data storage devices, sensors, molecular switches, studies of surface phenomena, etc. [1–6]. Among different photoactive units, azo and azomethine (imine) groups are considered as highly efficient ones and, therefore, great attention has been paid to the synthesis of polyazobenzenes [7–10] and polyazomethines [10–13]. It is important to highlight that the energy levels of the HOMO and LUMO of the molecule bearing the $N = N$ or $CH = N$ double bonds are lower than that of the $C = C$ analog. In fact, the HOMO and LUMO energy levels and energy gaps directly influence on optical properties of corresponding materials [10, 14, 15]. Generally, structures and functional optical properties (reversible *trans–cis* isomerization, photoinduced birefringence, photoluminescence, photovoltaic, etc.) of these polymers are well documented in the literature [1–21]. In addition to distinct optical properties, many studies have been dedicated to the synthesis of chelating agents based on polyazobenzenes (azobenzenes) and, especially, polyazomethines (azomethines) [22–24].

The introduction of novel and unique conjugated fragments into polymer main chains is an important way to realize superior properties from the final products

Yu. Kurioz (✉) · R. Kravchuk · V. Nazarenko
Institute of Physics, National Academy of Sciences of Ukraine, Prospect Nauky 46, Kyiv 03028, Ukraine
e-mail: kurioz@hotmail.com

I. Tkachenko · A. Kovalchuk · Ya. Kobzar · O. Shekera · V. Shevchenko
Institute of Macromolecular Chemistry, National Academy of Sciences of Ukraine, Kharkivske Shosse 48, Kyiv 02160, Ukraine
e-mail: ttkachenkoim@gmail.com

[15]. It has been recognized that azo-azomethine organic chromophores combine the valuable properties of both imine and azo groups. The simultaneous combination of such groups within the molecule conjugation system leads to the bathochromic shift of the absorption bands in the electronic spectra, increases stability of the *cis*-isomer of the azo group and photostability, and at the same time provides the low oxidation state of metal ions [25–27]. Thus, there are many motivations to explore new azo-azomethine conjugated systems and it is not surprising, therefore, that currently, a specific attention is drawn to the polymer-based materials [25, 27–29] as well as organic azo-azomethine chromophores [26, 30–33] having both azo and azomethine groups.

Previously, we developed two polyazomethines with azo groups in the backbone (Azo-Pam) by polycondensation of tetrafluorobenzene- or octafluorobiphenylene-based bis-hydroxybenzaldehydes with hexamethylenediamine [29, 34]. Both polymers showed promising potential as light-sensitive polymers for creation of polarization holograms and various liquid crystal device fabrications. Additionally, the obtained data show that used monomers, namely *meta*-linked azo-containing bis(2-hydroxybenzaldehyde)s with perfluorinated aromatic fragments, are effective building blocks for designing a wide range of stimuli-responsive and optical active materials. These monomers contain *ortho*-oriented hydroxy groups to aldehyde functions, and hence, the optical properties and the switching dynamics of azobenzenes can be controlled through *ortho*-substitution [35–37]. Next, it was determined that presence of fluorinated electron-withdrawing units in monomers and corresponding polymers resulted in their good optical properties, thermostability, and improved solubility [29, 38]. Though, an increased content of aliphatic units in the mentioned Azo-Pam polymers led to some natural deterioration of their thermal stability and shortening of the π-conjugation chain length. Extending the π-conjugated systems of chromophore-based compounds is the most promising strategy to design efficient visible-light-driven switches due to a more obvious red-shift of π-π* transition electronic bands [14, 16, 39]. In this context, it was anticipated that replacing of aliphatic diamine with aromatic one would improve functional properties of resulting Azo-Pam.

Insufficient solubility appeared to be a major drawback for fully aromatic polymers, especially for main-chain polyazobenzenes and polyazomethines [25, 40, 41]. It is generally recognized that the presence of flexible ether linkages and isomeric fragments in a polymer backbone allows regulating the different properties (optical and liquid crystalline properties, thermostability) of the final materials as well as enhances their solubility [29, 41]. Additionally, one of the successful approaches for enhancement of solubility is the decreasing of molecular weight of the targeted polymers, viz., the development of oligomers. To date, several types of azobenzene-[42, 43] or imine-based oligomers [14, 44, 45] have been reported.

Herein, we report on the synthesis of novel aldehyde-terminated azo-containing oligoazomethine with both tetrafluorobenzene and octafluorobiphenylene units as well as ether linkages and *meta*-oxyphenylene fragments in the backbone. Properties of the synthesized oligomer, such as solubility, tensile strength, thermal stability, photooptical behavior, and photoinductive birefringence, were investigated.

23.2   Experimental Section

23.2.1   *Materials*

Monomers 3,3'-{(2,3,5,6-tetrafluoro-1,4-phenylene)bis[oxy-3,1-phenylenediazene-2,1-diyl]}bis(6-hydroxybenzaldehyde) **1** and 3-{[4'-(3-aminophenoxy)-2,2',3,3',5,5',6,6'-octafluoro-1,1'-biphenyl-4-yl]oxy}phenyl amine **2** were prepared as described earlier [38, 46]. **2**-aminophenol (Acros Organics, 99%) was used as received. The other reagents and solvents were purified routinely.

23.2.2   *Synthesis of Azo-Oam-1*

A dry, 25 ml three-necked flask equipped with an oil bath, a mechanical stirrer, a cold water condenser, an argon inlet/outlet, and a thermometer was charged with monomer **1** (0.300 g, 0.476 mmol), diamine **2** (0.213 g, 0.416 mmol), and 3 ml of N,N-dimethylacetamide (DMAc). The mixture was then heated to 110 °C and stirred vigorously at this temperature for 24 h. The reaction mixture was quenched with methanol, and the resulting solid was collected by filtration. The oligomer was purified by reprecipitation from DMAc solution into methanol and then dried in a vacuum oven at 60 °C overnight—yield 86%; FTIR (KBr, cm^{-1}): 3600–3300 (–OH), 3100–2850 (C–H), 1668 (–CHO, end-group stretching), 1625 (–CH = N–), 1597, 1485 (C = C, arom.), 1221 (C–O–C), and 995, 980 (C–F); and UV–Vis spectrum (DMAc, 15.0 µg/mL): $\lambda_{max1} = 364$ nm and $\lambda_{max2} = 464$ nm.

23.2.3   **Synthesis of Model Compound 3 (4,4'-(((((perfluoro-1,4-phenylene)bis(oxy))bis(3,1-phenylene))bis(diazene-2,1-diyl))bis(2-(((2-hydroxyphenyl)imino)methyl)phenol)**

Compound **1** (0.500 g, 0.793 mmol), 2-aminophenol (0.173 g, 1.586 mmol), and DMAc (4.0 ml) were mixed and stirred until the solids were dissolved. Then, the solution was heated at 80 °C for 4 h. After cooling, the reaction mixture was precipitated into methanol. The resulting solid was collected by filtration, washed with hot methanol for three times, and finally dried at 60 °C under vacuum—yield 78% ^{1}H NMR (DMSO-d6, 400 MHz, ppm): δ 15.07 (s, 2H, OH), 10.10 (s, 2H, OH), 9.20 (s, 2H, CH = N), 8.24 (s, 2H, Ph), 7.99 (d, 2H, $J = 7.5$ Hz, Ph), 7.68–7.64 (m, 6H, Ph), 7.52 (d, 2H, $J = 5.6$ Hz, Ph), 7.41 (s, 2H, Ph), 7.02 (br.s., 4H, Ph), and 6.93 (d, 2H, $J = 5.6$ Hz, Ph); ^{19}F NMR (DMSO-d, 376 MHz, ppm): δ –154.85 (s, 4F, Ph), %; FTIR (KBr, cm^{-1}): 3600–3000 (-OH), 3050–2850 (C–H), 1618 (–CH = N-)– 1589,

1499 (C= C, arom.), 1246 (C–O–C), and 1016, 993 (C-F); and UV–Vis spectrum (DMAc, 6.0 µg/mL): $\lambda_{1max} = 368$ nm and $\lambda_{2max} = 459$ nm.

23.2.4 Characterization

Fourier transform infrared (FTIR) spectra (4000–400 cm^{-1}) of the synthesized compounds were recorded on a TENSOR 37 spectrometer in KBr pellets. ^{1}H and ^{19}F NMR spectra were recorded on a Bruker Avance instrument at room temperature in DMSO-d6. Chemical shifts for ^{1}H NMR are given relative to dimethyl sulfoxide ($\delta = 2.50$ ppm). For ^{19}F NMR, chemical shifts are reported in the scale relative to CFCl$_3$. The UV–Vis spectra of the obtained compounds were recorded on a Shimadzu UV-2450 spectrophotometer. The Azo-Oam-1 film for mechanical analysis was prepared by casting from DMAc solution (0.25 mg/mL) onto the Teflon plate. The obtained film was dried at room temperature for 24 h and then dried under vacuum for 24 h at 40 °C. Tensile strength (TS) was measured on a 2166 P-5 tensile-testing machine with uniaxial tension at a rate of clamp movement of 50 mm/min. The DSC analysis was run using a TA Q200 instrument; heating rate was 20 °C/min under an air atmosphere. The thermo-oxidative destruction of polymers was studied using the thermal gravimetric analysis (TGA) with a TA Instruments Q-50 apparatus (USA) in air. A heating rate of 20 °C/min with a temperature from 20 to 700 °C was applied.

The investigation of the pH influence upon the UV–Vis absorption maxima in DMAc was conducted at an oligomer concentration of 0.006 mg/mL by adding 1 drop of 1 N HCl solution to the corresponding oligomer solution in order to form an acid medium and by adding 2 drops of 1 N NaOH solution to the acid solution of oligomer in order to achieve acid neutralization and to form alkaline medium. Photoisomerization experiment in solution was performed by irradiating the samples at 10 cm distance with 365 nm UV light from DeLux EBT-01 mercury lamp (26 W) and then recorded. For the solid-state photoisomerization, the Azo-Oam-1 oligomer film was irradiated by UV light ($\lambda = 370$ nm, 3.4 mW/cm^2) at 4 cm distance.

The measurements of photoinduced birefringence in the Azo-Oam-1 oligomer film (film thickness ~ 80 µm) were carried out with an experimental optical setup as described in [29, 47]. Briefly, the Azo-Oam-1 film was irradiated with polarized light of an Ar laser ($\lambda = 532$ nm, 50 mW/cm^2) and was simultaneously located between the crossed polarizers for a He–Ne laser ($\lambda = 628$ nm, 5mW) as a probe beam. The polarization direction of the irradiating light made up a 45° to the directions of the polarizer and analyzer. The change in birefringence of the sample during the irradiation was monitored as a function of illumination time. In the Azo-Oam-1 film, the gratins were formed by two spatially modulated Ar laser with P = 10 mW/cm^2 at 532 nm with two linear p-polarizations. The recording of the polarized gratings was performed using experimental scheme represented in [48].

23.3 Results and Discussion

23.3.1 Synthesis and General Properties of Azo-Oam-1 Oligomer

The desired new fluorinated 2-hydroxybenzaldehyde-terminated oligomer (Azo-Oam-1) was prepared in good yield by the interaction of *meta*-linked diamine **2** with excess of azo-containing tetrafluorobenzene-based dialdehyde **1** in DMAc with following the general reaction pathway depicted in Fig. 23.1a. The oligomer repeating unit was targeted as n = 7 by controlling the molar ratio of dialdehyde **1** to diamine **2**. Note that we originally sought out to synthesize azo-based polyazomethine from equivalent molar amounts of monomers **1** and **2**, but the obtained polymer product was insoluble in any of the tested solvents. This phenomenon is ascribed by the high molecular weight of the rigid aromatic polymer chains, which limits the mobility of these chains.

The synthesized oligomer was obtained as yellow fibrous solid, soluble in DMAc and N-methyl-2-pyrrolidone, only partially soluble in N,N-dimethylformamide, and insoluble in the other organic solvents, such as DMSO, THF, acetone, and chloroform. The chemical structure of Azo-Oam-1 was studied by FTIR spectroscopy (Fig. 23.1b, spectrum 2); the FTIR spectrum of the initial monomer **1** is shown for comparison (Fig. 23.1b, spectrum 1). Thus, the appearance of the absorption band at 1625 cm^{-1}
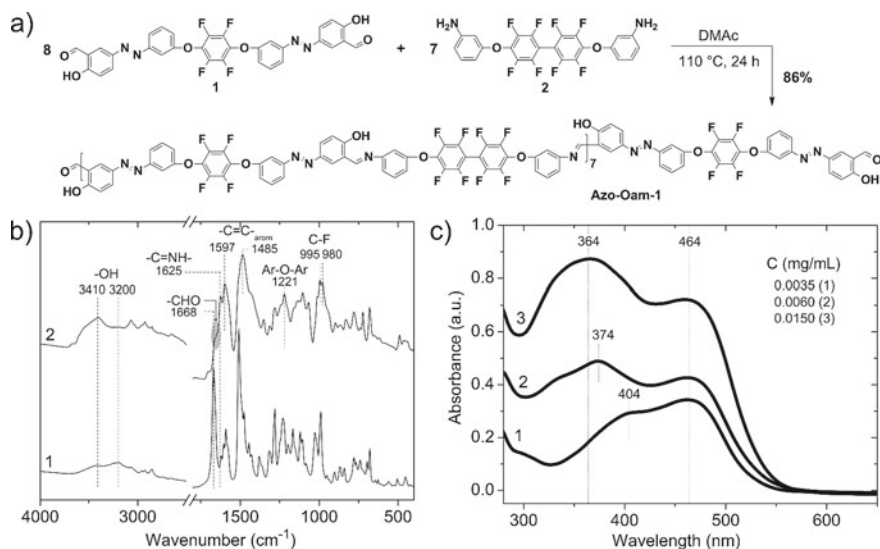
Fig. 23.1 a Synthesis of Azo-Oam-1 oligomer. **b** FTIR spectra of the initial monomer **1** (spectrum 1) and synthesized Azo-Oam-1 oligomer (spectrum 2). **c** UV–Vis absorbance spectra of Azo-Oam-1 at various concentrations (3.5, 6.0 and 15.0 µg mL^{-1}) in DMAc
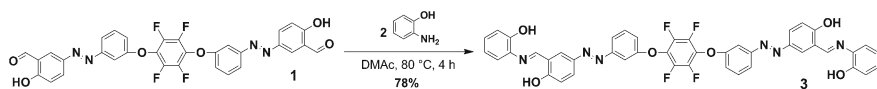
Fig. 23.2 Scheme of model compound **3** synthesis

indicates formation of -CH = N- linkages in oligomer. The strong absorption band at 1668 cm^{-1} in the spectrum of monomer **1** was assigned to the aldehyde groups, and because of polymerization process, this band almost completely disappeared in the spectrum of Azo-Oam-1. Meanwhile, the weak peak (as a shoulder) around 1660 cm^{-1} in the spectrum of Azo-Oam-1 indicates the presence of aldehyde end groups. The Ar-OH bands are located at about the range 3200–3600 cm^{-1} in azo-azomethine-based oligomer. Additionally, the FTIR spectrum of the target oligomer shows peaks which correspond to C—F (980 and 995 cm^{-1}), Ar–O-Ar (1221 cm^{-1}), C = C$_{arom}$ (1485 and 1597 cm^{-1}), and CH groups (2850–3100 cm^{-1}) (Fig. 23.1b).

^{1}H NMR analysis of the low molar mass material (a mixture of dimers and trimers) removed from the initial stage of polymer synthesis confirms the azomethine bond formation by the appearance of the characteristic imine peak in the range of 9.2–9.4 ppm. Note that two azomethine peaks were detected because the mixture of dimers and trimers possesses nonequivalent imines. Additionally, the formation of the azomethine linkage between dialdehyde **1** and aromatic amine was proved by the NMR, FTIR, and UV–Vis techniques on the base of the newly synthesized azo-azomethine model compound **3** (Fig. 23.2). The main characteristic peaks in the above-mentioned spectra for the Azo-Oam-1 coincide with similar peaks in the model compound **3**. Thus, for instance, the peak at 1618 cm^{-1} (FTIR) shows the presence of azomethine bond, as in the final oligomer.

Spectral features of the −CH = N− and −N = N− groups are closed, where their transitions are overlapped [33]. As it is depicted in Fig. 23.1c, the UV–Vis spectrum of Azo-Oam-1 are characterized by two absorption band, but position and relative intensity of these bands depend on the concentration of the oligomer in the DMAc. An absorption band related to the $\pi \rightarrow \pi^*$ transitions appears at 364–404 nm, while an abroad intense band in the visible region at 464 nm characterizes the $n \rightarrow \pi^*$ transitions, intramolecular charge transfer interaction involving the conjugated azo-azomethine blocks and hydrogen-bonded complexes of the obtained oligomers with the highly polar aprotic solvent such as DMAc [29, 46]. Generally, the reducing of the concentration of oligomer in a solution has caused a bathochromic shift of the $\pi \rightarrow \pi^*$ absorption band and increasing relative intensity of the $n \rightarrow \pi^*$ transition.

Importantly, despite the oligomeric nature, Azo-Oam-1 forms flexible free-standing film (the TS value of ca. 13 MPa) by casting from DMAc solution. From this point of view, the resulting oligomer can be considered as a polymer system. Notably, in general, the majority of azo-azomethine-containing polymers as well as aromatic main-chain polyazobenzenes and polyazomethines described in the literature have often a fairly low molecular weight [19, 25, 41].

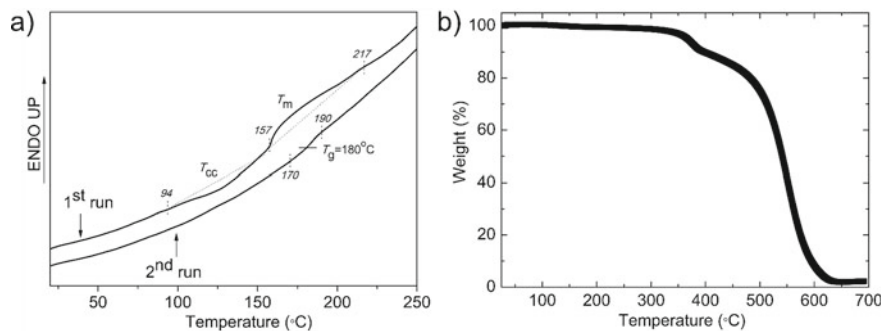The thermal properties of Azo-Oam-1 film were investigated using DSC and TGA techniques (Fig. 23.3).

Fig. 23.3 a DSC curves of Azo-Oam-1 oligomer recorded for film samples; depicted are the first and second heating runs (DSC curves are offset for clarity. Air atmosphere, heating rate of 20 °C/min. **b** TGA curve of Azo-Oam-1 in an air atmosphere (heating rate: 20 °C/min with a temperature from 25 to 700 °C)

Oligomer sample exhibited a broad exothermic peak at the temperature range of 94–157 °C followed by a broad endothermal peak from 157 to 217 °C in DSC analysis, during the first heating run (Fig. 23.3a). The first exothermic peak indicates formation of some ordered structures due to a cold crystallization process (T_{cc}), and the second peak (T_m) is related to the melting of such formed ordered phase. Generally, multiple phase transitions on the DSC profiles are characteristic of chromophore-containing polymers, especially polyazomethines [41, 49]. Nevertheless, during the second heating the oligomer showed only a glass transition (T_g) at 180 °C, which basically indicates the amorphous nature of this sample (Fig. 23.3a). The glass transition region value of the oligomer is 20 °C. The obtained oligomer is thermally stable in air up to 350 °C (Fig. 23.3b), showing only a 3% weight loss at this temperature. The replacement of the aliphatic diamine (namely 1,6-hexamethylenediamine) by an aromatic one (diamine **2**) induces an important increase in the thermostability of Azo-Oam-1. Thus, the results of TGA for Azo-Oam-1 obviously indicate the 5% weight-loss temperature ($T_{5\%}$) at 365 °C, which is higher than that of the azo-containing polyazomethine prepared from monomer **1** and aliphatic 1,6-hexamethylenediamine ($T_{5\%}$ is about 300 °C) [29, 34].

23.3.2 Optical Properties of Oligomer

As discussed above, it was found that changing the concentration of oligomer in solvent played a significant role in regulating its absorption maxima (Fig. 23.1c). Additionally, in DMAc solution, the absorption maxima of Azo-Oam-1 oligomer can be intentionally regulated by changing the pH values of a medium. For example, a hypsochromic shift from ~ 374 to 344 nm is clearly observed when increasing the proton concentration in the solution (pH ~2) while the peak at 464 nm disappears (Fig. 23.4a). When the neutralization of phenol groups of the oligomer in the alkaline
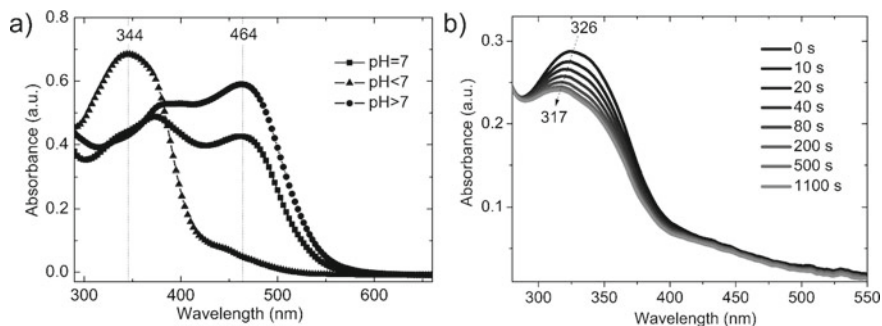
Fig. 23.4 a UV–Vis spectra of Azo-Oam-1 in DMAc at acidic (pH < 7), neutral (pH = 7), and alkaline medium (pH > 7). **b** Photoisomerization of Azo-Oam-1 in DMAc (0.006 mg/mL) upon irradiation at 365 nm

medium was performed (pH ∼12), the absorption spectrum changes significantly: The absorptivity in the visible wavelengths (the n–π* band at 464 nm) increases multifold in comparison to spectrum of protonated Azo-Oam-1 (Fig. 23.4a). Such distribution of the absorption maxima (the difference makes up 120 nm) is a consequence of the formation of ionic form in alkaline medium and azo form in acidic medium [29, 46].

The ability of azobenzene-based compounds to undergo photoisomerization is an effective tool for regulating their properties. The *trans–cis* transition of Azo-Oam-1 in the DMAc solution was not registered. At the same time, the reversible *trans–cis-trans* photoisomerization in the Azo-Oam-1 film is observed under UV illumination for *trans–cis* isomerization (Fig. 23.4b) and under deuterium lamp irradiation for the reversible *cis–trans* relaxation of azobenzene units.

23.3.3 Light-Induced Birefringence and Diffraction Gratings in the Azo-Oam-1 Film

One of the greatest opportunities for light-sensitive polymers comes from their ability to become anisotropic under a polarized light irradiation. Photoinduced anisotropy in the synthesized Azo-Oam-1 oligomer was investigated through birefringence and diffraction grating recording process. It is shown that after the beginning of irradiation with polarized light, the intensity of birefringence in the Azo-Oam-1 film increases and at a certain time reaches a constant value (Fig. 23.5a). After switching off the irradiation light, the relaxation process (between B and C time points, Fig. 23.5a) can be observed for oligomer sample due to *cis–trans* isomerization of azo groups. The obtained results are typical for the photoisomerization behavior in polymers accompanied by the motions of the azobenzene chromophores and the interactions of orientated azobenzene groups [25, 50, 51]. It is important to note that when the writing beam is turned off (point B, Fig. 23.5a), the remaining anisotropy continues to
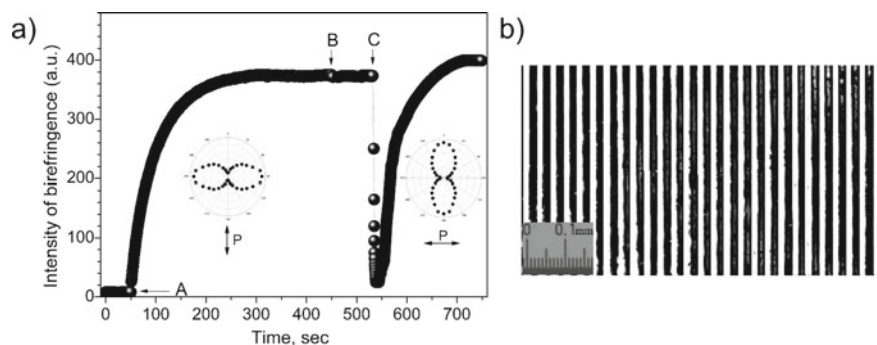
Fig. 23.5   a Dependence intensity of birefringence in Azo-Oam-1 film on irradiation time from Ar laser (λ = 532 nm, P = 10 mW). Linearly polarized light is switched on at point A (vertical polarization) and switched off at point B; irradiation when rotating the polarization of light by 90° (horizontal polarization) is switched on at point C. The insets show absorption spectra of Azo-Oam-1 for vertical (left inset) and horizontal (right inset) polarization of the incident polarized light. **b** Optical image of the diffraction pattern in Azo-Oam-1 film in a polarize microscope (scale = 0.1 mm)

hold at a certain value and this remnant birefringence is very stable for the oligomeric film. We assume that the main reason of the high residual anisotropy is the significant intermolecular interaction of macromolecules, which partially fix (stabilize) the *cis*-stationary state of azobenzene fragments in the Azo-Oam-1 film. Potentially, such interactions are possible with the groups $-OH$ and $-CH = N-$, which are capable of forming a stable hydrogen-bond network as well as between non-fluorinated and fluorinated aromatic fragments ($\pi_{Ar} - \pi_{ArF}$ stacking interactions) [23, 29].

While we observed the relaxation in the oligomer film, the direction of the irradiating polarization of Ar laser, due to the rotation of the Glan–Thompson prism, was changed by 90° and the irradiating beam was turned on again. Figure 23.5a shows that initially the intensity of birefringence decreases, apparently due to reduction or "erasure" of the anisotropy (Δn changes), and then increases rapidly, again reaching a steady state, which indicates an increase in anisotropy in the film according to new direction of polarization of the irradiating beam. Thus, so-called the phenomenon of "rewriting" was observed, which indicates a change in the birefringence in accordance with the change in the direction of irradiating polarization. Direction of the photoinduced anisotropy in the Azo-Oam-1 film is perpendicular to the direction of irradiation polarization light (λ = 532 nm). It was confirmed by the angular dependence of the polarized light absorption (Fig. 23.5a, insets).

Azo-Oam-1 oligomer was used for recording of diffraction gratings. Gratings were formed by 2-beam irradiation of Azo-Oam-1 film by spatially modulated Ar laser (wavelength λ = 532 nm, power $P \leq 10$ mW) with two linear ***p***-polarizations. The optical scheme for recording diffraction gratings was described in [48]. The observed diffraction patterns demonstrate equal intensities in each diffraction order (+1; −1) which is monitored as a function of recording time. The photo of the recorded diffraction grating with a resolution ~ 30 lines per millimeter made with polarized

microscope is represented in Fig. 23.5b. Having the probe beam intensities of the zero-diffraction order, I_0, and $I_{\pm 1}$ diffraction order, we can determine $\left(\eta_{+1} = \frac{I_{+1}}{I_0} * 100\% \right)$ the efficiency of diffraction as ~2%. This efficiency of diffraction gratings looks promising for further applications.

23.4   Conclusion

In a summary, we have developed synthetic route for a novel *meta*-linked aromatic oligomer with the aldehyde end groups and possessing both azo and azomethine groups as well as mono- and biphenylene perfluorinated aromatic units. The obtained oligomer has excellent solubility in common organic solvents and exhibited good thermal properties. The benefits of the proposed oligomer structure are its ability to form thermostable ($T_{5\%} = 365\,°C$) mechanically stable (TS = 13 MPa) free-standing film in which *trans–cis* photoisomerization occurs. The presence of OH groups at the *ortho* position with respect to the imine linkage in the azo-based oligoazomethine contributes to the reversible intramolecular migration of the proton of the hydroxyl groups, which allows to regulate their absorption maximum within the wide range by changing the concentration of oligomer and pH of the DMAc solution. It was found that after the irradiation by the polarized light the resulting oligomer acquired time stable anisotropic properties. Moreover, holographic gratings (efficiency of diffraction about 2%.) were observed in the oligomer film irradiated with two polarized beams. Doubtlessly, there are still many challenging options to be studied, but the obtained preliminary data show that the synthesis strategy of the azo-azomethine oligomer is an effective instrument for designing a wide range of stimuli-responsive and optical active materials.

Conflicts of Interest
On behalf of all authors, the corresponding author states that there is no conflict of interest.

References

1. Liu F, Urban MW (2010) Recent advances and challenges in designing stimuli-responsive polymers. Prog Polym Sci 35:3–23. https://doi.org/10.1016/j.progpolymsci.2009.10.002
2. Cao ZQ, Wang GJ (2016) Multi-stimuli responsive polymer materials: particles, films, and bulk gels. Chem Rec 16:1398–1435. https://doi.org/10.1002/tcr.201500281
3. Ohtani S, Yamada N, Gon M, Tanaka K, Chujo Y (2021) The effect of alkyl chain lengths on the red-to-near-infrared emission of boron-fused azomethine conjugated polymers and their film-state stimuli-responsivities. Polym Chem 12:2752–2759. https://doi.org/10.1039/D1PY00213A
4. Pang X, Lv JA, Zhu C, Qin L, Yu Y (2019) Photodeformable azobenzene-containing liquid crystal polymers and soft actuators. Adv Mater 31:1904224. https://doi.org/10.1002/adma.201904224
5. Stuart M, Huck W, Genzer J, Müller M, Ober C, Stamm M, Sukhorukov G, Szleifer I, Tsukruk V, Urban M, Winnik F, Zauscher S, Luzinov I, Minko S (2010) Emerging applications of stimuli-responsive polymer materials. Nature Mater 9:101–113. https://doi.org/10.1038/nmat2614
6. Moulin E, Faour L, Carmona-Vargas CC, Giuseppone N (2020) From molecular machines to stimuli-responsive materials. Adv Mater 32:1906036. https://doi.org/10.1002/adma.201906036
7. Kuenstler AS, Clark KD, Read de Alaniz J, Hayward RC (2020) Reversible actuation via photoisomerization-induced melting of a semicrystalline poly(azobenzene). ACS Macro Lett 9:902–909. https://doi.org/10.1021/acsmacrolett.0c00328
8. Wang HZ, Chow HF (2018) A photo-responsive poly(amide-triazole) physical organogel bearing azobenzene residues in the main chain. Chem Commun 54:8391–8394. https://doi.org/10.1039/C8CC05096A
9. Wu S, Butt HJ (2020) Solar-thermal energy conversion and storage using photoresponsive azobenzene-containing polymers. Macromol Rapid Commun 41:1900413. https://doi.org/10.1002/marc.201900413
10. Gon M, Tanaka K, Chujo Y (2021) Discovery of functional luminescence properties based on flexible and bendable boron-fused azomethine/azobenzene complexes with O, N, O-type tridentate ligands. Chem Rec 21:1358–1373. https://doi.org/10.1002/tcr.202000156
11. Lim W, Oo C, Choo Y, Looi S (2015) New generation of photosensitive poly(azomethine)esters: thermal behaviours, photocrosslinking and photoluminescence studies. Polymer 71:15–22. https://doi.org/10.1016/j.polymer.2015.06.041
12. Çulhaoğlu S, Kolcu F, Kaya İ (2021) Synthesis of phosphate and silane-based conjugated polymers derived from bis-azomethine: Photophysical and thermal characterization. React Funct Polym 166:104978. https://doi.org/10.1016/j.reactfunctpolym.2021.104978
13. Li G, Yu K, Noordijk J, Meeusen-Wierts M, Gebben B, oude Lohuis P, Schotman A, Bernaerts K (2020) Hydrothermal polymerization towards fully biobased polyazomethines. Chem Commun 56:9194−9197. https://doi.org/10.1039/D0CC03026K
14. Liu M, Yin L, Wang L, Miao T, Cheng X, Wang Y, Zhang W, Zhu X (2019) Synthesis of monodisperse aromatic azo oligomers toward gaining new insight into the isomerization of π-conjugated azo systems. Polym Chem 10:1806–1811. https://doi.org/10.1039/C9PY00001A
15. Gon M, Tanaka K, Chujo Y (2018) A highly efficient near-infrared emissive copolymer with a N=N double-bond π-conjugated cystem based on a fused azobenzene-boron complex. Angew Chem 130:6656–6661. https://doi.org/10.1002/ange.201803013
16. Anwar N, Willms T, Grimme B, Kuehne AJ (2013) Light-switchable and monodisperse conjugated polymer particles. ACS Macro Lett 2:766–769. https://doi.org/10.1021/mz400362g
17. Tkachenko IM, Ledin PA, Shevchenko VV, Tsukruk VV (2021) Mixed star-shaped POSS-based molecule with hydroxy group-containing units and azobenzene fragments as two types of arms. Mendeleev Commun 31:27–29. https://doi.org/10.1016/j.mencom.2021.01.007

18. Kang H, Joo K, Kang Y, Lee J, Lee Y, Jeon I, Lee T, Koh W, Choi J, Kim H, Ka J (2021) Highly sensitive updatable green hologram recording polymer with photoisomerizable azobenzene with highly birefringent acetylene as the side chain. Polym J 53:539–547. https://doi.org/10.1038/s41428-020-00447-x

19. Nitschke P, Jarząbek B, Damaceanu MD, Bejan AE, Chaber P (2021) Spectroscopic and electrochemical properties of thiophene-phenylene based Shiff-bases with alkoxy side groups, towards photovoltaic applications. Spectrochim Acta A Mol Biomol Spectrosc 248:119242. https://doi.org/10.1016/j.saa.2020.119242

20. Khalid N, Iqbal A, Siddiqi HM, Park OO (2017) Synthesis and photophysical study of new green fluorescent TPA based poly(azomethine)s. J Fluoresc 27:2177–2186. https://doi.org/10.1007/s10895-017-2157-4

21. Kato T, Gon M, Tanaka K, Chujo Y (2021) Modulation of stimuli-responsiveness toward acid vapor between real-time and write-erase responses based on conjugated polymers containing azobenzene and Schiff base moieties. J Polym Sci 59:1596–1602. https://doi.org/10.1002/pol.20210329

22. Ghoneim M, El-Sonbati A, Diab M, El-Bindary A, Serag L (2015) Supramolecular assembly on coordination of azopolymer complexes: a review. Polymer Plast Tech Eng 54:100−117. https://doi.org/10.1080/03602559.2014.935399

23. Iwan A, Sek D (2008) Processible polyazomethines and polyketanils: from aerospace to light-emitting diodes and other advanced applications. Prog Polym Sci 33:289–345. https://doi.org/10.1016/j.progpolymsci.2007.09.005

24. Sobarzo PA, Terraza CA, Maya EM (2020) New efficient tetraphenyl silylated poly (azomethine)s based on "pincer-like" bis(imino) pyridine iron (III) complexes as heterogeneous catalysts for CO_2 conversion. Eur Polym J 126:109567. https://doi.org/10.1016/j.eurpolymj.2020.109567

25. Kovalchuk AI, YaL K, Tkachenko IM, Shevchenko VV (2019) Polymers containing azo and azomethine groups: synthesis, properties, and application. Polym Sci Ser B 61:109–123. https://doi.org/10.1134/S1560090419020040

26. Georgiev A, Kostadinov A, Ivanov D, Dimov D, Stoyanov S, Nedelchev L, Nazarova D, Yancheva D (2018) Synthesis, spectroscopic and TD-DFT quantum mechanical study of azo-azomethine dyes. a laser induced *trans-cis-trans* photoisomerization cycle. Spectrochim Acta A Mol Biomol Spectrosc 192:263–274. https://doi.org/10.1016/j.saa.2017.11.016

27. Hajibeygi M, Shafiei-Navid S, Shabanian M, Vahabi H (2018) Novel poly(amide-azomethine) nanocomposites reinforced with polyacrylic acid-co-2-acrylamido-2-methylpropanesulfonic acid modified LDH: Synthesis and properties. Appl Clay Sci 157:165–176. https://doi.org/10.1016/j.clay.2018.03.004

28. Diana R, Panunzi B, Shikler R, Nabha S, Caruso U (2019) A symmetrical azo-based fluorophore and the derived salen multipurpose framework for emissive layers. Inorg Chem Commun 104:186–189. https://doi.org/10.1016/j.inoche.2019.04.016

29. Kovalchuk A, Kobzar Ya, Tkachenko I, Kurioz Yu, Tereshchenko O, Shekera O, Nazarenko V, Shevchenko V (2019) Photoactive fluorinated poly(azomethine)s with azo groups in the main chain for optical storage applications and controlling liquid crystal orientation. ACS Appl Polym Mater 2:455–463. https://pubs.acs.org/doi/https://doi.org/10.1021/acsapm.9b00906

30. Ozkan G, Kose M, Zengin H, McKee V, Kurtoglu M (2015) A new Salen-type azo-azomethine ligand and its Ni(II), Cu(II) and Zn(II) complexes: synthesis, spectral characterization, crystal structure and photoluminescence studies. Spectrochim Acta A Mol Biomol Spectrosc 150:966–973. https://doi.org/10.1016/j.saa.2015.06.038

31. Khanmohammadi H, Darvishpour M (2009) New azo ligands containing azomethine groups in the pyridazine-based chain: synthesis and characterization. Dyes Pigm 81:167–173. https://doi.org/10.1016/j.dyepig.2008.07.019

32. Iftime M, Cozan V, Airinei A, Varganici C, Ailiesei G, Timpu D, Sava I (2019) Asymmetric azomethine amines with azobenzene moieties-liquid crystalline and optical properties. Liq Cryst 46:1584–1594. https://doi.org/10.1080/02678292.2019.1640903

33. Stoilova A, Georgiev A, Nedelchev L, Nazarova D, Dimov D (2019) Structure-property relationship and photoinduced birefringence of the azo and azo-azomethine dyes thin films in PMMA matrix. Opt Mater 87:16–23. https://doi.org/10.1016/j.optmat.2018.07.010

34. Tkachenko I, Kurioz Y, Kovalchuk A, Ya K, Shekera O, Tereshchenko O, Nazarenko V, Shevchenko V (2020) Optical properties of azo-based poly(azomethine)s with aromatic fluorinated fragments, ether linkages and aliphatic units in the backbone. Mol Cryst Liq Cryst 697:85–96. https://doi.org/10.1080/15421406.2020.1731080

35. Dong M, Babalhavaeji A, Samanta S, Beharry A, Woolley G (2015) Red-shifting azobenzene photoswitches for in vivo use. Acc Chem Res 48:2662–2670. https://doi.org/10.1021/acs.accounts.5b00270

36. Ahmed Z, Siiskonen A, Virkki M, Priimagi A (2017) Controlling azobenzene photoswitching through combined ortho-fluorination and -amination. Chem Commun 53:12520–12523. https://doi.org/10.1039/C7CC07308A

37. Han M, Honda T, Ishikawa D, Ito E, Hara M, Norikane Y (2011) Realization of highly photoresponsive azobenzene-functionalized monolayers. J Mater Chem 21:4696–4702. https://doi.org/10.1039/C0JM03697H

38. Kovalchuk AI, YaL K, Tkachenko IM, Tolstov AL, Shekera OV, Shevchenko VV (2017) Synthesis and optical properties of new isomeric azo-containing bis(2-hydroxybenzaldehydes) with tetrafluorobenzene units. Mendeleev Commun 27:599–601. https://doi.org/10.1016/j.mencom.2017.11.020

39. Wang K, Yin L, Miu T, Liu M, Zhao Y, Chen Y, Zhou N, Zhang W, Zhu X (2018) Design and synthesis of a novel azobenzene-containing polymer both in the main-and side-chain toward unique photocontrolled isomerization properties. Mater Chem Front 2:1112–1118. https://doi.org/10.1039/C8QM00035B

40. Younis M, Long J, Peng S-Q, Wang X-S, Chai C, Bogliotti N, Huang M-H (2021) Reversible transformation between azo and azonium bond other than photoisomerization of azo bond in main-chain polyazobenzenes. J Phys Chem Lett 12:3655–3661. https://doi.org/10.1021/acs.jpclett.1c00750

41. YaL K, Tkachenko IM, Bliznyuk VN, Shekera OV, Turiv TM, Soroka PV, Nazarenko VG, Shevchenko VV (2016) Synthesis and characterization of fluorinated poly(azomethine ether)s from new core-fluorinated azomethine-containing monomers. Des Monomers Polym 19:1–11. https://doi.org/10.1080/15685551.2015.1092007

42. King ED, Tao P, Sanan TT, Hadad CM, Parquette JR (2008) Photomodulated chiral induction in helical azobenzene oligomers. Org Lett 10:1671–1674. https://doi.org/10.1021/ol8004722

43. Liu M, Shi X, Li L, Zhang J, Huang Z, Zhang W, Zhou N, Zhang Z, Zhu X (2021) Synthesis of discrete conjugated fluorine azo oligomers for the investigation of azobenzene position dependent physical properties and photoresponsive behavior. Macromol Chem Phys 222:2100092. https://doi.org/10.1002/macp.202100092

44. Özaytekin İ, Kar Y (2012) Synthesis and properties of composites of oligoazomethine with char. J Appl Polym Sci 123:815–823. https://doi.org/10.1002/app.34509

45. Tundidor-Camba A, González-Henríquez CM, Sarabia-Vallejos MA, Tagle LH, Hauyón RA, Sobarzo PA, González A, Ortiz PA, Maya EM, Terraza CA (2018) Silylated oligomeric poly(ether-azomethine)s from monomers containing biphenyl moieties: synthesis and characterization. RSC Adv 8:1296–1312. https://doi.org/10.1039/C7RA10929F

46. Kovalchuk AI, YaL K, Tkachenko IM, Tolstov AL, Shekera OV, Shevchenko VV (2018) Synthesis and optical properties of new isomeric core-fluorinated azo-containing bis(2-hydroxybenzaldehyde)s. J Mol Struct 1173:671–678. https://doi.org/10.1016/j.molstruc.2018.07.041

47. Kurioz YI (2013) Phototransformations in cellulose cinnamate films at illumination with polarized UV light. Ukr J Phys 58:1138–1138. https://doi.org/10.15407/ujpe58.12.1138

48. Parka J, Grudniewski T, Kurioz Y, Dąbrowski R (2004) Liquid crystals with high photorefractive index and different cell construction solutions for optical light modulators. Proc SPIE 5565:321. https://doi.org/10.1117/12.581204

49. Morgan PW, Kwolek SL, Pletcher TC (1987) Aromatic azomethine polymers and fibers. Macromolecules 20:729–739. https://doi.org/10.1021/ma00170a006
50. Bléger D, Liebig T, Thiermann R, Maskos M, Rabe JP, Hecht S (2011) Light-orchestrated macromolecular "accordions": reversible photoinduced shrinking of rigid-rod polymers. Angew Chem 123:12767–12771. https://doi.org/10.1002/ange.201106879
51. Robertus J, Reker S, Pijper T, Deuzeman A, Browne W, Feringa B (2012) Kinetic analysis of the thermal isomerisation pathways in an asymmetric double azobenzene switch. Phys Chem Chem Phys 14:4374–4382. https://doi.org/10.1039/C2CP23756C

Chapter 24
Surface Plasmon Enhanced Copper Monosulfide-Based Core–Shell Nanoparticles

R. Sadkovskyi, T. Bulavinets, and I. Yaremchuk

24.1 Introduction

The modern technologies development and the optoelectronic devices miniaturization are steadily leading to the need for the creation, research and use of nano- and micro-sized objects, such as nanocomposite systems, micro- and nanostructures, quantum dots, etc. [1–3]. Several modern photonic elements, such as filters, antennas, sensors, solar cells, and others can operate based on resonance phenomena [4–6]. Resonance effects are a powerful energy and information factor in new nanophotonic technologies in energy and biomedicine [7]. The usage of the plasmon resonance effect occurring on metal nanoparticles and nanostructures of various shapes and natures makes it possible to predictably scatter light of a certain spectral range in specified directions. Moreover, it can localize the electromagnetic field creating conditions for maximum absorption and generation of light. In addition, the resonance characteristics of specific metal-based nanocomposite structures depend both on the properties of the metal, primarily the value of the plasma resonance frequency of electron oscillations, and on a wide range of factors characterizing the metal–semiconductor interface and the nanostructure [8-10]. Generally, metal nanoparticles form a separate class of materials with unique properties [11]. Another class of nanoparticles characterized by plasmon resonance are nanoshells (a dielectric or semiconductor core covered with a metal shell or vice versa) [12–14], which provide the possibility of precise spectral tuning of the surface plasmon resonance frequencies using their morphology. It is possible due to the controlled plasmon interaction of the shell and the core through their ratio dimensions. In addition, it is expected that nanoshells exhibit higher sensitivity to changes in the dielectric medium, allow

R. Sadkovskyi · T. Bulavinets · I. Yaremchuk (✉)
Department of Photonics, Lviv Polytechnic National University, S. Bandery Street, 12, Lviv 79013, Ukraine
e-mail: iryna.y.yaremchuk@lpnu.ua

controlled redirection of electromagnetic radiation, and facilitate the study of multi-pole surface plasmon resonances [15]. It should be noted the growing interest in the use of the optical properties of plasmonic nanoshells as a functional component in various optical, biomedical systems [16–18]. The development of nanoparticles synthesis technology in recent years has allowed researchers to study nanoparticles of various shapes, ranging from nanorods [19, 20] to exotic structures such as nanoparticles or nanoris [20, 21]

In recent years, the study of molecular exciton–metal nanostructural complexes and the study of plasmon–exciton interaction have attracted the attention of researchers [22–25]. Excitons and plasmons are two types of collective electronic excitations in a condensed medium. Excitons studied in optical spectroscopy of semiconductor nanostructures [26] are very promising for many practical applications. Surface plasmons in the metal particles and their aggregates are also excited in the optical range and are widely used as nanoconcentrators of electromagnetic energy and optical sensors [27]. The role of plasmons in resonant interaction with excitons can be dual that they can decay exciton radiation or enhance it, depending on the nature of the interaction. In recent years, considerable interest has been associated with the creation of various "metal–semiconductor" nanostructures and the study of optical phenomena in them due to the interaction of large-radius excitons with plasmons [28]. It is shown that in the absence of electron transfer, the polarization interaction of excitons and plasmons significantly accelerates the spontaneous emission of excitons [29, 30], can lead to the formation of bound states [31, 32], and to the concentration of electromagnetic energy in nanometers, energy transfer in nanostructures [33], etc.

Therefore, today there are many well-studied applications of nanoparticles; however, new problems arise that require detailed study with the rapid development of the ability to produce and process nanomaterials. It is known that plasmonic properties are most clearly manifested in noble metals, since they demonstrate extraordinary optical properties in the visible range of the spectrum. However, recently, colloidal heavily doped nanocrystals of chalcogenides and metal oxides are of increasing interest [34]. This is primarily since such materials are characterized by both semiconductor and plasma nature [35]. As a result, they demonstrate a synergistic combination of the characteristic optoelectronic properties of nanoscale semiconductors and the optical response of localized surface plasmon resonance [36]. Outstanding representatives of such materials are semiconducting compounds of copper sulfides with a wide phase diversity. Copper monosulfide nanoparticles have several advantages. The most favorable features are the low cost, simple, and easy preparation, and small size for targeting [37]. Such nanoparticles in the presence of conductors and metals demonstrate the enhanced plasmonic characteristics in the near infrared range [38, 39].

Many questions remain open, even though in recent years, many scientific publications on composite nanoparticles based on copper monosulfide appear regularly. Until now, there is no unambiguous answer regarding the nature of the metal/semiconductor interaction and the ideal choice of the combination of materials. It is well known that the main factor affecting the position of the plasmon resonance maximum is the

size of nanoparticles; therefore, in our work, we studied in detail the optical response of spherical composite nanoparticles based on copper sulfide depending on the ratio of the shell core using the theoretical modeling. The study was carried out for dual plasmonic nanoparticles of the type of copper monosulfide-titanium dioxide, copper monosulfide-gold, and copper monosulfide-silver. The performance and practicality of copper monosulfide-based composite nanoparticles have been analyzed, which will allow their use in specialized applications.

24.2   Background

It is convenient to determine the optical properties of nanoshells in the form of a two-layer sphere using the above-described dipole equivalence method, which consists in finding the polarization of nanoparticles through their equivalent permeabilities [40]. The position of the localized plasmon resonance of nanoshells is determined by the ratio of the shell thickness to the core size, their dielectric functions, and environmental parameters.

The equivalent averaged permittivity $\varepsilon_{av}{}^{(1)}$ for a particle of radius r_1 in the medium with permittivity ε_m and with equivalent polarization $\varepsilon_{av}{}^{(1)}$ is determined by analogy with equation as follows:

$$\alpha_{av}^{(1)} = r_1^3 \frac{\varepsilon_{av}^{(1)} - \varepsilon_m}{\varepsilon_{av}^{(1)} + 2\varepsilon_m} \tag{24.1}$$

The equation that determines the equivalent nanoparticle permittivity $\varepsilon_{av}{}^{(2)}$ is obtained using the dipole equivalence method:

$$r_1^3 \frac{\varepsilon_{av}^{(1)} - \varepsilon_2}{\varepsilon_{av}^{(1)} + 2\varepsilon_m} = r_2^3 \frac{\varepsilon_{av}^{(2)} - \varepsilon_2}{\varepsilon_{av}^{(2)} + 2\varepsilon_2} \tag{24.2}$$

The average polarization of nanoparticles is determined by the expression:

$$\alpha_{av}^{(2)} = a_2^3 \frac{\varepsilon_{av}^{(2)} - \varepsilon_m}{\varepsilon_{av}^{(2)} + 2\varepsilon_m} \tag{24.3}$$

Thus, the core–shell ratio for a two-layer nanoparticle can be found from the expression as follows:

$$f_{12} = \frac{r_1^3}{r_2^3}, \tag{24.4}$$

where r_1 is core radius, r_2 is nanoparticle radius.

The average polarization α_{12} of a nanoparticle is determined by the following equation:

$$\alpha_{12} = \frac{\varepsilon_1 - \varepsilon_2}{\varepsilon_1 + 2\varepsilon_2}, \tag{24.5}$$

where ε_1 dielectric permittivity of core, and ε_2 is dielectric permittivity of shell.

Therefore, the dielectric constant of the equivalent particle $\varepsilon_{av}^{(2)}$ is equal to:

$$\varepsilon_{av}^{(2)} = \frac{\varepsilon_2(1 + 2f_{12}\alpha_{12})}{(1 - 2f_{12}\alpha_{12})} \tag{24.6}$$

The absorption C_{abs} and scattering C_{sca} cross sections for two-layer nanoparticles can be calculated as follows:

$$C_{abs} = \frac{12\pi k \varepsilon_m Im(\varepsilon_m)}{r^3 |\varepsilon - \varepsilon_m|^2} \left|\alpha_{av}^{(2)}\right|^2 \tag{24.7}$$

$$C_{sca} = \frac{8\pi}{3} k^4 \left|\alpha_{av}^{(2)}\right|^2 \tag{24.8}$$

The absorption cross section describes the energy absorbed by a nanoparticle and is expressed in terms of the ratio of the absorbed power to the energy flux in the incident light wave. The scattering cross section allows one to characterize that part of the energy flux that falls on the sphere and, after interacting with the sphere, is scattered in different directions.

More detailed description of the derivation of Eqs. (24.7, 24.8) can be founded in [40, 14]. In addition, it should be noted that in the same way, equation can be obtained for multilayer nanoparticles.

24.3 Optical Properties of the Core–shell Nanostructures Under Localized Plasmon Resonance Condition

At the first stage, the extinction spectrum of nanoshells of the type TiO_2 core-CuS shell and the CuS core-TiO_2 shell was calculated. In all calculations, air with a refractive index of 1.0 was chosen as the surrounding medium. The dependences of the extinction of TiO_2-CuS nanoshells on the wavelength are shown in Fig. 24.1a. Core radius varied from 15 to 40 nm at the total constant nanoparticle radius of 40 nm. Thus, the shell thickness varied from 15 to 30 nm. It can be seen from the figure that the core–shell ratio will affect both the position of the extinction maximum and the shape of the spectral curve. For example, it can be observed only one peak at shell thicknesses of 15 and 30 nm. The two extinction peaks are clearly pronounced at other shell thicknesses. The plasmon resonance peak shifts to the blue region of the spectrum with decreasing shell thickness. This is confirmed by

Fig. 24.1b, which shows the results of calculations for the constant core thickness of 20 nm with a change in the shell thickness from 1 to 15 nm. The plasmon peak splits into two peaks with increasing shell thickness and the intensity of the first peak is much higher than the intensity of the second one. It should be noted that the distance between the peaks decreases with increasing shell thickness. The extinction spectra of nanoparticles of copper monosulfide and titanium dioxide with a radius of 45 nm are presented in the inset in Fig. 24.1a. Comparing the extinction spectra of nanoparticles and nanoshells, the combination of a semiconductor with copper monosulfide leads to the enhancement of the spectra in the near infrared region of the spectrum.

Extinction spectra for $CuS-TiO_2$ nanoshells are shown in Fig. 24.1c and d. It can be seen from Fig. 24.1c that increase in the semiconductor shell thickness leads to the shift of the absorption peak to the infrared region of the spectrum and the decrease in its intensity. In this case, there is no splitting of the absorption peaks nor the ratio between the core and the shell. It should be noted that the enhancement of the extinction intensity of nanoshells of the $CuS-TiO_2$ type is very low compared to TiO_2-CuS. However, in such shells, it is possible to achieve the absorption peak at longer wavelengths, which means that they can be used in the near infrared range.
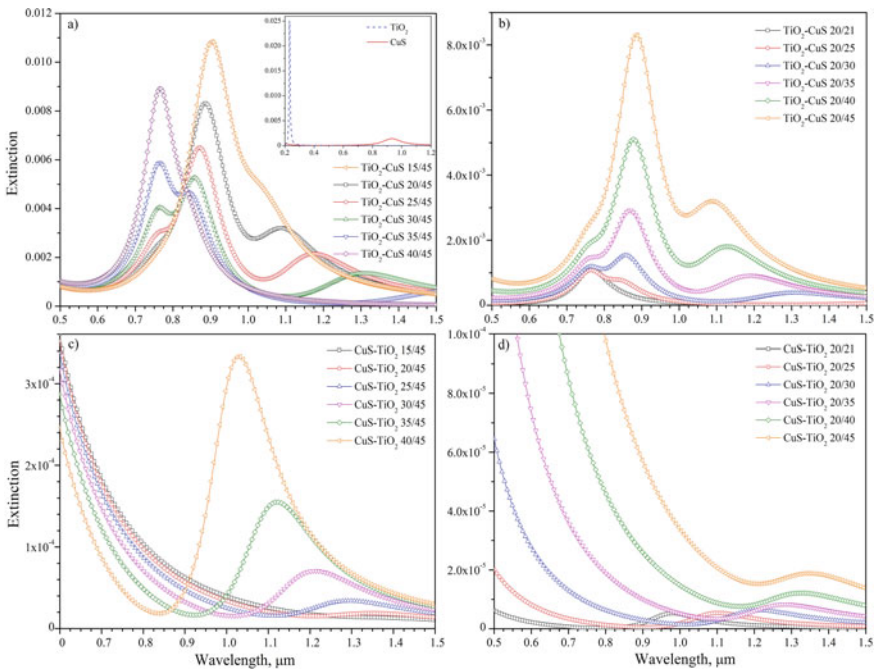
Fig. 24.1 Dependence of extinction of nanoshells TiO_2-CuS and $CuS- TiO_2$ on wavelength. (**a, c**) Core radius is varied from 15 to 40 nm. Shell thickness is varied from 1 to 10 nm. (**b, d**) Core radius is constant and equal 20 nm. Shell thickness is varied from 5 to 30 nm. Refractive index of surrounding medium is 1.0

The extinction of nanoshells of the type of Ag core, CuS shell, and CuS core, Ag shell were calculated (see Fig. 24.2). Dependences of the extinction of the Ag-CuS-type nanoshells are shown in Figs. 24.2a and b, where the core size varied from 20 to 29 nm, and the shell thickness varied from 1 to 10 nm. Such nanoshells are characterized by two pronounced peaks. The first peak is near to the plasmon absorption maximum of the silver nanoparticles, and the second one is near to the plasmon absorption maximum of the copper monosulfide nanoparticles. Extinction of the composite nanoparticle is higher in comparison to the simple nanoparticles. Thus, metal–semiconductor nanoparticles have enhanced optical response. Moreover, there is possibility to obtain plasmon peak position at the given wavelength changing geometrical parameters of nanoshells. Figures 24.2a and b indicate that the decrease in the size of the core and the increase in the shell lead to the shift of both extinction peaks to the region of shorter wavelengths. In addition, the peak responsible for the absorption of copper monosulfide splits in two with increasing shell thickness. Results of the calculations show that splitting depends not so much on the thickness of the shell as on the ratio between the thickness of the core and the shell, as shown in Fig. 24.2b. This splitting can be explained precisely due to the appearance of the strong plasmon–exciton interaction at the metal/semiconductor interface.
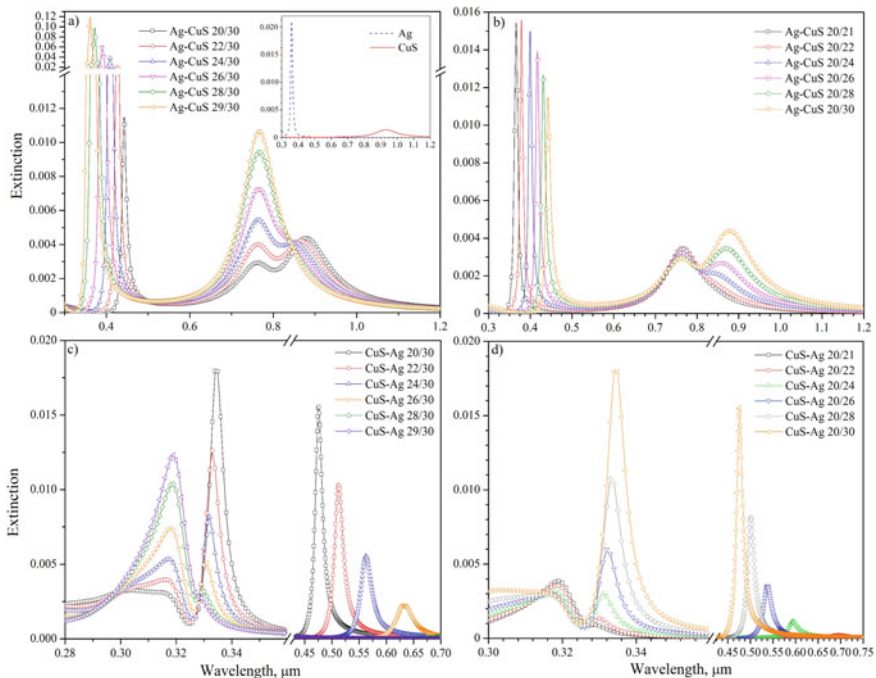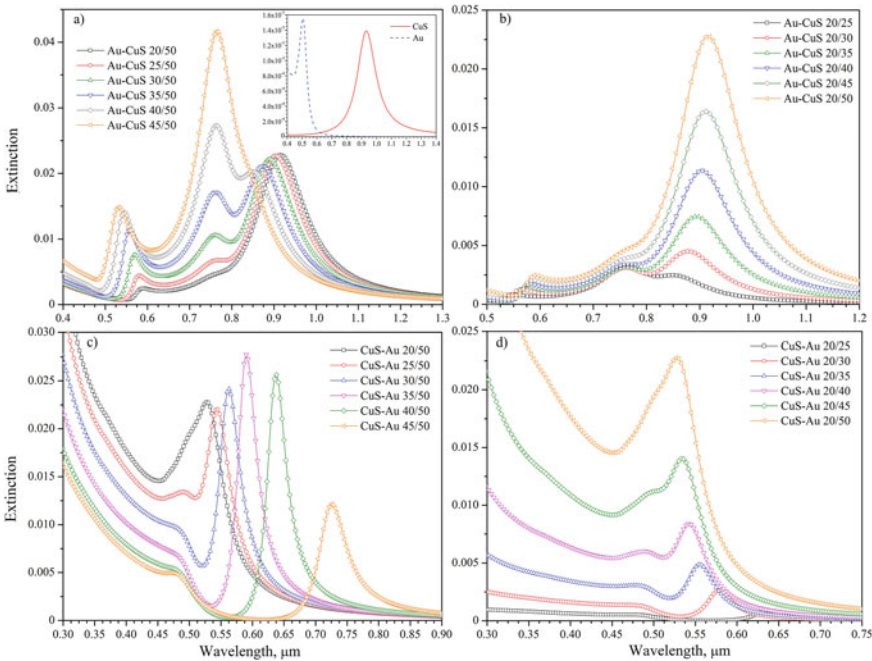

Fig. 24.2 Dependence of extinction of nanoshells Ag-CuS and CuS-Ag on wavelength. (a, c) Core radius is varied from 20 to 29 nm. Shell thickness is varied from 1 to 10 nm. (b, d) Core radius is constant and equal 20 nm. Shell thickness is varied from 5 to 30 nm. Refractive index of surrounding medium is 1.0

Similar calculations were performed for CuS-Ag nanoshells. There is also observed splitting of one of the peaks. In this case, splitting corresponds to first peaks. Perhaps, silver will play the dominant role in such type of nanoparticles. It should be noted that extinction spectrum for CuS-Ag nanoshells with bigger size consists only two peaks without any splitting. Thus, plasmon–exciton interaction depends on thickness ration of core–shell. After all, composite nanoparticles are characterized by the enhanced extinction comparing to pure nanoparticles. However, intensity of peaks in CuS-Ag nanoshells is higher than in Ag-CuS.

Another promising example of the use of plasmonic materials with excitonic materials is the combination of the gold and copper monosulfide. Figure 24.3 shows the results of extinction calculations of Au-CuS and CuS-Au types nanoshells. The core radius varied from 20 to 45 nm and the shell thickness varied from 5 to 30 nm in research of Au-CuS nanoshells (Fig. 24.3a).

In addition, the modeling of the extinction spectra of Au-CuS was carried out at a steady-state core size of 20 nm and a change in the shell thickness from 5 to 30 nm (Fig. 24.3b). It can be seen from the figures that extinction spectrum contains two main absorption peaks. For example, the first one with a low intensity is near 560 nm, which corresponds to the absorption peak of gold nanoparticles

Fig. 24.3 Dependence of extinction of nanoshells Au-CuS and CuS-Au on wavelength. (a, c) Core radius is varied from 20 to 45 nm. Shell thickness is varied from 5 to 30 nm. (b, d) Core radius is constant and equal 20 nm. Shell thickness is varied from 5 to 30 nm. Refractive index of surrounding medium is 1.0

and about 780 nm, which corresponds to the absorption of copper monosulfide for nanoshells with a core radius of 45 and a shell thickness of 5 nm. This second peak will also split into two peaks with the increase in the thickness of copper monosulfide, which indicates a pronounced plasmon–exciton coupling. It should be noted that the intensity of extinction of such nanoparticles will be the highest among those considered. Consequently, such nanoparticles can be successfully used to enhance the electromagnetic field, for example, in sensors applications. A somewhat different situation is observed when studying nanoshells of the CuS-Au type (Fig. 24.3c and d). Gold will play a dominant role here, since only one peak will be pronounced at wavelengths corresponding to the plasma absorption of gold nanoparticles. In addition, we see that the extinction intensity of such nanoparticles is lower than that of nanoshells of the Au-CuS type.

24.4 Conclusions

The dependences of extinction of monosulfide copper-based core–shell nanoparticles on wavelength were calculated. The study was carried out for dual plasmonic nanoparticles of the type of copper monosulfide-titanium dioxide, copper monosulfide-gold, and copper monosulfide-silver. It is shown that the core–shell ratio will affect both the position of the extinction maximum and the shape of the spectral curve for all considered core–shell nanoparticles. In case of core–shell based on titanium dioxide and copper monosulfide, there is plasmonic peak in infrared region. This peak splits into two under certain thicknesses core and shell. The nanoshells are characterized by two pronounced peaks in case of the metal and semiconductor materials combining. The first peak corresponds to the plasmon absorption maximum of the metal nanoparticles and the second one corresponds to the plasmon absorption maximum of the copper monosulfide nanoparticles. The second plasmon peaks can also split into two peaks at the given core–shell size ration. Such splitting can be explained by the appearance of the strong plasmon–exciton interaction. Researched core–shell nanoparticles demonstrate enhanced surface plasmon characteristics comparison to the nanoparticles, and it is useful for different sensors applications.

References

1. Ikumapayi OM, Akinlabi ET, Adeoye AOM, Fatoba SO (2021) Microfabrication and nanotechnology in manufacturing system–an overview. Mater Today: Proc 44:1154–1162
2. Khan S, Mansoor S, Rafi Z, Kumari B, Shoaib A, Saeed M, Shakeel F (2021) A review on nanotechnology: properties, applications, and mechanistic insights of cellular uptake mechanisms. J Molecular Liquids 118008
3. Pushparaj K, Liu W, Meyyazhagan A, Orlacchio A, Pappusamy M, Vadivalagan C, Balasubramanian B (2021) Nano-from nature to nurture: a comprehensive review on facets, trends,

perspectives and sustainability of nanotechnology in the food sector. Energy 122732

4. Cennamo N, Galatus R, Mattiello F, Sweid R, Zeni L (2016) Design of surface plasmon resonance sensor in plastic optical fibers based on nano-antenna arrays. Proc Eng 168:880–883

5. Yaremchuk I, Petrovska H, Fitio V, Bobitski Y (2018) Optimization and fabrication of the gold-coated GaAs diffraction gratings for surface plasmon resonance sensors. Optik 158:535–540

6. Samavati Z, Samavati A, Ismail AF, Rahman MA, Othman MHD, Yeganeh FN (2021) Optical fiber sensor for glycoprotein detection based on localized surface plasmon resonance of discontinuous Ag-deposited nanostructure. Opt Fiber Technol 62:102476

7. Bulavinets T, Kulpa-Greszta M, Tomaszewska A, Kus-Liśkiewicz M, Bielatowicz G, Yaremchuk I, Pązik R (2020) Efficient NIR energy conversion of plasmonic silver nanostructures fabricated with the laser-assisted synthetic approach for endodontic applications. RSC Adv 10(64):38861–38872

8. Yaremchuk I, Meškinis Š, Bulavinets T, Vasiliauskas A, Andrulevičius M, Fitio V, Tamulevičius S (2019) Effect of oxidation of copper nanoparticles on absorption spectra of DLC: Cu nanocomposites. Diam Relat Mater 99:107538

9. Bulavinets T, Varyshchuk V, Yaremchuk I, Bobitski Y (2017, August) Design and synthesis of silver nanoparticles with different shapes under the influence of photon flows. In: International conference on nanotechnology and nanomaterials, Springer Cham, pp 231–241

10. Kumar YR, Deshmukh K, Ali MMN, Abhijay G, Al-Onazi WA, Al-Mohaimeed AM, Pasha SK (2022) Structure, morphology and modelling studies of polyvinylalcohol nanocomposites reinforced with nickel oxide nanoparticles and graphene quantum dots. Environ Res 203:111842

11. Saravanan A, Kumar PS, Karishma S, Vo DVN, Jeevanantham S, Yaashikaa PR, George CS (2021) A review on biosynthesis of metal nanoparticles and its environmental applications. Chemosphere 264:128580

12. Pajor-Świerzy A, Szendera F, Pawłowski R, Szczepanowicz K (2021) Nanocomposite inks based on nickel-silver core–shell and silver nanoparticles for fabrication conductive coatings at low-temperature sintering. Colloids and Interf 5(1):15

13. Irani E, Yazdani E, Bayat A (2021) Enhancement and tuning of optical properties of CdTe/CdS core/shell quantum dots by tuning shell thickness. Optik 168198

14. Bulavinets T, Yaremchuk I, Bobitski Y (2016) Modeling optical characteristics of multi-layer nanoparticles of different sizes for applications in biomedicine. In: Nanophysics, nanophotonics, surface studies, and applications, Springer Cham, pp 101–115

15. Shishodia MS, Fainberg BD, Nitzan A (2011) Theory of energy transfer interactions near sphere and nanoshell based plasmonic nanostructures. Plasmonics: Metallic Nanostruct Their Opt Properties IX 8096:80961G-1–80961G-5

16. Kalele S, Gosavi SW, Urban J, Kulkarni SK (2006) Nanoshell particles: synthesis, properties and applications. Current Sci 1038–1052

17. Liang Z, Li X, Xie Y, Liu S (2014) 'Smart' gold nanoshells for combined cancer chemotherapy and hyperthermia. Biomed Mater 9(2):025012–1–025012–6

18. Tam F, Moran C, Halas N (2004) Geometrical parameters controlling sensitivity of nanoshell plasmon resonances to changes in dielectric environment. J Phys Chem B 108(45):17290–17294

19. Jiang X, Hu S, Li Z, Lv J, Si G (2016) Fabrication and characterization of plasmonic nanorods with high aspect ratios. Opt Mater 58:323–326

20. Liu Y, Yuan H, Kersey FR, Register JK, Parrott MC, Vo-Dinh T (2015) Plasmonic gold nanostars for multi-modality sensing and diagnostics. Sensors 15(2):3706–3720

21. Li M, Cushing SK, Liang H, Suri S, Ma D, Wu N (2013) Plasmonic nanorice antenna on triangle nanoarray for surface-enhanced Raman scattering detection of hepatitis B virus DNA. Anal Chem 85(4):2072–2078

22. Abid I, Bohloul A, Najmaei S, Avendano C, Liu HL, Péchou R, Lou J (2016) Resonant surface plasmon–exciton interaction in hybrid MoSe2@Au nanostructures. Nanoscale 8(15):8151–8159

23. Cao E, Lin W, Sun M, Liang W, Song Y (2018) Exciton-plasmon coupling interactions: from principle to applications. Nanophotonics 7(1):145–167
24. Fofang NT, Grady NK, Fan Z, Govorov AO, Halas NJ (2011) Plexciton dynamics: exciton-plasmon coupling in a J-aggregate-Au nanoshell complex provides a mechanism for nonlinearity. Nano Lett 11(4):1556–1560
25. Zhao W, Wang S, Liu B, Verzhbitskiy I, Li S, Giustiniano F, Oulton RF (2016) Exciton–plasmon coupling and electromagnetically induced transparency in monolayer semiconductors hybridized with Ag nanoparticles. Adv Mater 28(14):2709–2715
26. Scholes GD, Rumbles G (2011) Excitons in nanoscale systems. In: Materials for sustainable energy: a collection of peer-reviewed research and review articles from nature publishing group, World Scientific, pp 12–25
27. Luo X, Morrin A, Killard AJ, Smyth MR (2006) Application of nanoparticles in electrochemical sensors and biosensors. Electroanalysis 18(4):319–326
28. Achermann M (2010) Exciton-plasmon interactions in metal-semiconductor nanostructures. J Phys Chem Lett 1(19):2837–2843
29. Neogi A, Lee CW, Everitt HO, Kuroda T, Tackeuchi A, Yablonovitch E (2002) Enhancement of spontaneous recombination rate in a quantum well by resonant surface plasmon coupling. Phys Rev B 66(15):153305–1–153305–4
30. Toropov AA, Shubina TV, Belyaev KG, Ivanov SV, Kop'ev PS, Ogawa Y, Minami F (2011) Enhancement of excitonic emission in semiconductor heterostructures due to resonant coupling to multipole plasmon modes in a gold particle. Phys Rev B 84(8):085323–1–085323–9
31. Govorov AO, Bryant GW, Zhang W, Skeini T, Lee J, Kotov NA, Naik RR (2006) Exciton-plasmon interaction and hybrid excitons in semiconductor- metal nanoparticle assemblies. Nano Lett 6(5):984–994
32. Vasa P, Pomraenke R, Schwieger S, Mazur YI, Kunets V, Srinivasan P, Salamo G (2008) Coherent exciton–surface-plasmon-polariton interaction in hybrid metal-semiconductor nanostructures. Phys Rev Lett 101(11):116801–1–116801–4
33. Fedutik Y, Temnov VV, Schöps O, Woggon U, Artemyev MV (2007) Exciton-plasmon-photon conversion in plasmonic nanostructures. Phys Rev Lett 99(13):136802–1–136802–9
34. ZLiu Z, Zhong Y, Shafei I, Borman R, Jeong S, Chen J, Ye X (2019) Tuning infrared plasmon resonances in doped metal-oxide nanocrystals through cation-exchange reactions. Nature Commun 10(1):1−11
35. Xie Y, Carbone L, Nobile C, Grillo V, D'Agostino S, Della SF, Cozzoli PD (2013) Metallic-like stoichiometric copper sulfide nanocrystals: phase-and shape-selective synthesis, near-infrared surface plasmon resonance properties, and their modeling. ACS Nano 7(8):7352–7369
36. Sun S, Li P, Liang S, Yang Z (2017) Diversified copper sulfide (Cu 2–x S) micro-/nanostructures: a comprehensive review on synthesis, modifications and applications. Nanoscale 9(32):11357–11404
37. Sun M, Fu X, Chen K, Wang H (2020) Dual-plasmonic Gold@ copper sulfide core-shell nanoparticles: phase-selective synthesis and multimodal photothermal and photocatalytic behaviors. ACS Appl Mater Interfaces 12(41):46146–46161
38. Sun C, Liu M, Zou Y, Wei J, Jiang J (2016) Synthesis of plasmonic Au–CuS hybrid nanocrystals for photothermal transduction and chemical transformations. RSC Adv 6(31):26374–26379
39. Lv Q, Gao MY, Cheng ZH, Chen Q, Shen AG, Hu JM (2018) Rational synthesis of hollow cubic CuS@ Spiky Au core–shell nanoparticles for enhanced photothermal and SERS effects. Chem Commun 54(95):13399–13402
40. Khlebtsov NG, Dykman LA (2010) Optical properties and biomedical applications of plasmonic nanoparticles. J Quant Spectrosc Radiat Transfer 111(1):1–35

Chapter 25
Luminescent Properties of Opal–Active Dielectric Matrix Nanocomposites Activated by Ions of Rare-Earth Elements

O. V. Ohiienko, V. N. Moiseyenko, D. O. Holochalov, T. V. Shvets, and B. Abu Sal

25.1 Introduction and Background

Optical processes in nanostructured materials with a period close to the light wavelength are essentially different from those in bulk uniform media. The spontaneous emission spectrum is completely determined by the spectral distribution of transitions frequencies and the density of optical states within a region of these frequencies. The fabrication and research of the optical properties of new luminescent materials on the basis of synthetic opals are of both fundamental and practical interest. The properties of luminescent photonic crystals based on synthetic opals have been studied in numerous works [1–8]. The luminescence features of laser dyes [1–3], quantum dots, compounds of rare-earth elements in the pores of the opal matrix were studied [6]. The characteristic effects of the opal stopband and the density of optical states on the spectrum and the angular dependence of the luminescence intensity [9] are revealed. Of particular interest in this case are the luminescent properties of synthetic opals infiltrated with Eu^{3+} ions, in the spectrum of which narrow luminescence lines appear in the visible region of the spectrum, comparable with the width of the opal stopband.

O. V. Ohiienko (✉) · V. N. Moiseyenko · D. O. Holochalov · T. V. Shvets
Physics, Electronics and Computer Systems Department, Oles Honchar Dnipro National
University, Prospect Gagarina, 72, Dnipro 49010, Ukraine
e-mail: kombi21251@outlook.com

V. N. Moiseyenko
e-mail: vnmois@ukr.net

D. O. Holochalov
e-mail: holochalov_do@ffeks.dnu.edu.ua

B. Abu Sal
Applied Physics Department Faculty of Science, Tafila Technical University, Al-Eis, P.O. Box 40,
Tafila 66141, Jordan

The high sensitivity of the energy spectrum of europium to the local symmetry of the ion leads to a significant dependence of the luminescence characteristics on the structure of its local environment. Of particular interest from the scientific and practical points of view are opal nanocomposites–active dielectric activated by fluorescent centers.

This work is devoted to the study of the influence of nanocrystalline behavior and photonic crystal effects on the photoluminescence spectra of opal-$Bi_{12}SiO_{20}$, opal-Bi_2TeO_5, opal-$NaBi(MoO_4)_2$, and opal-TeO_2 nanocomposites infiltrated with salt europium (III) acetate hydrate ($C_6H_9EuO_6 \times H_2O$).

25.2 Sample Preparation and Experimental Techniques

25.2.1 Synthetic Opals and Nanocomposite Based on Them

Original synthetic opals were grown by natural sedimentation of monodisperse SiO_2 spheres synthesized by using the modified Stober technique [10]. We used the method of natural sedimentation in glass cylinders 4 cm in diameter under isothermal conditions at $T = 20\,°C$. The samples consisted of monodisperse α-SiO_2 globules forming a face-centered cubic (fcc) lattice. The center of the stopband at normal incidence for the original opal samples corresponded to 590–644 nm. To create luminescent centers, rare-earth ions were introduced into the samples of the initial opals. As fillers, we used 99.99% europium (III) acetate monohydrate ($C_6H_9EuO_6 \times H_2O$) from Aldrich (USA) in the form of a polycrystalline powder, as well as the oxides Eu_2O_3 and Dy_2O_3. To incorporate the $C_6H_9EuO_6 \times H_2O$ salt into the pores of the opal matrix, the opal samples under study were placed in a cuvette with an aqueous salt solution for 24 h, after which they were dried at room temperature. To fill the pores of the opal matrix with oxides Eu_2O_3 and Dy_2O_3, we used their solution in aqua regia. This process was carried out using the infiltration of the concentrated solutions of rare-earth element oxides (Eu_2O_3 and Dy_2O_3) in aqua regia (solution of nitric HNO_3 and perchloric HCl acids) into the samples. Next, the samples were heated to $110\,°C$ for an hour. The goal of this step was the evaporation of the liquid accumulated in synthetic opals through the process of infiltration. The opal pores were filled with active dielectrics from the melt [11, 12]. A polycrystalline powder of active dielectrics made from their single crystals was deposited on the (111) surface of an opal sample. Then the sample was placed in a resistance furnace, in which the temperature rose to the melting point of the powder. The melt penetrated the pores of the opal under the action of capillary forces. The melting temperature corresponded to the melting temperature of the corresponding active dielectric. Nanocomposites were manufactured: opal-$Bi_{12}SiO_{20}$, opal-Bi_2TeO_5, opal-$NaBi (MoO_4)_2$, and opal-TeO_2. The fact that the melt entered the pores of the opal was recorded by the shift of the maximum of the Bragg reflection band. The characteristics of the manufactured nanocomposites are presented in Table 25.1.

Table 25.1 Position of the center of the stopband for the obtained samples of opal–active dielectric nanocomposites

Sample	Interplanar distance (d), nm	Effective refractive index	Stopband center position, nm		
			$\Theta = 60°$	$\Theta = 30°$	$\Theta = 0°$
Opal-Bi_2TeO_5	250	1.52	624	717	760
Opal-$Bi_{12}SiO_{20}$	245	1.56	635	724	764
Opal-$NaBi(MoO_4)_2$	241	1.50	590	682	723
Opal-TeO_2	250	1.51	618	713	755
Original opal	245	1.27	455	572	621
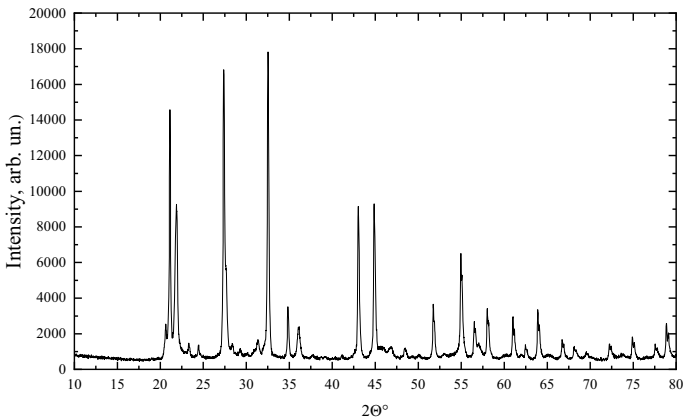
Fig. 25.1 X-ray diffractogram of the opal-$Bi_{12}SiO_{20}$ sample, on which the most intense peaks correspond to the crystal phase $Bi_4Si_3O_{12}$

25.2.2 X-ray Diffraction Patterns of Nanocomposites

XRD measurements on polycrystals powder of active dielectrics and composite on them were carried out on a X-ray diffractometer PW3040/60 using Cu K_α radiation ($\lambda = 1.5418°A$). Figures 25.1, 25.2 and 25.3 shows X-ray diffraction patterns of nanocomposites, which indicate the crystalline state of active dielectrics in the pores of the opal matrix.

25.2.3 Measurement of Luminescence Spectra

The photoluminescence spectra were excited by the radiation of a semiconductor laser ($\lambda_{ex} = 405$ nm) in the geometry "reflected" from the surface (111) of the
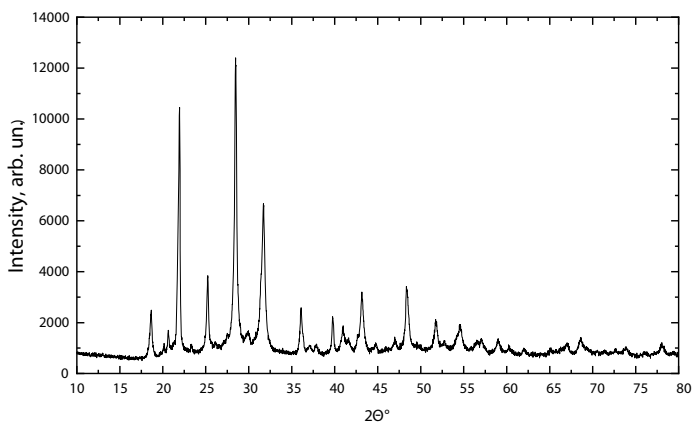
Fig. 25.2 X-ray diffractogram of the opal-Bi$_2$TeO$_5$
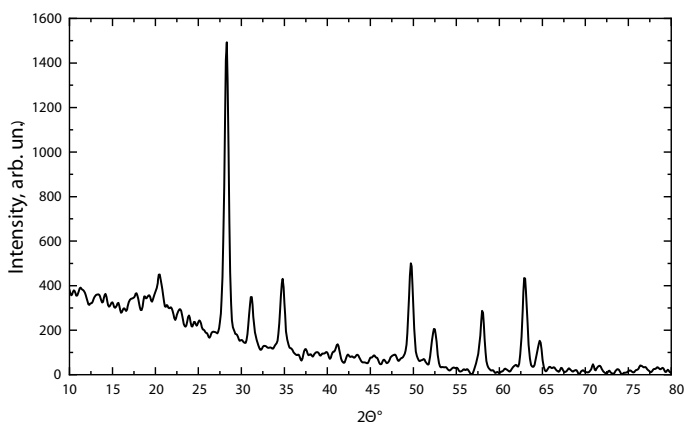
Fig. 25.3 X-ray diffractogram of the opal-NaBi(MoO$_4$)$_2$

sample. The angle between the direction of registration of luminescence and the [111] axis of the sample was 55° (Fig. 25.4).

The luminescence spectra were recorded using a modified laser spectrometer based on a DFS-12 double monochromator. The signal from the photomultiplier tube (FEU-79) after preliminary amplification was recorded in the mode of counting one-electron pulses with accumulation.

Fig. 25.4 Optical scheme of sample excitation and photoluminescence registration system: 1—spectrometer DFS-12, 2—photomultiplier FEU-79, 3—analog-to-digital converter, 4—PC
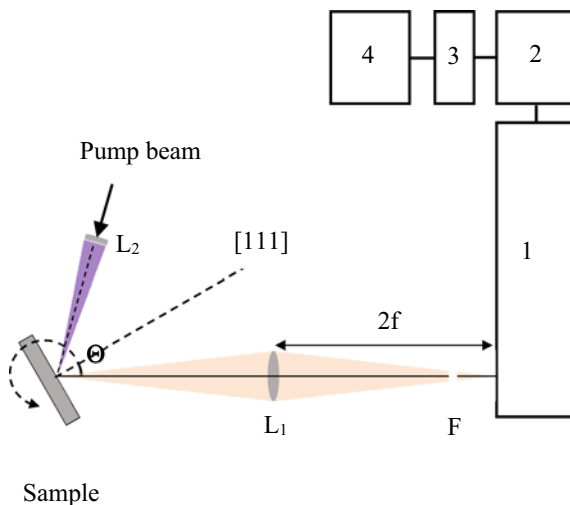
25.3 Luminescence Spectra

25.3.1 Luminescence of Initial Active Dielectric Crystals

Figure 25.5 shows the photoluminescence spectra of the $Bi_{12}SiO_{20}$ crystal and the photoluminescence spectrum of the opal-$Bi_{12}SiO_{20}$ nanocomposite.

It was found for the opal-$Bi_{12}SiO_{20}$ matrix nanocomposite that the substance in the pores of the opal is in a crystalline state (Fig. 25.1). In addition to the crystalline phase $Bi_{12}SiO_{20}$, the dominant presence of nanocrystals of bismuth orthosilicate $Bi_4Si_3O_{12}$, formed due to the interaction of the BSO melt with the structure of SiO_2 globules, was found in the pores of the opal. Figure 25.6 shows the photoluminescence spectra of the $NaBi(MoO_4)_2$ crystal and the photoluminescence spectrum of the opal-$NaBi(MoO_4)_2$ nanocomposite.

25.3.2 Luminescence of the Starting Compounds of Rare-Earth Elements

Figure 25.7 shows the luminescence spectra of the starting europium (III) acetate salt and europium oxide at room temperature.

The luminescence spectra demonstrate high intensity and radiative transitions characteristic of europium ions: forbidden electric-dipole transition $^5D_0 \rightarrow {}^7F_0$, magnetic-dipole $^5D_0 \rightarrow {}^7F_1$, and electric-dipole $^5D_0 \rightarrow {}^7F_2$. For all three transitions, additional splitting of the luminescence bands appeared.
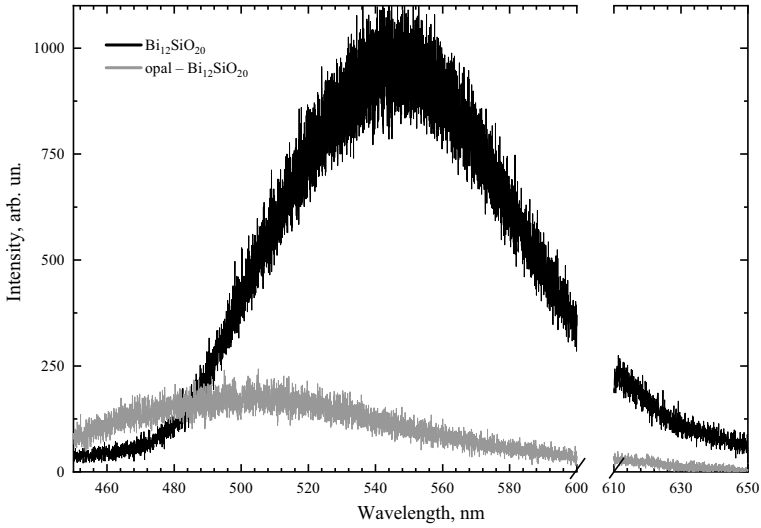
Fig. 25.5 Luminescence spectra of a sample of a $Bi_{12}SiO_{20}$ crystal (black curve) and an opal-$Bi_{12}SiO_{20}$ nanocomposite (gray curve) [13]
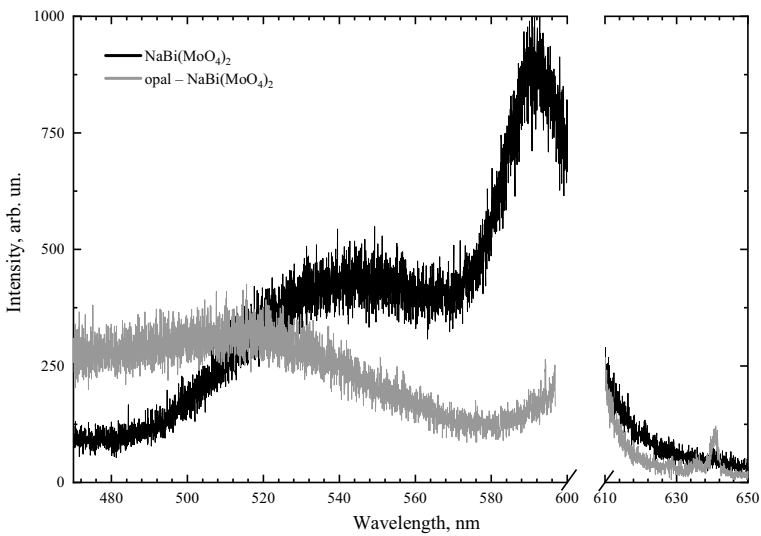

Fig. 25.6 Luminescence spectra of a sample of a crystal $NaBi(MoO_4)_2$ (black curve) and nanocomposite opal-$NaBi(MoO_4)_2$ (gray curve)
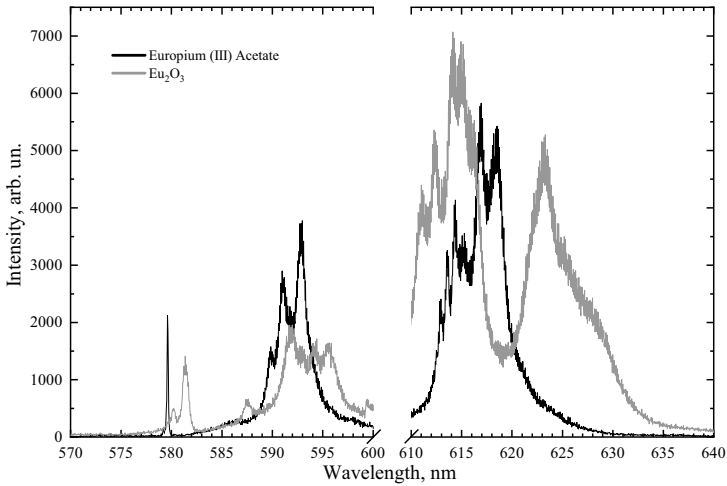
Fig. 25.7 Luminescence spectra of the initial europium (III) acetate salt and europium oxide at room temperature [14]

25.3.3 Luminescence of Rare-Earth Elements in the Pores of the Opal Matrix

Figure 25.8 shows the luminescence spectra of europium oxide in the pores of the opal matrix.
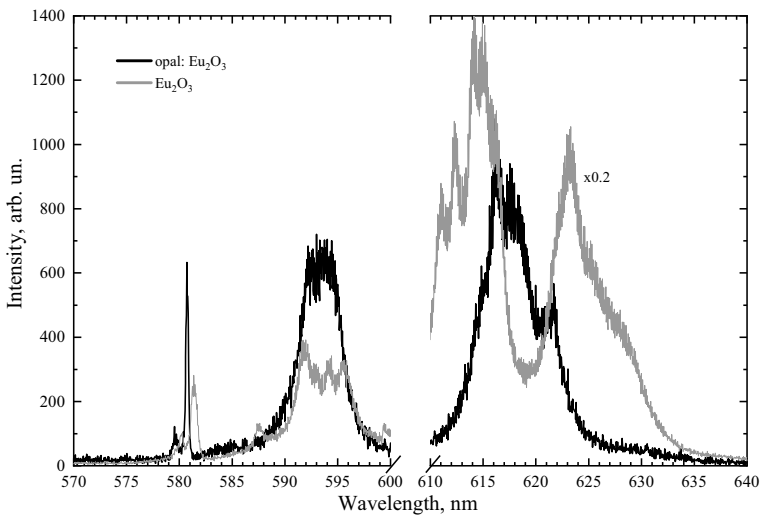
Fig. 25.8 Photoluminescence spectrum of opal sample infiltrated by europium oxide [14]
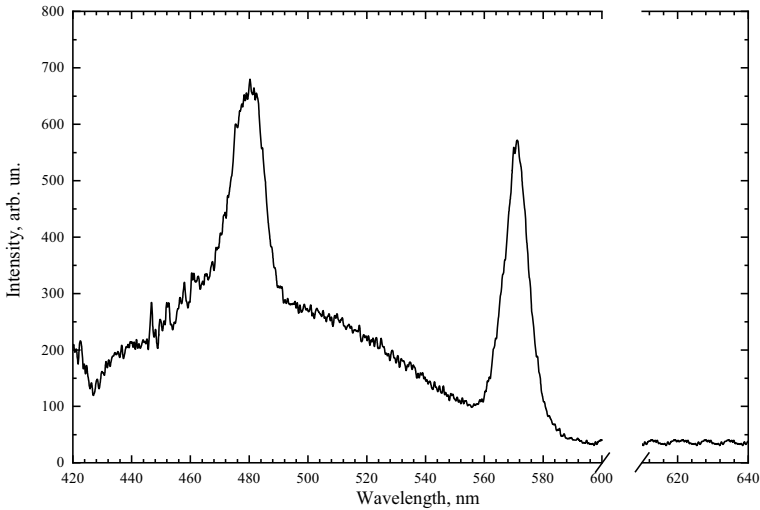
Fig. 25.9 Photoluminescence spectrum of opal sample infiltrated by dysprosium oxide [14]

Figure 25.9 shows the luminescence spectra of dysprosium oxide in the pores of the opal matrix.

On the spectrum of the sample infiltrated by europium (Fig. 25.8), there are distinctive europium lines at 580, 593, and 618 nm, which correspond to the typical transitions of this rare-earth element, such as $^{5}D_0 \rightarrow {}^{7}F_J$, where $J = 0, 1, 2$. Distinctive spectral lines of dysprosium luminescence at wavelengths of 480 and 572 nm are shown in Fig. 25.9. The maxima of these wavelengths correspond to the typical lines of luminescence of trivalent dysprosium—specifically transitions $^{4}D_{9/2} \rightarrow {}^{6}H_J$, where $J = \frac{13}{2}, \frac{11}{2}$. The luminescence spectra in Fig. 25.9 have a wide band on the range of 420–560 nm which is not present in pure and infiltrated by europium opal samples. It can be caused by the glow of the defects in opal matrix appeared as a result of dysprosium oxides infiltration [14]. The luminescence spectra of europium (III) acetate in the pores of synthetic opal at room temperature are shown in Fig. 25.10.

The spectrum demonstrates high intensity of europium radiative transitions:

- $^{5}D_0 \rightarrow {}^{7}F_0$—forbidden electro-dipole transition at wavelength interval from 575 to 581 nm;
- $^{5}D_0 \rightarrow {}^{7}F_1$—magnetic-dipole transition at wavelength interval from 581 to 605 nm;
- $^{5}D_0 \rightarrow {}^{7}F_2$—hypersensitive electro-dipole transition at wavelength interval from 605 to 635 nm.

Comparison of the luminescence spectra of europium ions in the pores of opal in the composition of the oxide (Fig. 25.8) and the salt $C_6H_9EuO_6 \times H_2O$ (Fig. 25.10) shows that in the latter case, a more detailed splitting of bands is manifested, which is due to the different coordination environment of europium ions. With an increase in
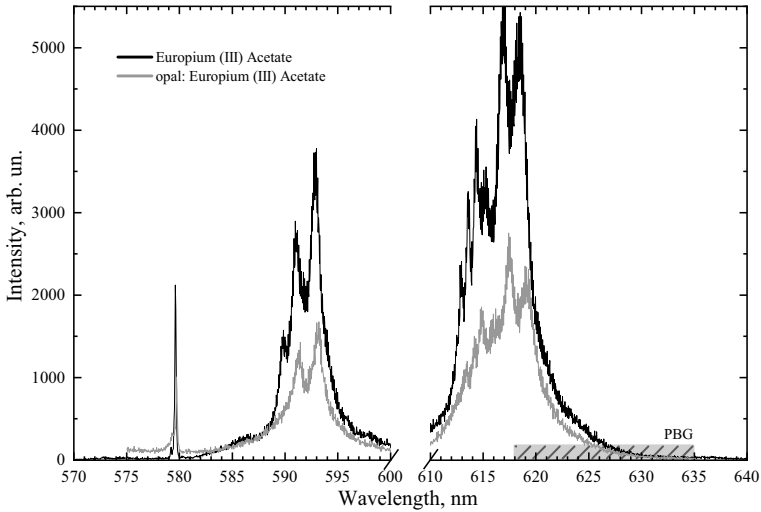
Fig. 25.10 Luminescence spectra of europium (III) acetate in the pores of synthetic opal. For comparison, the luminescence spectrum of the initial europium (III) acetate salt is given, and the position of the opal stopband is indicated [14]

the annealing temperature of the opal-salt $C_6H_9EuO_6 \times H_2O$ sample, in comparison with the spectra of the powder and its aqueous solution, the integrated luminescence intensity of europium (III) acetate in the pores of the opal decreases, and the spectral intensity distribution within each band acquires continual character (Fig. 25.11).

It should be noted that the changes in the salt spectra in the opal pores are caused not only by a change in the coordination environment of Eu^{3+} ions as a result of
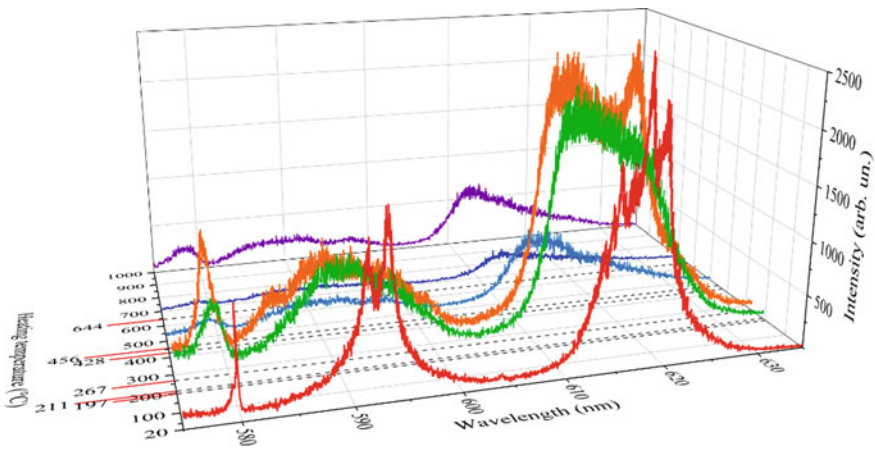
Fig. 25.11 Luminescence spectra of europium (III) acetate in the opal pores for different annealing temperatures [14]
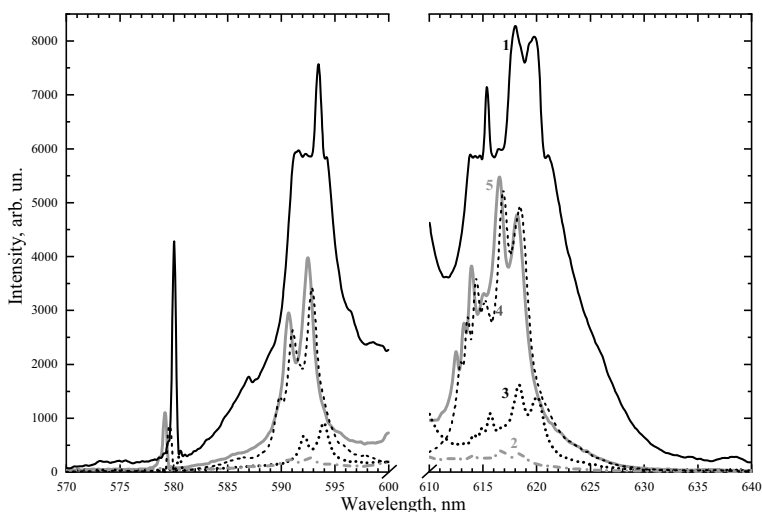
Fig. 25.12 Luminescence spectra of opal–active dielectric composites infiltrated with europium (III) acetate salt: 1—opal-$Bi_{12}SiO_{20}$: Eu^{3+}; 2—opal-Bi_2TeO_5: Eu^{3+}; 3—opal-$NaBi(MoO_4)_2$: Eu^{3+}; 4—opal-TeO_2: Eu^{3+}; 5—opal: europium (III) acetate salt

thermal decomposition of the salt, but also by the influence of photonic crystal effects [14].

25.3.4 Luminescence of Rare-Earth Elements in the Pores of Nanocomposites

Figure 25.12 shows the luminescence spectra of opal–active dielectric composites infiltrated with europium (III) acetate salt.

All the luminescence spectra of europium ions in the pores of the nanocomposites were shifted to longer wavelengths by 2–3 nm in comparison with the luminescence spectrum of the initial europium (III) acetate salt (Fig. 25.7). In the measured spectra, radiative transitions in the energy spectrum of europium ions $^5D_0 \rightarrow {}^7F_0$, $^5D_0 \rightarrow {}^7F_1$, and $^5D_0 \rightarrow {}^7F_2$ were manifested for wavelengths of 580 nm, 592 nm, and 619 nm, respectively. This may be due to the influence of the position of the stopband (Table 25.1) and the spectral distribution of the density of optical states, as well as the nanocrystalline environment of europium ions in the pores of the opal matrix. Among the nanocomposites containing bismuth, the highest luminescence intensity was observed in the opal sample—$Bi_{12}SiO_{20}$: Eu^{3+}. This is due to the participation of Bi^{3+} ions in optical processes as a coactivator of the luminescence of Eu^{3+} ions (Fig. 25.5).

25.4   Conclusions

The influence of coordination and crystalline environment, as well as photonic-crystalline effects on the luminescence spectra of ions of rare-earth elements in the pores of nanocomposites based on synthetic opals, has been studied. To study the effect of the nanocrystalline environment on the luminescence spectra of rare-earth ions in the opal pores, dielectrics were additionally introduced by the melting method. Opal-$Bi_{12}SiO_{20}$, opal-Bi_2TeO_5, opal-$NaBi(MoO_4)_2$, and opal-TeO_2 nanocomposites were made, and their own luminescence spectra were measured. The luminescence spectra of europium and dysprosium ions in the pores of synthetic opals and europium ions in the pores of nanocomposites were measured. High intensity radiation transitions for europium ions $^5D_0 \rightarrow {}^7F_0$, $^5D_0 \rightarrow {}^7F_1$, $^5D_0 \rightarrow {}^7F_2$, and less intense transitions for dysprosium ions $^4D_{9/2} \rightarrow {}^6H_{13/2}$, $^4D_{9/2} \rightarrow {}^6H_{11/2}$ were revealed. The spectral intensity distribution and the band splitting in the luminescence spectra of the starting compounds and compounds in the pores of the nanocomposites differed significantly. The influence of the coordination and nanocrystalline environment, as well as the position of the stop zone and the density spectrum of optical states on the luminescence spectra is revealed. A significant increase in the integral luminescence intensity of Eu^{3+} ions in the pores of the opal-$Bi_{12}SiO_{20}$ nanocomposite was found, which is due to the co-activation of luminescence due to Bi^{3+} ions.

References

1. Bechger L, Lodah P, Vos WL (2005) Directional fluorescence spectra of laser dye in opal and inverse opal photonic crystals. J Phys Chem B 109:9980–9988
2. Nikolaev IS, Lodahl P, Vos WL (2005) Quantitative analysis of directional spontaneous emission spectra from light sources in photonic crystals. Phys Rev A 71:053813
3. Alimov OK, Basiyev TT, Olovskiy UV, Osiko VV, Samoylovich MI (2008) Conversion of the luminescence of laser dyes in opal matrices to stimulated emission. Quantum Electron 38(7):665
4. Gruzintsev AN, Yemel'chenko GA, Masalov VM, Yakimov YeYe, Barthou C, Maitre A (2009) Lyuminestsentsiya kvantovykh tochek CdSe/ZnS, infil'trovannykh v opalovuyu matritsu. Fizika i tekhnika poluprovodnikov 43(2):209–213
5. Gadzhiyev GM, Golubev VG, Zamoryanskaya MV, Kurdyukov DA, Medvedev AV, Merz J, Mintairov A, Pevtsov AB, Sel'kin AV, Travnikov VV, Sharenkova NV (2003) Fotonnyye kristally na osnove kompozitov opal-GaP i opal-GaPN: polucheniye i opticheskiye svoystva. Fizika i tekhnika poluprovodnikov 37(12):1449–1455
6. Gorelik VS, Ivicheva SN, Lepnev LS, Litvinova AO, Moiseenko VM (2015) Vtorichnoye izlucheniye v globulyarnykh fotonnykh kristallakh na osnove opalovykh matrits, zapolnennykh yevropiyem. Neorg Mater 51(6):583–587
7. Boyko VV, Dovbeshko GI, Fesenko OM, Gorelik VS, Moiseyenko VM, Romanyuk VR, Shvets TV, Vodolazkyy P (2011) New optical properties of synthetic opals infiltrated by DNA. Mol Cryst Liq Cryst 535(537888):30–41
8. Dovbeshko GI, Fesenko OM, Boyko VV, Romanyuk VR, Gorelik VS, Moiseyenko VM, Sobolev VB, Shvalagin VV (2012) Secondary emission from synthetic opal infiltrated by colloidal gold and glycine. Ukr J Phys 57(2):154–158

9. Boiko VV, Dovbeshko GI, Dolgov L, Kiisk V, Sildos I, Loot A, Gorelik VS (2015) Angular shaping of fluorescence from synthetic opal-based photonic crystal. Nanoscale Res Lett 10(97)
10. Stöber W, Fink A, Bohn E (1968) Controlled growth of monodisperse silica spheres in the micron size range. J Colloid Interface Sci 26(2):62–69
11. Moiseienko V, Derhachov M, Abu Sal B, Holze R, Brynza M (2017) Nanocomposites on the base of synthetic opals and nanocrystalline phases of Bi-containing active dielectrics. Springer Proc Phys 50(195):661–674
12. Moiseienko VM, Gorelik SV, Bilal Abu Sal, Ohiienko OV, Golochalov DO (2019) Luminescent properties of nanocomposite - $Bi_{12}SiO_{20}$, filled with $C_6H_9EuO_6 \times H_2O$. J Phys Conf Ser 1348:012096
13. Posmahnyi SV, Ohiienko OV, Shvets TV (2018) Investigation of the photoluminescence spectra of rare-earth elements in pores of an opal matrix. J Phys Electron 2:67–72
14. Ohiienko OV, Moiseyenko VM, Shvets TV (2020) Molecular crystals and liquid crystals, vol 701

Chapter 26
Nanostructured Optical Composites of $TiO_2(C_3N_4Ox)$/PANI for Photocatalytic Application

M. M. Zahornyi, O. M. Lavrynenko, O. Yu. Pavlenko, M. E. Bondarenko, P. M. Silenko, Yu. M. Solonin, O. Y. Khyzhun, T. F. Lobunets, and A. K. Melnyk

26.1 Actuality

The work is devoted to TiO_2 $(C_3N_4O_x)$/PANI materials with effective optical properties. It has been found that the bandgap decreased from 3.2 to 2.3 eV in nanocomposites, respectively. The one-step nanostructured composites synthesis can be used as a cost-effective way to avoid the disadvantages of each component and realize the synergistic effect with heterojunction to enhance photocatalytic activity.

The researches have been shown that the synergistic effect of the combination g-C_3N_4 and TiO2 (anatase) led to an improvement in the absorption of visible light and further enhances photocatalytic activity, in particular, for the inactivation of bacteria in water under the influence of visible light. However, when we use g-C_3N_4/TiO_2 and g-C_3N_4, the limited use of solar energy is possible because they exhibit photoactivity in the near-blue visible region only (wavelength less than 460 nm).

We suppose that combining O-doped g-C_3N_4 with TiO_2 and polyaniline is a good strategy to obtain a new effective semiconductor photocatalyst.

Function components of synthesized nanocomposites:

1. The synthesized titanium dioxide nanoparticles have a virucidal and antiviral effect against adenovirus serotype 5. (https://doi.org/10.15407/microbiolj81.05.073). Such nanoparticles have a good application for photoelectrocatalysis process (https://doi10.15421/081.914).

M. M. Zahornyi · O. M. Lavrynenko (✉) · O. Yu. Pavlenko · M. E. Bondarenko · P. M. Silenko · Yu. M. Solonin · O. Y. Khyzhun · T. F. Lobunets
I.N. Frantsevich Institute for Problems of Materials Science of NASU (IPMS), Kyiv, Ukraine
e-mail: alena.lavrynenko@gmail.com

A. K. Melnyk
Institute for Sorption and Problems of Endoecology, Kyiv, Ukraine
e-mail: mak106@ukr.net

2. The combination of PANI nanoparticles with TiO_2 will create an excited-state of electron (e^-) and hole ($h+$) pairs, that react with O_2 and water vapor in the atmosphere to produce superoxide ions (O^{2-}) and hydroxyl radicals (OH·) under irradiation. Both O_2^-, OH· are extremely powerful agents in the destruction of toxic chemical compounds, bacteria cells to form CO_2 and water. In addition, polyaniline with a mesoporous structure, taking into account the electrical charge of microorganisms and products of their destruction through the regulation of electrical potential, will allow us to actively influence the adsorption of microorganisms in the first stage, their inactivation thereby increasing the intensity of the whole process, as well as the desorption of products of their destruction. This makes it possible to increase the performance of the photocatalyst and the duration of its operation until its next regeneration. Due to electronic structure and conductivity, PANI produces important h^+.

3. Defects in the structure of $C_3N_4O_x$ with a good optical characteristic allow us to combine it with TiO_2 and PANI to increase the optical and photocatalytic activity for use in optics and disinfection air.

26.2 Introduction

Conducting polymers find increasing use in various electronic devices, such as chemical sensors, light-emitting diodes, electrochromic displays. Among these polymers, polyaniline (PANI) occupies a special place, due to: (1) availability and ease of synthesis, (2) resistance to oxidation in air, and, finally, (3) PANI exhibits several properties, such as multicolor electrochromism, chemical sensitivity, and inherent properties in metals to semiconductors [1].

The TiO_2 and polyaniline complex have become the hot research field. TiO_2 nanomaterials have high catalytic activity, good stability, high yield hydroxyl radicals, light corrosion in the anticorrosion coatings, water purification, and bacteria sterilization [2]. Polyaniline has a good environmental stability in the visible region and has energetic absorption, strong electron donors, and excellent hole transport material. When both efficient composite, the contact interface will form a heterojunction, can not only increase the separation efficiency of the light-generated charge, but the spectral response can broaden the range of composite materials to improve the utilization of sunlight [3]. In previous publications, it has been shown that TiO_2 is an excellent photocatalyst due to its high chemical stability and photocatalytic activity. But TiO_2 has a wide bandgap of 3.2 eV, which restricts its use to UV light occupies only 3–5% of solar energy utilization. So, it is important to modify the optical response of TiO_2 from UV to visible light range by shortening its bandgap [4–9]. However, TiO_2, Fe_3O_4 photocatalytic activity under Vis (>400 nm) can be increased by doping [10, 11]; and thus, numerous groups utilize transition metal ions, such as Fe, Au, Ag, V, Cr, and Ni, to hinder the recombination process [5–7] and no metal elements (C, S) [8].

Recently, conducting polymers showed great potential as photosensitizers at UV action due to its low bandgap and π-π^* transition which the electron can be excited from highest occupied molecular orbital (HMO) to lowest unoccupied molecular orbital (LUMO) [12, 13].

Zhu et al. reported the photocatalytic degradation of methyl orange using polythiophene/titanium dioxide composites [14]. Gu et al. reported the photocatalytic degradation of Rhodamine B using a novel TiO_2-Polyaniline composite [15]. It was found that the prepared composites were found to be a very efficient photocatalysts under visible light irradiation.

The present study [4] was undertaken to evaluate the degradation of phenol and p-cresol as recalcitrant aromatic compounds in abattoir wastewater using TiO_2/ZnO composite doped by PANI. Cleaning detergents and residual blood were the main sources of organic matter in wastewater. The method used to prepare the composite was "in situ" chemical oxidative polymerization of aniline and was tested on an annular reactor fitted with a 25 W UV-C lamp.

PANI/TiO_2 composites can be prepared by the chemical oxidation of aniline in the presence of TiO_2 particles. Generally, aniline oxidation can yield different products as oligomers and oxidation products with an amino group in the ortho-position [16], which presents imperfections that might influence aggregate size. In addition, PANI properties were shown to be perturbed when monomers with an amino group in the ortho-position were added to the synthesis solution. However, in the literature, the impact of the initial synthesis conditions on the in situ PANI/TiO_2 synthesis has not been clarified yet [1, 17, 18].

g-C_3N_4 presents a partly similar effect to the incorporation of nitrogen atoms in the carbon matrix, which would improve the electron-donor properties, surface polarity, electrical conductivity, and wettability in the electrolyte, resulting in efficient charge transfer with polymer matrix [19]. These characteristics of the g-C_3N_4 and PANI make them ideal materials to reduce the recombination rate of photoinduced e^-/h pairs and enhance the production of the active radical species for the achievement of the highest photocatalysis. Recently, the combination of the TiO_2, g-C_3N_4, or PANI with other materials has been synthesized to make the binary and ternary photocatalyst [20].

Harvesting solar light based on graphite-like g-C_3N_4 semiconductor materials for the production of renewable energy, wastewater treatment, and effectively removing biohazards is considered a promising solution to address the imperative energy and environmental issues [21–24]. Currently, various bandgap-engineering strategies, including non-metal doping, especially by oxygen, are used to further enhance the light-harvesting capability of g-C_3N_4 [24–27]. Thus, the O-g-C_3N_4 catalyst exhibited outstanding photocatalytic activity toward overall water splitting and intractable organic pollutant degradation with simultaneous H_2 production under visible light [25]. For example, ozone-treated carbon nitride increases photocatalytic rhodamine B (RhB) degradation constants by approximately 6 times [26], accelerating the photodegradation of methylene blue by a factor of 5 times and 2 times accelerates the generation of H_2 compared with untreated graphitic carbon nitride [27]. It is assumed [28] that the significant enhancement of the photocatalytic activity of

O-modified carbon nitride is ascribed to the synergistic effects of narrowed bandgap and improved charge transfer efficiency.

Unfortunately, the single-layer g-C_3N_4 is easily reduced due to the van der Waals force, which leads to a low specific power and energy density [29]. Therefore, coupling g-C_3N_4Ox with PANI may be an effective strategy to overcome both limitations.

Herein, we report a facile method synthesis of PANI/$C_3N_4O_x$ (TiO_2) composites via an "in situ" chemical oxidative polymerization of aniline hydrochloride monomer in the presence of g-C_3N_4 (O ~ 5%), anatase. The prepared hybrid material took full use of the characteristics of PANI and $C_3N_4O_x$, with specific morphology and optical properties of prepared samples.

26.3 Experimental Part

Materials. All reagents and solvents were purchased from commercial sources.

Instrumentation. Powder X-ray diffraction was performed using Bruker A8 advanced with monochromatized CuKα radiation with an accelerating voltage of 40 kV. Polymerization medium with different oxide nanoparticles represented by homogenizer ULAB2200 (Germany) at speed of $300 \, min^{-1}$. High-resolution electron microscopy and EDS were performed with MIRA 3 TESCAN. X-Ray photoelectron spectroscopy (XPS) was done with Surface Nano Analysis Company SPECS (Germany). All UV–visible spectroscopic analysis done on PerkinElmer Lambda Bio 35 UV–Vis. EPR spectra of systems were recorded on an X-band spectrometer Bruker Elexsys E580 at temperature 298 K; spectra recording conditions were following: frequency—9.38 GHz; microwave power—2 mW; modulation intensity—from 0.1 to 1G with modulation frequency 100 kHz; scan width—100 G; and resolution—1024 points. All measurements were performed using variable temperature unit BVT3000; every value was set for at least 3 min, the stability of measurements was ± 0,2 K.

26.4 Synthesis of TiO_2 Nanoparticles and Polyaniline

Titanium dioxide (anatase) is obtained from $TiO(OH)_2$ raw material that is a product of the intermediate stage of the titanium concentrates and slags processing "Sumykhimprom" Compony. Characteristics of TiO_2 nanoparticles are presented. https://doi.org/10.15407/microbiolj81.05.073.

Polyaniline synthesis was carried out according to methodic [12] using oxidative radical polymerization at 0 °C.

26.5　Modifications of TiO_2 Followed by Polymerization with Layer Polyaniline

PANI/TiO_2, PANI/$C_3N_4O_x$ formed by the in situ polymerization method. First, nanoparticles of TiO_2, $C_3N_4O_x$ were modified by the water solution of aniline hydrochloride (GHAn) using homogenizer ULAB2200 (Germany) at speed of $300\ min^{-1}$ during 1 h. Then, the APS solution was added dropwise at 0 °C. Polymerization on surface oxide nanoparticles was carried out at pH medium 2–4 depending on the GHAn content in the mixture. The in situ polymerization process resulted in a dark green product. After that, the obtained nanocomposites were washed with deionized water, acetone, ethanol, respectively. Lastly, nanocomposites were dried at 50 °C for 24 h.

26.6　Synthesis of Doped $O\text{-}C_3N_4$

$C_3N_4O_X$ (~ 5 wt% O) powder was obtained following the development in Frantsevich Institute for Problems of Materials Science of the National Academy of Sciences of Ukraine (IPM NASU)—the one-step method for the synthesis oxygen modified graphite-like carbon nitride from various precursors [27, 30–32, 33]. Note that another known method for producing oxygen-doped carbon nitride suggests a two-stage process since the synthesis involves post-treatment of the presynthesized undoped g-C_3N_4 with hydrogen peroxide, ozone, or nitric acid [31, 32, 34–36]. According to the proposed in IPM NASU [30] facile one-step procedure, C_3N_4Ox (~ 5 wt% O)-powdered product was synthesized by the pyrolysis of melamine at the presence of a fixed volume of air. To produce a partially oxidized product, the melamine in the open ceramic crucible occurred in a tubular quartz reactor. For this experiment, the synthesis of O-doped carbon nitride was carried out at heating of ceramic crucible up to 560 °C under ambient pressure.

26.7　Results and Discussion

It has been shown that different concentrations of oxidizer in the reaction mixture with monomer and acid medium change the morphology of the PANI. A ratio of oxidizer/monomer 1.25 allows us to obtain the PANI [12] with a developed mesoporous structure (an average pore size of 10–14 nm). So, this ratio is used by us for PANI-$TiO_2(C_3N_4O_x)$ synthesis.

At first 10 min, with the addition of an oxidizer, the pH of the mixture decreased to 2.5. After adding all amounts of oxidizer, the pH was 2.45 and 2.3 (green mixture with precipitation). As we can see, the polymerization behavior of the monomer

Table 26.1 Parameters for polymerization "in situ" *on the TiO₂, C₃N₄Ox nanoparticles*

Sample No.	Monomer (mg)	pH	t (min) (polymerization)
1	25	2.75	25
2	50	2.37	30
3	100	2.45	–
4	150	2.6	35
5	25	3.2	30
6	50	–	15
7	100	2.3	30

on the surface of TiO_2, $C_3N_4O_x$ is different due to defects on the surface of such nanopowders and the molecular weight of the polymer layer (Table 26.1).

26.8   XPS_SEM

It can be seen that the surface of both TiO_2 and $C_3N_4O_x$ promotes the rapid decomposition of the oxidizer ammonium persulfate with the formation of free radicals formed on the surface of nanoparticles. The monomer itself is adsorbed on its surface at low temperature, while protons with hydroxyl groups are also present on the surface of TiO_2 and $C_3N_4O_x$ during polymerization in an acidic medium (Fig. 26.1a–c). For example, the survey X-ray spectrum of the sample PANI-$C_3N_4O_x$ (No. 6) (Fig. 26.1b) contains four signals that correspond to C1s, N1s, O1s, and S2s, 2p spectral lines.

The surface of $C_3N_4O_x$ particles is covered with a layer of polymer. This fact explains the weak signal intensity for element N (Fig. 26.1c) and the strong signal intensity for element C. We can assume a conjugation between the polymer and $C_3N_4O_x$.

26.9   XRD

The PANI loaded on the porous g- $C_3N_4O_x$ sheet was confirmed by X-ray diffraction too (Fig. 26.2). The neat PANI shows partial crystallinity with at least three Bragg diffraction peaks (curve 2). The crystalline reflex at $2\theta=15°$ is indicative of the crystalline structure of the emeraldine salt. The broad bands centered at $2\theta = 20.42°$ and 25.38° are the characteristic Bragg diffraction peaks of PANI. For porous g-$C_3N_4O_x$ (curve 1), the XRD peak at 27.5 can be indexed as the (002) diffraction plane, which belongs to the stacking distance of the conjugated aromatic system. Another pronounced additional peak was found at 13.1, relating to an in-plane structural packing motif, such as the hole-to-hole distance of the nitride pores in the crystal. In the case of porous g-C_3N_4/PANI composite (curve 3), the peak of the porous
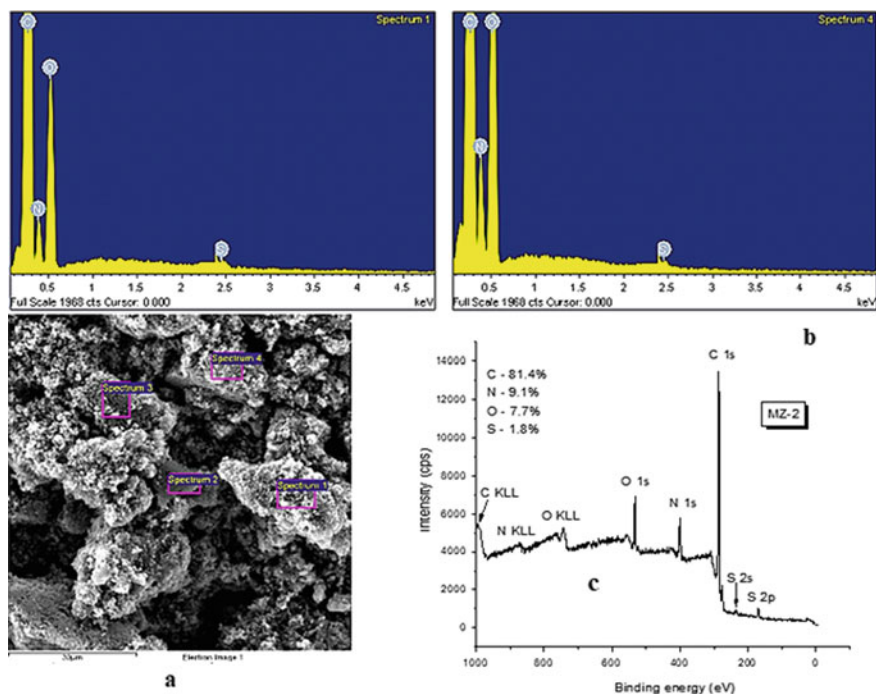
Fig. 26.1 Total analysis structure of PANI-C$_3$N$_4$O$_x$ (sample 6). **a** SEM image surface. **b** EDS spectra. **c** Total XPS spectrum

g-C$_3$N$_4$ sheet stacking disappeared, suggesting that the porous g-C$_3$N$_4$ has almost no aggregation and is fully used as the substrate of PANI to produce composites. Two broad peaks of the porous g-C$_3$N$_4$/PANI composite centered at $2\theta = 20.12°$ and $25.26°$ were almost the same as that of pure PANI. In the case of a porous composite g- C$_3$N$_4$/PANI (curve 3, Fig. 26.2), the peak in the region of 13.1–13.5° disappears, the intensity of the reflex (002) decreases, the peak expands, and we assume that the structure is disordered as for PANI@g-C$_3$N$_4$ (curve 4, Fig. 26.2). A similar pattern occurred for the samples, which were synthesized by the authors in hydrochloric acid by polymerization of aniline on the surface of carbon nitride nanoparticles g-C$_3$N$_4$ [35].

26.10   TEM and SEM

The morphological studies have shown with increasing concentration of the polymer formed particles in the form of rolled balls. The titanium dioxide particles themselves are predominantly spherical. In Fig. 26.3a–d shows the capture of spherical TiO$_2$
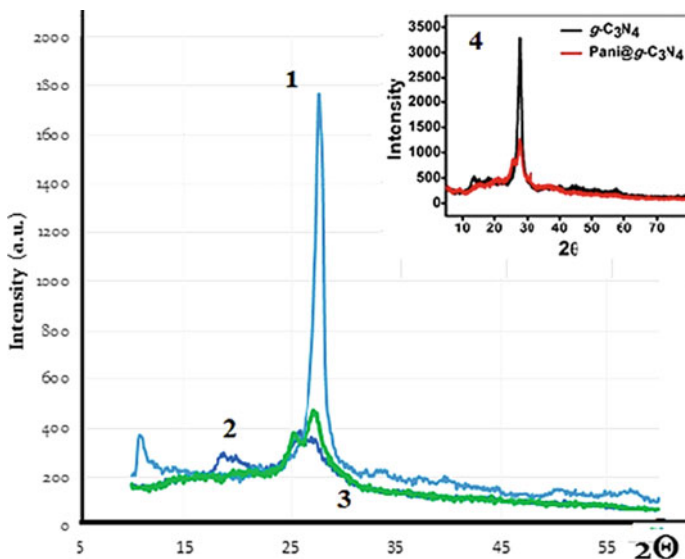
Fig. 26.2 XRD patterns of systems: 1—$C_3N_4O_x$; 2-PANI: 3—C_3N_4/PANI (sample 6)

particles, $C_3N_4O_x$ plates by the polymer mesh. The polymer itself is formed by tubular nanoparticles with a diameter of 70–100 nm with different orientation.

SEM images have shown that spherical TiO_2 nanoparticles, depending on the concentration of the polymer can be covered by half or completely with a polymer grid PANI (Fig 26.4).

26.11 Optical Properties Study

For anatase intensively band absorbance in short wave numbers UV region. For pure conductive polymer, two intensive bands especially in the region are visible of 550–600 nm (polymer has conjugated system bonds). The band absorbance at 402–420 nm is due to the polaron-π^* transition in polyaniline [12]. When added smaller concentration polymer, the absorbance band was wide in comparison with pure TiO_2 and polymer. We can see the physicochemical interaction between TiO_2 and polymer. TiO_2 anatase can absorb light with wavelengths below 400 nm. Pure PANI presents the characteristic band at 350–415, 550–600 nm which are attributed to the π-π^* transition of the benzenoid ring, π-polaron exaction transition of the quinonoid rings, respectively. So, doped PANI has high absorption either in the visible light region. For the sample of composite (Fig. 26.5), we observed two bands of absorption at 250–300 nm and 350–500 nm and 550–750 nm in comparison with spectra of [12]. Maybe there is a strong π-π^* transition of the benzenoid ring and interaction between anatase (10 nm) and doped polyaniline. It is possible
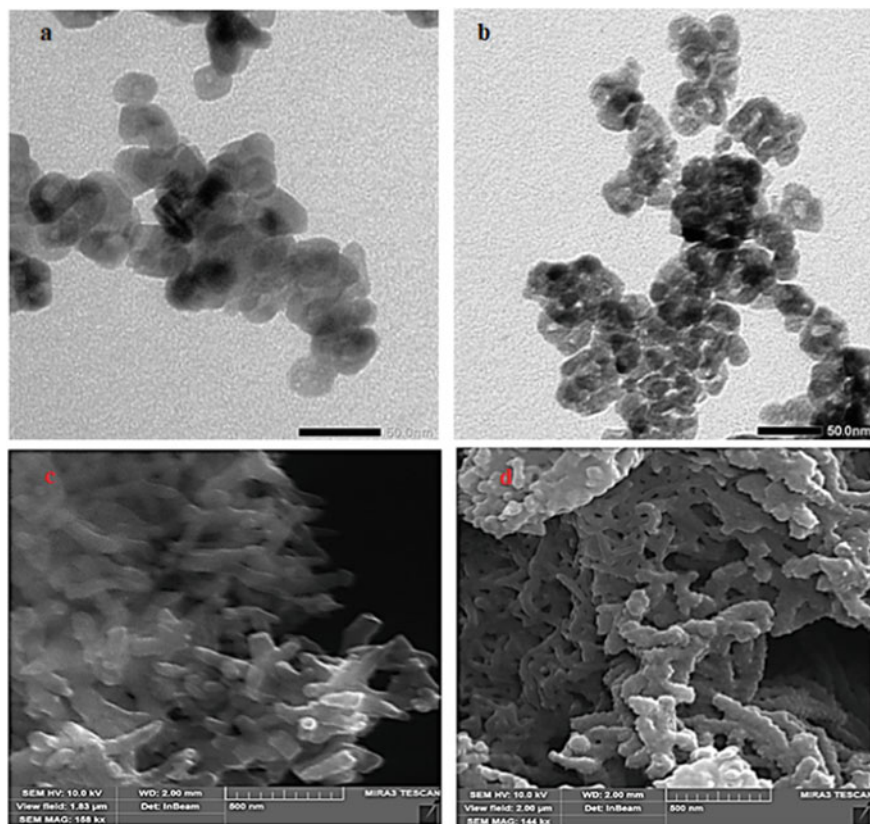
Fig. 26.3 Morphology of TiO$_2$ (C$_3$N$_4$O$_x$)/PANI systems. **a** TEM image of TiO$_2$ (scale 50 nm). **b** TEM image of TiO$_2$/PANI (scale 50 nm). **c** SEM image of PANI (scale 500 nm). **d** SEM image of C$_3$N$_4$O$_x$/PANI (scale 500 nm)

because of charge carrier delocalization due to the extended chain conformation of the PANI. PANI-TiO$_2$ nanocomposites produce more electron–hole pairs under light illumination, and this is expected to increase the photocatalytic activity.

The semiconductor C$_3$N$_4$O$_x$ consists of carbon atoms and nitrogen, which enables its functionalization in wide limits to control the reactivity of the material. Graphite carbon nitride is the most stable modification of carbon nitride, which attracts the interest of researchers due to its unique electronic properties, catalytic, including photocatalytic activity. Ideal carbon nitride contains only C–N bonds and is a π-conjugated polymer "poly (tri-triazine)". Given the aromatic nature of the component blocks (s-triazine rings), the corresponding 2D polymer is capable of forming π-conjugated flat layers, similar to that of graphite.

The hydrogen presence in the structure of carbon nitride testifies to its incomplete condensation and the existence of surface defects. It gives catalytic properties to carbon nitride in the reactions of hydrogenation, oxidation, transesterification,

Fig. 26.4 Morphology of TiO$_2$/PANI: No 2 (**a**), No 3 (**b**)

a

b
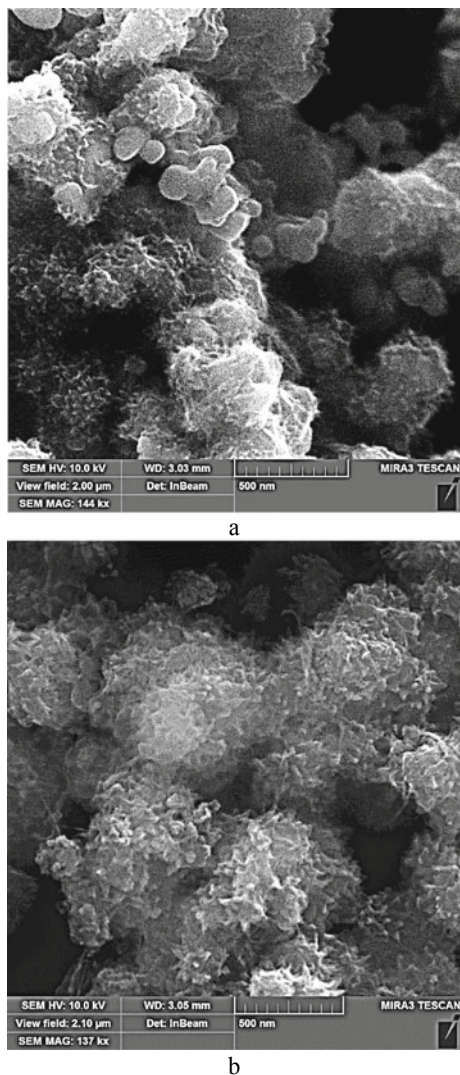
etc. Surface structural defects of carbon nitride, TiO$_2$, C$_3$N$_4$O$_x$ (EPR) can act as active centers and provide the possibility of additional chemical modification of the surface material for purposeful regulation of the structure of catalytically active systems and for performing heterogeneous catalytic reactions [36, 37]. The high nitrogen content of carbon nitride makes it possible to use carbon nitride as a major non-metal catalyst. Besides, the deposition of nanoparticles of metal oxides, metals, in particular noble, on graphitic carbon nitride, TiO$_2$ increases the Schottky barrier, which, in turn, will contribute to a better separation of charges at the boundary of the metal–semiconductor heterojunction. Therefore, conducting oxide nanoparticles
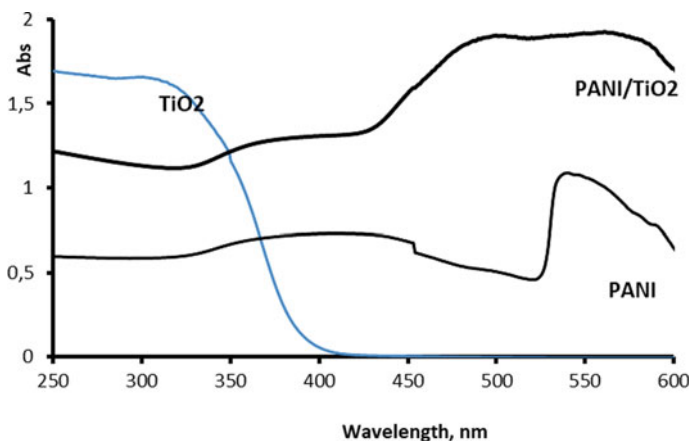
Fig. 26.5 UV–Vis spectra of PANI nanocomposites

can act as an "active" carrier of metal nanoparticles, contributing to the increase in catalytic activity and selectivity of catalysts.

As we can see, the contribution of the morphology of TiO$_2$ nanoparticles is obvious. The difference in the width and intensity of the spectral line for the spectra of composites recorded at room temperature (298 K) with phases TiO$_2$, C$_3$N$_4$Ox (Fig. 26.6), which can be explained both by the nature of the phases and on the other hand by the morphology of the surface TiO$_2$, C$_3$N$_4$Ox. The mechanism of interaction requires a detailed study of the contribution of each component.

The synthesis of C$_3$N$_4$O$_x$/TiO$_2$ was performed using methodic [36]. To increase opportunities of photochemistry-related applications of C$_3$N$_4$O$_x$/TiO$_2$ composite are decisive the phase composition and morphology of nanoparticles of the TiO$_2$ matrix and their optical properties. SEM images (Fig. 26.7a, b) of nanoparticles of both C$_3$N$_4$O$_x$/TiO$_2$ (~5% O) composites (anatase and rutile phase) demonstrate the arrangement of TiO$_2$ as separate globular nanoparticles and clusters between the plates and in the channels of the porous scaly plates C3N4Ox. However, the anatase phase nanoparticles (developed in IPM NASU) have a significantly higher dispersion, the average size of non-aggregated almost monodisperse particles of which is 10 nm. Using UV/Vis spectroscopy, it was found that in the series from TiO$_2$ (anatase), TiO$_2$ (rutile), C$_3$N$_4$, C$_3$N$_4$O$_x$/TiO$_2$ (anatase), C$_3$N$_4$O$_x$/TiO$_2$ (rutile) to C$_3$N$_4$O$_x$, a redshift of the long-wavelength edge of the fundamental absorption band is observed in the spectra (Fig. 26.7c) and the bandgap (Fig. 26.7d).

26.12 Summary

The development of new effective composite nanocrystalline photocatalysts has been demonstrated. The combination of PANI nanoparticles with TiO$_2$, C$_3$N$_4$O$_x$ will create
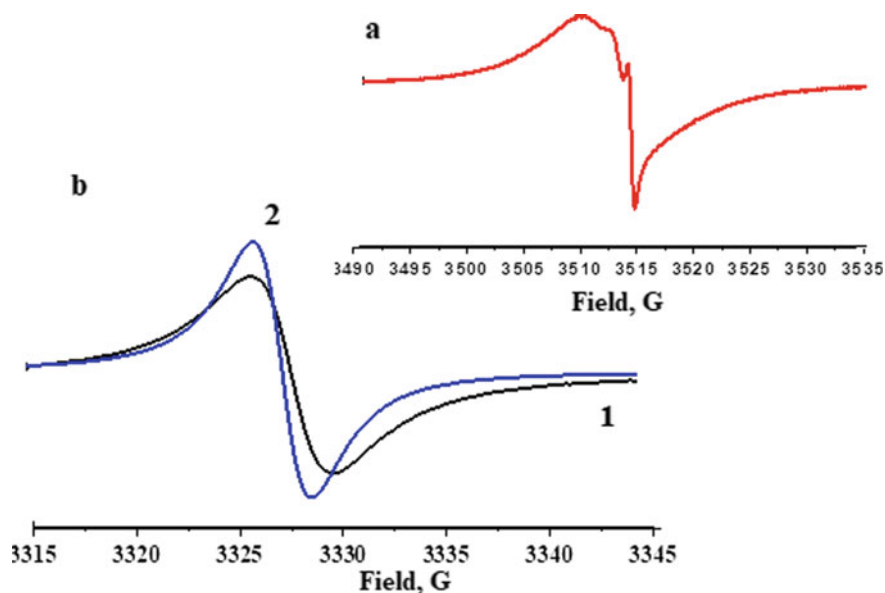
Fig. 26.6 EPR spectra of systems based on PANI at 298 K. **a** pure C_3N_4Ox. **b** PANI/TiO$_2$ (1), PANI/C_3N_4Ox (2)

an excited state of the electron (e$^-$) and hole (h$^+$) pairs, which can react with O_2 and water vapor in the atmosphere to produce superoxide ions and hydroxyl radicals (OH·) under irradiation. Both $O_2{}^-$ and OH· are agents in the destruction of toxic chemical compounds and bacteria cells to form CO_2 and water. This process allows increasing the performance of the photocatalyst and the duration of its operation until its next regeneration. Due to molecular structure and conductivity, PANI produces important h$^+$ in the valence band. $C_3N_4O_x$ combination with TiO$_2$ anatase nanoparticles and $C_3N_4O_x$, TiO$_2$ (anatases) with polyaniline allows designing the efficient electronic heterojunctions with possible regulation of molecular structure, which will be promise for increasing their photocatalytic activity with more efficient use of solar energy.
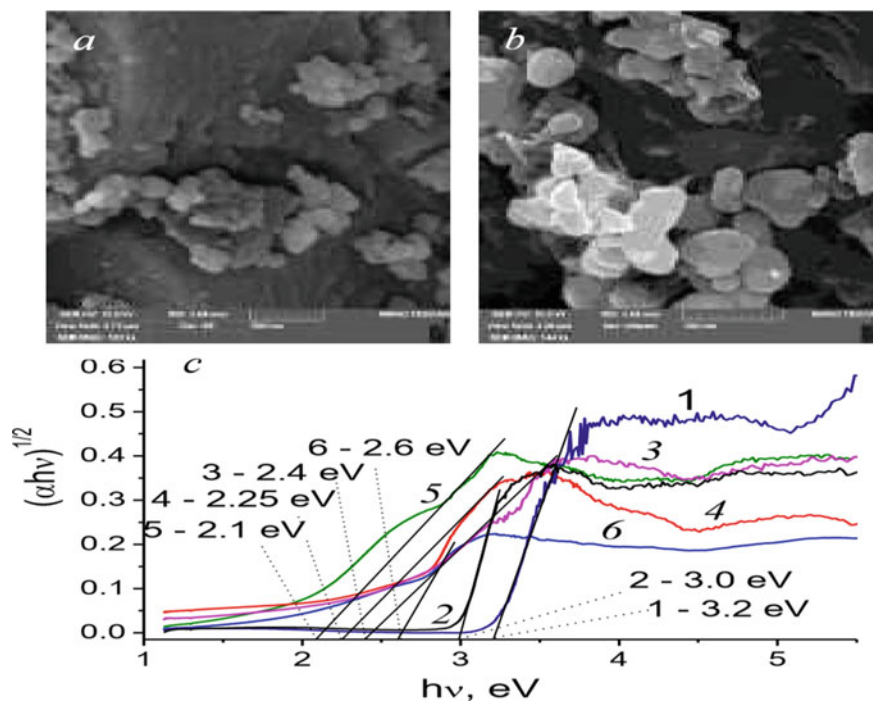
Fig. 26.7 SEM images of composites $C_3N_4O_x$/TiO_2 (anatase) (**a**) and $C_3N_4O_x$/TiO_2 (rutile) (**b**), UV–Vis DRS estimation of bandgap energies (**c**) of: *1*—anatase TiO_2, *2*—rutile TiO_2, *3*—$C_3N_4O_x$/TiO_2 (anatase), *4*—$C_3N_4O_x$/TiO_2 (rutile), *5*—$C_3N_4O_x$, *6*—pristine C_3N_4

Conflicts of Interest The authors have no conflicts of interest to declare.

References

1. Gilja V, Novakovic K, Travas-Sejdic J, Hrnjak-Murgic Z et al (2017) Stability and synergistic effect of polyaniline/TiO_2 photocatalysts in degradation of azo dye in wastewater. Nanomaterials 412(7):1–16. https://doi.org/10.3390/nano7120412
2. Jumat NA, Wai PS, Ching JJ, Basirun WJ (2017) Synthesis of polyaniline-Tio_2 nanocomposites and their application in photocatalytic degradation. Poly Poly Compos 25(7):507–511
3. Zahornyi M (2017) Nanosized powders as reinforcement for photoactive composites (Overview). Powder Metall Metal Ceram 56(3–4):130–147
4. Brooms TJ, Onyango MS, Ochieng A (2014) Photocatalytic activity of polyaniline/Tio_2/Zno composite for degradation of aromatic compounds in abattoir wastewater. In: International conference on chemical, integrated waste management and environmental engineering (ICCIWEE'2014) April 15–16, 2014 Johannesburg, pp. 124–130

5. Ghazzal MN, Kebaili U, Joseph M et al (2012) Photocatalytic degradation of rhodamine 6G on mesoporous titania films: combined effect of texture and dye aggregation forms. Appl Catalysis B: Environ 115:276–284

6. Lavrynenko OM (2021) Comparative analysis of CeO_2&Ag^0 and TiO_2&Ag^0 nanoparticles formed under the co-precipitation. In: Lavrynenko OM, Zahornyi MM, Pavlenko OY, Tyschenko NI, Bykov OI (eds) 2021 IEEE 11th international conference on "nanomaterials: applications properties" (NAP 2021) Odesa, Ukraine, Sept. 5–11. https://doi.org/10.1109/NAP51885.2021.9568577

7. Lavrynenko O, Pavlenko O, Dudchenko N, Brik A (2021) Physical–chemical properties of magnetite nanoparticles doped with Ag (I) and Au(III) Cations. In: Springer proceedings in physics, vol 246. https://doi.org/10.1007/978-3-030-51905-6_37

8. Khalyavka TA, Shapovalova MV, Korzhak GV et al (2021) Photocatalytic hydrogen evolution and Rifampicinum destruction over carbon-modified TiO_2. Res Chem Intermed. https://doi.org/10.1007/s11164-021-04609-1

9. Zahornyi MM, Lavrynenko OM, Pavlenko OY, Tyschenko NI, Skoryk MA, Kornienko OA (2021) Synthesis, structure, optical and biomedical application of nanosized composites based on TiO_2, Fe_3O_4 . In: Fesenko O, Yatsenko L (eds) Nanooptics and photonics, nanochemistry and nanobiotechnology, and their applications. NANO, 2021. Chapter springer proceedings in physics, vol 264. Springer, Cham, pp 153–164. https://doi.org/10.1007/978-3-030-74800-5_10

10. Xu H, Jia FL, Ai ZH, Zhang LZ (2007) A general soft interface platform for the growth and assembly of hierarchical rutile TiO_2 nanorods spheres. Cryst Growth Des. 7:1216–1219

11. Gopalakrishnan K, Elango M, Thamilselvan M (2012) Optical studies on nano-structured conducting polyaniline prepared by chemical oxidation method. Arch Phys Res 3:315–319

12. Zahornyi MM (2021) Optical and photocatalytic activity of polyaniline/TiO_2 composites with anatase and P25 nanoparticles; Zahornyi MM, Tyschenko NI, Ragulya AV, Lavrynenko OM, Kasumov AM, Melnyk AK, Kuzma OV, Ievtushenko AI (2021) J Nano-And Electron Phys 13(N5):05034–05035. https://doi.org/10.21272/jnep.13(5).05034

13. Ghosh S, Kouamé NA, Ramos L, Remita S, Dazzi A, Deniset-Besseau A, Beaunier P, Goubard F, Aubert PH, Remita H (2015) Conducting polymer nanostructures for photocatalysis under visible light. Nat Mater 14(5):505–511. https://doi.org/10.1038/nmat4220

14. Zhu Y, Xu S, Yi D (2010) Photocatalytic degradation of methyl orange using polythiophene/titanium dioxide composites. React Funct Polym 70:282–287

15. Liuan G, Wang J, Qi R, Wang X, Ping X, Han X (2012) A novel incorporating style of polyaniline/TiO_2 composites as effective visible photocatalysts. J Mol Catal A: Chem 357:19–25

16. Zaleska-Medynska A (2018) Metal oxide-based photocatalysis 1st edition fundamentals and prospects for application. Elsiver, p 350. Book ISBN: 9780128116340

17. Heshmatpour F, Zarrin S (2017) A probe into the effect of fixing the titanium dioxide by a conductive polymer and ceramic on the photocatalytic activity for degradation of organic pollutants. J Photochem Photobiol A: Chem 346:431–443

18. Radoičić M, Ćirić-Marjanović G, VukSpasojević P, Mitrić M, Novaković T, Šaponjić Z (2017) Superior photocatalytic properties of carbonized PANI/TiO_2 nanocomposites. Appl Catal B: Environ 213:155–166

19. Zhou S-X, Tao X-Y, Ma J, Guo L-T, Zhu Y-B, Fan H-L, Liu Z-S, Wei X-Y (2018) Synthesis of flower-like PANI/g-C3N4 nanocomposite as supercapacitor electrode. Vacuum. https://doi.org/10.1016/j.vacuum.2017.12.019

20. Chen X, Zhu X, Xiao Y, Yang X (2015) J Electroanal Chem 743:99–104

21. Putri LK, Ng B-J, Er C-C (2020) Appl Surf Sci 504:144427

22. Pisanu A, Speltini A, Vigani B et al (2018) Enhanced hydrogen photogeneration by bulk g-C3N4 through a simple and efficient oxidation route. Dalton Trans 47:6772–6778

23. Xue J, Fujitsuka M, Majima T (2019) Phys Chem Chem Phys 21:2318–2324

24. Wen J, Xie J, Chen X, Li X (2017) A review on g-C3N4-based photocatalysts. Appl Surf Sci 391:72

25. Wang H, Guan Y, Hu S, Pei Y, Ma W, Fan Z (2019) NANO 14(02):1950023
26. Qu X, Hu S, Bai J, Li P, Lu G, Kang X (2018) A facile approach to synthesize oxygen doped g-C$_3$N$_4$ with enhanced visible light activity under anoxic conditions via oxygen-plasma treatment. New J Chem 42(7):4998
27. Liu X, Ji H, Wang J, Xiao J, Yuan H, Xiao D (2017) Ozone treatment of graphitic carbon nitride with enhanced photocatalytic activity under visible light irradiation. J Colloid Interface Sci 505:919
28. Wei F, Liu Y, Zhao H, Ren X, Liu J, Hasan T, Chen L, Li Y, Su B (2018) Oxygen self-doped g-C3N4 with tunable electronic band structure for unprecedentedly enhanced photocatalytic performance. Nanoscale 10(9):4515
29. Alenizi MA, Kumar R, Aslam M, Alseroury FA, Barakat MA (2019) Construction of a ternary g-C3N4/TiO2@polyaniline nanocomposite for the enhanced photocatalytic activity under solar light. Sci Rep 9(1). https://doi.org/10.1038/s41598-019-48516-3
30. Kharlamov A, Bondarenko M, Kharlamova G (2016) Method for the synthesis of water-soluble oxide of graphite-like carbon nitride. Diamond Relat Mater 61:46
31. Kharlamov A, Bondarenko M, Kharlamova G, Gubareni N (2016) Features of the synthesis of carbon nitride oxide (g-C$_3$N$_4$)O at urea pyrolysis. Diamond Relat Mater 66:16
32. Bondarenko M, Silenko P, Gubareni N, Khyzhun O, Ostapovskaya N, Solonin Y (2018) Synthesis of multilayer azagraphene and carbon nitride oxide. Him Fiz Tehnol Poverhni 9(4):393
33. Li J, Shen B, Hong Z (2012) A facile approach to synthesize novel oxygen-doped g-C$_3$N$_4$ with superior visible-light photoreactivity. Chem Commun 48(98):12017
34. Bondarenko ME, Influence of the phase composition of the TiO$_2$ matrix on the optical properties and morphology of deposited C$_3$N$_4$O$_x$ nanoparticles; Bondarenko ME, Silenko PM, Solonin YM, Ragulya AV, Zahornyi MM, Shvalagin VV, Gubareni NI, Khyzhun OY (2020) Chem Phys Technol Surface 11:492
35. Oves M, Synthesis and antibacterial aspects of graphitic C3N4@Polyaniline composites; Oves M, Omaish Ansari M, Darwesh R, Hussian A, Alajmi MF, Qari HA (2020) Coatings 10. https://doi.org/10.3390/coatings10100950
36. Bondarenko ME, Sylenko PM, Solonin YM, Ragulya AV, Gubareni NI, Zahornyi MN, Khyzhun OY, Ostapovska NY (2020) «Nanostructured composite O-g-C3N4/TiO2 for photocatalytic application fabricated by means of synthesis of O-doped carbon nitride on the surface of anatase nanoparticles. Nanosistemi, Nanomateriali, Nanotehnologii 81(2):265–282. https://doi.org/10.15407/nnn.18.02.265
37. Shvalagin V (2021) Acid treated crystalline graphitic carbon nitride with improved efficiency in photocatalytic ethanol oxidation under visible light. In: Shvalagin V, Kuchmiy S, Skoryk M, Bondarenko M, Khyzhun O (eds) Materials science and engineering: B., vol 271, P 115304

Chapter 27
Local Modes and Local Resonances in Defect Containing 1D Photonic Structures: Signal Processing and Collimation of THz Irradiation

E. Ya. Glushko

27.1 Introduction

The photonic resonators have an extremely wide spectrum of applications in technique and technology beginning with night-vision applications, safety and defense, sensing, communication applications, signal processing, and many other areas [1–8]. Depending on frequency region and geometry of resonator, some unusual forms of reflection and transmission occur accompanied by extremely sharp local resonances of transmission inside the area of perfect reflective reflection windows [9–12]. It was found that for a normally incident electromagnetic wave (EMW), the presence of metal generates narrow spectral wells in the middle of reflection windows existing for the same free photonic crystal. An investigation of properties including the resonances shape showed that they are of Fano type. Quite another manifestation of metal-resonator interinfluence takes place at whispering incident angles when reflection spikes of a p-polarized wave coincide with modes of photonic crystal resonator and they are absent throughout the stopband areas between modes. This behavior is typical for a surface plasmon (SP) resonance. The effect is strongly depended on polarization, number of periods, and angle of incidence. The s-polarized field exhibits more complicate features: At whispering incident angles, the resonances in vicinity of low energy modes of each band arise between them (Fano-type resonances) whereas the resonances with higher energy close to the top of band became to be matched with the mode frequencies (SP resonances).

The 1D photonic crystals (PhCr) in photonics to a certain extent play a role similar to the role of hydrogen atom in quantum mechanics of atomic spectra: They have analytical solution of the eigenstates problem and also can serve as a ground of classification of the photonic states for 2D and 3D photonic structures. An attempt to

---

E. Ya. Glushko (✉)

Institute of Semiconductor Physics, 41 Nauki Prsp, Kyiv 03028, Ukraine
e-mail: scientist.com_eugene.glushko@mail.com

build a classification scheme for a two-dimensional photonic resonator was undertaken in [13] using an exact eigenfunctions basis found for a 1D structure. A formal link between 1 and 2D spectra was analyzed. A generalized description of reflection spectra for metalized photonic resonators was considered in [12, 14] where an effect of needle-like dips of reflection accompanying by enhanced resonant absorption of electromagnetic energy in a metal film (piercing) was found. It was shown there that the arising sharp dips in reflection have interference nature: They originate due to a property of resonator to concentrate electromagnetic energy immediately near the metalized end of the resonator.

Also, the 1D PhCr resonators are convenient to study the practical applications of local states, both surface and intrinsic ones, existing in defected resonators. Very attractive are their technological simplicity and an opportunity to prognose the parameters of electromagnetic devices. Due to the well-known scaling property of the 1D periodic structures [15], one can fabricate resonators with needed spectrum and tune the spectrum structure including the corresponding local states. The use of latter instead the described in [16] shifting band method can give an essential advantage in energy of a signal needed to perform logic operations. The reason is that local states of a resonator with doubled defect may be situated close enough one to another and can give a sharp transfer from perfect reflection to perfect transmission. In the THz region under consideration, as well as in optical region, the physics of signal processing may be based on the $\chi^{(3)}$ Kerr effect [17–20]. An important circumstance is also an opportunity to create in this frequency region optically high contrastive structures with practically absent losses of electromagnetic energy inside [21].

In general, the existence of a local electromagnetic state is a sign of high optical contrastivity of the structure. In the case of surface states, it is a contrastivity regarding external medium. The intrinsic local state arising inside a defect containing resonator indicates a high optical contrast between defect and photonic resonator. It is worth noting that though the optics of 1D photonic structures were analyzed in a lot of publications, the THz frequency region cannot be considered as a comprehensive studied area. First, it concerns a physical link between the modes of total intrinsic reflection (TIR) region and spectra of reflection in external geometry of incidence out the TIR region. Besides, it concerns the physical nature of sharp absorption resonances of polarized EMW piercing a metal film contacting the resonator [12, 14]. The peaks of resonant transmission against the backdrop of the perfect reflection windows in visual and IR frequency region were considered in [10, 11, 22, 23] for some partial cases at the normal incidence only and regardless of the resonator's mode spectrum. A more comprehensive study of phenomena accompanying the EMW behavior in defected/metalized resonators for both external reflection spectra and intrinsic resonator modes structure in a more wide frequency region was presented in [12–16] to recognize the entire operational field more exactly. This very approach gives an opportunity to consider some new effects of filtering and collimating.

In this study, we consider several kinds of a planar central defect containing photonic crystal resonator which allow to excite both standing waves inside TIR region and waves transmitting through and reflected from the structure. The found

local modes of resonators containing a binary defect are proposed to use in transformation of the physically added signals with intensities 1, 2, or 3 into the corresponding binary sequences. We also concentrate on the use of extremely sharp transmission resonances existing on the background of wide reflection windows in spectra of a defect contained resonator to concentrate the initially diverged input THz radiation inside a very narrow angular interval of output beam.

27.2 Transmission Spikes of a Double Central Defect Containing 1D Resonator: Signal Processing Schemes

Let we consider a p-polarized EMW in layered N-period silicon-air structure containing two intrinsic defect layers in the center. The thicknesses of Si-layers d_1 and air voids d_2 were chosen to consider effects of resonant reflection and transmission in the chosen frequency region. The position of left defect layer with thickness d_d corresponds to number $2N_d + 1$. The same second defect layer occupies position $2N_d + 4$; a period of the PhCr is inserted between two defect layers D. It means that a polarized EMW passes through N_d periods of the PhCr, meets the defect layer, then propagates through a period, again meets a defect, and then propagates through the remaining $N-N_d$ periods of the structure with an additional ending Si-layer of same size (Fig. 27.1).

According to the chosen geometry, a p-polarized plane electromagnetic wave with the refraction vector $\boldsymbol{n_s} = n_s\,(cos\theta_s,\,sin\theta_s)$ inside an arbitrary s-layer can be expressed in a view containing Z and Y components:

$$e^{-ik_{sy}z}k_s\mathbf{E}_s = (-k_{sy}, k_{sz})A_s e^{ik_{sz}z} - (k_{sy}, k_{sz})B_s e^{-ik_{sz}z}, \qquad (27.1)$$
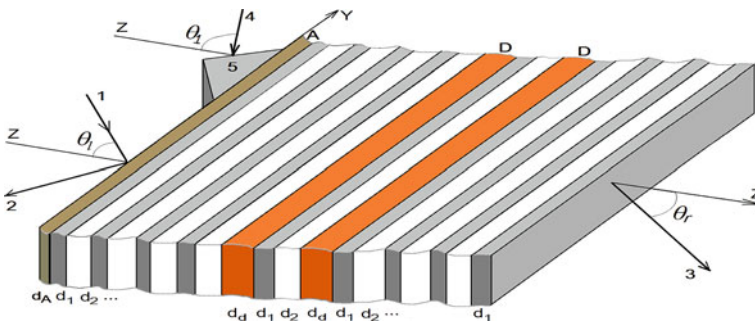

Fig. 27.1 A planar layered double defect containing 7-period photonic crystal resonator. One more period is inserted between defect layers D; 1, 2, incident and reflected beams in external geometry of incidence, respectively; 3, transmitted beam of θ_l, incident angle; 4, intrinsic geometry incident beam, angle of wavevector in layer d_1 is θ_1; 5, input prism; and θ_r, output angle

where A_s and B_s are electric field amplitudes, and z indicates projection of refraction vector and wave vector $\mathbf{k_s}$ into axes OZ in geometry of p-polarization. The light passing through the system is determined by Maxwell boundary conditions of continuous tangential components of fields is obeyed a self-consistent chain of 2 N + 6 matrix equations for field amplitudes A and B (from left to right):

$$\begin{cases} \mathbf{M}_l \begin{pmatrix} A_l \\ B_l \end{pmatrix} = \mathbf{L}_1 \begin{pmatrix} A_1 \\ B_1 \end{pmatrix}; \ \mathbf{M}_1 \begin{pmatrix} A_1 \\ B_1 \end{pmatrix} = \mathbf{L}_2 \begin{pmatrix} A_2 \\ B_2 \end{pmatrix}; \\ \mathbf{M}_2 \begin{pmatrix} A_2 \\ B_2 \end{pmatrix} = \mathbf{L}_3 \begin{pmatrix} A_3 \\ B_3 \end{pmatrix}; \ \mathbf{M}_2 \begin{pmatrix} A_2 \\ B_2 \end{pmatrix} = \mathbf{L}_3 \begin{pmatrix} A_3 \\ B_3 \end{pmatrix}; \\ \dots \\ \mathbf{M}_{2N_d} \begin{pmatrix} A_{2N_d} \\ B_{2N_d} \end{pmatrix} = \mathbf{L}_{2N_d+1} \begin{pmatrix} A_{2N_d+1} \\ B_{2N_d+1} \end{pmatrix}; \ \mathbf{M}_{2N_d+1} \begin{pmatrix} A_{2N_d+1} \\ B_{2N_d+1} \end{pmatrix} = \mathbf{L}_{2N_d+2} \begin{pmatrix} A_{2N_d+2} \\ B_{2N_d+2} \end{pmatrix}; \\ \mathbf{M}_{2N_d+3} \begin{pmatrix} A_{2N_d+3} \\ B_{2N_d+3} \end{pmatrix} = \mathbf{L}_{2N_d+4} \begin{pmatrix} A_{2N_d+4} \\ B_{2N_d+4} \end{pmatrix}; \ \mathbf{M}_{2N_d+4} \begin{pmatrix} A_{2N_d+4} \\ B_{2N_d+4} \end{pmatrix} = \mathbf{L}_{2N_d+5} \begin{pmatrix} A_{2N_d+5} \\ B_{2N_d+5} \end{pmatrix}; \\ \dots \\ \mathbf{M}_{2N+4} \begin{pmatrix} A_{2N+4} \\ B_{2N+4} \end{pmatrix} = \mathbf{L}_{2N+5} \begin{pmatrix} A_{2N+5} \\ B_{2N+5} \end{pmatrix}; \ \mathbf{M}_{2N+5} \begin{pmatrix} A_{2N+5} \\ B_{2N+5} \end{pmatrix} = \mathbf{L}_r \begin{pmatrix} A_r \\ B_r \end{pmatrix} \end{cases} \qquad (27.2)$$

where indexes l and r mark the left and right media, correspondingly; A_r is the amplitude of the wave running away into the right-hand semi-space at θ_r output angle, whereas the amplitude B_r should be set equal to zero. The central two rows in (27.2) describing amplitudes from $2N_d + 1$ to $2N_d + 4$ correspond to the double defect with an intermediate Si/air period in the middle. The system of Eq. (27.2) describes all possible cases of passing through the structure for a polarized wave. If the electromagnetic field is excited inside the total internal region of the PhCr (internal problem), we must take $A_l = 0$ and Eq. (27.2) transforms into the eigenvalue problem describing spectrum of standing waves and their density distribution in space—eigenfunctions. If the beam 1 falls onto the resonator like it is shown in Fig. 27.1, the module of amplitude A_l should be taken equal to $1,$ and therefore, all other amplitudes have absolute meaning. In this case (external problem), the system (2) issues a continuous spectrum and can be described in terms of reflection and transmission. The matrices of transfer through the right boundary $\mathbf{M_s}$ and left boundary $\mathbf{L_s}$ of the s-layer are:

$$\mathbf{M}_s = \begin{pmatrix} \cos\theta_s e^{ik_{sz}d_s}, & -\cos\theta_s e^{-ik_{sz}d_s} \\ k_{sz}e^{ik_{sz}d_s}, & k_{sz}e^{-ik_{sz}d_s} \end{pmatrix}, \quad \mathbf{L}_s = \begin{pmatrix} \cos\theta_s, & -\cos\theta_s \\ k_{sz}, & k_{sz} \end{pmatrix} \qquad (27.3)$$

where d_s is the width of s-layer. If a nonlinear layer d_A is present (Fig. 27.1), the amplitudes A_l and B_l include the corresponding parameters of the nonlinear layer d_A.

The boron-doped silicon is one of the lowest loss materials in the entire millimeter wave region [21, 24]. Therefore, we consider a boron-doped silicon photonic resonator $(Si/Air)_5/D/(Si/Air)/D(Si/Air)_5/Si$ with central disposition of doubled defect $D/(Si/Air)/D$. The resonator contains 5 periods from both sides of the binary central defect. Our evaluations give for resonators with central disposition of a defect a much more distinctive and sharper local transmission resonances against wide

windows of reflection (Fig. 27.2, lower panel). Any deviation from the central position of the defect leads to weakening and widening of the resonance. In Fig. 27.2 (top panel), the bandgap structure for a 10-period PP/air D-D defect containing photonic crystal in frequency interval (0−1.4) THz is presented. The angle interval of the resonator eigenstates pertains to the TIR region. The latter for Si occupies an interval (17°, 90°) of incident angles θ_1 in silicon. The chosen interval contains 3 bands; each of them includes 12–13 modes uniting into pairs inside the band and 2–4 additional photonic states having a tendency to detach from the bottom or top of a corresponding band with following transformation into the local states. The points of local-band transformation of states are shown by changed color. The number of local states varies from 1 to 4 depending on angle of incidence so that the total number of band + local eigenstates equals to 14. If the angle between wavevector k_1 and axis OZ inside a Si-layer growths from the minimal one 17° (TIR angle) up to 27°, then the first three photonic bands occupying intervals (0, 364) GHz, (476, 784) GHz, and (924, 1176) GHz up to 27° where the first band narrows: (406, 441) GHz and width of another one is approximately 1 GHz. The doublet structure of band modes arises due to influence of the central double defect zone which "cuts" the resonator's 10-period body into two islands of the similar design interacting with each other through the central defect zone. The interaction between photonic islands leads to the well-known effect of mode repulsion and that is the reason of paired structure. The intrinsic local states generated by the defect zone arise if their optical contrast relatively the PhCr is high enough. For instance, states D vanish if d_d becomes less than 1.4 μm. In the case under consideration, the intrinsic local states D occupy positions in the first half of each gap. The resonator's surface local states cannot exist in any periodic binary structure if one of its components coincides with surrounding medium. If the interaction between islands decreases, then the paired band modes draw together though perfect degeneracy of states is principally unattainable in 1D systems [25]. It is worth noting that the width of bands is not changing in the process of such transformation.

An application arises due to a well-expressed angular dependence of resonances that gives an opportunity to organize one of the existing all-optical signal processing schemes TR or RT where, for instance, in expression TR the first "T" corresponds to perfect transmission of signal of intensity I_0 and second "R" means perfect reflection of the signal $2I_0$. The RT schemes proposed in [15, 16] need $s(s + 1)/2$ logic gates to organize an s-digit all-optical adder that gives 131,328 cells connected by optical channels for a 512-digit capacity adder. Here, we include into consideration one more signal intensity $3I_0$. Our analysis shows that a combination of TRT and TRR schemes of processing in logic devices allows to decrease the number of cells in adder to 2 s-1 (1023 for a 512-digit capacity adder). One can consider how the local modes of a planar photonic crystal resonator containing two symmetrical defect layers occupying a central position inside the structure can be used to organize more effective operation of signals in an all-optical logic device. Two defect layers are divided by the structure's period (Si/air). In Fig. 27.2 (top panel), the bandgap structure in frequency interval (0–1.4) THz is presented in dependence on the wave incident angle θ_1 in the total internal reflection (TIR) range of silicon layers (17°, 90°).
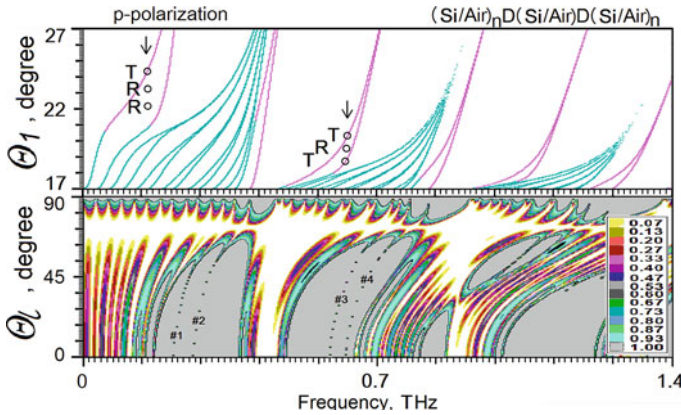
Fig. 27.2 (Si/Air)$_5$/D/(Si/Air)/D(Si/Air)$_5$/Si photonic structure. P-polarized modes/resonances and signal processing. **Top part**: Bandgap structure and local modes of the 10-period Si/air photonic crystal containing a binary one-period divided defect D-D of thickness $100\,\mu$m, $d_{Si} = 100\,\mu$m, period $300\,\mu$m, and air void size $200\,\mu$m. External incident angle θ_l (see Fig. 27.1), intrinsic angle θ_1 inside the Si material. Three bands each of them containing 10–13 resonator band eigenmodes and from 1 to 4 detached local states. Arrows, operating frequencies of TRR (left) and TRT (right) signal processing schemes. **Bottom part**: Angle-frequency diagram of reflection at external incidence (Fig. 27.1). Notations #1, #2, #3, and #4 enumerate the first four transmission spikes having its beginning at 225.69 GHz, 260.62 GHz, 588.47 GHz, and 624.64 GHz, correspondingly, for normal incidence $\theta_l = 0°$. **Inset:** Scale of colors

The chosen interval contains 3 bands; each of them includes 12–13 modes uniting into pairs inside the band and 2–4 additional photonic states having a tendency to detach from the bottom or top of a corresponding band with following transformation into the local states. The number of local states varies from 1 to 4 depending on angle of incidence so that the total number of band + local eigenstates equals to 14. If the angle between wavevector k_1 and axis OZ inside the Si-layers growths from the minimal one 17° (TIR angle) up to 27°, then the first three photonic bands occupying intervals (0, 0.289) THz, (0.324, 0.781) THz, and (0.914, 1.128) THz essentially decrease their width to where is narrowed to (0.226, 0.261) THz for the lowest band whereas the width of the next one becomes < 1 GHz. The angle-frequency positions are shown by circles in vicinity of local branches for two types of logic gates TRR and TRT, where the last R/T shows the perfect reflection or transmission of signal $3I_0$. The latter is needed to organize a more compact all-optical adder based on the $\chi^{(3)}$ nonlinear effect of shifting bands (or local states). In Fig. 27.2 (bottom panel), the angle-frequency color map of reflection at external incidence is presented. The upper part of diagram $\theta_l \approx 90°$ in general repeats the TIR region structure of resonator's eigenstates: Each TIR mode has a continuation out the TIR region as resonance peaks of transmission. The Brewster effect can be observed at $\theta_l \approx 73.65°$—it is the reason of perfect reflection of p-polarized EMW at all frequencies. At $\theta_l < 73.65°$, the map exhibits several perfect reflection areas—windows of reflection. The first two windows contain four extremely sharp double

defect caused transmission resonance lines marked as #1, #2, #3, and #4 which have at normal incidence the frequencies (GHz)/HWHM(MHz) $\approx 225/0.74$, $\approx 260/0.21$, $\approx 588/2.51$, and $\approx 624/45.2$, correspondingly. The Fano type of these resonances was discussed in [12] for the case of p-polarization. In the case of whispered incidence $\theta_l \sim 90°$, the reflection spectrum of p-polarized (s-polarized) waves demonstrates a system of sharp dips matching the position of resonator's eigenmodes inside the TIR region at the angle of TIR 17°. Due to the angle dependence of resonant transmission lines, they are sensible to intensity of EMW in the structures containing a $\chi^{(3)}$ nonlinear layer and an opportunity to use these resonances in a TRR logic gate exists.

The operational angle-frequency positions are shown in Fig. 27.2 (upper panel) by circles in vicinity of local branches for two types of logic gates TRR and TRT, where the last R/T shows the perfect reflection or transmission of signal $3I_0$. The latter is needed to organize a more compact all-optical adder based on the $\chi^{(3)}$ nonlinear effect of shifting bands or local states.

Our evaluations show that the shape of resonance lines depends on the number of periods: Both frequency and angle widths of resonances essentially decrease with increasing of the number of periods. Any deviation from the central positioning of defect (including odd numbers N) leads to widening the HWHM of resonance lines and decreasing the transmission peak maximum.

27.3 Energy Concentration and Collimation Effect in a Resonator Structure with Unitary Central Defect

Let we consider one of the promising applications of PhCr with a unitary central defect. It was discussed in [26] how the existing sharp peaks of transmission can be used to control the divergence of the incident beam if a peak is situated against the backdrop of perfect reflection in a wide angle interval. Here, we develop the approach presented there considering a much more optically contrastive Si-air structure to improve the collimating properties of device.

The system under consideration is shown in Fig. 27.3a. A monochromatic diverged incident beam I_l passes from the source S into the resonator $(Si/Air)_4/D(Si/Air)_3/Si$ through the electromagnetic field reservoir (EFR) 3. The initial beam divergence $\Delta\theta$ may be large enough depending on the quality of the source. After interaction with resonator, any wave with wavevector out the transmission peak reflects back into the EFR whereas waves inside the peak angular interval pass through the collimator with essentially lowered divergence $\delta\theta$. Owing to perfection of mirror walls of the reservoir, the density of field inside the EMR increases up to state of saturation when the energy flux of the output beam I_r plus flux of losses become equal to energy flux of the input beam I_l.

We have calculated the bandgap structure, local modes, and angle-frequency map of reflection for a 10-period Si/air photonic crystal containing a central unitary Si-defect D of thickness 0.45 mm, $d_{Si} = 0.5$ mm, period 1.3 mm, and air void size
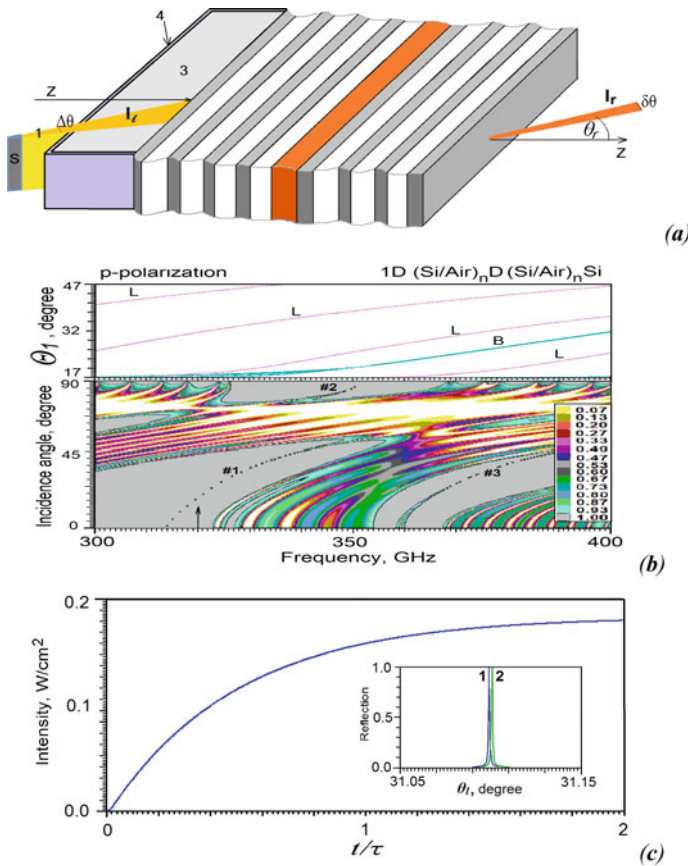
Fig. 27.3 **a** (Si/Air)$_4$/D(Si/Air)$_3$/Si THz collimating system. 1, monochromatic diverged incident beam I_l; 2, collimated output beam I_r; 3, EM field reservoir; 4, mirror walls of the reservoir; θ_r, output angle; and $\Delta\theta$ and $\delta\theta$ are input and out divergencies of beam, correspondingly. **b** Spectrum of (Si/Air)$_5$/D (Si/Air)$_5$/Si photonic resonator. **Top part**: Bandgap structure and local modes of the 10-period Si/air photonic crystal containing a central unitary defect D of thickness 0.45 mm, d_{Si} =0.5 mm, period 1.3 mm, and air void size 0.8 mm. External incident angle θ_l, intrinsic angle θ_1 inside the Si material. Inside the interval (300−400) GHz, two bands with first of them containing 10–11 resonator eigenmodes B and from 1 to 4 local states L detached from bands. **Bottom part**: Notations #1, #2, and #3 enumerate the defect caused transmission resonances. Section of the reflection diagram in angle interval (0°, 40°) is shown by vertical arrow. **Inset:** Scale of colors. **c** Time dependence of collimated flow I_r for υ_l= 320.011 GHz, $\tau \approx$ 2.26 μs. **Inset:** Sharp peaks of angular dependencies of reflection at 320.011 GHz (curve 1) and 320.012 GHz (curve 2). Reflection dip position of the curve 1 is θ_l= 31.1009° with divergency $\delta\theta$= 0.0007° (Fig 27.3a, lower panel, vertical arrow) at input divergency 40°

0.8 mm. Inside the chosen interval (300−400) GHz, two bands exist with first of them containing 10–11 resonator eigenmodes B and from 1 to 4 local states L detached from bands. It is important for our study of collimation effect the map of reflection calculated in the external geometry of incidence and shown in the lower panel of Fig. 27.3b. Notations #1, #2, and #3 enumerate the defect caused transmission resonances. Section of the reflection diagram in angle interval (0°, 40°) is shown by vertical arrow.

   To collimate a monochromatic diverged beam passing through the resonator, one can choose the angle-frequency region around a separate dip curve. For.

   instance, in [26] a 90 GHz beam being initially diverging in angle interval (0°, 90°) after passing the silicon-propylene resonator $(Si/PP)_5Si(Si/PP)_5$ decreased its divergence up to 0.4° in vicinity of direction 22.5 at the given parameters. A problem arises if the region of perfect reflection containing a sharp peak of transmission is not omnidirectional one like it is in the case of resonator under consideration. We suppose that a mirror EMW reservoir of special form can support the trapped radiation inside the needed angle interval between 0° and 40° (Fig. 27.3a, b, lower panel). Then, we have a system which accumulates the electromagnetic energy from a source of intensity I_l and fixed frequency υ_l inside the angle interval of perfect reflection. When the average density of energy inside the EMW reservoir reaches its saturation, then a stable energy flow I_r through the resonator window is establishing along the direction determined by angle position of transmission resonance $\theta_1 = 31.1009°°$ (Fig. 27.3b, vertical arrow on lower panel). The flow outside the EMW reservoir depends on the accumulated density of electromagnetic energy W inside the reservoir.

   We should take into account two possible channels of energy leakage: through the PhCr and one more arising due to the reverse flow immediately through the source window A simplified kinetic equation for W can be written as:

$$\frac{dW}{dt} = \frac{I_l S_l}{V} - \frac{cW}{V}(S_r \Omega_r f_r + S_l \Omega_l f_l), \tag{27.4}$$

where V is the volume of reservoir, Ω is spatial angle, and f_l and f_r are the integral characteristic of transmission through the corresponding window of the reservoir— left or right. We suppose here that intensity of radiation I_r transmitted through the metalized PhCr is proportional to average density of energy W:

$$I_r = Wc\frac{\Omega_r f_r}{4\pi}, \; I_l' = Wc\frac{\Omega_l f_l}{4\pi}. \tag{27.5}$$

   The characteristic time τ of the process of energy accumulation depends on the input and output sections S_l and S_r, the angle dependence of transmission at the chosen frequency $\upsilon_l = 320.011$ GHz (shown by arrow in Fig. 27.3a), and volume V of the EMW reservoir. In Fig. 27.3, time dependence of the collimated output flow I_r is shown for different thicknesses of metal film. The integral parameter of transmission f_r represents geometrically area under the curve of transmission 1-R

shown in the Insertion. On account of perfect reflection and small spike width, the calculated f_r was of the order of 10^{-3}–10^{-4}. The characteristic time τ of the process of energy accumulation depends on the input and output sections S_l and S_r, the angle dependence of transmission at the chosen frequency $\upsilon_1 = 320.011$ GHz (shown by arrow in Fig. 27.3b, lower panel), and volume V of the EMW reservoir. In Fig. 27.3c, time dependence of the collimated output flow I_r is shown for different thicknesses of metal film. The integral parameter of transmission f_r represents geometrically area under the curve of reflection R shown in the Insertion. On account of perfect reflection and small width of the transmission peak, the calculated f_r is of the order of 10^{-3}. For the parameters taken: $I_l = 0.5$ W/cm^2, $S_l = 8$ cm^2, $S_r = 18$ cm^2, EMW reservoir volume $V = 54$cm^3, energy losses on the reservoir walls, and reverse flow through the source section S_l as 20%, we have a strongly collimated beam with angular HWHM close to 0.0007° and intensity $I_1 = 0.1818$ W/cm^2. Our evaluations show that electromagnetic energy of saturation inside the EMW box depends on leakage through the windows. In the considered case, this energy approximately equals to *9.04* μJ and it is reached with the characteristic time 2.26 μs. The angular HWHM essentially depends on the structure optical contrastivity: A considerably lesser contrastive structure considered in [26] gave a much weaker divergency.

27.4 Resonant Transmission-Based Filtering

The sharp resonances of transmission looking like thin lines onto the angle-frequency diagram also give an opportunity to organize tunable ultranarrow filtering of a collimated terahertz beam. The filter spectral width depends on the resonator quality, chosen frequency interval, and the incident angle of a collimated beam. A resonator based on materials of higher contrast like boron contained silicon has issues more wide windows of reflection and sharper local states with correspondingly narrower HWHM. One can predict two cases of possible application. (**1**) If the frequency band of the collimated source matches one of the considered in above windows of reflection (Fig. 27.2, lower panel and Fig. 27.3b, lower panel) at the corresponding direction of incidence, then only frequencies inside the peak of transmission will pass through the resonator whereas the rest will be reflected. It means a sufficient weakening of the output signal because the resonator bandpass is narrow. The use of the discussed above stochastic EMW reservoir allows to enhance the output beam intensity regardless the narrow angular area of the resonator. (**2**) Another possible application corresponds to the case when a source generates a collimated but instable monochromatic frequency. When the instable source scans an interval which includes the transmission resonance frequency, then only the resonant frequency will be transmitted through the resonator; therefore, the filter of that kind can play the role of a frequency stabilizer.

References

1. Zhang X-C, Xu J (2010) Introduction to THz wave photonics. Springer Science+Business Media, LLC
2. Lova P, Manfredi G, Comoretto D (2018) Advances in functional solution processed planar 1D photonic crystals. Adv Optical Mater 6:1800730
3. Tonouchi M (2007) Cutting-edge THz technology. Nat Photonics 1:97–105
4. Dhillon SS, Vitiello MS, Linfield EH et al (2017) The 2017 terahertz science and technology roadmap. J Phys D: Appl Phys 50:043001
5. Hesler J, Prasankumar R, Tignon J (2019) Advances in terahertz solid-state physics and devices. J Appl Phys 126:110401
6. Kyaw C, Yahiaoui R, Chase ZA et.al (2020) Guided-mode resonances in flexible 2D terahertz photonic crystals. Optica 7(5):537–541
7. Shi X, Han Z (2017) Enhanced terahertz fingerprint detection with ultrahigh sensitivity using the cavity defect modes. Sci Rep 7:13147
8. Sizov FF (2017) Infrared and terahertz in biomedicine. Semiconduct Phys Quantum Electron Optoelectron 20:273
9. Wu C-J, Wang Z-H (2010) Properties of defect modes in one-dimensional photonic crystals. Progress In Electromagnet Res 103:169–184
10. Jena S, Tokas RB, Thakur S, Udupa DV (2021) Thermally tunable terahertz omnidirectional photonic bandgap and defect mode in 1D photonic crystals containing moderately doped semiconductor. Physica E: Low-dimensional Syst Nanostruct 126:114477
11. Chang Y-H, Jhu Y-Y, Wu C-J (2011) Temperature dependence of defect mode in a defective photonic crystal. Opt Commun 285:1501–1504
12. Glushko EY (2020) Mixed Fano-SP resonant absorption of THz electromagnetic waves in a photonic resonator contacting with a metal film. Phys Lett A 384(23):126564
13. Glushko EY (2017) Island-kind 2D photonic crystal resonator. Ukr Phys J 62(11):945–952
14. Glushko EY (2021) Induced resonant electromagnetic piercing in metalized photonic crystal structures. Optik 231:166502
15. Glushko EY (2005) All-optical signal processing in photonic structures with nonlinearity. Opt Commun 247(4–6):275–280
16. Glushko EY (2008) Logical gates on trapped modes in photonic crystals with nonlinear coating. In: Proceedings SPIE 6903, 69030G -69030G-10
17. Mizzioni P et al (2019) Roadmap on all-optical processing. J Opt 21:063001
18. Hoffmann MC, Brandt NC, Hwang HY, Yeh K-L, Nelson KA (2009) Terahertz Kerr effect. Appl Phys Lett 95:231105
19. Tomchuk PM, Brodyn MS, Volkov VI, Lyakhovetskii VR (2013) Third-order optical nonlinearity of noble metal nanostructures. Ukr J Phys 8(1):50–69
20. Chen C, Ning T, Zhou Y, Zhang D, Wang P, Ming H, Yang G (2008) Large optical nonlinearity of Au nanoparticle-dispersed $BaSrTiO_3$ films prepared by pulsed laser deposition. J Phys D: Appl Phys 41:225301
21. Sanjuan F, Tocho JO (2012) Optical properties of silicon, sapphire, silica and glass in the Terahertz range,. In: Latin America optics and photonics conference, paper LT4C.1
22. Treshin IV, Klimov VV, Melentiev PN, Balykin VI (2013) Optical Tamm state and extraordinary light transmission through a nanoaperture. Phys Rev A 88:023832
23. Kaliteevski M, Iorsh I, Brand S, Abram RA, Chamberlain JM, Kavokin AV, Shelykh IA (2007) Tamm plasmon-polaritons: possible electromagnetic states at the interface of a metal and a dielectric Bragg mirror. Phys Rev B 76:165415
24. Afsar MN, Chi H (1994) Millimeter wave complex refractive index, complex dielectric permittivity and loss tangent of extra high purity and compensated silicon. Int J Infrared Milli Waves 15:1181–1188
25. Landau LD, Lifshitz EM (1977) Quantum mechanics. nonrelativistic theory, vol 3. Pergamon Press, New York

26. Glushko EY (2021) Collimation effect on THz transmission resonances in metalized and defected photonic structures. In: Shi-Hai Dong BP (ed) Research trends and challenges in physical science, International UK, vol 1, Chapter 7, pp 83–89

Chapter 28
Features of Surface Structuring of Direct and Indirect Band Gap Semiconductors by Femtosecond Laser

N. I. Berezovska, I. M. Dmitruk, Ye. S. Hrabovskyi, R. S. Kolodka, O. P. Stanovyi, A. M. Dmytruk, and I. V. Blonskyi

28.1 Introduction

In recent years, promising applications of micro- and nanotextured surfaces in different areas of science and technology stipulate the active study of the surface modification with different methods that results in the formation of the surface micro- and nanostructures. In contrast to such complex techniques, as, for example, lithographical techniques, ultrashort laser processing could create in one-step regime 3D periodic structures at the surface of various materials, such as metals [1–3], semiconductors [4–7], and dielectrics [8–10]. The interest to the formation of laser-induced periodic surface structures (LIPSS) or ripples is constantly growing since 1965, when Birnbaum [11] demonstrated the occurrence of the periodic structures at the surface of single-crystal specimens of high-purity semiconductors of germanium, silicon, GaAs, GaSb, InSb, and InAs after an irradiation by a ruby laser. The method of direct femtosecond laser structuring allows to treat a relatively large area of the sample with controllability and reproducibility of the processing results. Practical benefits of LIPSS at semiconductor surfaces cover wide range of applications in

N. I. Berezovska (✉) · I. M. Dmitruk · Ye. S. Hrabovskyi · R. S. Kolodka · O. P. Stanovyi
Faculty of Physics, Taras Shevchenko National University of Kyiv, Volodymyrska Street, 64/13, Kyiv 01601, Ukraine
e-mail: n_berezovska@univ.kiev.ua

I. M. Dmitruk
e-mail: igor_dmitruk@univ.kiev.ua

A. M. Dmytruk · I. V. Blonskyi
Photon Processes Department, Institute of Physics of NAS of Ukraine, Prospect Nauky, 46, Kyiv 03028, Ukraine
e-mail: admytruk@iop.kiev.ua

I. V. Blonskyi
e-mail: blon@iop.kiev.ua

photonics, plasmonics, optoelectronics, biochemical sensing, wettability changes, etc. Thus, the texturing of the surface of photovoltaic elements belongs to a standard treatment procedure aimed at reducing the reflection losses [12, 13], increasing the robustness against defects and perturbations [14]. The combination of semiconductor surface relief with metal features induces the efficient light trapping and an increase of the absorption in thin layers due to the involvement of the surface plasmons-polaritons (SPPs) [15–17]. Formation of LIPSS on semiconductors and subsequent plating with gold or silver nanofeatures can be used for the producing of the substrates for surface-enhanced Raman scattering (SERS) [18, 19].

In general, both the fs-laser beam parameters and material properties determine the results of the light–matter interaction. The classification of the LIPSS could be found for example, in [20, 21]. LIPSS with the structure period close to the laser wavelength ($\Lambda \cong \lambda$) is called low spatial frequency LIPSS (LSFL). Commonly, their orientation is perpendicular to the laser beam polarization. Usually, this type of ripples is inherent to the strong absorbing materials, such as semiconductors and metals. In some cases, LIPSSs manifest direction parallel to the laser beam polarization, and frequently, their period is larger than the laser wavelength. Such structures are also called grooves. Another type of LIPSS is called high spatial frequency LIPSS (HSFL). Such LIPSS are characterized with spatial periods significantly smaller than the laser wavelength ($\Lambda < \lambda/2$). They are often revealed for the weakly absorbent materials such as dielectrics. HSFL is also observed for the semiconductor materials. HSFL can exhibit both orientations (parallel or perpendicular to the laser beam polarization). Different types of LIPSS are associated with different formation mechanisms.

Along with accelerating experimental research activity on LIPSS formation on different materials, theories and numerical methods concerning origin of LIPSS are actively developed. Leading scientists who intensively study LIPSS formation divide the approaches to the LIPSS creation into two types, i.e., electromagnetic approach describing the impact of optical energy into the solid and matter reorganization approach describing the redistribution of surface near the area of laser-excited material [21]. Within electromagnetic theory on the formation of LIPSS, the incident light scatters at the roughness of the sample surface exciting surface electromagnetic waves (SEWs) including surface plasmon polaritons (SPP). LIPSS formation usually is a result of multi-pulse laser treatment in the ablative regime. In addition to the interference between the incident laser beam and SEWs (i.e., SPPs), additional second-order contributions can be caused by the interference of counterpropagating plasmon waves [22]. This approach can be applied to the initially plasmonically nonactive materials, such as semiconductors and dielectrics, which can be turned into a metallic state at an excess of a critical density of electrons in the conduction band during fs-laser irradiation [5, 23–25]. Thus, Bonse and co-workers [23] combined the Sipe's theory with a Drude model to quantify the change of dielectric permittivity as a function of the laser-induced electron density N_e in the conduction band of silicon. Furthermore, after the initial formation of the periodic profiles, it should be also taken into account the subsequent coupling of the electronic system

and the lattice of the solid through electron–phonon coupling, as well as thermal diffusion, electron diffusion, and phase transitions of melting substance [26, 27].

Regardless the progress of elucidation of the LIPSS origin, further investigations of the nature of LIPSS in different materials and hybrid structures are of great importance [28].

We present a survey of the impact of femtosecond laser impulses on set of semiconductors with direct and indirect band gap (GaAs, ZnSe, GaSe, PbI$_2$, CdZnTe and Si), compare the peculiarities of morphology of textured surfaces obtained in similar fs-laser processing setup, and discuss the nature of these patterns, as well as spectroscopic manifestation of the effect of fs-laser treatment on optical properties of corresponding semiconductor.

28.2 Experimental Details

Micro- and nanostructuring of semiconductors under study have been carried out with a femtosecond laser, namely a Ti–sapphire laser system which consists of a Mira-900F femtosecond oscillator with a Legend-HE chirped pulse amplifier (both from Coherent, USA). The main characteristics of the laser have been the following: central wavelength of 800 nm, a pulse duration of $130-150$ fs, a pulse repetition rate of 1 kHz, and a pulse energy about $0.8-1$ mJ. Cylindrical lenses and spherical lens (in the case of GaAs texturing) are used for the beam focusing onto the surface sample. A typical power density at the sample surface is of the order of 10^{12} W/cm^2. A laser power meter "Field Master GS" with a detector head "LM-10" (Coherent, USA) was used for the measurements of the average laser power. In some experiments, the diaphragm for the incident beam has been used, and its presence in the setup was taken into account while the pulse irradiation energy density was evaluated. The surface texturing has been realized in scanning beam regime at a velocity range of 0.45…1 mm/s. During the laser processing, a vertically standing sample stage moves at a defined velocity. The horizontally polarized laser beam is incident normally onto the sample surface. The laser processing has been performed in air environment in the multi-pulse regime.

The influence of fs-laser radiation parameters on surface morphology of the samples has been analyzed by scanning electron microscopy (SEM) with AURA 100 SEM (SERON Technology Inc.) and 2D Fourier transform (2D-FFT) of SEM images. 2D Fourier transform has been performed using Gwyddion 2.60 software. We also present the resultant 2D-FFT in 3D view for the better visualization of its shape. Sometimes, 3D view presentation has been rotated relative to the orientation of the corresponding SEM image and its 2D-FFT presentation. It should be noted that for a more convenient presentation of 2D-FFT results, we show its profile in a certain direction in μm^{-1} (end bars represent the signal summation width in specified direction), and its low-frequency corrected variant in nanometers, where spatial periods of the structure are clearly seen. This graph of the profile could be further analyzed by the peak deconvolution.

The photoluminescence (PL) spectra have been measured with the setup based on a single-grating spectrometer MDR-3 (LOMO) under an excitation of semiconductor lasers $\lambda_{ex} = 406$ nm ($E_{ex} = 3.05$ eV), $\lambda_{ex} = 532$ nm ($E_{ex} = 2.3$ eV) and pulsed nitrogen laser $\lambda_{ex} = 337$ nm ($E_{ex} = 3.68$ eV).

28.3   Peculiarities of Femtosecond Light-Semiconductor Interaction in the Case of Direct Band Gap Semiconductors

Direct band gap semiconductor zinc selenide (ZnSe) belongs to the popular opto-electronic materials. ZnSe is used in light-emitting diodes, photodetectors, X-ray detectors, field emitters, elements of solar cells, and other devices. It has wide band gap—$E_g = 2.7$ eV at 300 K. There are only a few papers describing the fs-laser treatment of ZnSe [29–35]. As a rule, LIPSSs with periods around 160−180 nm have been observed.

We also studied fs-laser processing of ZnSe single crystal with maximum resistivity ($\rho \geq 10^{12}$ Ω cm) and a minimum concentration of impurities using linearly polarized Ti/sapphire fs-laser [36]. The fs-laser pulses with the central wavelength of 800 nm with the energy density of around 0.04–0.05 J/cm^2, the effective number of laser pulses varied in the range of ~300–400, the pulse duration of 140 fs at a repetition rate of 1 kHz have been applied for the ZnSe texturing. As impurities and native defects could affect electronic and optical properties of ZnSe, the influence of the fs-laser processing on luminescent properties of ZnSe has been investigated to elucidate the changes in the quality of ZnSe single crystals after fs-laser processing. During fs-laser processing at the regime of the lower fluence, LIPSSs of two periods 220 and less pronounced 640 nm were revealed at the surface (see Fig. 28.1). The periods values were defined by 2D Fourier transform of SEM images. Figure 28.1a, represents the central and peripheral fields of the fs-laser beam action on the sample surface. At Fig. 28.1b, the incipient periodic structures are seen. These structures are forming along the existing cracks at the sample surface or located randomly. At the same time, the obtained structures trace the laser beam polarization; namely these structures are oriented perpendicular to laser beam polarization. Figure 28.1c, represents the central part of the area processed with the fs-laser beam, d—its Fourier transform. LIPSS are rather homogeneous along the surface.

The occurrence of the LSFL and HSFL at the fs-laser treated ZnSe surface indicates the complicated nature of the process of fs-laser influence at the semiconductor surface. The laser-induced changes of ZnSe carrier concentrations specify periods of obtained LIPSS. Authors of [23, 29, 35] emphasize that transient changes in material properties under laser irradiation are of crucial importance in the LIPSS formation. The energy of incident light 800 nm (1.55 eV) is less than the band gap of ZnSe single crystal, so the electrons in the valence band will be excited up to conduction band via two-photon absorption when the sample is irradiated by femtosecond laser
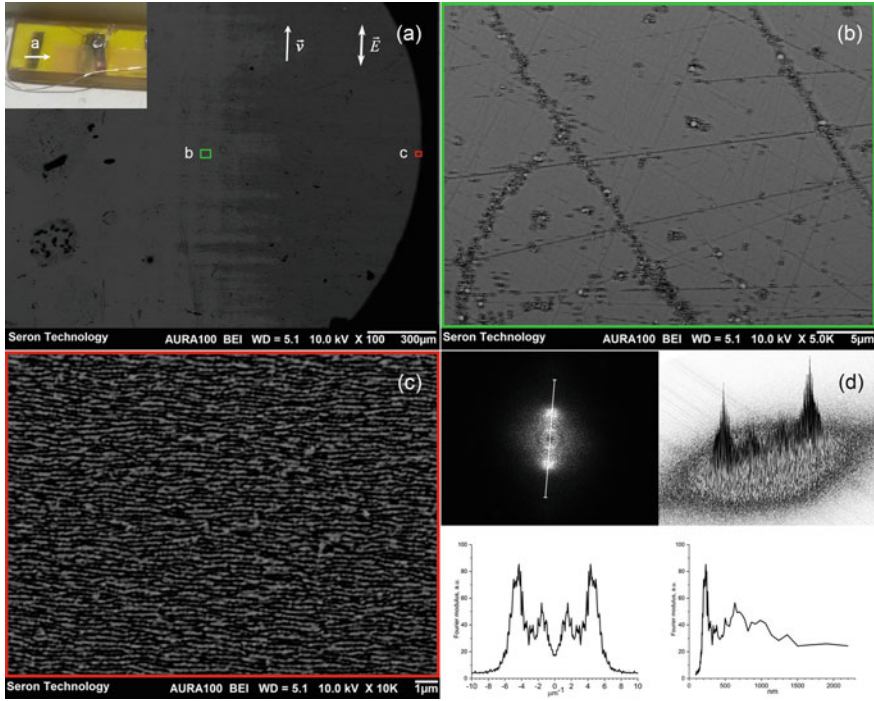
Fig. 28.1 SEM images of ZnSe surface treated with fs-laser beam focused with cylindrical lens (**a**, **b**, **c**): **a** general view of the treated sample, **b** surface irradiated by the beam periphery part, **c** central part of structured area; **d** 2D Fourier transforms of a SEM image **c** in two views; lower part of **d** presents the Fourier transform profile along the line at 2D Fourier transform and the Fourier transform profile in nanometers. The inset in **a** presents the view of fs-laser treated ZnSe single crystal

pulses. Therefore, the complex refractive index of the laser treated ZnSe is a function of the carrier density of conduction band electrons.

LSFLs are characterized by the periods smaller than the laser wavelength, since the surface damage begins at carrier concentrations close to the critical carrier density of surface plasmon polaritons excitation [23]. For semiconductors, it appears in a relatively narrow fluence range.

The period of HSFL in transparent materials usually follows the empirical formula $\Lambda \simeq \lambda/2n$, where n is the refractive index of an untreated material, and λ is the wavelength of the incident fs-laser beam. We obtained slightly higher periods of LIPSS (from 182 to 214 nm depending on a slight change in processing parameters for corresponding ZnSe surface). The modified fs-laser-excited refractive index n* for ZnSe is lower than that for untreated material [29, 33]. Thus, the periods of HSFL obtained in our experiments are in good accordance with the periodicity around 200 nm for bulk ZnSe demonstrated in other papers [33, 34].

For the evaluation of the possibility of further perspective applications of textured semiconductors, in particular ZnSe, the optical properties of modified surface should be examined. We studied near-band-edge emission and emission related to the impurities or structural defects of untreated and fs-laser treated ZnSe single crystal at room and liquid nitrogen temperatures (see Fig. 28.2). PL bands in the region from 500 to 700 nm determined by intrinsic point defects are of the same order of magnitude for untreated and textured areas of ZnSe. In general, it should be stated that the high structural perfection of ZnSe single crystal is not affected significantly under fs-laser processing at the levels of the energy density of around 0.04–0.05 J/cm^2, that do not exceed an ablation threshold for ZnSe which is about 0.7 J/cm^2 [37].

Direct Band Gap Semiconductor Gallium Arsenide (GaAs) ($E_G = 1.42$ eV at 300 K) belongs to A3B5 semiconductors. GaAs characterized with a higher electron mobility and higher thermal stability than silicon is perspective for the application in multi-junction or cascade solar cells, micro-optical components, and terahertz emitters. Production of functional surface frequently requires the texturing of GaAs surface. Femtosecond laser modification of GaAs has been reported in a number of papers [4, 38–40].

In our experiments, GaAs wafers were treated with linearly polarized fs-pulses (wavelength of 800 nm, the pulse energy density of ~0.4 J/cm^2). Observed LIPSS is orientated perpendicular to the laser beam polarization with period of 725 nm, additional feature in FFT (360 nm) corresponds to splitting of LSFL ridges. This process is sometimes associated with formation of some types of HSFL. There are several proposed mechanisms, namely enhancement of local electric field by
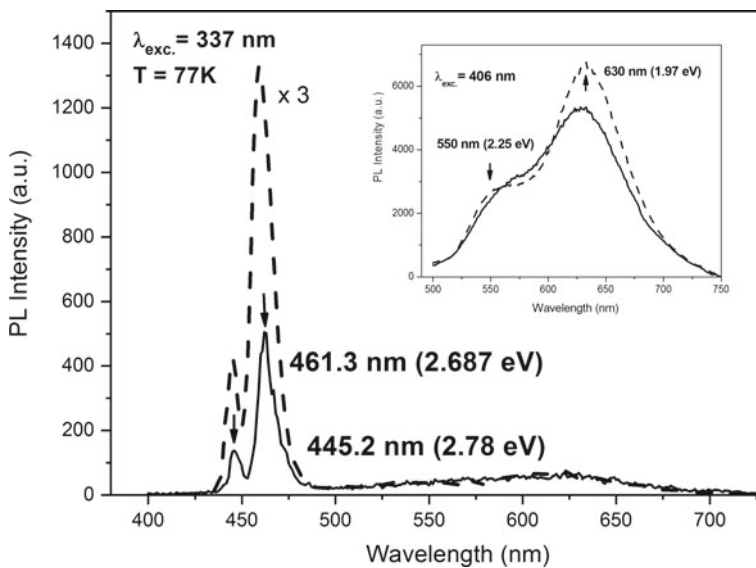

Fig. 28.2 PL spectra of fs-laser treated (solid line) and untreated (dashed line) surface of ZnSe sample at 77 K under an excitation of 337 and 406 nm (inset)

surface morphology [41] or laser-induced point defect accumulation and diffusion [38]. Supra-wavelength-sized quasi-gratings oriented parallel to the laser beam polarization, although known as grooves [42] with period of ~1.7 µm (see Figs. 28.3, and 28.4) although can be seen. Their formation is associated with heat accumulation and hydrodynamic effects [6]. The origin of the LSFL attributed to the electromagnetic approach, in particular the interference between the incident laser beam and SEWs including SPPs.

Cylindrical lens provides more smooth spatial variation of irradiation parameters athwart structured line. In combination with diaphragms of different shape, this allows to create large areas of homogeneous structures in a single scan, or one can study effects of different fluence and effective pulse number in different parts of the scan.

Figure 28.4 shows the same sample irradiated with beam focused by spherical lens. Resulting structures are less regular, and structures on beam periphery are quite different (Figs. 28.3b and 28.4b).
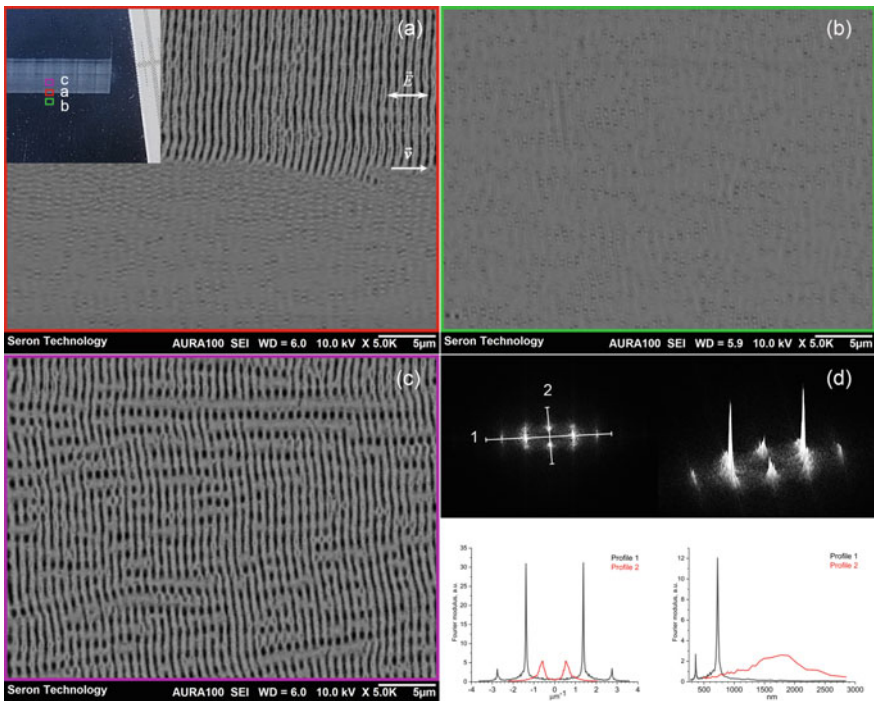

Fig. 28.3 SEM images of edge, outlying and central parts of an area scanned by laser beam focused with cylindrical lens at GaAs surface (**a**, **b**, **c**); 2D Fourier transform of a SEM image **c** of fs-laser treated GaAs surface (**d**); lower part of **d** presents the Fourier transform profiles along the lines 1, 2 in 2D Fourier transform **d** and the Fourier transform profiles in nanometers. An inset presents view of the fs-laser beam scanning area at GaAs surface
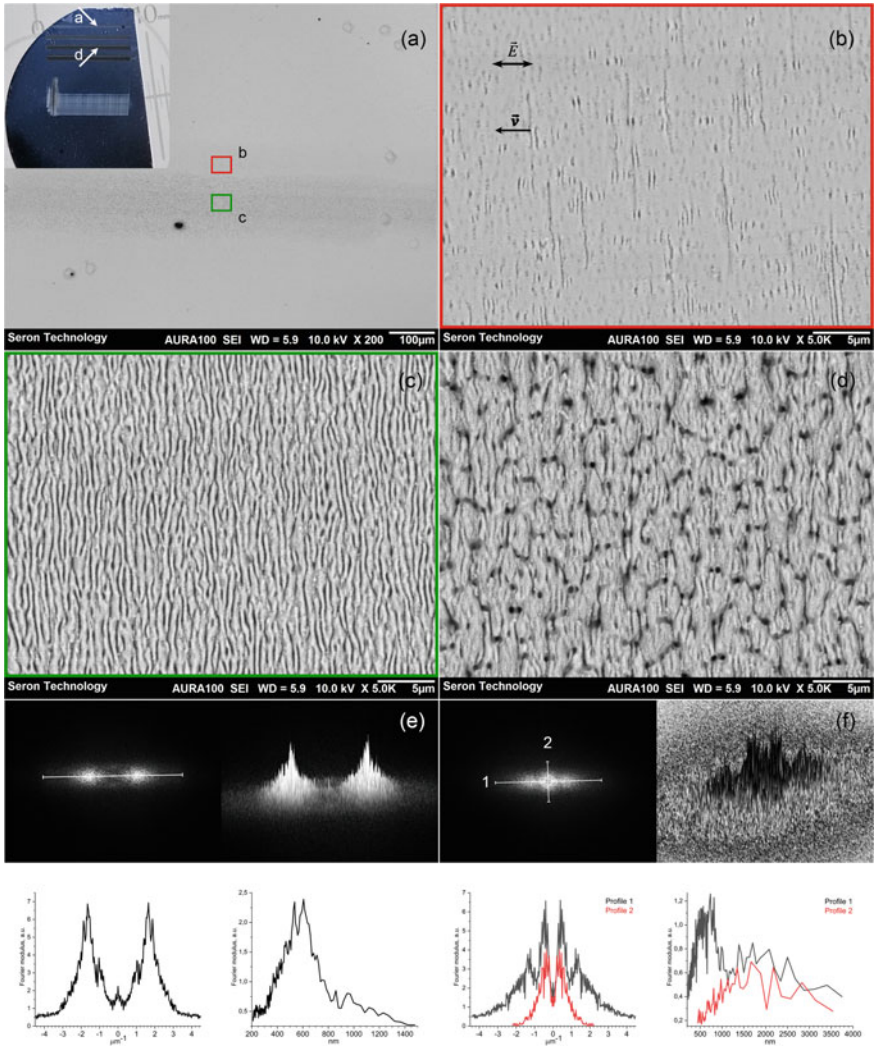
Fig. 28.4 SEM images of GaAs surface structured by scanning with spherical lens focused laser beam. **a** general view of structured area, **b**, **c** central and outlying parts of (**a**); **d** central part of area structured with higher fluence; **e** 2D Fourier transform of a SEM image (**c**); **f** 2D Fourier transform of a SEM image (**d**); lower part of the figure presents the Fourier transform profile along the line at 2D Fourier transform **e** and the Fourier transform profiles along lines 1, 2 at 2D Fourier transform (**f**), and corresponding Fourier transform profiles in nanometers. An inset in **a** presents view of the fs-laser beam scanning areas at GaAs surface

The laser fluence change results in change of morphology, namely appearance of porous and grain structures, periodicity violation, etc. (see Fig. 28.4c−d). The topology of the surface undergo drastic changes under increased fluence—the grain-porous structure is forming. On the grains with characteristic size of 1.7 μm, LSFL with period around 500–800 nm is formed. 2D Fourier transform of corresponding SEM image demonstrates the existence of two structural features in two perpendicular directions. The origin of such structure may be related to the effects of matter reorganization, in particular hydrodynamic effects of the transiently melted surface, material instabilities or defect creation, diffusion, or erosion effects enforced by ultrafast laser processing.

Obtained porous structure at the GaAs surface after the fs-laser treatment with higher power density (Fig. 28.4d) resembles chemically etched GaAs surface. It is characterized with rather high homogeneity.

To evaluate possible changes in optical properties, the near-band-edge emission of untreated and fs-laser treated GaAs samples represented at Fig. 28.3 has been studied at liquid nitrogen temperatures under an excitation of 532 nm (see Fig. 28.5). PL band at around 1.51 eV caused by the recombination of free excitons has been observed for untreated and fs-laser treated surfaces at T = 77 K. The intensity of PL band at fs-laser treated GaAs surface 2.5 times smaller than the one for untreated GaAs surface.
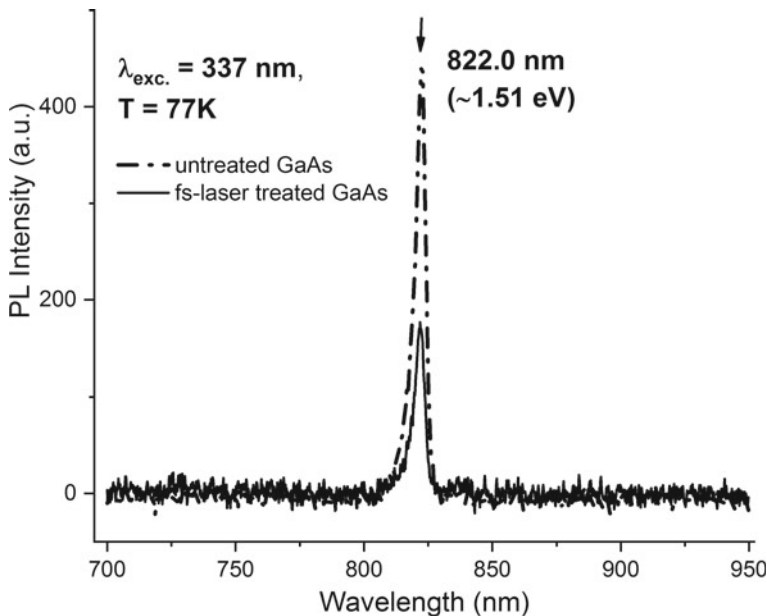

Fig. 28.5 PL spectra of fs-laser treated (solid line) and untreated (dashed line) surface of GaAs sample at 77 K under an excitation of 532 nm

Direct Band Gap Semiconductor Cadmium Zinc Telluride (CdZnTe) or CZT is an alloy of zinc telluride and cadmium telluride. CdZnTe is a direct band gap semiconductor with the band gap that varies from approximately 1.4 to 2.2 eV depending on Zn concentration. It possesses a high electro-optic coefficient and transparency in the mid-infrared region. CdZnTe is perspective for some applications, including semiconductor radiation detectors, photorefractive gratings, electro-optic modulators, solar cells, and terahertz detectors. Graded CdZnTe was proposed as an alternative for the pure CdTe in thin film solar cells for the increasing their efficiency [43].

Most of the experiments on laser processing of CdZnTe have been carried out with nanosecond (ns) laser pulses [43–47]. Nivas and co-authors [48] stated that the fs-laser-induced surface processing of CdZnTe has not been investigated yet. They carried out an experimental study of laser ablation and surface structuring of CdZnTe in air. The fs-laser pulses with the central wavelength around 800 nm, a pulse duration of $\approx$35 fs, have been used for three sets of the laser processing conditions (from the low peak fluence of 0.64 J/cm^2 up to the highest peak fluence of $\approx$7.0 J/cm^2). Both LSFL and HSFL perpendicular to the laser beam polarization have been observed. These LIPSSs are attributed to the progressive aggregation of randomly distributed nanoparticles, accompanied by the process of laser ablation at high pulse energy that produces a deep crater.

In our experiments on fs-laser treatment of CdZnTe the linearly polarized fs-laser radiation with central wavelength of 800 nm, the pulse energy density of ~0.4 J/cm^2 has been used. Slight change of fluence was attained by the sample shift from the focusing lens. The HSFLs with period of 220 nm are seen at Fig. 28.6c, e. It should be pointed out at the observed changes of the morphology at different edge areas of the laser beam scanning line at CdZnTe surface (see Fig. 28.6d, g, h). At the part of the laser beam scanning line, the clearly defined LSFL with the period of 550 nm has been formed. In Fig. 28.6 g, we can see that LSFL area exists in a strip near the edge of structured area and the structure become dominated by grooves closer to the middle. HSFL comprised of aggregated nanoparticles can be obtained not only around the crater but although by prolonged irradiation by low intensity beam as in our case. Less pronounced outlying structure on the upper part of b as well as structure in corresponding area for GaAs (Fig. 28.3b) needs further investigation.

The specific view of the scanned area (Fig. 28.6b) is due to the fact that scanning on short distances with subsequent change in the beam intensity was performed. Therefore, the scanned strip consists of places where the beam stopped and stood, and areas where the scanning took place. The technical features of mechanics lead to the accelerated movement at speed-up and braking mode that results in specific view of the structured area.
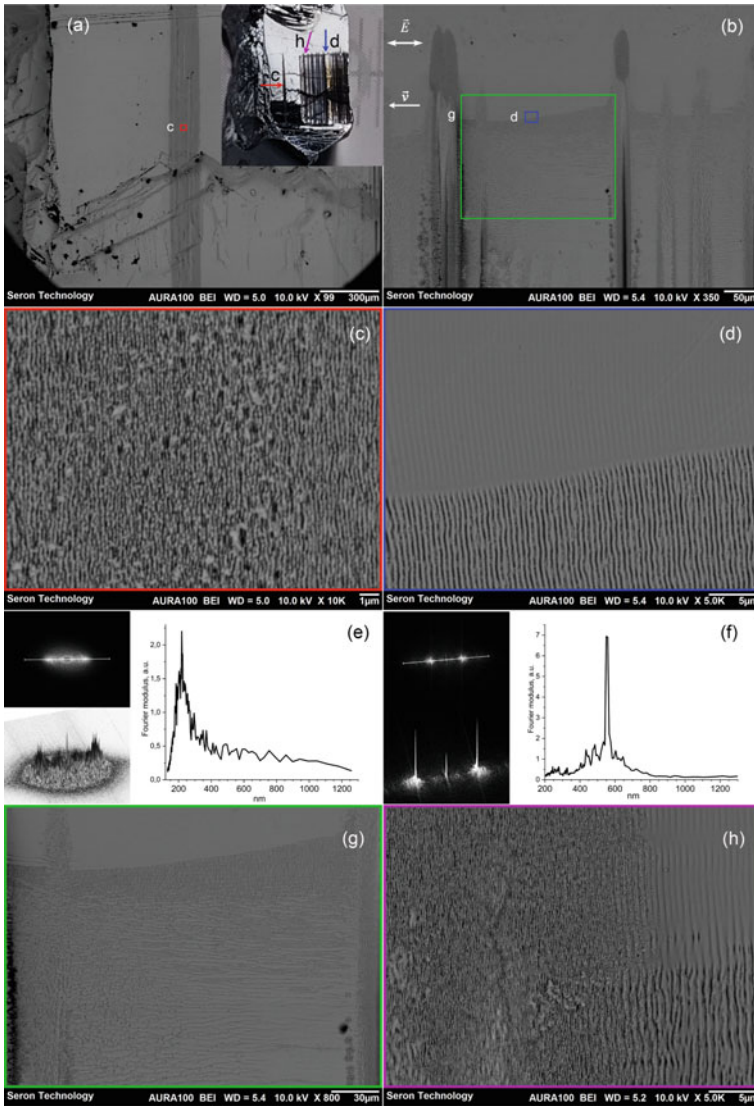
Fig. 28.6 SEM image of stationary fs-laser treated area at CdZnTe surface (**a**); SEM images of different edge laser beam scanning areas at CdZnTe surface (**b, d**); SEM image of the central part of the area structured by the stationary beam (**c**); 2D Fourier transform of a SEM image **c** presented in two views and the Fourier transform profile along the line at 2D Fourier transform presented in nanometers (**e**); 2D Fourier transform of a SEM image **d** in two views and corresponding Fourier transform profile along the line at 2D Fourier transform presented in nanometers (**f**); SEM image of the laser beam scanning area (**g**); SEM image of the place where adjoin areas formed by the stationary beam and by the scanning beam (**h**). An inset in **a** presents the view of the fs-laser treated areas at CdZnTe surface

28.4   Femtosecond Laser Processing of the Semiconductors with the Transition of Band Gap from a Direct Type to an Indirect Type

Layered semiconductor lead iodide (PbI$_2$) belongs to the transition metal halides (TMH) family applicable for perovskite solar cells, photodetectors, nuclear radiation detectors. This semiconductor is characterized with specific structure and interesting optical properties. Direct band gap of 2.26 eV in bulk PbI$_2$ transforms to an indirect band gap with an energy of 2.64 eV for a single-layer PbI$_2$ [49]. This thickness-dependent band gap determines the photoluminescence and optoelectronic properties of PbI$_2$.

In the literature, we did not find any scientific articles directly related to fs-laser processing of PbI$_2$. There were attempts of laser patterning of the solar cell layers of perovskite solar modules by nanosecond laser pulses with durations of about ≈ 30 ns at a wavelength of 532 nm [50]. Authors observed LIPSS with residuals composed of PbI$_2$ remains even at higher fluences.

In our experiments, we carried out the direct fs-laser texturing of PbI$_2$ surface with the linearly polarized fs-laser radiation with central wavelength of 800 nm, the pulse energy density of ~0.4–0.5 J/cm^2. The results of morphology analysis of untreated and fs-laser treated surfaces of PbI$_2$ are presented at Fig. 28.7. We discovered the exfoliation of the PbI$_2$ layers during fs-laser treatment (see Fig. 28.7b). We observed the beginning of the LSFL formation with a period of around 700 nm at applied fluences (see Fig. 28.7c−d). The obtained LSFLs are irregular and weakly pronounced.

Layered semiconductor gallium selenide (GaSe) is a layered semiconductor with an indirect band gap of ~2.1 eV. The thickness of GaSe films has a strong influence on its electronic structure. 2D GaSe thin films have a larger band gap than the bulk GaSe. A single layer consists of covalently bonded Se-Ga-Ga-Se atoms. Each Ga atom is tetragonally oriented to three Se atoms and one Ga atom. The layers are stacked together via van der Waals interaction. According to theoretical calculations [51–53], bulk GaSe has a direct band gap. A direct-to-indirect band gap transition occurs as the number of layers is decreasing below some critical value. As the number of layers decreases to below 7, the calculations show that the conduction band minimum remains at the Brillouin zone center (Γ point), but the valence band maximum shifts away from Γ point to nearby k points [52]. The energy band in the vicinity of the Γ point exhibits a Mexican-hat-like dispersion. GaSe crystals are characterized with wide optical transparency of 0.65−18 μm. GaSe has been used as a photoconductor, a second-harmonic generation crystal in nonlinear optics. GaSe is used to generate THz radiation up to 31 THz and above. GaSe also is perspective for applications in solar cells. According to available literature data, there are only few articles devoted to GaSe laser processing [54]. There is lack of information about fs-laser processing of GaSe semiconductor.
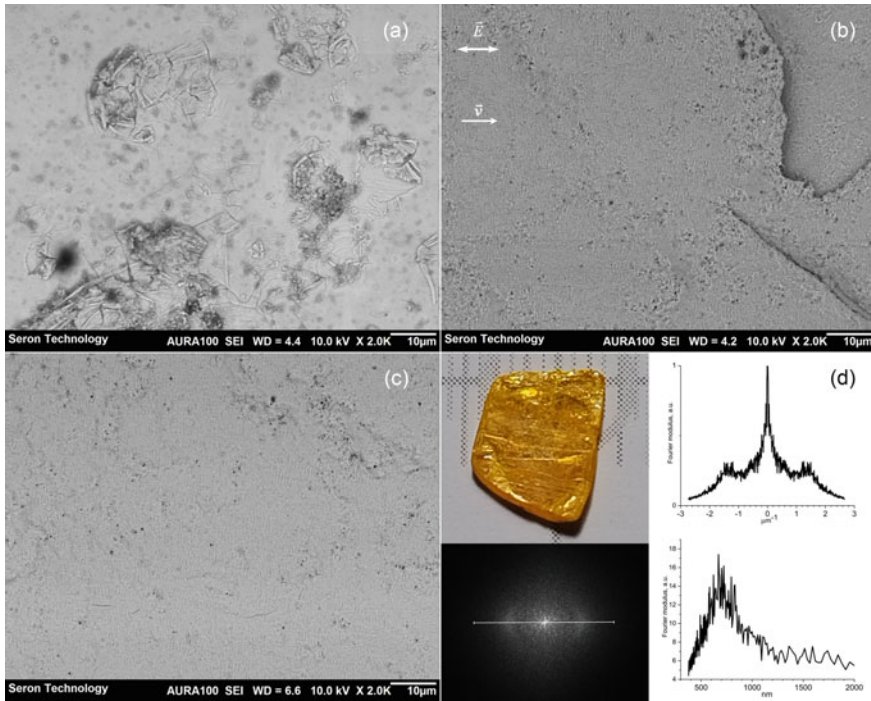
Fig. 28.7   SEM image of untreated PbI$_2$ surface (**a**); SEM images of different fs-laser treated areas of PbI$_2$ surface (**b**, **c**); **d** represents the view of PbI$_2$ sample, 2D Fourier transform of a SEM image (**c**), the Fourier transform profile along the line in 2D Fourier transform and corresponding Fourier transform profile in nanometers

After fs-laser treatment at the pulse energy density of ∼ 0.5–0.6 J/cm^2, the LSFL with period of 620 nm and HSFL with period around 230–250 nm have been discovered (see Fig. 28.8). Figure 28.8b−c, demonstrates the beginning of modification of GaSe surface assisted with surface defects. This process has been observed at lower fluence. At Fig. 28.8d−e, one can see exfoliated area of GaSe sample. At Fig. 28.8f, the fingerprints of typical LIPSS formed at GaSe surface under fs-laser radiation are marked with 1, 2, 3, and corresponding profiles are presented in Fig. 28.8i. Periodic structures marked with 1, 3 have similar direction of ripples but different periods. The period of LIPSS labeled by 2 correlates with the value of period of structure marked 3, but the directions are perpendicular each other. To elucidate the origin of such variety of structures, more careful experiments should be carried out.
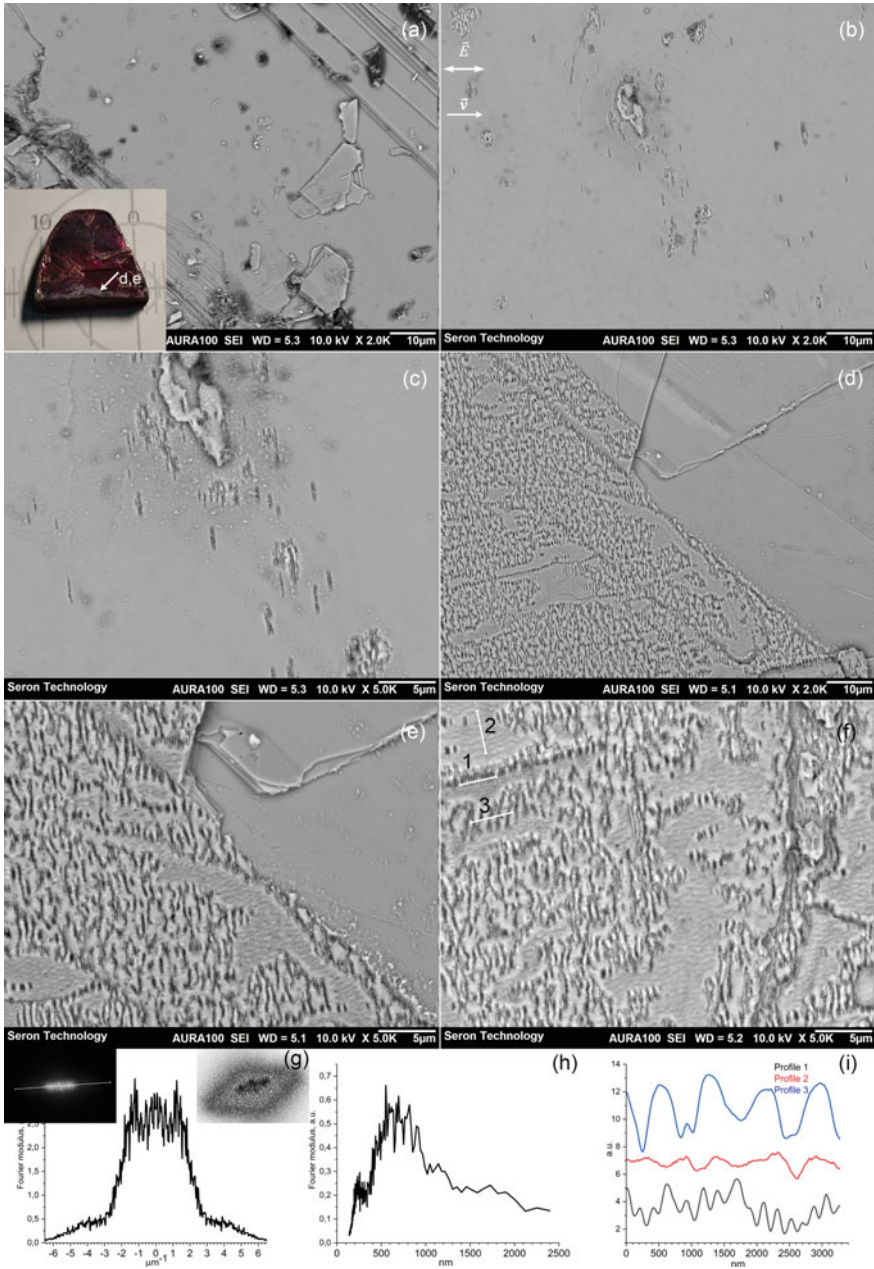
Fig. 28.8 **a** SEM image of untreated GaSe surface; **b** SEM image of GaSe surface treated at the pulse energy density of ~0.5 J/cm^2; **c** enlarged view of SEM image (**b**); an area with exfoliated part of the sample **d** and its enlarged view (**e**); SEM image of treated GaSe and different types of LIPSSs marked with 1, 2, 3 (**f**); insets in **g** present 2D Fourier transform of SEM image (**f**), corresponding Fourier transform profile along the line on 2D Fourier transform and corresponding Fourier transform profile in nanometers (**g**, **h**), surface profiles marked with 1, 2, 3 (**i**). An inset in **a** presents the view of the GaSe sample

28.5   The Femtosecond Laser Processing of Indirect Band Gap Semiconductors

Indirect band gap semiconductor silicon (Si) belongs to the most widely used semiconductors for various applications. Laser processing of silicon is actively studied, as Si demonstrates some specific characteristics under irradiation with ultrashort laser pulses [7, 12, 13, 23, 24, 55]. Different mechanisms of the formation of LIPSS at the Si surface have been considered, namely self-organization of LIPSS, the interference of the incident laser radiation with SEWs, including SPP and counterpropagating plasmon waves. Main characteristics of LIPPS depend on the laser processing conditions (laser polarization, frequency, pulse irradiation energy density, angle of incidence, and scanning velocity).

In this research, we briefly present the LIPSS formation on silicon surface, paying special attention on the LIPSS morphology. Polished n-doped silicon (100) wafers have been used for LIPSS formation. Micro- and nanostructuring of silicon surfaces have been obtained by irradiation of fs-laser pulses of the wavelength of 800 nm, the pulse energy of about 1.44 mJ, the pulse duration of ~150 fs, and the repetition rate of 1 kHz. At Fig. 28.9, one can see typical LIPSS formed at silicon surface. The orientation of the LIPSS is perpendicular to the laser beam polarization. 2D-FFT analysis of SEM image at Fig. 28.9a, determines the period of corresponding LSFL of approximately 540 nm. Additional feature in FFT (310 nm) corresponds to the splitting of LSFL ridges. The existence of ripples with the reduced period could be determined by the second-harmonic generation of laser radiation at the silicon surface. SEM images analysis reveals the presence of the strip breaks and loops at LSFL. These defects resemble edge dislocations. Figure 28.9b corresponds to the irradiation conditions with bigger fluence. LSFL at Fig. 28.9b, is characterized with the period of about 590 nm. At this SEM image, the grooves with supra-micron period perpendicular to LSFL are clearly seen.

Figure 28.9e−f demonstrate SEM images of silicon surface treated at a half-velocity compared to the processing conditions of silicon presented at SEM image (b). In this case, we obtained more prolonged impact of the laser radiation on the viewed area (e, f) that causes the enlarged efficacy of thermal and ablation processes at this area due to the processing conditions. Accidentally, we discovered LSFL under the layer that probably consists of ablated products and/or oxides after mechanical remove of upper layer in this part of the fs-laser treated area. Morphologies on Fig. 28.9 suggest that we are observing structured surface on (a) and a layer of periodically aggregated particles on (b). Whether there is although structured surface beneath them needs further investigation.

In our previous paper [56], emission from the processing area of silicon samples has been also studied to clarify the LIPSS formation on silicon. The emission spectra from a moving silicon sample during femtosecond laser treatment revealed wide PL band attributed to the oxidized silicon, second-harmonic generation (SHG) of the laser radiation on the LIPSS, and sharp emission lines (EL) of the silicon atoms or
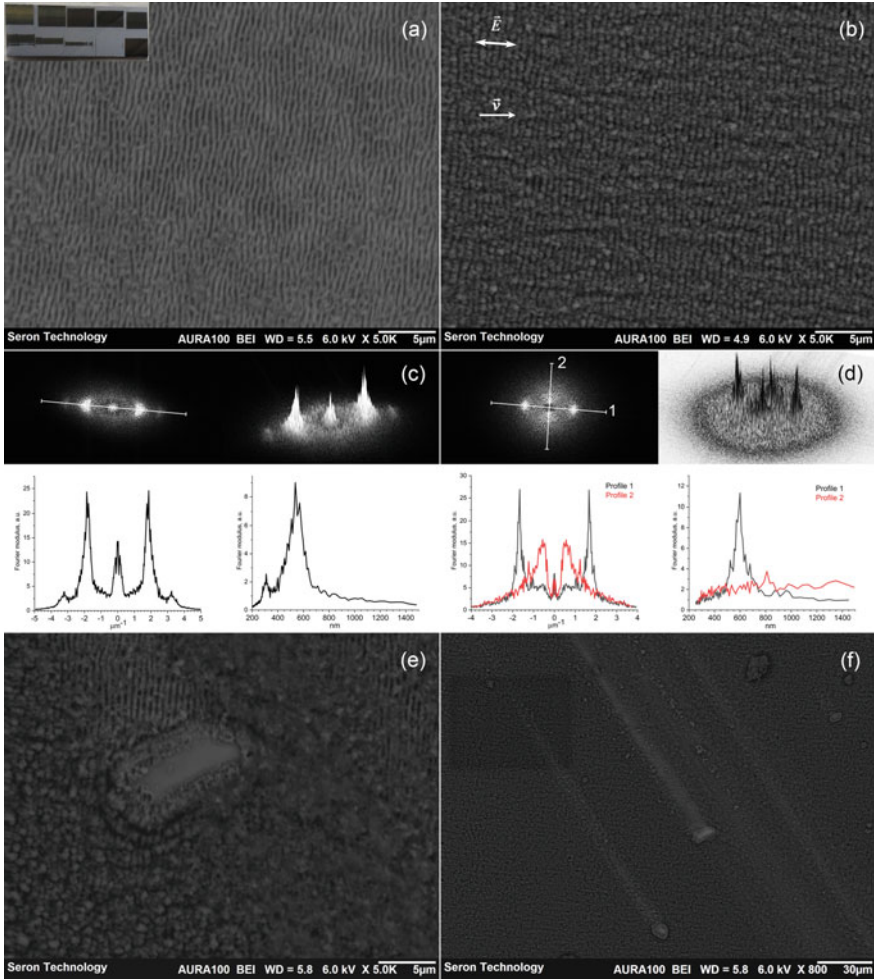
Fig. 28.9 SEM image of the fs-laser treated silicon surface (**a**, **b**); **e** SEM image of surface of fs-laser treated silicon surface at a half-velocity compared to the conditions of SEM image (**b**); **f** enlarged view of SEM image (**e**); **c** 2D Fourier transform of a SEM image (**a**), at the low part of **c**—Fourier transform profile along the line in 2D Fourier transform and corresponding Fourier transform profile in nanometers; **d** 2D Fourier transform of a SEM image (**b**), at the low part of **d**—Fourier transform profiles along the lines in 2D Fourier transform and corresponding Fourier transform profiles in nanometers. An inset in **a** presents the view of the silicon sample

ions produced during laser ablation of silicon. The ratio of SHG to PL (or SHG to EL) intensities is suggested as a real-time quality measure for LIPSS generation.

There are few scientific works comparing fs-laser structuring of semiconductors with direct and indirect band gaps [21, 26, 57]. This situation is obviously due to the fact that the resembling kinds of LIPSS are observed in both types of semiconductors,

and their nature is considered from more general approaches that take into account the nature of electromagnetic effects or effects of matter reorganization.

Sei and co-authors [57] underline the longer relaxation time of the excited carrier in an indirect band gap semiconductor that requires a certain correlation of the positions of not only electrons and holes but also phonons. In the case of fs-laser processed semiconductors such as silicon, the interference between the laser beam and the SEW electromagnetic field, as well as the subsequent coupling of the electronic system and the lattice of the solid through electron–phonon coupling, thermal diffusion, electron diffusion, and the phase transition of thermal melting have to be considered [26, 27].

28.6 Conclusions

The peculiarities of laser-induced surface structures produced with the femtosecond laser radiation on semiconductors with direct (ZnSe, GaAs, CdZnTe) band gap, with the structurally induced direct-to-indirect band gap transition (PbI_2, GaSe) and indirect band gap (Si) have been analyzed by scanning electron microscopy, 2D Fourier transform of SEM images, optical spectroscopy. The fs-laser treatment of semiconductors has been performed in the multi-pulse regime in air environment. Under the treatment with the fundamental fs-laser radiation (800 nm, about 130–150 fs), both low spatial frequency LIPSS and high spatial frequency LIPSS have been observed. Other features at the surface (different defects in periodic structure, ablation products, etc.) have been also revealed. In spite of a lot of similar features of formed LIPSSs at semiconductors with direct and indirect band gaps, some factors such as the electron–phonon coupling could have different effectiveness in each of these semiconductors. Information about laser structuring of some of presented materials in literature is sparse. Thus, further investigations are reasonable.

References

1. Vorobyev AY, Makin VS, Guo C (2007) Periodic ordering of random surface nanostructures induced by femtosecond laser pulses on metals. J Appl Phys101(3):034903. https://doi.org/10.1063/1.2432288
2. Colombier JP, Garrelie F, Faure N, Reynaud S, Bounhalli M, Audouard E, Stoian R, Pigeon F (2012) Effects of electron-phonon coupling and electron diffusion on ripples growth on ultrafast-laser-irradiated metals. J Appl Phys 111(2):024902. https://doi.org/10.1063/1.3676221

3. Gurevich EL, Levy Y, Bulgakova NM (2020) Three-step description of single-pulse formation of laser-induced periodic surface structures on metals. Nanomaterials 10(9):1836. https://doi.org/10.3390/nano10091836

4. Borowiec A, Haugen HK (2003) Subwavelength ripple formation on the surfaces of compound semiconductors irradiated with femtosecond laser pulses. Appl Phys Lett 82(25):4462–4464. https://doi.org/10.1063/1.1586457

5. Huang M, Zhao F, Cheng Y, Xu N, Xu Z (2009) Origin of laser-induced near-subwavelength ripples: interference between surface plasmons and incident laser. ACS Nano 3(12):4062–4070. https://doi.org/10.1021/nn900654v

6. Tsibidis GD, Fotakis C, Stratakis E (2015) From ripples to spikes: A hydrodynamical mechanism to interpret femtosecond laser-induced self-assembled structures. Phys Rev B 92(4):041405. https://doi.org/10.1103/PhysRevB.92.041405

7. Florian C, Fischer D, Freiberg K, Duwe M, Sahre M, Schneider S, Hertwig A, Krüger J, Rettenmayr M, Beck U, Undisz A, Bonse J (2021) Single femtosecond laser-pulse-induced superficial amorphization and re-crystallization of silicon. Materials 14(7):1651. https://doi.org/10.3390/ma14071651

8. Reif J, Costache F, Henyk M, Pandelov SV (2002) Ripples revisited: non-classical morphology at the bottom of femtosecond laser ablation craters in transparent dielectrics. Appl Surf Sci 197–198:891–895. https://doi.org/10.1016/S0169-4332(02)00450-6

9. Buividas R, Mikutis M, Juodkazis S (2014) Surface and bulk structuring of materials by ripples with long and short laser pulses: recent advances. Prog Quantum Electron 38(3):119–156. https://doi.org/10.1016/j.pquantelec.2014.03.002

10. Rudenko A, Colombier J-P, Höhm S, Rosenfeld A, Krüger J, Bonse J, Itina TE (2017) Spontaneous periodic ordering on the surface and in the bulk of dielectrics irradiated by ultrafast laser: a shared electromagnetic origin. Sci Rep 7(1):12306. https://doi.org/10.1038/s41598-017-12502-4

11. Birnbaum M (1965) Semiconductor surface damage produced by ruby lasers. J Appl Phys 36(11):3688–3689. https://doi.org/10.1063/1.1703071

12. Vorobyev AY, Guo C (2011) Antireflection effect of femtosecond laser-induced periodic surface structures on silicon. Opt Expr 19(S5):A1031. https://doi.org/10.1364/OE.19.0A1031

13. Dostovalov A, Bronnikov K, Korolkov V, Babin S, Mitsai E, Mironenko A, Tutov M, Zhang D, Sugioka K, Maksimovic J, Katkus T, Juodkazis S, Zhizhchenko A, Kuchmizhak A (2020) Hierarchical anti-reflective laser-induced periodic surface structures (LIPSSs) on amorphous Si films for sensing applications. Nanoscale 12(25):13431–13441. https://doi.org/10.1039/D0NR02182B

14. Öktem B, Pavlov I, Ilday S, Kalaycıoğlu H, Rybak A, Yavaş S, Erdoğan M, Ilday FÖ (2013) Nonlinear laser lithography for indefinitely large-area nanostructuring with femtosecond pulses. Nat Photonics 7(11):897–901. https://doi.org/10.1038/nphoton.2013.272

15. Mokkapati S, Beck FJ, Polman A, Catchpole KR (2009) Designing periodic arrays of metal nanoparticles for light-trapping applications in solar cells. Appl Phys Lett 95(5):053115. https://doi.org/10.1063/1.3200948

16. Dmitruk NL, Borkovskaya OY, Mamontova IB, Mamykin SV, Malynych SZ, Romanyuk VR (2015) Metal nanoparticle-enhanced photocurrent in GaAs photovoltaic structures with microtextured interfaces. Nanoscale Res Lett 10(1):72. https://doi.org/10.1186/s11671-015-0786-6

17. Berezovska N, Dmitruk I, Kalyuzhnyy A, Dmytruk A, Blonskyi I (2018) Self-organized structuring of the surface of a metal–semiconductor composite by femtosecond laser processing. Ukr J Phys 63(5):406. https://doi.org/10.15407/ujpe63.5.406

18. Saikiran V, Dar MH, Kuladeep R, Desai NR (2016) Ultrafast laser induced subwavelength periodic surface structures on semiconductors/metals and application to SERS studies. MRS Adv 1(49):3317–3327. https://doi.org/10.1557/adv.2016.468

19. Hamad S, Bharati Moram SS, Yendeti B, Podagatlapalli GK, Nageswara Rao SVS, Pathak AP, Mohiddon MA, Soma VR (2018) Femtosecond laser-induced, nanoparticle-embedded periodic surface structures on crystalline silicon for reproducible and multi-utility SERS platforms. ACS Omega 3(12):18420–18432. https://doi.org/10.1021/acsomega.8b02629

20. Bonse J, Hohm S, Kirner SV, Rosenfeld A, Kruger J (2017) Laser-induced periodic surface structures—a scientific evergreen. IEEE J Sel Top Quantum Electron 23(3):9000615. https://doi.org/10.1109/JSTQE.2016.2614183

21. Bonse J, Gräf S (2020) Maxwell meets Marangoni—a review of theories on laser-induced periodic surface structures. Laser Photonics Rev 14(10):2000215. https://doi.org/10.1002/lpor.202000215

22. Vorobyev AY, Guo C (2013) Direct femtosecond laser surface nano/microstructuring and its applications. Laser Photonics Rev 7(3):385–407. https://doi.org/10.1002/lpor.201200017

23. Bonse J, Rosenfeld A, Krüger J (2009) On the role of surface plasmon polaritons in the formation of laser-induced periodic surface structures upon irradiation of silicon by femtosecond-laser pulses. J Appl Phys 106(10):104910. https://doi.org/10.1063/1.3261734

24. Tsibidis GD, Barberoglou M, Loukakos PA, Stratakis E, Fotakis C (2012) Dynamics of ripple formation on silicon surfaces by ultrashort laser pulses in subablation conditions. Phys Rev B 86(11):115316. https://doi.org/10.1103/PhysRevB.86.115316

25. Zhang H, Colombier J-P, Witte S (2020) Laser-induced periodic surface structures: arbitrary angles of incidence and polarization states. Phys Rev B 101(24):245430. https://doi.org/10.1103/PhysRevB.101.245430

26. Derrien T, Sarnet T, Sentis M, Itina T (2010) Application of a two-temperature model for the investigation of the periodic structure formation on Si surface in femtosecond laser interactions. J Optoelectron Adv Mater12(3):610–615. https://hal-ujm.archives-ouvertes.fr/ujm-00530631

27. Levy Y, Derrien TJ-Y, Bulgakova NM, Gurevich EL, Mocek T (2016) Relaxation dynamics of femtosecond-laser-induced temperature modulation on the surfaces of metals and semiconductors. Appl Surf Sci 374:157–164. https://doi.org/10.1016/j.apsusc.2015.10.159

28. Florian C, Kirner SV, Krüger J, Bonse J (2020) Surface functionalization by laser-induced periodic surface structures. J Laser Appl 32(2):022063. https://doi.org/10.2351/7.0000103

29. Jia TQ, Chen HX, Huang M, Zhao FL, Qiu JR, Li RX, Xu ZZ, He XK, Zhang J, Kuroda H (2005) Formation of nanogratings on the surface of a ZnSe crystal irradiated by femtosecond laser pulses. Phys Rev B 72(12):125429. https://doi.org/10.1103/PhysRevB.72.125429

30. Ma HL, Guo Y, Zhong MJ, Li RX (2007) Femtosecond pulse laser-induced self-organized nanogratings on the surface of a ZnSe crystal. Appl Phys A 89(3):707–709. https://doi.org/10.1007/s00339-007-4147-x

31. Jia T, Baba M, Huang M, Zhao F, Qiu J, Wu X, Ichihara M, Suzuki M, Li R, Xu Z, Kuroda H (2007) Femtosecond laser-induced ZnSe nanowires on the surface of a ZnSe wafer in water. Solid State Commun 141(11):635–638. https://doi.org/10.1016/j.ssc.2006.12.025

32. Wang HI, Tang WT, Liao LW, Tseng PS, Luo CW, Yang CS, Kobayashi T (2012) Femtosecond laser-induced formation of Wurtzite phase ZnSe Nanoparticles in Air. J Nanomater 2012:1–6. https://doi.org/10.1155/2012/278364

33. Wang L, Chen Q-D, Yang R, Xu B-B, Wang H-Y, Yang H, Huo C-S, Sun H-B, Tu H-L (2014) Rapid production of large-area deep sub-wavelength hybrid structures by femtosecond laser light-field tailoring. Appl Phys Lett 104(3):031904. https://doi.org/10.1063/1.4832878

34. Xiao Y, Deng G, Feng G, Ning S, Wang S, Chen X, Yang H, Zhou S (2019) Femtosecond laser induced nano-meter size surface structures on ZnSe film. AIP Adv 9(1):015106. https://doi.org/10.1063/1.5067307

35. Wang S, Feng G, Zhou S (2014) Microsized structures assisted nanostructure formation on ZnSe wafer by femtosecond laser irradiation. Appl Phys Lett 105(25):253110. https://doi.org/10.1063/1.4904998

36. Dmitruk I, Berezovska N, Degoda V, Hrabovskyi Y, Kolodka R, Podust G, Stanovyi O, Blonskyi I (2021) Luminescence of femtosecond laser-processed ZnSe Crystal. J Nanomater 2021:1–9. https://doi.org/10.1155/2021/6683040

37. Wang X, Jia T, Li X, Li C, Feng D, Sun H, Xu S, Xu Z (2005) Ablation and ultrafast dynamics of zinc selenide under femtosecond laser irradiation. Chin Opt Lett 3(10):615–617. http://www.osapublishing.org/col/abstract.cfm?URI=col-3-10-615

38. Abere MJ, Torralva B, Yalisove SM (2016) Periodic surface structure bifurcation induced by ultrafast laser generated point defect diffusion in GaAs. Appl Phys Lett 108(15):153110. https://doi.org/10.1063/1.4946861

39. Margiolakis A, Tsibidis GD, Dani KM, Tsironis GP (2018) Ultrafast dynamics and subwavelength periodic structure formation following irradiation of GaAs with femtosecond laser pulses. Phys Rev B 98(22):224103. https://doi.org/10.1103/PhysRevB.98.224103

40. Sun X, Zhou F, Dong X, Zhang F, Liang C, Duan L, Hu Y, Duan J (2020) Fabrication of GaAs micro-optical components using wet etching assisted femtosecond laser ablation. J Mod Opt 67(20):1516–1523. https://doi.org/10.1080/09500340.2020.1869849

41. Hou S, Huo Y, Xiong P, Zhang Y, Zhang S, Jia T, Sun Z, Qiu J, Xu Z (2011) Formation of long- and short-periodic nanoripples on stainless steel irradiated by femtosecond laser pulses. J Phys D: Appl Phys 44(50):505401. https://doi.org/10.1088/0022-3727/44/50/505401

42. Bonse J, Krüger J (2010) Pulse number dependence of laser-induced periodic surface structures for femtosecond laser irradiation of silicon. J Appl Phys 108(3):034903. https://doi.org/10.1063/1.3456501

43. Morales-Acevedo A (2011) Analytical model for the photocurrent of solar cells based on graded band-gap CdZnTe thin films. Sol Energy Mater Sol Cells 95(10):2837–2841. https://doi.org/10.1016/j.solmat.2011.05.045

44. Medvid' A, Fedorenko L, Korbutjak B, Kryluk S, Yusupov M, Mychko A (2007) Formation of graded band-gap in CdZnTe by YAG:Nd laser radiation. Radiation MeasureM 42(4–5):701–703. https://doi.org/10.1016/j.radmeas.2007.01.070

45. Medvid A, Mychko A, Strilchyk O, Litovchenko N, Naseka Y, Onufrijevs P, Pludonis A (2009) Exciton quantum confinement effect in nanostructures formed by laser radiation on the surface of CdZnTe ternary compound. Phys Stat Sol (c) 6(1):209–212. https://doi.org/10.1002/pssc.200879869

46. Gnatyuk VA, Vlasenko OI, Levytskyi SN, Aoki T (2015) Laser-induced modification of properties of CdZnTe crystals. AMR 1117:15–18. https://doi.org/10.4028/www.scientific.net/AMR.1117.15

47. Medvid' A, Mychko A, Dauksta E, Kosyak V, Grase L (2016) Laser ablation in CdZnTe crystal due to thermal self-focusing: secondary phase hydrodynamic expansion. Appl Surf Sci 374:77–80.https://doi.org/10.1016/j.apsusc.2015.09.225

48. Nivas JJJ, Allahyari E, Vecchione A, Hao Q, Amoruso S, Wang X (2020) Laser ablation and structuring of CdZnTe with femtosecond laser pulses. J Mater Sci Technol 48:180–185. https://doi.org/10.1016/j.jmst.2020.01.059

49. Frisenda R, Island JO, Lado JL, Giovanelli E, Gant P, Nagler P, Bange S, Lupton JM, Schüller C, Molina-Mendoza AJ, Aballe L, Foerster M, Korn T, Angel Niño M, de Lara DP, Pérez EM, Fernandéz-Rossier J, Castellanos-Gomez A (2017) Characterization of highly crystalline lead iodide nanosheets prepared by room-temperature solution processing. Nanotechnology 28(45):455703. https://doi.org/10.1088/1361-6528/aa8e5c

50. Schultz C, Schneider F, Neubauer A, Bartelt A, Jost M, Rech B, Schlatmann R, Albrecht S, Stegemann B (2018) Evidence of PbI$_2$—containing debris upon P2 nanosecond laser patterning of perovskite solar cells. IEEE J Photovoltaics 8(5):1244–1251. https://doi.org/10.1109/JPHOTOV.2018.2858934

51. Zhu Z, Cheng Y, Schwingenschlögl U (2012) Topological phase transition in layered GaS and GaSe. Phys Rev Lett 108(26):266805. https://doi.org/10.1103/PhysRevLett.108.266805

52. Li X, Lin M-W, Puretzky AA, Idrobo JC, Ma C, Chi M, Yoon M, Rouleau CM, Kravchenko II, Geohegan DB, Xiao K (2015) Controlled vapor phase growth of single crystalline, two-dimensional GaSe crystals with high photoresponse. Sci Rep 4(1):5497. https://doi.org/10.1038/srep05497

53. Ma Y, Dai Y, Guo M, Yu L, Huang B (2013) Tunable electronic and dielectric behavior of GaS and GaSe monolayers. Phys Chem Chem Phys 15(19):7098. https://doi.org/10.1039/c3cp50233c

54. Cheshev D, Rodriguez RD, Matković A, Ruban A, Chen J-J, Sheremet E (2020) Patterning GaSe by high-powered laser beams. ACS Omega 5(17):10183–10190. https://doi.org/10.1021/acsomega.0c01079

55. Stratakis E, Bonse J, Heitz J, Siegel J, Tsibidis GD, Skoulas E, Papadopoulos A, Mimidis A, Joel A-C, Comanns P, Krüger J, Florian C, Fuentes-Edfuf Y, Solis J, Baumgartner W (2020)

Laser engineering of biomimetic surfaces. Mater Sci Eng: R: Reports 141:100562. https://doi.org/10.1016/j.mser.2020.100562

56. Dmytruk A, Dmitruk I, Berezovska N, Karlash A, Kadan V, Blonskyi I (2021) Emission from silicon as a real-time figure of merit for laser-induced periodic surface structure formation. J Phy D: Appl Phys 54(26):265102. https://doi.org/10.1088/1361-6463/abf22a

57. Sei T, Shimotsuma Y, Sakakura M, Miura K (2016) Self-assembled nanostructures inside indirect bandgap semiconductor by using ir femtosecond double-pulses. J Laser Micro Nanoeng 11(1):76–80. https://doi.org/10.2961/jlmn.2016.01.0014

Chapter 29
Dielectric and Photoluminescent Properties of the Water–Cellulose–NaCl Systems in a Wide Range of Temperatures: What is the Role of Ions?

M. M. Lazarenko, S. G. Nedilko, D. O. Shevtsov, V. P. Scherbatskyi, V. A. Barbash, K. S. Yablochkova, V. I. Kovalchuk, D. A. Andrusenko, R. V. Dinzhos, N. M. Fialko, E. A. Lysenkov, S. V. Gryn, and O. M. Alekseev

29.1 Introduction

Composite materials are gaining in increasing recognition in the world [1–5]. Nanocellulose is one of the most promising substances to fill the composites [6–11], as it gives composites biodegrading properties [12, 13].

M. M. Lazarenko (✉) · S. G. Nedilko · D. O. Shevtsov · V. P. Scherbatskyi · K. S. Yablochkova · V. I. Kovalchuk · D. A. Andrusenko · S. V. Gryn · O. M. Alekseev
Taras Shevchenko National University of Kyiv, Kyiv, Ukraine
e-mail: maxs@univ.kiev.ua

D. A. Andrusenko
e-mail: and_@univ.kiev.ua

O. M. Alekseev
e-mail: alan@univ.kiev.ua

V. A. Barbash
National Technical University of Ukraine "Igor Sikorsky Kyiv Polytechnic Institute", Kyiv, Ukraine
e-mail: v.barbash@kpi.ua

R. V. Dinzhos
V.O. Sukhomlynskyi Mykolaiv National University, Nikolaev, Ukraine

R. V. Dinzhos · N. M. Fialko
Institute of Engineering, Thermophysics of NAS of Ukraine, Kyiv, Ukraine
e-mail: nmfialko@ukr.net

E. A. Lysenkov
Petro Mohyla Black Sea National University, Mykolayiv, Ukraine
e-mail: ealysenkov@ukr.net

Nanocellulose extraction from the raw plant material begins with its acid or alkaline delignification (step 1), when the lignin shells of native microfibrils and hemicellulose layers are destroyed, and the lateral contacts between the nanofibrils and their co-crystallization become possible, leading to the creation of the cellulose microfibrils. Next, weak acid hydrolysis (step 2) can be carried out to destroy molecular segments in mesomorphic domains, which, unlike the crystalline ones, are accessible to water and reagents. Such a procedure decreases the polymerization degree of the cellulose molecules down to the "level off" degree of polymerization, which is determined by the length of the crystalline domains in the nanofibrils. These nanofibrils become cellulose nanocrystals: cylindrical in shape, with sharpened ends (whiskers), the aspect ratio of which depends on the source origin of the cellulose [10]. The cross section of the whiskers can be either hexagonal or rectangular, depending on the socket geometry of the terminal complex of the cellulose source cells [10, 14]. The nanocrystals formed are prone to aggregation in the liquid environment, with the degree of this aggregation determined by the chemical composition of their lateral sides. The nanocrystals least prone to aggregation are nanocrystals with a negative charge on the surface SO_3H groups [10], which form when the sulfuric acid is used during step 2. After the multiple cycles of filtration and flushing on a centrifuge and the ultrasound dispersion (step 3), the water suspension of the cellulose nanocrystals is formed. The structure and the rheological properties of this suspension are determined by the temperature and the concentration of the nanocrystals in it.

The nanocellulose materials are widely used in water purification processes [15], in electronics [16, 17], in pharmaceutical industry [18, 19], in oil production industry, [20], and in food industry [21]. One of the important properties of nanocellulose, which makes it useful in the industries listed above, is its moisture content. [22]. Hence, the study of how the water content affects the properties of the nanocellulose attracts wide attention [23–26]. Among the most popular in this regard systems are hydrogel [27–29] and water suspensions [30, 31] based on nanocellulose. Another set of the nanocellulose composites' properties that attracts attention is their dielectric properties [32–35], which are affected by the moisture content as well [26, 36–38]. When the moisture content in the nanocellulose composite is high, lyotropic liquid crystal phase is observed in the composites, whose rheological, optical, and structural properties were abundantly studied. [28, 29, 33, 39–41]. However, the data on other physical properties of the solid water–nanocellulose–ions systems, in particular, its electrical properties, is clearly lacking.

Solid water–nanocellulose–ions systems are characterized by a significant spatial heterogeneity arising due to the aggregation and/or co-crystallization of nanocrystals when the specimens are obtained by freezing or evaporating aqueous suspensions. In such a case, ions of different types can be trapped in the intercrystalline layers of ice or cellulose nanocrystals, their presence significantly affecting phase transitions and relaxation processes in such composites. Thus, it is particularly important to study the physical properties of the water–nanocellulose–ions systems in the temperature range in which phase transitions are observed.

In the present work, we aim to elucidate how the concentration of the nanocellulose affects dielectric and photoluminescent properties of the water–nanocellulose–NaCl

system in a wide range of temperatures and to determine the molecular mechanisms of relaxation processes that take place in these systems.

29.2 Experiment

29.2.1 Composites

Nanocellulose was obtained by hydrolysis of the organosolvent cellulose from the stems of *Miscanthus x giganteus* using procedures described in [42–44]. Hydrolysis of the never dried organosolvent miscanthus pulp (OMP) was carried out by solution of sulfuric acid with a concentration of 43%, at the liquid to solid ratio 10:1, at temperature 60 °C for the duration of 60 min for obtaining of nanocellulose. The calculated amount of sulfate acid with the corresponding concentration was slowly added into the flask with the OMP suspension. Upon expiration of the reaction time, the hydrolysis was stopped by tenfold dilution with distilled water and subsequent cooling of the suspension to room temperature. The hydrolyzed nanocellulose was rinsed with distilled water three times through centrifugation at 4000 rev/min and subsequent dialysis until reaching a neutral pH. Ultrasound treatment of nanocellulose (NC) with concentration 0.6% was performed using ultrasound disintegrator UZDN-A (SELMI, Ukraine) with 22 kHz for 60 min. The nanocellulose suspension was placed in an ice bath to prevent overheating during treatment.

«Ultra pure water» H_2O purchased from Anton Paar was used to prepare composites, as well as 9gNaCl per 1 L of water solutions of NaCl.

The following solutions were prepared: 0.8 g NC/9gNaCl per 1 l of water (further referred to in the text as 0.08NC/NaCl/H_2O), 1.5gNC/9gNaCl per 1 l of water (0.15NC/NaCl/H_2O), and 3 g/NC/9gNaCl per 1 l of water (0.3NC/NaCl/H_2O).

29.2.2 Methods

The dielectric properties were studied in the 1 to 50 kHz frequency range and –190 to 100 °C temperature range using an automated installation based on a P5083 AC bridge and a four-electrode thermostatted cell, with an option of a sample thickness control. The samples were placed into enclosed polyethylene capsules, allowing us to perform measurements in a temperature interval that includes phase transitions regions [45, 46].

Luminescent characteristics were measured using DFS-12 spectral monochromator equipped with two grates (1200 grooves/mm; linear dispersion 1 mm/nm) and FEU-79 photomultiplier. A diode-pumping lasers with a radiation wavelengths of $\lambda_{ex} = 405$ and 473 nm were used as a source of photoluminescence excitation. All

the PL spectra were corrected for the spectral response of the registering system. The monitoring solution was in quartz cuvette of 10 mm thickness.

Transmission spectra of the solution placed in noted cuvette were measured using the same spectral monochromator. The KGM halogen lamp was used as source of wide band radiation, and empty cuvette was used as reference sample.

29.3   Results and Discussion

29.3.1   Dielectric Properties

The dielectric properties of our system were determined by recording the real $\varepsilon'(T)$ and imaginary $\varepsilon''(T)$ parts of the complex dielectric permittivity for pure H_2O first. The data were obtained in the temperature range from –100 to 50 °C at frequencies f = 5, 10, 20 and 50 kHz (Fig. 29.1).

The temperature dependence of the real component of the complex dielectric permittivity for H_2O has an inflection point (Fig. 29.1a). The position of this inflection point shifts to higher temperatures with increasing frequency. The imaginary component of the complex dielectric permittivity, on the other hand, has a peak value (Fig. 29.1a), whose position shifts to higher temperatures at higher frequencies. These two observations indicate that a relaxation process takes place in this temperature interval [47–50]. A further steep increase in the dielectric permittivity is due to the melting of the sample.

We then recorded the temperature dependencies of the real $\varepsilon'(T)$ and imaginary $\varepsilon''(T)$ parts of the complex dielectric permittivity in the temperature range from –100 to 50 °C at the frequencies f = 5, 10, 20, 50 kHz for the 9 g/l NaCl water solution (Fig. 29.2).

Finally, we have recorded the temperature dependencies of the real $\varepsilon'(T)$ (a) and imaginary $\varepsilon''(T)$ parts of the complex dielectric permittivity at f = 5, 10, 20, 50 kHz for the water solutions of all three nanocellulose composites: 0.08NC/NaCl/H_2O (Fig. 29.3), 0.15NC/NaCl/H_2O (Fig. 29.4), and 0.3NC/NaCl/H_2O (Fig. 29.5). The measurements were taken in a wider range of temperatures: from −190 to 70 °C.

Each of the temperature dependencies of the real part of dielectric permittivity for 0.08NC/NaCl/H_2O, 0.15NC/NaCl/H_2O, and 0.3NC/NaCl/H_2O has an inflection point (Figs. 29.3a, 29.4a and 29.5a). This inflection point tends to shift to higher temperatures with increasing frequency. Concurringly, the imaginary component of the dielectricpermittivity for all three composites has a peak value (Figs. 29.3b, 29.4b and 29.5b), whose position also shifts to higher temperatures with increasing frequency. We may thus infer that a relaxation process occurs in each of the three composites and that this relaxation process is due to thermal dipole polarization. The steep increase of the dielectric permittivity above the relaxation process can be attributed to the melting of 0.08NC/NaCl/H_2O, 0.15NC/NaCl/H_2O, and 0.3NC/NaCl/H_2O (Figs. 29.3a, 29.4a and 29.5a).
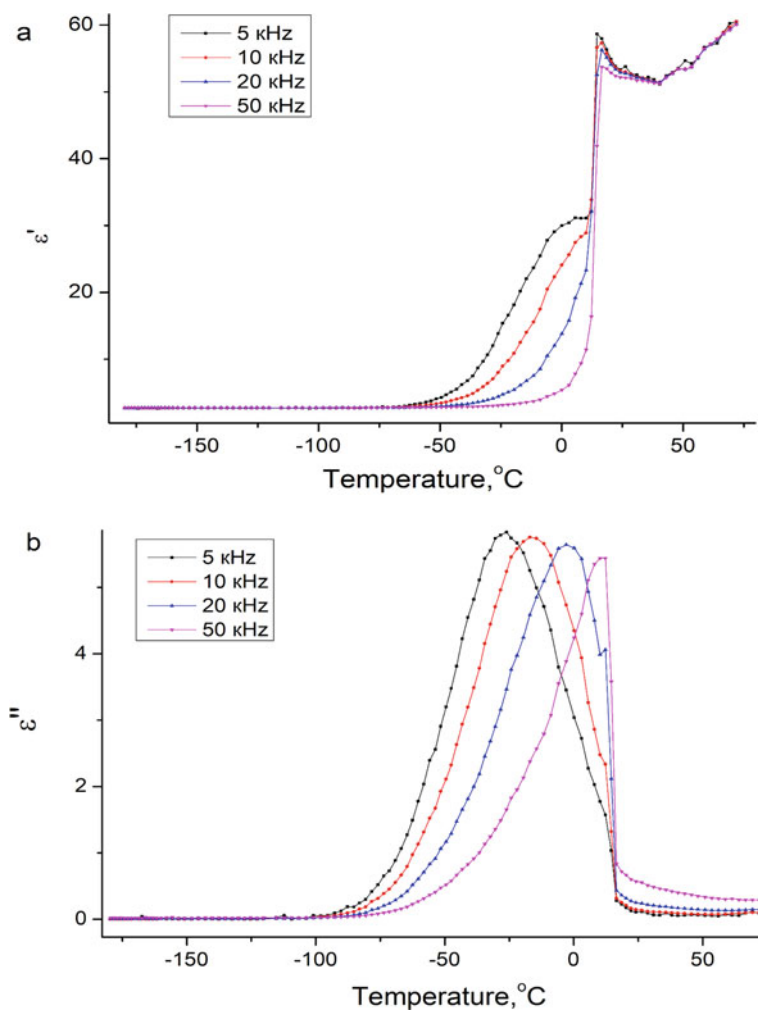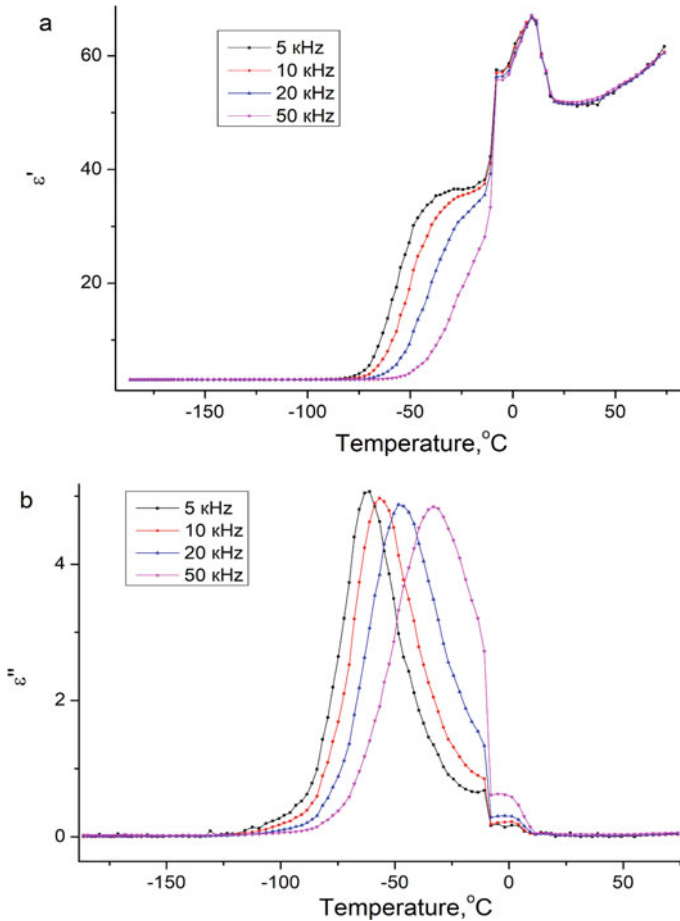
Fig. 29.1 Temperature dependence of the real $\varepsilon'(T)$ **a** and imaginary $\varepsilon''(T)$ **b** parts of the complex dielectric permittivity at different frequencies for the pure H_2O (Anton Paar «Ultra pure water»)

29.3.2   Transmission Spectra

Transmission spectra of $0.6NC/H_2O$ (curve 1) solutions $0.08NC/NaCl/H_2O$, $0.15NC/NaCl/H_2O$, and $0.3NC/NaCl/H_2O$ (curves 2–4) are shown in Fig. 29.6. All spectra were recorded in the wavelength range in which the photoluminescence of samples was excited (the excitation wavelengths λ_{ex} used were 405, 473, and 532 nm) at 20 °C.

The transmission spectrum of the initial suspension in the 400−800 nm range agrees with the available data [51–53]. Its main characteristics are the absence of

Fig. 29.2 Temperature dependence of the real $\varepsilon'(T)$ (**a**) and imaginary $\varepsilon''(T)$ (**b**) parts of the complex dielectric permittivity at different frequencies for 9 g/l NaCl water solution

any peculiarities and a tendency of the transmission to increase with increasing wavelengths.

The presence of the NaCl in the solution changes this trend: A small (about 1%) increase is observed at wavelengths above 630 nm; conversely, a small decrease is observed between 400 and 620 nm: from 11.4% at $\lambda = 479$ nm to 10.1% at $\lambda = 630$ nm (see curves 2 and 4 on Fig. 29.6). The decrease of the nanocellulose content increases these changes: The transmission decreases from 21 to 15% in the wavelength range from 470 to 630 nm, while at higher wavelengths of 630−800 nm, the transmission increases from 15 to 18% (curve 3 on Fig. 29.6). Consequently, the solutions which contain NaCl have a wide absorption band with the maximum at 630−650 nm.
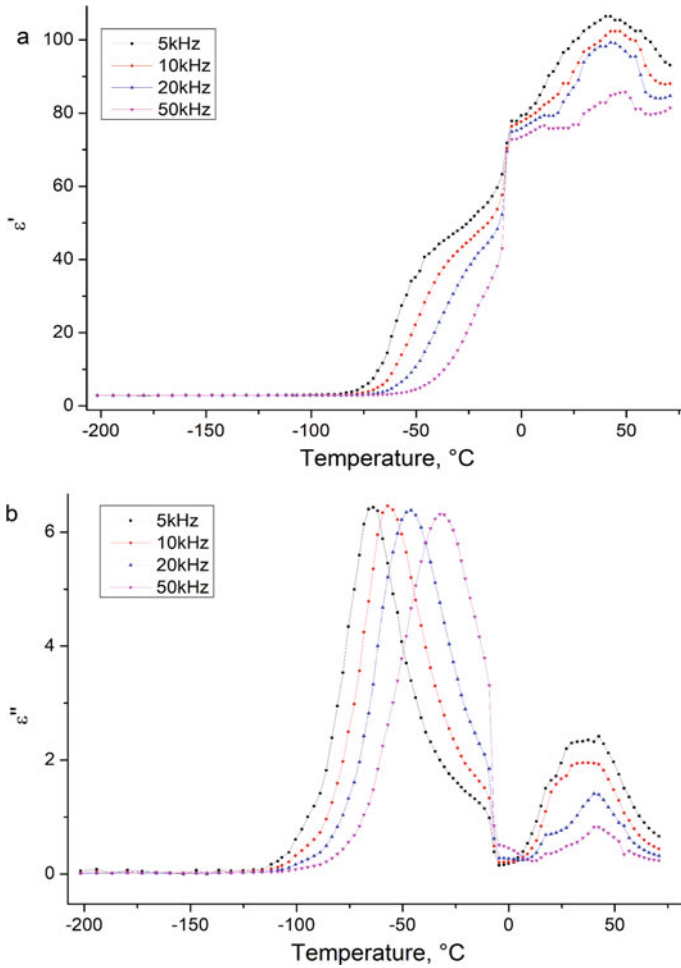
Fig. 29.3 Temperature dependence of the real $\varepsilon'(T)$ (**a**) and imaginary $\varepsilon''(T)$ (**b**) parts of the complex dielectric permittivity at different frequencies for 0.08NC/NaCl/H$_2$O composite

The increase of the transmission, in general, when the amount of the nanocellulose in the solution decreases, is expected; however, it doesn't appear to vary strictly linearly with the nanocellulose concentration. One explanation for this is that the decrease in the intensity of light passing through the sample is not due to absorption exclusively, but rather the combination of the absorption and the scattering of the light in the solution, its cloudiness. Thus, the wide absorption band at 600 nm may be attributed both to the change in the distribution of the nanocellulose particle's size, as the solution becomes more dilute, and to the impact of NaCl ions on the change in this distribution.
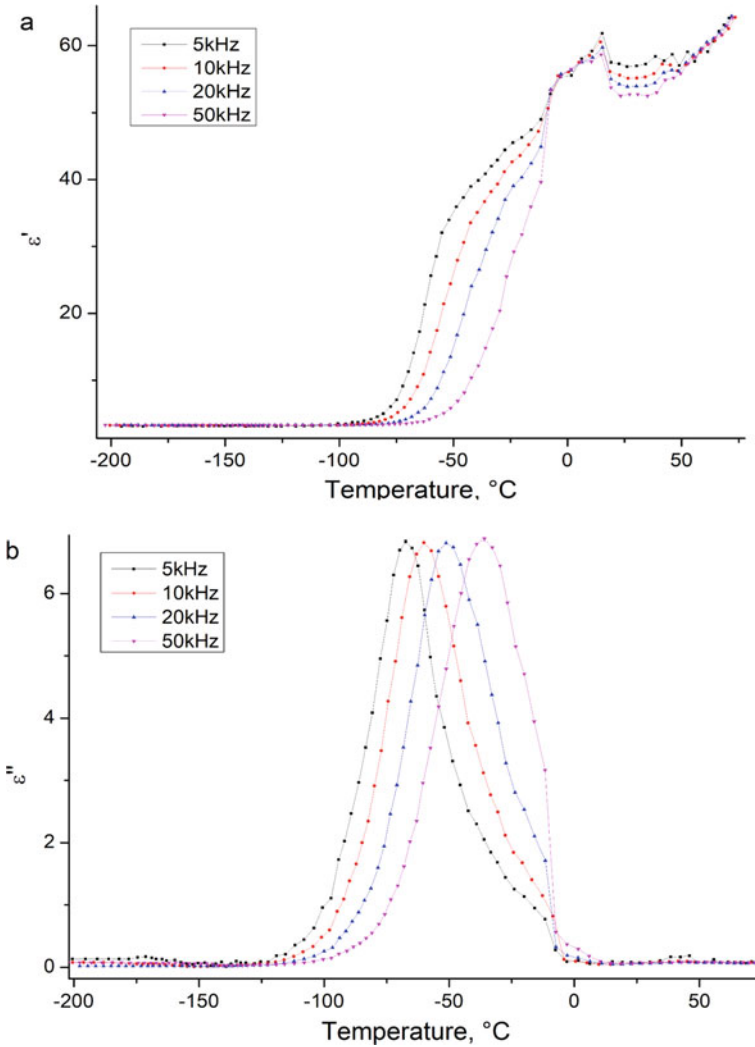
Fig. 29.4 Temperature dependence of the real $\varepsilon'(T)$ (**a**) and imaginary $\varepsilon''(T)$ (**b**) parts of the complex dielectric permittivity at different frequencies for 0.15NC/NaCl/H$_2$O composite

Another way to explain why the presence of ions affects the transmission spectra of NC/NaCl/H$_2$O solutions is to suppose that the sodium ions can interact with certain molecular groups concentrated on the surface of nanocellulose fibrils. Indeed, 400−800 nm is the transparency region for the molecular cellulose, and thus for cellulose nanofibrils. Consequently, the appearance of a wide absorption band in this region can be explained by a selective interaction of the sodium ions with the functional groups of the nanocellulose molecules. An additional argument in favor of this speculation is the appearance of a relatively narrow absorption band at 400
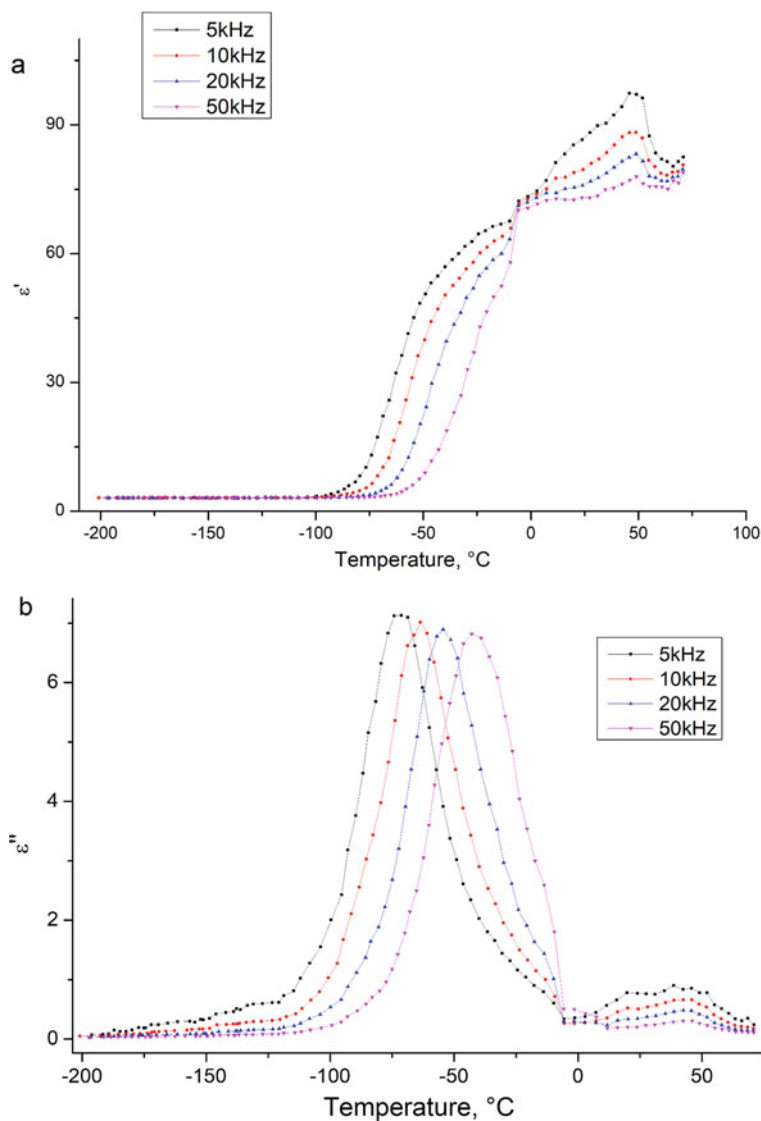
Fig. 29.5 Temperature dependence of the real $\varepsilon'(T)$ (**a**) and imaginary $\varepsilon''(T)$ (**b**) parts of the complex dielectric permittivity at different frequencies for 0.3NC/NaCl/H_2O composite

to 550 nm with a maximum at 490 nm (see an arrow indicating the position of the band on curves 3 and 4 on Fig. 29.6).

To clarify, which of the explanations for the wide absorption band is, indeed, correct, and how the sodium chloride ions affect the properties of the water–cellulose–NaCl systems, their luminescence spectra were recorded.

Fig. 29.6 Transmission spectra of 0.08NC/NaCl/H$_2$O (1), 0.15NC/NaCl/H$_2$O (2), 0.3NC/NaCl/H$_2$O (3), and 0.6NC/H$_2$O (4) composites
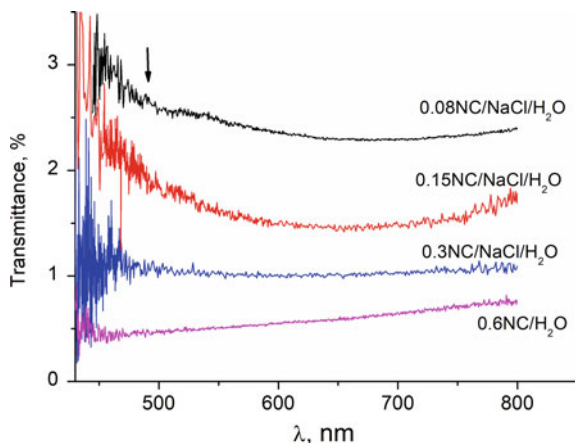
29.3.3 Luminescence Spectra

The luminescence spectra of the solutions were excited using laser radiation of wavelengths λ_{ex} = 405 and 473 nm at 20 °C. A wide radiation band in the spectral region of 450 to 800 nm is observed on the photoluminescence (PL) spectrum. This band is, evidently, a superposition of several distinct bands. Roughly, three components: short-wave (450 to 550 nm), mid-wave (500 to 625 nm), and long-wave (575−800 nm) can be identified in this band (see Figs. 29.7 and 29.8). The relative impact of these three components on the resulting spectrum is determined by the excitation wavelengths: As the wavelength of the excitation wave increases (from 405 to 473 nm), the input of the long-wave component increases, and the band's maximum shifts to longer wavelengths by about 20 nm (see vertical lines in Figs. 29.7a and 29.8a).

When the nanocellulose content in the solution changes, so does the shape of the PL spectrum. This becomes evident in Figs. 29.7b and 29.8b, which show the spectra from Figs. 29.7a and 29.8a normalized to the maxima of the respective intensities.

Another important observation is that the shape of the spectra changes most significantly when NaCl is added into the water–cellulose solution (the change from spectrum 3 to spectrum 4 in Fig. 29.7). The change in the shape of the spectrum is less pronounced with the longer wavelength of excitation (Fig. 29.8a).

The observation described supports the previously expressed assumptions about several possible sources of the luminescence of solutions with nanocellulose [54–56]. The components of the solutions that can act as the PL centers are molecular fluorophores, which are not the constituents of the cellulose molecules, but rather the defects or impurities present in the solution [31].

The spectra in Fig. 29.7b demonstrate clearly that the PL of the samples is the superposition of the radiation of different, possibly molecular groups. There, among the relatively wide overlapping components, several narrow spectral bands are present in the 525−575 nm range. Such spectral features are characteristic for the PL spectra
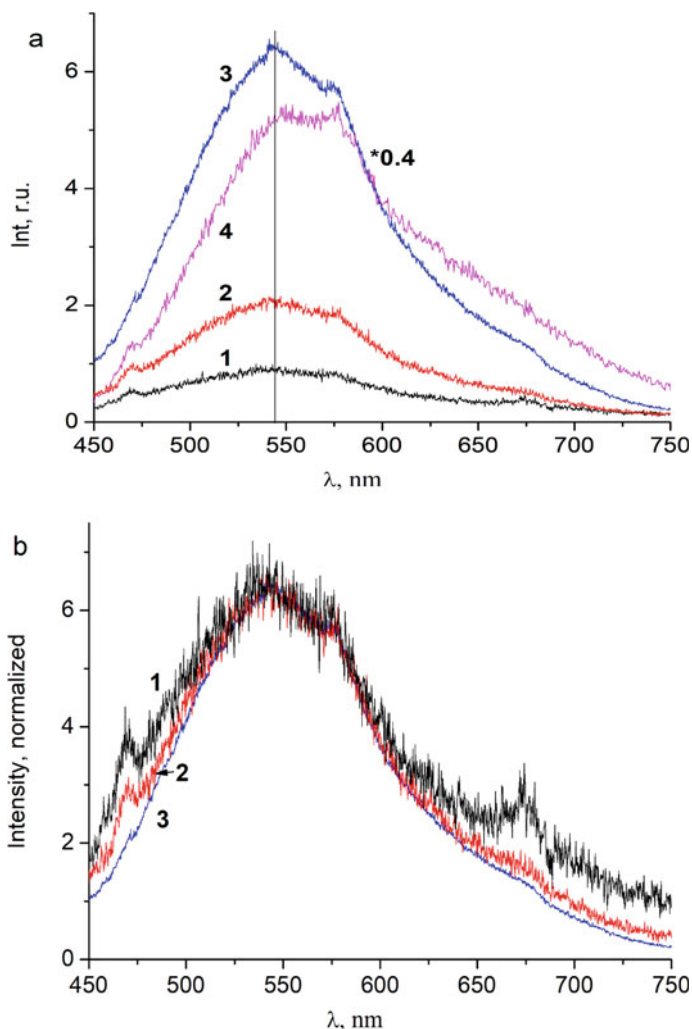
Fig. 29.7   a PL spectra of 0.08NC/NaCl/H$_2$O (1), 0.15NC/NaCl/H$_2$O (2), 0.3NC/NaCl/H$_2$O (3) and 0.6NC/H$_2$O (4) solutions, excitation wavelength 405 nm; **b** PL spectra of 0.08NC/NaCl/H$_2$O (1), 0.15NC/NaCl/H$_2$O (2), 0.3NC/NaCl/H$_2$O (3) and 0.6NC/H$_2$O (4) solutions normalized by their respective maxima

of many organic compounds, in particular the aromatic molecules [57, 58]. It is thus evident, that when exciting PL by different wavelengths, the different types of PL centers excite differently, with varying efficiency, resulting in the redistribution of their input into the emission spectrum.

As shown earlier, in the aqueous solutions, water molecules surround the molecular groups on the surface of cellulose nanofibrils and thus can dampen their photoluminescence. Consequently, as the amount of nanocellulose in the solution

Fig. 29.8 **a** PL spectra of 0.08NC/NaCl/H$_2$O (1), 0.15NC/NaCl/H$_2$O (2), 0.3NC/NaCl/H$_2$O (3), and 0.6NC/H$_2$O (4) solutions, excitation wavelength 473 nm; **b** PL spectra of 0.08NC/NaCl/H$_2$O (1), 0.15NC/NaCl/H$_2$O (2), 0.3NC/NaCl/H$_2$O (3), and 0.6NC/H$_2$O (4) solutions normalized by their respective maxima
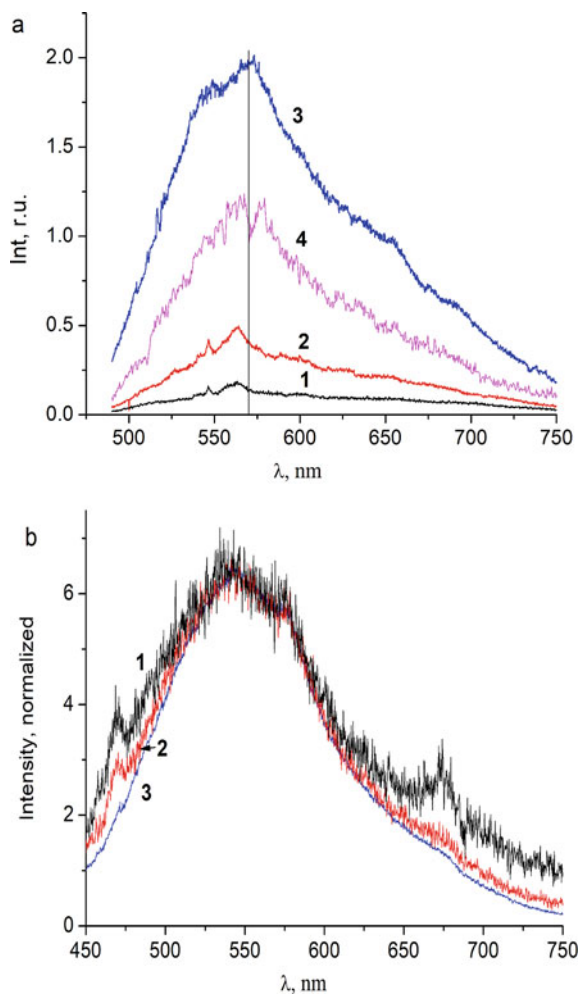
increases, the number of the fluorophore molecules interacting with water molecules decreases, and the intensity of the photoluminescence can thus increase—just as the data in Fig. 29.8 suggests. The increase in the intensity occurs at different rates for different excitations, again pointing at the fact that different excitations affect different photoluminescence centers.

Sodium cations in the solution are known to "pull" the hydrogen bonds of the water molecules and limit their access to the surface molecules of cellulose. As a result, the damping of the PL by water molecules may become less pronounced. Thus, it is Na cations that increase the intensity of PL in water–cellulose–NaCl solutions, compared to the samples where NaCl is absent (see curves 3 and 4 on Figs. 29.7 and 29.8, respectively, as well as Fig. 29.9, in which the last point C $= 0.6\%$ corresponds to the solution with no NaCl present).

Fig. 29.9 PL spectra intensity versus the concentration of nanocellulose for different excitations: $\lambda_{ex} = 405$ nm (1) and 473 nm (2); concentration 0.6% corresponds to the water–nanocellulose solution with no NaCl present
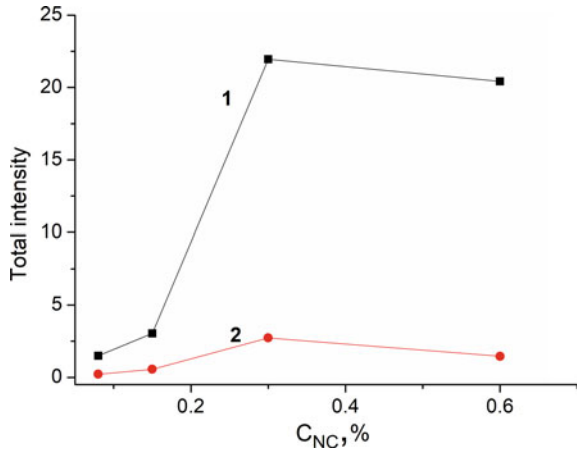
29.4 Discussion

All three nanocellulose–water–NaCl systems we have studied in the present work demonstrate a low-temperature dielectric relaxation. To find out how the parameters of the relaxation processes are affected by the system's component, a comparison of the behavior of the nanocellulose–water composites with that of the nanocellulose–water–NaCl composites can be beneficial. Thus, the temperature dependence of the dielectric permittivity $\varepsilon'(T)$ at 10 kHz for the pure H_2O, $0.15NC/H_2O$, $0.3NC/H_2O$, and $0.6NC/H_2O$ composites [31] was plotted on Fig. 29.10, and $\varepsilon'(T)$ at 10 kHz for H_2O, $NaCl/H_2O$, $0.08NC/NaCl/H_2O$, $0.15NC/NaCl/H_2O$, and $0.3NC/NaCl/H_2O$ was plotted on Fig. 29.11. Noticeably, the change in the dielectric permittivity $\Delta\varepsilon$ during the dielectric process increases with the increasing concentration of the nanocellulose in both NC/H_2O and $NC/NaCl/H_2O$ nanocomposites. That is, the energy characteristics of the relaxation process appear to change with the increasing nanocellulose content.

To calculate the energy characteristics of the relaxation process, the model of the identical relaxator system can be used: Each of these relaxators has two non-equivalent energy states, separated by a potential barrier [59–61].

In such a model, the real and the imaginary components of the dielectric permittivity obey the following equations [62]:

$$\varepsilon'(\omega, T) = \varepsilon_\infty + \frac{\Delta\varepsilon(T)}{1 + \omega^2 \tau^2(T)} \qquad (29.1)$$

$$\varepsilon''(\omega, T) = \frac{\Delta\varepsilon(T)\omega\tau(T)}{1 + \omega^2 \tau^2(T)} \qquad (29.2)$$
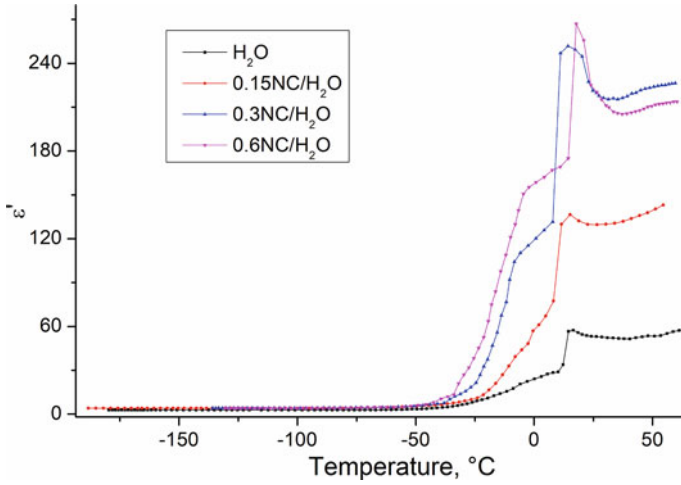
only one relaxation time exists:

Fig. 29.10 Temperature dependence of the real part of the complex dielectric permittivity at 10 kHz for H_2O, 0.15NC/H_2O [31], 0.3NC/H_2O [31], 0.6NC/H_2O [31]
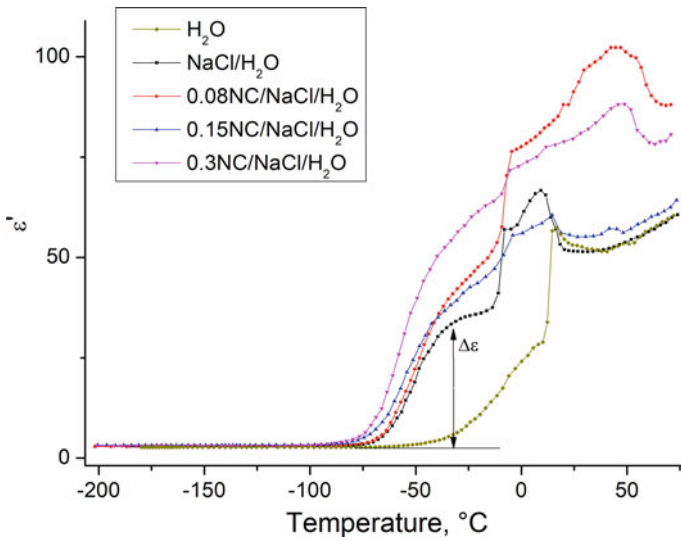

Fig. 29.11 Temperature dependence of the real part of the complex dielectric permittivity at 10 kHz for H_2O, NaCl/H_2O, 0.08NC/NaCl/H_2O, 0.15NC/NaCl/H_2O, 0.3NC/NaCl/H_2O

$$\tau = \frac{2\pi}{\omega_0} \frac{\exp(U/kT)}{1 + \exp(-V/kT)},$$

(29.3)

and the increment of the dielectric permittivity is described by

Table 29.1 Energy characteristics of the relaxation processes in nanocellulose–water [31] and nanocellulose–water–NaCl solid solutions

Sample	$\Delta S/k$	U, kJ·mol^{-1}	$\frac{N\mu^2}{3k\varepsilon_0}$, $\times 10^3$ K
H_2O	0	31.9 ± 5.2	118.1 ± 3.2
0.15NC/H_2O	8.5 ± 1.8	50.6 ± 3.8	415.1 ± 3.5
0.3NC/H_2O	8.8 ± 1.1	49.4 ± 2.3	461.5 ± 3.7
0.6NC/H_2O	7.8 ± 0.6	47.0 ± 0.5	532.6 ± 4.1
NaCl/H_2O	2.1 ± 0.5	30.9 ± 6.2	75.3 ± 1.5
0.08NC/NaCl/H_2O	1.3 ± 0.4	29.3 ± 1.7	169.4 ± 2.0
0.15NC/NaCl/H_2O	1.9 ± 0.7	30.1 ± 1.9	178.7 ± 1.9
0.3NC/NaCl/H_2O	2.1 ± 0.6	29.7 ± 3.2	195.1 ± 2.1

$$\Delta\varepsilon = \varepsilon_0 - \varepsilon_\infty = \frac{N\mu^2}{3k\varepsilon_0 T} \cdot \frac{\exp(-V/kT)}{\left[1 + \exp(-V/kT)\right]^2}, \tag{29.4}$$

where N– relaxator concentration, μ^2– mean square of the difference of the relaxator dipole moments in states 1 and 2, V—the difference in energies in states 1 and 2 [62].

Fitting the ε'(T) dependence using formula (29.4), the values of $\frac{N\mu^2}{3k\varepsilon_0}$ can be calculated (Table 29.1). As NaCl is added to water, the value of $\frac{N\mu^2}{3k\varepsilon_0}$ decreases, that is, the concentration of relaxators in the solid solution decreases. One of the ways to explain this observation is to assume that ions bind some of the water's molecules in ice so that these molecules lose the ability to change their orientation in the relaxation process temperature region.

As the water is added to nanocellulose, the hydration shells are formed around the nanocellulose, and the value of $\frac{N\mu^2}{3k\varepsilon_0}$ increases with the increasing nanocellulose content. Such behavior can be attributed to the impact of the conformational motion of the groups of nanocellulose molecules bound to the hydration shell on the overall relaxation process. When NaCl is added to the nanocellulose–water solution, it positions itself between the ice and the nanocellulose, so $\frac{N\mu^2}{3k\varepsilon_0}$ decreases (compared to its value in nanocellulose–water systems). Thus, the ions of salt partially block the formation of hydration shells around the nanocellulose. This, in turn, leads to the increase in the intensity of the photoluminescence (see curves 3 and 4 on Figs. 29.7 and 29.8, respectively, as well as Fig. 29.9, in which the last point C = 0.6% corresponds to the solution with no NaCl present).

To support the explanations offered above, the temperature dependencies of the imaginary part of the dielectric permittivity for nanocellulose–water and nanocellulose–water–NaCl solutions are compared. Figure 29.12 shows $\varepsilon''(T)$ at 10 kHz for H_2O, 0.15NC/H_2O, 0.3NC/H_2O, and 0.6NC/H_2O [31], whereas Fig. 29.13 shows $\varepsilon''(T)$ at 10 kHz for H_2O, NaCl/H_2O, 0.08NC/NaCl/H_2O, 0.15NC/NaCl/H_2O, 0.3NC/NaCl/H_2O.
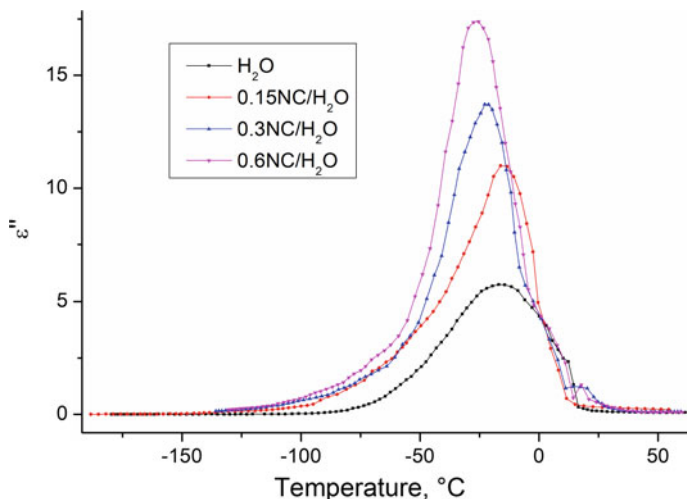
Fig. 29.12 Temperature dependence of the imaginary part of the complex dielectric permittivity at 10 kHz for H_2O, 0.15NC/H_2O [31], 0.3NC/H_2O [31], 0.6NC/H_2O [31]
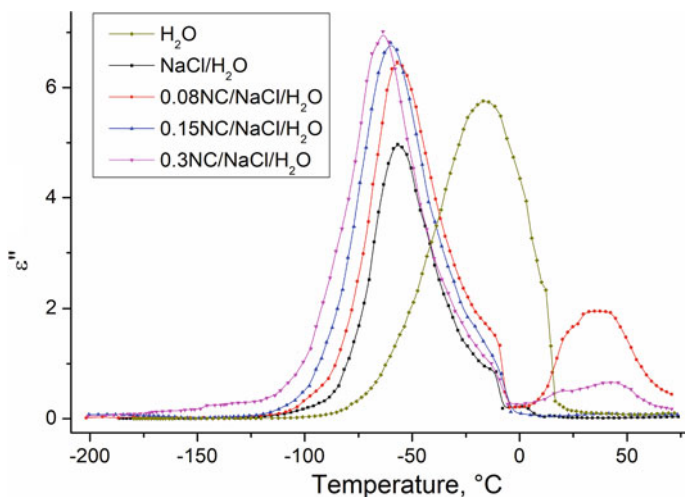

Fig. 29.13 Temperature dependence of the imaginary part of the complex dielectric permittivity at 10 kHz for H_2O, NaCl/H_2O, 0.08NC/NaCl/H_2O, 0.15NC/NaCl/H_2O, 0.3NC/NaCl/H_2O

To obtain additional insight, the temperatures at which the peak of ε'' is observed (the maximum of the relaxation process) are plotted against the concentration of nanocellulose in NC/H_2O and NC/NaCl/H_2O solutions (Fig. 29.14). The peak's position shifts toward lower temperatures with the increasing concentration of cellulose in both NC/H_2O and NC/NaCl/H_2O. Additionally, the presence of Na^+ and Cl^- ions in the solutions significantly decreases the temperature of the relaxation process.
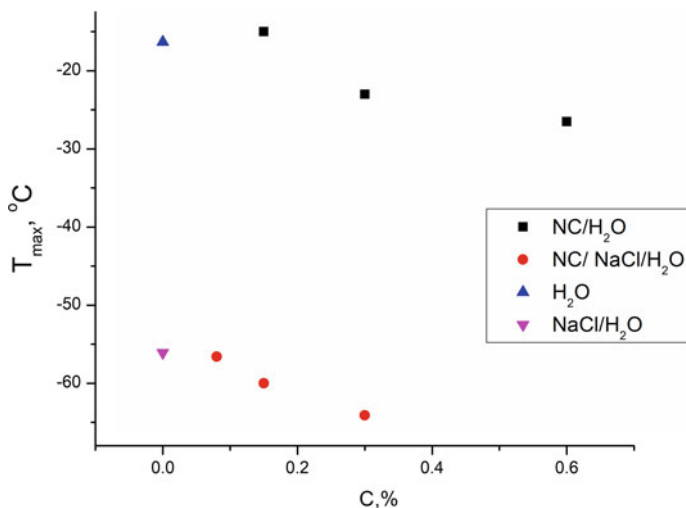
Fig. 29.14 Temperature of the maximum of the relaxation process versus the concentration of the nanocellulose in NC/H$_2$O and NC/NaCl/H$_2$O solutions at 10 kHz

The height of the maximum of the relaxation process also appears to be affected by the concentration of nanocellulose in the NC/NaCl/H$_2$O systems. Figure 29.15 shows that the height of this peak increases with increasing concentration of nanocellulose in both NC/H$_2$O and NC/NaCl/H$_2$O solutions. At the same time, the addition of NaCl to the solution decreases the height of the peak. The latter observation gives additional evidence that the Na$^+$ and Cl$^-$ ions bind the water molecules of the hydration shell, forbidding the conformational motion of some of the cellulose molecule's side chains.

The energy characteristics of the dielectric relaxation in solutions can be calculated: If the activation entropy is considered, then the time of the relaxation can be expressed as

$$\tau = \tau_0 exp\left((U - T\Delta S)/kT\right), \tag{29.5}$$

where $\tau_0 = 10^{-12}$ s, U—activation energy; T—absolute temperature; ΔS—entropy of activation; k—Boltzmann's constant [36].

The maximum on the $\varepsilon''(T)$ dependency is attained when $\omega\tau = 1$, where $\omega = 2\pi f$ is the angular frequency of the external field oscillation. Consequently, $\ln f = -\ln 2\pi \tau_0 + \Delta S/k - U/kT$. Then, plotting the Arrhenius equation $\ln f(1/T)$ (Fig. 29.16) we can obtain the values of the activation entropy $\Delta S/k$ and activation energy U (Table 29.1). The $\ln f(1/T)$ dependencies demonstrate that the dielectric relaxation processes shift toward lower temperatures with the increasing concentration of nanocellulose. When nanocellulose is added to the water, the activation energy, compared to that of pure water, tends to increase. However, this effect disappears when ions are introduced into the solution (Table 29.1). Additionally, when nanocellulose is added to water, the activation entropy $\Delta S/k$ increases. We can thus suppose that the entropy
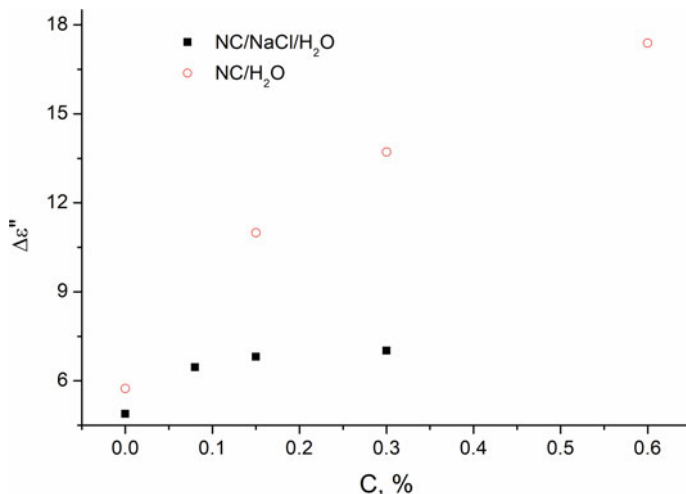
Fig. 29.15 Height of the ε" peak (relaxation process maximum) versus the concentration of nanocellulose in NC/H$_2$O and NC/NaCl/H$_2$O solutions at 10 kHz

of the relaxation process activation is due to the formation of the hydrogen bonds between the nanocellulose and the surrounding molecules of the hydration shell [63]. The identical values of $\Delta S/k$ at different concentrations of nanocellulose are then due to the formation of the single hydration shell around nanocellulose crystals. The value of $\Delta S/k$ decreases with increasing content of salt, serving as additional evidence that the ions in the solid aqueous solutions are located at the nanocellulose–ice interface and block the formation of h-bonds between the water and nanocellulose molecules. Consequently, the ions partially block the formation of the hydration shells around the cellulose nanocrystals.

As we have commented earlier, the activation energy U is almost identical for 0.15NC/H$_2$O, 0.3NC/H$_2$O, and 0.6NC/H$_2$O solutions but is higher than for the pure H$_2$O. We can thus speculate that the nature of the relaxation process in 0.15NC/H$_2$O, 0.3NC/H$_2$O, and 0.6NC/H$_2$O is different from that in pure H$_2$O and is due to the superposition of two relaxation processes: one of them related to the relaxation in ice, and the other to the relaxation at the surface of the nanocellulose crystals surrounded by hydration shell.

In [36, 37], the relaxation processes of the microcrystal cellulose with a small moisture content (0.4−16.4% H$_2$O) were examined. In the case of such systems, the dielectric relaxation in the −100 to 0 °C range was shown to occur in the surface layers of cellulose crystallites, surrounded by the hydration shell and caused by the reorientation of the surface methylol groups of the cellulose molecule by means of its conformation change $tg \leftrightarrow tt$. Thus, by way of analogy with the microcrystal cellulose studies results, the relaxation processes in 0.15NC/H$_2$O, 0.3NC/H$_2$O, and 0.6NC/H$_2$O are also due to the conformational motion of the methylol groups on the surface of the nanocellulose crystals, surrounded by the hydration shell. And,
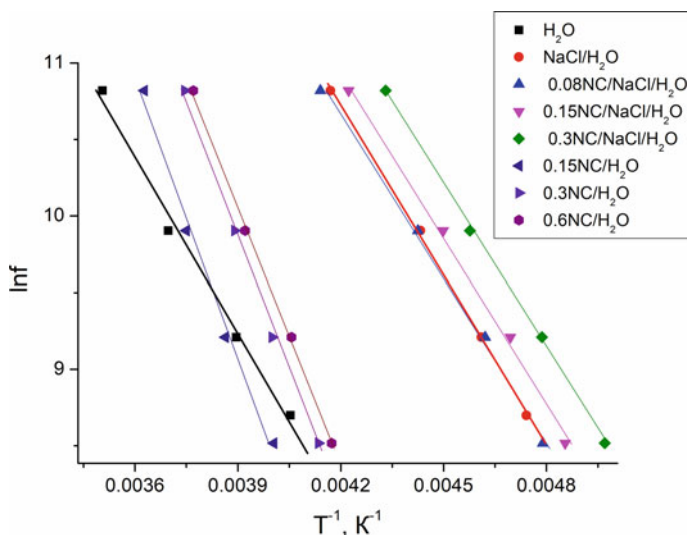
Fig. 29.16 Arrhenius equation $\ln f (1/T)$ for all NC/H$_2$O, NC/NaCl/H$_2$O samples

as the ions are found to partially block the formation of the hydration shell around the nanocrystal cellulose, they also block the relaxation process in the surface layers surrounded by the hydration shell. Thus, the entropy of the relaxation process activation for the nanocellulose–water–ions system decreases compared to the nanocellulose–water solutions (Table 29.1). The decrease in the intensity of the dielectric relaxation in solid solutions of the nanocellulose with ions, compared to the solid solutions without ions, is caused by the binding of water molecules by the NaCl salt's ions, which blocks the formation of the bonds between the water molecules in the hydration shell and the methylol groups on the surface of nanocellulose. This, in turn, leads to a decrease in the number of methylol groups that can take part in conformation motion.

29.5 Conclusions

Dielectric and spectral properties of the solid nanocellulose solutions have been studied in detail to elucidate the impact of the presence of the Na$^+$ та Cl$^-$ ions in them. Dielectric relaxation is observed in the temperature range from -100 to 0 °C for all 0.15NC/H$_2$O, 0.3NC/H$_2$O, and 0.6NC/H$_2$O solutions, whose nature is different from the relaxation in the pure water, and which is caused by the dipole thermal polarization. The intensity of the dielectric relaxation is shown to increase with the increasing nanocellulose content. Consequently, the relaxation process in the solid solutions of 0.15NC/H$_2$O, 0.3NC/H$_2$O, and 0.6NC/H$_2$O can be viewed as the superposition of two processes: the dielectric relaxation in ice and the dielectric

relaxation in the surface layers of the nanocellulose particles surrounded by the hydrations shell. The mechanism of the relaxation process in the surface layers of nanocellulose is due to the reorientation of the cellulose molecule's surface methylol groups by changing their conformation from *tg* to *tt*. The change in the orientation of the methylol group coincides with the breaking and the subsequent formation of the hydrogen bond with one of the water molecules in the hydration shell. There are several ways for this process to occur, as demonstrated by the presence of the entropy of the relaxation process activation. Nevertheless, the results obtained by both dielectric and optical spectroscopy methods agree: The ions of NaCl disrupt the formation of the hydration shell around the cellulose molecules. In particular, when the composites are in the solid state, the Na^+ and Cl^- ions get distributed along the nanocellulose–ice interface and partially block the formation of the hydration shell around the cellulose. Consequently, they partially block the dielectric relaxation process, which takes place in the surface layers of the nanocellulose surrounded by the hydration shell. Thus, the concentration of relaxators in the solid aqueous solutions of nanocellulose in the presence of Na^+ and Cl^- ions decreases (compared to the solid aqueous solutions of nanocellulose). The decrease in the intensity of the dielectric relaxation in the solid aqueous solutions of nanocellulose with ions, compared to water–nanocellulose solutions, is due to the binding of the water molecules in the hydration shell of the nanocellulose by the ions, blocking the formation of the h-bonds between the bound molecules of water and methylol groups. In other words, the conformation motion of some of the surface methylol groups gets blocked.

References

1. Thostenson ET, Li C, Chou TW (2005) Nanocomposites in context. Compos Sci Technol 65(3–4):491
2. Hsissou R, Seghiri R, Benzekri Z, Hilali M, Rafik M, Elharfi A (2021) Polymer composite materials: a comprehensive review. Compos Struct 262:113640
3. Demchenko V, Shtompel V, Riabov S, Lysenkov E (2015) Constant electric and magnetic fields effect on the structuring and thermomechanical and thermophysical properties of nanocomposites formed from pectin–Cu_2^+–polyethyleneimine interpolyelectrolyte–metal complexes. Nanoscale Res Lett 10(1):1
4. Lysenkov EA, Klepko VV, Yakovlev YV (2016) Specifics of percolation behavior in the polyether–carbon nanotube systems doped with $LiClO_4$. Surf Eng Appl Electrochem 52(2):186
5. Fialko N, Dinzhos R, Sherenkovskii J, Meranova N, Navrodska R, Koseva N, Korzhyk V, Izvorska D, Lazarenko M (2021) Establishing patterns in the effect of temperature regime when manufacturing nanocomposites on their heat-conducting properties. EEJET 4(5):112
6. Kim JH, Shim BS, Kim HS, Lee YJ, Min SK, Jang D, Abas Z, Kim J (2015) Review of nanocellulose for sustainable future materials. IJPEM—GT 2(2):197
7. Saurabh CK, Adnan AS, Fazita MN, Syakir MI, Davoudpour Y, Rafatullah M, Abdullah CK, Haafiz MKM, Dungani R (2016) A review on chitosan-cellulose blends and nanocellulose reinforced chitosan biocomposites: properties and their applications. Carbohydr Polym 150:216
8. Rebouillat S, Pla F (2013) State of the art manufacturing and engineering of nanocellulose: a review of available data and industrial applications. JBNB 4(02):165

9. Marinho NP, de Cademartori PHG, Nisgoski S, de Andrade Tanobe VO, Klock U, de Muñiz GIB (2020) Feasibility of ramie fibers as raw material for the isolation of nanofibrillated cellulose. Carbohydr Polym 230:115579

10. Moon RJ, Martini A, Nairn J, Simonsen J, Youngblood J (2011) Cellulose nanomaterials review: structure, properties and nanocomposites. Chem Soc Rev 40:3941

11. Kargarzadeh H, Mariano M, Huang J, Lin N, Ahmad I, Dufresne A, Thomas S (2017) Recent developments on nanocellulose reinforced polymer nanocomposites: a review. Polymer 132:368

12. Li F, Mascheroni E, Piergiovanni L (2015) The potential of nanocellulose in the packaging field: a review. Packag Technol Sci 28(6):475

13. Zinge C, Kandasubramanian B (2020) Nanocellulose based biodegradable polymers. Eur Polym J 133:109758

14. Zabashta U, Lazarenko M, Alekseev A, Tkachev S, Vasylyuk S, Kovalchuk V, Bulavin L (2021) Mechanism of disorder genesis in cellulose microfibrils. Cellul Chem Technol 55(3–4):223–230

15. Voisin H, Bergström L, Liu P, Mathew AP (2017) Nanocellulose-based materials for water purification. Nanomaterials 7(3):57

16. Tao J, Jiao L, Deng Y (2021) Cellulose-and nanocellulose-based dielectric materials. In: nanocellulose based composites for electronics, Elsevier, pp 73–100

17. Nizam PA, Gopakumar DA, Pottathara YB, Pasquini D, Nzihou A, Thomas S (2021) Nanocellulose-based composites: fundamentals and applications in electronics. Elsevier, In nanocellulose based composites for electronics, pp 15–29

18. Wadher KJ, Bajaj GS, Trivedi RV, Trivedi SS (2021) Investigation of the influence of cellulose polymer on solid phase transformation of carbamazepine. J Cryst Growth 575:126358

19. Plackett D, Letchford K, Jackson J, Burt H (2014) A review of nanocellulose as a novel vehicle for drug delivery. Nord Pulp Paper Res J 29(1):105

20. Negi H, Sharma S, Singh RK (2021) Assessment of cellulose substituted with varying short/long, linear/branched alkyl groups for inhibition of wax crystals growth in crude oil. J Ind Eng Chem 104:458

21. Serpa A, Velásquez-Cock J, Gañán P, Castro C, Vélez L, Zuluaga R (2016) Vegetable nanocellulose in food science: a review. Food Hydrocoll 57:178

22. Gorade VG, Chaudhary BU, Kale RD (2021) Moisture management of polypropylene non-woven fabric using microcrystalline cellulose through surface modification. Appl Surf Sci Adv 6:100151

23. Hoeng F, Denneulin A, Bras J (2016) Use of nanocellulose in printed electronics: a review. Nanoscale 8(27):13131

24. Du X, Zhang Z, Liu W, Deng Y (2017) Nanocellulose-based conductive materials and their emerging applications in energy devices-a review. Nano Energy 35:299

25. Chornii V, Nedilko SG, Alekseev A, Terebilenko K, Boyko V, Lazarenko M, Revo S, Scherbatskyi V, Teselko P (2020) Properties of the micro/nanocrystalline cellulose filled with ZrO2: Eu, F particles. In: 2020 IEEE 40th international conference on electronics and nanotechnology ELNANO 2020. Proceedings, pp 297–301

26. Zhao H, Chen Z, Du X, Chen L (2019) Contribution of different state of adsorbed water to the sub-Tg dynamics of cellulose. Carbohydr polym 210:322

27. Due France KJ, Hoare T Cranston ED (2017) Review of hydrogels and aerogels containing nanocellulose. Chem Mater 29(11):4609

28. Alekseev O, Zabashta Y, Kovalchuk V, Lazarenko M, Bulavin L (2019) The structure of polymer clusters in aqueous solutions of hydroxypropyl cellulose. Ukr J Phys 64(3):238

29. Alekseev OM, Zabashta YF, Kovalchuk VI, Lazarenko MM, Rudnikov EG, Bulavin LA (2020) Structural transition in dilute solutions of rod-like macromolecules. Ukr J Phys 65(1):50

30. Kedzior SA, Gabriel VA, Dubé MA, Cranston ED (2020) Nanocellulose in emulsions and heterogeneous water-based polymer systems: a review. Adv Mater 33(28):2002404

31. Lazarenko MM, Nedilko SG, Alekseev SA, Tkachov SY, Shevtsov DO, Scherbatskyi VP, Barbash VA, Yablochkova KS, Ushcats MV, Kovalchuk VI, Andrusenko DA, Izvorska D,

Dinzhos RV, Alekseev OM (2021) Electric and spectral properties of solid water-nanocellulose systems in a wide range of temperatures. International conference on nanotechnology and nanomaterials. Springer, Cham, pp 51–73

32. , Khouaja A, Koubaa A (2021) Daly HB Dielectric properties and thermal stability of cellulose high-density polyethylene bio-based composites. Ind Crops Prod 171:113928

33. Le Bras D, Strømme M, Mihranyan A (2015) Characterization of dielectric properties of nanocellulose from wood and algae for electrical insulator applications. J Phys Chem B 119(18):5911

34. Zhou Y, Huang X, Huang J, Zhang L, Zhou Z (2018) Predicting the dielectric properties of nanocellulose-modified presspaper based on the multivariate analysis method. Molecules 23(7):1507

35. Jose J, Thomas V, John J, Mathew RM, Salam JA, Jose G, Abraham R (2021) Effect of temperature and frequency on the dielectric properties of cellulose nanofibers from cotton. J Mater Sci Mater Electron 32(16):21213

36. Kovalov KM, Alekseev OM, Lazarenko MM, Zabashta YF, Grabovskii YE, Tkachov SY (2017) Influence of water on the structure and dielectric properties of the microcrystalline and nano-cellulose. Nanoscale Res Lett 12(1):468

37. Alekseev OM, Kovalov KM, Lazarenko MM, Lazarenko MV, Grabovskii YE, Tkachov SY (2019) Cell Chem Technol 53(1–2):15

38. Lazarenko M, Alekseev A, Zabashta Y, Tkachev S, Kovalchuk V, Andrusenko D,.Grabovsky Y, Bulavin L (2020) Estimation of water content in cellulose materials Cell Chem Technol 54(3−4):199

39. Marchessault RH, Morehead FF, Walter NM (1959) Liquid crystal systems from fibrillar polysaccharides. Nature 184:632

40. Mihranyan A, Llagostera AP, Karmhag R, Strømme M, Ek R (2004) Moisture sorption by cellulose powders of varying crystallinity. Int J Pharm 269(2):433

41. Kocherbitov V, Ulvenlund S, Kober M, Jarring K, Arnebrant T (2008) Hydration of micro-crystalline cellulose and milled cellulose studied by sorption calorimetry. J Phys Chem B 112(12):3728

42. Barbash VA, Yaschenko OV, Shniruk OM (2017) Preparation and properties of nanocellulose from organosolv straw pulp. Nanoscale Res Lett 12(1):241

43. Barbash V, Yashchenko O, Kedrovska A (2017) Preparation and properties of nanocellulose from peracetic flax pulp. J Sci Res Rep 16(1):1

44. Barbash VA, Yashchenko OV, Opolsky VO (2018) Effect of hydrolysis conditions of organosolv pulp from kenaf fibers on the physicochemical properties of the obtained nanocellulose. Theor Exp Chem 54(3):193

45. Alekseev AN, Lazarenko MM, Lazarenko MV, Kovalev KN, Tkachev SY (2017) Characterization of dielectric properties in liquid–solid phase transition. Inorg Mater 53(15):1473

46. Lazarenko MM, Hnatiuk KI, Alekseev SA, Yablochkova KS, Dinzhos RV, Ublekov F, Lazarenko MV, Andrusenko DA, Alekseev AN (2020) Low-temperature dielectric relaxation in the system silica gel–undecylenic acid. In: 2020 IEEE 10th international conference nanomaterials: applications and properties, IEEE, 01NIC02–1

47. Hölzl C, Forbert H, Marx D (2021) Dielectric relaxation of water: assessing the impact of localized modes, translational diffusion, and collective dynamics. Phys Chem Chem Phys 23(37):20875

48. Zarzycki P, Gilbert B (2020) Temperature-dependence of the dielectric relaxation of water using non-polarizable water models. Phys Chem Chem Phys 22(3):1011

49. Popov I, Ishai PB, Khamzin A, Feldman Y (2016) The mechanism of the dielectric relaxation in water. Phys Chem Chem Phys 18(20):13941

50. Nandi N, Bagchi B (1997) Dielectric relaxation of biological water. J Phys Chem B 101(50):10954

51. Yang W, Jiao L, Liu W, Dai H (2019) Manufacture of highly transparent and hazy cellulose nanofibril films via coating TEMPO-oxidized wood fibers. Nanomaterials 9(1):107

52. Nogi M, Iwamoto S, Nakagaito AN, Yano H (2009) Optically transparent nanofiber paper. Adv Mater 21(16):1595
53. Simão CD, Reparaz JS, Wagner MR, Graczykowski B, Kreuzer M, Ruiz-Blanco YB, García Y, Malho JM, Goñi AR, Ahopeltoc J, Sotomayor Torre CM (2015) Optical and mechanical properties of nanofibrillated cellulose: towards a robust platform for nextgeneration green technologies. Carbohydr Polym 126:40
54. Pikulev V, Loginova S, Gurtov V (2012) Luminescence properties of silicon-cellulose nanocomposites. Nanoscale Res Lett 7:426
55. Nedielko M, Hamamda S, Alekseev O, Chornii V, Dashevskii M, Lazarenko M, Scherbatskyi V (2017) Mechanical, dielectric, and spectroscopic characteristics of "micro/nanocellulose+oxide" composites. Nanoscale Res Lett 12(1):98
56. Grönroos P, Bessonoff M, Salminen K, Paltakari J, Kulmala S (2018) Phosphorescence and fluorescence of fibrillar cellulose films. Nord Pulp Paper Res J 33:246
57. Ding Q, Zhang P (2021) Revealing the autofluorescence properties of nanocellulose isolated from different raw materials by different methods. In IOP Conf Ser: Earth Environ Sci 639(1):012037
58. Adachi C, Tsutsui T (2006) Fundamentals of luminescence: luminescence of organic compounds. Applied Chemistry. CRC Press, pp 51–59
59. Lazarenko MM, Alekseev AN, Alekseev SA, Yablochkova KS, Bokhvan SI, Demidiuk OF, Lazarenko MV (2020) Topological solitons in aliphatic systems with a restricted translational mobility. Chem Phys 539:110959
60. Lazarenko MM, Alekseev AN, Alekseev SA, Hnatiuk KI, Demidiuk OF, Yablochkova KS, Atamas NO, Lazarenko MV (2020) Topological solitons in chain molecular crystals with stoichiometric obstacles and hydrogen bonds. J Phys Chem Solids 144:109514
61. Tkachev SY, Alekseev OM, Lazarenko MM, Lazarenko MV, Kovalov KM, Bokhvan SI, Grabovskii YE, Hoshylyk NV (2018) Topological solitons in branched aliphatic molecules. Mol Cryst Liq Cryst 665(1):166
62. Hoffman JD, Williams G, Passaglia E (1966) Analysis of the α, β, and γ relaxations in polychlorotrifluoroethylene and polyethylene: Dielectric and mechanical properties. J Polym Sci C (14)1:173
63. Fröhlich H (1958) Theory of dielectrics: dielectric constant and dielectric loss. Clarendon Press, pp 192